METHODS OF X-RAY AND NEUTRON SCATTERING IN POLYMER SCIENCE

TOPICS IN POLYMER SCIENCE

A Series of Advanced Textbooks and Monographs

Series Editor

JAMES E. MARK, University of Cincinnati

K. Binder (editor)

Monte Carlo and Molecular Dynamics Simulations in Polymer Science

B. Erman and J.E. Mark

Structures and Properties of Rubberlike Networks

R.J. Roe

Methods of X-Ray and Neutron Scattering in Polymer Science

Oxford University Press

Oxford New York
Athens Auckland Bangkok Bogotá Buenos Aires Calcutta
Cape Town Chennai Dar es Salaam Delhi Florence Hong Kong Istanbul
Karachi Kuala Lumpur Madrid Melbourne Mexico City Mumbai
Nairobi Paris São Paulo Singapore Taipei Tokyo Toronto Warsaw

and associated companies in
Berlin Ibadan

Published by Oxford University Press, Inc.
198 Madison Avenue, New York, New York 10016
http://www.oup-usa.org

Library of Congress Cataloging-in-Publication Data

Roe, R. J. (Ryong-Joon)
Methods of X-ray and neutron scattering in polymer science / Ryong
-Joon Roe.
p. cm.—(Topics in polymer science)
Includes bibliographical references and index.
ISBN 0-19-511321-7 (cloth)
1. Polymers—Analysis. 2. X-rays—Scattering. 3. Neutrons—
Scattering. I. Title. II. Series.
QD139.P6R64 2000
547'.7046—dc21 99-37446
CIP

9 8 7 6 5 4 3 2 1

Printed in the United States of America
on acid-free paper

Contents

Preface

X-Ray scattering and diffraction are among the principal tools for studying polymers, with their utility proven since the very inception of polymer science. Neutron scattering has been applied only more recently to the study of polymers, starting from the late 1960s, but the method, particularly in combination with the deuterium labeling technique, is now well established as an indispensable tool that complements the x-ray methods. This book presents the basic theories underlying x-ray and neutron scattering, as well as the various techniques that have been developed for their application to the study of polymers.

There is a great deal of similarity between the x-ray and neutron scattering methods as applied to the study of the structure of matter. Historically, however, the two methods were developed in different time periods by different groups of scientists, and as a result very different terminologies often evolved to explain the same phenomena. In this book emphasis is given to presenting the two methods together, so that readers will become equally familiar with both from the outset. In a similar vein, to allow readers to gain a unified view of diffraction, the distinction between wide-angle diffraction and small-angle scattering has been delayed as far as possible. As part of such an effort, a consistent set of terminologies and symbols is carried through the book, encompassing diverse topics, such as x-ray and neutron scattering, wide- and small-angle scattering, and elastic and inelastic scattering. This attention to consistency sometimes made it necessary to deviate from the symbols and nomenclatures established in specialized areas of the literature.

This is an introductory textbook, and it emphasizes basic concepts rather than the details of specific techniques. It assumes the reader has had little prior exposure to scattering phenomena, except perhaps some elementary concepts such as the Bragg law and Miller indices of crystallographic planes. Throughout the book all relationships introduced are derived from first premises, except in those instances that would otherwise require long excursions into subject areas beyond the scope of this book. The book is certainly not meant to be a review of the literature on the topics discussed, and experimental results are quoted only to the extent that they illustrate how the theoretical concepts or the methods of analysis just explained are utilized in practice. Being introductory and at the same time covering a wide range of topics at a modest length, the book obviously leaves out many advanced topics of importance,

and for these a list of further readings is attached to the end of each chapter so that readers can explore these topics on their own.

The book starts with the basic properties of x-rays and neutrons and the principles of their scattering from matter. This is followed by a brief discussion of experimental techniques. The remainder of the book is then devoted to discussing methods of studying specific types of samples or specific properties. Chapters 3 and 4 deal with the study of single-component crystalline and amorphous polymers, respectively. The small-angle scattering technique is discussed mainly in Chapter 5, but Chapters 4 and 6 also deal with some aspects of it. Chapter 6 is concerned with binary, single-phase systems such as a polymer blend and polymer solution, and here the issues related to deuterium labeling in neutron scattering studies are discussed. Chapter 7 deals with the technique of reflectivity measurements, which gained importance in recent years. Here, too, emphasis is given to the fact that the theoretical relationships for the analysis of reflectivity data follow from the same set of basic equations used in wide- and small-angle scattering measurements. The study of polymer dynamics by means of inelastic neutron scattering involves concepts and techniques somewhat different from those discussed in Chapters 2 to 7 and is therefore treated separately, in the last chapter.

This book grew out of the lecture notes for a course I have given at the University of Cincinnati in the past 20 years or so. In the course, the first six weeks are devoted to the materials in Chapter 1 and Appendices B (Fourier transform) and C (reciprocal lattice). The Fourier transform technique is freely utilized throughout the discussions in the book, and students are encouraged to become familiar with the technique as early as possible. Once acquainted thoroughly with the fundamentals of diffraction phenomena and the Fourier transform technique, it is hoped that the students are equipped to pursue the rest of the topics with little difficulty. To facilitate such a plan of study, exercise problems are attached to Chapter 1 and Appendices B and C. After studying Chapter 1 and the Appendices and the material in Chapter 2 on experimental techniques (which is mostly descriptive), the student or reader may choose one or more chapters from the rest of the book for more detailed reading according to the type of structures he or she plans to investigate. Each of Chapters 3 to 8 stands largely on its own and can be studied independently of others.

It is a great pleasure to acknowledge Drs. Greg Beaucage, Al Hurd, Hyun-Hoon Song, and Wang-Cheol Zin for reading parts of the manuscript and offering valuable comments and my son TaiYun for checking grammatical errors throughout the manuscript.

Cincinnati, Ohio *R. J. Roe*

METHODS OF X-RAY AND NEUTRON SCATTERING IN POLYMER SCIENCE

Basics of X-Ray and Neutron Scattering

1

1.1 PROPERTIES OF X-RAYS AND NEUTRONS

X-Rays are electromagnetic radiation occupying the spectrum from about 10^{-2} to 10^{2} Å in wavelength, but those used for the study of the structure of materials have wavelengths more narrowly confined to the approximate range of 0.5–2.5 Å. Studies on polymers are performed mostly with the $K\alpha$ characteristic radiation from a copper target tube having a (weighted average) wavelength of 1.5418 Å, but occasional work is also done with the $K\alpha$ line of wavelength 0.7107 Å from a molybdenum target tube. X-Rays of a similar wavelength can also be selected, by means of a monochromator, from a broad spectrum emitted by a synchrotron radiation source. As with light, x-rays propagate with the speed of light $c = 2.998 \times 10^{8}$ m/s, and the wavelength λ and the frequency ν are related to each other by

$$\lambda = \frac{c}{\nu} \tag{1.1}$$

The x-ray wavelength of around 1 Å is of the same order of magnitude as most interatomic distances of interest in condensed matter, and this is why x-rays play such an important role in probing the structure, that is, the arrangement of atoms in matter.

X-Rays, like light, exhibit a wave–particle duality. Certain properties of x-rays are better understood when a beam of x-rays is regarded as a stream of photons. Whereas a wave is characterized by wavelength λ and frequency ν, a photon is characterized by its energy E and momentum p, which are related to λ and ν by

$$E = h\nu \tag{1.2}$$

and

$$p = \frac{h}{\lambda} \tag{1.3}$$

where h is Planck's constant ($= 6.626 \times 10^{-34}$ J s). Equation (1.3) is called the *de Broglie relation*. A photon does not possess a mass or an electric charge. Note that the shorter the wavelength, the higher the energy of the photon. For Cu$K\alpha$ and Mo$K\alpha$ characteristic radiations, the energy of a photon is 8.04 and 17.44 keV, respectively.

A neutron is an uncharged elementary particle, possessing a mass m equal to 1.675×10^{-24} g and spin 1/2. Its kinetic energy E and momentum p are

$$E = \tfrac{1}{2}m\upsilon^2 \tag{1.4}$$

and

$$p = m\upsilon \tag{1.5}$$

where υ is its velocity. The source of neutrons in most scattering experiments is traditionally a nuclear reactor, although spallation sources have gained importance in recent years. Whether produced by a nuclear fission reaction in a reactor or by bombardment of high-energy protons onto a heavy metal in a spallation source, the neutrons that emerge are of very high velocities, and for neutron scattering studies they must be moderated, that is, allowed to slow down through repeated collisions with atoms in the moderating material. After a sufficient number of collisions, they achieve an approximate equilibrium as a "gas" at the temperature of the moderator. The velocity spectrum of the neutrons in the moderator thus approaches the Maxwell–Boltzmann distribution in a gas in equilibrium, given by

$$f(\upsilon) = 4\pi \left(\frac{m}{2\pi\, kT}\right)^{3/2} \upsilon^2 \exp\left(-\tfrac{1}{2}m\upsilon^2/kT\right) \tag{1.6}$$

where $f(\upsilon)\, d\upsilon$ is the fraction of gas molecules with velocities between υ and $\upsilon + d\upsilon$ and k is Boltzmann's constant (1.381×10^{-23} J/K). The maximum of the function $f(\upsilon)$ occurs at

$$\upsilon = \left(\frac{2kT}{m}\right)^{1/2} \tag{1.7}$$

The so-called cold source neutrons emerge from a small volume ($\sim$ 20 liters) of liquid deuterium maintained at around 25 K. Thermal neutrons are those moderated usually with heavy water D_2O at around 330 K. A block of hot graphite at $T \sim 2000$ K functions as a source of hot neutrons. The Maxwell–Boltzmann distributions for $T = 25$, 330, and 2000 K are illustrated in Figure 1.1. The flux, that is, the number of neutrons of velocity υ that emerge from the moderator per second is proportional to υ times $f(\upsilon)$, and therefore in terms of the neutron flux that is available for scattering measurement the distribution is a little skewed in favor of higher υ in comparison to that shown in Figure 1.1.

Neutrons also exhibit wave-like behavior, with the wavelength λ given by the de Broglie relation

$$\lambda = \frac{h}{p} = \frac{h}{m\upsilon} \tag{1.8}$$

In Table 1.1 the most probable velocity υ in the Maxwell–Boltzmann distribution, given by Equation (1.7), the corresponding kinetic energy $E = m\upsilon^2/2 = kT$, and wavelength λ are listed for the three typical moderator temperatures 25, 330, and 2000 K. It is significant that the wavelengths of these neutrons are again of the

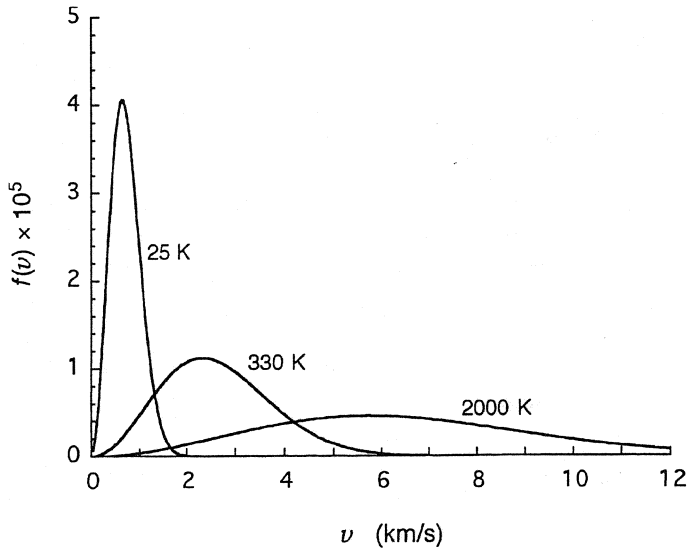

Figure 1.1 Maxwell–Boltzmann distribution $f(v)$, Equation (1.6), for $T = 25$, 330, and 2000 K.

order of 1 Å, as with x-rays, and as a result neutron scattering can also be a very useful tool for investigating the structure of materials. In many ways the properties of neutrons and their scattering behavior are similar to those exhibited by x-rays, so that most of the theoretical tools and experimental techniques developed with x-rays can be applied to neutron scattering and vice versa. There are, however, some important differences between x-rays and neutrons, as will be seen shortly, and these differences often make the two methods complementary to each other, making the range of information obtainable by the two methods combined even larger.

One of the differences of fundamental importance between x-ray photons and neutrons is in the energies of the particles. Whereas the energy of an x-ray photon is, as mentioned before, of the order of 10 keV, the kinetic energy of a thermal neutron is of the order of 10 meV. The average energy associated with the motion of atoms, arising from vibrational, rotational, and translational motions of molecules, is of the order of kT . At ambient temperatures kT is about 20 meV.

TABLE 1.1
Comparison of Typical Values of v, E, and λ of Neutrons from Cold, Thermal, and Hot Sources

	Cold	Thermal	Hot
T (K)	25	330	2000
v (m/s)	642	2333	5743
E (meV)	2.16	28.4	172
λ (Å)	6.16	1.696	0.689

Thus, when x-rays are scattered by matter, even when there is an exchange of energies between the motion of atoms and the x-ray photon, the energy of the photon is scarcely affected. On the other hand, when neutrons are scattered inelastically, their energies can be modified to an appreciable extent that can be measured experimentally.

This difference can be understood also from a slightly different viewpoint as follows. The time ($\tau = 1/\nu$) associated with one wave period is of the order of 10^{-19} s for x-rays and 10^{-13} s for thermal neutrons. Since a typical time period for atomic motions is 10^{-13} s, an x-ray, unlike a neutron, does not see a change in the atomic position. Measuring the inelastic scattering of neutrons is a very useful method for investigating the motions of atoms in materials, and this is one area in which neutron scattering clearly distinguishes itself from x-ray scattering. In most of this book we discuss only the study of structures by means of elastic scattering of neutrons as well as x-rays. The topic of dynamics is deferred until inelastic neutron scattering is specifically taken up in Chapter 8.

We note here, in passing, another important property of neutrons. Since the neutron has a magnetic moment, it can interact with magnetic moments of unpaired electrons in certain atoms. Such magnetic scattering can furnish important information about the magnetic structure of materials such as ferro- and antiferromagnets. In this book we will not, however, be concerned with magnetic scattering of neutrons.

1.2 SCATTERING AND INTERFERENCE

1.2.1 Flux, Scattering Cross Section, and Intensity

The term *flux* is used to describe the *strength* of a beam of radiation. If the beam is a *plane* wave, consisting of parallel rays, the flux J is measured as the amount of energy that is transmitted per unit area per second. When the radiation is regarded as a stream of particles, the flux J is more conveniently represented by the particle flux, that is, the number of photons or neutrons passing through a unit area per second. When the radiation is regarded as a wave, the flux J is proportional to the square of the *amplitude* A of the oscillating wave field. With the amplitude expressed as a complex number, J is thus given by

$$J = |A|^2 = AA^* \tag{1.9}$$

where A^* is the complex conjugate of A.

In the case of a *spherical* wave, that is, radiation emitted or scattered by a point source, it is more convenient to express the flux J by the amount of energy transmitted per second through a *unit solid angle* rather than a *unit area*. In this way the measure of the flux becomes independent of the distance R from the source to the point of observation. In terms of the particle stream, the flux is then given as the number of photons or neutrons transmitted per solid angle per second. It is also understood that the amplitude A of the spherical wave is so defined that its square still gives the flux J independent of R.

Suppose an incident plane wave of flux J_0 irradiates a sample, from which the scattered spherical wave emanates in all directions (see Figure 1.2). Our task is then to measure the flux J of the scattered ray as a function of the scattering direction and to interpret this information to learn about the structure of the sample. Since under a given experimental condition J will increase or decrease in proportion with J_0, we are really interested in the ratio J/J_0 as a function of the scattering direction. Because J_0 refers to a plane wave and J to a spherical wave, the ratio J/J_0 has dimension of area per solid angle. In the neutron-scattering community the ratio J/J_0 is invariably referred to as the *differential scattering cross section*

$$\frac{d\sigma}{d\Omega} \equiv \frac{J}{J_0} \tag{1.10}$$

In terms of the particle language, the differential scattering cross section $d\sigma/d\Omega$ is the probability that a photon or a neutron impinging on the sample is scattered into a unit solid angle in the given direction, or

$$\frac{d\sigma}{d\Omega} = \frac{\text{number of particles scattered into a unit solid angle in a given direction per second}}{\text{flux of the incident beam}} \tag{1.11}$$

Integrating the differential scattering cross section throughout the solid angle Ω gives the *total scattering cross section*

$$\begin{aligned} \sigma_{\text{tot}} &= \int_{\text{all directions}} \left(\frac{d\sigma}{d\Omega}\right) d\Omega \\ &= \int_0^{2\pi} \int_0^{\pi} \left(\frac{d\sigma}{d\Omega}\right) \sin\Theta \, d\Theta \, d\Phi \end{aligned} \tag{1.12}$$

The total scattering cross section is therefore

$$\sigma_{\text{tot}} = \frac{\text{total number of particles scattered in all directions per second}}{\text{flux of the incident beam}} \tag{1.13}$$

and has dimension of area, as the word *cross section* implies.

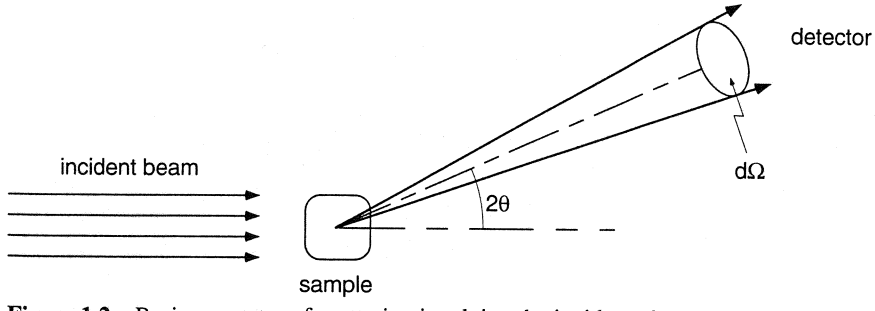

Figure 1.2 Basic geometry of scattering involving the incident plane wave, the sample, the scattered spherical wave, and the detector.

The various theoretical results, described in the rest of this book, show how the differential scattering cross section $d\sigma/d\Omega$ is related to the structure of matter. Experimentally one measures the flux J of the scattered beam as a function of the scattering angle. The result may be converted to the differential scattering cross section J/J_0 if the incident beam flux J_0 is known, or else the flux J may simply be recorded in some arbitrary units, such as counts per second. Traditionally the term *intensity* has been used, especially in the x-ray scattering community, to denote both the flux J and the differential scattering cross section J/J_0. The word *intensity* is, however, reserved in this book exclusively to designate the differential scattering cross section and is represented by the symbol I to differentiate it from flux J.

1.2.2 Interference Calculation

The diffraction of x-rays and neutrons by matter results from the combination of two different phenomena: (1) scattering of x-rays by individual electrons in the sample or scattering of neutrons by individual atomic nuclei in it, and (2) interference among the waves scattered by these primary events. It is essentially because of this interference effect that the fluxes of the waves emanating in different directions vary with direction. Experimentally, we measure the flux as a function of the scattering direction and analyze and interpret the data to obtain information about the relative placement of electrons or atomic nuclei in the sample. Strictly speaking the term *scattering* refers only to phenomenon (1) above, whereas the term *diffraction* refers to the combination of (1) and (2), but this distinction is often blurred. In current practice the term *diffraction* tends to be used only when the sample is crystalline or otherwise sufficiently regular to make the scattered beam concentrated around a number of sharply defined scattering directions. When the scattering pattern is diffuse, and especially when the pattern of interest is mainly in the small-angle region, the term *scattering* is almost exclusively used even when the phenomena involve the combination of (1) and (2). Following this practice, in this book, the word *scattering* is used rather loosely in this broader sense and often interchangeably with the word *diffraction*.

Scattering as the primary event must be discussed separately for x-rays and for neutrons because of the difference in the nature of the two types of radiation and their mechanism of interaction with matter. Despite these differences the interference effects exhibited by them are exactly the same and can be discussed as a single common phenomenon. Most theoretical results developed for the interpretation of diffraction of x-rays or neutrons are equally applicable to both types of radiation. Historically, however, the methods for using x-rays and neutrons have been developed by diverse groups of scientists, and very different terminologies have evolved to describe the same phenomenon or physical quantity. In this text we pay particular attention to developing common terminologies and symbols applicable to both x-ray and neutron scattering. In line with this approach, we confine our attention, as stated earlier, initially to the methods for studying structures by elastic scattering only.

The *amplitude* A of a wave of frequency ν and wavelength λ traveling in the x direction can be expressed as

$$A(x,t) = \mathcal{A}\cos[2\pi(\nu t - x/\lambda)] \tag{1.14}$$

where $\mathcal{A}$ is the *modulus* or the absolute value of $A(x,t)$. The term $2\pi x/\lambda$ gives the change in the phase ϕ of the wave that results on travel by distance x. It is usually more convenient to use a complex notation for $A(x,t)$ (see Appendix A for a review on complex numbers) and write it as

$$A(x,t) = \mathcal{A}e^{i2\pi(\nu t - x/\lambda)} \tag{1.15}$$

If we take the real part of the complex $A(x,t)$ we recover the original expression (1.14).

In Figure 1.3 a plane incident wave traveling in the direction specified by the unit vector $\boldsymbol{S}_0$ is scattered by the particles located at two points, O and P. A detector is placed in the direction specified by the unit vector $\boldsymbol{S}$ at a distance far from these scattering centers. If the scattering is coherent and there is no phase change on scattering, the phase difference $\Delta\phi$ between the two waves scattered at O and P and arriving at the detector depends only on the path length difference δ between the two rays:

$$\Delta\phi = \frac{2\pi\delta}{\lambda} \tag{1.16}$$

Designating the position of the second scatterer relative to the first as $\boldsymbol{r}$, we have QP $= \boldsymbol{S}_0 \cdot \boldsymbol{r}$ and OR $= \boldsymbol{S} \cdot \boldsymbol{r}$, and therefore the phase difference is

$$\begin{aligned}\Delta\phi &= \frac{2\pi}{\lambda}(\boldsymbol{S}_0 \cdot \boldsymbol{r} - \boldsymbol{S} \cdot \boldsymbol{r}) \\ &= -2\pi \boldsymbol{s} \cdot \boldsymbol{r}\end{aligned} \tag{1.17}$$

where $\boldsymbol{s}$ is defined as

$$\boldsymbol{s} = \frac{\boldsymbol{S} - \boldsymbol{S}_0}{\lambda} \tag{1.18}$$

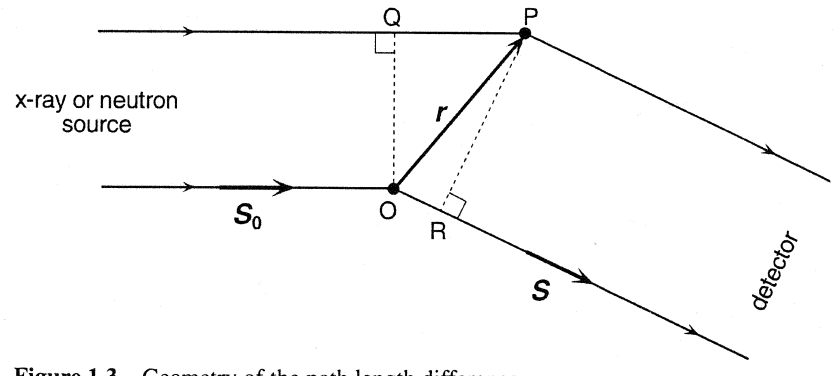

Figure 1.3 Geometry of the path length difference.

The vector s is referred to as the *scattering vector*, and it completely characterizes the scattering geometry: the incident and scattered beam directions and the wavelength. Its magnitude is related to the scattering angle 2θ (see Figure 1.4) by

$$|s| = s = \frac{2\sin\theta}{\lambda} \tag{1.19}$$

Let us now represent the spherical wave $A_1(x,t)$ scattered at O by particle 1 as

$$A_1(x,t) = A_0\, b e^{i2\pi(\nu t - x/\lambda)} \tag{1.20}$$

where A_0 is the amplitude of the incident radiation and b is the *scattering length* that expresses the efficiency of scattering by the particle. The magnitude of b depends on the nature of the radiation and the scattering particle. It has dimension of length in view of the fact that $A_1(x,t)$ represents the amplitude of a spherical wave whereas A_0 is that of a plane wave. Then the wave scattered at P by particle 2 can be written as

$$\begin{aligned} A_2(x,t) &= A_1(x,t)e^{i\Delta\phi} \\ &= A_0 b e^{i2\pi(\nu t - x/\lambda)}\, e^{-i2\pi s\cdot r} \end{aligned} \tag{1.21}$$

The combined wave $A(x,t)$ that reaches the detector is the sum of $A_1(x,t)$ and $A_2(x,t)$:

$$\begin{aligned} A(x,t) &= A_1(x,t) + A_2(x,t) \\ &= A_0 b e^{i2\pi(\nu t - x/\lambda)}\left(1 + e^{-i2\pi s\cdot r}\right) \end{aligned} \tag{1.22}$$

When the flux is evaluated, as in (1.9), by squaring the amplitude, we have

$$\begin{aligned} J(s) &= A(x,t)A^*(x,t) \\ &= A_0^2 b^2\left(1 + e^{-i2\pi s\cdot r}\right)\left(1 + e^{i2\pi s\cdot r}\right) \end{aligned} \tag{1.23}$$

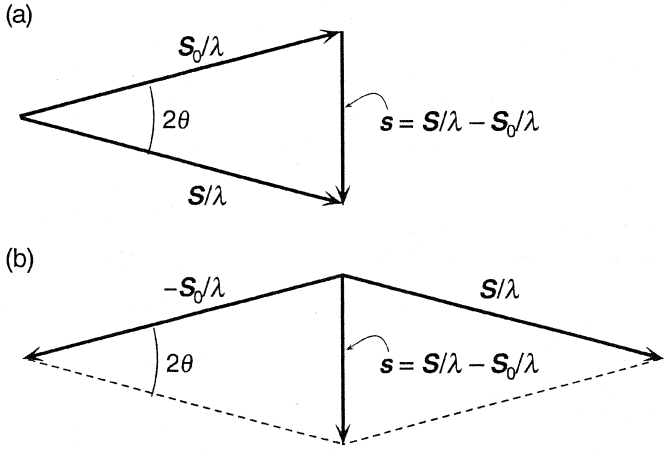

Figure 1.4 (a, b) Definition of the scattering vector s.

where the factors $e^{i2\pi(\nu t - x/\lambda)}$ and $e^{-i2\pi(\nu t - x/\lambda)}$ that depend on t and x have canceled each other out. It therefore suffices to write the scattered wave in (1.22) as

$$A(\boldsymbol{s}) = A_0\, b\left(1 + e^{-i2\pi \boldsymbol{s}\cdot\boldsymbol{r}}\right) \tag{1.24}$$

The flux $J(\boldsymbol{s})$ and amplitude $A(\boldsymbol{s})$ are written in (1.23) and (1.24) explicitly as a function of $\boldsymbol{s}$ to emphasize their dependence on the scattering geometry as embodied in $\boldsymbol{s}$. [Equations (1.20) and (1.21) ignore any phase change that may take place on scattering. As long as the extent of phase change at each scattering event is the same, the effect is canceled out when the flux is evaluated as in (1.23).]

When there are N, rather than two, identical scatterers, Equation (1.24) can easily be generalized to

$$A(\boldsymbol{s}) = A_0\, b \sum_{j=1}^{N} e^{-i2\pi \boldsymbol{s}\cdot\boldsymbol{r}_j} \tag{1.25}$$

where $\boldsymbol{r}_j$ denotes the position of the jth scatterer relative to an arbitrary origin. When Equation (1.24) for the two scatterers was derived, the origin was placed to coincide with one of the scatterers, but that was not necessary. What really matters is only the relative difference in the path length between the rays scattered at different centers, and any effect of the change in the origin would have simply canceled out when the flux was evaluated by taking the absolute square of the amplitude.

We may replace the summation in (1.25) with an integral, when the scatterers are numerous and are more or less continuously dispersed in space in the sample. Thus, taking $n(\boldsymbol{r})\, d\boldsymbol{r}$ to represent the number of scatterers within a volume element $d\boldsymbol{r} = dx\, dy\, dz$ around $\boldsymbol{r}$, (1.25) can be written as

$$A(\boldsymbol{s}) = A_0\, b \int_V n(\boldsymbol{r}) e^{-i2\pi \boldsymbol{s}\boldsymbol{r}}\, d\boldsymbol{r} \tag{1.26}$$

where V in the integration sign denotes that the integration is to be performed over the *scattering volume*, that is, the entire sample volume when the incident beam cross section is larger than the sample dimension, or over the illuminated volume when the sample volume is larger. Equation (1.26) shows that the wave amplitude $A(\boldsymbol{s})$ is proportional to the three-dimensional Fourier transform of the *local number density* $n(\boldsymbol{r})$ of scattering centers in the sample. The Fourier transform plays a central role in the interpretation of diffraction phenomena. Some of the properties of the Fourier transform are described in Appendix B. Many of the discussions in the rest of the book make use of these properties of the Fourier transform, and the reader is expected to be thoroughly familiar with them.

In some articles the quantity $\boldsymbol{q}$, related to $\boldsymbol{s}$ by

$$\boldsymbol{q} = 2\pi \boldsymbol{s} \tag{1.27}$$

is defined as the scattering vector instead of $\boldsymbol{s}$. The vector $\boldsymbol{q}$ can also be defined as

$$\boldsymbol{q} = \boldsymbol{k} - \boldsymbol{k}_0 \tag{1.28}$$

where $\boldsymbol{k}_0 = 2\pi \boldsymbol{S}_0/\lambda$ and $\boldsymbol{k} = 2\pi \boldsymbol{S}/\lambda$ are the *wave vectors* characterizing the incident and scattered radiation. All the equations developed above can be restated in terms of $\boldsymbol{q}$ by simply replacing $2\pi \boldsymbol{s}$, wherever it occurs, with $\boldsymbol{q}$. Since, as stated before, scientists working in many different fields of study came to use and develop various diffraction methods, it is not surprising that two different notations are used to represent the same physical quantity. The majority of literature on x-ray diffraction is in terms of $\boldsymbol{s}$, whereas work on neutron scattering is almost exclusively given in terms of $\boldsymbol{q}$. We will mix the use of $\boldsymbol{s}$ and $\boldsymbol{q}$ in this book. The reader should become equally familiar and comfortable with both of them. A different symbol such as $\boldsymbol{h}$, $\boldsymbol{K}$, $\boldsymbol{Q}$, or κ is also used in place of $\boldsymbol{q}$ by some authors. The scattering vector $\boldsymbol{q}$ is also referred to as the *momentum transfer vector* by some. This is because, when Equation (1.18) is written as

$$\hbar \boldsymbol{q} = h\boldsymbol{s} = \frac{h}{\lambda}\boldsymbol{S} - \frac{h}{\lambda}\boldsymbol{S}_0 \tag{1.29}$$

where $\hbar \equiv h/2\pi$, it is seen that the third member of (1.29) represents the change in the momentum that was suffered by the incident photon or neutron, from $(h/\lambda)\boldsymbol{S}_0$ before the scattering to $(h/\lambda)\boldsymbol{S}$ after the scattering. Thus the momentum transferred from the radiation to the scattering particle is equal to $\boldsymbol{q}$ when measured in units of $\hbar$ and equal to $\boldsymbol{s}$ when measured in units of h.

1.3 SCATTERING OF X-RAYS

1.3.1 Classical Scattering from an Electron

X-Rays, being electromagnetic radiation, interact with electric charges in matter. We first consider the scattering of x-rays by a single electron. Suppose a free electron is placed at position O and is irradiated with a beam of x-rays of flux J_0 propagating in the direction of the X axis, as in Figure 1.5. The detector is placed at point P which is in the XY plane at a large distance R from O. The scattering angle between OX and OP is 2θ. Since the electromagnetic wave is a transverse wave, its electric field vector E_0 is in the plane YZ perpendicular to the propagation direction X.

Let us first consider the case in which the beam is polarized in the Z direction, with the magnitude of its electric field vector being equal to E_{0z}. The electromagnetic field of the beam sets the free electron oscillating in the Z direction. The alternating acceleration of the oscillating electron in turn induces emission of an electromagnetic radiation of the same frequency propagating in all directions. The magnitude of the electric field vector due to the oscillating electron that reaches point P is given, according to classical electromagnetic theory, by

$$E_z = E_{0z}\frac{e^2}{mc^2}\frac{1}{R} \tag{1.30}$$

where e and m are the electronic charge and mass, respectively. Next consider a beam polarized to have its electric field vector confined to the Y direction. The resulting

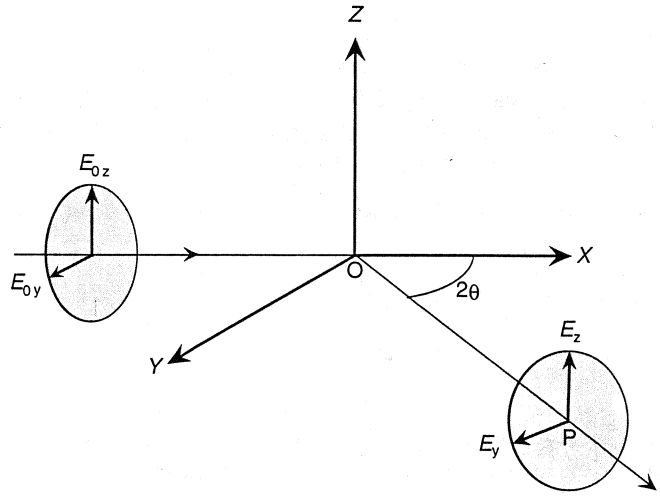

Figure 1.5 Scattering of an unpolarized x-ray by a single free electron at the origin.

oscillation of the electron is no longer perpendicular to the direction OP of the scattered beam, and hence the magnitude of the electric field vector reaching P is now

$$E_y = E_{0y}\frac{e^2}{mc^2}\frac{\cos 2\theta}{R} \tag{1.31}$$

For a beam polarized in an arbitrary direction its electric field vector E_0 can be decomposed into its Y and Z components as in

$$E_0^2 = E_{0y}^2 + E_{0z}^2 \tag{1.32}$$

and E_{0y} and E_{0z} each gives rise to the scattered beam electric field according to (1.31) and (1.30), respectively. For an *unpolarized* x-ray beam the direction of its electric field vector varies randomly with time, but in view of (1.32) the time averages of E_{0y}^2 and E_{0z}^2 obey

$$E_0^2 = \langle E_{0y}^2\rangle + \langle E_{0z}^2\rangle, \qquad \langle E_{0y}^2\rangle = \langle E_{0z}^2\rangle = \frac{1}{2}E_0^2 \tag{1.33}$$

The flux of energy reaching a unit area per second at P is proportional to $E^2 = \langle E_y^2\rangle + \langle E_z^2\rangle$ and is therefore given by

$$J_0\left(\frac{e^2}{mc^2}\right)^2\frac{1}{R^2}\frac{1+\cos^2 2\theta}{2} \tag{1.34}$$

where $J_0 = E_0^2$. This unit area at P subtends a solid angle $1/R^2$ at O, and therefore the energy scattered in the direction OP per unit solid angle per second, i.e., the flux J_e of the scattered x-rays is

$$J_e = J_0\left(\frac{e^2}{mc^2}\right)^2\frac{1+\cos^2 2\theta}{2} \tag{1.35}$$

This is called the *Thomson formula* for the scattering of x-rays by a single electron.

The factor e^2/mc^2 in (1.35) has dimension of length and is called the *classical radius of the electron*, r_e. Its numerical value is 2.818×10^{-15} m. The physical fact embodied in (1.35) can be expressed in an alternative language. Thus, the differential scattering cross section of an electron for unpolarized x-rays is

$$\left(\frac{d\sigma}{d\Omega}\right)_e = r_e^2 \frac{1 + \cos^2 2\theta}{2} \tag{1.36}$$

and the scattering length of an electron for unpolarized x-rays is

$$b_e = r_e \left(\frac{1 + \cos^2 2\theta}{2}\right)^{1/2} \tag{1.37}$$

By integrating (1.36) throughout the solid angle Ω, that is, over $\Theta(\equiv 2\theta)$ from 0 to π and over Φ from 0 to 2π [cf. Equation (1.12)], we find the total scattering cross section of an electron to be

$$\sigma_e = \frac{8}{3}\pi r_e^2 \tag{1.38}$$

the numerical value of which is 6.65×10^{-29} m^2 = 0.665 barn (1 barn = 10^{-28} m^2). [The cross section σ_e given by (1.38) is independent of the state of polarization of the incident x-rays.]

According to (1.35) the scattered beam exhibits the highest flux in the forward ($2\theta = 0$) and backward ($2\theta = 180°$) directions and the lowest in the transverse ($2\theta = 90°$) directions. From the derivation leading to (1.35) it should be clear that the scattered beam is unpolarized in the forward and backward directions, whereas it is totally polarized in the transverse direction. The factor $(1+\cos^2 2\theta)/2$ in (1.35) is commonly referred to as the *polarization factor*. It should be kept in mind that this particular form of the polarization factor is valid only when the incident beam is unpolarized. When the incident x-ray beam is partially polarized, a modified form of the polarization factor, different from the one in (1.35), must be used. An x-ray beam emanating from a tube is generally unpolarized, but the beam that has been monochromatized by reflection from a monochromator single crystal is partially polarized. The beam from a synchrotron radiation source is highly polarized.

The derivation leading to Equation (1.35) is valid for scattering from any unconstrained charged particle, whether an electron or an atomic nucleus. The scattered beam flux is seen to be proportional to $1/m^2$, however, and because atomic nuclei are of much higher mass compared to an electron, scattering of x-rays from them is extremely small and can safely be neglected. Thus the scattering of x-rays from matter results entirely from the presence of electrons around atomic centers.

1.3.2 Electron Unit

The amplitude of x-rays scattered from a sample containing N electrons at positions $\mathbf{r}_j$ ($j = 1 \ldots N$), when the interference effect is fully taken into account according to (1.25), is given by

$$A(s) = A_0\, b_e \sum_{j=1}^{N} e^{-i2\pi s r_j} \tag{1.39}$$

The intensity of scattering, in the sense defined in Section 1.2.1, is then

$$I(s) = \frac{J(s)}{J_0} = \frac{|A(s)|^2}{|A_0|^2} = b_e^2 \left| \sum_{j=1}^{N} e^{-i2\pi s r_j} \right|^2 \tag{1.40}$$

The intensity of scattered x-rays is often expressed in *electron units*. The intensity in electron units is defined as

$$I_{eu}(s) = I(s)/b_e^2 \tag{1.41}$$

By rewriting (1.41) as

$$I_{eu}(s) = \frac{J(s)}{J_0 b_e^2} \tag{1.42}$$

it is seen that, experimentally, $I_{eu}(s)$ is obtained if the observed flux $J(s)$ is compared to $J_0 b_e^2$, where the latter is the scattering that would have been realized if a single electron were placed at the sample position under the same experimental condition. The advantage of expressing the intensity in electron units, from a theoretical point of view, is that it depends only on the structure of the sample (that is, the positions $\boldsymbol{r}_j$) and not on any other factors related to experiments. The intensity in electron units is dimensionless in the strict sense but is commonly expressed in (number of electrons)^2.

1.3.3 Atomic Scattering Factor

The amplitude of x-ray scattering from an atom, measured in units of $A_0 b_e$, is called the *atomic scattering factor*:

$$f(s) = \int n(\boldsymbol{r}) e^{-i2\pi s r} d\boldsymbol{r} \tag{1.43}$$

where $n(\boldsymbol{r})$ is the time-averaged electron density distribution belonging to the atom, $\boldsymbol{r}$ being measured from the center of the atom as the origin. If $n(r)$ is spherically symmetrical, as it is in a free atom, $f(s)$ is a function of the magnitude of s only. Performing the transformation given by (B.50), we can then write $f(s)$ as

$$f(s) = \int_0^\infty 4\pi r^2 n(r) \frac{\sin 2\pi s r}{2\pi s r} dr \tag{1.44}$$

In Figure 1.6, the atomic scattering factors $f(s)$ for hydrogen, carbon, and oxygen are plotted against $s = 2(\sin\theta)/\lambda$. In the forward direction ($s = 0$) the x-ray waves scattered from different parts of the electron cloud in an atom are all in phase, and the wave amplitudes simply add up, rendering $f(0)$ equal to the atomic number Z. As s increases, the waves from different parts of the atom develop more phase differences, and the overall amplitude begins to decrease. The exact shape of the curve $f(s)$ reflects the shape of the electron density distribution in the atom. The

atomic scattering factors for all the atoms and some important ions, calculated from various approximations to the electron density distribution derived theoretically, are available in the *International Tables for Crystallography*, Vol. C[15] in tabulated form and also as coefficients in analytical approximations.

In Equation (1.39) giving the amplitude of scattering from a sample containing N electrons, we now group the electrons according to the atoms to which they belong. The position vector $\boldsymbol{r}_j$ of an electron can be written (see Figure 1.7) as

$$\boldsymbol{r}_j = \boldsymbol{r}_k + \boldsymbol{r}_{k,m} \tag{1.45}$$

where $\boldsymbol{r}_k$ denotes the position of the center of the kth atom ($k = 1 \ldots N_{\text{atom}}$), and $\boldsymbol{r}_{k,m}$ is the position of the electron ($m = 1 \ldots Z$) within the kth atom measured from its center. Thus Equation (1.39) can be written as

$$A(\boldsymbol{s}) = A_0 b_e \sum_{k=1}^{N_{\text{atom}}} \left(\sum_{m=1}^{Z} e^{-i2\pi \boldsymbol{s}\boldsymbol{r}_{k,m}} \right) e^{-i2\pi \boldsymbol{s}\boldsymbol{r}_k} \tag{1.46}$$

The quantity within the parentheses in (1.46), when averaged over time, is in effect identical to the integral in (1.43), and therefore (1.46) can be written as

$$A(\boldsymbol{s}) = A_0 b_e \sum_{k=1}^{N_{\text{atom}}} f_k(s) e^{-i2\pi \boldsymbol{s}\boldsymbol{r}_k} \tag{1.47}$$

where $f_k(s)$ is the atomic scattering factor of the kth atom. If the atoms are all of the same kind, $f(s)$ can be factored out in front of the summation sign, and (1.47) becomes

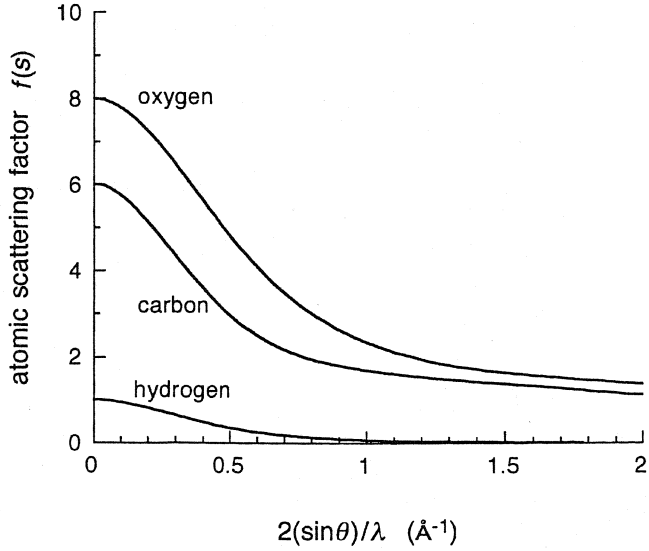

Figure 1.6 Atomic scattering factors $f(s)$ for hydrogen, carbon, and oxygen atoms plotted against $s = 2(\sin\theta)/\lambda$.

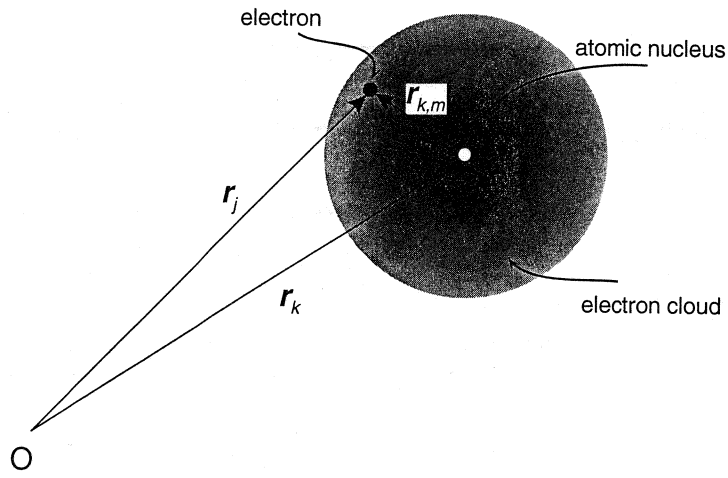

Figure 1.7 Vectors r_j and r_k denote the positions of an electron and the atomic center measured from the origin O, and $r_{k,m}$ denotes the position of the electron measured from the atomic center.

$$A(s) = A_0 b_e f(s) \sum_{k=1}^{N_{\text{atom}}} e^{-i2\pi s r_k} \tag{1.48}$$

Equation (1.48) is what one would have deduced directly from (1.25) when the scattering length b of the individual scatterer there is replaced by $b_e f(s)$. If the structure is represented not by the position of each atom but by the density distribution $n_{\text{at}}(r)$ of atomic centers, then in the case of a sample with a single species of atom, we can write (1.48) as

$$A(s) = A_0 b_e f(s) \int n_{\text{at}}(r) e^{-i2\pi s r}\, dr \tag{1.49}$$

If there are more than one type of atom, then $A(s)$ is a sum of terms each of the form (1.49) pertaining to a single atomic species.

1.3.4 Compton-Modified Scattering

The scattering of x-rays discussed above is elastic, in the sense that there is no transfer of energy from the photon to the electron, and therefore the scattered x-ray retains the same wavelength. The scattering is also coherent, because the phase relationships between the incident and scattered rays are maintained so that interference phenomena can occur among the scattered rays. There is, however, another mechanism by which the electrons scatter x-rays, and this is called the *Compton-modified scattering*. This is best explained in terms of the particle nature of the x-rays.

Suppose a photon of energy $h\nu$ strikes an electron at rest. At the collision some of the energy of the photon is imparted to the electron, which now moves away at

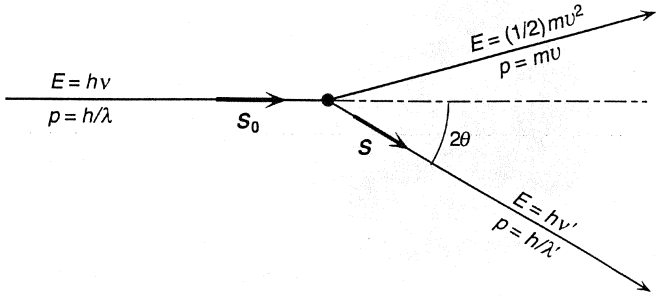

Figure 1.8 Geometry of the Compton-modified scattering. The electron, initially at rest, moves away at velocity $\boldsymbol{v}$ after having been struck by an x-ray photon of energy $h\nu$ and momentum h/λ.

velocity $\boldsymbol{v}$, while the energy of the photon has been reduced to $h\nu'(\nu' < \nu)$ (see Figure 1.8). The conservation of energy and momentum requires that

$$h\nu = h\nu' + \frac{1}{2}m\upsilon^2 \tag{1.50}$$

and

$$\frac{h}{\lambda}\boldsymbol{S}_0 = \frac{h}{\lambda'}\boldsymbol{S} + m\boldsymbol{\upsilon} \tag{1.51}$$

Solving these two equations in the approximation that $(\lambda' - \lambda)/\lambda << 1$ we obtain

$$\Delta\lambda = \lambda' - \lambda = \frac{h}{mc}(1 - \cos 2\theta) = \frac{h}{mc}2\sin^2\theta \tag{1.52}$$

where h/mc is equal to 0.02426 Å. The maximum wavelength shift, occurring at $2\theta = 180°$, is equal to 0.048 Å, which is still a small fraction of the Cu$K\alpha$ wavelength 1.54 Å.

In this process of inelastic scattering, the phase relationship between the incident and the scattered wave is not maintained. The Compton-modified scattering is therefore incoherent, and no interference effect occurs among the rays scattered from different electrons and atoms. As a result no information about the structure of the sample is contained in it. Equation (1.52) for the wavelength shift has been derived for an electron initially at rest. Atomic electrons are not at rest, and as a result the wavelengths of Compton-modified scattering actually observed cover a narrow band centered around the value given by (1.52). The study of the inelastic scattering spectrum of x-rays can provide information about the electronic motion in atoms, in much the same way as the inelastic scattering of neutrons is used to obtain information on the atomic motion in matter. Only the coherently scattered intensity is, however, of relevance in experiments aimed at elucidating the structure of the sample, and the intensity of the Compton-modified scattering must be subtracted from the observed intensity before the data can be interpreted.

A rigorous discussion of the scattering of x-rays from atomic electrons should be based on quantum mechanics. The intensity of the Compton-modified scattering and its dependence on the scattering angle can, however, be explained in a very approximate manner by the following argument. For more detailed discussions, the reader is referred to advanced texts.[16] According to quantum mechanical treatments, the total intensity of scattering by an electron, including both the coherent and Compton-modified scattering, is the intensity I_e given by (1.36) that is based on the Thomson formula (1.35). Each electron in an atom, with total Z electrons, contributes $I_e[f(s)/Z]^2$, on the average, to the coherent scattering. The Compton-modified intensity is equal to the difference between these two: $I_e - I_e[f(s)/Z]^2$. The Compton-modified scattering intensity for an atom containing Z electrons is therefore given approximately by

$$I_{\text{Compton}} \cong b_e^2 \left[Z - \frac{f^2(s)}{Z} \right] \left(\frac{\lambda}{\lambda'} \right)^3 \tag{1.53}$$

where the factor $(\lambda/\lambda')^3$, called the *Breit–Dirac recoil factor*, corrects for the effect that arises from the change in the wavelength on scattering. Values of I_{Compton} for atoms (except for very heavy atoms) are tabulated as a function of s in the *International Tables for Crystallography*, Vol. C.[15] Since $f(s)$ is, roughly speaking, proportional to Z, and I_{Compton} as given by (1.53) is, again very approximately, proportional to Z, the ratio $I_{\text{Compton}}/b_e^2 f^2(s)$ decreases with increasing Z. The Compton-modified scattering can therefore be neglected sometimes for materials containing heavy atoms, such as metals, but it is important with polymers having only light elements. In Figure 1.9, I_{Compton} for a carbon atom is plotted along with the square of $f(s)$ for carbon. It shows that for small θ the Compton-modified intensity is small and can be ignored, but at large θ it exceeds the coherently scattered intensity. When one is interested in diffuse scattering at large angles, as for example in the study of amorphous materials, accurate subtraction of the Compton component from the observed total intensity is important, and, especially in view of the rather small wavelength shift for the modified scattering, its elimination can become a significant experimental challenge.

1.4 SCATTERING OF NEUTRONS

1.4.1 Scattering Length of a Single Nucleus

We first consider the scattering of neutrons by a single atomic nucleus resulting from their interaction with it through nuclear forces. The efficacy of neutron scattering by a nucleus is expressed by the *scattering length* b of the nucleus. In other words, the differential scattering cross section of the nucleus is

$$\frac{d\sigma}{d\Omega} = b^2 \tag{1.54}$$

The value of the scattering length is independent of the wavelength of the incident neutrons. For a particular nucleus concerned it depends on the spin state of the

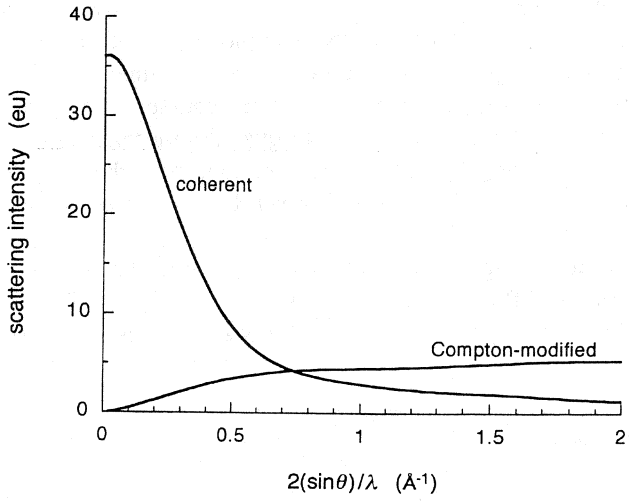

Figure 1.9 Plot of the Compton-modified scattering intensity I_{Compton} for a carbon atom and the square of the atomic scattering factor $f(s)$ of carbon.

nucleus–neutron system. The neutron has spin 1/2. If the nucleus has nonzero spin i, the spin of the nucleus–neutron system is either $i + 1/2$ or $i - 1/2$, and the associated scattering length is either b^+ or b^-, respectively. If the spin of the nucleus is zero, the nucleus–neutron system has a single spin state of spin 1/2, and there is only one value of the scattering length. Normally the value refers to the case in which the atom is tightly bound to a matrix, which is relevant to the study of polymers and other condensed matter. If the atom is free to recoil, as for example in gases, the value of the *free-atom scattering length* is slightly different from the *bound-atom scattering length.*

The strength of the nucleus–neutron interaction depends on the details of the nuclear structure, which is not related to the atomic number in any simple way. Therefore, the magnitude of the scattering length b can vary greatly between elements neighboring in terms of atomic number or mass, and even between isotopes of the same element. In contrast to this, the strength of interaction of x-rays with an atom depends primarily on the number of electrons it contains, and therefore the atomic scattering factor $f(s)$ increases linearly with atomic number.

The radius of an atomic nucleus is very small, and the range of nuclear forces that cause scattering is even smaller, being of the order of 10^{-14} to 10^{-15} m. The size scale of the scattering event is thus several orders of magnitude smaller than the wavelength of the neutrons being scattered. As a result the scattering of neutrons from an atomic nucleus is spherically symmetric, and the value of b does not change with scattering angle. This is in strong contrast to the case of x-rays discussed in Section 1.3. In the case of x-rays the equivalent to b is the product of the x-ray scattering length b_e of a single electron with the atomic scattering factor $f(s)$ of the atom concerned. The θ dependence of b_e arises from the polarization of x-ray waves, which has no counterpart with neutrons (the spin polarization of neutrons

is an entirely different phenomenon and refers to relative populations of the spin-up and spin-down states of neutrons in the beam). The atomic scattering factor $f(s)$ for x-rays decreases with increasing s; this is because the range of atomic electron clouds is comparable to the x-ray wavelength, and as a result rays scattered from different parts of the atom experience a phase difference that increases with increasing 2θ.

1.4.2 Coherent and Incoherent Scattering Length

Now we consider an assembly of nuclei of a single element. If it is isotopically pure, and at the same time the nuclear spin is zero, all the nuclei in the assembly have an identical value of b, and no complication arises. On the other hand, if the assembly is a mixture of isotopes, as is the case with the majority of the elements, the value of b will vary randomly from nucleus to nucleus. Even when the element consists of a single isotope, the nucleus can take one of two very different scattering lengths b^+ or b^-, if its nuclear spin is nonzero. This is because the neutron, with spin 1/2, interacts with a nucleus of spin i, and the resulting nucleus–neutron system has the total spin either $i + 1/2$ or $i - 1/2$. The number of states associated with spin $i + 1/2$ is

$$2(i + 1/2) + 1 = 2i + 2 \tag{1.55}$$

and the number of states associated with spin $i - 1/2$ is

$$2(i - 1/2) + 1 = 2i \tag{1.56}$$

giving a total of $(4i + 2)$ states. Each spin state has the same a priori probability when the neutron beam is unpolarized so that the nuclear spin is randomly oriented. Therefore the probability that the b^+ scattering length is realized is

$$f^+ = \frac{2i + 2}{4i + 2} = \frac{i + 1}{2i + 1} \tag{1.57}$$

and for the b^- scattering length the probability is

$$f^- = \frac{2i}{4i + 2} = \frac{i}{2i + 1} \tag{1.58}$$

The consequence of such a random variability in the scattering lengths, resulting either from the presence of isotopes or from nonzero nuclear spin, is that the scattered intensity contains not only a component that reflects the structure as usual, but also another component that arises simply from this randomness and has nothing to do with the structure. Let us examine the consequence of this randomness in more detail. For the sake of simplicity we assume that there is only one kind of atom, but its scattering length b varies from nucleus to nucleus due to either the nonzero spin or the presence of isotopes. As was shown in Section 1.2.2, the amplitude $A(\boldsymbol{q})$ of scattering as a function of $\boldsymbol{q}$ can be written as

$$A(\boldsymbol{q}) = A_0 \sum_{j=1}^{N} b_j e^{-i\boldsymbol{q}\boldsymbol{r}_j} \tag{1.59}$$

where, unlike in Equation (1.25), b_j is written inside the summation in view of its variability. Since $J(\boldsymbol{q}) = A(\boldsymbol{q})A^*(\boldsymbol{q})$ we have for $d\sigma/d\Omega \equiv J/J_0$

$$\frac{d\sigma}{d\Omega} = \sum_{j,k} \langle b_j b_k \rangle e^{-i\boldsymbol{q}(\boldsymbol{r}_j - \boldsymbol{r}_k)} \tag{1.60}$$

where $\langle b_j b_k \rangle$ is the expectation value of $b_j b_k$ in view of the random variability of b_j and b_k. For j equal to k, we have

$$\langle b_j b_j \rangle = \langle b_j^2 \rangle = \langle b^2 \rangle \tag{1.61}$$

while for $j \neq k$, since there is no correlation between the values of b_j and b_k,

$$\langle b_j b_k \rangle_{j \neq k} = \langle b_j \rangle \langle b_k \rangle = \langle b \rangle^2 \tag{1.62}$$

Combining (1.61) and (1.62) we can write

$$\langle b_j b_k \rangle = \langle b \rangle^2 + \delta_{j,k} \left(\langle b^2 \rangle - \langle b \rangle^2 \right) \tag{1.63}$$

where $\delta_{j,k}$ is the Kronecker delta, which is equal to 1 if $j = k$ and equal to 0 otherwise. Substitution of (1.63) into (1.60) then gives

$$\frac{d\sigma}{d\Omega} = \langle b \rangle^2 \sum_{j,k} e^{-i\boldsymbol{q}(\boldsymbol{r}_j - \boldsymbol{r}_k)} + N \left(\langle b^2 \rangle - \langle b \rangle^2 \right) \tag{1.64}$$

The first term in (1.64) is equal to the total intensity that would have been obtained if all the nuclei had the identical scattering length equal to the average $\langle b \rangle$. The second term does not depend on $\boldsymbol{r}_j$s and therefore contains no information about the structure of the sample. It is simply proportional to the variance $\langle b^2 \rangle - \langle b \rangle^2 = \langle (b - \langle b \rangle)^2 \rangle$, showing that it arises from the fluctuation in the scattering lengths. The two terms are therefore called the coherent and incoherent components of the intensity. Correspondingly, the *coherent* and *incoherent scattering lengths* of an element or an isotope are defined as

$$b_{\text{coh}} = \langle b \rangle \tag{1.65}$$

and

$$b_{\text{inc}} = \left(\langle b^2 \rangle - \langle b \rangle^2 \right)^{1/2} \tag{1.66}$$

The total scattering cross section σ_{tot} is equal to $4\pi b^2$ when b is independent of $\boldsymbol{q}$ [cf. Equation (1.12)], and therefore the *coherent* and *incoherent cross sections* are given by

$$\sigma_{\text{coh}} = 4\pi \langle b \rangle^2 \tag{1.67}$$

$$\sigma_{\text{inc}} = 4\pi \left(\langle b^2 \rangle - \langle b \rangle^2 \right) \tag{1.68}$$

Note that the incoherence of the Compton-modified x-ray scattering occurs by a mechanism that is very different from what is considered here. The Compton-modified scattering is incoherent because the phase coherence is lost in the inelastic scat-

tering, but in neutron scattering the incoherent component arises because of the random variability in the scattering lengths of individual nuclei. They are similar only with respect to the fact that no structural information is contained in the incoherent intensity.

The values of b_{coh}, σ_{coh}, and σ_{inc} for some common elements and isotopes likely to be encountered in polymer studies are listed in Table 1.2. Except for ^{1}H, ^{2}D, ^{19}F, ^{23}Na, and ^{31}P, the values are for elements with naturally occurring abundance of isotopes. A negative value of b means that the scattering from the nucleus undergoes a 180° phase shift in comparison to the scattering from those nuclei having positive b values. These values have been taken from the *International Tables for Crystallography*, Vol. C.[15] Similar tabulations are also given by Koester *et al.*[17] and by Sears.[18] Unlike the atomic scattering factors $f(s)$ for x-rays, which are calculated from theoretical electron density distributions in atoms, the neutron scattering cross sections are obtained experimentally, since we do not understand the nuclear forces in enough detail to permit their accurate calculation. To allow comparison with scattering lengths for x-rays, the last two columns in Table 1.2 list the values of the product $r_e f(s)$ where r_e is the classical radius of the electron (discussed in Section 1.3.1) and $f(s)$ is the atomic scattering factor. Since $f(s)$ depends on the scattering angle the values of $r_e f(s)$ are given for $s = 0$, relevant for small-angle scattering, and for $s = 1$ Å^{-1} ($2\theta \cong 100°$ for Cu$K\alpha$ radiation), relevant for wide-angle scattering. It is seen that except for very light nuclei, the coherent neutron scattering length b_{coh} is in general much smaller than the corresponding x-ray scattering lengths.

Hydrogen ^{1}H, with spin 1/2, has the spin-up and spin-down scattering lengths equal to $b^+ = 1.080 \times 10^{-12}$ cm and $b^- = -4.737 \times 10^{-12}$ cm. With the probabilities f^+ and f^- given by (1.57) and (1.58), the cross sections calculated according to (1.67)

TABLE 1.2
Scattering Lengths and Cross Sections for Some Common Elements and Isotopes

	Atomic Number	b_{coh} (10^{-12} cm)	σ_{coh} (10^{-24} cm^2)	σ_{inc} (10^{-24} cm^2)	$r_e f(s)$ (10^{-12} cm)	
					$s = 0$	$s = 1$ Å^{-1}
^{1}H	1	−0.374	1.76	79.9	0.28	0.02
^{2}D	1	0.667	5.59	2.04	0.28	0.02
C	6	0.665	5.55	0.001	1.69	0.48
N	7	0.936	11.01	0.49	1.97	0.53
O	8	0.580	4.23	0.000	2.25	0.62
^{19}F	9	0.565	4.02	0.001	2.53	0.75
^{23}Na	11	0.363	1.66	1.62	3.09	1.14
Si	14	0.415	2.16	0.015	3.95	1.72
^{31}P	15	0.513	3.31	0.006	4.23	1.83
S	16	0.285	1.02	0.007	4.5	1.9
Cl	17	0.958	11.53	5.2	4.8	2.0
K	19	0.371	1.73	0.25	5.3	2.2
V	23	−0.0382	0.018	5.19	6.5	2.8
Ni	28	1.03	13.3	5.2	7.9	3.6
Br	35	0.680	5.80	0.10	9.8	4.7

and (1.68) are $\sigma_{coh} = 1.76$ barns and $\sigma_{inc} = 79.7$ barns. Such a large incoherent cross section is unique to hydrogen among all nuclei. For the purpose of studying their structures, the large incoherent scattering from hydrogenous materials is an unwanted complication that must be eliminated either experimentally or otherwise before the data can be interpreted. Substituting all the hydrogens with deuteriums, for example, serves the purpose. On the other hand, for the purpose of studying the dynamics of polymeric materials by inelastic scattering, the large incoherent cross section of hydrogen is actually a blessing, as will be seen later when inelastic scattering is discussed in Chapter 8.

In many ways neutron scattering plays a role complementary to x-ray scattering in the study of the structure of materials, and this is mainly because the neutron cross section varies seemingly randomly among elements, whereas the x-ray atomic scattering factor increases smoothly with atomic number. With x-rays, scattering from heavy atoms, such as metal atoms, present in an organic molecule can often overwhelm the scattering from the rest of the molecule. This can be advantageous, for example, in solving the phase problem in crystal structure analysis, but in many instances it makes it difficult to see the structure of the other lighter atoms. The use of neutron, instead of x-ray, scattering is then called for. Since hydrogen is almost invisible to x-rays, even when the other atoms present in the material are only light atoms such as carbon or oxygen, it is almost impossible to determine the positions of hydrogens by x-ray crystal structure analysis. This difficulty can be avoided with neutron diffraction, especially by using a crystal in which all hydrogen atoms have been replaced by deuterium atoms. The large difference in the scattering cross section between hydrogen and deuterium plays a crucial role in the use of neutron scattering for the study of polymers. By substituting hydrogens with deuteriums in only some of the molecules, we can effectively make the molecules selectively "visible" to neutron beams, without altering their thermodynamic properties in any appreciable way. This technique, known as *deuterium labeling*, is discussed in more detail in Section 6.3.

1.5 AUTOCORRELATION FUNCTION AND RECIPROCAL SPACE

1.5.1 A Note on Notations

In Section 1.3 it was shown that the amplitude $A(\boldsymbol{q})$ of scattered x-rays is given, when the positions $\boldsymbol{r}_j$ of all the electrons in the sample are known, by

$$A(\boldsymbol{q}) = A_0 \, b_e \sum_j e^{-i\boldsymbol{q}\boldsymbol{r}_j} \tag{1.39}$$

where A_0 is the amplitude of the incident beam and b_e is the x-ray scattering length of an electron, given by (1.37) in the case of an unpolarized incident beam. If, on the other hand, the structure is defined by the positions $\boldsymbol{r}_j$ of atoms, the amplitude can be written (provided the atoms are all of the same kind) as

$$A(\boldsymbol{q}) = A_0 \, b_e \, f(q) \sum_j e^{-i\boldsymbol{q}\boldsymbol{r}_j} \tag{1.48}$$

where $f(q)$ is the atomic scattering factor. In the case of neutron scattering, the amplitude of (coherent) scattering from the same sample can, on the other hand, be written as

$$A(\boldsymbol{q}) = A_0\, b_{\text{coh}} \sum_j e^{-i\boldsymbol{q}\boldsymbol{r}_j} \tag{1.69}$$

where b_{coh} is the coherent neutron scattering length of the atomic nuclei, located at positions $\boldsymbol{r}_j$ and assumed to be all of the same element. To be able to discuss the scattering of both x-rays and neutrons at the same time, we will from now on use a single expression

$$A(\boldsymbol{q}) = b \sum_j e^{-i\boldsymbol{q}\boldsymbol{r}_j} \tag{1.70}$$

to represent any of the three, (1.39), 1.49), or (1.69). The *generalized scattering length* b in (1.70) represents either b_e, $b_e f(q)$, or b_{coh} as the case may be, and $\boldsymbol{r}_j$ gives either the electronic or nucleic position. By writing the amplitude as in (1.70) it is further understood that $A(\boldsymbol{q})$ now stands for the *normalized amplitude*, i.e., the ratio $A(\boldsymbol{q})/A_0$. If the material contains more than one species of element, (1.70) becomes

$$A(\boldsymbol{q}) = \sum_j b_j e^{-i\boldsymbol{q}\boldsymbol{r}_j} \tag{1.71}$$

If the structure is defined in terms of the density distribution $n(\boldsymbol{r})$ of the electrons or nucleic centers instead of the individual positions $\boldsymbol{r}_j$, again a single expression

$$A(\boldsymbol{q}) = b \int_V n(\boldsymbol{r}) e^{-i\boldsymbol{q}\boldsymbol{r}}\, d\boldsymbol{r} \tag{1.72}$$

will be used for both x-ray and neutron scattering. More generally (1.72) may be written as

$$A(\boldsymbol{q}) = \int_V \rho(\boldsymbol{r}) e^{-i\boldsymbol{q}\boldsymbol{r}}\, d\boldsymbol{r} \tag{1.73}$$

where $\rho(\boldsymbol{r})$ is the *scattering length density distribution*, equal, in the case of x-ray scattering, to the electron density distribution $n(\boldsymbol{r})$ multiplied by b_e, or, in the case of neutron scattering, to

$$\rho(\boldsymbol{r}) = \sum_\alpha b_\alpha n_\alpha(\boldsymbol{r}) \tag{1.74}$$

where the subscript α refers to the different atomic species present.

It has already been mentioned in Section 1.2.1 that the term *intensity* will be used to denote the differential scattering cross section $d\sigma/d\Omega$, i.e., the ratio $J(\boldsymbol{q})/J_0$. The normalized amplitude defined here is therefore related to the intensity by $I(\boldsymbol{q}) = |A(\boldsymbol{q})|^2$.

The scattering length b_e for scattering of x-rays by an electron includes the square root of the polarization factor as discussed in Section 1.3.1. Since the polarization factor varies according to the state of polarization of the incident x-ray beam and thus

depends on the experimental setup, the intensity data are normally reported after the observed intensity has been corrected for the polarization effect. In keeping with this practice we will assume, in all the discussions that follow, that b_e is redefined as equal to the classical electron radius r_e without any polarization factor involved.

1.5.2 Autocorrelation Function

We take Equation (1.73), or its equivalent

$$I(\boldsymbol{q}) = |A(\boldsymbol{q})|^2 = |\int_V \rho(\boldsymbol{r}) e^{-i\boldsymbol{q}\boldsymbol{r}} d\boldsymbol{r}|^2 \tag{1.75}$$

as the fundamental starting point for interpretation of all scattered intensity. Stated in words, the scattered intensity $I(\boldsymbol{q})$ is the absolute square of the Fourier transform of the scattering length density $\rho(\boldsymbol{r})$. [Strictly speaking, the integral in (1.75) is only over the finite illuminated volume V and therefore it only approximates the Fourier transform, but we will ignore the subtlety here.] Although not expressed explicitly in the derivation leading to (1.73) and (1.75), these equations were obtained under the assumption that the scattering is weak (as is true in most of the cases we consider), so that the scattering occurs only once within the sample. Such an approach is called *kinematic theory*. In a large, perfect crystal, a diffracted ray may be diffracted many times in different regions before finally leaving the crystal, and such an effect is taken into account in the *dynamic theory*,[19] which, however, is not discussed in this book.

During the time period of a scattering measurement, the positions $\boldsymbol{r}_j$ of atoms and hence the scattering length density distribution $\rho(\boldsymbol{r})$ may change due to the thermal motion of the atoms, and the intensity $I(\boldsymbol{q})$ that is actually measured is the average over the time. In an equilibrium system such a time average is equivalent to an ensemble average, which is more convenient to calculate from theoretical considerations. Thus it is more appropriately to write (1.75) as

$$I(\boldsymbol{q}) = \langle |A(\boldsymbol{q})|^2 \rangle = \left\langle |\int_V \rho(\boldsymbol{r}) e^{-i\boldsymbol{q}\boldsymbol{r}} d\boldsymbol{r}|^2 \right\rangle \tag{1.76}$$

where $\langle \cdots \rangle$ denotes the ensemble average. The simpler expression (1.75) will continue to be used, however, as long as there is no danger of ambiguity.

We now rewrite (1.75) as

$$\begin{aligned} I(\boldsymbol{q}) &= A(\boldsymbol{q}) \cdot A^*(\boldsymbol{q}) \\ &= \left[\int \rho(\boldsymbol{u}') e^{-i\boldsymbol{q}\boldsymbol{u}'} d\boldsymbol{u}'\right]\left[\int \rho(\boldsymbol{u}) e^{i\boldsymbol{q}\boldsymbol{u}}\, d\boldsymbol{u}\right] \end{aligned} \tag{1.77}$$

Adopting a new variable $\boldsymbol{r} = \boldsymbol{u}' - \boldsymbol{u}$ instead of $\boldsymbol{u}'$, we then have

$$\begin{aligned} I(\boldsymbol{q}) &= \int \left[\int \rho(\boldsymbol{u})\rho(\boldsymbol{u}+\boldsymbol{r}) d\boldsymbol{u}\right] e^{-i\boldsymbol{q}\boldsymbol{r}} d\boldsymbol{r} \\ &= \int \Gamma_\rho(\boldsymbol{r}) e^{-i\boldsymbol{q}\boldsymbol{r}} d\boldsymbol{r} \end{aligned} \tag{1.78}$$

where $\Gamma_\rho(\boldsymbol{r})$ is defined as

$$\Gamma_\rho(\boldsymbol{r}) = \int \rho(\boldsymbol{u})\rho(\boldsymbol{u}+\boldsymbol{r})d\boldsymbol{u} \tag{1.79}$$

and is called the *autocorrelation function* of $\rho(\boldsymbol{r})$.$\Gamma_\rho(\boldsymbol{r})$ is related to the average of $\rho(\boldsymbol{u})\rho(\boldsymbol{u}')$, taken throughout the sample space while $\boldsymbol{u}' - \boldsymbol{u}$ is kept equal to $\boldsymbol{r}$, since

$$\langle \rho(\boldsymbol{u})\rho(\boldsymbol{u}') \rangle = \frac{\int \rho(\boldsymbol{u})\rho(\boldsymbol{u}+\boldsymbol{r})d\boldsymbol{u}}{\int d\boldsymbol{u}} = \frac{\Gamma_\rho(\boldsymbol{r})}{V} \tag{1.80}$$

The autocorrelation function $\Gamma_\rho(\boldsymbol{r})$ thus specifies how the densities $\rho(\boldsymbol{u})$ and $\rho(\boldsymbol{u}')$ in neighboring regions separated by $\boldsymbol{r}$ are correlated to each other on the average. When $\boldsymbol{r}$ equals 0, we obviously have

$$\Gamma_\rho(0) = \langle \rho^2 \rangle V \tag{1.81}$$

whereas, between any two points separated by a large distance $\boldsymbol{r}$ there is no correlation in the density (except when the object has a long range order), so that

$$\Gamma_\rho(\boldsymbol{r} \to \infty) = \langle \rho(\boldsymbol{u}) \rangle \langle \rho(\boldsymbol{u}') \rangle V = \langle \rho \rangle^2 V \tag{1.82}$$

For a one-dimensional function $f(x)$, the operation leading to $\Gamma_f(x)$ can be described as follows. First, shift the curve $f(x)$ by $-X$ to obtain a curve representing $f(x + X)$, next multiply $f(x)$ with $f(x + X)$, and then integrate the product over the whole range of x. This gives the value of $\Gamma_f(x)$ at $x = X$, and this operation is to be repeated for other values of X in the whole range. Figure 1.10 gives an example of $f(x)$ and its autocorrelation function $\Gamma_f(x)$. This illustrates a few general properties of an autocorrelation function. $\Gamma_f(x)$ is even (or centrosymmetric in two or three dimension) even when $f(x)$ is not, and the maximum of $\Gamma_f(x)$ is at $x = 0$. If $f(x)$ consists of islands of finite densities (representing "particles"), islands also occur in $\Gamma_f(x)$ at positions that correspond to the interparticle distances in $f(x)$, but the islands in $\Gamma_f(x)$ are more smeared (less sharply peaked) than the corresponding islands in $f(x)$.

The autocorrelation function is sometimes referred to simply as the *correlation function.* Among those working in crystal structure analysis, the autocorrelation function is known as the *Patterson function.* Many of the distribution functions obtained from scattering intensity data are in the nature of the correlation function, with possible differences in the normalization constant or a constant term. Functions in this vein include the *pair correlation function* or the *radial distribution function* (and its uniaxial variant *cylindrical distribution function*), discussed in Chapter 4.

Equation (1.78) shows that the intensity of scattering $I(\boldsymbol{q})$ is given by the Fourier transform of the autocorrelation function $\Gamma_\rho(\boldsymbol{r})$ of the scattering length density distribution $\rho(\boldsymbol{r})$ defining the structure. This should be contrasted with Equation (1.73), which states that the amplitude of scattering $A(\boldsymbol{q})$ is given by the Fourier transform of the density distribution $\rho(\boldsymbol{r})$ itself. We can regard (1.78) as the alternative to (1.75) in its role as the starting point for discussion of all scattering and diffraction phenomena.

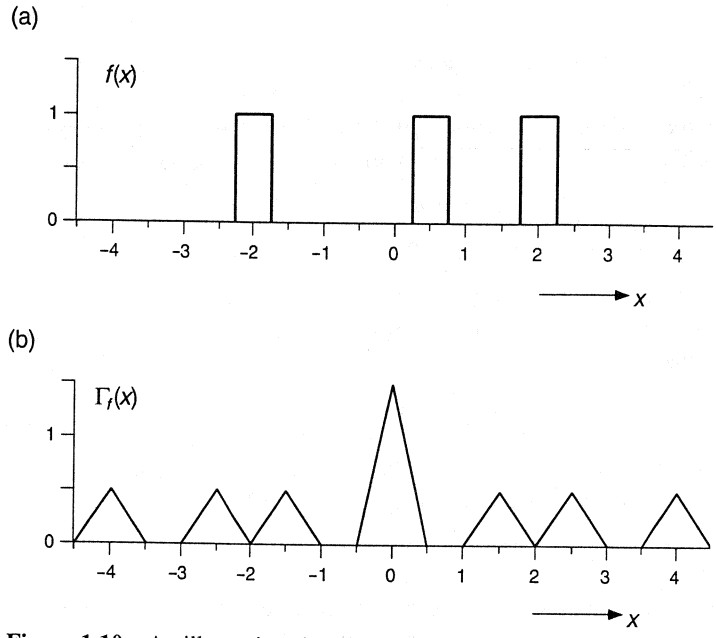

Figure 1.10 An illustration showing the relationship between a function $f(x)$ plotted in (a) and its autocorrelation function $\Gamma_f(x)$ plotted in (b).

1.5.3 Ewald Sphere and Reciprocal Space

Suppose we place our sample at the origin O (see Figure 1.11) with the incident beam directed along MO, and we measure the intensity $I(s)$ of the beam scattered in the direction OX. The corresponding scattering vector s is pointing to P in Figure 1.11, if the length MO and OX in the figure is $1/\lambda$. As we change the direction OX in which the scattered beam intensity is measured, s moves along the surface of a sphere of radius $1/\lambda$ centered on M. Measuring the intensity with the detector pointing in all possible directions OX is in effect determining the values of $I(s)$ as a function of s over the surface of the said sphere. This sphere is called the *Ewald sphere*. If we change the orientation of the sample in the scattering experimental setup, it amounts to changing the incident beam direction MO in Figure 1.11. Measurements with the detector placed in different directions then amount to determining $I(s)$ over the Ewald sphere, which has been rotated to a new position around the origin O. With many different orientations of the sample, one can eventually determine $I(s)$ for all values of s within the *limiting sphere* of radius $2/\lambda$ shown in Figure 1.11. One can, in principle, repeat the whole measurement with a radiation of smaller and smaller wavelength λ and thus explore $I(s)$ for the complete three-dimensional range of s. This Ewald sphere construction is very useful in interpreting the effect of various geometric arrangements of scattering measurements.

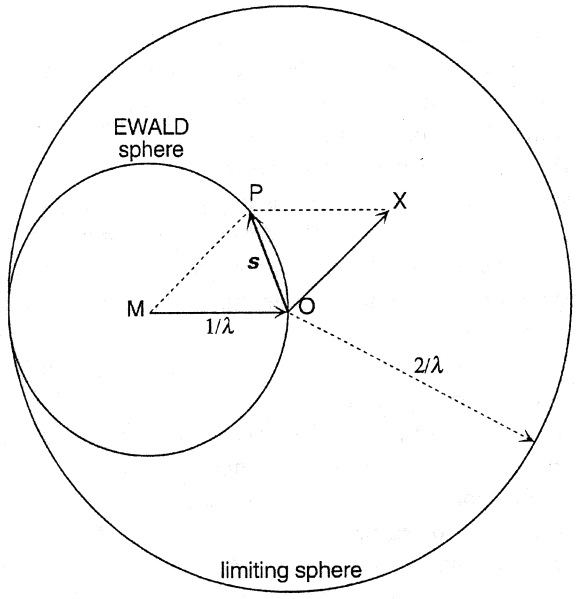

Figure 1.11 Ewald sphere construction.

The scattering vector $\boldsymbol{s}$ or $\boldsymbol{q}$ has dimension of length^{-1} and spans a three-dimensional *reciprocal space.* The origin of the reciprocal space is located at the same origin O of the real space spanned by $\boldsymbol{r}$. The information on the structure of the sample is contained in the function $\rho(\boldsymbol{r})$ in real space, and its Fourier transform gives the amplitude $A(\boldsymbol{s})$, a function in reciprocal space. If $A(\boldsymbol{s})$ could be determined over all $\boldsymbol{s}$, the real space function $\rho(\boldsymbol{r})$ is recovered by the inverse Fourier transform

$$\rho(\boldsymbol{r}) = \int A(\boldsymbol{s}) e^{i2\pi \boldsymbol{s}\boldsymbol{r}} d\boldsymbol{s} \tag{1.83}$$

The information contents of $\rho(\boldsymbol{r})$ and $A(\boldsymbol{s})$ are therefore entirely equivalent to each other. Since, in Equation (1.78), the intensity $I(\boldsymbol{s})$ in reciprocal space is given by the Fourier transform of $\Gamma_\rho(\boldsymbol{r})$ in real space, one can also derive the latter from the former by the inverse Fourier transform operation

$$\Gamma_\rho(\boldsymbol{r}) = \int I(\boldsymbol{s}) e^{i2\pi \boldsymbol{s}\boldsymbol{r}} d\boldsymbol{s} \tag{1.84}$$

The relationship among $\rho(\boldsymbol{r})$, $\Gamma_\rho(\boldsymbol{r})$, $A(\boldsymbol{s})$, and $I(\boldsymbol{s})$ can be represented by the diagram in Figure 1.12. The functions $\rho(\boldsymbol{r})$ and $A(\boldsymbol{s})$ can be converted to each other through the Fourier transform operation. Similarly, $\Gamma_\rho(\boldsymbol{r})$ and $I(\boldsymbol{s})$ can be converted to each other. However, there is only a one-way street from $\rho(\boldsymbol{r})$ to $\Gamma_\rho(\boldsymbol{r})$ and from $A(\boldsymbol{s})$ to $I(\boldsymbol{s})$. In the autocorrelation operation, represented by Equation (1.79),

or in the squaring $A(s)A^*(s)$ to obtain $I(s)$, some of the information contained in $\rho(r)$ or $A(s)$ is lost, and there is no way the reverse operation can be performed. The amplitude is a complex quantity, and in the process of converting it to the intensity, which is a real quantity, the information on the phase angle is completely lost. Our main objective in measuring $I(s)$ is to obtain the structural information $\rho(r)$ from it. We can always assume a model structure and see whether the intensity pattern calculated from it agrees with experimental $I(s)$. Aside from the difficulty of coming up with a satisfactory model in some instances, there is always the question of whether the assumed model represents the unique solution to the problem. In the crystal structure analysis aimed at determining the atomic positions in a crystal unit cell, the absolute value of $A(s)$ is derived from the square root of observed $I(s)$, and the phase is deduced by one of several ingenious methods relying on some additional physical facts and/or additional experimental measurements. The task of deducing the phases, called the phase problem, is central to the pursuit for those engaged in crystal structure analysis. With polymers and other noncrystalline materials, the alternative route is usually taken, where the intensity itself or the autocorrelation function derived from it is analyzed directly to extract structural parameters under some broad assumptions concerning the type of structure it contains. The interpretation of small-angle scattering data is largely of this nature.

1.5.4 Invariant

The *invariant* Q is defined as the quantity obtained when $I(s)$ is integrated with respect to s throughout the reciprocal space, that is,

$$Q = \int I(s)\, ds = \frac{1}{(2\pi)^3} \int I(q)\, dq \tag{1.85}$$

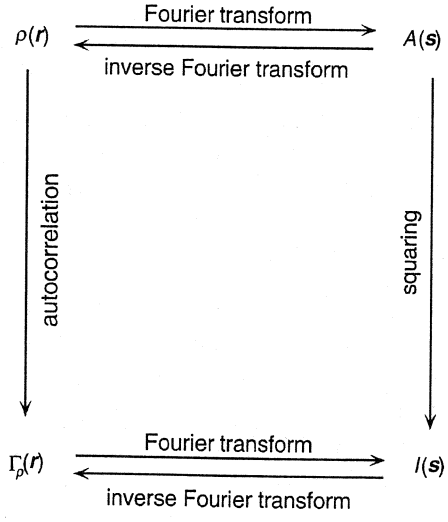

Figure 1.12 Relationship among $\rho(r)$, $\Gamma_\rho(r)$, $A(s)$, and $I(s)$.

In the case of an isotropic material for which $I(s)$ depends only on the magnitude of s, Equation (1.85) can be written as

$$Q = 4\pi \int_0^\infty s^2 I(s)\, ds = \frac{1}{2\pi^2} \int_0^\infty q^2 I(q)\, dq \tag{1.86}$$

The invariant Q can be regarded as representing the overall scattering power of the sample that takes into account the intensity of scattering that is expected from it under all possible scattering geometry. Substituting (1.78) for $I(q)$ in (1.85) and changing the order of integration, we obtain

$$\begin{aligned} Q &= \int \Gamma_\rho(r) \left[\int e^{-i2\pi sr}\, ds \right] dr \\ &= \int \Gamma_\rho(r)\delta(r)\, dr \\ &= \Gamma_\rho(0) \end{aligned} \tag{1.87}$$

which, from (1.81), is seen to be equal to $\langle \rho^2 \rangle V$. The word *invariant* stresses the fact that its value depends only on the mean square fluctuation of the scattering length density in the sample and not on particulars of how the fluctuations are distributed. As long as the material constitution remains the same, the value of Q should remain invariant even after the structure has been disturbed and the positions of constituent atoms have been altered. The invariant was originally defined by Porod[20] in connection with small-angle scattering only, but the concept is more general and can be applied to the overall scattering that includes both small- and wide-angle scattering.

1.6 SCATTERING DUE TO THE SAMPLE AS A WHOLE

Let us designate the mean value of $\rho(r)$ throughout the sample by $\langle \rho \rangle$ and the deviation of $\rho(r)$ from its mean by

$$\eta(r) = \rho(r) - \langle \rho \rangle \tag{1.88}$$

The autocorrelation function of $\eta(r)$ is

$$\Gamma_\eta(r) = \int \eta(u)\eta(u+r) du \tag{1.89}$$

The autocorrelation function $\Gamma_\rho(r)$ of $\rho(r)$ can then be written as

$$\begin{aligned} \Gamma_\rho(r) &= \int [\eta(u) + \langle \rho \rangle][\eta(u+r) + \langle \rho \rangle]\, du \\ &= \int \eta(u)\eta(u+r)\, du + \langle \rho \rangle^2 \int du + \langle \rho \rangle \int \eta(u)\, du \\ &\quad + \langle \rho \rangle \int \eta(u+r)\, du \end{aligned} \tag{1.90}$$

The third integral in (1.90) is zero by the definition of $\eta(\boldsymbol{r})$. The fourth is also zero except when $\boldsymbol{r}$ is of the same order of magnitude as the sample dimension so that the effect of the edge of the sample becomes important. Since we are not interested in an effect that becomes noticeable only when $\boldsymbol{r}$ is of macroscopic dimension, the fourth term in (1.90) can be neglected. Thus (1.90) reduces to

$$\Gamma_\rho(\boldsymbol{r}) = \Gamma_\eta(\boldsymbol{r}) + \langle\rho\rangle^2 V \tag{1.91}$$

Substitution of (1.91) into (1.78) then gives the intensity as

$$I(\boldsymbol{q}) = \int \Gamma_\eta(\boldsymbol{r}) e^{-i\boldsymbol{q}\boldsymbol{r}} d\boldsymbol{r} + \langle\rho\rangle^2 V\delta(\boldsymbol{q}) \tag{1.92}$$

where the second term results from the Fourier transform of unity, which is equal to the delta function (see Appendix B). The scattered intensity therefore consists of two terms, and the second term represents the scattering due to the sample volume as a whole, as if it is a body of uniform density $\langle\rho\rangle$, and is called by some the *null scattering*. The null scattering is experimentally unobservable because, at $\boldsymbol{q} = 0$, it is swamped by the much stronger, unmodified transmitted beam. The second term in (1.92) is therefore neglected for all practical purposes, and we then obtain the result that the intensity $I(\boldsymbol{q})$ is equal to the Fourier transform of $\Gamma_\eta(\boldsymbol{r})$. The reader may wonder why $I(\boldsymbol{q})$ should be given as the Fourier transform of $\Gamma_\rho(\boldsymbol{r})$ in (1.78) and at the same time as that of $\Gamma_\eta(\boldsymbol{r})$ as implied in (1.92). To resolve this question, we have to compare the behavior of the autocorrelation functions $\Gamma_\rho(\boldsymbol{r})$ and $\Gamma_\eta(\boldsymbol{r})$ for large $\boldsymbol{r}$. From Equation (1.82) it is seen that in the limit of $\boldsymbol{r} \to \infty$, $\Gamma_\rho(\boldsymbol{r})$ approaches $\langle\rho\rangle^2 V$ whereas $\Gamma_\eta(\boldsymbol{r})$ approaches $\langle\eta\rangle^2 V = 0$. The attempt to perform the Fourier transform in (1.78), in its unmodified form, will not succeed because the integral will not converge, whereas the Fourier transform of $\Gamma_\eta(\boldsymbol{r})$ in (1.92) can be accomplished without difficulty.

The results of the above analysis can be stated in words as follows: What determines the strength and pattern of scattering from a sample is not the absolute value of the scattering length density but rather the fluctuations or the heterogeneities in the scattering length density present in the sample. The absolute value of the scattering length density governs the intensity of the null scattering, which is of course unmeasurable and therefore has no practical meaning. If we are to increase the scattered intensity from a sample for ease of measurement, we have to increase the *contrast* in the scattering length density among different molecules, species, or regions in the sample.

An examination of the definition of the autocorrelation function $\Gamma_\eta(\boldsymbol{r})$ in (1.89) reveals another interesting aspect. Suppose we have a "positive" and a complimentary "negative" image of an object, in which, when the density $\rho(\boldsymbol{r})$ is high in the "positive" image, the density at the same spot $\boldsymbol{r}$ in the "negative" image is low, and vice versa (just imagine a photographic negative film and its positive print). The variations in $\eta(\boldsymbol{r})$ in these two images will be very similar, except that when $\eta(\boldsymbol{r})$ is positive (or negative) in the "positive" image, it will be negative (or positive) in the "negative" image by the same absolute amount. Since in the definition of the

autocorrelation function in (1.89) the function $\eta(\boldsymbol{r})$ occurs twice in the integrand, the reversal in the signs between the "positive" and "negative" images cancels out and the same autocorrelation function and hence the same scattered intensity result. This is called the *Babinet principle*. The same principle applies to optical diffraction, so that, for example, the diffraction pattern obtained with an opaque screen having a circular hole in the center is the same as the pattern obtainable from an opaque circle of the same radius pasted in the middle of an otherwise transparent sheet. The Babinet principle is a direct consequence of the fact that it is the deviation $\eta(\boldsymbol{r})$ rather than the absolute value of the density $\rho(\boldsymbol{r})$ that determines the scattered intensity pattern.

1.7 DIFFRACTION BY CRYSTALS

A crystal consists of a large number of unit cells arranged regularly in three-dimensional space, with each unit cell having the identical atomic content. The shape and size of the unit cell are defined by the three unit cell vectors $\boldsymbol{a}, \boldsymbol{b}, \boldsymbol{c}$. The origin of each unit cell is on a lattice point, whose position is specified as

$$\boldsymbol{r}_{uvw} = u\boldsymbol{a} + v\boldsymbol{b} + w\boldsymbol{c} \tag{1.93}$$

where u, v, w are positive or negative integers or zero. The lattice consisting of all these lattice points is then represented mathematically as

$$z(\boldsymbol{r}) = \sum_{u=-\infty}^{\infty} \sum_{v=-\infty}^{\infty} \sum_{w=-\infty}^{\infty} \delta(\boldsymbol{r} - \boldsymbol{r}_{uvw}) \tag{1.94}$$

The content of the unit cell is defined by specifying the positions of all the atoms it contains. It is more convenient, however, to specify the unit cell content by the distribution $\rho_u(\boldsymbol{r})$ of the appropriate scattering length density, so that the same expression can be used in discussing both x-ray and neutron diffraction. The convolution product

$$\rho(\boldsymbol{r}) = \rho_u(\boldsymbol{r}) * z(\boldsymbol{r}) \tag{1.95}$$

then gives the scattering length distribution $\rho(\boldsymbol{r})$ in the crystal as a whole. In Figure 1.13a–c, an example in one-dimensional space illustrates how the convolution of $\rho_u(r)$ and $z(r)$ leads to $\rho(r)$.

The amplitude $A(\boldsymbol{s})$ of scattered x-rays or neutrons is equal to the Fourier transform of $\rho(\boldsymbol{r})$, and therefore, by taking the Fourier transform of (1.95) and using the convolution theorem (see Appendix B), we obtain

$$A(\boldsymbol{s}) = F(\boldsymbol{s})Z(\boldsymbol{s}) \tag{1.96}$$

where $F(\boldsymbol{s})$, called the *structure factor* of the unit cell, is the Fourier transform of $\rho_u(\boldsymbol{r})$, and $Z(\boldsymbol{s})$, called the *lattice factor*, is the Fourier transform of $z(\boldsymbol{r})$. As is shown in Appendix C, $Z(\boldsymbol{s})$ is itself a lattice in reciprocal space, and its lattice points are given by

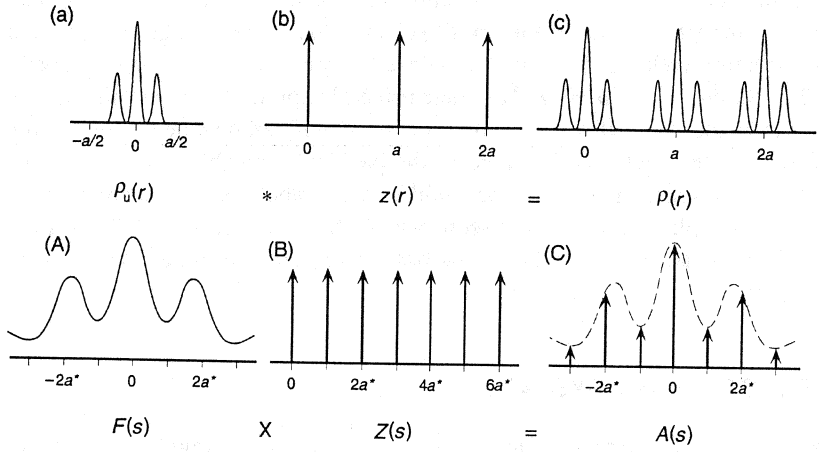

Figure 1.13 A one-dimensional example illustrating the mathematical operations represented by Equations (1.95) and (1.96). The convolution of the unit cell content $\rho_u(r)$ with the lattice $z(r)$ produces an infinite repetition of the unit cell pattern, while the product of the structure factor $F(s)$ with the reciprocal lattice $Z(s)$ produces the discrete amplitude function whose magnitude at the reciprocal lattice point is modulated by $F(s)$. Note that (a) and (A), (b) and (B), and (c) and (C) are, respectively, the Fourier transforms of each other.

$$\boldsymbol{r}^*_{hkl} = h\boldsymbol{a}^* + k\boldsymbol{b}^* + l\boldsymbol{c}^* \tag{1.97}$$

where h, k, l are integers. The three vectors $\boldsymbol{a}^*$, $\boldsymbol{b}^*$, and $\boldsymbol{c}^*$ in reciprocal space define the *reciprocal lattice* and are related to the unit cell vectors $\boldsymbol{a}$, $\boldsymbol{b}$, and $\boldsymbol{c}$ in real space in the manner described in Appendix C. The concept of the reciprocal lattice is very useful and important in understanding diffraction phenomena from crystalline materials.

The structure factor $F(\boldsymbol{s})$ is in general a smoothly varying function defined over the whole range of reciprocal space. Its product with the lattice factor $Z(\boldsymbol{s})$, however, produces the amplitude function $A(\boldsymbol{s})$ that is nonzero only at the reciprocal lattice points, as can be seen from the one-dimensional illustration given in Figure 1.13A–C. The scattered beam intensity, which is given by the square of $A(\boldsymbol{s})$, is therefore also nonzero only at the reciprocal lattice points. It is thus seen that in diffraction by crystals, the scattering vector $\boldsymbol{s}$ and hence the direction in which finite diffraction intensity is observed is determined solely by the lattice factor $Z(\boldsymbol{s})$, which in turn depends uniquely on the lattice structure represented by the unit cell vectors $\boldsymbol{a}$, $\boldsymbol{b}$, and $\boldsymbol{c}$. The intensities of scattering observed at these various reciprocal lattice points are "modulated" by the structure factor $F(\boldsymbol{s})$, which is governed by the atomic content, represented by $\rho_u(\boldsymbol{r})$, of the unit cell only. Thus the interpretation of diffraction patterns from crystals cleanly separates into two aspects, the diffraction directions giving information about the lattice structure and the intensities of diffraction at various $\boldsymbol{s}$ giving information about the placement of atoms in the unit cell.

While $F(\boldsymbol{s})$ is a continuously varying function of $\boldsymbol{s}$, its magnitude is experimentally observable and therefore is meaningful only at discrete values of $\boldsymbol{s}$ corresponding to

the reciprocal lattice points. Therefore the structure factor $F(s)$ can in fact be replaced, without loss of information, by a triply infinite series F_{hkl} $(h, k, l = -\infty \cdots \infty)$ with

$$F_{hkl} \equiv F(\boldsymbol{r}^*_{hkl}) = \int \rho_u(\boldsymbol{r}) \exp(-i2\pi \boldsymbol{r}^*_{hkl}\, \boldsymbol{r}) d\boldsymbol{r} \tag{1.98}$$

If F_{hkl} is known for a large number of hkl reflections, (1.98) can be inverted to obtain $\rho_u(\boldsymbol{r})$ and hence the positions of all the atoms in the unit cell. Such an endeavor is called the *crystal structure analysis* and is explained in more detail in Section 3.3. The intensity of reflection, I_{hkl}, observed at $s = \boldsymbol{r}^*_{hkl}$ is equal to $|F_{hkl}|^2$. The absolute value of F_{hkl} can therefore be obtained as the square root of the observed intensity of the hkl reflection, but the intensity data do not provide any direct information about the phase angle of the complex F_{hkl}. A major task in crystal structure analysis is solving the *phase problem* to determine the phases of the structure factors.

1.7.1 Effect of Temperature

In the above discussion, we have tacitly assumed that the atomic positions, with respect to the origin of the unit cell, are held fixed exactly identical in every unit cells. In reality atoms vibrate about their average positions, and therefore the scattering length density distribution $\rho_u(\boldsymbol{r})$ is slightly different among different unit cells. As a result of such thermal vibrations, the structure factor F'_{hkl} that is actually observed is modified from the F_{hkl} that is given by (1.98) and applicable to ideal crystals, so that

$$F'_{hkl} = e^{-M} F_{hkl} \tag{1.99}$$

The observed intensities of the diffraction peaks are therefore reduced, in comparison to those expected from an ideal crystal, by the ratio

$$D = e^{-2M} \tag{1.100}$$

which is called the *Debye–Waller factor*.[21,22]

The reason for the Debye–Waller factor can be understood by the following simplified argument. The vibration displaces atoms from their average positions in random directions, and as a result, when viewed over time, the atoms look as though they are smeared and spread out in all directions. Similarly, the scattering length density distribution $\rho'_u(\boldsymbol{r})$ in the unit cell is also smeared out. The smeared distribution $\rho'_u(\boldsymbol{r})$ can be represented by a convolution of $\rho_u(\boldsymbol{r})$ with a "smearing function" that may be given by a Gaussian function, so that

$$\rho'_u(\boldsymbol{r}) = \rho_u(\boldsymbol{r}) * g(\boldsymbol{r}) \tag{1.101}$$

and

$$g(\boldsymbol{r}) = \left(\frac{3}{2\pi\sigma^2}\right)^{3/2} \exp\left(-\frac{3}{2\sigma^2}\boldsymbol{r}^2\right) \tag{1.102}$$

where σ is the root-mean-square displacement of the atoms about their average positions. Taking the Fourier transform of (1.101) then leads to

$$F'_{hkl} = F_{hkl} \exp\left(-\frac{2}{3}\pi^2\sigma^2 s^2\right) \tag{1.103}$$

The exponent $2M$ in the Debye–Waller factor is thus equal to $(2/3)\pi^2\sigma^2 s^2$. Note that the exponent is proportional to s^2, and this means that the intensity of diffraction is progressively more attenuated as the diffraction angle 2θ is increased. The reason for this can be seen as follows. The diffraction peak at a larger angle occurs as a result of reflections from crystallographic planes having a smaller interplanar spacing d, and the smaller spacing is proportionately more severely disturbed by the same absolute amount of displacement of atoms.

FURTHER READING

X-Ray Scattering

1. Cullity, B. D., *Elements of X-ray Diffraction*, 2nd ed., Addison-Wesley, Reading, MA, 1978.
2. Klug, H. P., and Alexander, L. E., *X-ray Diffraction Procedures for Polycrystalline and Amorphous Materials*, 2nd ed., Wiley-Interscience, New York, 1974.
3. James, R. W., *The Optical Principles of the Diffraction of X-rays*, Ox Bow Press, Woodbridge, CN, 1982.
4. Guinier, A., *X-ray Diffraction in Crystals, Imperfect Crystals, and Amorphous Bodies*, Freeman, San Francisco, 1963.
5. Warren, B. E., *X-ray Diffraction*, Addison-Wesley, Reading, MA, 1969.

Neutron Scattering

6. Bacon, G. E., *Neutron Diffraction*, 3rd ed., Clarendon Press, Oxford, 1975.
7. Squires, G. L., *Introduction to the Theory of Thermal Neutron Scattering*, Cambridge University Press, Cambridge, 1978.
8. Lovesey, S. W., *Theory of Neutron Scattering from Condensed Matter*, Clarendon Press, Oxford, 1984.

Scattering, General

9. Cowley, J. M., *Diffraction Physics*, 3rd ed., Elsevier, Amsterdam, 1995.

Scattering from Polymers

10. Vainshtein, B. K., *Diffraction of X-Rays by Chain Molecules*, Elsevier, Amsterdam, 1966.
11. Alexander, L. E., *X-Ray Diffraction Methods in Polymer Science*, Wiley-Interscience, New York, 1969.
12. Kakudo, M., and Kasai, N., *X-ray Diffraction by Polymers*, Elsevier, Amsterdam, 1972.
13. Baltá-Calleja, F. J., and Vonk, C. G., *X-ray Scattering of Synthetic Polymers*, Elsevier, Amsterdam, 1989.
14. Higgins, J. S., and Benoît, H. C., *Polymers and Neutron Scattering*, Clarendon Press, Oxford, 1994.

REFERENCES

15. *International Tables for Crystallography*, Vol. C, Wilson, A. J. C., Ed., Kluwer Academic Publications, Dordrecht, 1992.
16. See, for example, Chapter 3 of Further Reading 3, and pp. 11–20 of Further Reading 4.
17. Koester, L., Rauch, R., and Seymann, E., *Atomic Data and Nuclear Data Tables* **49**, 65 (1991).
18. Sears, V. F., *Neutron News* **3**, 26 (1992).
19. See, for example, Chapter 14 of Further Reading 5.
20. Porod, G., *Kolloid-Z.* **124**, 83 (1951).
21. Debye, P., *Ann. Phys.* **40**, 49 (1914).
22. Waller, I., *Z. Phys.* **17**, 398 (1923); **51**, 213 (1928).

EXERCISES

1. For x-rays of wavelength 1 Å, the energy of a photon is 12.4 keV. For neutrons of wavelength 1 Å, the energy of a neutron is 82 meV. Explain why there is such a large difference in the energy of x-rays and neutrons when their wavelengths are the same.

2. The geometry of scattering from two scattering centers, shown in Figure 1.3, is redrawn in Figure 1.14. The incident beam direction is here characterized by the angle θ_0 between S_0 and $\boldsymbol{r}$, and the scattered beam direction is characterized by the angles Θ and Φ, where Θ is the angle between S and $\boldsymbol{r}$ and Φ is the angle between the plane that contains S_0 and $\boldsymbol{r}$ and the plane that contains S and $\boldsymbol{r}$. Express the amplitude of scattering, (1.24), as a function of θ_0, Θ, and Φ, and show that the intensity of scattering is maximal at $\Theta = \theta_0$ and is independent of Φ.

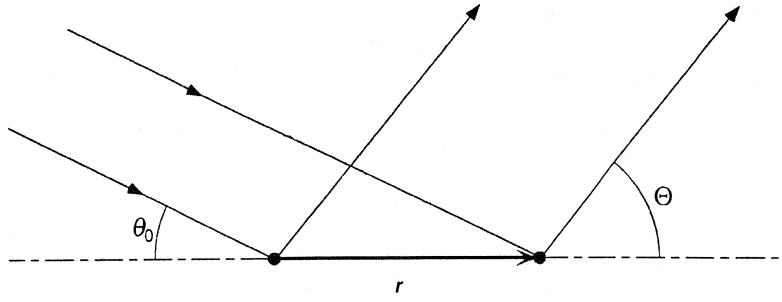

Figure 1.14 Geometry of scattering from two scattering centers.

3. The total cross section σ_e of an electron for x-ray scattering, given in Equation (1.38), was calculated for an unpolarized incident x-ray. Calculate the total scattering cross section for a linearly polarized incident beam.

4. When the incident x-ray beam is unpolarized, will the beam scattered in the direction $2\theta = 90°$ be polarized or unpolarized?

5. Solving the Schrödinger equation for a hydrogen atom in the ground state gives an electron density distribution around the nucleus that is spherically symmetric and obeys

$$n(r) = \left(1/\pi a^3\right) e^{-2r/a}$$

with $a = 0.528$ Å. Calculate the atomic scattering factor f as a function of s and compare it with the tabulated value in the literature.

6. In Figure 1.6, it is seen that the ratio of f_O to f_C, where f_O and f_C are the atomic scattering factors for an oxygen and carbon atom, respectively, is seen to decrease with increasing value of $2 \sin\theta/\lambda$. What can one infer from this fact about the orbital electron clouds around the nuclei in these two atoms?

7. Derive Equation (1.52) giving the extent of wavelength shift for Compton-modified x-rays, starting from the energy and momentum conservation relationships (1.50) and (1.51).

8. According to the Thomson equation giving the intensity of x-rays scattered from a single electron, the intensities scattered in the forward and backward directions are the same. When scattering of x-rays from a dilute gas is measured, the intensity decreases monotonically with increasing scattering angle. On the other hand, when scattering from a liquid or glass is determined, the intensity goes through a maximum as the scattering angle is increased. How would you explain these differences?

9. Using the values of neutron scattering cross sections in Table 1.2, calculate the coherent and incoherent scattering length densities for the following polymers, and also for the corresponding polymers in which all the hydrogens are replaced by deuteriums (the number in parentheses refers to the mass density of the polymer): (a) polyethylene (0.95 g/cm^3); (b) polystyrene (1.05); (c) poly(methyl methacrylate) (1.18); (d) poly(vinyl chloride) (1.4); (e) polytetrafluoroethylene (2.3).

10. Given that the spin-up and spin-down neutron scattering lengths of a proton are 1.080×10^{-12} cm, and -4.737×10^{-12} cm, respectively, verify that the incoherent scattering cross section σ_{inc} is indeed as high as 79.7 barns.

11. Think of a possible reason why the incoherent neutron scattering cross sections of carbon and oxygen are both practically equal to zero, and confirm it by consulting a table of relevant nuclear data.

12. Show that the autocorrelation function of $\exp(-\pi x^2)$ is $(1/\sqrt{2})\exp(-\frac{1}{2}\pi x^2)$ and that of $e^{-|x|}$ is $e^{-|x|}(1 + |x|)$.

13. Show that, given a function $f(x)$, its autocorrelation function $\Gamma_f(x)$ defined by Equation (1.79) can be expressed as

$$\Gamma_f(x) = f(x) * f(-x)$$

14. Show that the autocorrelation function $\Gamma_f(x)$ of any function $f(x)$ has its maximum at $x = 0$.

Experimental Techniques 2

2.1 RADIATION SOURCE

2.1.1 X-Ray

Traditionally x-rays are generated in the laboratory by means of a filament tube, originally invented by Coolidge in 1913. Electrons released from a hot tungsten filament are accelerated toward a metal target in an evacuated tube, and x-rays are generated on impact of the electrons at the target. X-Ray tubes are generally classified into two types, sealed and rotating anode, depending on whether the assembly is permanently sealed or whether the target metal (anode) is rotated rapidly through a mechanical linkage driven from the outside of the seal. The latter is usually capable of generating a much higher flux of x-rays. The quest for ever intense x-ray beams led to the development of synchrotron radiation sources in recent years. A synchrotron is a large facility in which high-energy electrons, circulating in a storage ring at speeds approaching the speed of light, are led to emit intense beams of x-rays and other electromagnetic radiations such as ultraviolet light.

2.1.1.1 X-Ray Tubes

Figure 2.1 presents a schematic drawing of a *sealed x-ray tube*. A tungsten filament is heated by a filament current and emits electrons into the surrounding vacuum. The filament is maintained at a high negative voltage (30 ~ 50 kV) relative to the anode, toward which the electrons are attracted and accelerated. The small metal cup surrounding the filament is at the same potential as the filament itself and helps to focus the electron beam to a small area (*focal spot*) on the surface of the *target metal* bonded to the anode. The striking electrons induce emission of x-rays, which then exit the tube through small windows (about 1 cm in diameter) made of materials relatively transparent to x-rays (usually beryllium). Only a small fraction of the kinetic energy of the electrons is converted into x-rays; the rest is dissipated as heat, which must be removed with cooling water to prevent damage to the target. The maximum output of an x-ray tube is limited by its cooling capacity. The *tube current* due to the flow of electrons from the filament to the target is usually on the order of 20–40 mA, and therefore the cooling water must dissipate heat at the rate of up to about 2 kW from the small focal spot area. In a *rotating anode tube* a band of target metal is bonded to the surface of a cylindrical block of anode that is rapidly rotated. Since, as the

anode rotates, a fresh surface of the target is continuously brought to the electron beam focus, a much higher tube current can be tolerated, and a tube power rating of up to about 100 kW can be achieved. The design of such a rotating anode tube is, however, more complicated, because a good vacuum seal must be maintained around the rotating shaft, while the focal spot position on the surface of the rotating target metal must remain stable.

The shape of the focal spot on the target irradiated by the electron beam is essentially a projection of the coiled filament, and its size is typically 1 × 10 mm. When the x-rays from such a focal spot exit through the tube window at a *take-off angle* α of 6°, the beam has a roughly 1 × 1 mm cross section, if the window is along the extension of the long dimension of the focal spot, as in Figure 2.2. The beam, on the other hand, appears to have a 0.1 × 10 mm cross section, if the window is

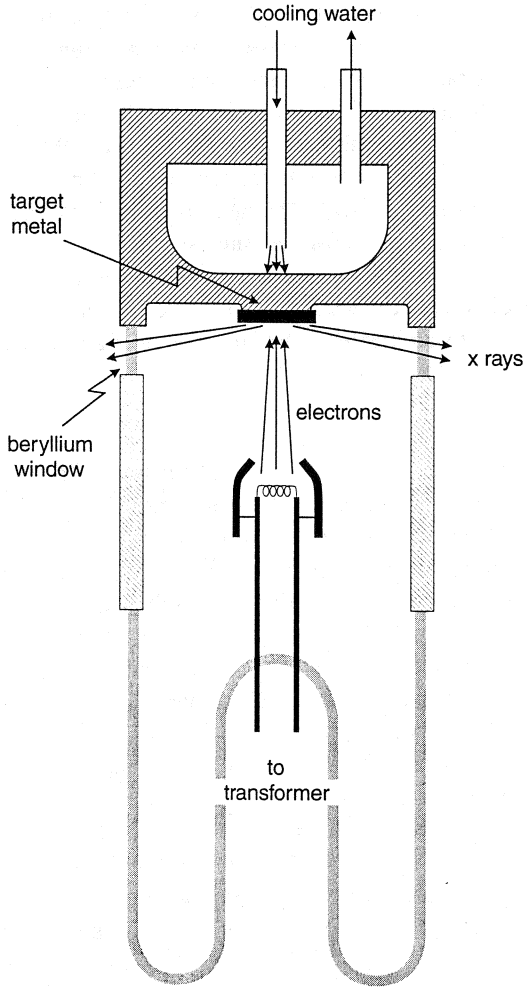

Figure 2.1 Schematic illustration of a sealed x-ray tube.

in the direction normal to the long dimension of the focal spot (and hence normal to the plane of the drawing of Figure 2.2). These are called, respectively, *square-focus* and *line-focus* geometry. An x-ray tube typically has windows on three or four sides, allowing both types of geometry, and the choice depends on the nature of the measurement intended and the design of the camera or diffractometer being used.

2.1.1.2 Spectrum of X-Rays Generated

White Radiation. X-Rays are produced when a charged particle is rapidly accelerated or decelerated. In an x-ray tube, the filament electrons, raised to high speed under the influence of the anode potential, hit the target metal and suffer a sudden deceleration. This induces emission of x-rays in all directions. If E is the part of the kinetic energy of the electron that is actually converted to an x-ray photon, its wavelength λ is given, from Equations (1.1) and (1.2), as

$$\lambda = \frac{hc}{E} \tag{2.1}$$

The wavelengths of the x-rays produced in an x-ray tube are spread over a broad spectrum, since the fraction of energy actually converted is different for each electron striking the target. Such a spectrum is called *white radiation, continuous radiation,* or *bremsstrahlung* (German for *brake radiation*). The broad, continuous spectrum is bound at the lower end by the *short wavelength limit* λ_{SWL}, which corresponds to the wavelength of x-rays produced when the kinetic energy of an electron is wholly

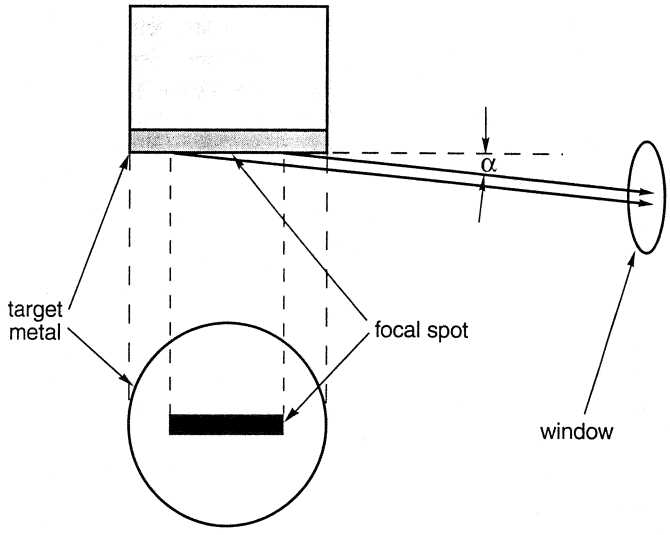

Figure 2.2 The diagram illustrates how the beam has an approximately square cross section if it emerges from the metal target at a take-off angle α of 6° ($\sin 6° \approx 0.1$). The beam emerging in the direction perpendicular to the plane of the diagram, at a similarly small take-off angle, would have a thin, line-shaped cross section.

converted to a single photon. Since the kinetic energy of an electron at the moment of impact is equal to eV, where e is the electronic charge and V is the anode potential, the short wavelength limit is given by

$$\lambda_{SWL} = \frac{hc}{eV} = \frac{12.40 \times 10^3}{V} \tag{2.2}$$

where the numerical value of hc/e given is valid when λ is in Ångstroms and V is in volts.

Characteristic Radiation. In addition to white radiation, the spectrum of x-rays produced in a tube contains sharp maxima confined within narrow ranges of wavelengths. They are called *characteristic radiation*, since the peak positions in the spectrum are characteristic of the target metal used. The mechanism of production of characteristic radiation is very different from that of white radiation. The impact of the highly accelerated filament electrons on the target metal can cause ejection of one or more orbital electrons from the target metal atoms. The binding energy of the inner K shell electron in a copper atom is 8.98 keV, so that it takes filament electrons accelerated by an *excitation voltage* higher than about 9 kV to eject a K electron. (In a molybdenum atom, the binding energy of the K shell electron is 20.0 keV.) The vacancy left by the ejected K shell electron is subsequently filled when one of the L or M shell electrons is transferred to it. Since the K shell is at a lower energy level than the L or M shell (i.e., the K shell electron is more tightly bound to the nucleus), the excess energy is released on this transition and is emitted as an X-ray photon. The transition of an electron from the L shell to the K shell produces either a $K\alpha_1$ or $K\alpha_2$ line, depending on the subshell of L from which the electron came. The transition from the M to K shell produces $K\beta$ lines. Since the energy differences involved in these transitions are determined by the structure of the atom, the wavelengths of these characteristic lines depend on the metal atoms themselves and not on the operating conditions of the x-ray tube, except that the applied tube voltage must be higher than the excitation voltage mentioned above. Table 2.1 gives the wavelengths and relative fluxes of the characteristic lines of Cu and Mo target tubes. The $K\alpha_1$ and $K\alpha_2$ lines have wavelengths very close together and, if they are unresolved, they are considered as components of a single $K\alpha$ doublet line.

2.1.1.3 Synchrotron Radiation Source

In a synchrotron, a beam of electrons is accelerated to nearly the speed of light and is made to circulate on a closed orbit under high vacuum in a storage ring. The closed orbit is achieved by bending the path with a series of *bending magnets* placed along the ring circumference. In some facilities, positrons, instead of electrons, are used. The circumference of the storage ring ranges from about 50 to over 1000 m, and the electron beams are accelerated typically to an energy on the order of GeV. A charged particle that is accelerated emits electromagnetic radiation, and bending is a form of acceleration. The radiation emitted by the orbiting electrons covers an extremely broad range of the electromagnetic spectrum. The flux of x-rays emitted is many orders of magnitude greater than that obtainable with conventional x-ray tubes, making the

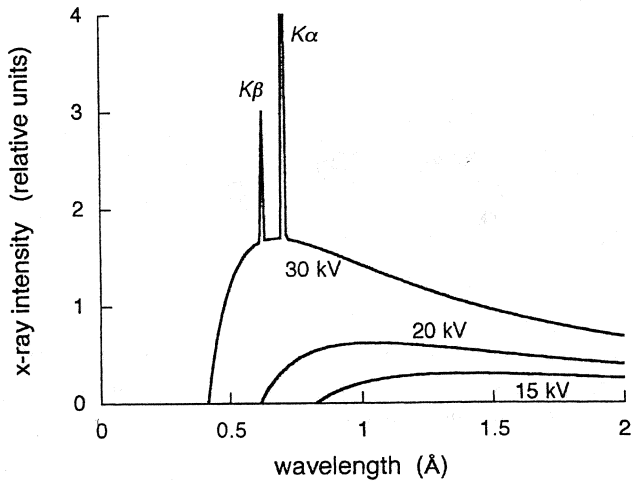

Figure 2.3 X-Ray spectrum of molybdenum as a function of applied voltage (schematics). The spectral line widths are not to scale. The $K\alpha$ doublet consists of unresolved $K\alpha_1$ and $K\alpha_2$ lines, with the former about twice as intense as the latter.

TABLE 2.1
Wavelengths and Relative Fluxes of Characteristic Lines

Target	Excitation Voltage (kV)	Line	Wavelength (Å)	Relative Flux
Cu	8.98	$K\alpha_1$	1.5405	1
		$K\alpha_2$	1.5443	0.497
		$K\beta_1$	1.3922	0.200
Mo	20.0	$K\alpha_1$	0.7093	1
		$K\alpha_2$	0.7135	0.499
		$K\beta_1$	0.6323	0.279

Data from *International Tables for Crystallography*.[6]

required time for any single measurement very short and therefore allowing rapid time series measurements with samples undergoing dynamic evolution.

Figure 2.4 illustrates schematically the major components of the storage ring.

1. The *injection system* (**IS** in Figure 2.4), which generates electrons, accelerates them, and injects them into the vacuum chamber.
2. The *vacuum chamber*, i.e., the metal tube in which the electrons circulate along a closed trajectory. The vacuum is maintained at $10^{-10} \sim 10^{-11}$ Torr.
3. The *radiofrequency cavity* system (**RF** in Figure 2.4), which acts on the circulating electrons and restores the energy they lose through the emission of electromagnetic radiation.
4. The *bending magnets* (**BM** in Figure 2.4), which bend the trajectory of the electrons and force them to circulate in a closed orbit.

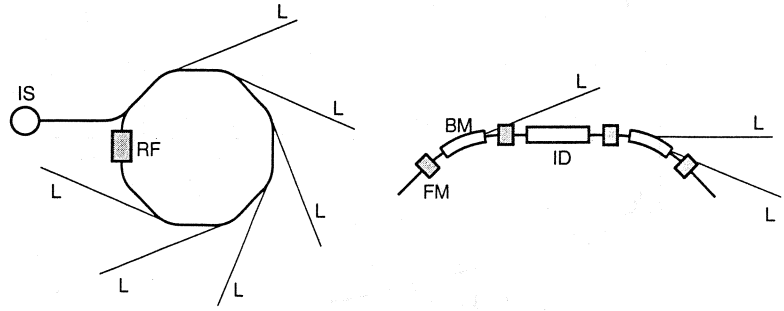

Figure 2.4 Schematics of a synchrotron radiation facility. The closed circuit on the left represents the storage ring. IS, injection system; RF, radiofrequency cavity; L, beamline; BM, bending magnets; FM, focusing magnets; ID, insertion device.

5. The *focusing magnets* (**FM** in Figure 2.4), which fine tunes the electron beam trajectory to keep the electrons within a narrow range of a defined path.
6. The *beam lines* (**L** in Figure 2.4) through which the electromagnetic radiation exits into the user's experimental chambers.
7. The *insertion devices* (**ID** in Figure 2.4), which are additional devices, such as *wigglers* and *undulators*, inserted into straight sections of the ring. They further modify the electron trajectories from a straight line, and thereby induce emission of additional synchrotron radiations, as explained shortly.

Emission Spectrum. The spectral distribution of synchrotron radiation is extremely broad, ranging from the infrared ($\lambda \sim 10^{-2}$ cm) to the hard x-ray ($\lambda \sim 10^{-2}$ nm). The spectrum depends on the energy E of the circulating electron beam in the storage ring and the radius of curvature R of its trajectory. The whole spectrum shifts toward shorter wavelengths as the energy E of the beam is increased and as its path is more tightly bent (making R smaller). Figure 2.5 shows the spectral distributions at three different electron beam energies E, calculated for $R = 12.7$ m. The position of the spectral curve along the wavelength axis can be characterized by the value of the *critical wavelength* λ_c, which is indicated by the small vertical bar on each curve in Figure 2.5. The critical wavelength λ_c is defined so that half of the entire radiated power is contained in the radiations with wavelengths smaller than λ_c. It is related to R and E by

$$\lambda_c = \left(\frac{4}{3}\pi m^3 c^3\right)\frac{R}{E^3} \tag{2.3}$$

where m is the rest mass of an electron and c is the speed of light. The numerical value of the quantity within the parentheses is equal to 5.6 when R, E, and λ_c are in m, GeV, and Å, respectively.

Angular Divergence and Source Size. At relativistic speed, the electrons forced along a curved path emit radiation that is sharply concentrated in the direction of their

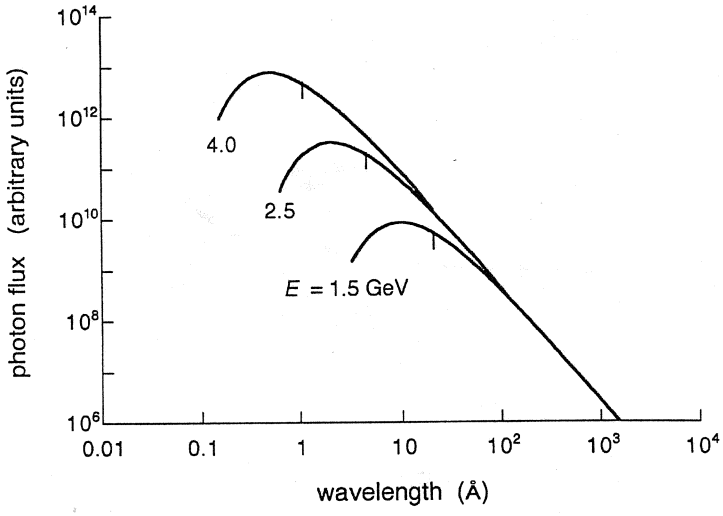

Figure 2.5 Spectral distribution of the radiation emitted by a storage ring, calculated for the radius of curvature R equal to 12.7 m, and the energies E of the circulating electron beam as indicated. The vertical bars identify the critical wavelength λ_c.

motion. The radiation emerging from the storage ring therefore has a very small angular divergence in the direction perpendicular to the plane of the electron orbit. The vertical divergence $\Delta\psi$ (see Figure 2.6) is of the order of mc^2/E. Since mc^2 is equal to 5.11×10^{-4} MeV, $\Delta\psi$ is only a fraction of a milliradian when the electron energy is in the GeV range. The synchrotron radiation is thus highly collimated as it emerges. To make the apparent source size small, the spread of the orbiting electrons in the circulating beam in the storage ring is also kept very small by means of a series of focusing magnets, designated **FM** in Figure 2.4. As a result, the radiation emitted from the storage ring not only has an overall high flux of photons, but also a high brightness (that is, a high photon flux per unit source area). The small apparent source size is important, since it permits, among others, the use of very small samples.

Polarization. The emitted synchrotron radiation is also highly polarized. For those x-rays emitted in the plane of the electron orbit, that is, in the direction $\psi = 0$, the radiation is completely linearly polarized, with the electric vector of the radiation parallel to the electron orbit. For the x-rays emerging in the direction not exactly on the orbital plane, that is, $\psi \neq 0$, the radiation is elliptically polarized, with a small vertically polarized component present. The polarization factor given in Equation (1.35) for the scattering of x-rays from an electron is valid only for unpolarized incident x-rays and has to be suitably modified for measurements with synchrotron radiation.

Wigglers and Undulators. The beam orbit in a storage ring is not circular and consists instead of an alternating sequence of straight sections and curved sections,

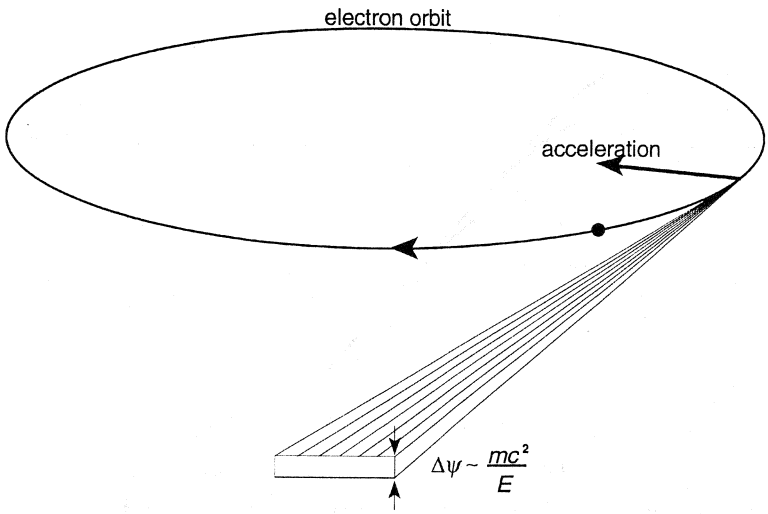

Figure 2.6 Angular distribution of the radiation emitted by an electron circulating at a speed close to the speed of light. The radiation emerges tangential to the electron orbit, and the vertical divergence of the radiation is very small and is inversely proportional to the energy E of the circulating electron.

the latter equipped with bending magnets (**BM** in Figure 2.4). The straight sections can accommodate so-called insertion devices (**ID** in Figure 2.4) that locally modify the beam path. To see the function of these insertion devices, let us look at the simple three-magnet sequence shown in Figure 2.7, in which the polarity of the central magnet is opposite to that of the other two. This device "wiggles" the path of the electrons, forcing them through a trajectory with a small radius of curvature, while leaving the overall direction of the beam unchanged. This wiggle induces an emission of radiation, which is independent of the radiation produced by the action of the bending magnets. The radius of curvature of such a wiggled path depends on the strength of the wiggler magnets used, and therefore the spectrum of the radiation produced by such a device can be made very different from that of the bending magnet radiation. In practice, a *wiggler* consists of a series of magnets of alternating polarities that are placed in succession. The total flux from a wiggler is the sum of the emissions from each magnet, only if, of course, the radiations emitted by successive wiggler magnets do not interfere with each other, which is true with wigglers as they are designed in practice. However, in the type of insertion devices called *undulators*, the angle of deflection of the electron trajectory from the straight line is kept small compared to mc^2/E, and in this case the emissions from successive magnets retain coherence and interfere with each other. The result of the interference is to enhance the intensity in certain regions of wavelengths at the expense of other regions, and with a sufficient number of magnets, the spectrum becomes concentrated to a single or a few narrow, strong lines.

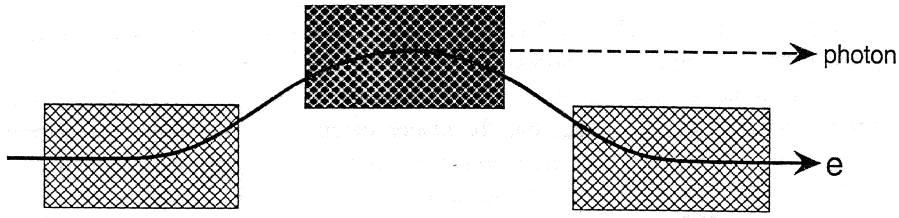

Figure 2.7 Schematics illustrating how a sequence of three magnets forces an electron trajectory to deviate momentarily from a straight line and thereby induces emission of radiation.

2.1.2 Neutron

Nuclear reactors are by far the most commonly available source of neutrons for scattering experiments. The flux of neutrons emanating from the reactor is steady in time. As explained in Section 2.1.2.3, there are other neutron sources available, in which neutrons are produced as a rapid sequence of very short, intense pulses. Such pulsed neutrons are particularly well suited for the time-of-flight method of measuring the energy (or wavelength) of neutrons. Since, for every neutron in a single pulse, the departure time from the source is essentially identical, determining its time of arrival at the detector gives information about the energy change it suffered in inelastic scattering. It is possible to create such a pulsed stream of neutrons by intercepting a steady neutron flow with a rotating chopper, but only by wasting a large fraction of the initially available neutrons.

2.1.2.1 Nuclear Reactor

In the nuclear reactor a sustained nuclear fission reaction takes place in the fuel rods of enriched ^{235}U and produces fast neutrons with energy in the 1–2 MeV range. Aside from the fuel itself, three other elements of the nuclear reactor are of direct concern to the users of the neutron beam. They are the moderators, which slow down the speed of the neutrons to usable ranges, the radiation shield, which protects the users, and the neutron guides, which bring the neutron flux to the area where the measuring instruments are installed. A thick concrete wall surrounds the reactor core, the moderators, and other control elements of the reactor and protects the users in adjoining chambers from harmful effects of radiation. The radiation shield is also important to minimize the background count due to stray neutrons and gamma rays. The neutron flux is led out from the vicinity of the moderator to the user instrument area by means of neutron guides that pass though the thick shield wall.

In the reactor core the fuel rods are surrounded by a thermal moderator, usually a pool of D_2O, which also acts as coolant and is maintained at near ambient temperature (for example, 50°C). The neutrons repeatedly collide with the atomic nuclei in the moderator, and their average energy is reduced to that corresponding to the thermal motion at the moderator temperature. As is shown in Table 1.1, at $T = 57°C$ (330 K), the thermal energy amounts to 38 meV, which corresponds to 2000 m/s in speed, or

1.7 Å in de Broglie wavelength. Neutrons with a different average wavelength can be produced by having a small moderator placed near the reactor core and maintained at a much higher or lower temperature. Thus a container of liquid H_2 or D_2 or solid methane a few liters in volume may be placed close to the core where the neutron flux is high and maintained at a temperature around 25 K through circulation of liquid helium coolant. The neutrons from such a cold source emerge with a reduced average speed of about 600 m/s, which corresponds to an average wavelength of around 6 Å. Similarly, a hot source is a moderator, usually a block of graphite maintained at about 2000 K by the heat of the radiation only, that shifts the spectrum of neutrons to shorter wavelengths.

2.1.2.2 Neutron Guide

To serve as many scientific experiments as possible with a single reactor source, the measurement instruments are placed around the reactor some distances away from the core. This creates a need to channel the neutron beams from the moderator to the instruments without losing their strength. In the case of the synchrotron, emitted x-rays are already highly collimated, and a straight beamline is all that is necessary. Neutrons from a reactor core or a moderator, however, emerge in all directions with equal probabilities, and unless some special measures are taken, the neutron flux (the number of neutrons per second through a unit cross-sectional area) decreases as the inverse square of the distance. This difficulty is alleviated by the use of a *neutron guide*. The guide is an evacuated tube with thick glass walls and a rectangular cross section of the order of 10×10 cm^2. The inner surface is coated with an evaporated layer of nickel about 1000 Å thick. The function of the guide tube is based on the principle of total internal reflection.

In Figure 2.8 a ray of radiation is traveling from medium 1 of a higher refractive index toward medium 2 of a lower refractive index. At the interface, in general, part of the beam is refracted into medium 2 and the rest is reflected back into medium 1. However, if the angle θ_1 of incidence at the interface is smaller than some critical angle θ_c, the beam is totally reflected without any loss of energy. In optical fibers light is confined within the glass medium because the refractive index of glass is higher than that of air. For x-rays and neutrons, the refractive index n of any (nonabsorbing) material medium is slightly less than unity, and is given by

$$n = 1 - \frac{1}{2\pi}\rho\lambda^2 \tag{2.4}$$

where ρ is the scattering length density (equal to the product of the scattering length b of an atomic nucleus and its number density). For a ray traveling in a vacuum and hitting the surface of a material the critical angle θ_c is therefore given by

$$\theta_c = \cos^{-1} n = \left(\frac{\rho}{\pi}\right)^{1/2} \lambda \tag{2.5}$$

(See Section 7.2 for a more extended discussion of the reflection of x-rays and neutrons at an interface.) For nickel, which has the largest scattering length density among commonly available metals, $(\rho/\pi)^{1/2}$ is equal to 1.73×10^{-3} Å^{-1}. The critical angle

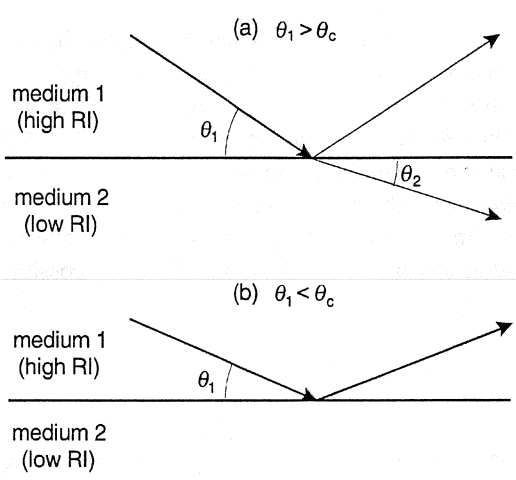

Figure 2.8 Schematics illustrating total reflection. A ray of radiation is traveling from medium 1 of higher refractive index (RI) to medium 2 of lower refractive index. If the incident angle θ_1 of the ray striking the interface is smaller than the critical angle θ_c, all the energy of the ray is reflected back to medium 1. The critical angle θ_c is equal to $\cos^{-1}(n_2/n_1)$, where n_1 and n_2 are the refractive indices of the two media.

for neutrons of $\lambda = 5$ Å, for example, is thus equal to 8.6 mrad or about 0.5°. All the neutrons entering the guide tube at angles smaller than θ_c travel unmodified along the guide through repeated reflections at the walls, as long as the tube is straight and the wall surfaces are very smooth. By making the tube slightly curved, it is also possible to make short wavelength neutrons, for which $(\rho/\pi)^{1/2}\ \lambda$ is too small, fail to be transmitted. This aids suppressing the background of fast neutrons reaching the measurement instruments.

2.1.2.3 Pulsed Neutron Source

There are two types of nuclear reactions that are used for the production of pulsed neutrons. One is the photoneutron production from electrons and the other is the spallation of atomic nuclei by protons. In the *electron linear accelerator source*, electrons accelerated to a high energy (up to 100 MeV) in a linear accelerator are aimed at a heavy metal target, usually ordinary uranium or depleted uranium (uranium from which ^{235}U has been almost completely depleted). The sudden deceleration of electrons produces γ-rays, in exactly the same way as white radiation is generated in an x-ray tube. Some of the produced γ-rays induce photoneutron reactions, in which the γ-ray excites a target nucleus that subsequently decays with the emission of a neutron. Accelerating electrons is relatively cheap, and the technology is well established, but the process suffers from inefficiency, yielding only about 5 neutrons for every 100 electrons, and most of the energy of the electrons is dissipated as heat that must be removed by cooling. In the *proton spallation source*, a much heavier particle, a proton, is accelerated in a linear accelerator, a synchrotron, or a combination of the two, to a much higher energy, for example, 800 MeV. When such a particle strikes a heavy metal target (such as uranium or tungsten), neutrons are literally chipped off the target nuclei, as the word *spallation* implies. The efficiency is high, each proton yielding about 30 neutrons. Moreover, the depth of penetration of protons is up to tens of centimeters, so that the heat is dissipated over a larger volume of the target metal, lessening the problem of cooling the target.

These pulsed sources produce extremely fast neutrons, which have to be slowed down for scattering measurements. Moderators are placed around the target and are aided by reflectors that direct neutrons toward the moderators. When initially produced, the pulse has an extremely short duration, on the order of a microsecond, but repeated collisions within the moderator broaden the pulse width considerably. The neutrons are often left *undermoderated,* with their effective temperature remaining higher than the moderator temperature. In this way a compromise is sought between the need for relatively short pulse widths and the desire for as much flux as possible in the useful wavelength range.

2.2 MONOCHROMATIZATION

Most of the diffraction and scattering techniques used in the study of polymers require an x-ray or neutron radiation that is essentially monochromatic. All the radiation sources discussed above, however, produce a broad spectrum of wavelengths, and a means of admitting only a very narrow range of wavelengths while discarding the rest of the spectrum is needed. A crystal monochromator performs well in this regard. A narrowly limited range of wavelengths can be selected by reflecting the beam from a selected crystallographic plane in a single crystal. However, the beam flux is considerably weakened as a result of this process. In the case of neutrons, another equally important method available for monochromatization is the selection of neutrons according to their velocities by a mechanical means. In the case of x-rays the characteristic $K\alpha$ line from a tube is sufficiently narrow and strong already for most measurement purposes, except that the contamination by the $K\beta$ line and the white radiation must still be eliminated. As an aid to monochromatization a filter is convenient and widely used, especially for x-rays, and allows the transmission of radiation in some broad region of the spectrum to be severely curtailed. The functioning of filters will be discussed in Section 2.3.3 after some general aspects of absorption of x-rays and neutrons have been described. Electronic discrimination of the energies (and hence the wavelengths) of x-ray photons detected by a detector also plays some limited role in preventing unwanted radiation from being registered, as will be discussed in Section 2.4.

2.2.1 Crystal Monochromator

When a beam of white radiation impinges, as in Figure 2.9a, on a crystal with its surface cut parallel to a crystallographic plane (*hkl*), reflection can take place only for the component of the beam having a single wavelength λ that satisfies the Bragg relation

$$2d \sin\theta = \lambda \tag{2.6}$$

where d is the spacing of the (*hkl*) planes. The wavelength λ can be selected, as desired, by setting the crystal so that the incident beam strikes it at a glancing angle θ that meets the condition (2.6). The same aim can be accomplished by cutting the

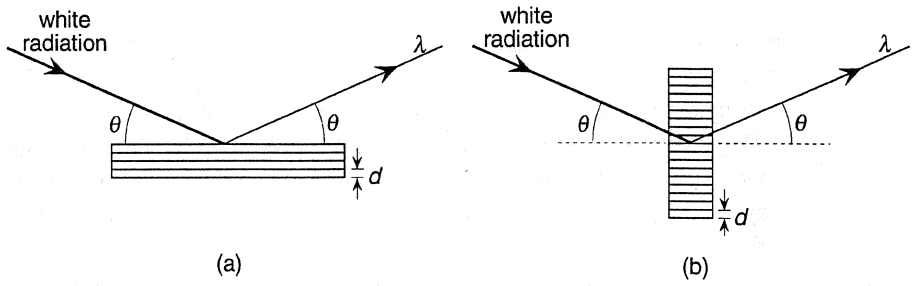

Figure 2.9 Crystal monochromator in reflection geometry (a) and transmission geometry (b). The incident beam is drawn with a thick line to indicate that it contains a continuous spectrum, whereas the reflected beam, containing a single wavelength, is drawn with a thin line.

monochromator crystal with its faces perpendicular to the (*hkl*) plane, as in Figure 2.9b. Such a transmission geometry is preferable only when the attenuation of the beam through absorption is minor, as is more often the case with neutrons.

The monochromator crystal, set to reflect the wavelength λ from the (*hkl*) planes, will also simultaneously reflect the radiation of wavelengths λ/n ($n = 2, 3, \ldots$) from the (*nh,hk,hl*) planes. The spectral distribution in the incident beam is often such that the reflected beam at wavelengths equal to $\lambda/2$, $\lambda/3$, etc. is very weak, and this poses no serious problem. Otherwise, a filter (or pulse height discrimination in the case of x-rays) may eliminate much of such higher order contaminations. In any case, it is desirable that the crystal be chosen with an eye not only for a high reflectivity at the chosen (*hkl*) plane but also for a low (or absence of) reflectivity at the (2*h*,2*k*,2*l*) plane. For example, when (111) is chosen as the reflecting plane with a germanium crystal, the reflection from (222) is forbidden by the crystal symmetry.

If the monochromator crystal is perfect, and if, at the same time, the incident beam is perfectly collimated to have only parallel rays, then at any given setting of the crystal there is only one wavelength λ that satisfies the Bragg condition (2.6). The flux of the beam that is reflected under these conditions would be very low and would not be sufficient to allow useful measurement. Fortunately, the incident beam in practice contains a certain degree of divergence (i.e., misorientation of individual rays from the average direction). The crystal is also rarely a perfect single crystal. In fact a good monochromator crystal is required to possess a degree of mosaic spread sufficient so that in effect it consists of an assembly of mosaic blocks, each displaced in its orientation from others by a small degree. The combined effect of the beam divergence and the mosaic spread is to make the reflected beam much stronger, as is diagrammed in Figure 2.10. Figure 2.10a depicts the idealized case in which the incident beam of white radiation is perfectly collimated and the crystal is also perfect. In Figure 2.10b the incident beam has a directional divergence, where α represents the extent of misorientations present. The reflected beam is also divergent to the same extent, since each ray in the beam, striking the crystal at an incident angle slightly different from θ, still satisfies the Bragg condition for a wavelength

slightly different from λ. In Figure 2.10c, the mosaic spread present in the crystal is equivalent to having a perfect single crystal rocked over an angular range β. With a perfectly collimated incident beam impinging, the reflected beam is spread over a range 2β. The individual ray in the reflected beam still contains only a single wavelength and is thus of low flux. In Figure 2.10d both effects are present. If the central ray in the reflected beam is taken as a representative example, it is readily seen that it contains a band of wavelengths ranging from $2d \sin(\theta - \alpha/2)$ to $2d \sin(\theta + \alpha/2)$ (provided $\beta > \alpha/2$), and the overall flux is now orders of magnitude greater.

The monochromator crystal need not always be flat as illustrated in Figures 2.9 and 2.10 but may be bent or otherwise shaped in such a way to have the reflected rays from different parts of the crystal focus at a single line or a single point. In this way a large gain in the monochromatized beam flux can be achieved. There are a

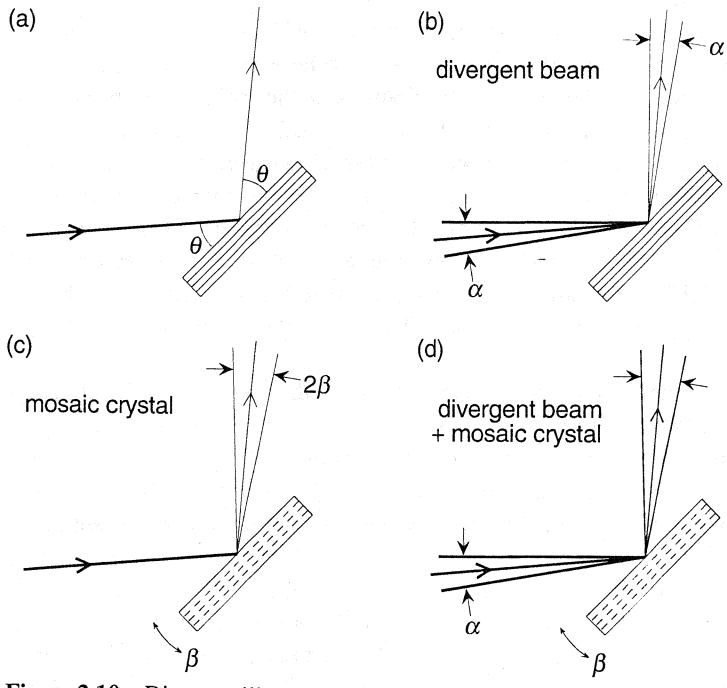

Figure 2.10 Diagrams illustrating the combined effect of beam divergence and crystal mosaic spread. In (a) a beam of white radiation, perfectly collimated, impinges on a perfect single crystal, and gives rise to a reflection containing a single wavelength λ. In (b) a divergent incident beam gives rise to a reflected beam, which is again divergent, with each ray in it still containing a single wavelength. In (c) a crystal with a mosaic spread is equivalent to having a single crystal rocked over the angular range β. A perfectly collimated beam can give rise to a divergent beam of spread equal to 2β. Each ray in the beam still contains a single wavelength. In (d), with both effects present, each reflected ray contains a band of wavelengths, rendering the overall flux much greater.

number of different focusing arrangements possible, depending on the way the crystal is shaped and on the geometry of the sample and the camera or diffractometer used. The article by Roberts and Parrish[7] discusses many of these possible arrangements. One illustrative example is the Johansson crystal. The crystal, with its surface initially cut parallel to the reflecting planes, is bent cylindrically at radius $2R$, and its surface is then further ground to cylindrical radius R, where R is the radius of the focusing circle shown in Figure 2.11. A spreading beam of radiation emanating from a line source (long in the direction perpendicular to the plane of the drawing), such as the line focus of an x-ray tube, is allowed to illuminate a fairly wide area of the bent and ground crystal. Due to a geometric property of a circle, the reflected rays all converge to a single line (parallel to the line source). In this way a considerable enhancement in the reflected beam flux as a whole can be achieved, provided of course that the diffractometer is designed to make full use of the monochromatic beam diverging from the line-shaped focus.

2.2.2 Neutron Velocity Selector

X-Rays have the same velocity as light irrespective of the wavelength. The velocity of a neutron, on the other hand, depends on its wavelength and varies as $h/m\lambda$, as given by Equation (1.8). Monochromatization of neutrons can therefore be achieved

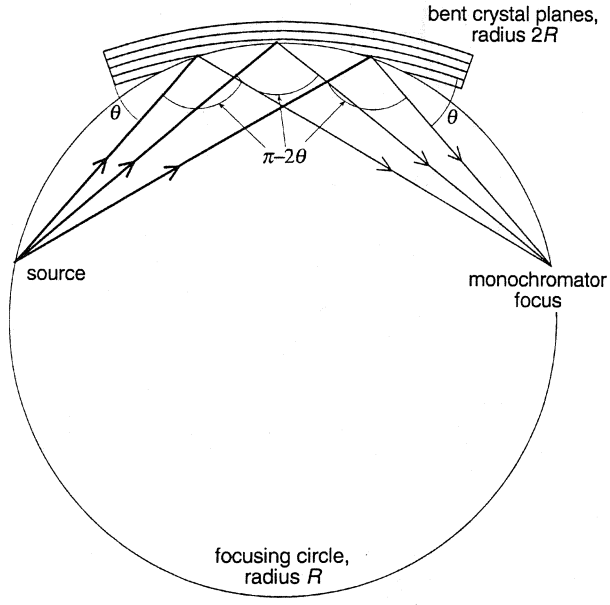

Figure 2.11 Focusing monochromator, using a bent and ground crystal.

with a device that selects neutrons according to their velocity. The numerical value of h/m is equal to 4.0×10^{-7} m^2/s, so that for a neutron of 4 Å in λ, the velocity is about 1000 m/s, far below the speed of light, and in the range quite manageable by mechanical means. Figure 2.12a illustrates the principle of one of such devices. Two disks opaque to neutrons rotate on the same axis parallel to the neutron beam. A small opening in the first disk periodically chops the neutron beam, yielding a pulse of "white" neutrons. Neutrons within the pulse arrive at the second disk at different times according to their velocities. The opening in the second disk allows only neutrons of a selected band of velocities to pass. The time delay between the two openings and hence the wavelength selected depends on the phase lag between the first and second choppers, the distance between them, and the speed of their rotation. The so-called mechanical velocity selector is an extension of this method. It consists of a cylinder rotating about an axis that is parallel to the neutron beam, and the cylinder contains helical slots cut along its curved surface where it intersects the beam. Only neutrons with the correct velocity can travel along the slots without being absorbed. Another design of the velocity selector is illustrated in Figure 2.12b. Here the axis of rotation of the curved slot rotor is perpendicular to the direction of the neutron flux, and a steady beam of "white" neutrons is again chopped into pulses of monochromatic neutrons.

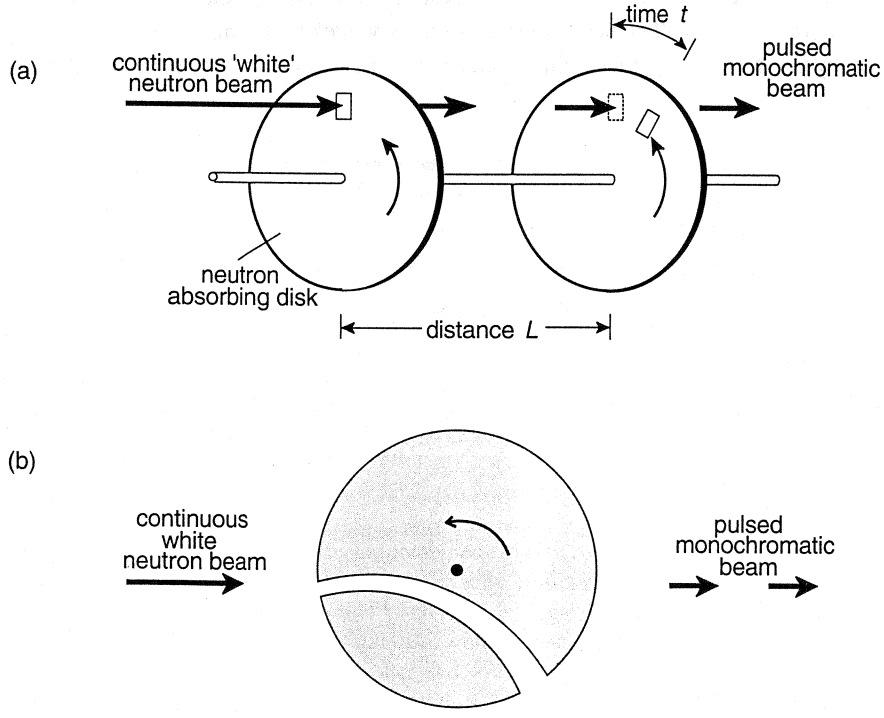

Figure 2.12 (a) Schematic diagram illustrating the principle of neutron wavelength selection on a continuous neutron source by use of mechanical choppers and the neutron time of flight. (b) Curved slot rotor: another design for neutron velocity selection.

2.3 ABSORPTION

2.3.1 Absorption Coefficient

When radiation impinges on a sample, a fraction of the incident beam is scattered (either elastically or inelastically), and the x-ray photons or neutrons thereby change their direction of propagation. Another fraction of the particles is absorbed, through conversion of their energy into other forms of energy. The transmitted beam, which is unmodified and propagates in the original incident direction, is of lower flux as a result of both the scattering and absorption processes. Absorption of x-rays occurs mostly through photoionization of atoms in the sample, with ejection of electrons from their inner atomic shells. The excited atoms may subsequently decay with emission of other radiation, as in the case of x-ray fluorescence. Absorption of neutrons results from the capture of neutrons by atomic nuclei with excitation of the latter, followed often by emission of secondary radiation that is not normally detected in the scattering measurement.

The efficiency at which an atom absorbs x-rays or an atomic nucleus absorbs neutrons can be expressed several ways. The more fundamental way of expressing it is in terms of the *absorption cross section* σ_{abs}, which is defined as *the number of photons (or neutrons) absorbed per second by an atom (or a nucleus), divided by the flux of the incident radiation*. Since the flux is the number of particles passing through unit area per second, σ_{abs} has the dimension of area, usually given in barns (10^{-24} cm^2).

The efficacy of absorption by a material depends on the density of its atoms as well as on the absorption cross section of individual atoms. The absorption cross section Σ_{abs} *per unit volume* of the material is then given, in the case of a monatomic substance, by

$$\Sigma_{abs} = \sigma_{abs} n = \sigma_{abs} \frac{\tilde{\rho}}{m} N_A \tag{2.7}$$

where n is the number density of atoms, m is the atomic mass, $\tilde{\rho}$ is the mass density of the material, and N_A is Avogadro's number. Σ_{abs} has dimension of inverse length, and is more commonly referred to as the *linear absorption coefficient* μ. It denotes the probability of a photon (or neutron) being absorbed while traversing the material to the depth of a unit length. In other words, $1/\mu$ is the mean free path of the photon (or neutron) in the material. The radiation, initially of flux J_0, will emerge, after passage through the material of thickness x, with flux J_x given by

$$J_x = J_0 e^{-\mu x} \tag{2.8}$$

For a given type of radiation (and wavelength), σ_{abs} is an intrinsic property of the element, whereas Σ_{abs} ($\equiv \mu$) is a property of the particular material sample, being dependent on its mass density $\tilde{\rho}$ and therefore on temperature and whether the sample is crystalline or amorphous, etc. X-Ray literature usually cites, instead of σ_{abs}, the *mass absorption coefficient* $\mu/\tilde{\rho} (= \sigma_{abs} N_A/m)$, which is the absorption cross section per *unit mass*, an intrinsic property of the element.

The process of absorption of x-rays or neutrons is not affected by the state of bonding of the atoms in the material, and therefore for a material consisting of more than one element, the overall absorption coefficient depends only on the relative numbers of various atoms present in it. Thus the linear absorption coefficient of a sample can be calculated by

$$\mu = \tilde{\rho} \sum_j \left(\frac{\mu}{\tilde{\rho}}\right)_j w_j \tag{2.9}$$

where $\tilde{\rho}$ is the overall mass density of the sample, and $(\mu/\tilde{\rho})_j$ and w_j are the mass absorption coefficient and weight fraction of the jth atomic component in the sample. The values of σ_{abs} and $\mu/\tilde{\rho}$, for both x-rays and neutrons, of some of the atoms commonly encountered in the study of polymers are listed in Table 2.2. The table also includes four elements, lithium, boron, cadmium, and gadolinium, that are unusually high absorbers of neutrons. The numbers there show clearly that neutrons are generally far more penetrating than x-rays through matter.

TABLE 2.2
Absorption Coefficients for X-rays and Neutrons

Element	Atomic Number	Absorption Cross-Section σ_{abs} (10^{-24} cm^2)		Mass Absorption Coefficient $\mu/\tilde{\rho}$ (cm^2/g)	
		x-Ray	Neutron	x-Ray	Neutron
H	1	0.655	0.3326	0.391	0.199
D	1		0.00051		0.00015
Li	3	5.76	70.5	0.500	6.12
Be	4	16.6	0.0076	1.11	0.00051
B	5	41.5	767	2.31	42.7
C	6	89.9	0.0035	4.51	0.00018
N	7	173	1.90	7.44	0.0817
O	8	304	0.00019	11.5	7.2×10^{-6}
F	9	498	0.0096	15.8	0.000304
Na	11	1140	0.530	29.7	0.0139
Al	13	2220	0.231	49.6	0.00516
Si	14	2970	0.171	63.7	0.00367
P	15	3880	0.172	75.5	0.00335
S	16	4970	0.53	93.3	0.0100
Cl	17	6240	33.5	106	0.569
K	19	9400	2.1	145	0.0324
Fe	26	28000	2.56	302	0.0276
Ni	28	4760	4.49	48.8	0.0461
Cu	29	5470	3.78	51.8	0.0358
Cd	48	41500	2520	222	13.50
Gd	64	105000	48890	403	187.2
Pb	82	79800	0.171	235	0.00050

[a] The absorption values for x-rays are for the Cu$K\alpha$ radiation ($\lambda = 1.542$ Å), and those for neutrons are for $\lambda = 1.8$ Å. The neutron data are from Bée[8] and are for the elements with the natural abundance of isotopes, except for H and D. The x-ray data are from the *International Tables of Crystallography*.[9]

Strictly speaking, Equation (2.8), which describes the attenuation of the transmitted beam, is true only when the loss of flux due to scattering is negligible in comparison to the loss due to absorption. If the fractional *transmission* $T = J_x/J_0$ through a sample of thickness x is measured and the apparent linear absorption coefficient μ_{app} is evaluated as $-(\ln T)/x$, one should write

$$\mu_{app} = \mu_{abs} + \mu_{scat} \tag{2.10}$$

where μ_{abs} is the linear coefficient of true absorption and μ_{scat} is the total scattering cross section per unit volume. For x-rays μ_{abs} is much greater than μ_{scat}, whereas for neutrons the reverse is true with most elements, except with a few highly absorbent ones, such as boron.

2.3.2 Wavelength Dependence

The absorption cross section σ_{abs} and the linear absorption coefficient μ are highly wavelength dependent. The values given in Table 2.2 are for $\lambda = 1.54$ Å in the case of x-rays and for 1.8 Å in the case of neutrons. The absorption cross section for neutrons is always proportional to λ, with a few exceptions in the form of resonance capture peaks observed with elements of no concern to polymer studies. Therefore the values in Table 2.2 for neutrons can easily be converted to other wavelengths. In the case of x-rays, the absorption also increases in general with wavelength approximately as λ^3, but the smoothly varying curve of μ vs. λ is frequently interrupted by a discontinuous change. Such an *absorption edge* is illustrated in Figure 2.13 where the mass absorption coefficient $\mu/\tilde{\rho}$ of Ni is plotted against the wavelength. The wavelength at which the absorption edge occurs is characteristic of the absorbing element, and the existence of absorption edges is easily explained as follows. The absorption of x-rays occurs as a result of photoionization of atoms, that is, ejection of one or more electrons from the atomic orbitals. As the wavelength of the x-rays is gradually increased (or as the energy of the photons is reduced), the probability of interaction of the photons with the electrons is enhanced, and the absorption coefficient becomes larger. With further increase in the wavelength, the photon energy eventually falls below the binding energy of K electrons, which are then no longer ejected. At this K absorption edge (1.488 Å for Ni) therefore the mass absorption coefficient exhibits an abrupt decrease. If the data beyond $\lambda = 2.5$ Å were plotted in Figure 2.13, we would find that the λ^3 branch beyond the K edge would be interrupted again by L_I, L_{II}, and L_{III} absorption edges, at wavelengths corresponding to the binding energy of the subshells of L electrons. Both the absorption edge of a metal and the characteristic radiation emitted by the target metal in an x-ray tube are related to the electronic energy levels of the metal atom. Whereas the absorption edge reflects the binding energy of an electron directly, the characteristic radiation is determined by the difference between two energy levels.

2.3.3 Filters

When the characteristic $K\alpha$ radiation from an x-ray tube is used as the radiation source, it is necessary, unless a crystal monochromator is used, to remove as much of

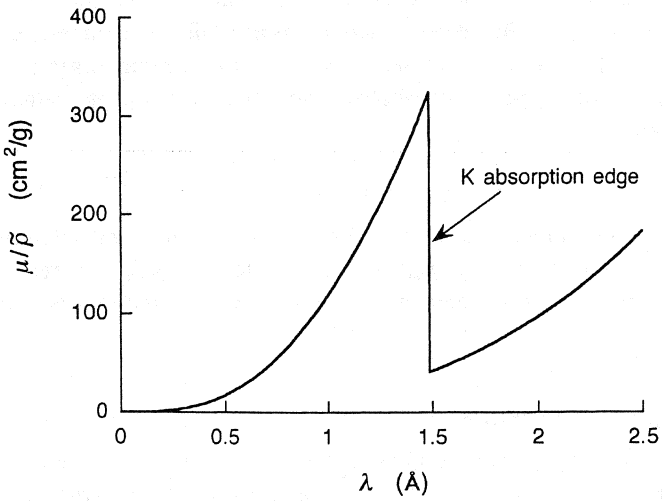

Figure 2.13 Variation with wavelength of the x-ray mass absorption coefficient of nickel. The K absorption edge is at $\lambda = 1.488$ Å.

the $K\beta$ line as possible by use of a so-called β filter. The K absorption edge of nickel is at wavelength 1.488 Å, which lies between the Cu$K\alpha$ line of wavelength 1.542 Å and the Cu$K\beta$ line of wavelength 1.392 Å. The mass absorption coefficient of nickel for x-rays at these two wavelengths is 445 and 2690 cm^2/g, respectively. Therefore, by inserting a foil of nickel in the beam path of x-rays from a copper tube, the $K\beta$ line intensity can be reduced substantially while attenuating the $K\alpha$ line intensity only moderately. With a nickel foil of thickness 20 μm, the intensity ratio of Cu$K\beta$ to Cu$K\alpha$, originally 1/7.5 at the target, can be reduced to about 1/500, whereas the Cu$K\alpha$ line itself is attenuated only 60%. In the case of a molybdenum target tube, a zirconium foil can serve as the β filter.

The so-called *polycrystalline filter* can be used to restrict the transmission of neutrons of wavelength below a certain threshold. It operates by a mechanism entirely different from that of x-ray filters. A neutron beam, passing through a fairly thick (20 $\sim$ 40 cm) block of a polycrystalline material, suffers repeated diffractions by the various crystal planes in it, and the transmitted beam is greatly attenuated as a result. Because there are many lattice planes with different d_{hkl} values and because the crystals are oriented in all directions, the Bragg condition is satisfied with neutrons of any wavelength, as long as the wavelength is shorter than a limiting value λ_{max}. The upper limit λ_{max} is set by the largest spacing d_{max} available in the crystal and the largest diffraction angle possible $\theta_{max} = 90°$ and is therefore equal to $2d_{max}$. Because the true absorption cross section of most elements for neutrons is very small, as is seen in Table 2.2, neutrons with wavelength longer than λ_{max} are transmitted with little attenuation. Figure 2.14[10] gives the total scattering cross section of polycrystalline Be at 77 K plotted against wavelength. It has a sharp cutoff at 3.96 Å. Be metal is

particularly suited for this type of filter because of its high scattering cross section and low absorption cross section. Used in conjunction with a crystal monochromator, such a filter is suitable for removal of higher order harmonics, if the fundamental wavelength selected is longer than 3.96 Å, as is the case with a pyrolytic graphite monochromator.

2.4 DETECTORS

Historically fluorescent screens and photographic film have long been the primary means of detecting x-rays. Fluorescent screens are made of a thin layer of zinc sulfide, containing a trace of nickel. Irradiated with an x-ray beam, this compound fluoresces and emits faint yellow light. A photographic film leaves a permanent record of exposure to x-rays and, when used in conjunction with a microdensitometer, it can provide a nearly quantitative measure of the relative intensities of different diffraction spots recorded on a single sheet of film.

Electronic counters are devices in which absorption of an x-ray photon or a neutron generates a short electric pulse in the associated electronic circuitry. By "counting" the rate of generation of such pulses, the flux of the x-ray or neutron beam to which the device is exposed can be measured. These counters are the outgrowth of the initial efforts made by nuclear physicists for detection of radioactivities of materials. Most useful among them for x-ray and neutron scattering studies are the proportional and scintillation counters described in Section 2.4.1. Further elaboration on these counters led to the development of position-sensitive detectors, explained in Section 2.4.2. Very recently, a number of novel devices based on new technologies have become available, and these are briefly introduced in Section 2.4.4.

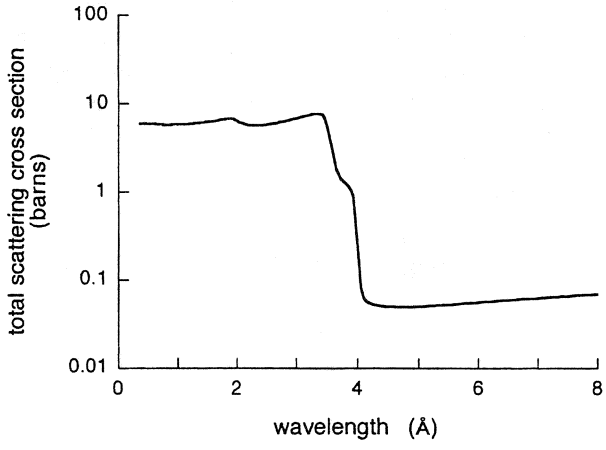

Figure 2.14 The total scattering cross section of polycrystalline beryllium at 77 K, showing the sharp cutoff at $\lambda_{max} = 3.96$ Å. (From Stirling.[10])

2.4.1 Proportional and Scintillation Counters

2.4.1.1 Proportional Counter

The proportional counter is a gas-filled counter, with a long metal cylinder (typically a few centimeters in diameter and about 10 ~ 30 cm in length) that acts as the cathode, and a thin metal wire, an anode, running along the center of the cylinder (see Figure 2.15). The counter for x-ray detection is filled with a rare gas such as Ar, Kr, or Xe. The incident x-ray photon ionizes gas molecules and leaves a trail of positive ions and liberated electrons. Since the ionization potential of Ar, for example, is 26 eV and the energy of a Cu$K\alpha$ photon is 8.04 keV, a large number of ion-electron pairs are generated from each absorbed x-ray photon. The electrons are rapidly attracted to the anode wire, while the heavier positive ions drift toward and are eventually collected by the cathode.

The electrons, while moving toward the central anode wire, are further accelerated under the influence of the anode potential and ionize additional gas molecules they encounter. Because of such secondary ionization the number of electrons collected at the anode into a single pulse is far greater than was initially generated by the primary ionization event. This is called *gas amplification*, and the amplification factor is dependent on the anode voltage and the gas pressure. At anode voltages within an optimal range (usually 1 ~ 2 kV), the gas-filled counter performs as a *proportional counter*, in the sense that the size of the pulse generated is approximately proportional to the energy of the incoming x-ray photon. At voltages too high or too low such a proportionality is not maintained.

Operating the gas-filled counter as a proportional counter is very useful, since incoming photons of different wavelengths, producing pulses of different heights, can be easily differentiated electronically. *Energy resolution* by means of *pulse height discrimination* cannot, however, eliminate the need for a crystal monochromator or other means of monochromatization, since the proportionality between the photon energy and the pulse height is not accurately maintained. For a strictly monochromatic incident beam, the size distribution of the pulses generated is found to have a spread of about 20% (full width at half maximum). This means essentially that there has to

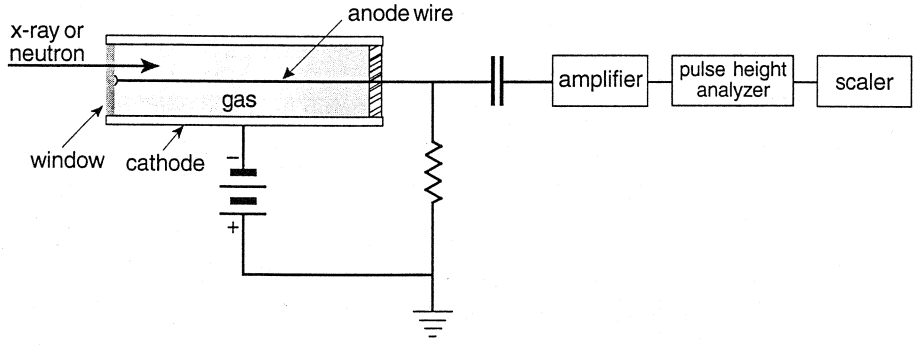

Figure 2.15 Schematic of a proportional counter.

be at least a 20% difference in wavelengths before the contaminating radiation can be effectively removed through pulse height discrimination in the electronic circuit. Used in conjunction with a β filter, the pulse height discrimination is nevertheless useful in isolating the $K\alpha$ radiation from the white radiation background.

Because neutrons are essentially nonionizing when passing through matter, their detection is accomplished by first inducing nuclear reactions that produce ionizing particles. The gas counter is thus filled with either ^{3}He or BF_3 (enriched in ^{10}B). In the nuclear reaction

$$^3\text{He} + \text{n} \rightarrow {}^3\text{H} + \text{p} + 0.77\ \text{MeV}$$

a helium absorbs a neutron and produces α proton and a tritium nucleus of high energies. In the reaction

$$^{10}\text{B} + \text{n} \rightarrow {}^7\text{Li} + \alpha + 2.30\ \text{MeV}$$

absorption of a neutron by a ^{10}B produces an α particle and a ^{7}Li nucleus. These energetic, charged particles induce further secondary ionization in the gas, resulting in a gas amplification. The counter, however, does not function as a "proportional" counter, since the size of the electric pulses observed is determined by the energies of the ionizing particles produced by the nuclear reaction and not by the energies of the incident neutrons. However, the capability of pulse height discrimination is still useful as a means of discriminating against background γ-rays.

2.4.1.2 Scintillation Counter

A *scintillator* crystal emits visible light when it absorbs ionizing radiation. The scintillator commonly used for the detection of x-rays is a sodium iodide crystal activated with a small amount of thallium [abbreviated as NaI(Tl)]. Absorption of an x-ray photon produces ionization in the crystal, which in turn induces fluorescence of blue visible light (~420 nm) in the thallium sites. Other substances that can be used for x-ray detection are CsI(Tl), CaI_2(Eu), and ZnS(Ag) (see Arndt and Willis[11]). In the case of a neutron detector, the inability of neutrons to produce ionization is overcome, as in a gas-filled proportional counter, by incorporating a substance that induces a nuclear reaction producing ionizing particles. The "scintillator" used is thus a glass or plastic loaded with ^{6}Li and ZnS(Ag). The neutron absorbed by ^{6}Li first undergoes a nuclear reaction

$$^6\text{Li} + \text{n} \rightarrow {}^3\text{H} + \alpha + 4.79\ \text{MeV}$$

producing an α particle and a tritium nucleus. These charged, high-energy particles in turn stimulate emission of visible light (~450 nm) by ZnS(Ag).

The flash of light produced by the scintillator is fed to a photomultiplier tube. The photocathode in the photomultiplier converts the light energy to an electric pulse, which then goes through several stages of amplification. As with the proportional counter, the size of the pulse generated on absorbing an x-ray photon is roughly proportional to its energy, but the energy resolution is much worse with the scintillation counter. The distribution of the pulse heights generated in the latter by a

monochromatic x-ray beam is as much as 40–50% (full width at half maximum). This broadening of the pulse height distribution arises mainly as a cumulative result of the modest pulse height scrambling that occurs at each amplification stage of the photomultiplier. Counterbalancing the poorer energy resolution, other factors favor the scintillation over the proportional counter. The very short decay time of scintillator crystals, about 10^{-7} s, allows a very fast counting rate of the order of 1 MHz. In the proportional counter, collecting ions moving through the gas medium is much slower, and the maximum possible counting rate is about 50 kHz. The efficiency of detection of x-rays by the scintillation counter is very high, approaching 100% for both Cu$K\alpha$ and Mo$K\alpha$ lines. This high efficiency is due to the high absorption coefficient for x-rays of the dense scintillator crystals. The detection efficiency of the Ar-filled proportional counter is much lower, usually in the 40 $\sim$ 60% range for Cu$K\alpha$ and less than 30% for Mo$K\alpha$. It can be increased by increasing the gas pressure, by increasing the pass length of the radiation (for example, by having the window at the end, rather than the side, of the counter tube), and by using higher absorbing Xe gas instead of Ar or Kr gas.

2.4.2 Position-Sensitive Detectors

A position-sensitive detector allows measurement of intensities over a range of scattering angles simultaneously, affording a great saving in time compared with the point-by-point detectors, discussed in the previous section, that have to be moved in steps to different angular positions. A photographic film is a good example of a position-sensitive detector that is simple to use. A position-sensitive detector is either a one-dimensional ("linear") detector or two-dimensional ("area") detector.

Figure 2.16 illustrates the working of a *one-dimensional position-sensitive proportional counter*. The detector tube itself is very similar in construction and operation to the simple proportional counter shown in Figure 2.15. The difference is that the anode wire at the axial center of the long cylindrical cathode tube is now connected to the electronic circuit at both ends. The window that admits the incident x-rays or neutrons is now on the side of the cathode tube. The photoelectrons generated by the primary and secondary ionization events following absorption of an x-ray photon or a neutron are collected at a localized spot on the anode wire, and a fraction of the electric charge is led out of the right channel and the rest out of the left. After amplification, the pulses in the right and left channels are combined, and the height of the combined pulse is then analyzed as before for the purpose of energy resolution. The information about the position of the ionization event along the anode wire can be obtained by one of two ways depending on the details of the circuitry. In the *resistance-capacitance encoding*,[12] which is depicted in Figure 2.16, the difference in the rise time of the two pulses coming out of the two ends is noted and translated into the position coordinate. In the *charge-division encoding*, the magnitudes of the charges in the pulses coming out of the two ends are compared.

Various *multiwire proportional counters* (MWPC) have been designed for use as two-dimensional position-sensitive detectors. An example of such a design is illustrated in Figure 2.17. Here a plane of fine, equally spaced parallel wires functions

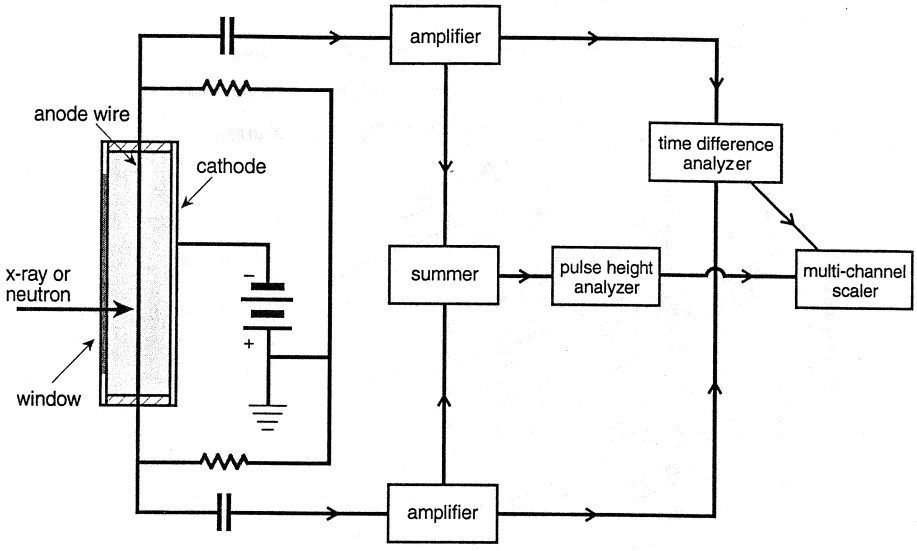

Figure 2.16 Schematic illustration of a one-dimensional position-sensitive detector. The gas-filled detector operates as a proportional counter, and the position information is encoded in the difference in the rise time between the pulses coming out of the two ends of the anode wire.

as the anode and is positioned between two cathode planes. The latter are themselves planes of fine wires (or narrow conductive strips) oriented parallel to the anode wires in one plane and perpendicular in the other. These electrodes are encased as a whole in a flat housing that is filled with a proportional counter gas such as Ar or Xe for x-ray detectors and ^{3}He or BF_3 for neutron detectors. As in any proportional counter, the absorption of incoming radiation produces photoionization of the gas, and, after gas amplification, the electrons are collected at the central anode wires. Simultaneously, corresponding positive pulses are induced on a few of the neighboring cathode wires in the two cathode planes. These positive pulses are collected through delay lines. The time delay between the anode pulse (the prompt pulse) and the pulse from the end of the delay line gives the X or Y coordinate of the cathode wire where the pulse originated. A computer algorithm then determines the centroid of the pulses and locates the ionization event on one of the 512 × 512 pixels.

2.4.3 Counting Statistics

For each absorbed x-ray photon or neutron, the proportional or scintillation counter produces a discrete electric pulse. The flux J of the beam of x-rays or neutrons is measured as the number of counts of such pulses observed per second. If measurements are made repeatedly with a beam of constant flux, the number of counts observed during a fixed time period is not exactly the same, but is rather subject to statistical fluctuations. The arrival time of any one particle (x-ray photon or neutron) is totally uncorrelated with the arrival time of the next particle. The flux J of the particles,

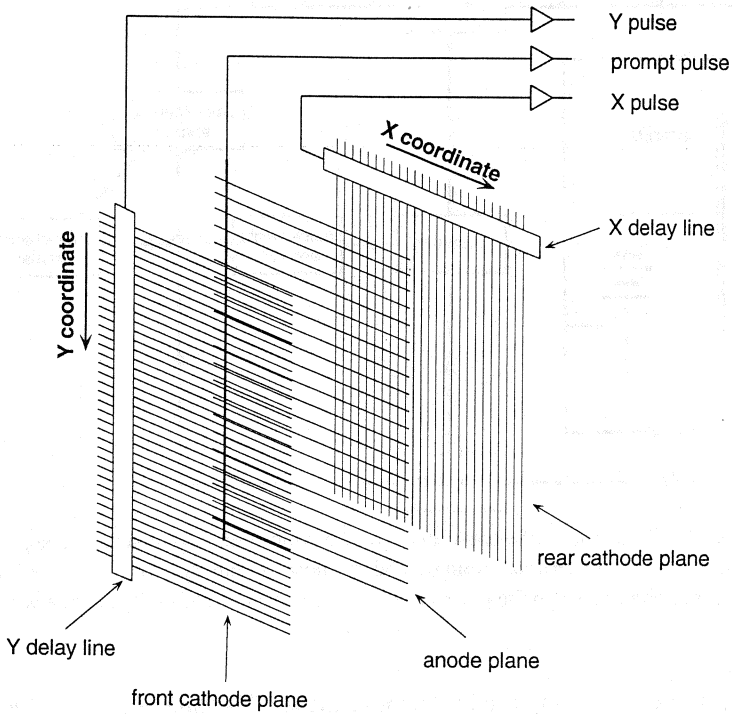

Figure 2.17 Schematic of a two-dimensional position-sensitive multiwire proportional counter (MWPC). (The spacing between electrode planes is not to scale.)

averaged over a long period of time, is the only characteristic of the beam that we are interested in measuring. Under these circumstances, the probability of actually observing x counts during a time period t is given by the Poisson distribution

$$p(x; X) = \frac{X^x}{x!} e^{-X} \tag{2.11}$$

where X $(= Jt)$ is the expectation value of x. The average and average square of x, calculated from (2.11), is $\langle x \rangle = X$ and $\langle x^2 \rangle = X^2 + X$. Therefore, if many measurements are made, each for the same length of time t under identical conditions, the numbers of counts observed will show a spread with a variance σ^2 equal to $\langle x^2 \rangle - \langle x \rangle^2 = X$ and a standard deviation σ equal to $X^{1/2}$. If in a single measurement over a time period t the number of counts observed is x, the best estimate of the flux is $J = x/t$, and its standard deviation σ is $x^{1/2}/t = (J/t)^{1/2}$. The precision of the measured intensity improves with the square root of the time spent to measure the intensity.

Often the flux to be determined, J_{net}, is obtained by subtracting the background J_{bkgd} from the gross (or overall) flux J_{gross}. When the total amount of time t_{total} available for measuring both J_{gross} and J_{bkgd} is constrained, it is necessary to decide on the best strategy to minimize the error in J_{net}. Suppose the total time t_{total} is apportioned into $t_{\text{gross}} = f\, t_{\text{total}}$ for the measurement of J_{gross} and $t_{\text{bkgd}} = (1 - f)\, t_{\text{total}}$ for the

measurement of J_{bkgd}. Since the variance of the difference of two quantities is equal to the sum of the variances of individual quantities, we have

$$\begin{aligned}\sigma_{net}^2 &= \sigma_{gross}^2 + \sigma_{bkgd}^2 \\ &= \frac{J_{gross}}{t_{gross}} + \frac{J_{bkgd}}{t_{bkgd}} \\ &= \frac{J_{gross}}{f\, t_{total}} + \frac{J_{bkgd}}{(1-f)t_{total}}\end{aligned} \tag{2.12}$$

Minimization of σ_{net}^2 with respect to f shows that the optimum value of $f = t_{gross}/t_{total}$ is given by

$$\left(\frac{f}{1-f}\right)^2 = \frac{J_{gross}}{J_{bkgd}} \tag{2.13}$$

Thus, for example, when J_{bkgd} and J_{gross} are in the ratio of 1 to 4, the measurement times t_{bkgd} and t_{gross} should be apportioned in the ratio of 1 to 2.

Detectors have a finite resolving time. If two or more pulses arrive within a time period shorter than this "dead" time, they are not resolved and are recognized as a single larger pulse. Since the times of arrival of x-ray photons or neutrons are uncorrelated with each other, there is always a finite chance that the arrivals of two such particles will overlap. When the counting loss due to the dead time is moderate, it can be estimated and corrected for as follows. If the observed, or "apparent," counting rate is x_{app} counts per second and the dead time of the detector is τ seconds, the detector will be inactive for a period $x_{app}\,\tau$ during each second. During this period the number of counts lost will be $x(x_{app}\,\tau)$, where x is the true counting rate that would have been observed in the absence of counting loss. We then have

$$x = x_{app} + x(x_{app}\tau) \tag{2.14}$$

from which we obtain

$$x = x_{app} + \frac{x_{app}^2\tau}{1 - x_{app}\tau} \tag{2.15}$$

This derivation ignores the possibility of more than two pulses piling up and is therefore applicable only when the counting losses are not too high.

2.4.4 Integrating Detectors

Detector technology is presently undergoing a rapid evolution, and several newer types of area detectors have recently become commercially available and are gaining popularity in many laboratories. The development of these detectors undoubtedly is the result of the advancement of electronics technology in general and the availability at low cost of many required components already developed for other mass-market purposes. The development has been stimulated also by the increasing accessibility of synchrotron radiation sources in recent years and by the resulting acute need[13] for

detectors not limited by the count rate capabilities of multiwire proportional counters. The traditional counters discussed in Sections 2.4.1 and 2.4.2 are all "pulse-counting" detectors, producing an electric pulse for each photon or neutron absorbed. In contrast, these newer ones are "integrating" detectors, producing output signals that give the number of such absorption events detected and integrated over a period of time. In this sense they function the same way as a photographic film. We briefly discuss here three types of these newer detectors[14] based on (1) image plate, (2) TV cameras, and (3) charge-coupled device (CCD) chips.

An *image plate* is a sheet of plastic on which a thin coating of fine phosphor crystals has been applied. The phosphor, BaFBr doped with Eu^{2+}, has the property that the energy deposited by the absorbed x-ray (or ultraviolet light) photon produces a "color center" of metastable state, which decays with a half-time of about 10 h at room temperature. The x-ray diffraction pattern is thus stored as a latent image consisting of the distribution of these quasistable color centers. After a period of exposure, the latent image is read off by scanning the image plate pixel by pixel with a focused laser beam. When illuminated with a beam of red He–Ne laser light (633 nm), the "trapped" energy is released with emission of blue fluorescence (390 nm). The blue light signal is filtered to remove scattered laser light, detected by a photomultiplier, and digitized. Currently, a spatial resolution of 100 μm is easily attained. The image plate is then ready for reuse, after any residual image is cleared by exposure to a bright light for a few minutes. It is an important replacement of photographic film, with additional advantages that it is reusable, does not need wet development in the dark room, and has a much better spatial resolution and dynamic range.[15]

In the same way as the x-ray or neutron radiation is first converted into visible light in the scintillation counter, the diffraction pattern falling on the detector plane of an area detector may first be converted into a pattern of visible light by use of a suitable phosphor. The phosphor has to be applied as a thin coating to increase the spatial resolution. The substances $Gd_2O_2S(Tb)$, $Y_2O_2S(Eu)$, and $Y_2O_2S(Tb)$ are used for this purpose because they have high absorption coefficient for x-rays and short decay time constants for the fluorescence (of the order of 1 ms). The task to be performed is then to sense this pattern of light, digitize it pixel by pixel, and accumulate the digitized data into computer memory. One obvious tool for such a task is a TV camera such as a *vidicon tube*. More recently, CCD chips are rapidly gaining popularity. Usually the light pattern in the phosphor screen is first enhanced by passing it through an image intensifier. The active sensing area of a vidicon tube or a CCD chip is usually fairly small (typically a few centimeters square for the vidicon tube and 1–2 cm square for the CCD chip) and is much smaller than the detector window size that is normally desirable from the viewpoint of the detector users (10 cm square or larger). The light image pattern from the phosphor screen (or from the image intensifier) is therefore reduced in size by use of either an optical fiber taper or an optical lens system before it is sent to the sensing device. Figure 2.18 gives a schematic illustration of such an arrangement.[16,17] On the vidicon tube target the image is formed as 525 raster lines at the commercial TV rate of 30 frames per second (in the United States). The video image may be scanned by an electron beam and digitized into 512 pixels per line

that are accumulated in the 512 × 512 pixel data in the computer memory. In such a "fast scan" mode, useful for time-lapse studies, the period of integration in the camera target is 33 ms. In the alternative "slow scan" mode an exposure period as long as 1000 s is allowed before the charge image is scanned. A *CCD* is a solid-state chip, with individual light-sensing pixels already built in as integral components on the silicon substrate. The pixels are each as small as 27 × 27 μm in size and there are 512 × 512, 1024 × 1024, or 2048 × 2048 pixels in total on a single chip of only a few centimeters square in size. Compared to a vidicon tube, which is a bulky vacuum tube, a CCD is compact, stable, and reliable, and moreover offers enhanced resolution, linearity, dynamic range, and read-out speed. CCD sensors have been enthusiastically embraced by the astronomy community and are likely to be as popular in their application as x-ray detectors.

2.5 CAMERAS AND DIFFRACTOMETERS

To perform scattering measurements, the various components of the measuring instrument, that is, the radiation source, monochromater, beam collimator, sample holder, detector, etc., have to be physically arranged in some fixed geometric relationships to each other. The equipment that is set up to facilitate such an arrangement is called either a camera, a diffractometer, or a spectrometer. A camera is an instrument in which all the components are, in general, held at fixed positions during the measurement, while the word diffractometer is used when the detector (and often the sample holder as well) rotates to allow measurements at different scattering angles. Of course such a distinction is not a strict rule obeyed by all. A spectrometer is an instrument whose primary purpose is to analyze the wavelength distribution in the scattered beam, as in x-ray fluorescence analysis and neutron inelastic scattering. Spectrometers are not considered in this section, but the designs of some neutron spectrometers will be examined later when the subject of inelastic scattering of neutrons is taken up in Chapter 8. Over the years so many different cameras and diffractometers have been

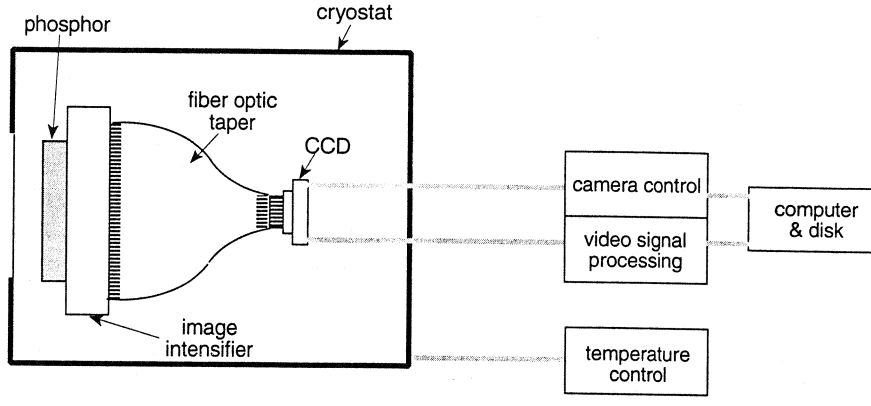

Figure 2.18 Schematic of a CCD-based area detector.

designed, each tailored to different measurement needs, that it is not worth discussing all of them or even representative ones. Instead, we will discuss only some important design features that are common to most of them.

2.5.1 Collimation

The flat film camera, schematically illustrated in Figure 2.19, embodies the essential elements of a camera. A good camera design should facilitate satisfying the two most important requirements, that is, defining the scattering angle 2θ as accurately as possible, while maximizing the flux of the scattered beam to allow its accurate and speedy measurement. These two requirements often conflict with each other. To reduce the divergence in the incident beam, the size of the pinholes in the collimator may be made small, but then the amount of incident bean energy that reaches the sample is severely limited and the flux of the scattered beam is correspondingly curtailed. Here we look into some factors that have to be taken into consideration in the design of pinhole collimators.

Figure 2.20a illustrates the simplest collimating system, in which the radiation emanating from a point source is allowed to pass through a pinhole of diameter d. The beam divergence α is given by d/L_1, where L_1 is the distance from the point source to the pinhole. The profile of the beam falling on the sample is depicted on the right of the diagram, showing the circular area that is uniformly illuminated. This diagram also illustrates the following two points. First, the presence of parasitic scattering, that is, scattering of the beam from the edges of the collimating material itself, makes the beam emerge from the pinhole with a divergence larger in practice than the idealized divergence α calculated on the basis of the pinhole diameter alone. The presence of parasitic scattering is indicated in the beam profile in Figure 2.20a by the low level flux spreading out beyond the central illuminated area. Second, the angle α can be made smaller by either reducing d or increasing L_1. Changing d and L_1 simultaneously by the same factor does not affect α, and therefore the optimum value of d is to be decided on the basis of other criteria.

In Figure 2.20b the detector is brought into the picture. The area on the detector illuminated by the direct beam of divergence α has diameter p_0 equal to

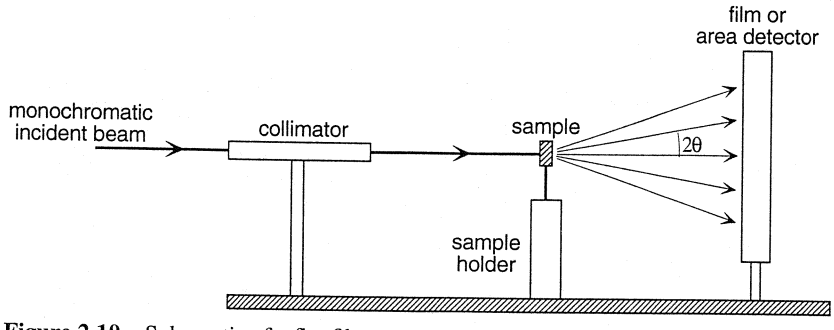

Figure 2.19 Schematic of a flat film camera.

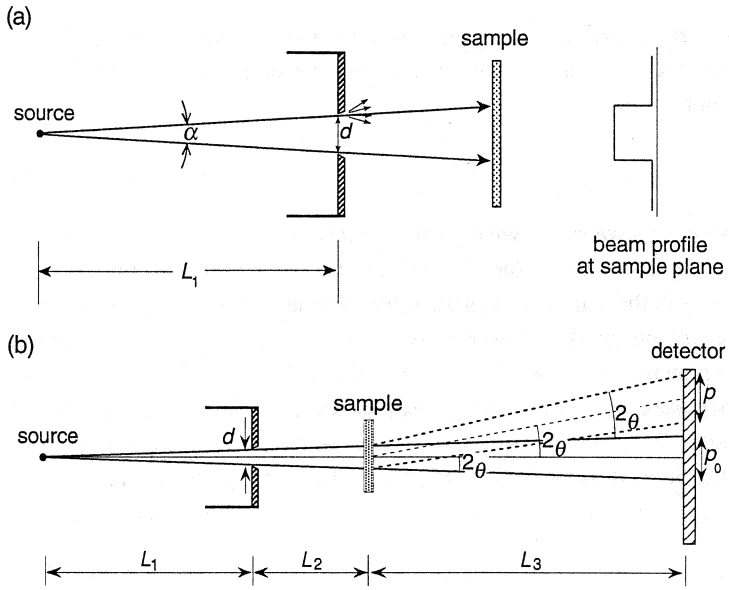

Figure 2.20 (a, b) Collimator with a single pinhole, with radiation from a point source.

$$p_0 = \alpha(L_1 + L_2 + L_3) = \frac{d}{L_1}(L_1 + L_2 + L_3) \tag{2.16}$$

Rays scattered at the sample at a scattering angle 2θ also illuminate a circle of diameter p at the detector plane, where p is approximately equal to p_0 when 2θ is fairly small. The distance Δ between the centers of the two circles of diameter p_0 and p is

$$\Delta = 2\theta L_3 \tag{2.17}$$

For the scattered rays to be resolved from the direct beam, the distance Δ has to be at least as large as p_0 ($\approx p$). Thus the minimum 2θ that can be resolved is given by

$$2\theta_{\min} = \frac{d}{L_1}\frac{L_1 + L_2 + L_3}{L_3} \tag{2.18}$$

The resolution limit $2\theta_{\min}$ defined by (2.18) is again scale invariant, that is, it does not change when all the lengths, d, L_1, L_2, and L_3, are altered by the same scaling factor. At this point, however, the spatial resolution of the detector has to be brought into consideration. If the detector can resolve two points only if they are separated by at least δ, we may have to make the minimum value of Δ as large as δ by increasing the scale of all the lengths involved, d, L_1, L_2, and L_3.

In Figure 2.21a the size of the radiation source has been increased from the point source depicted in Figure 2.20. For the same pinhole diameter d and the source-to-pinhole distance L_1, the divergence α in Figure 2.21a is now larger than in Figure 2.20, and the flux profile of the beam is now trapezoidal instead of rectangular. The beam divergence α increases without limit as the source size is made still larger and

can be limited only by having a second pinhole introduced as in Figure 2.21b (for the sake of simplicity we assume the two pinholes are the same size). Now the beam divergence is given by

$$\alpha = \frac{2d}{L_0} \tag{2.19}$$

where L_0 is the distance between the two pinholes, and the distance between the source and the pinholes no longer plays a role. The effect of having a pair of pinholes is to limit the effective size of the source to the area within diameter h. As was pointed out in Figure 2.20, the divergence angle α does not change when d and L_0 are both increased by the same scaling factor. However, with increased d and L_0, the effective diameter h of the source increases, and more beam energy is admitted through the collimator and onto the sample. Thus the dimensions of the collimator must be designed with the source size taken into consideration. In Figure 2.21c a third pinhole is added after the first and second. If the diameter of the third pinhole is carefully adjusted to be

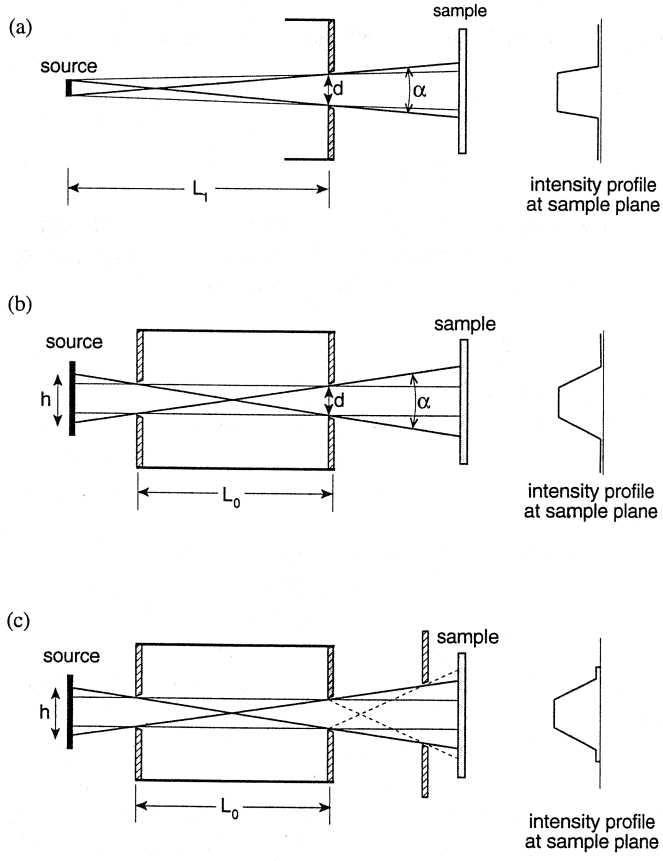

Figure 2.21 Illustration showing various elements (a–c) in the design of a pinhole collimator.

slightly larger than the outer envelope of the primary beam (indicated by the thicker ray lines in the diagram), most of the parasitic scattering originating from the second pinhole is blocked, without the third pinhole itself becoming a source of parasitic scattering. In the beam flux profile, the parasitic scattering is shown to extend only a short distance beyond the main illuminated area indicated by the trapezoid.

The series of diagrams in Figures 2.20 and 2.21 illustrates some of the salient points to be attended to in the design of a collimator system, especially that the spatial resolution of the detector and the size of the radiation source must be taken into account. With improvement in detector technology, the spatial resolution of the detector is becoming less of a limiting factor in the design. When an x-ray tube with a relatively small focus area in the target is used, it is feasible to design an instrument fairly compact as a whole. With any radiation source what really matters is the brilliance (the flux per unit area of the source) rather than the total flux emanating from the source. The real or the apparent size of a neutron source is always far larger than x-ray source sizes, and thus neutron scattering instruments are in general an order of magnitude larger than corresponding x-ray instruments.

In some collimating systems, slits are used instead of pinholes. This is often the case when the radiation source is itself a line (as, for example, with the line focus of an x-ray tube) rather than a circle or a square. A slit can be considered as a row of pinholes spaced close together on a straight line. The total energy in the primary beam admitted through the collimator is thereby increased by a large factor, but the beam divergence in the direction of the long dimension of the slit is also greatly enhanced. The resulting smearing in the observed scattering curve is especially pronounced in the small-angle scattering pattern, and a "desmearing" correction is required, as will be discussed later in Section 5.6. In wide-angle scattering, the extent of slit smearing is usually restricted at the time of measurement by the use of a *Soller slit*. The Soller slit consists of a number (10 to 20) of closely spaced, thin metal plates parallel to each other, with their normal set in the direction of the long length of the slit. A pair of neighboring metal plates in it then act as a collimator limiting the divergence of the beam in the slit length direction.

2.5.2 Focusing Geometry

In striving to limit the divergence of rays in the incident beam by use of ever smaller pinholes, one inevitably discards much of the incident beam energy and hence weakens the flux of the scattered beam. An alternative approach in collimation is to use a diverging (or converging) primary beam in a focusing geometry, thereby achieving much greater flux of the scattered beam without sacrificing angular resolution. All such focusing arrangements rely on a geometric property of a circle that can be stated as follows: given two fixed points S and F on the circumference of a circle (see Figure 2.22), the angle subtended by these two at every point on the arc between S and F is identical.

In the reflection mode depicted in Figure 2.22a, the radiation emanating divergent from a point source S illuminates the sample that is spread over an arc of the *focusing circle*. All the rays that are scattered by the same angle 2θ but from different points

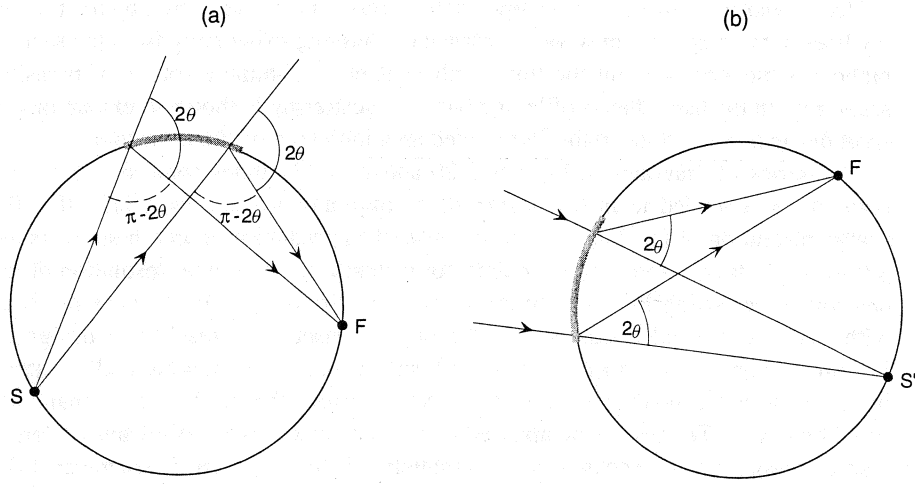

Figure 2.22 Geometry of focusing arrangements in reflection (a) and transmission (b) modes.

on the sample converge to a single point F on the focusing circle. For each possible scattering angle, the rays converge to another point on the circle, whose location depends on the scattering angle. A film placed near F along the focusing circle then records the scattered intensity pattern. The bent and ground crystal monochromator, discussed in Section 2.2.1, is based on the same principle. The source S can be an actual physical source such as the focal spot on an x-ray tube target or can be a small opening through which divergent rays emerge, as when rays reflected by a crystal monochromator are made to focus on the opening. When the source is a line source, or when the small opening is a slit, the same geometric arrangement can still work, as long as the long dimension of the source or the slit is perpendicular to the focusing plane.

Figure 2.22b shows a similar focusing arrangement in a transmission mode, where the incident rays converge to a "virtual source" S′ situated on the focusing circle. On their way toward S′, through the sample spread over an arc on the circle, the rays are scattered, and those that are scattered at an angle 2θ from different points on the sample all converge to a single point F on the circle. A primary beam initially emerging divergent from a point source can be made to converge toward a point by means of either a curved crystal monochromator or a curved mirror.

The focusing arrangement discussed here can be combined with the focusing achieved by means of a curved crystal monochromator in a number of different ways. Many of these arrangements are discussed by Roberts and Parrish.[7] In the above discussion we have considered only the rays that are confined within the plane of the drawing and ignored the consequences of the rays diverging in the perpendicular direction. When a line source or a slit is used in practice, the perpendicular divergence is often limited with Soller slits. In most cases the "circle" in the above discussion is in reality a cylindrically curved surface. A pair of cylindrical mirrors, one focusing in the "horizontal" plane and the other in the "vertical" plane, can be used to achieve

true focusing to a single point, and such an arrangement is actually found in some designs of small-angle scattering cameras.

2.5.3 Diffractometer

In a typical design of a diffractometer, the radiation source is stationary, and the detector, a proportional or scintillation counter, rotates to various 2θ positions on the "diffractometer circle" (see Figure 2.23). The "source" could be the focal spot of an x-ray tube or an opening to which the diffracted beam of a crystal monochromator is focused. The sample holder at the center of the diffractometer circle also rotates about the same axis, and this rotation is coupled to the detector arm movement such that when the detector rotates by an angle 2θ the sample holder simultaneously turns itself half as much, that is, by θ. Because of such a 2θ–θ coupling, once a flat sample is placed in a position to approximate the focusing geometry as in Figure 2.23a, the approximate focusing geometry is maintained irrespective of a subsequent change in the rotational position of the detector. In transmission mode, focusing is of course not attained, but once a sheet sample is placed, as in Figure 2.23b, in a symmetric orientation that bisects the angle between the source and the detector, the symmetric transmission geometry is maintained again irrespective of the rotational position of the detector.

Maintaining a symmetric geometry at all scattering angles, either in reflection or transmission mode, is important, especially when the sample is not isotropic and its scattering pattern depends on the direction in the sample that is being investigated. The scattering vector $\boldsymbol{q}$ (or $\boldsymbol{s}$) bisects the angle subtending the source and detector at the point of scattering, and in the symmetrical reflection mode $\boldsymbol{q}$ is always in the direction normal to the sheet surface. Similarly, in the symmetrical transmission mode, the scattering vector remains in the direction parallel to the sheet surface. Symmetrical placement of the sample in the diffractometer also

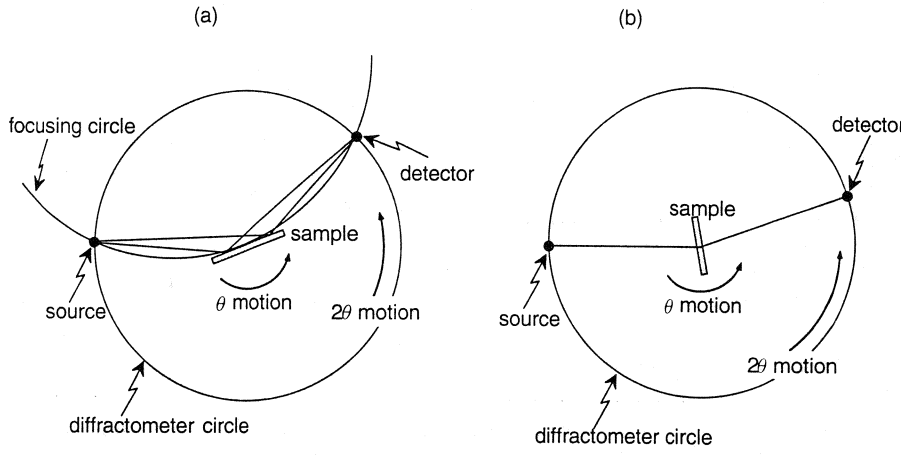

Figure 2.23 Geometry of a diffractometer in reflection (a) and transmission (b) mode.

simplifies the calculation of the absorption factor. When the intensity of scattering is measured by scanning through a range of 2θ, the observed intensity varies not only because of the variation in the scattering power of the sample with q, but also because of the variation in the absorption factor with 2θ angle. The absorption factor accounts for the change with 2θ in the attenuation of the beam due to absorption within the sample and also for the change in the irradiated volume with 2θ. The absorption factors AF in the reflection and transmission modes can be calculated as follows.

Suppose a beam of cross-sectional area A falls on a sheet sample of thickness t in the symmetrical reflection geometry, as in Figure 2.24a. We assume, for the sake of simplicity, that the rays in the beam are all parallel to each other. Now consider a layer of thickness dx inside the sample, at depth x below the flat surface, where the irradiated volume is equal to $dx \cdot A/\sin\theta$. Before reaching this depth the beam has traveled distance l within the sample, where l is equal to $x/\sin\theta$, and has suffered attenuation by a factor $\exp(-\mu l)$, μ being the linear absorption coefficient. The scattered beam must travel the same distance within the sample again on its way out. If $i(2\theta)$ is the intensity of scattering *per unit volume* of the sample, then the contribution $dI(2\theta)$ to the total scattering intensity by the layer dx at depth x is

$$dI(2\theta) = i(2\theta)\frac{dx\ A}{\sin\theta}\exp\left(-2\mu\frac{x}{\sin\theta}\right) \tag{2.20}$$

On integration of (2.20) with respect to x from 0 to t, the total scattered intensity $I(2\theta)$ from a sample of thickness t is given by

$$I(2\theta) = i(2\theta)\frac{A}{2\mu}\left[1 - \exp\left(-2\mu\ \frac{t}{\sin\theta}\right)\right] \tag{2.21}$$

The absorption factor in symmetrical reflection is therefore

$$AF_{\text{refl}} = \frac{1}{2\mu}\left[1 - \exp\left(-2\mu\frac{t}{\sin\theta}\right)\right] \tag{2.22}$$

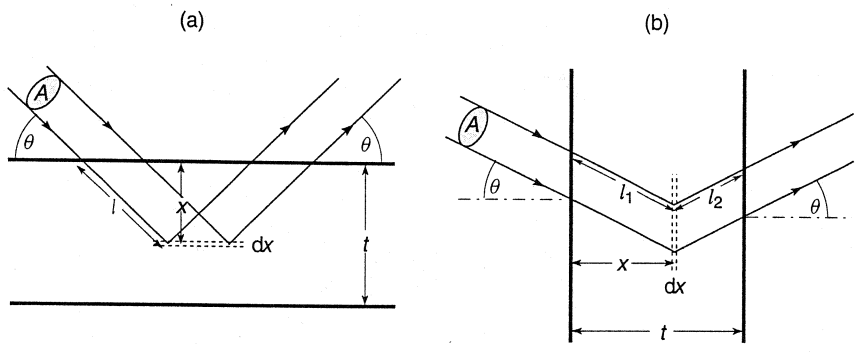

Figure 2.24 Geometry in the calculation of the absorption factor in the (a) symmetrical reflection and (b) symmetrical transmission mode with a sheet sample.

If the sample is sufficiently thick in comparison to $1/\mu$, that is, if the penetration of the beam to the other side of the sheet is negligibly small, we may let $\mu t \to \infty$ in (2.22), and the absorption factor becomes equal to $1/2\mu$, which is independent of the scattering angle and thus obviates the need for absorption correction.

A similar calculation for the symmetrical transmission mode can be made as follows. In the layer of thickness dx at depth x within the sample, the volume irradiated by a beam of cross-sectional area A is equal to $dx \cdot A/\cos\theta$. The distance of travel by the beam within the sample is equal to $l_1 + l_2$, where $l_1 = x/\cos\theta$ and $l_2 = (t - x)/\cos\theta$. The intensity of scattering due to the layer dx is then

$$dI(2\theta) = i(2\theta)\frac{dx\ A}{\cos\theta}\exp\left(-\mu\frac{t}{\cos\theta}\right) \tag{2.23}$$

Integrating (2.23) with respect to x from 0 to t gives

$$I(2\theta) = i(2\theta)\frac{At}{\cos\theta}\exp\left(-\mu\frac{t}{\cos\theta}\right) \tag{2.24}$$

and the absorption factor is

$$AF_{\text{trans}} = \frac{t}{\cos\theta}\exp\left(-\mu\frac{t}{\cos\theta}\right) \tag{2.25}$$

In a transmission mode the intensity of scattering obviously depends on the thickness of the sample, and, while the irradiated volume increases in proportion to t, this increase is counterbalanced by the absorption effect attenuating the beam by the factor $\exp(-\mu t/\cos\theta)$. By differentiating (2.24) with respect to t and setting the result equal to zero, we find that the intensity is the maximum when t is equal to $1/\mu$. Taking polystyrene (density 1.05 g/cm^3) and poly(vinyl chloride) (density 1.39 g/cm^3) as typical examples of polymers, we find, with the use of the data in Table 2.2, that the linear absorption coefficients μ of the two polymers are 4.12 and 88.1 cm^{-1}, respectively, for Cu$K\alpha$ x-rays and 0.016 and 0.46 cm^{-1}, respectively, for 1.8 Å neutrons. Thus, in x-ray studies with hydrocarbon polymers and other relatively weakly absorbing materials, samples of thickness $2 \sim 3$ mm offer the maximum scattered intensity. In neutron scattering where the linear absorption coefficient is usually much smaller, one can afford a much thicker sample. In choosing the optimum sample thickness, it is, however, necessary that the effect of sample thickness on the angular resolution and the extent of multiple scattering is also taken into account. The multiple scattering effect is discussed in the next section. Reflection mode, by allowing the use of a divergent incident beam in a focusing geometry, in general affords higher flux of scattering than transmission mode. At relatively small scattering angles, say, 2θ less than 30°, however, the area of the sample irradiated in reflection mode becomes too large, and it then becomes difficult to prepare a sufficiently large sample with a good flat surface. Moreover, when the sample is not isotropic and some degree of preferred orientation is present, one may be interested in knowing the variation in the structure in different directions, and in such cases transmission method is usually the preferred choice.

2.6 MULTIPLE SCATTERING

Theoretical expressions relating the scattered intensity to the structure of the material usually assume that the incident rays are scattered only once in the sample. In practice, however, some of the scattered rays may undergo additional scattering before they leave the sample. The observed intensity data, therefore, must be corrected for the multiple scattering effect before they can be analyzed and compared with theoretical expressions. The extent of multiple scattering is more appreciable when the sample is large (and thick), thus presenting more opportunities for a scattered beam to undergo scattering again, and also when the scattering power of the material is high and the absorption coefficient is small. The calculation given below illustrates how the extent of double scattering can be estimated under a given sample and scattering geometry. The method can of course be extended in principle to estimate the extent of triple and higher order scatterings, but these are much weaker than double scattering and can usually be safely ignored (Vineyard[18] and Sears[19] discuss more general methods of estimating the effect of multiple scattering that includes higher order scattering).

In Figure 2.25 we assume the sample is an infinitely large sheet of thickness t placed in a transmission geometry, but any other sample and scattering geometry may be treated in the same way. The sheet is illuminated by an incident beam of cross-sectional area A, traveling in the direction given by unit vector $\boldsymbol{S}_0$. The flux J_0 of the incidnet beam represents the number of x-ray photons or neutrons traveling in it per second per unit cross-sectional area. If ξ_0 is the angle of incidence at the sheet surface (see Figure 2.25), the total volume V_0 of the sample illuminated by the incident beam is

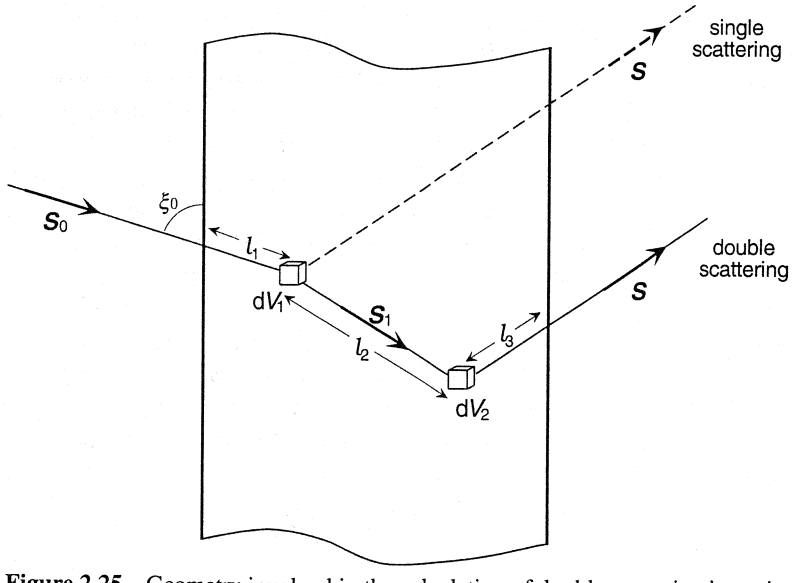

Figure 2.25 Geometry involved in the calculation of double scattering intensity.

$$V_0 = \frac{At}{\sin \xi_0} \tag{2.26}$$

The detector is placed at distance R from the center of the illuminated volume, in the direction defined by unit vector $\boldsymbol{S}$. The distance R is considered to be sufficiently far in comparison to the sheet thickness t or the beam cross-sectional area A. The detector window is also open sufficiently wide that the detector is able to "view" all of the illuminated volume V_0.

Before proceeding further, a remark is added here to clarify the meaning of the symbol used in this section to designate the scattering power of the material. The intensity $I(\boldsymbol{q})$ of scattering by a sample, as defined in Sections 1.2.1 and 1.5.1 and used throughout this book, denotes the scattering power of the sample as a whole and is therefore proportional to the scattering volume V_0 (which is equal to the irradiated volume when the detector is able to view all the irradiated volume, as we have assumed in the above). We here use the notation $i(\boldsymbol{q})$ to designate the scattering power *per unit volume* of the sample (this notation has already been used in the discussion of absorption factor in Section 2.5.3). In other words, $i(\boldsymbol{q}) = I(\boldsymbol{q})/V_0$. In the case of neutron scattering, $i(\boldsymbol{q})$ is a unique property of the material, dependent only on the structure (i.e., the types of atoms it contains and their relative positions in it), but is independent of the sample size, shape, or any other experimental conditions . In the case of x-ray scattering, however, $i(\boldsymbol{q})$ in the present discussion includes the polarization factor in addition to the structure-dependent factor and therefore depends on the state of polarization of the incident x-ray beam.

Let us now look at a volume element dV_1 located within the illuminated volume V_0. The flux of the incident radiation reaching this volume element is $J_0 \exp(-\mu l_1)$, where μ is the linear absorption coefficient and l_1 is the path length of the beam within the material from the point of entry to the volume element dV_1. A fraction of this flux is scattered at dV_1, and the magnitude of the flux that would actually reach the detector, in the absence of multiple scattering, is

$$dJ_1(\boldsymbol{q}) = J_0 e^{-\mu l_1} i(\boldsymbol{q}) e^{-\mu l_2} \frac{1}{R^2} dV_1 \tag{2.27}$$

where l_2 is the path length of the beam from dV_1 to the point of exit from the sample on its way to the detector. $\boldsymbol{q}$ is, as usual, equal to $2\pi(\boldsymbol{S} - \boldsymbol{S}_0)/\lambda$. The presence of the factor $1/R^2$ shows that the magnitude of the flux $dJ_1(\boldsymbol{q})$ is here expressed per unit cross-sectional area at the detector position, instead of per unit solid angle. In the absence of multiple scattering, the total flux reaching the detector would be

$$J_1(\boldsymbol{q}) = J_0 \int_{V_0} e^{-\mu l_1} i(\boldsymbol{q}) e^{-\mu l_2} \frac{1}{R^2} dV_1 \tag{2.28}$$

In other words, the intensity $I_1(\boldsymbol{q})$ of single scattering, when the intensity is expressed in the sense defined in Section 1.2.1, is

$$I_1(\boldsymbol{q}) = \int_{V_0} i(\boldsymbol{q}) e^{-\mu l_1} e^{-\mu l_2} dV_1 \tag{2.29}$$

Next, we look at the flux of the scattered beam due to double scattering. The flux reaching the volume element dV_2, after having been scattered once at dV_1, is

$$(J_0 e^{-\mu l_1})[i(\boldsymbol{q}_1) dV_1] e^{-\mu l_2} \frac{1}{l_2^2} \tag{2.30}$$

where $\boldsymbol{q}_1 = 2\pi(\boldsymbol{S}_1 - \boldsymbol{S}_0)/\lambda$ and l_2 is the distance from dV_1 to dV_2. The flux $dJ_2(\boldsymbol{q})$ reaching the detector, after having been scattered at dV_1 and again at dV_2, is then

$$dJ_2(\boldsymbol{q}) = \left[J_0 e^{-\mu l_1} i(\boldsymbol{q}_1) e^{-\mu l_2} \frac{1}{l_2^2} dV_1 \right] i(\boldsymbol{q}_2) e^{-\mu l_3} \frac{1}{R^2} dV_2 \tag{2.31}$$

where $\boldsymbol{q}_2 = 2\pi(\boldsymbol{S} - \boldsymbol{S}_1)/\lambda$ and l_3 is the distance from dV_2 to the point of exit on the way to the detector. The total flux at the detector that is due to double scattering is therefore

$$J_2(\boldsymbol{q}) = \int_V \left[\int_{V_0} J_0 e^{-\mu l_1} i(\boldsymbol{q}_1) e^{-\mu l_2} \frac{1}{l_2^2} dV_1 \right] i(\boldsymbol{q}_2) e^{-\mu l_3} \frac{1}{R^2} dV_2 \tag{2.32}$$

where the integration with respect to dV_2 is over all the sample volume V that is viewed by the detector. Written in the intensity notation defined in Section 1.2.1, (2.32) becomes

$$I_2(\boldsymbol{q}) = \int_V \int_{V_0} i(\boldsymbol{q}_1) i(\boldsymbol{q}_2) e^{-\mu l_1} e^{-\mu l_2} e^{-\mu l_3} \frac{1}{l_2^2} dV_1 dV_2 \tag{2.33}$$

As stated earlier, the scattering function $i(\boldsymbol{q})$ for x-rays must include the polarization factor. If the incident beam is unpolarized, the function $i(\boldsymbol{q})$ in Equation (2.29) for single scattering should include the polarization factor $P_1(\boldsymbol{q})$, which, as given in Equation (1.35), is

$$P_1(\boldsymbol{q}) = \frac{1}{2}(1 + \cos^2 2\theta) \tag{2.34}$$

Similarly, in the case of an unpolarized incident beam, the product of intensity functions, $i(\boldsymbol{q}_1) i(\boldsymbol{q}_2)$, in Equation (2.33) should include the polarization factor $P_2(\boldsymbol{q})$ for double scattering given by

$$P_2(\boldsymbol{q}, \boldsymbol{q}_1, \boldsymbol{q}_2) = \frac{1}{2}\left[\cos^2 2\theta_1 + \cos^2 2\theta_2 + (\cos 2\theta - \cos 2\theta_1 \cos 2\theta_2)^2\right] \tag{2.35}$$

where $|\boldsymbol{q}|$ is $4\pi \sin\theta/\lambda$, and θ_1 and θ_2 are similarly related to $\boldsymbol{q}_1$ and $\boldsymbol{q}_2$, respectively. For a partially polarized incident beam, expressions for P_1 and P_2 can be derived by the procedure suggested by Strong and Kaplow.[20]

To evaluate $I_1(\boldsymbol{q})$ and $I_2(\boldsymbol{q})$ given by Equations (2.29) and (2.33), $\boldsymbol{q}_1$, $\boldsymbol{q}_2$, l_1, l_2, and l_3 must first be expressed explicitly as functions of the position coordinates of dV_1 and dV_2, under the boundary conditions appropriate to the sample and the scattering geometry being considered. The six-fold integration required for the evaluation of $I_2(\boldsymbol{q})$ was in the past performed by resorting to the Monte Carlo method, but with the computational power of computers now available, straightforward numerical integrations over grids of positions of dV_1 and dV_2 can readily be accomplished. Certain

characteristics of the scattering and sample geometry may also allow introduction of simplifications into the integration procedure. For example, in integrating with respect to dV_2 over the sample volume V, the outlying regions of the sample may be excluded as soon as the absorption factor $e^{-\mu(l_1+l_2+l_3)}$ drops below a certain, sufficiently small level. With a sample in the form of a flat sheet, the incident beam can be represented, without loss of generality, by a beam with an infinitesimally small cross-sectional area A, and the six-fold integration is then reduced to a four-fold integration.

Once $I_1(\boldsymbol{q})$ and $I_2(\boldsymbol{q})$ are evaluated according to (2.29) and (2.33), the observed intensity is multiplied by $I_1(\boldsymbol{q}) / [I_1(\boldsymbol{q}) + I_2(\boldsymbol{q})]$ to obtain the intensity corrected for the double scattering effect. Throughout the above discussion, it has been tacitly assumed that the scattering function $i(\boldsymbol{q})$, representing the scattering power per unit volume of the sample, is known. Of course in practice $i(\boldsymbol{q})$ is not known at the outset and is rather to be determined as the end result of the double scattering correction. Fortunately, this is not a serious problem, since the fraction of double scattering, $I_2(\boldsymbol{q}) / [I_1(\boldsymbol{q}) + I_2(\boldsymbol{q})]$, is not very sensitive to the exact form of $i(\boldsymbol{q})$, so that the experimentally observed $I(\boldsymbol{q})$, after a suitable normalization, can be used as the first approximation to $i(\boldsymbol{q})$. What is more important in the double scattering correction, however, is that $i(\boldsymbol{q})$, in Equations (2.29) and (2.33), must be expressed in absolute units, whereas the observed intensity is usually determined at first in arbitrary units. The procedure for calibrating the instrument to allow conversion of the intensity into absolute units is discussed in the next section.

As an example illustrating the magnitude of the double scattering correction, we present in Figure 2.26 the result of calculations performed for the scattering of x-rays from amorphous bulk polystyrene. Here the thick broken curve shows the single scattering intensity curve (given in electron units per CH). The three solid curves are the double scattering intensities, calculated for samples with thickness 1, 3, and 5 mm, respectively, placed in symmetric transmission mode. The single scattering intensity is referred to the scale on the left axis, and the double scattering intensities are referred to the expanded scale on the right axis. As expected the extent of double scattering increases progressively as the sample thickness is increased from 1 to 5 mm. The overall intensity of scattering due to double scattering is a relatively small fraction of the single scattering intensity, and when the single scattering is very strong, for example, at q around 1.3 Å^{-1}, the effect of double scattering can be safely ignored. However, when the single scattering is weak, as at very small q values, the magnitude of the double scattering intensity is of the same order of magnitude as the single scattering intensity, and a double scattering correction from the observed intensity is clearly required.

2.7 ABSOLUTE INTENSITY CALIBRATION

In the majority of experimental studies what is of interest is the variation in the scattering intensity as a function of the scattering angle, and it is sufficient in such cases to have the observed intensity $I(\boldsymbol{q})$ expressed in any arbitrary units, for example, counts per second. There are, however, cases in which the observed intensity must

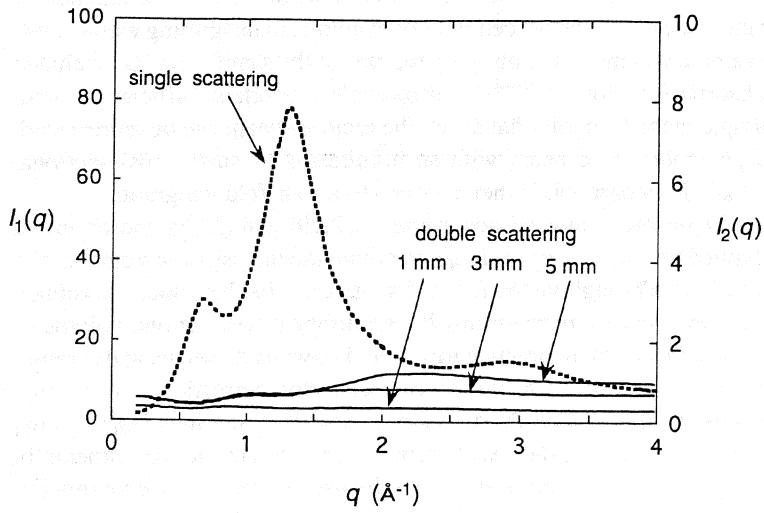

Figure 2.26 The thick broken curve gives the single scattering intensity obtained with amorphous bulk polystyrene. The thin solid curves show the calculated double scattering intensities for samples of the indicated thickness placed in a symmetric transmission geometry. The single scattering intensity is referred to the scale on the left axis; the double scattering intensities are referred to the expanded scale on the right axis.

be placed in absolute units, and to accomplish this the flux of the scattered beam has to be compared to the flux of the incident beam. When a calculation based on a theoretical model is compared against observed data, the confidence in the model is strengthened by agreement not only in the relative magnitudes but also in the absolute values. When the observed intensity consists of both coherent and incoherent scattering, as is usually the case, the coherent component can often be obtained by subtracting the incoherent part known theoretically, but this subtraction can be done only if the overall intensity is obtained on an absolute scale. In the analysis of small-angle scattering results, intensities in absolute units are required to evaluate molar masses of suspended particles and the invariant Q, from which, for example, the phase volumes of immiscible components in a blend can be determined.

There are essentially three types of experimental procedures for determining the absolute intensity. These are (1) determining the intensity of the primary beam itself after attenuating it by some known factor, (2) measuring the scattering intensity from a material whose scattering power is known from theoretical considerations, and (3) using a secondary standard sample that has been calibrated by one of the above two methods.

An unattenuated primary beam is so much stronger than the scattered beam that no detector is capable of measuring both the primary and the scattered beam under similar conditions. Attenuating the primary beam by inserting a filter of known absorption coefficient naturally comes to mind, but the method is difficult and can give erroneous results unless the beam has been rendered strictly monochromatic. Spectral components in the beam with even a small difference in wavelength and in absorption

coefficient can undergo a large difference in attenuation after passage through several layers of the filter. Even with the use of a carefully constructed crystal monochromator, the harmonics with wavelengths $\lambda/2$, $\lambda/3$, etc. can present complications. Another method of attenuating the beam is to use a rotating disk with a small opening. If the rotation speed is low and the opening is relatively large, the beam is simply chopped up into pulses, and the flux in each pulse will remain still too high for the detector to measure without serious counting losses. In fact the rotor has to be designed such that the number of x-ray photons or neutrons that pass the hole at any one occasion is smaller than one on average. Only in this way can one ensure that the interval between the arrivals of two successive radiation particles exceeds the deadtime of the counter.[21] For the comparison to be meaningful, of course the primary and the scattered beams must be measured under the exact same instrumental conditions, including the collimation geometry and the detector operation parameters, except for the presence of the attenuator with the former and the sample with the latter.

For neutron scattering, vanadium metal is a convenient material for calibrating both wide-angle and small-angle instruments. The coherent scattering cross section of a vanadium nucleus is 0.0184 barns, the smallest among all the elements, and its incoherent scattering cross section is 5.187 barns, a relatively large value. The scattering of neutrons from vanadium is therefore almost completely incoherent and depends very little on the scattering angle, as seen in the data given in Figure 2.27.[22] With x-rays, there is no comparably convenient material. For x-ray wide-angle instruments, the integrated intensities of Bragg diffraction peaks from nickel metal can be used as the calibration standard, as was shown by a study performed by a commission of the International Union of Crystallography (Suortti[23], see also Suortti *et al.*[24]). For small-angle x-ray instruments the scattering due to density fluctuation in an amorphous material can be utilized. As discussed in Chapter 4, the intensity of scattering from a single component liquid or gas, when extrapolated to zero scattering angle, is given by

$$\lim_{q \to 0} I(q) = V b^2 \langle n \rangle^2 kT \beta_T \tag{2.36}$$

where V is the scattering volume, b is the scattering length per molecule, $\langle n \rangle$ is the number density of the molecules, and β_T is the isothermal compressibility. Since the compressibility of a gas or liquid can be determined accurately, its calculated zero-angle scattering intensity can serve as a reliable reference. Scattering from water has been used for this purpose (Hendricks *et al.*[25]). Because of its fairly weak scattering, accumulation of counts over some length of time is required, but on the other hand the need for multiple scattering correction is only moderate. The use of a gas, especially octafluorocyclobutane in view of its high scattering power (Hendricks and Shaffer[26]), has been suggested, but with a gas a careful regulation of its pressure is important.

Other material specimens, once carefully calibrated by one of the primary methods explained above, can be used as a secondary standard. The material for such a secondary standard should be easy to handle, give a moderately strong scattering intensity, and remain unaltered over a long period of time under repeated usage. Polyethylene and glassy carbon have been used for this purpose.

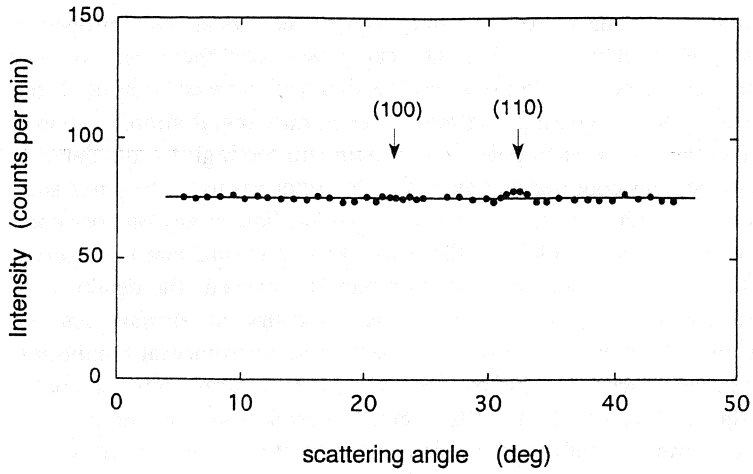

Figure 2.27 Neutron scattering pattern of vanadium at 20 K, showing the extremely weak coherent scattering. (From Shull and Wilkinson.[22])

FURTHER READING

Synchrotron Radiation Source

1. Winick, H., in *Synchrotron Radiation Research*, Chapter 2, H. Winick and S. Doniach, Eds., Plenum Press, New York, 1980.
2. Elsner, G., Riekel, Ch., and Zachmann, H. G., *Adv. Polym. Sci.* **67**, 1 (1985).
3. Margaritondo, G., *Introduction to Synchrotron Radiation,* Oxford University Press, New York, 1988.
4. Helliwell, J. R., *Macromolecular Crystallography with Synchrotron Radiation*, Cambridge University Press, Cambridge, 1992, chapter 4.

Pulsed Neutron Source

5. Windsor, C. G., *Pulsed Neutron Scattering*, Taylor & Francis, London, 1981.

REFERENCES

6. *International Tables for Crystallography*, Vol. C, Kluwer Academic Publishers, Dordrecht, 1992, Section 4.2.1, and *International Tables for X-ray Crystallography*, Vol. III, Kynoch Press, Birmingham, 1968, p. 71.
7. Roberts, B. W., and Parrish, W., in *International Tables for X-ray Crystallography,* Vol. III, Kynoch Press, Birmingham, England, 1968, Section 2.3.
8. Bée, M., *Quasielastic Neutron Scattering*, Adam Hilger, Bristol, 1988.
9. *International Tables for Crystallography*, Vol. C, Kluwer Academic Publishers, Dordrecht, 1992, Section 4.2.4.

10. Stirling, G. C., in *Chemical Application of Thermal Neutron Scattering,* B. T. M. Willis, Ed., Oxford University Press, Oxford, 1973, p. 31.
11. Arndt, U. W., and Willis, B. T. M., *Single Crystal Diffractometry,* Cambridge University Press, Cambridge, 1966, Chapter 4.
12. Borkowski, C. J., and Kopp, M. K., *Rev. Sci. Instr.* **39**, 1515 (1968).
13. Helliwell, J. R., *Macromolecular Crystallography with Synchrotron Radiation*, Cambridge University Press, Cambridge, 1992, p. 181.
14. Faruqi, A. R., *Nucl. Instr. Method* **A310**, 14 (1991).
15. Amemiya, Y., Matsushita, T., Nakagawa, A., Satow, Y., Miyahara, J., and Chikawa, J., *Nucl. Instr. Methods* **A266**, 645 (1988).
16. Arndt, U. W., *J. Appl. Crystallogr.* **19**, 145 (1986).
17. Hendrix, J., *Adv. Polymer Sci.* **67**, 59 (1985).
18. Vineyard, G. H., *Phys. Rev.* **96**, 93 (1954).
19. Sears, V. F., *Adv. Phys.* **24**, 1 (1975).
20. Strong, S. L., and Kaplow, R., *Acta Crystallogr.* **23**, 38 (1967).
21. Kratky, O., in *Small-Angle X-Ray Scattering*, H. Brumberger, Ed., Gordon and Breach, New York, 1967, Chapter 4.
22. Shull, C. G., and Wilkinson, M. K., *Rev. Mod. Phys.* **25**, 100 (1953).
23. Suortti, P., *Acta Crystallogr.* A**33**, 1012 (1977).
24. Suortti, P., Hastings, J. B., and Cox, D. E., *Acta Crystallogr.* A**41**, 413 (1985).
25. Hendricks, R. W., Mardon, P. G., and Shaffer, L. B., *J. Chem. Phys.* **61**, 319 (1974).
26. Hendricks, R. W., and Shaffer, L. B., *USAEC Report ORNL-TM 3407*, Oak Ridge National Laboratory, Oak Ridge, TN, 1971.

Crystalline Polymers

3

3.1 INTRODUCTION

Figure 3.1 illustrates a typical x-ray diffraction pattern that can be obtained with a semicrystalline polymer, in this example poly(3-hydroxybutyrate), by means of a flat film camera such as the one shown in Figure 2.19. The sample is isotropic, having been crystallized from the melt by lowering the temperature without any application of deformation. The semicrystalline polymer therefore contains many crystallites oriented in all directions with equal probabilities and, as a consequence, exhibits circular diffraction patterns as seen in Figure 3.1. Such a photograph is often called a *powder diagram* in analogy to the diffraction pattern obtainable with a crystalline powder. If a microdensitometer scan of the diagram in Figure 3.1 is taken from the center in a radial direction, or, alternatively, if a diffractometer scan of diffracted beam intensity is made over a range of diffraction angle 2θ from small to large, an intensity curve such as given in Figure 3.2 is obtained. Here a number of relatively sharp diffraction peaks, indicative of a crystalline material, are superimposed on a broad, diffuse scattering, with its maximum around 20° in 2θ, which arises from the amorphous phase of the polymer. If the sample is stretched uniaxially after it has been crystallized so that the crystallites in it are highly oriented, the diffraction pattern obtained may look like the one shown in Figure 3.3. Here the diffraction pattern was obtained with an ultradrawn sample of poly(α, α'-dimethylpropiolactone), taken with a film placed cylindrically around the fiber. Such a diffraction pattern is called a *fiber diagram*. The reason for the appearance of the diffraction spots arranged in horizontal lines is explained in Appendix C. If the degree of orientation of the crystallites is much more modest, a diffraction pattern in which the circles in Figure 3.1 are reduced to arcs is obtained, and the length of such arcs then gives a measure of the degree of crystallite orientation.

Given diffraction data such as those illustrated in Figures 3.1–3.3, several different types of information can be derived from them about the structure of the semicrystalline polymer.

1. From the set of diffraction angles at which sharp Bragg peaks are observed, the lattice parameters a, b, and c and the angles among them that define the unit cell geometry can be calculated. Studying the changes in the lattice parameters

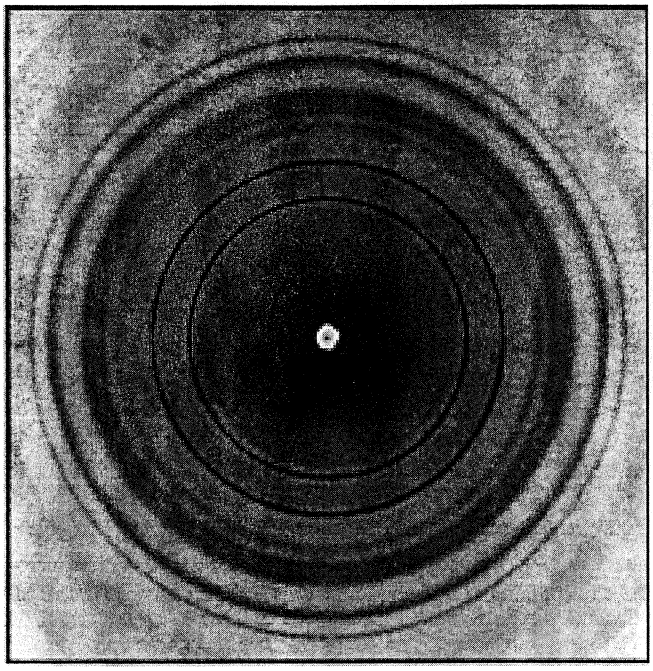

Figure 3.1 Diffraction pattern obtained with an isotropic, semicrystalline polymer, poly(3-hydroxybutyrate) by means of a flat film camera. (Courtesy of M. M. Satkowsky.)

resulting from changes in temperature, pressure, stress, etc. provides insight into the ways crystals respond to outside influences imposed on them.

2. By collecting the integrated intensities of diffraction peaks and subjecting them to a sequence of analyses, it is possible to determine the positions of the atoms packed in the crystalline unit cell. Such an endeavor constitutes the traditional process of crystal structure analysis, and much of the information that is available today about the shape of polymer molecules and their arrangement in crystals was derived by this method.
3. The diffraction peaks obtained with a perfect crystal are in theory expected to be infinitely sharp. The finite widths of the observed diffraction peaks as seen in Figure 3.2 reflect the fact that crystallites in semicrystalline polymers are not perfect, and the analysis of the line widths can tell us about the nature and degree of imperfection in the polymer crystal lattices and the size of the polymer crystallites if they are small.
4. The degree of crystallinity can be determined if the intensities due to the amorphous scattering can be separated, by an appropriate method, from the Bragg diffraction peaks due to crystalline phases. The broadening of diffraction peaks due to crystal imperfections and the consequent overlapping of the diffraction peaks, however, make accurate determination of the degree of crystallinity sometimes difficult.

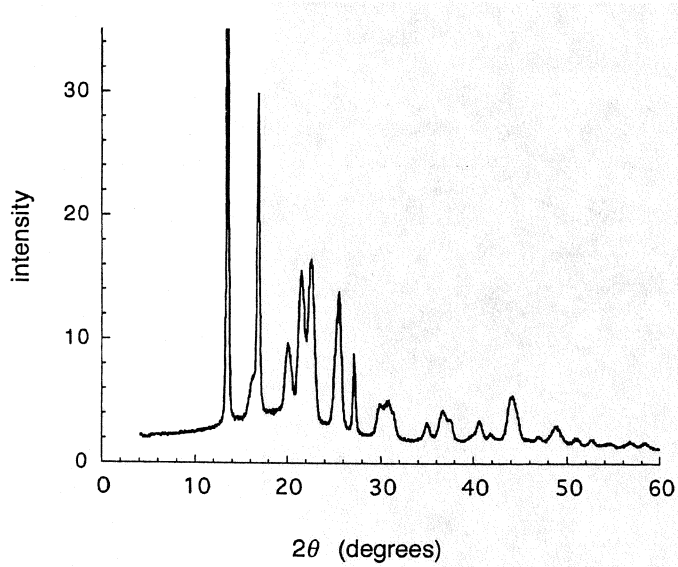

Figure 3.2 Diffraction pattern of poly(3-hydroxybutyrate), obtainable by a radial microdensitometer scan of the powder diagram such as shown in Figure 3.1. (Courtesy of M. M. Satkowsky.)

5. With an anisotropic sample, by measuring the variation in the intensities along one or more diffraction arcs, as mentioned in the preceding paragraph, the degree of preferred orientation and the orientation distribution of crystallographic planes in the crystalline phase can be determined. A combined analysis of several such distributions of crystallographic plane orientations can lead to the determination of the distribution of the crystallite orientation itself.

In the following five sections of this chapter methods of obtaining each of these five types of information from the analysis of the diffraction data are discussed.

3.2 LATTICE PARAMETERS

3.2.1 Indexing

The *lattice parameters* (or *lattice constants*) that define the unit cell geometry are the lengths a, b, and c of the unit cell edges and the angles α, β, and γ between the b and c axes, c and a axes, and a and b axes, respectively. The first step in

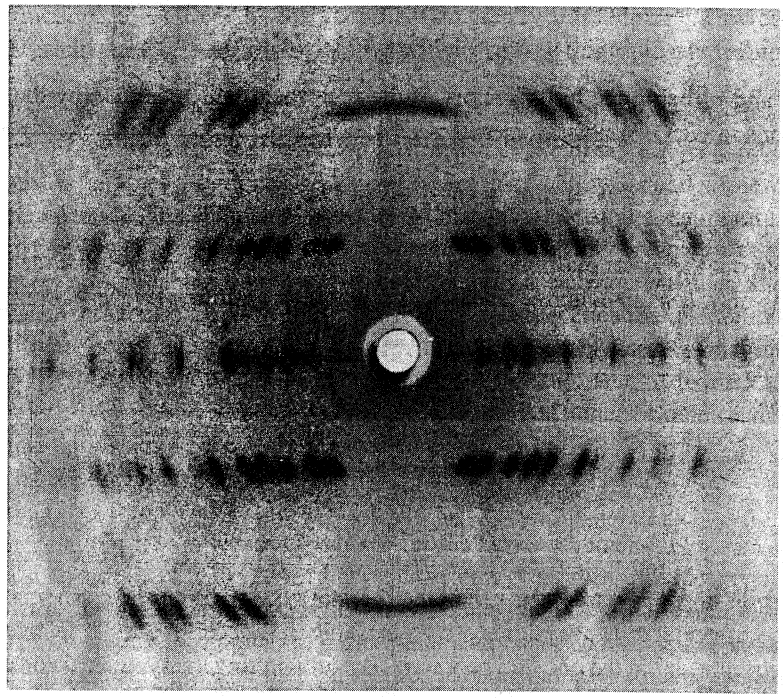

Figure 3.3 Fiber diagram obtained with a highly stretched poly(α, α'-dimethylpropiolactone). (Courtesy of E. S. Clark.)

the determination of accurate lattice parameters is to *index* the observed diffraction peaks, that is, to identify the Miller indices h, k, and l for each of the crystallographic planes that gave rise to the reflections. When the unit cell parameters are already known even approximately, indexing a diffraction peak is a relatively simple matter and consists of deciding on the set of integers h, k, and l that makes the observed diffraction angle 2θ match the one calculated from the *Bragg relationship* (or *Bragg law*)

$$\frac{2 \sin \theta}{\lambda} = \frac{1}{d_{hkl}} \tag{3.1}$$

where d_{hkl} is the interplanar spacing between parallel crystallographic planes (hkl). For this purpose we need an expression giving d_{hkl} as a function of h, k, and l and of the lattice constants. As noted in Appendix C, $1/d_{hkl}$ is equal to the absolute value of $\mathbf{r}^*_{hkl}$, where $\mathbf{r}^*_{hkl}$ is the reciprocal lattice vector given by

$$\boldsymbol{r}^*_{hkl} = h\boldsymbol{a}^* + k\boldsymbol{b}^* + l\boldsymbol{c}^* \tag{3.2}$$

$\boldsymbol{a}^*$, $\boldsymbol{b}^*$, and $\boldsymbol{c}^*$ being the basis vectors of the reciprocal lattice defined by the set of equations in (C.1). We therefore write

$$\frac{1}{d^2_{hkl}} = (h\boldsymbol{a}^* + k\boldsymbol{b}^* + l\boldsymbol{c}^*) \cdot (h\boldsymbol{a}^* + k\boldsymbol{b}^* + l\boldsymbol{c}^*) \tag{3.3}$$

Carrying out the scalar multiplications on the right of (3.3) and expressing the results in terms of a, b, c, α, β, and γ leads, after some heavy arithmetic (see Warren[10]), to

$$\frac{1}{d^2_{hkl}} = \left[\frac{h^2 \sin^2\alpha}{a^2} + \frac{k^2 \sin^2\beta}{b^2} + \frac{l^2 \sin^2\gamma}{c^2} + \frac{2hk}{ab}(\cos\alpha \cos\beta - \cos\gamma) + \frac{2kl}{bc}(\cos\beta \cos\gamma - \cos\alpha) + \frac{2lh}{ca}(\cos\gamma \cos\alpha - \cos\beta) \right] / \left(1 + 2\cos\alpha \cos\beta \cos\gamma - \cos^2\alpha - \cos^2\beta - \cos^2\gamma\right) \tag{3.4}$$

This expression is general and is valid for all crystal systems. A crystal can be classified into one of seven crystal systems, given in Table 3.1, according to the elements of symmetry present in the unit cell geometry. By substituting the symmetry constraints listed in Table 3.1 for the unit cell axes and angles, Equation (3.4) for $1/d^2_{hkl}$ can be simplified considerably for crystal systems of higher symmetry, while for triclinic crystal systems Equation (3.4) stands as given.

For most of the semicrystalline polymers that have been synthesized and studied to any extent to date the unit cell parameters are known at least approximately, and a good tabulation of such data is found in reference books such as *Polymer Handbook*.[11] When the unit cell geometry is entirely unknown, indexing the Bragg reflections is a more involved process. Having a fiber diagram rather than a powder diagram alone is then useful, since the two-dimensional information about the x and y coordinates of

TABLE 3.1
Seven Crystal Systems

Crystal System	Constraints due to Symmetry
Cubic	$a = b = c, \alpha = \beta = \gamma = 90°$
Tetragonal	$a = b, \alpha = \beta = \gamma = 90°$
Orthorhombic	$\alpha = \beta = \gamma = 90°$
Rhombohedral[a]	$a = b = c, \alpha = \beta = \gamma \neq 90°$
Hexagonal	$a = b, \alpha = \beta = 90°, \gamma = 120°$
Monoclinic[b]	$\alpha = \gamma = 90°$
Triclinic	None

[a] Also called trigonal.
[b] By convention the unique axis (the axis perpendicular to the other two axes) is designated as the b axis, unless there is a specific reason for designating otherwise.

the diffraction spots offered by the fiber diagram greatly aids indexing. However, the need for such a task seldom arises, and we will not pursue this topic any further here.

3.2.2 Precision Measurement of Lattice Parameters

For a given polymer the precise values of lattice parameters depend somewhat on the circumstances in which the material is placed, such as the temperature, the deformation history, the crystallization conditions, etc. The changes in the lattice parameters brought about by these outside influences are always much smaller than the parameters themselves, and for their accurate determination the diffraction angle 2θ has to be measured with good accuracy. The experimental precautions that must be taken for this purpose have been discussed by many, among them Klug and Alexander,[3] Parrish and Wilson,[12] and Baltá-Calleja and Vonk.[4] Some of the more important points among them are mentioned below.

For each Bragg reflection for which the diffraction angle 2θ is accurately measured, Equation (3.1), into which expression (3.4) is substituted for $1/d_{hkl}$, is set up. The set of such equations is simultaneously solved for the lattice parameters a, b, c, α, β, and γ (or a subset of them in the case of crystal systems other than triclinic) regarded as unknowns. The number of Bragg reflections included in the measurement preferably should be larger than the number of lattice parameters to be determined. In solving the overdetermined set of equations by a method such as the least-square, more weight should be given, in general, to reflections at larger diffraction angles 2θ. The reason for this is easily seen if we differentiate the Bragg relationship (3.1) to obtain

$$\frac{\Delta d}{d} = -\cot\theta\ \Delta\theta \tag{3.5}$$

which shows that the relative error, $\Delta d/d$, in the plane spacing d due to the error $\Delta\theta$ in the diffraction angle decreases as θ approaches 90° (or as the diffraction angle 2θ approaches 180°). This strategy may not always work with some polymers, however, since the shape of the diffraction peaks observed may deteriorate rather rapidly with increasing 2θ angle, and moreover these higher order peaks may overlap severely with each other.

When a flat, sheet-like sample is mounted in a diffractometer in reflection geometry (see Figure 2.23a), two factors induce the line shape to broaden asymmetrically, causing the reflection positions to shift to smaller angles. The first of these effects arises from the failure to achieve a perfect focusing geometry. With a divergent incident beam, a perfect focusing is achieved only when the sample surface is bent so as to conform to the focusing circle that passes through the source, the detector, and the diffractometer axis. It is impractical to have the sample bent at a variable curvature as the diffraction angle is altered continuously during a 2θ scan. In the usual practice a flat sheet is mounted, and a small geometric aberration is thereby created. The second effect arises from the penetration of the beam below the surface of the sample. The depth of the penetration varies with the diffraction angle, so that the effective center of the sample also shifts with 2θ. According to Wilson,[13] the shift

in the center of gravity of the diffraction line profile, when the sample is mounted with the center of its front surface coincident with the diffractometer axis, is given by

$$\Delta(2\theta) = -\frac{L^2 \sin 2\theta}{12R^2} - \frac{\sin 2\theta}{2\mu R} + \frac{2t \cos\theta}{R[\exp(2\mu t/\sin\theta) - 1]} \tag{3.6}$$

where R is the diffractometer radius, t is the thickness of the sample, μ is the linear absorption coefficient, and L, the length of the sample illuminated by the beam, is given by

$$L = \frac{2\alpha R}{\sin\theta} \tag{3.7}$$

2α being the full angular aperture of the incident beam in the diffractometer plane. The first term in (3.6) arises from the "flat sample effect" and the second and third terms from the "beam penetration effect." The first effect is minimized by using an incident beam with a small divergent angle α. For small t it is easily seen that the second and third terms are about equal in magnitude and cancel each other out, and therefore a thin sample should be used to minimize the error due to the second effect.

A practical way of obtaining good accuracy in the lattice parameters, without requiring accurate calibration of all the elements in a diffractometer, is to make use of a calibration standard, that is, to have a material of known lattice parameters mixed in the polymer sample being investigated. Best results are obtained when such a standard material is not simply spread thinly over the surface but is blended with the polymer so that the standard is dispersed throughout the sample. Powders of inorganic materials such as quartz and silicon, for example, are used for this purpose.

3.2.3 Examples of Lattice Parameter Measurements with Polymers

Changes in the lattice parameters of polymers can be observed under a variety of circumstances. Information on changes in the lattice parameters provides insight into the forces that bind the atoms and molecules in the crystal and the factors that determine the crystal structure. The unit cell dimensions change with temperature as a result of thermal expansion. With polymers the thermal expansion is always highly anisotropic, the change in the direction of the chain axis being the smallest. Figure 3.4 shows the results obtained (by Davis *et al.*[14]) with polyethylene, which has an orthorhombic structure with the c axis along the direction of the planar zig-zag chain backbone. Application of pressure brings about densification of materials, which is reflected in the unit cell dimensions. If any polymorphic transformation takes place as a result of changes in temperature or pressure, it can be detected as an abrupt change in the lattice parameters. Application of stress also induces changes in the lattice dimensions, and if the true stress that is actually borne by the crystalline lattices can be estimated, the measurement of the change in the lattice parameters leads to determination of the true elastic moduli of the crystalline polymer.

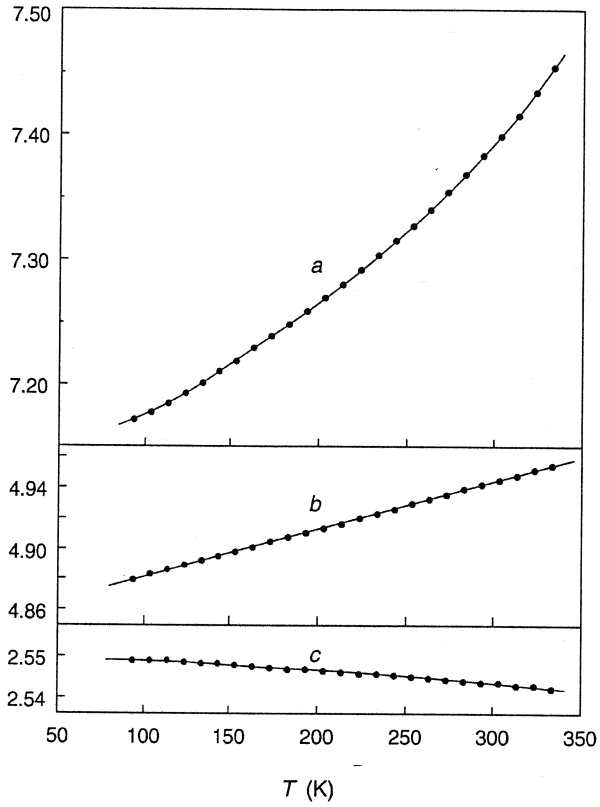

Figure 3.4 Effect of temperature on the lattice parameters of linear polyethylene. (From Davis *et al.*[14])

There are many examples in the literature showing that incorporation of foreign comonomer units into the chain backbone of a crystallizable polymer can lead to expansion of the unit cell dimensions. Figure 3.5[15,16] plots the cell parameters of isotactic polypropylenes, which were randomly copolymerized with various mole fractions of butene-1. Isotactic polypropylene crystal is monoclinic, its chain backbone forming a 3_1 helix in the c direction. The lattice expansion may result either from inclusion of foreign comonomer units into the crystalline phase creating lattice imperfections or from accumulation of rejected noncrystallizable units in the surface region of the crystallites, the strain resulting from it propagating to the interior. Arguments for either case can be made depending on the specifics of the polymer crystals being investigated, and evidence from other sources is required to give support to either case. For example, with melt-crystallized and solution-crystallized polyethylene (Davis *et al.*[17]), the lattice parameters depend on the lamellar thickness, suggesting that the lattice expansion arises from the surface strain effect.

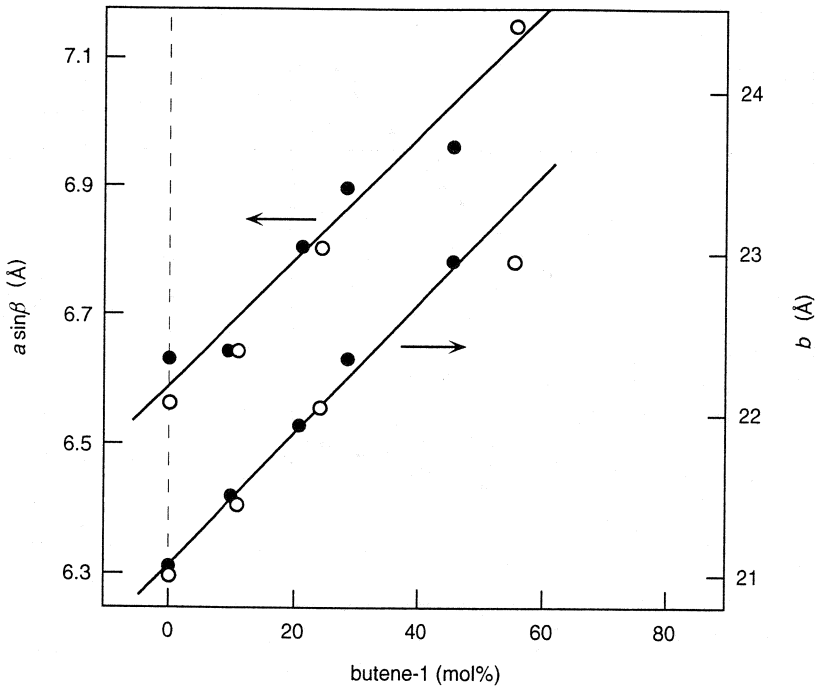

Figure 3.5 Lattice parameters of isotactic polypropylenes randomly copolymerized with various proportions of butene-1. The crystal is monoclinic, with the chain helical axis in the *c* direction. The data include the results (in solid symbols) obtained with single crystals prepared from solution (Cavallo *et al.*[15]) and those (in open symbols) obtained with melt crystallized samples (Turner-Jones[16]).

3.3 CRYSTAL STRUCTURE ANALYSIS

3.3.1 Fourier Synthesis

The term *crystal structure analysis* or *crystal structure determination* refers to the endeavor by which the positions of the atoms in a unit cell are determined from analysis of x-ray or neutron diffraction data. As discussed in Section 1.7, the information contained in observed intensities of diffraction from a crystalline material can be separated into two distinct factors, one relating to the lattice structure of the crystal and the other to the atomic content within a unit cell. The former can be obtained from the measurement of the diffraction angles or more generally from the determination of the scattering vectors s at which Bragg reflections are observed. On the other hand the information about the atomic structure (or the distribution of scattering length density within the unit cell) is contained in the variation in the intensities among observed Bragg reflections. Thus, as discussed in Section 1.7, the amplitude of scattering $A(s)$ can be written as

$$A(s) = F(s)Z(s) \tag{1.96}$$

where the *structure factor* $F(s)$ is the Fourier transform of the scattering length density distribution $\rho_u(r)$ within a unit cell and the lattice factor $Z(s)$ is the Fourier transform of the lattice itself. For the purpose of crystal structure analysis, it is necessary to determine $F(s)$, since its inverse Fourier transform gives the scattering length density distribution and therefore the positions of all atoms in the unit cell.

The bulk of crystal structure analysis work, especially of polymers, is traditionally carried out with data obtained with x rays. X-Ray facilities have been more readily available to polymer scientists, and the flux from an x-ray source is generally much higher than from a neutron source. The discussions that follow in the next few sections are therefore given in the terminology of x-ray analysis. It is to be noted, however, that there are certain advantages to neutrons in crystal structure analysis, especially when used as a supplement to x-ray analysis. A hydrogen atom, with only a single electron, does not contribute much to x-ray scattering, and its position is not easily revealed in the Fourier map synthesized from x-ray intensities. Neutron diffraction data are needed for determining the precise positions of hydrogen atoms or the bond lengths involving hydrogen atoms. It is also possible with neutrons to distinguish atoms with nearly the same atomic number that cannot readily be differentiated with x-rays (for example, Fe, Co, and Ni).

The intensity of scattering from a crystal (assumed to be large and devoid of any lattice defects) is nonzero only when the scattering vector $\boldsymbol{s}$ coincides with the reciprocal lattice $\boldsymbol{r}^*_{hkl}$ given by Equation (3.2). The square root of the intensity I_{hkl} observed at $\boldsymbol{s} = \boldsymbol{r}^*_{hkl}$ (and properly normalized) provides the absolute magnitude of the structure factor $F(s)$ at $\boldsymbol{r}^*_{hkl}$, that is,

$$|F_{hkl}| \equiv |F(\boldsymbol{r}^*_{hkl})| = \sqrt{I_{hkl}} \tag{3.8}$$

To be able to construct the scattering length density distribution $\rho_u(\boldsymbol{r})$ by inverse Fourier transform of the structure factors, additional information on the phase angles of F_{hkl} is needed, which is not directly available from the observed intensity data. Some of the methods by which the phase angles are determined are discussed in Section 3.3.2. For the moment we assume that the full complex value of F_{hkl}, i.e., its absolute magnitude as well as the phase angle, is available for a large number of hkl reflections. The following gives an account of the process by which the scattering length density distribution $\rho_u(\boldsymbol{r})$ is actually calculated when the structure factors are available.

The structure factor F_{hkl} defined by (1.98) can be written as

$$F_{hkl} = \int \rho_u(\boldsymbol{r}) \exp[-i2\pi(h\boldsymbol{a}^* + k\boldsymbol{b}^* + l\boldsymbol{c}^*) \cdot \boldsymbol{r}]\, d\boldsymbol{r} \tag{3.9}$$

If we take the inverse Fourier transform of (3.9) we obtain

$$\rho_u(\boldsymbol{r}) = \frac{1}{V_u} \sum_{h=-\infty}^{\infty} \sum_{k=-\infty}^{\infty} \sum_{l=-\infty}^{\infty} F_{hkl} \exp\left[i2\pi(h\boldsymbol{a}^* + k\boldsymbol{b}^* + l\boldsymbol{c}^*) \cdot \boldsymbol{r}\right] \tag{3.10}$$

where V_u is the volume of the unit cell. In obtaining (3.10) from (3.9) the integration associated with the inverse Fourier transform is replaced by summations in view of the fact that F_{hkl} is assumed nonzero only at integral values of h, k, and l. Note also that $1/V_u$ is the volume of the reciprocal lattice unit cell, which is equal to the volume in reciprocal space that corresponds to incrementing h, k, and l each by one. For crystal structure analysis it is convenient to express the position vector $\boldsymbol{r}$ as

$$\boldsymbol{r} = X\boldsymbol{a} + Y\boldsymbol{b} + Z\boldsymbol{c} \tag{3.11}$$

where X, for example, is the coordinate measured in units of a in the direction of the crystallographic axis $\boldsymbol{a}$. Because of the orthogonality relationships between $(\boldsymbol{a}, \boldsymbol{b}, \boldsymbol{c})$ and $(\boldsymbol{a}^*, \boldsymbol{b}^*, \boldsymbol{c}^*)$, as given in (C.3), (3.10) can be written as

$$\begin{aligned}\rho_u(X, Y, Z) &= \frac{1}{V_u} \sum_{h=-\infty}^{\infty} \sum_{k=-\infty}^{\infty} \sum_{l=-\infty}^{\infty} \\ &\quad F_{hkl} \exp\left[i2\pi(h\boldsymbol{a}^* + k\boldsymbol{b}^* + l\boldsymbol{c}^*)(X\boldsymbol{a} + Y\boldsymbol{b} + Z\boldsymbol{c})\right] \\ &= \frac{1}{V_u} \sum_{h=-\infty}^{\infty} \sum_{k=-\infty}^{\infty} \sum_{l=-\infty}^{\infty} F_{hkl} \exp\left[i2\pi(hX + kY + lZ)\right]\end{aligned} \tag{3.12}$$

The operation represented by (3.12) is often called the *Fourier synthesis*. Equation (3.12) shows that if the knowledge of a complete set of F_{hkl} is available, the scattering length density distribution $\rho(X,Y,Z)$ can be synthesized. In the case of neutron scattering, the scattering length density is concentrated on atomic nuclei and therefore the positions of individual atoms can easily be identified. In the case of x-ray scattering, the electron density distribution, which is proportional to the scattering length density distribution, is again centered around atomic positions but is more smeared out. Figure 3.6[18] illustrates the electron density map of polyethylene, obtained by such a Fourier synthesis, showing that, while the carbon centers are revealed as maxima in the contour map, the positions of hydrogens with single electrons cannot be identified as easily.

3.3.1.1 Effect of Symmetry

In a unit cell the positions of many of the atoms are related to each other by symmetry relationships. Recognizing the presence of such symmetry elements is an important step in solving the structure of a crystal. The symmetry implies that the content of the unit cell can be grouped into several equivalent parts, and the structure of only one of these parts need be determined. Knowledge of the various symmetry elements present may also give valuable hints about the packing of atoms even before the structure analysis has begun.

The various symmetry elements that can be present in a crystal with three-dimensional lattices are (1) n-fold rotation axes, (2) n-fold rotation-inversion axes, (3) mirror planes, (4) n-fold screw axes, and (5) glide planes. The n-fold rotation

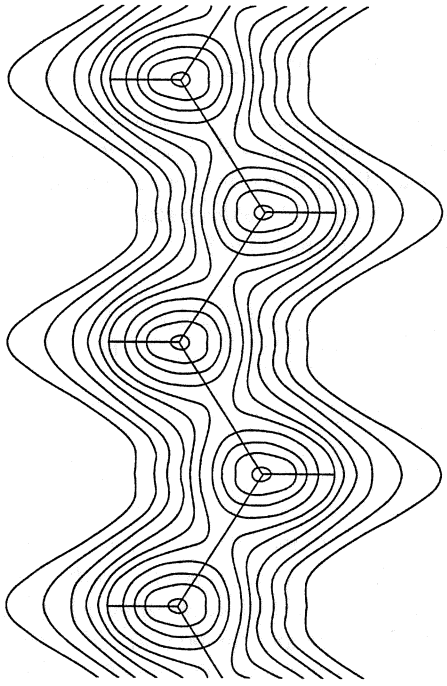

Figure 3.6 Electron density map of polyethylene, in the section through the molecular plane containing all carbon atoms. (From Bunn.[18])

axes can be either one-, two-, three-, four-, or six-fold axes. An n-fold rotation-inversion axis combines an n-fold rotation axis with a center-of-symmetry operation. A mirror plane is equivalent to a two-fold rotation-inversion axis. An n-fold screw axis consists of a combination of an n-fold axis with a translation. A glide plane is a combination of a mirror plane with a translation. These various symmetry elements can be combined to give a three-dimensional infinite lattice in one of 230 distinct ways, or 230 space groups. Detailed description of each of these space groups is found in the *International Tables for Crystallography*, Vol. A.[19] The space group to which the crystal under study belongs is usually determined from the examination of systematic absences of Bragg reflections. In other words, some of the *hkl* reflections, having certain simple relationships among the *h, k,* and *l* indices, are missing from the observed reflections, and the type of relationships that dictates such absences depends on the particular space group concerned.

To illustrate how the presence of symmetry elements gives rise to a systematic absence of certain *hkl* reflections, consider a crystal, for example, that possesses a two-fold screw axis passing through the origin and parallel to the a axis. The symmetry element implies that whenever there is an atom at (X,Y,Z), there is another atom of the same type at $(\frac{1}{2}+X, -Y, -Z)$. We now rewrite Equation (3.9) in terms of atomic positions (X_j, Y_j, Z_j) rather than in terms of scattering length density distribution $\rho_u(\boldsymbol{r})$ as

$$F_{hkl} = \sum_{j=1}^{m} b_j \exp\left[-i2\pi(hX_j + kY_j + lZ_j)\right] \tag{3.13}$$

where b_j is the scattering length of the jth atom and j runs from 1 to m, m being the total number of atoms in the unit cell. (For x-ray diffraction b_j is to be replaced by $b_e f_j$ where b_e is the scattering length of an electron and f_j is the atomic scattering factor.) For the crystal considered in this example F_{h00} is calculated to be

$$\begin{aligned} F_{h00} &= \sum_{j=1}^{m/2} b_j \left\{\exp\left[-i2\pi(hX_j)\right] + \exp\left[-i2\pi\left(\frac{h}{2} + hX_j\right)\right]\right\} \\ &= \sum_{j=1}^{m/2} b_j \exp\left[-i2\pi(hX_j)\right](1 + e^{-i\pi h}) \end{aligned} \tag{3.14}$$

which shows that F_{h00} is equal to zero whenever h is odd.

The systematic absence of hkl reflections for each of the 230 space groups is listed in the *International Table.* Sometimes, noting the systematic absence of reflections is not sufficient to uniquely identify the space group. In such cases some additional information is relied on to narrow the choice. For example, the presence of a center of symmetry (one-fold inversion axis) is inferred from the distribution of intensities among the reflections, or from the lack of certain physical effects such as piezoelectricity or the second harmonic generation of light. An important simplification in the solution of the phase problem arises when the crystal possesses a center of symmetry. Then for every atom at (X, Y, Z) there exists another atom of the same kind at $(-X, -Y, -Z)$, and substituting these atomic coordinates in (3.13) it is seen that all structure factors F_{hkl} are real. The phase angle is therefore equal to either 0 or π, and the task of solving the phase problem, that is, figuring out the phase angles, is now reduced to assigning a correct + or − sign to observed reflections.

3.3.1.2 Resolution of the Fourier Map

The number of reflections for which the intensity can be measured experimentally is limited since, as is seen from the Ewald sphere construction discussed in Section 1.5.3, the range of reciprocal space that can be explored with a radiation of wavelength λ is limited by

$$r^*_{hkl} < s_{\max} \tag{3.15}$$

where $s_{\max}$ is equal to $2/\lambda$. The range of reciprocal space for which the intensity can be measured in practice is often even smaller than $2/\lambda$ for experimental reasons. The limited set of F_{hkl} thus available, under the assumption that the phase problem is completely solved, can be thought of as

$$[\text{a finite set of } F_{hkl} \text{ satisfying (3.15)}] = [\text{an infinite set of } F_{hkl}] \times \sigma(s) \tag{3.16}$$

where $\times$ denotes multiplication and $\sigma(s)$ is a function equal to unity when $|s| \leq s_{\max}$ and equal to zero when $|s| > s_{\max}$. Applying the multiplication theorem (B.24)

to (3.16), we find that the inverse Fourier transform of the function represented by the finite set of F_{hkl} is then equal to the convolution product of the inverse Fourier transform of the infinite set of F_{hkl}, as given by (3.12), and the inverse Fourier transform of $\sigma(s)$. In other words,

$$\frac{1}{V_u}\sum_{\substack{h\\ r^*_{hkl}<s_{max}}}\sum_{k}\sum_{l} F_{hkl}\,\exp[i2\pi(hX+kY+lZ)] = \rho_u(X,Y,Z) * \mathcal{F}^{-1}\{\sigma(s)\} \quad (3.17)$$

The inverse Fourier transform $\mathcal{F}^{-1}\{\sigma(s)\}$ of the function $\sigma(s)$ representing a sphere is the same as its Fourier transform, which has a central peak with a width (HWHM) equal to ca. $1/2s_{max}$ followed by small oscillations of ever decreasing amplitudes at higher r (see the discussion of the Fourier transform of a sphere in Section 5.2.2.1). The scattering length density distribution calculated by (3.17) from the limited set of F_{hkl} is equivalent to the one obtained when the true scattering length density distribution is "smeared" by a "smearing function" $\mathcal{F}^{-1}\{\sigma(s)\}$, and therefore the resolution of the structure that can be deduced from such a smeared distribution is limited to about $1/2s_{max}$.

3.3.2 Performing the Structure Analysis

As can be seen from the discussion in the previous section, producing an electron density map, once observed intensities I_{hkl} are available, could have been an almost routine process of performing a Fourier sum, except for the fact that the information for the phase angles is not directly available from experiment. Almost all of the efforts and ingenuity of those engaged in crystal structure analysis are devoted to figuring out the phase angles. In this scientists have been enormously successful, as judged from the vast number of crystalline structures that have been determined, including many complicated substances such as biological macromolecules containing many thousands of atoms. For the fascinating story of how this is accomplished, the reader is referred to other standard textbooks of crystal structure analysis (for example Glusker and Trueblood[5] and Glusker *et al.*[6]). Here only an extremely brief account of some important aspects of the methods is given.

3.3.2.1 Patterson Function

It was shown in Section 1.5 that the inverse Fourier transform of intensity $I(s)$

$$\Gamma_\rho(r) = \int I(s)e^{i2\pi sr}ds \quad (1.84)$$

gives the autocorrelation function $\Gamma_\rho(r)$ defined as

$$\Gamma_\rho(r) = \int \rho(u)\rho(u+r)\,du \quad (1.79)$$

In the context of diffraction from crystals where $I(s)$ is nonzero only at the reciprocal lattice points, Equation (1.84) can be written, in analogy to (3.12), as

$$P(X, Y, Z) = \frac{1}{V_u} \sum_{h=-\infty}^{\infty} \sum_{k=-\infty}^{\infty} \sum_{l=-\infty}^{\infty} I_{hkl} \exp[i2\pi(hX + kY + lZ)] \quad (3.18)$$

where $P(X,Y,Z)$, called the *Patterson function*, is the autocorrelation function of the scattering length density distribution $\rho_u(X,Y,Z)$ in the unit cell.

A two-dimensional example is given in Figure 3.7 as an aid to understanding the relationship between the scattering length density map $\rho_u(X,Y,Z)$, obtained from a Fourier synthesis of F_{hkl} according to (3.12), and the Patterson map $P(X,Y,Z)$ obtained by (3.18). Here Figure 3.7a depicts a four-atom molecule, the black circle representing the atomic centers where the electron densities are at a maximum. The Patterson map in Figure 3.7b is drawn by placing each atom of Figure 3.7a in succession at the origin and noting the positions of the other atoms. The pattern in Figure 3.7b has a center of symmetry, and the number of maxima is now 12, which is twice the number of interatomic vectors present in (a), that is, $N(N—1)$ with $N = 4$. The Patterson map therefore presents all the inter-atomic vectors present in the unit cell. (The same point is also brought out in the one-dimensional example shown in Figure 1.10.) Once the Patterson map is synthesized from the observed intensities I_{hkl} according to (3.18) an attempt can be made to decipher it and figure out the positions of the N atoms that give rise to the $N(N - 1)$ interatomic vectors in the map. This task may be aided by other supplementary knowledge about the bond distances, bond angles, crystal symmetry, and so forth. The trial structure thus devised can then be tested and improved on by the process of refinement to be discussed in Section 3.3.2.3. However, it must be said that when more than a small number of atoms are involved in a unit cell, deciphering the Patterson function is not an easy task.

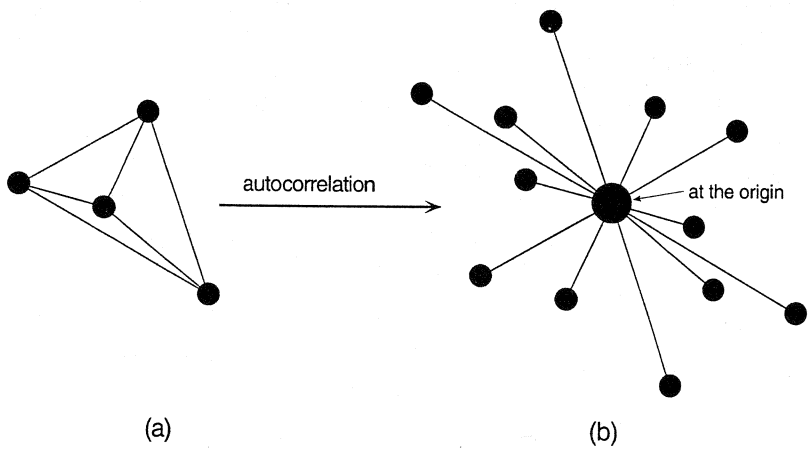

Figure 3.7 Autocorrelation of the simple four-atom molcule in (a) gives the Patterson map shown in (b). Note that the Patterson pattern has a center of symmetry, and the positions of the peaks in it relative to the origin represent all the interatomic vectors present in the molecule (a).

3.3.2.2 Methods of Phase-Angle Determination

Solving the phase problem, that is, obtaining an estimate of the structure factor phase angles that cannot be directly determined from the observed intensity data, is the central task in crystal structure analysis. Three of the more commonly used among the general methods are briefly discussed.

The **heavy atom method** can be used, in x-ray studies, when the material contains one or a few atoms of atomic number Z considerably greater than those of the rest of the atoms. If the material of interest does not contain such a heavy atom, a derivative, containing, for example, an iodine or a heavy metal atom, can often be synthesized, with the hope that the structure of interest is not modified by this substitution. The scattering of x-rays from the material is then dominated by the scattering from the heavy atom, and it can be assumed that the phase angle for the whole structure for most of the *hkl* reflections will be not far from that due to the heavy atom alone. The structure is therefore solved first for the heavy atom alone, for example, by analyzing a Patterson map, and the phase angles for various Bragg reflections are calculated on the basis of this heavy atom structure. The calculated phase angle is then assigned to the square root of the observed intensity to form the set of structure factors that will be subjected to further refinement as described below.

Isomorphous crystals have almost identical structures, but with one or more atoms replaced by chemically similar ones (with different scattering power). With substances having a large number of atoms in a unit cell, for example, with crystals of biological macromolecules, it is often possible to prepare derivatives forming isomorphous crystals. In the following brief description illustrating how the **isomorphous replacement method** works, we assume, for simplicity, that the crystal is centrosymmetric so that the phase angle is either 0 or π only, that is, the value of F_{hkl} is either $+\sqrt{I_{hkl}}$ or $-\sqrt{I_{hkl}}$. If the replaceable atoms are heavy, they can be located by a Patterson map. If the structure factors are F_1 and F_2 for a given Bragg reflection from the two crystals, we can write

$$F_1 = F_{M1} + F_C \tag{3.19}$$

and

$$F_2 = F_{M2} + F_C \tag{3.20}$$

where F_C is the contribution from the component common to both crystals and F_{M1} and F_{M2} are the contributions from the atoms or groups of atoms that are interchanged in the isomorphous pair. From the knowledge of the location of M1 (and M2) both F_{M1} and F_{M2} can be calculated, and therefore the value of $F_1 - F_2$ is obtained, as it is equal to $F_{M1} - F_{M2}$. The calculated value of $F_1 - F_2$ is then compared with the four possible values derived from experimental intensities: $+\sqrt{I_1}+\sqrt{I_2}$, $+\sqrt{I_1}-\sqrt{I_2}$, $-\sqrt{I_1}+\sqrt{I_2}$, and $-\sqrt{I_1}-\sqrt{I_2}$. The one that gives the best match provides the signs of $\sqrt{I_1}$ and $\sqrt{I_2}$.

It has been stated several times that although experimental measurements provide information on the magnitude of the structure factors, the phase-angle information is lost in the observed intensity data. This assertion, however, turns out to be not completely true, since in the **direct methods** the phase angles can be estimated

by comparing the magnitudes of structure factors among different reflections. This fortunate circumstance arises from the fact that there are restrictions to the possible phase angles that individual reflections can take. These restrictions are due to the physical fact that (1) the electron density is everywhere nonnegative and moreover (2) the electron density is concentrated around atomic centers. If phase angles are arbitrarily assigned to the structure factors, in most cases they produce an electron density map that is clearly incompatible with the above conditions. These physical constraints give rise to inequality relationships and statistical distributions that must be obeyed among the structure factors (Harker and Kasper,[20] Karle and Hauptman,[21] Sayre,[22] and Giacovazzo[23]). Application of these criteria to the analysis of observed intensity data is tedious but is fortunately amenable to automatic computer analysis, and the direct methods are fast becoming the preferred choice in the structure analysis of large molecule crystals.

3.3.2.3 Structure Refinement

Once a tentative assignment has been made to phase angles by a method such as one discussed above, a trial structure can be derived. For this purpose, a Fourier synthesis, indicated by (3.12), is performed using the structure factors F_{hkl} that are based on the observed intensities and the estimated phase angles. The electron density map obtained is then interpreted to locate the positions of various atoms, taking into account other available knowledge about the structure, such as the atomic constitution of the substance, bond lengths, bond angles, symmetry, etc.

The trial structure derived in this way or directly from the analysis of a Patterson map is then subjected to an iterative process of refinement. Taking the atomic coordinates in the trial structure, the structure factors are calculated according to (3.13). If the trial structure is a sufficiently good approximation to the true structure, the magnitude $|F_{hkl}|_{\text{calc}}$ of a calculated structure factor should agree fairly well with the observed one $|F_{hkl}|_{\text{obs}} = (I_{hkl})^{1/2}$ for most of the Bragg reflections. The degree of agreement is usually expressed in terms of the *R factor* or *R value,* which is defined as

$$R = \frac{\sum_{\text{all } hkl} \left| |F_{hkl}|_{\text{obs}} - |F_{hkl}|_{\text{calc}} \right|}{\sum_{\text{all } hkl} |F_{hkl}|_{\text{obs}}} \tag{3.21}$$

An R value sufficiently small, such as a number 0.1 or less, is expected if the trial structure is deemed good enough to be accepted as substantially correct. It is unlikely that the first trial structure will give such a good agreement and further refinement is needed. The simplest approach is to take the phase angles of the calculated structure factors as the new set of assigned phase angles to be associated with the observed $(I_{hkl})^{1/2}$, and to repeat the above process. Hopefully, the R value may show an improvement. This process may then be repeated many times until the R values fall below some acceptable value, which depends in part on the estimated accuracy of the intensity measurements. If the initial trial structure is not a good enough approximation, the R value may fail to fall beyond the first several iterations, and a new trial structure then needs to be proposed.

A more systematic way of improving on the trial structure is to use the least-square method. In this method the parameters of the system (such as the atomic coordinates and Debye–Waller factors) are altered by a numerical algorithm in the direction toward minimizing the sum

$$D = \sum_{\text{all } hkl} w_{hkl} \left(|F_{hkl}|_{\text{obs}} - |F_{hkl}|_{\text{calc}}\right)^2 \tag{3.22}$$

where w_{hkl} is a suitably chosen weighting factor that, for example, reflects the difference in the accuracy of measuring different *hkl* reflections. The least-square minimization is well suited for automatic processing by means of a computer.

3.3.3 Examples of Crystal Structure of Polymers

The methods of crystal structure analysis discussed are equally applicable to determining the structure of polymer crystals as well as organic or inorganic, small-molecule crystals and crystals of biological macromolecules. To accurately determine the intensities of Bragg reflections the sample is preferably prepared in the form of a single crystal. With polymers it is, however, not possible to grow single crystals large enough for the purpose; a solution-grown single crystal is much too small to give sufficiently strong diffraction intensities for measurement. In some instances single crystal mats, in which solution-grown lamellar crystals are sedimented to lie in parallel stacks, were used. In the case of polyoxymethylene, a highly crystalline, three-dimensionally oriented crystal was prepared by solid-state polymerization of a single crystal of tetraoxane through γ-irradiation. More usually a bulk-crystallized polymer sample is used, which is treated to attain a high degree of orientation, either by elongation or rolling. Such a treatment enhances the degree of crystallinity, and at the same time helps index the reflections and reduce overlaps among high-order reflections. Sometimes a bidirectional orientation is given by elongating or rolling the sample in the direction perpendicular to the orientation already given. Even after such a treatment the quality of the intensity data obtained is inferior to those obtained with a well-grown single crystal. It is heartening to see that despite these difficulties, the methods of crystal structure analysis have been successfully applied (see Tadokoro[7]) to the determination of the crystal structure of a large number of polymers. A good compilation of crystal structures of polymers is found in Wunderlich.[24] The tabulation in *Polymer Handbook*[11] gives, in addition to lattice parameters, the space group, the type of chain conformation, and a reference to original literature for most crystalline polymers.

A few illustrative examples of crystal structures of polymers are given here. The electron density map of polyethylene obtained by Fourier synthesis is given in Figure 3.6, and it shows that the polymer molecule adopts a planar zig-zag conformation in which the torsional angle of the C–C bonds are all in *trans*. Figure 3.8 shows that in polyoxymethylene (Uchida and Tadokoro[25]) all the backbone C–O bonds adopt a *gauche* conformation, with the result that the overall chain conformation is helical. The helical structure is clearly seen in Figure 3.8b, which gives the electron density distribution on a cylindrical section of radius 0.691 Å surrounding the helix axis

and cut open flat for presentation. The alternate peaks of lower and higher densities correspond to carbon and oxygen atoms. The *c* repeat distance of 17.39 Å is spanned, as seen clearly in the electron density map, by five turns of the helix involving nine –CO– units.

Helical conformations occur frequently in crystalline polymers (Wunderlich[24]). The type of helical structure is designated by a nomenclature of the form $A*u/t$ where A is the number of backbone atoms in a repeat unit of the polymer chain, u is the number of such units required for a crystallographic repeat distance in the chain axis direction, and t is the number of turns the helix makes in this crystallographic repeat. Thus the above mentioned polyoxymethylene has a helix structure 2∗9/5. According to this scheme, the planar zig-zag conformation of polyethylene can be regarded as a helix of a 2∗1/1 or 1∗2/1 designation. In polyethylene the hydrogens atoms attached to adjacent carbon atoms are separated by 2.5 Å, which is greater than the sum of the van der Waals radii of 2.4 Å for the two hydrogens. If one of the hydrogens in alternate carbons is replaced by another atom or a group of atoms, as is the case in all vinyl polymers, the larger size can no longer be accommodated within the all-*trans*

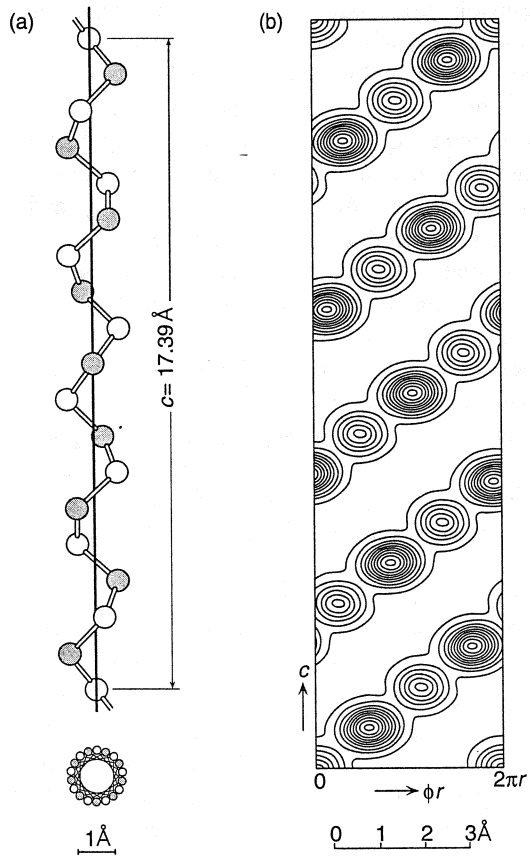

Figure 3.8 Crystal structure of polyoxymethylene. (a) Skeletal model; open circle, oxygen atom; solid circle, methylene group. (b) Electron density map on a cylindrical section of radius 0.691 Å, which is cut open flat for presentation purpose. (From Uchida and Tadokoro.[25])

planar zig-zag conformation. With some of the backbone C–C bonds forced to *gauche* conformations, the chain settles down to a helical structure, as illustrated in Figure 3.9. For example, isotactic polypropylene and isotactic polystyrene adopt alternate *trans* and *gauche* conformations for the backbone C–C bonds and result in a 2∗3/1 helix shown in Figure 3.9a. With larger side groups a more loose helix is needed, and structures such as those shown in Figure 3.9b and c are then realized (Natta and Corradini[26]).

3.4 LINE BROADENING AND CRYSTAL IMPERFECTIONS

A diffraction pattern obtained from a large, perfect crystal is expected to consist of a number of extremely sharp diffraction peaks at s coinciding with the reciprocal lattice r^*_{hkl}. The diffraction peaks actually observed with a crystalline sample and especially those observed with a crystalline polymer, however, have finite widths. Three distinct reasons for such line broadening, examined in this section, are (1) instrumental effects, (2) an effect due to the small crystal size, and (3) effects due to lattice imperfections.

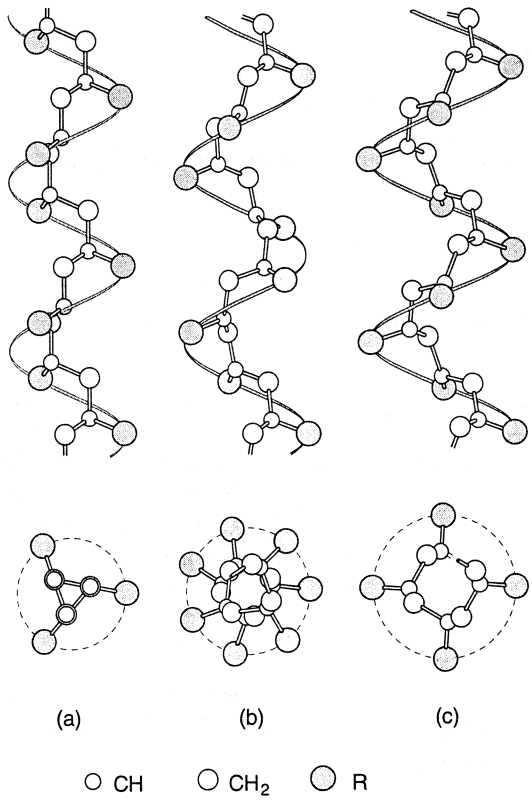

Figure 3.9 Helical structures adopted by various isotactic vinyl polymers (Natta and Corradini[26]). The side group R-of the polymers that form the helical structures shown is $-CH_3$, $-C_2H_5$, $-CH{=}CH_2$, $-CH_2-CH_2-CH-(CH_3)_2$, $-O-CH_3-O-CH_2-CH-(CH_3)_2$, and $-C_6H_5$ for (a), $-CH_2-CH-(CH_3)-C_2H_5$ and $-CH_2-CH-(CH_3)_2$ for (b), and $-CH-(CH_3)_2$ and $-C_2H_5$ for (c).

3.4.1 Instrumental Broadening

A diffraction line may be broadened as a result of instrumental effects, such as an imperfection in the collimation geometry, the finite width of the detector window, imperfect focusing, less than perfect monochromatization of the incident beam, etc. Suppose that $I(s)$ represents the intensity pattern that could be obtained under an ideal instrumental condition producing no instrumental broadening, and $I_{obs}(s)$ represents the smeared intensity pattern that is actually observed. The relationship between these two can be expressed in most cases as

$$I_{obs}(s) = I(s) * G(s) \tag{3.23}$$

where $G(s)$ is the "smearing" function that characterizes the effect of smearing due to the finite resolution of the instrument. In principle, $G(s)$ can be determined experimentally by measuring the diffraction line shape with the same instrument under exactly the same conditions but using a sample that is known to give a perfectly sharp diffraction line. A "standard" powder sample of a strain-free crystalline material of sufficiently large crystal sizes, to rule out any particle-size broadening, can in practice serve the purpose. A fairly good approximation to $G(s)$ can also be obtained from an intimate knowledge of the instrumental geometry and the conditions of measurement. With a good approximation to $G(s)$ thus available, a correction to the observed intensity $I_{obs}(s)$ to remove the effect of smearing can be easily accomplished. Taking the Fourier transform of (3.23) gives

$$\mathcal{F}\{I_{obs}(s)\} = \mathcal{F}\{I(s)\}\mathcal{F}\{G(s)\} \tag{3.24}$$

Therefore $I(s)$ can be obtained as the inverse Fourier transform of the ratio $\mathcal{F}\{I_{obs}(s)\}/\mathcal{F}\{G(s)\}$.

3.4.2 Small Crystal Size

In representing the scattering length density distribution in the crystal in Section 1.7 as

$$\rho(\boldsymbol{r}) = \rho_u(\boldsymbol{r}) * z(\boldsymbol{r}) \tag{1.95}$$

we have tacitly assumed that the crystal is of infinite size and $z(\boldsymbol{r})$ represents the crystal lattice extending to infinite extent in three dimensions. Now we examine what modification is brought to the amplitude $A(s)$ and intensity $I(s)$ of scattering when the crystal is of finite size. The scattering length density distribution in a finite crystal can be written as

$$\rho(\boldsymbol{r}) = \rho_u(\boldsymbol{r}) * [z(\boldsymbol{r}) \cdot \sigma(\boldsymbol{r})] \tag{3.25}$$

where $\sigma(\boldsymbol{r})$ is the *shape function,* which is equal to 1 for $\boldsymbol{r}$ inside the crystal and equal to 0 outside of it (see Figure 3.10). Taking the Fourier transform of (3.25) and making use of the multiplication theorem we obtain

$$A(s) = F(s) \cdot [Z(s) * \Sigma(s)] \tag{3.26}$$

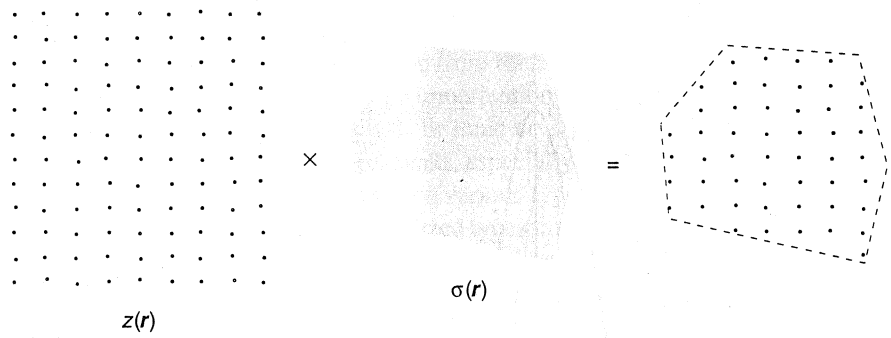

Figure 3.10 Action of the shape function $\sigma(\boldsymbol{r})$.

and

$$I(\boldsymbol{s}) = |F(\boldsymbol{s})|^2 \; |Z(\boldsymbol{s}) * \Sigma(\boldsymbol{s})|^2 \tag{3.27}$$

where $F(\boldsymbol{s})$ is the structure factor, $Z(\boldsymbol{s})$ is the Fourier transform of $z(\boldsymbol{r})$ and is equal to the reciprocal lattice (within a proportionality constant, as mentioned in Appendix C), and $\Sigma(\boldsymbol{s})$ is the Fourier transform of $\sigma(\boldsymbol{r})$. To examine more closely what $Z(\boldsymbol{s}) * \Sigma(\boldsymbol{s})$ and its square are like, we now consider a specific example of the shape function $\sigma(\boldsymbol{r})$.

Suppose the crystal has the shape of a parallelepiped with edges of lengths L_x, L_y, L_z in the x, y, z directions. The Fourier transform of such a shape can be obtained by integrating for x, y, and z separately, and is given by

$$\Sigma(\boldsymbol{s}) = \left(L_x \frac{\sin \pi s_x L_x}{\pi s_x L_x}\right)\left(L_y \frac{\sin \pi s_y L_y}{\pi s_y L_y}\right)\left(L_z \frac{\sin \pi s_z L_z}{\pi s_z L_z}\right) \tag{3.28}$$

where s_x, s_y, s_z are the components of $\boldsymbol{s}$ in the x, y, z directions. The function $\sin \pi sL / \pi sL$, as shown in Figure 3.11, has a peak of height unity at $s = 0$ and oscillates around zero with progressively decreasing amplitudes at larger s, and its zeros are at $s = \pm 1/L, \pm 2/L, \pm 3/L$, etc. The width of its central peak is of the order of $1/L$, which is much smaller than the reciprocal lattice parameters a^*, b^*, c^*. We recall that $Z(\boldsymbol{s})$ can be written as

$$Z(\boldsymbol{s}) = (1/V_u) \sum_{h=-\infty}^{\infty} \sum_{k=-\infty}^{\infty} \sum_{l=-\infty}^{\infty} \delta(\boldsymbol{s} - \boldsymbol{r}^*_{hkl}) \tag{C.10}$$

where V_u is the unit cell volume. The convolution of $\Sigma(\boldsymbol{s})$ with an individual term $\delta(\boldsymbol{s} - \boldsymbol{r}^*_{hkl})$ in $Z(\boldsymbol{s})$ gives $\Sigma(\boldsymbol{s} - \boldsymbol{r}^*_{hkl})$ representing a $\Sigma(\boldsymbol{s})$ peak located at $\boldsymbol{r}^*_{hkl}$. Since the mutual overlap among these peaks is negligibly small, we can write

$$Z(\boldsymbol{s}) * \Sigma(\boldsymbol{s}) = (1/V_u) \sum_{h=-\infty}^{\infty} \sum_{k=-\infty}^{\infty} \sum_{l=-\infty}^{\infty} \Sigma(\boldsymbol{s} - \boldsymbol{r}^*_{hkl}) \tag{3.29}$$

Thus, the lattice factor $Z(\boldsymbol{s})$, which, for an infinite crystal, is an infinite set of delta functions located at the reciprocal lattice points $\boldsymbol{r}^*_{hkl}$, is replaced for a finite crystal by

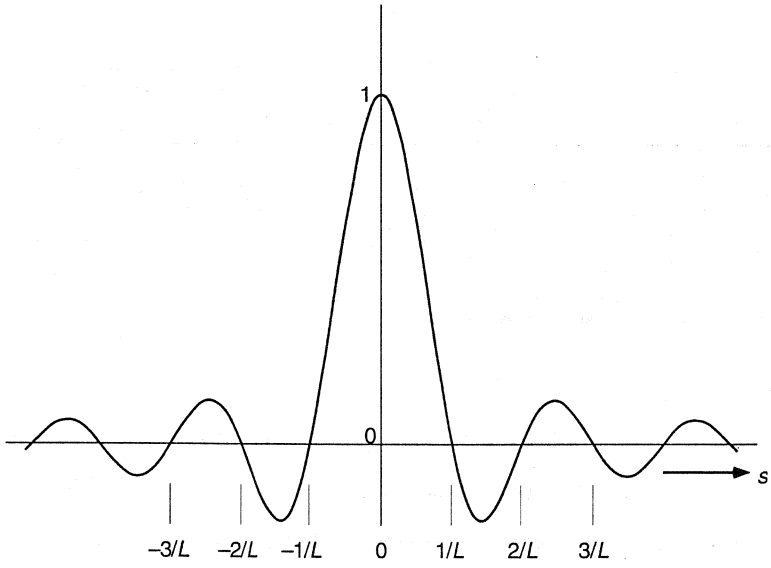

Figure 3.11 Plot of $\sin \pi sL / \pi sL$ against s.

$Z(s) * \Sigma(s)$, which is a similarly infinite set of slightly broadened peaks $\Sigma(s)$ located at the same reciprocal lattice points. The lattice factor $|Z(s) * \Sigma(s)|^2$ that articulates the intensity in (3.27) is a similar set of broadened peaks located at the reciprocal lattice points. The shape of the individual peaks for the intensity function is given by $\Sigma^2(s)$, which has a width, in terms of FWHM, about $1/\sqrt{2}$ of that of $\Sigma(s)$.

It should be noted that the small crystal size broadens all (*hkl*) diffraction lines to the same extent. This is true even for the (000) reflection. The (000) reflection is normally unobservable, since it is hidden by the much stronger primary beam. However, when the line broadening is fairly large and the collimation of the beam is sufficiently fine, it becomes possible to measure the broadening of the (000) reflection. This is significant, since the (000) reflection is not affected by line broadening caused by lattice imperfections, and therefore the line width of the (000) reflection, after correction for instrumental broadening, can be directly interpreted in terms of the size effect. The (000) reflection in fact arises from the constructive interference of scattering from all parts of the sample and is therefore observable with any kind of sample, whether crystalline or not. The line broadening of the (000) reflection therefore provides a means of determining the sample size irrespective of the nature of the sample. The line broadening of the zero angle scattering thus provides a logical bridge to the technique of small-angle scattering discussed in Chapter 5.

3.4.3 Crystal Imperfections

Crystal imperfections of many different kinds can occur in real crystals for a variety of reasons. Occasional substitution of atoms in the crystal with foreign atoms produces imperfection. A vacancy, an interstitial atom, or a chain end in the case of polymer

crystals are all examples of imperfections. Temperature vibrations of atoms in the crystal produce displacements of atoms from their strictly regular lattice positions. In crystalline polymers the degree of imperfection encountered is generally much higher than in small molecule crystals or ionic crystals, as is reflected in the much more ill-defined shape of diffraction peaks, especially at high diffraction angles, that are observed with polymers. Among the various types of imperfections that can be imagined, there are two somewhat idealized types that can be unambiguously defined and quantitatively analyzed. They are called the *crystal imperfections of the first kind* and *of the second kind.* A crystal under study may contain elements of imperfections of both kinds in a differing degree.

In the imperfections of the first kind, we imagine that an ideal lattice, or an ideal average lattice, exists throughout the crystal, and the actual positions of atoms are displaced from their ideal positions to the extent governed by some statistical law. The displacements are assumed to be small compared with the interatomic distances, and moreover the displacement of one atom from its ideal position is totally uncorrelated with that of a neighboring atom. The effect of thermal vibrations of atoms approximates this type of imperfection, if, as in the Einstein model of crystal, we ignore that the vibrations of neighboring atoms are in reality correlated with each other to some extent. A crystal with imperfection of the first kind may also contain a substitutional disorder, in which some of the atoms are replaced by foreign atoms, but we here confine our discussion to displacement disorders only.

In the imperfections of the second kind, the distance between nearest-neighbor atoms fluctuates moderately around an average value according to a statistical law, but there is no longer any average lattice to which the atomic positions can be referred. Thus, although a short-range order is maintained, there is no longer a long-range order. If the fluctuation in the nearest-neighbor distance is large, a liquid structure is realized, with the short-range order decaying rapidly beyond the third or fourth neighbors. But when the extent of imperfection is less severe, a semblance of crystalline order may persist to longer distances. Crystals with this type of imperfection were named *paracrystals* by Hosemann.[8]

The difference between the two types of imperfection can be seen more easily in terms of a one-dimensional lattice, as is illustrated in Figure 3.12. Figure 3.12a represents an ideal lattice in which the distances between neighboring atoms are strictly maintained at d. In Figure 3.12b, which depicts the imperfection of the first kind, atom j is displaced from its ideal position by Δx_j, and the distance between the jth and kth atoms is given by

$$\begin{aligned} x_{jk} &= (kd + \Delta x_k) - (jd + \Delta x_j) \\ &= (k - j)d + (\Delta x_k - \Delta x_j) \end{aligned} \tag{3.30}$$

The deviation of x_{jk} from its expectation value $(k - j)d$ is equal to $(\Delta x_k - \Delta x_j)$, the magnitude of which does not depend on the difference $k - j$. In Figure 3.12c, which depicts the imperfection of the second kind, the distance between the $(j - 1)$th and jth atoms is $d + \Delta x_j$, and the distance between the jth and kth atoms is given by

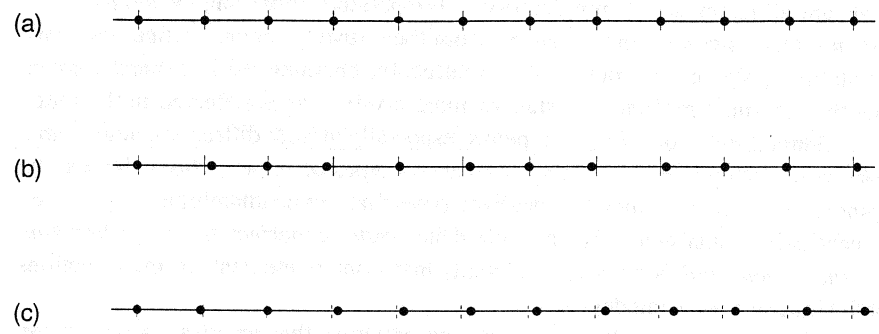

Figure 3.12 One-dimensional examples illustrating lattice distortions. (a) Ideal lattice. (b) Lattice with imperfections of the first kind. (c) Lattice with imperfections of the second kind.

$$x_{jk} = (k - j)d + (\Delta x_j + \Delta x_{j+1} + \cdots + \Delta x_{k-1} + \Delta x_k) \tag{3.31}$$

The deviation of x_{jk} from its mean can therefore grow larger as the difference $k - j$ increases.

Another way of seeing the differences between the two kinds of imperfections is as follows (Hermans[27]). In the imperfection of the first kind, if the distance between the $(j-1)$th and jth atoms happens to be unusually large (as a result of the jth atom being displaced to the right), there is a high probability that the distance between the jth and $(j+1)$th atoms is smaller than usual. In other words, there is a negative aftereffect. In the imperfection of the second kind, if the jth atom happens to be unusually displaced to the right, the probability that the $(j+1)$th atom is also displaced to the right is very high. In other words, there is a positive aftereffect.

Under the assumption that the arrangement of atoms in all the unit cells remains undisturbed by the lattice imperfections, the scattering length density distribution $\rho(\boldsymbol{r})$ of the imperfect crystal can still be represented by (1.95) where $z(\boldsymbol{r})$ now stands for the lattice with imperfections. The intensity of scattering is then given by

$$I(\boldsymbol{s}) = |F(\boldsymbol{s})|^2 \, |Z(\boldsymbol{s})|^2 \tag{3.32}$$

where $F(\boldsymbol{s})$ is the structure factor and $Z(\boldsymbol{s})$ is the Fourier transform of the imperfect lattice $z(\boldsymbol{r})$. It was shown in Section 1.5.3 that the intensity of scattering can be calculated either by taking the Fourier transform of $\rho(\boldsymbol{r})$ first and then squaring it, or alternatively by evaluating the autocorrelation function $\Gamma_\rho(\boldsymbol{r})$ first and then taking the Fourier transform of it. By applying the same reasoning, it is easy to show that $|Z(\boldsymbol{s})|^2$ can be obtained by first evaluating the autocorrelation function $\Gamma_z(\boldsymbol{r})$ of $z(\boldsymbol{r})$ and then taking the Fourier transform of $\Gamma_z(\boldsymbol{r})$.

The crystalline lattice, irrespective of whether perfect or imperfect, can be represented mathematically by

$$z(\boldsymbol{r}) = \sum_{j=1}^{N} \delta(\boldsymbol{r} - \boldsymbol{r}_j) \tag{3.33}$$

where $\boldsymbol{r}_j$ specifies the position of the jth lattice point. The autocorrelation function of $z(\boldsymbol{r})$ is

$$\Gamma_z(\boldsymbol{r}) = \sum_{j=1}^{N}\sum_{k=1}^{N}\delta(\boldsymbol{r}-\boldsymbol{r}_{jk}), \qquad \boldsymbol{r}_{jk} = \boldsymbol{r}_k - \boldsymbol{r}_j \tag{3.34}$$

Separating the terms for $j = k$, (3.34) can be rewritten as

$$\Gamma_z(\boldsymbol{r}) = N\delta(\boldsymbol{r}) + \sum_{j\neq k}\sum\delta(\boldsymbol{r}-\boldsymbol{r}_{jk}) \tag{3.35}$$

For a perfect crystal, $\boldsymbol{r}_{jk}$ all lie on a perfect lattice, and therefore the correlation function $\Gamma_z(\boldsymbol{r})$ is nonzero only when $\boldsymbol{r}$ coincides with the lattice. However, for crystals with imperfections, $\boldsymbol{r}_{jk}$ are subject to statistical fluctuations, and the correlation function $\Gamma_z(\boldsymbol{r})$ described by (3.35) is no longer strictly on a lattice but is smeared out, as illustrated in Figure 3.13. Note that in the imperfection of the first kind the autocorrelation function is smeared out equally at every lattice point except at the origin, but in the imperfection of the second kind the degree of smearing of the autocorrelation function becomes more severe as the distance from the origin is increased.

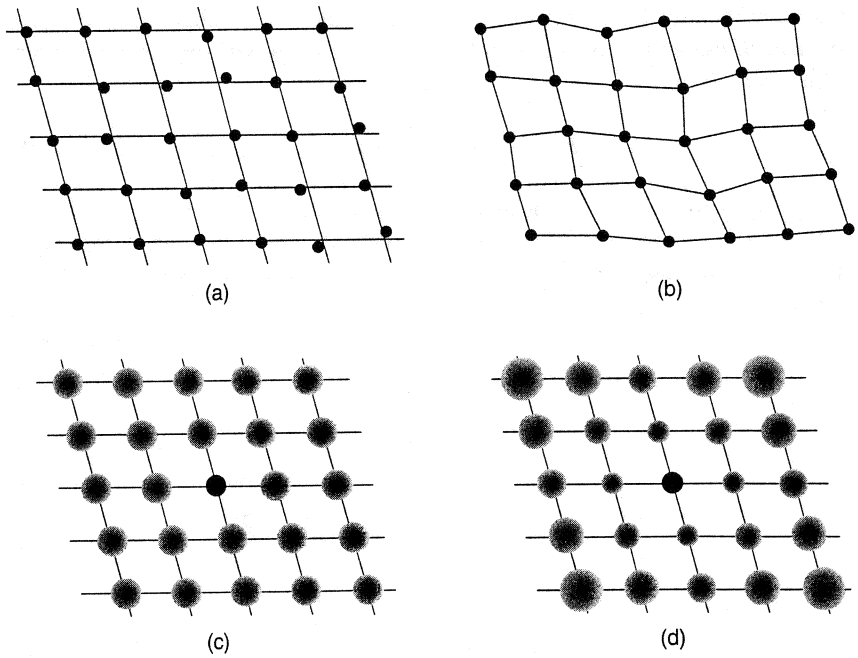

Figure 3.13 Imperfections of (a) the first and (b) the second kind in two-dimensional crystals. (c) and (d) are the corresponding autocorrelation functions.

In the next two sections we derive the autocorrelation functions $\Gamma_z(\boldsymbol{r})$ of the lattices with imperfections of the first and second kind separately.

3.4.4 Crystal Imperfection of the First Kind

We write the position $\boldsymbol{r}_j$ of the jth atom as

$$\boldsymbol{r}_j = \boldsymbol{r}_j^0 + \boldsymbol{a}_j \tag{3.36}$$

where $\boldsymbol{r}_j^0$ is the position where the atom should have been if the crystal were perfect, and $\boldsymbol{a}_j$ represents the displacement of the atom from this ideal position. The displacement $\boldsymbol{a}_j$ will vary from atom to atom according to a probability function $p(\boldsymbol{a})$, which we expect to resemble, in general, a Gaussian function. The interatomic vector $\boldsymbol{r}_{jk}$ between the jth and kth atoms can similarly be written as

$$\boldsymbol{r}_{jk} = \boldsymbol{r}_{jk}^0 + \boldsymbol{b}_{jk} \tag{3.37}$$

where

$$\boldsymbol{r}_{jk}^0 = \boldsymbol{r}_k^0 - \boldsymbol{r}_j^0 \tag{3.38}$$

We are interested in the probability distribution $w(\boldsymbol{b})$ of the deviation $\boldsymbol{b}_{jk}$ of the interatomic vector $\boldsymbol{r}_{jk}$ from its ideal value $\boldsymbol{r}_{jk}^0$. As is implied in Equation (3.30), $w(\boldsymbol{b})$ is independent of the difference $k - j$. A deviation $\boldsymbol{b}$ is realized whenever the displacement of the first atom is $\boldsymbol{a}$ and that of the second atom is $\boldsymbol{b} + \boldsymbol{a}$ (see Figure 3.14). Thus, we can write

$$w(\boldsymbol{b}) = \int p(\boldsymbol{a})\, p(\boldsymbol{b} + \boldsymbol{a})\, d\boldsymbol{a} \tag{3.39}$$

This shows that $w(\boldsymbol{b})$ is actually the autocorrelation function of $p(\boldsymbol{a})$.

In Equation (3.35) for the autocorrelation function $\Gamma_z(\boldsymbol{r})$, there are many terms under the double summation that correspond to the same value of $\boldsymbol{r}_{jk}^0$ but with different extent of deviation. The function $\Gamma_z(\boldsymbol{r})$ around each lattice points $\boldsymbol{r}_{jk}^0$ therefore consists

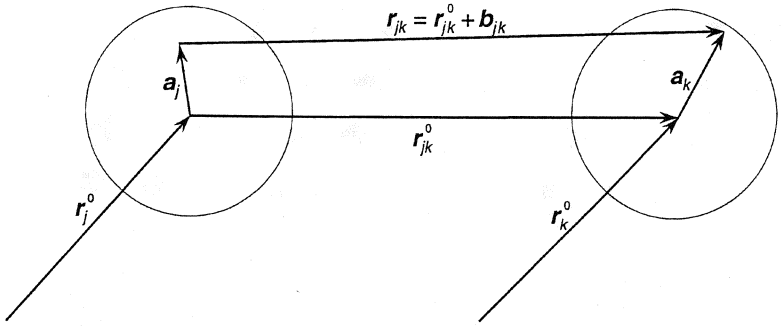

Figure 3.14 Diagram illustrating that $\boldsymbol{a}_k = \boldsymbol{a}_j + \boldsymbol{r}_{jk} - \boldsymbol{r}_{jk}^0 = \boldsymbol{a}_j + \boldsymbol{b}_{jk}$.

of a superposition of many points spread according to $w(\boldsymbol{b})$. This fact is schematically represented in Figure 3.13c. We therefore rewrite (3.35), for the present case of the imperfection of the first kind, as

$$\Gamma_z(\boldsymbol{r}) = N\delta(\boldsymbol{r}) + \sum_{j\neq k}\sum w(\boldsymbol{r} - \boldsymbol{r}_{jk}^0) \tag{3.40}$$

Its Fourier transform is

$$\mathcal{F}\{\Gamma_z(\boldsymbol{r})\} = N + \sum_{j\neq k}\sum \exp(-i2\pi \boldsymbol{s}\boldsymbol{r}_{jk}^0)\mathcal{F}\{w(\boldsymbol{r})\} \tag{3.41}$$

$\mathcal{F}\{w(\boldsymbol{r})\}$ is related to $P(\boldsymbol{s})$, the Fourier transform of $p(\boldsymbol{r})$, by

$$\mathcal{F}\{w(\boldsymbol{r})\} = |P(\boldsymbol{s})|^2 \tag{3.42}$$

in view of the fact that $w(\boldsymbol{r})$ is the autocorrelation function of $p(\boldsymbol{r})$. Restoring the terms with $j = k$ in the double summation, (3.41) is rewritten as

$$\begin{aligned} I(\boldsymbol{s})/|F(\boldsymbol{s})|^2 &= N\left\{1 - |P(\boldsymbol{s})|^2\right\} + |P(\boldsymbol{s})|^2 \sum_{j=1}^{N}\sum_{k=1}^{N} \exp(-i2\pi \boldsymbol{s}\boldsymbol{r}_{jk}^0) \\ &= N\left\{1 - |P(\boldsymbol{s})|^2\right\} + |P(\boldsymbol{s})|^2 Z_0(\boldsymbol{s}) \end{aligned} \tag{3.43}$$

where $Z_0(\boldsymbol{s})$ represents the perfect reciprocal lattice, which is equal to the infinite sum of $\exp(-i2\pi \boldsymbol{s}\boldsymbol{r}_{jk}^0)$, as explained in Appendix C.

The second term in the last member of (3.43) gives the Bragg diffraction peaks. The fact that $Z_0(\boldsymbol{s})$ is simply multiplied by $|P(\boldsymbol{s})|^2$ means that the widths of the diffraction peaks are not broadened, and only their heights are modified. A good approximation to $p(\boldsymbol{r})$ is a Gaussian function, given in (1.102), with σ representing the root-mean-square displacement of atoms about their mean positions. In such a case, $|P(\boldsymbol{s})|^2$ can be represented by

$$|P(\boldsymbol{s})|^2 = e^{-2M} \tag{3.44}$$

where

$$M = \frac{2}{3}\pi^2\sigma^2 s^2 \tag{3.45}$$

Since the exponent M is proportional to s^2, the effect of the imperfection of the first kind is to suppress the height of the diffraction peaks progressively more as the diffraction angle 2θ is increased. When the cause of the imperfection is thermal vibration, $|P(\boldsymbol{s})|^2$ is identical to the Debye–Waller factor D already mentioned in Section 1.7.1. The first term in the last member of (3.43) shows that there is another component of scattering that is a continuous function of s. In the case of the imperfection due to thermal vibration, this continuous component is called the *thermal diffuse scattering*. This diffuse scattering, $N\left\{1 - |P(\boldsymbol{s})|^2\right\}$, shows up as a continuous background scattering observable between Bragg diffraction peaks, and moreover the intensity of the diffuse scattering increases with increasing 2θ. In fact the intensity

component that has been lost from the diffraction peaks as a result of the reduction in the peak heights is reappearing in the form of the continuous component in the background.

3.4.5 Crystal Imperfection of the Second Kind

Examination of the imperfection of the second kind in quantitative detail is difficult unless some simplifying assumptions are made. For example, in the so-called "ideal paracrystals" proposed by Hosemann,[8] a simplifying assumption, somewhat unrealistic, has been made to the effect that all the unit cells are in the shape of a parallelepiped, although the edge lengths and axis angles may vary from one unit cell to the next. Instead, we here treat in some detail only a one-dimensional version of the imperfection of the second kind. The one-dimensional case can be treated exactly without simplifying assumptions. Moreover, the essential features in the deterioration of the diffraction lines due to the imperfection of the second kind are all brought out in the one-dimensional case. One-dimensional paracrystals are actually realized in physical systems, for example, when lamellar structures are stacked on top of each other, such as in a smectic liquid crystal or in a membrane assembly. A closely similar system of diblock copolymer forming a lamellar morphology is examined again in Section 5.5.1.

For a one-dimensional crystal, Equation (3.35) can be rewritten, by grouping the first neighbor pairs, second neighbor pairs, etc., separately, as

$$\Gamma_z(x) = N\delta(x) + \sum_{j=1}^{N-1} \delta(x - x_{j,j+1}) + \sum_{j=1}^{N-1} \delta(x + x_{j,j+1}) + \cdots$$
$$+ \sum_{j=1}^{N-m} \delta(x - x_{j,j+m}) + \sum_{j=1}^{N-m} \delta(x + x_{j,j+m}) + \cdots \tag{3.46}$$

The placement of atoms in the one-dimensional lattice is characterized by the probability function $p_1(x)$ specifying that the probability of finding a nearest-neighbor pair at a distance between x and $x + dx$ is equal to $p_1(x)\,dx$. The function $p_1(x)$ is normalized to unity and the mean distance d between first neighbors is given by

$$d = \int_0^\infty x p_1(x) dx \tag{3.47}$$

Equation (3.47) implies that $p_1(x)$ is defined only for positive values of x. We also define a function $p_{-1}(x)$ by

$$p_{-1}(-x) = p_1(x) \tag{3.48}$$

that is, $p_{-1}(x)$ is defined only for negative values of x and is symmetrical to $p_1(x)$ about $x = 0$ (see Figure 3.15). The second term on the right of (3.46), $\sum \delta(x - x_{j,j+1})$, can then be equated to $(N-1)p_1(x) \sim Np_1(x)$, and the third term, $\sum \delta(x + x_{j,j+1})$, to $Np_{-1}(x)$.

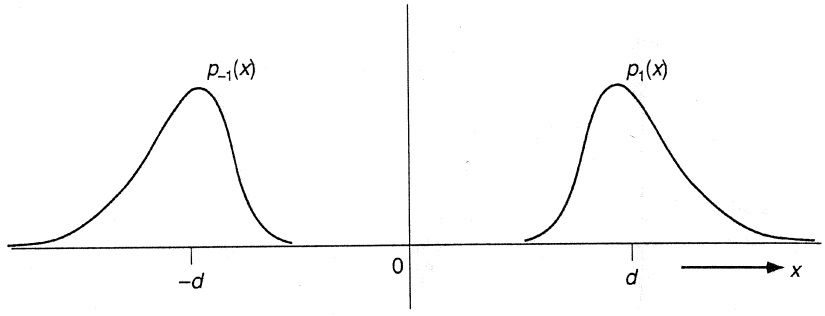

Figure 3.15 Probability functions for first neighbors, $p_1(x)$ and $p_{-1}(x)$.

The probability $p_2(x)\,dx$ of finding a second neighbor pair at a distance between x and $x + dx$ is then equal to

$$\begin{aligned} p_2(x) &= \int_0^x p_1(u)p_1(x-u)\,du \\ &= \int_{-\infty}^{\infty} p_1(u)p_1(x-u)\,du \\ &= p_1(x) * p_1(x) \end{aligned} \tag{3.49}$$

In going from the second to the third member of (3.49), $p_1(x)$ is regarded equal to zero for negative values of x. By a similar reasoning it can be seen that the probability function $p_m(x)$ describing the distance between mth nearest neighbors is given by

$$p_m(x) = \underbrace{p_1(x) * p_1(x) * \cdots * p_1(x) * p_1(x)}_{m \text{ times}} \tag{3.50}$$

and similarly $p_{-m}(x)$ is given by an m-fold convolution of $p_{-1}(x)$. Equation (3.46) is then rewritten as

$$\Gamma_z(x)/N = \delta(x) + p_1(x) + p_2(x) + \cdots + p_{-1}(x) + p_{-2}(x) + \cdots \tag{3.51}$$

From the definition of $p_m(x)$, given by (3.50), it can be easily seen that its center of mass is located at $x = md$. The normalized autocorrelation function given by (3.51) is therefore a linear lattice with a series of $p_m(x)$ located at $x = md$, for $m = 0, \pm 1, \pm 2, \cdots$. As illustrated in Figure 3.16, the function $p_m(x)$ is progressively broader as the distance from the origin is increased, while its height is correspondingly reduced to maintain a unit area under the curve. Figure 3.13d illustrates the same effect with a two-dimensional lattice.

The intensity of scattering is given by the product of $|F(s)|^2$ with the Fourier transform of (3.51). We designate the Fourier transform of $p_1(x)$ as $P(s)$. Then the Fourier transform of $p_m(x)$ is given, by virtue of the convolution theorem, as the mth power of $P(s)$. Because of the symmetry property (3.48), the Fourier transforms of $p_{-1}(x)$ and $p_{-m}(x)$ are given by $P^*(s)$ and $[P^*(s)]^m$, respectively, where the asterisk denotes the complex conjugate. The intensity of scattering is then given by

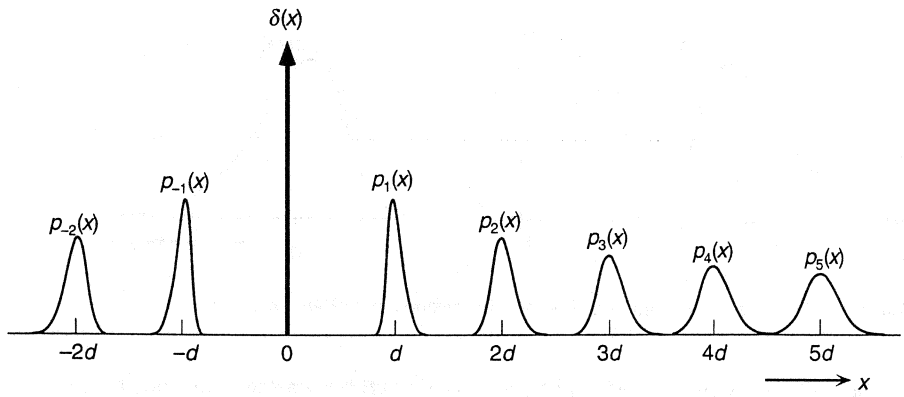

Figure 3.16 Plot of the autocorrelation function (3.51). The curve $p_m(x)$ centered around md is the m-fold convolution of $p_1(x)$ and is accordingly broader in width and shorter in height with increasing $|m|$.

$$\frac{I(s)}{N|F(s)|^2} = 1 + \frac{P(s)}{1-P(s)} + \frac{P^*(s)}{1-P^*(s)}$$
$$= \mathrm{Re}\left[\frac{1+P(s)}{1-P(s)}\right] \tag{3.52}$$

where Re[Z] denotes the real part of a complex quantity Z.

Although it is possible to examine (3.52) analytically (see Hosemann and Bagchi[8] and Vainshtein[9]) to see its general behavior, we here take a simple example of $p_1(x)$ and study its numerical result. A Gaussian function is taken for $p_1(x)$ as given by

$$p_1(x) = \frac{1}{\sqrt{2\pi}\Delta} \exp\left[-\frac{1}{2\Delta^2}(x-d)^2\right] \tag{3.53}$$

where Δ is the standard deviation around its mean d. The Fourier transform of (3.53) is then

$$P(s) = \exp(-i2\pi sd)\exp(-2\pi^2\Delta^2 s^2) \tag{3.54}$$

The plot of (3.52) with (3.54) substituted for $P(s)$ is shown in Figure 3.17, where Δ is taken to be equal to $0.1d$. The maxima of the peaks are located very nearly at $s = h/d$, where h is a positive or negative integer. The behavior of the plot can be understood by writing (3.52) as

$$\frac{I(s)}{N|F(s)|^2} = \frac{1-|P(s)|^2}{1-2|P(s)|\cos\phi + |P(s)|^2} \tag{3.55}$$

where ϕ is the phase angle of $P(s)$. For $P(s)$ given by (3.54), Equation (3.55) can be further rewritten as

$$\frac{I(s)}{N|F(s)|^2} = \frac{1-e^{-4\pi^2\Delta^2 s^2}}{1-2e^{-2\pi^2\Delta^2 s^2}\cos(2\pi ds) + e^{-4\pi^2\Delta^2 s^2}} \tag{3.56}$$

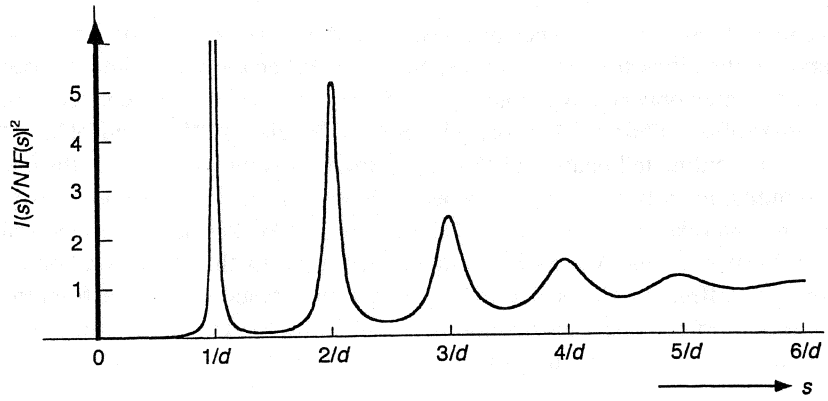

Figure 3.17 Plot of the intensity function (3.56) for a one-dimensional paracrystal, with $\Delta = 0.1d$.

The maxima in the plot in Figure 3.17 occur approximately at the minima of the denominator and therefore at $s = h/d$ at which $\cos(2\pi ds)$ is equal to unity when h is an integer. For $\Delta/d \ll 1$, the heights of the peak in (3.56) can be approximated by

$$\frac{I(h/d)}{N|F(s)|^2} = \frac{1}{\pi^2(\Delta/d)^2h^2} \tag{3.57}$$

showing that the peak heights decay with an inverse square of the reflection order h. The area under the curve for each $1/d$ period is a constant and equal to $1/d$. Therefore for a small value of h, when the overlap between neighboring peaks is not severe, the integral width of the peak is given by

$$\Delta s = \frac{1}{d}\pi^2\left(\frac{\Delta}{d}\right)^2 h^2 \tag{3.58}$$

3.4.6 Summary

Aside from the instrumental effect, there are three main causes that degrade the diffraction line shape from the ideal delta function. They are the small crystal size and imperfections of the first and second kinds. The small crystal size effect broadens all the diffraction lines, including the 000 line, to the same extent. The imperfection of the first kind does not actually cause any line broadening, but instead simply reduces the height of the diffraction peaks according to the Debye–Waller factor e^{-2M} where M is proportional to s^2. At the same time, the scattering energy that has been lost from the diffraction lines as a result of the reduced height reappears as a diffuse scattering in the region of non-Bragg angles, its intensity increasing with s as $1 - e^{-2M}$. The imperfection of the second kind produces a line broadening in which the width of the diffraction line increases with s^2. It is therefore possible, at least in principle,

to differentiate these different types of crystal imperfections by analyzing how the degradation of the diffraction line shape depends on s. When the line width is plotted against s^2, the value obtained by extrapolation to $s = 0$ can be interpreted in terms of the crystal size effect, while the slope of such a plot can be related to the extent of lattice distortion Δ according to Equation (3.58). Experimental examples that show the line width depending linearly on s^2 were obtained by Hosemann and his co-workers with polyethylene and other polymer crystals (Hosemann and Wilke[28] and Hindeleh and Hosemann[29]). Warren and Averbach[30,31] suggest a similar method based on Fourier coefficients of diffraction line shape for separating the crystal size effect from the lattice distortion effect, and their method was applied by Buchanan and Miller[32] to the data obtained with isotactic polystyrene.

3.5 DEGREE OF CRYSTALLINITY

Scattering from an amorphous material such as a melt or a glass gives an intensity pattern that is broad and essentially featureless except for the so-called amorphous halo. The diffraction pattern obtainable from a good crystalline material, on the other hand, consists of a series of sharp Bragg peaks, which can be easily and clearly distinguished from the diffuse background. A semicrystalline polymer gives a scattering pattern consisting of a superposition of both of these features, their relative contributions reflecting the relative amounts of the noncrystalline and crystalline phases present. Scattering is in fact the primary means by which the presence of any crystalline order in a material can be detected. These observations naturally lead to the expectation that x-ray or neutron diffraction should provide a method well suited to determining the degree of crystallinity of a semicrystalline polymer.

To turn diffraction measurements into a quantitative tool for determining the degree of crystallinity, however, it is necessary to be able to separate the observed intensity into crystalline and noncrystalline components. A simple-minded approach to this would be to connect the lowest points between diffraction peaks with a smooth curve and call it the amorphous component. This is not always easy, since with polymers the effect of lattice imperfections and small crystal size makes the diffraction peaks broaden and overlap with each other appreciably, especially at high diffraction angles, and the extent of such overlap must be estimated in drawing the amorphous scattering curve. A somewhat better result is achieved if the shape of the amorphous curve is known independently. Such an amorphous curve is obtained if a totally amorphous sample of the same polymer can be produced by quenching from the melt state as, for example, with poly(ethylene terephthalate) or polystyrene. Another possible approach is to measure the scattering from the polymer at several temperatures above its melting point and then extrapolate the result to the temperature at which the degree of crystallinity is to be determined, as has been done, for example, with polyethylene.[33] Such an approach still does not ensure a complete accuracy, since the presence of lattice imperfections in the crystalline phase causes some of the diffracted beam intensities to be diverted from the Bragg peaks to the diffuse background, as explained in Section 3.4. Unless a proper allowance is made for the effects of

imperfections, the evaluation based on the intensities of the observed Bragg peaks alone would severely underestimate the degree of crystallinity. A procedure, proposed by Ruland,[34] that properly takes account of the lattice imperfections is described in Section 3.5.2.

3.5.1 Evaluation of the Degree of Crystallinity

Once the separation into the crystalline and amorphous components of scattering has been achieved, the degree of crystallinity is determined by comparing the relative magnitudes of the "total scattering" by the two phases. Stated more explicitly, the quantity to be evaluated and compared for such a purpose is the invariant Q, defined in Section 1.5.4 as

$$\begin{aligned} Q &= \int I(s)\, ds \\ &= 4\pi \int_0^\infty s^2 I(s)\, ds \end{aligned} \tag{3.59}$$

where the last member is applicable when the sample is isotropic. The invariant Q represents the total scattering power of the sample and is related, as stated in Section 1.5.4, to the scattering length density distribution $\rho(\boldsymbol{r})$ in the sample by

$$Q = \Gamma_\rho(0) = \int_V \rho^2(\boldsymbol{r})\, d\boldsymbol{r} \tag{3.60}$$

For x̄-ray scattering, $\rho(\boldsymbol{r})$ is equal to the scattering length of an electron, b_e, times the electron density distribution. The latter is localized around individual atomic centers except for a small fraction present between atoms as bonding electrons. Therefore the integral represented by (3.60) is essentially independent of the way atomic centers are distributed in the matter and depends only on the atomic contents, that is, the type and number of atoms present. This statement is even more true in the case of neutron scattering, since the scattering length is then totally concentrated in the atomic nuclei. Considering isotropic materials only for the sake of simplicity, we can therefore write

$$\begin{aligned} Q &= 4\pi \int_0^\infty s^2 I(s)\, ds \\ &= 4\pi N \int_0^\infty s^2 \langle b^2 \rangle\, ds \end{aligned} \tag{3.61}$$

The last member of (3.61) gives the scattering power of an assembly of N independent atoms, where b stands, in the case of x-ray scattering, for the product of b_e and the atomic scattering factor $f(s)$.

By defining the degree of crystallinity x as N_{cr}/N, where N_{cr} is the number of atoms in the crystalline phase, we obtain

$$x = \frac{Q_{cr}}{Q} = \frac{4\pi \int_0^\infty s^2 I_{cr}(s) ds}{4\pi \int_0^\infty s^2 I(s) ds} \tag{3.62}$$

where $I_{cr}(s)$ is the crystalline component of the scattered intensity and Q_{cr} is the corresponding invariant. Experimentally the intensities $I(s)$ and $I_{cr}(s)$ are available only to a finite upper limit in s, and a way to avoid the error that might result from the truncation of the integrals in (3.62) is discussed when the method proposed by Ruland is considered in Section 3.5.2.

Although the evaluation of the degree of crystallinity on the basis of Equation (3.62) is theoretically more satisfying, the method is tedious, and over the years many workers have devised and suggested simpler but more approximate methods, many of which rely on the availability of a reference sample of a known degree of crystallinity. For example, if scattering curves are obtained, under identical experimental conditions, from a reference sample and a test sample, it is possible to compare the crystalline (or amorphous) components of the scattering at selected diffraction angles from these two samples and thereby evaluate the degree of crystallinity. When a series of samples of the same polymer are being examined, there may sometimes be interest in obtaining not the absolute value, but rather some relative measure of the degree of crystallinity expressed as, for example, the "crystallinity index." A survey of such approximate methods proposed in the past is given by Baltá-Calleja and Vonk.[4]

3.5.2 Ruland's Method

The method suggested by Ruland[34] addresses two problems associated with the use of Equation (3.62) to evaluate the degree of crystallinity. The first is that lattice imperfections in the crystalline phase cause some of the diffracted intensities to be diverted from the Bragg peaks to the diffuse background. The second is that the intensity is measured experimentally only up to some finite upper limit in s and not to infinity as demanded by (3.62).

Suppose that the scattered intensity $I(s)$ is separated into its crystalline and amorphous components in such a way that $I_{cr}(s)$ obtained includes only the scattered intensity in the Bragg peaks and not the one diverted to the background. The invariant Q_{cr} based on $I_{cr}(s)$ can then be written as

$$\begin{aligned} Q_{cr} &= 4\pi \int_0^\infty s^2 I_{cr}(s)\, ds \\ &= 4\pi N_{cr} \int_0^\infty s^2 \langle b^2 \rangle D(s)\, ds \end{aligned} \tag{3.63}$$

where the *distortion factor* $D(s)$ accounts for the diversion of the scattered intensity to the diffuse background. The distortion factor can be expressed, as a first approximation, by

$$D(s) = e^{-Bs^2} \tag{3.64}$$

The fact that the effect of thermal vibrations and other imperfections of the first kind can be represented by an expression of the form (3.64) has been explained in Section 3.4.4. Ruland[34] showed that for the imperfections of the second kind the distortion effect can also be expressed in the form of (3.64) at least approximately.

Thus, by writing the distortion factor $D(s)$ as in (3.64), the constant B is understood to incorporate the effect of imperfections of these different kinds together.

The degree of crystallinity x, defined as N_{cr}/N, is now given, in view of (3.61) and (3.63), by

$$x = \frac{\int_0^\infty s^2 I_{cr}(s)\, ds}{\int_0^\infty s^2 I(s)\, ds} \frac{\int_0^\infty s^2 \langle b^2 \rangle\, ds}{\int_0^\infty s^2 \langle b^2 \rangle\, D(s)\, ds} \tag{3.65}$$

To deal with the second problem concerning the upper limit of integration in (3.65), we note that in any material there is always a shortest distance r_{min} below which two atoms cannot approach each other, and thus the intensity function $I(s)$ for s beyond $s_{max} \sim 1/r_{min}$ merely reflects the electron density distribution within individual atoms only, so that the equality

$$\int_0^{s_{max}} s^2 I(s)\, ds = \int_0^{s_{max}} s^2 \langle b^2 \rangle\, ds \tag{3.66}$$

holds, irrespective of the structure or the crystallinity of the material. Thus, in evaluating the degree of crystallinity x by means of (3.65), the upper integration limit may be replaced with any s value larger than s_{max}. The distortion factor $D(s)$ or the distortion parameter B as defined in (3.64) is usually not known for the material of study. This problem was resolved by Ruland by noting that for several different values of the upper integration limit, the degree of crystallinity x should remain constant, and therefore the value of B, regarded as an adjustable parameter, must be chosen so as to ensure the constancy of x irrespective of the value of the upper integration limit. This ingenious method of obtaining both the degree of crystallinity and the degree of crystal imperfections at the same time apparently works well, as seen from the results obtained with samples of polypropylene,[34] nylons,[35] polyethylene,[36] polytetrafluoroethylene,[37] and poly(ethylene terephthalate).[38,39] Methods for automating some of the numerical procedures have also been proposed.[38–40]

3.5.3 A Method Based on Small-Angle Scattering

An entirely different method of determining the degree of crystallinity from x-ray or neutron scattering data, without relying on the separation of Bragg peaks from the overall scattering curve, is available through use of the small-angle scattering technique. This method requires determination of the invariant Q evaluated by integrating the observed intensity obtained over the scattering vector s in the small-angle range. This small-angle version of the invariant Q reflects the mean square fluctuation of the scattering length density on a size scale much larger than atomic dimensions. When the sample is assumed to have a two-phase structure and when the average scattering length density in each phase is known, it is possible to evaluate the relative amounts of the two phases, as discussed in Section 5.3.2.1. The method is thus very similar to the widely used method based on the measurement of mass density, in which a two-phase structure is assumed and knowledge of the mass densities of totally crystalline and totally amorphous phases is required. In both the small-angle scattering method and the mass density method, the presence of imperfections in the crystalline phase

does not seriously affect the result as long as the average mass density or the average scattering length density in the crystalline phase is not altered appreciably by the imperfections.

3.6 ORIENTATION

When a polymer is crystallized from its isotropic melt, without ever being subjected to stress or deformation either during or after the crystallization, the resulting semicrystalline polymer remains isotropic, and the individual crystallites formed in it are oriented in all different directions with equal probabilities. The diffraction pattern from such a sample, taken, for example, with a flat film camera shown in Figure 2.19, consists of a series of concentric circles, each circle corresponding to a Bragg reflection *hkl*, as illustrated in Figure 3.1. If, on the other hand, the polymer has been deformed in some way, the crystallites may no longer be randomly oriented in all directions. The presence of such a *preferred orientation* is readily recognized from the diffraction pattern, where the diffraction circles may no longer be of uniform intensity along their circumferences and may even be broken up into longer or shorter arcs, depending on the degree of preferred orientation imparted. Many of the mechanical, optical, and other properties of a semicrystalline polymer exhibit anisotropy when a preferred orientation exists, and it is important that a method is available for determining the state of orientation distribution of crystallites present in the polymer.

Diffraction of x-rays or neutrons provides the best method for determining the orientation of crystallites. There are other techniques available for determining the orientation of chain elements in a polymer, such as those relying on the measurement of birefringence, infrared dichroism, fluorescence polarization, nuclear magnetic resonance, etc. However, the diffraction technique is unique in that it provides information on the preferred orientation of polymer segments only in the crystalline regions. Combining the diffraction method with another method, which responds to orientations in both crystalline and amorphous regions such as the birefringence method, therefore makes it possible to discriminate the orientation of segments in amorphous regions from those in crystalline regions.

What is actually determined by the diffraction method is the orientation distribution, in the polymer sample, of a reciprocal lattice vector $\boldsymbol{r}^*_{hkl}$ or the normal to a crystallographic plane (*hkl*). The orientation distribution of such *plane-normals* or *poles* should be distinguished from the orientation distribution of crystallites themselves. The latter can be inferred, as will be explained in Section 3.6.3, only when the orientation distributions of a sufficient number of plane-normals become available through diffraction measurements.

3.6.1 Orientation Distribution of Plane-Normals (Poles)

3.6.1.1 Uniaxial and Biaxial Orientation

In an undeformed, isotropic polymer all directions are equivalent: crystallites are oriented in different directions with equal probabilities. When a polymer is uniaxially

stretched, the direction of stretch becomes the unique axis along which a certain crystallographic direction of the crystallites (usually the one parallel with the chain axis direction) tends to align. At the same time the distribution of crystallites (and of plane-normals) exhibits a cylindrical symmetry around this unique axis. Such a pattern of orientation is called *uniaxial orientation* and the unique axis is sometimes referred to as the *fiber axis*. In a more general pattern of deformation, such as that caused by extrusion, calendaring, or blow molding, the direction in which the highest degree of deformation has occurred is usually referred to as the *machine direction* (MD), and the designations *transverse direction* (TD) and *normal direction* (ND) are given to the two directions perpendicular to the machine direction, the normal direction often being assigned to the normal to the finished surface of the prepared article. Such an orientation pattern is usually called *biaxial orientation*, although no axes of rotation symmetry are actually present.

Let us take vector w to be a unit vector normal to the (hkl) crystallographic planes in a crystallite. The orientation of w can be specified by reference to a coordinate system O-XYZ fixed to the semicrystalline polymer sample. For a sample with biaxial orientation the X, Y, and Z axes may be chosen, for example, to coincide with the normal, transverse, and machine directions, respectively. In the case of uniaxial orientation, the Z axis is invariably chosen to coincide with the symmetry axis. Two angles are required to specify the orientation of vector w within the coordinate system. The most common practice is to choose the polar and azimuthal angles Θ and Φ, as are used in the spherical polar coordinate system (see Figure 3.18a). An alternative approach preferred by some workers, for a reason to be explained below, is to choose any two angles among the three Θ_X, Θ_Y, and Θ_Z, where Θ_X, for example, is the angle between w and X (see Figure 3.18b). The relationship between these two sets of angles is given by

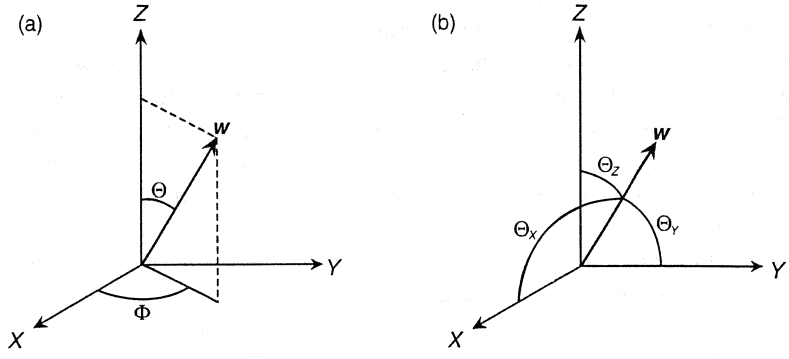

Figure 3.18 Definition of the angles defining the orientation of a pole (normal to a crystallographic plane) within a sample. The coordinate system O-XYZ is fixed to the sample. In scheme (a) two angles Θ and Φ, defined as illustrated, are used to specify the direction; in scheme (b) any two of the three angles Θ_X, Θ_Y, and Θ_Z are used.

$$\cos\Theta_X = \cos\Phi\ \sin\Theta, \qquad \cos\Theta_Y = \sin\Phi\ \sin\Theta, \qquad \Theta_Z = \Theta \tag{3.67}$$

while Θ_X, Θ_Y, and Θ_Z are related among themselves by

$$\cos^2\Theta_X + \cos^2\Theta_Y + \cos^2\Theta_Z = 1 \tag{3.68}$$

The statistical distribution of the orientation of $\boldsymbol{w}$ in the sample can be represented, in a general way, by a function $t(\Theta, \Phi)$ defined for $0 \leq \Theta < \pi$ and $0 \leq \Phi < 2\pi$. In other words, the probability, weighted according to the mass of the crystallites, of finding the vector $\boldsymbol{w}$ in the direction specified by the range $(\Theta, \Theta + d\Theta)$ and $(\Phi, \Phi + d\Phi)$ is equal to $t(\Theta, \Phi)\, d\Theta\, d\Phi$. We call $t(\Theta, \Phi)$ the *plane-normal (or pole) orientation distribution function*, or the *pole distribution* for short. For a sample having uniaxial orientation, directions having the same Θ but different Φ are all equivalent, and therefore the pole distribution can be written as a function of Θ only, $t(\Theta)$, defined for $0 \leq \Theta < \pi$. The pole distributions $t(\Theta, \Phi)$ or $t(\Theta)$ are normalized so as to have

$$\int_0^{2\pi} \int_0^{\pi} t(\Theta, \Phi) \sin\Theta\, d\Theta\, d\Phi = 1 \tag{3.69}$$

and

$$\int_0^{\pi} t(\Theta) \sin\Theta\, d\Theta = 1 \tag{3.70}$$

The diffraction phenomenon is unable to distinguish the diffraction by (hkl) planes from the diffraction by $(\bar{h}\bar{k}\bar{l})$ planes. As a result, the pole distribution $t(\Theta, \Phi)$ as determined experimentally is centrosymmetric, that is, $t(\Theta, \Phi) = t(-\Theta, -\Phi)$. The pole distribution therefore needs to be determined in practice only for the range $0 \leq \Theta < \pi/2$ and $0 \leq \Phi < 2\pi$.

3.6.1.2 Methods of Measurement

Experimental determination of the pole distribution $t(\Theta)$ is relatively simple when the sample possesses uniaxial symmetry. If the sample is in the form of a thin sheet with the symmetry axis parallel with the sheet surface, the symmetric transmission method (see Section 2.5.3) is the most convenient experimental method. If the sample, in the form of a sheet, has its symmetry axis normal to the sheet surface, the symmetric reflection method should be used. In Figure 3.19, the diffractometer axis is normal to the plane of the drawing. The radiation source (S), the center of the sample (O), and the detector (D) are held fixed during the whole measurement so that the scattering vector $\boldsymbol{q}$, which is in the plane of the drawing, and the Bragg angle 2θ remain unchanged. At first the sample is placed to have the symmetry axis Z coincide with the scattering vector $\boldsymbol{q}$ and the X axis coincide with the diffractometer axis. The intensity measured at this point is proportional to $t(0)$. The sample is then rotated by an angle Θ around the axis AOA′, which is perpendicular to both $\boldsymbol{q}$ and the diffractometer axis. In the transmission method, the sample volume irradiated and the beam path length within the sample remain unaltered at different Θ, so that the measured intensity is proportional to $t(\Theta)$.

In the reflection method both the irradiated volume and the beam path length change with Θ, but any absorption correction that needs to be applied is small when Θ is not excessively large and when the divergence of the beam entering the detector is properly controlled by means of a receiving slit. It is, however, obvious that $t(\Theta)$ for Θ approaching 90° is inaccessible to the reflection method.

For a biaxially oriented sample, the above process of measurement as a function of Θ must be repeated for different Φ values. Thus, in the initial positioning, the sample, with its Z axis coinciding with the q vector, is first rotated around Z by Φ. The intensity measured at this point is proportional to $t(0,\Phi)$. Rotating the sample around the AOA′ axis by Θ then enables measurement of the intensity, that is proportional to $t(\Theta, \Phi)$. In the transmission method the absorption correction depends on Φ and can become large when Φ approaches 90°. In the reflection method, on the other hand, the absorption correction is independent of Φ. To determine $t(\Theta, \Phi)$ for the complete ranges of Θ and Φ, two or more test specimens must be cut from a large piece of the sample, with their exposed surfaces oriented differently with respect to the symmetry axes, and the results of the measurement obtained with each piece must in the end be combined. The sequence of movements by which different Θ and Φ values are brought into diffraction can of course be chosen differently from the one described above, and there are in fact available automated devices designed to explore a range of Θ and Φ unattended.

The absorption correction (correcting for the effects arising from variations in irradiated volume as well as in beam path length within the sample) is important, and one way to ensure its accuracy is to obtain a reference sample having the same constitution and shape as the test sample but known to be isotropic and to make sure that the intensity measured with this reference sample is truly constant after the absorption correction is applied. From the intensity $I(\Theta)$ or $I(\Theta, \Phi)$ obtained after the absorption correction, the pole distribution $t(\Theta)$ or $t(\Theta, \Phi)$, for a sample of uniaxial or biaxial orientation, respectively, is evaluated according to

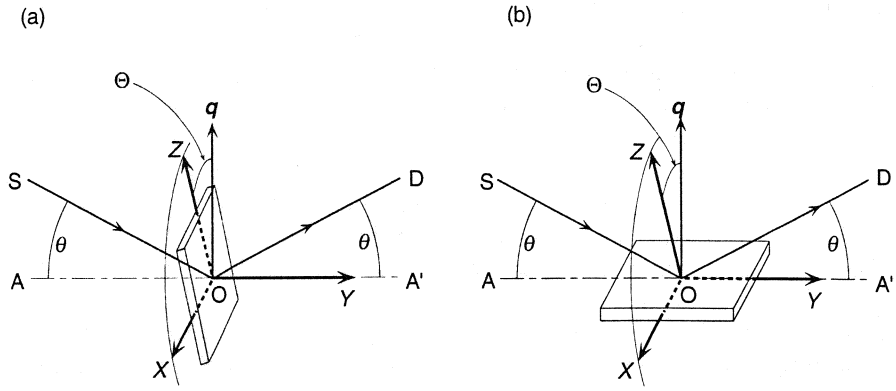

Figure 3.19 Geometry of sample orientation in the diffractometer in (a) symmetric transmission technique and (b) symmetric reflection technique.

$$t(\Theta) = \frac{I(\Theta)}{\int_0^{\pi} I(\Theta) \sin \Theta \, d\Theta} \tag{3.71}$$

or

$$t(\Theta, \Phi) = \frac{I(\Theta, \Phi)}{\int_0^{2\pi} \int_0^{\pi} I(\Theta, \Phi) \sin \Theta \, d\Theta \, d\Phi} \tag{3.72}$$

3.6.1.3 Pole Figure

For biaxial orientation the pole distribution $t(\Theta, \Phi)$ may be visualized as a density distribution defined on the surface of a sphere. The method of *stereographic projection* is then used to transcribe the density distribution from the spherical surface onto a sheet of paper. The contour map thus obtained is called a *pole figure.*

The stereographic projection can be explained with the aid of Figure 3.20 as follows. The *plane of projection* is placed tangent to the sphere. The line drawn from the point of contact, A, to the center of the sphere, B, is extended, until it crosses the surface of the rear hemisphere at point C, which is then chosen as the *point of projection.* For a point P on the surface of the front hemisphere, the extension of the line from C to P gives its projection P′ on the projection plane. All the points on the surface of the front hemisphere are therefore mapped to points within the *circle of projection* of radius twice that of the sphere. The great half circle from the north pole N to the south pole S through A is mapped as the vertical diameter N′AS′, and the equatorial half circle EAW is mapped as the horizontal diameter E′AW′. Some of the more important properties of the stereographic projection can be described as follows:

1. The angle between two crossing lines on the sphere is equal to the angle between the projections of these lines.
2. A circle on the sphere is projected as a true circle. However, the center of a circle on the sphere is not projected as the center of its projected circle.
3. Two lines of equal length on the sphere do not necessarily produce two projected lines of equal length. As a result the projection is not true to area. For example, a small circle of radius a at point A on the sphere gives rise to a circle of radius a on the projection, but the same circle near the north pole N or south pole S will produce a projected circle of twice the radius.

Figure 3.21 shows a *Wulff net*, which gives the stereographic projection of a complete set of longitude lines (of constant Φ) and latitude lines (of constant Θ).

Figure 3.22 gives illustrative examples of pole figures obtained with a stretched sample of lightly cross-linked polyethylene (Desper and Stein[41]). The contour lines drawn with light solid curves denote densities higher than that of the heavy curves, and the broken contour lines are of lower densities. Although the sample was uniaxially deformed, the orientation distribution in the sample has apparently acquired a degree of biaxial character, as evidenced from the fact that the contour lines do not follow the lines of equal latitude shown in Figure 3.21.

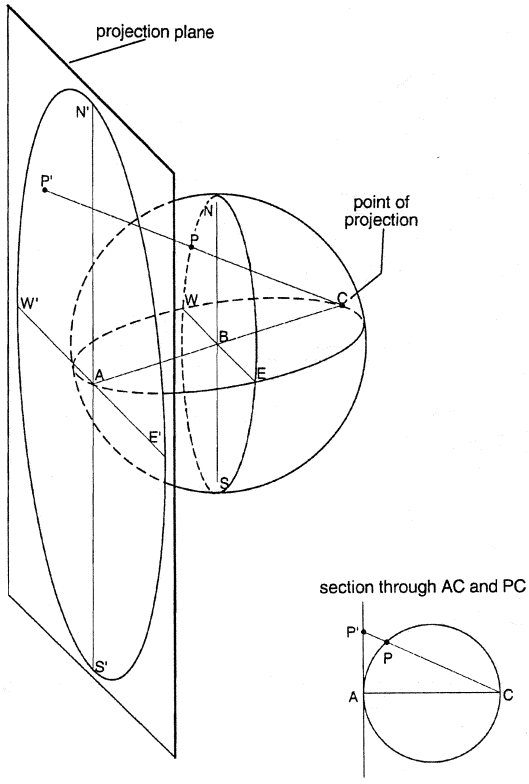

Figure 3.20 Diagram illustrating the stereographic projection.

3.6.2 Orientation Parameters

3.6.2.1 Hermans Orientation Parameter

It is often desirable that the degree of orientation of a pole is designated by a single number rather than by a complete distribution function $t(\Theta)$ or $t(\Theta, \Phi)$. Such a practice would be akin to representing the size distribution of polymer molecules by means of a number- or weight-average. Since the pole distribution function is centrosymmetric due to our inability to distinguish the positive from the negative direction of a pole, the average of $\cos\Theta$ is equal to zero. The most natural choice for representing the average orientation of a pole is therefore to evaluate the average of $\cos^2\Theta$. In view of the normalization denoted by (3.69) or (3.70), the averaging is performed according to

$$\langle \cos^2\Theta \rangle = \int_0^{\pi} \cos^2\Theta \, t(\Theta) \sin\Theta \, d\Theta \tag{3.73}$$

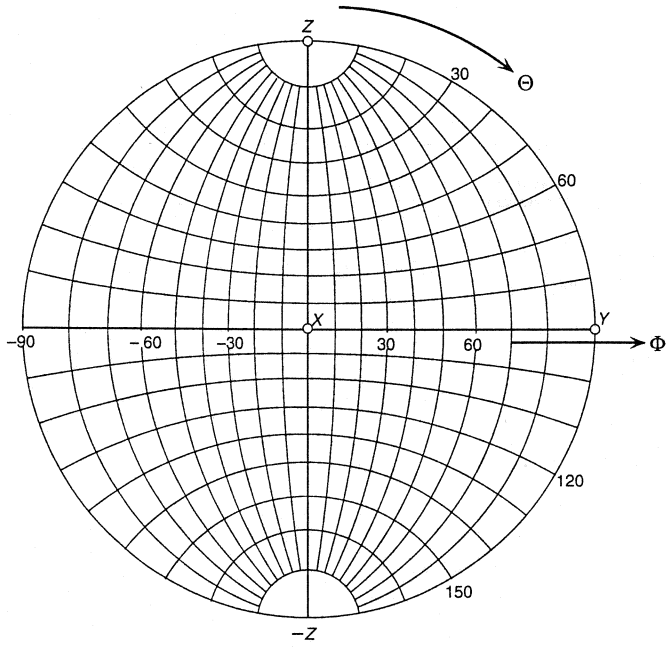

Figure 3.21 Wulff net that shows the stereographic projection of lines of equal longitude and equal latitude at 10° intervals.

or

$$\langle \cos^2 \Theta \rangle = \int_0^{2\pi} \int_0^{\pi} \cos^2 \Theta \, t(\Theta, \Phi) \sin \Theta \, d\Theta \, d\Phi \tag{3.74}$$

depending on whether the orientation is uniaxial or biaxial. The value of $\langle \cos^2 \Theta \rangle$ is equal to 1, 1/3, or 0, respectively, when the pole is perfectly aligned with Z, randomly oriented, or perpendicular to Z. Hermans and Platzek[42] proposed using, in place of $\langle \cos^2 \Theta \rangle$, the second-order Legendre function of $\cos \Theta$, i.e.,

$$f = \langle P_2(\cos \Theta) \rangle = \frac{3}{2} \langle \cos^2 \Theta \rangle - \frac{1}{2} \tag{3.75}$$

The parameter f defined by (3.75) is called the *Hermans orientation parameter* or simply the *orientation parameter.* The value of f is equal to 1, 0, or $-1/2$ when the pole is parallel to Z, random, or perpendicular to Z, respectively.

The pole distribution $t(\Theta)$ or $t(\Theta, \Phi)$ and the orientation parameter f are defined and measured for individual poles. The pole orientation parameter by itself does not specify the state of orientation of *crystallites* in the sample. The orientation of an individual crystallite in space is uniquely defined when the orientations of at least two nonparallel directions associated with the crystallite are given. Thus, in an effort to specify the "average orientation of crystallite" in a sample, one may evaluate the orientation parameters f_a and f_b of two nonparallel poles, a and b, and represent

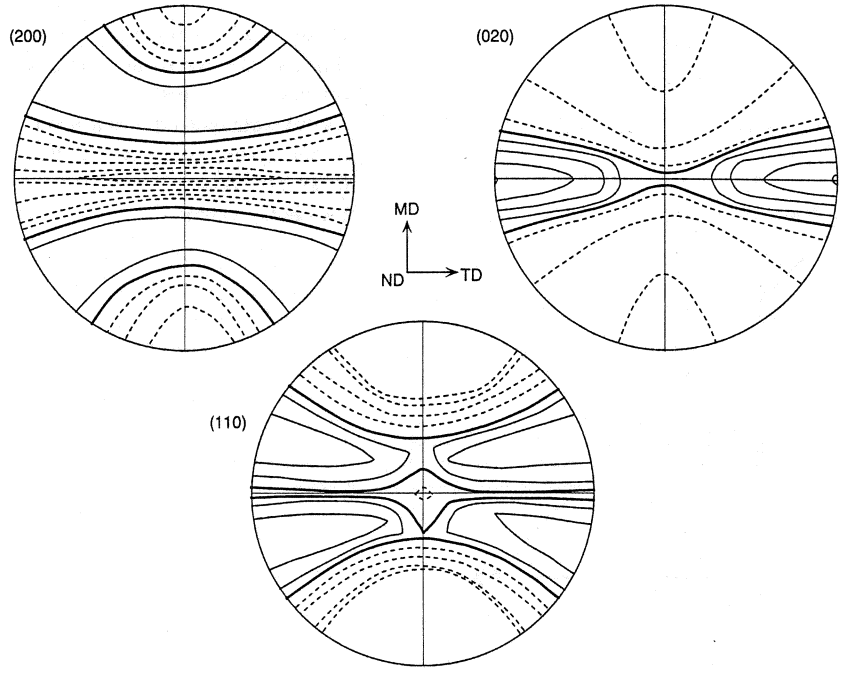

Figure 3.22 Examples of pole figures obtained with a stretched polyethylene sample for (100), (010), and (110) plane-normals. (From Desper and Stein.[41])

the state of preferred orientation by a point plotted on a two-dimensional diagram having f_a and f_b as the Cartesian axes. Such a plot will be more meaningful if the two poles selected are orthogonal to each other, as, for example, the a and b axes of an orthorhombic unit cell. Such a representation, proposed first by Stein,[43] is illustrated in Figure 3.23. For two poles a and b that are orthogonal to each other, the polar angles Θ_a and Θ_b measured from the Z axis are constrained by

$$\cos^2 \Theta_a + \cos^2 \Theta_b \leq 1 \tag{3.76}$$

from which it follows that

$$f_a + f_b \leq \frac{1}{2} \tag{3.77}$$

This inequality, combined with the fact that the parameters f_a and f_b can vary only from $-1/2$ to 1, restricts the points in Figure 3.23 to within the triangular area shown. In the diagram the corners A, B, and C correspond to the cases in which the a, b, and c axes, respectively, are perfectly oriented toward the Z direction. The lines BC, CA, and AB represent the cases in which the a, b, and c axes, respectively, are normal to the Z axis. An isotropic sample is represented by a point at the origin. When, for example, a series of samples are prepared as a function of processing variables, the resulting changes in their state of crystallite orientation could be graphically represented by a curved line on the diagram in Figure 3.23.

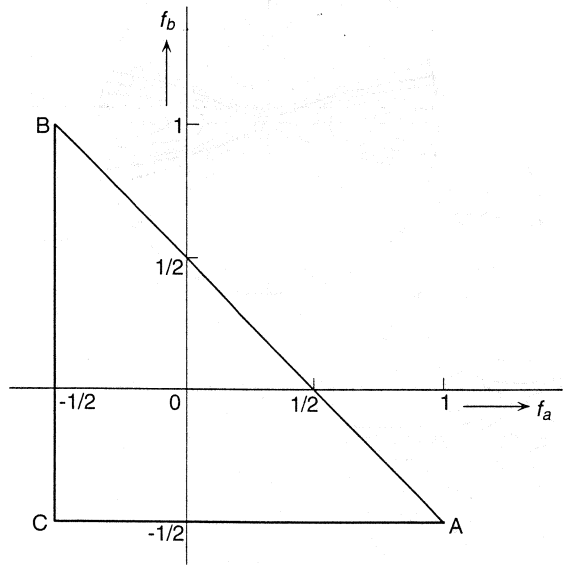

Figure 3.23 A point plotted on this diagram, giving the Hermans orientation parameters f_a and f_b for two orthogonal poles a and b in the crystal, represents the state of average orientation of crystallites in the sample.

3.6.2.2 Biaxial Orientation Parameters

The Hermans orientation parameter is always evaluated with reference to the Z axis. For a biaxially oriented sample, the machine, transverse, and normal directions are usually of comparable significance, and therefore an alternative definition of the orientation parameter that places the three directions on a more equal footing is desirable. The scheme of specifying the orientation of a pole by means of two angles Θ_Z and Θ_Y as defined in Figure 3.18b is more appropriate for this purpose. In the simplest of such schemes two averages $\langle\cos^2\Theta_Z\rangle$ and $\langle\cos^2\Theta_Y\rangle$ are specified to give the average orientation of a single pole. The state of average orientation of a pole can then be conveniently represented by a point within an equilateral triangle of unit height, as shown in Figure 3.24. For any pole the relationships

$$\cos^2\Theta_X + \cos^2\Theta_Y + \cos^2\Theta_Z = 1 \tag{3.78}$$

and

$$\langle\cos^2\Theta_X\rangle + \langle\cos^2\Theta_Y\rangle + \langle\cos^2\Theta_Z\rangle = 1 \tag{3.79}$$

always hold. When the distances from a point P to the sides YZ, ZX, and XY are chosen to equal $\langle\cos^2\Theta_X\rangle$, $\langle\cos^2\Theta_Y\rangle$, and $\langle\cos^2\Theta_Z\rangle$, respectively, their sum is identically equal to the height of the triangle, which is unity, thus satisfying condition (3.79). A pole with random orientation is represented by a point at the center of gravity of the triangle, whereas points designated as X, Y, and Z in Figure 3.24 represent the cases in which the pole is perfectly aligned with the respective axis.

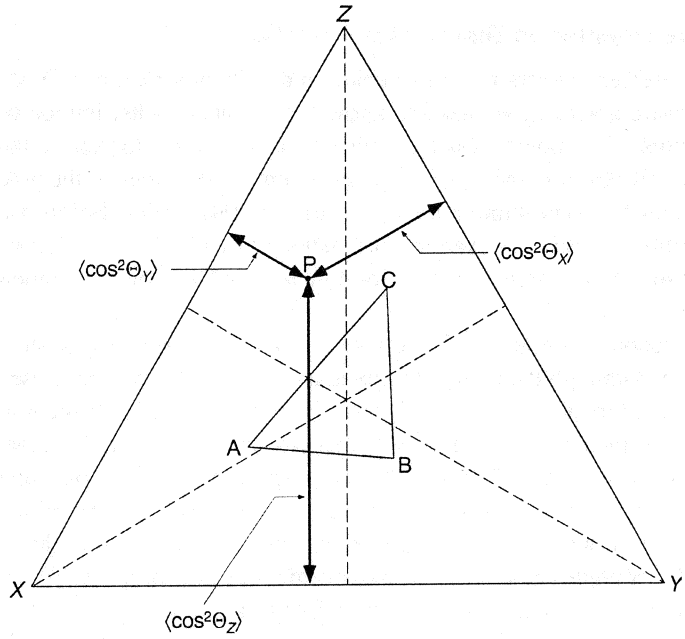

Figure 3.24 Point P plotted in the equilateral triangle of unit height represents the average cosines $\langle\cos^2\Theta_X\rangle$, $\langle\cos^2\Theta_Y\rangle$, and $\langle\cos^2\Theta_Z\rangle$ of a pole in the sample, while the small triangle ABC specifies the state of average orientation of crystallites in the sample. (From Desper and Stein.[41])

It should be noted that a point in the diagram in Figure 3.24 represents the state of average orientation of a single pole, in contrast to the diagram in Figure 3.23 in which a point gives the average orientations of two poles simultaneously, thereby specifying the state of average orientation of crystallites. Thus in Figure 3.24 we need to specify at least two points simultaneously if we are to represent the state of average orientation of crystallites. Suppose we choose two poles, a and b, that are mutually orthogonal in the crystallite, and represent their average cosines by points A and B in the diagram in Figure 3.24. If we choose another pole c in the crystallite that is orthogonal to both a and b, the following relationship among the three holds

$$\langle\cos^2\Theta_{Xa}\rangle + \langle\cos^2\Theta_{Xb}\rangle + \langle\cos^2\Theta_{Xc}\rangle = 1 \tag{3.80}$$

and so do similar relationships resulting when X in (3.80) is replaced by Y or Z. A consequence of these relationships (see Desper and Stein[41]) is that the three points A, B, and C in Figure 3.24 representing the average cosines of poles a, b, and c also form a triangle with its center of gravity coinciding with that of the larger triangle XYZ.

3.6.3 Crystallite Orientation Distribution Function

The diffraction measurement determines the orientation distribution $t(\Theta)$ or $t(\Theta, \Phi)$ of a pole. In most cases, however, we need to know the orientation distribution of crystallites in the sample. The question is then whether it is possible to deduce the crystallite orientation distribution once we have experimentally determined the pole orientation distributions for some finite number of different (*hkl*) poles. Before we can answer this question, we have to examine and define more clearly the relationship between the crystallite orientation distribution function and the pole orientation distribution functions.

To specify the direction of a pole within a crystallite, we fix a coordinate system *o-xyz* to the crystallite. Although the three orthogonal axes *x, y*, and *z* may be chosen without any reference to the unit cell axes *a, b,* and *c*, it will be more convenient in practice to choose *z* to coincide with *c*, which is usually the polymer chain direction. The normal to the *j*th crystallographic plane is then specified by the polar and azimuthal angles ζ_j and ψ_j, as shown in Figure 3.25. In the case of a crystallite, a three-dimensional object, we need three angles to specify its orientation in three-dimensional space. Euler angles α, β, and γ are convenient for this purpose. To see the definition[44] of these angles, imagine that the crystallite is initially placed such that the crystallite coordinate system *o-xyz* coincides with the coordinate system *O-XYZ* fixed to the sample. First rotate the crystallite by α around the *z* axis, which is also the *Z* axis (see Figure 3.26a). Next rotate the crystallite by β around the *y* axis (see Figure 3.26b). Finally rotate the crystallite by γ around the *z* axis (see Figure 3.26c). In other words, β and α are the polar and azimuthal angles specifying the orientation of the crystallite *z* axis in the sample coordinate system *O-XYZ*, and γ defines the rotation of the crystallite around its own *z* axis.

The distribution of crystallite orientation can therefore be expressed as a function of Euler angles $w(\alpha, \beta, \gamma)$ defined for $0 < \alpha \leq 2\pi$, $0 < \beta \leq \pi$, and $0 < \gamma \leq 2\pi$. The question raised above can now be rephrased as follows: (1) When the pole distributions $t_j(\Theta, \Phi)$ are known for a finite number of poles $j = 1, 2, 3, \ldots, \nu$, is it possible to derive $w(\alpha, \beta, \gamma)$? A related question is: (2) When $w(\alpha, \beta, \gamma)$ is known, is it possible to calculate $t(\Theta, \Phi)$ for any crystallographic plane (*hkl*)? If the answers to these two questions are both affirmative, it follows that when the pole distributions for a finite number of poles are experimentally determined, the pole distribution for any other pole can be calculated. This last possibility is a useful one, since this implies that if, for example, the intensity of (001) reflection is too weak to allow direct experimental determination of the orientation distribution of polymer chain backbones, measurements of (100), (010), (110), etc., might allow the (001) orientation distribution to be derived indirectly.

The observed pole distribution $t_j(\Theta, \Phi)$ may be expanded in a series of spherical harmonics

$$t_j(\Theta, \Phi) = \sum_{l=0}^{\infty} \sum_{m=-l}^{l} T_{lm}^{j} P_l^m(\cos\Theta) e^{-im\Phi} \tag{3.81}$$

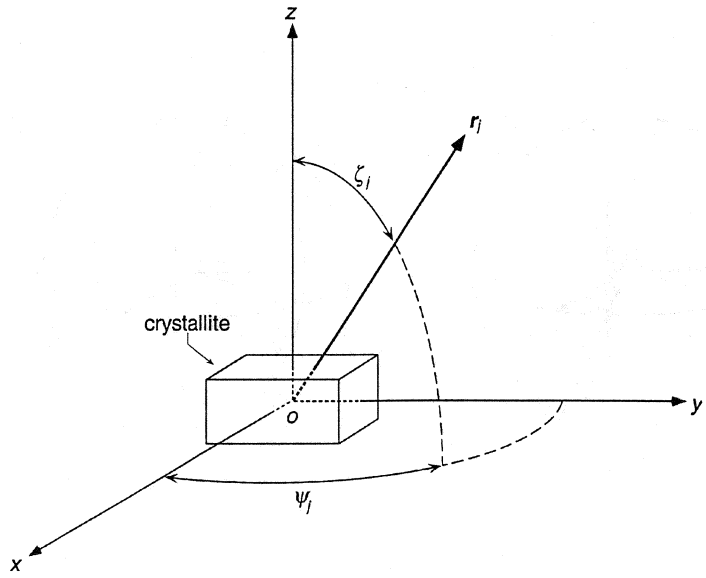

Figure 3.25 The direction of the reciprocal lattice vector r_j in the crystallite is specified by means of angles ζ_j and ψ_j defined with reference to the coordinate system o-xyz fixed to the crystallite.

where $P_l^m(X)$ is the normalized associated Legendre function, and the coefficients T_{lm}^j can be determined, once $t_j(\Theta, \Phi)$ is available from experiment, by

$$T_{lm}^j = \frac{1}{2\pi} \int_0^{2\pi} \int_0^{\pi} t_j(\Theta, \Phi) P_l^m(\cos\Theta) e^{im\Phi} \sin\Theta \, d\Theta \, d\Phi \tag{3.82}$$

Equation (3.82) follows from the orthonormal properties of spherical harmonics that can be stated as

$$\frac{1}{2\pi} \int_0^{2\pi} \int_0^{\pi} P_l^m(\cos\Theta) e^{-im\Phi} \, P_{l'}^{m'}(\cos\Theta) e^{im'\Phi} \sin\Theta \, d\Theta \, d\Phi = \delta_{ll'}\delta_{mm'} \tag{3.83}$$

where $\delta_{ll'}$ is the Kronecker's delta equal to 1 when $l = l'$ and equal to 0 when $l \neq l'$. In (3.81) the summation with respect to l is for all integer values 0, 1, 2, etc. However, as mentioned earlier, x-ray and neutron diffraction cannot distinguish the positive and negative directions of a pole, and as a result $t(\Theta, \Phi)$ is centrosymmetric. Since $P_l^m(x)$ is an odd function of x when l is odd, the coefficient T_{lm} evaluated according to (3.82)

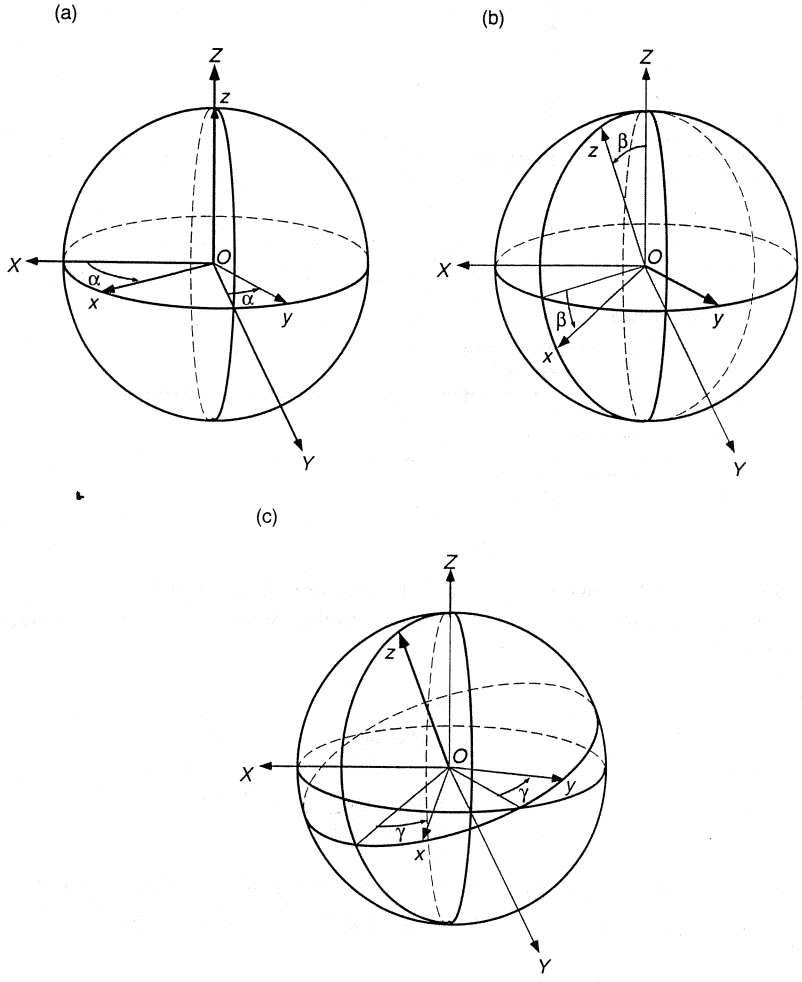

Figure 3.26 Definition of Euler angles (a) α, (b) β, and (c) γ.

is equal to zero when l is odd. Thus the series expansion (3.81) contains only terms with l even.

The crystallite orientation distribution $w(\alpha, \beta, \gamma)$ can similarly be expanded in a series. Since the distribution is a function of three variables, the series expansion requires orthonormal functions more general than the spherical harmonics. The generalized spherical harmonics to be used are now of the form[45]

$$Z_{lmn}(\cos\beta)\, e^{-im\alpha}\, e^{-in\gamma} \tag{3.84}$$

where $Z_{lmn}(X)$ is a generalized Legendre function that arises, for example, in the quantum mechanical treatment of angular momentum.[46] In the same way as $P_l^m(X)$ is a polynomial of X that depends on integer indices l and m, $Z_{lmn}(X)$ is also a polynomial of X that depends on indices l, m, and n. The generalized spherical harmonics (3.84)

also have the orthonormal property similar to that expressed by (3.83). The crystallite orientation distribution $w(\alpha, \beta, \gamma)$ is now expanded in a series as

$$w(\alpha, \beta, \gamma) = \sum_{l=0}^{\infty} \sum_{m=-l}^{l} \sum_{n=-l}^{l} W_{lmn} Z_{lmn}(\cos \beta) e^{-im\alpha} e^{-in\gamma} \tag{3.85}$$

where W_{lmn} are the coefficients that need to be determined.

Question (1) we raised earlier, that is, whether the crystallite orientation distribution $w(\alpha, \beta, \gamma)$ can be determined once the pole orientation distributions $t_j(\Theta, \Phi)$ for some numbers of (hkl) reciprocal lattice vectors have been measured experimentally, can be answered affirmatively if it is possible to calculate the coefficients W_{lmn} from the knowledge of T_{lm}^js obtained for a finite number of poles ($j = 1, 2, \ldots, \nu$). The answer to this question is fortunately yes, but with some qualifications. The desired relationship linking W_{lmn} to T_{lm}^js is[45]

$$T_{lm}^j = 2\pi \left(\frac{2}{2l+1}\right)^{1/2} \sum_{n=-l}^{l} W_{lmn} P_l^n(\cos \varsigma_j) e^{im\psi_j} \tag{3.86}$$

where ζ_j and ψ_j, as illustrated in Figure 3.25, are the angles specifying the direction of reciprocal lattice vector $\boldsymbol{r}_j$ with reference to the crystallite frame of reference o-xyz. In the context of question (1), there are in (3.86) $2l + 1$ unknowns $W_{lm\bar{l}}, \ldots, W_{lm0}, \ldots, W_{lml}$, for fixed l and m, that need to be determined. Thus, if measurements are made for the pole distributions $t_j(\Theta, \Phi)$ for ν different poles ($\nu \geq 2l + 1$), then relations (3.86) give ν simultaneous linear equations (with fixed l and m) that can be solved to give $2l+1$ W_{lmn}s. Depending on the number ν of poles for which the pole orientation distribution was measured, the crystallite distribution, as represented by (3.85), is obtained as a series with higher order terms truncated beyond $l = (\nu - 1)/2$. This means that to be able to determine $w(\alpha, \beta, \gamma)$ to a sufficiently large number of terms in the series, the pole distributions have to be measured also for a correspondingly large number of (hkl) planes. Fortunately, the symmetry elements present, such as the uniaxial rather than biaxial symmetry in the sample and any axis of rotation or mirror plane present in the crystal structure, make many of the coefficients T_{lm}^j and W_{lmn} equal to zero, and the number n of poles for which the pole distribution must be determined is greatly reduced.[45,47]

A further, more subtle complication in the determination of $w(\alpha, \beta, \gamma)$ is that, since all T_{lm}^js for l odd are equal to zero (due to the nature of diffraction phenomenon), there is no way that the coefficients W_{lmn} with l odd can be determined. This does not mean that W_{lmn} with l odd are identically equal to zero.[48] Thus the crystallite orientation distribution $w(\alpha, \beta, \gamma)$ determined by means of (3.86) is incomplete, aside from the series truncation error, because terms with l odd are missing in the series. The effect of these missing terms shows up, when the crystallite orientation distribution is plotted, as aberrations in the form of "ghost peaks" or regions of negative values of $w(\alpha, \beta, \gamma)$. Methods for remedying such faults are now available[49] but will not be discussed here. This difficulty in determining the coefficient W_{lmn} with l odd does not affect question (2) raised above, that is, the question of deriving a pole distribution $t_j(\Theta, \Phi)$ indirectly

once $w(\alpha, \beta, \gamma)$ has been determined. Once the coefficients W_{lmn} are available, the coefficients T_{lm}^{j} for any other pole j can be readily calculated by means of (3.86), and since T_{lm}^{j} with l odd is always zero there is no need to know W_{lmn} for l odd.

FURTHER READING

1. Alexander, L. E., *X-Ray Diffraction Methods in Polymer Science*, Wiley-Interscience, New York, 1969.
2. Kakudo, M., and Kasai, N., *X-ray Diffraction by Polymers,* Elsevier, Amsterdam, 1972.
3. Klug, H. P., and Alexander, L. E., *X-ray Diffraction Procedures*, 2nd ed., Wiley, New York, 1974, Chapter 8.
4. Baltá-Calleja, F. J., and Vonk, C. G., *X-ray Scattering of Synthetic Polymers*, Elsevier, Amsterdam, 1989, Chapters 3–6.

Crystal Structure Analysis

5. Glusker, J. P., and Trueblood, K. N., *Crystal Structure Analysis, A Primer*, 2nd ed., Oxford University Press, New York, 1985.
6. Glusker, J. P., Lewis, M., and Rossi, M., *Crystal Structure Analysis for Chemists and Biologists*, VCH, New York, 1994.
7. Tadokoro, H., *Structure of Crystalline Polymers*, Wiley, New York, 1979.

Crystal Imperfection

8. Hosemann, R., and Bagchi, S. N., *Direct Analysis of Diffraction by Matter*, North-Holland, Amsterdam, 1962.
9. Vainshtein, B. K., *Diffraction of X-rays by Chain Molecules*, Elsevier, New York, 1966.

REFERENCES

10. Warren, B. E., *X-ray Diffraction*, Addison-Wesley, Reading, 1969, p. 20.
11. Brandrup, J., and Immergut, E. H., *Polymer Handbook.*, 3rd ed., Wiley, New York, 1989.
12. Parrish, W., and Wilson, A. J. C., in *International Tables for X-ray Crystallography*, Vol. II, Kynoch Press, Birmingham, 1972, p. 217.
13. Wilson, A. J. C., *J. Sci. Instr.* **27**, 321 (1950).
14. Davis, G. T., Eby, R. K., and Colson, J. P., *J. Appl. Phys.* **41**, 4316 (1970).
15. Cavallo, P., Martuscelli, E., and Pracella, M., *Polymer* **18**, 42 (1977).
16. Turner-Jones, A., *Polymer* **7**, 23 (1966).
17. Davis, G. T., Weeks, J. J., Martin, G. M., and Eby, R. K., *J. Appl. Phys.* **45**, 4175 (1974).
18. Bunn, C. W., *Trans. Faraday Soc.* **35**, 482 (1939).
19. *International Tables for Crystallography*, Vol. A, 2nd ed., Th. Hahn, Ed., Kluwer Academic Publishing, Dordrecht, 1987.
20. Harker, D., and Kasper, J. S., *Acta Crystallogr.* **1**, 70 (1948).
21. Karle, J., and Hauptman, H., *Acta Crystallogr.* **3**, 181 (1950).
22. Sayre, D., *Acta Crystallogr.* **5**, 60 (1952).

23. Giacovazzo, C., in *International Tables for Crystallography*, Vol. B, U. Shmeuli, Ed., Kluwer Academic Publication, Dordrecht , 1993, Section 2.2.
24. Wunderlich, B., *Macromolecular Physics*, Vol. 1, Academic Press, New York, 1973, Chapter 2.
25. Uchida, T., and Tadokoro, H., *J. Polymer Sci., Part A-2* **5**, 63 (1967).
26. Natta, G., and Corradini, P., *Rubber Chem. Technol.* **33**, 703 (1960).
27. Hermans, J. J., *Rec. Trav. Chim.* **63**, 211 (1944).
28. Hosemann, R., and Wilke, W., *Makromol. Chem.* **118**, 230 (1968).
29. Hindeleh, A. M., and Hosemann, R., *Polymer Commun.* **23**, 1101 (1982).
30. Warren, B. E., and Averbach, B. L., *J. Appl. Phys.* **21,** 595 (1950).
31. Warren, B. E., and Averbach, B. L., *J. Appl. Phys.* **23,** 497 (1952).
32. Buchanan, D. R., and Miller, R. L., *J. Appl. Phys.* **37**, 4003 (1966).
33. Kakudo, M., and Ullman, R., *J. Polymer Sci.* 45, 91 (1960).
34. Ruland, W., *Acta Crystallogr.* **14**, 1180 (1961).
35. Ruland, W., *Polymer* **5**, 89 (1964).
36. Killian, H. G., *Kolloid-Z. Z. Polymere* **183**, 1 (1962).
37. Killian, H. G., *Kolloid-Z. Z. Polymere* **185**, 13 (1962).
38. Riello, P., Fagherazzi, G., Canton, P., Clemente, D., and Signoretto, M., *J. Appl. Crystallogr.* **28**, 121 (1995).
39. Polizzi, S., Fagherazzi, G., Benedetti, A., Battagliarin, M., and Asano, T., *J. Appl. Crystallogr.* **23**, 359 (1990).
40. Vonk, C. G., *J. Appl. Crystallogr.* **6**, 148 (1973).
41. Desper, C.R., and Stein, R. S., *J. Appl. Phys.* **37**, 3990 (1966).
42. Hermans, P. H., and Platzek, P., *Kolloid Z.* **87**, 246 (1939).
43. Stein, R. S., *J. Polymer Sci.* **31**, 327 (1958).
44. Margenau, H., and Murphy, G. M., *The Mathematics of Physics and Chemistry*, Van Nostrand, New York, 1943, p. 272.
45. Roe, R. J., *J. Appl. Phys.* **36**, 2024 (1965).
46. Rose, M. E., *Elementary Theory of Angular Momentum*, Wiley, New York, 1957, Chapter 4.
47. Roe, R. J., and Krigbaum, W. R., *J. Chem. Phys.* ***40***, 2608 (1964).
48. Matthies, S., *Phys. Stat. Sol.* **b92**, K135 (1979).
49. Matthies, S., Vinel, G. W., and Helming, K., *Standard Distributions in Texture Analysis*, Akademie-Verlag, Berlin, 1987.

Amorphous Polymers

4

The scattering from an amorphous material, whether a liquid, an inorganic glass, or a glassy or rubbery polymer, lacks the sharp diffraction peaks that are characteristic of crystalline materials. At first glance the scattering appears totally featureless except for the presence of an amorphous halo. However, much information about the structure of the amorphous material can still be extracted from a detailed analysis of such apparently featureless scattering curves. Broadly speaking, two types of studies can be performed to obtain information about the structure of amorphous polymers, as discussed in this chapter. One is a study of the local structure, or the short-range order, present in these polymers, and this usually is accomplished through the determination of the radial distribution function. In the case of a uniaxially oriented amorphous polymer a similar analysis may lead to the determination of the so-called cylindrical distribution function, which gives information about the short-range order in the polymer as well as some measure of the state of orientation of chain segments. The second is a study to determine the extent of large-scale density fluctuations present in the polymer by means of a small-angle scattering measurement. In this chapter we discuss studies that are made with a pure, single-component, amorphous polymer. In the case of a multicomponent system, such as a polymer blend or a solution of a polymer in a solvent, the presence of a concentration fluctuation produces an additional, usually much stronger, scattering effect. Aspects of studies of such multicomponent systems are presented separately in Chapter 6, after the technique of small-angle scattering is discussed in detail in Chapter 5.

4.1 SHORT-RANGE ORDER

4.1.1 Pair Distribution Function: Cases with a Single Atomic Species

The method of studying the short-range structure in an amorphous polymer, as long as the polymer is isotropic, is essentially the same as that used for the study of an ordinary liquid. In crystal structure analysis the aim is to determine the positions of all the atoms in a unit cell as well as to find the lattice structure by which the unit cell is repeated in the crystal. In an amorphous substance, the environment surrounding

an atom is never exactly the same as the one surrounding the next atom. The short-range structure can therefore be defined only in a statistical sense. Yet there clearly exists a short-range order in a liquid, resulting from repulsive and attractive forces of interaction acting among neighboring atoms and molecules. Such a local structure may extend to a distance of a few atomic radii or more depending on the nature of the interaction forces, the density, and other factors. The information about the local structure can be summarized concisely in a *pair distribution function* (or *pair correlation function*) $g(r)$, which will be defined below. In the case of a monatomic liquid, such as liquid argon, the knowledge of $g(r)$ is all that is required to evaluate most of its thermodynamic properties through standard statistical mechanics methods. To define the local structure of amorphous polymers completely, additional information about chain connectivity and conformation is required, but the pair distribution function is certainly the starting point in understanding the packing of chains. It is the x-ray or neutron scattering technique that provides the experimental data from which the pair distribution function can be derived.

At first, for the sake of simplicity, we consider cases in which the amorphous material contains only one kind of atom and defer a discussion of cases involving more than one atomic species to Section 4.1.2. Suppose we select an arbitrary atom and then note that in a volume element $d\boldsymbol{r}$ separated from it by $\boldsymbol{r}$, the number of atoms found is equal, on average, to $n_2(\boldsymbol{r})\, d\boldsymbol{r}$. Because the space occupied by an atom is excluded to others, $n_2(\boldsymbol{r})$ is clearly equal to zero for r less than twice the radius of the atom. As r increases, the density $n_2(\boldsymbol{r})$ attains a maximum at the distance r that corresponds to the first coordination shell. Beyond this maximum, with increasing r, $n_2(\boldsymbol{r})$ goes through alternate minima and maxima with gradually diminishing depths and heights. At very large r it reaches a constant value equal to the average number density of atoms $\langle n \rangle$. The pair distribution function $g(\boldsymbol{r})$ is the normalized version of $n_2(\boldsymbol{r})$, given by

$$g(\boldsymbol{r}) = n_2(\boldsymbol{r}) / \langle n \rangle \tag{4.1}$$

so that $g(\boldsymbol{r})$ approaches unity at large r. Figure 4.1 gives an example of the pair distribution function obtained with liquid argon by means of neutron scattering measurement. When the amorphous material under consideration is an ordinary liquid or an undeformed polymer, its properties are isotropic, and $n_2(\boldsymbol{r})$ and $g(\boldsymbol{r})$ are functions of scalar distance r only. The term *radial distribution function* is then often used in place of the pair distribution function. When the polymer has been deformed uniaxially and thus possesses cylindrical symmetry, the term *cylindrical distribution function* is used instead.

To see how the pair distribution function can be determined from the scattering data, we start from Equation (1.70) for the amplitude $A(\boldsymbol{q})$ of scattering, which on squaring gives the intensity

$$I(\boldsymbol{q}) = \left\langle \left(b \sum_{j=1}^{N} e^{-i\boldsymbol{q}\boldsymbol{r}_j} \right) \left(b \sum_{k=1}^{N} e^{i\boldsymbol{q}\boldsymbol{r}_k} \right) \right\rangle \tag{4.2}$$

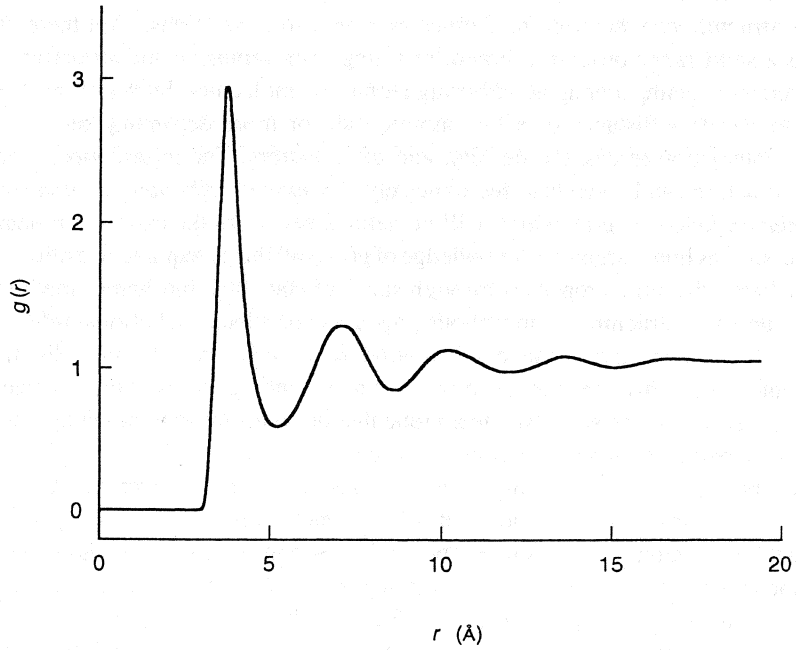

Figure 4.1 Pair distribution function of liquid argon at 84 K obtained by neutron scattering measurement.

where N is the number of atoms in the scattering volume and $\boldsymbol{r}_j$ is the position of the jth atom. The angle bracket $\langle \cdots \rangle$ in (4.2) indicates that the intensity observed is the time average, which in an equilibrium system is equal to the ensemble average. Splitting the terms with $j = k$ from the summation in (4.2), we can write it as

$$I(\boldsymbol{q}) = Nb^2 + b^2 \sum_{j=1}^{N} \sum_{k \neq j} \left\langle e^{-i\boldsymbol{q}\boldsymbol{r}_{jk}} \right\rangle \tag{4.3}$$

where $\boldsymbol{r}_{jk} = \boldsymbol{r}_j - \boldsymbol{r}_k$. The first term on the right of (4.3) represents the sum of independent scattering from each of the N atoms, and the second term represents the effect of interference among the waves scattered from different atoms. We replace the summation with respect to k by an integral, and in doing so note that when $\boldsymbol{r}_{jk}$ is between $\boldsymbol{r}$ and $\boldsymbol{r} + d\boldsymbol{r}$, the number of atoms to be included in the sum is equal, on the average, to $n_2(\boldsymbol{r})\, d\boldsymbol{r}$. Thus (4.3) becomes

$$I(\boldsymbol{q}) = Nb^2 + Nb^2 \int_V n_2(\boldsymbol{r}) e^{-i\boldsymbol{q}\boldsymbol{r}}\, d\boldsymbol{r} \tag{4.4}$$

Subtracting $\langle n \rangle$ from $n_2(\boldsymbol{r})$ we find

$$I(\boldsymbol{q}) = Nb^2 + Nb^2 \int_V [n_2(\boldsymbol{r}) - \langle n \rangle] e^{-i\boldsymbol{q}\boldsymbol{r}}\, d\boldsymbol{r} + Nb^2 \int_V \langle n \rangle\, e^{-i\boldsymbol{q}\boldsymbol{r}}\, d\boldsymbol{r}$$

$$= Nb^2 + Nb^2 \langle n \rangle \int_V [g(\boldsymbol{r}) - 1] e^{-i\boldsymbol{q}\boldsymbol{r}}\, d\boldsymbol{r} + Nb^2 \langle n \rangle\, \delta(\boldsymbol{q}) \tag{4.5}$$

The last term in (4.5) represents the unobservable "null scattering" or the scattering from the sample as a whole (see Section 1.6), and it will be ignored in the discussion from now on. At this point we define the *interference function* (or *reduced intensity function*) $i(\boldsymbol{q})$ by

$$i(\boldsymbol{q}) \equiv \frac{I(\boldsymbol{q}) - Nb^2}{Nb^2} \tag{4.6}$$

Equation (4.5) can then be rewritten as

$$i(\boldsymbol{q}) = \langle n \rangle \int_V [g(\boldsymbol{r}) - 1] e^{-i\boldsymbol{q}\boldsymbol{r}}\, d\boldsymbol{r} \tag{4.7}$$

Equation (4.7) shows that $g(\boldsymbol{r}) - 1$ can be evaluated by taking the inverse Fourier transform of the interference function $i(\boldsymbol{q})$ derived from the observed intensity $I(\boldsymbol{q})$ in accordance with (4.6).

4.1.2 Pair Distribution Function: Cases with More Than One Atomic Species

In organic polymers, there is always more than one kind of atoms present. Even a hydrocarbon polymer, the simplest among polymers in chemical structure, is made up of two types of atoms, carbons and hydrogens. To specify the short-range order in a hydrocarbon polymer, three *partial pair distribution functions,* $g_{CC}(\boldsymbol{r})$, $g_{HH}(\boldsymbol{r})$, and $g_{CH}(\boldsymbol{r})$, are needed. The definition of $g_{CH}(\boldsymbol{r})$, for example, is as follows. We pick an arbitrary C atom and look at the volume element $d\boldsymbol{r}$ at a position displaced from it by $\boldsymbol{r}$. We note the number of H atoms present in this volume element to be equal, on the average, to $n_{CH}(\boldsymbol{r})\, d\boldsymbol{r}$. The function $g_{CH}(\boldsymbol{r})$ is obtained on normalization as

$$g_{CH}(\boldsymbol{r}) = n_{CH}(\boldsymbol{r}) / \langle n_H \rangle \tag{4.8}$$

where $\langle n_H \rangle$ is the average number density of H atoms in the sample. Thus $g_{CH}(\boldsymbol{r})$ is a measure of the concentration of H atoms present at distance $\boldsymbol{r}$ around a C atom. The fact that

$$g_{CH}(\boldsymbol{r}) = g_{HC}(\boldsymbol{r}) \tag{4.9}$$

can be demonstrated as follows. We note that

$$\langle n_C \rangle\, n_{CH}(\boldsymbol{r}) = \langle n_H \rangle\, n_{HC}(-\boldsymbol{r}) = \langle n_H \rangle\, n_{HC}(\boldsymbol{r}) \tag{4.10}$$

where the first member is the number of C–H pairs in which the H atom is displaced from the C atom by $\boldsymbol{r}$, and the second member is the number of H–C pairs in which the C atom is displaced from the H atom by $-\boldsymbol{r}$. The second and third members in (4.9)

are equal to each other because liquid properties are centrosymmetric and therefore $n_{HC}(-\boldsymbol{r}) = n_{HC}(\boldsymbol{r})$. Dividing (4.10) with $\langle n_C \rangle \langle n_H \rangle$ then gives (4.9).

Assuming that the polymer contains m different atomic species and letting indices α and β denote the types of atoms ($\alpha, \beta = 1, \ldots, m$), we can generalize Equation (4.4) to

$$I(\boldsymbol{q}) = \sum_{\alpha=1}^{m} N_\alpha b_\alpha^2 + \sum_{\alpha=1}^{m} N_\alpha b_\alpha \sum_{\beta=1}^{m} b_\beta \int_V n_{\alpha\beta}(\boldsymbol{r}) e^{-i\boldsymbol{q}\boldsymbol{r}}\, d\boldsymbol{r} \tag{4.11}$$

where N_α is the number of atoms of type α, of scattering length b_α, contained in the scattering volume. In terms of the atomic number fractions x_α, N_α and $\langle n_\alpha \rangle$ can be written as Nx_α and $\langle n \rangle x_\alpha$, respectively (where N is now the total number of atoms of all types and $\langle n \rangle = N/V$ is the average number of all atoms per unit volume). When the null scattering is removed from (4.11), it can be rewritten as

$$I(\boldsymbol{q}) = N \sum_{\alpha=1}^{M} x_\alpha b_\alpha^2 + N \langle n \rangle \sum_{\alpha=1}^{m} \sum_{\beta=1}^{m} x_\alpha x_\beta b_\alpha b_\beta \int_V \left[g_{\alpha\beta}(\boldsymbol{r}) - 1 \right] e^{-i\boldsymbol{q}\boldsymbol{r}}\, d\boldsymbol{r} \tag{4.12}$$

With m atomic species, there are $m(m+1)/2$ partial pair distribution functions $g_{\alpha\beta}(\boldsymbol{r})$ that are distinct from each other. When only a single intensity function $I(\boldsymbol{q})$ is available from experiment, no method of ingenious analysis can lead to determination of all these separate partial pair distribution functions from it. Different and independent intensity functions $I(\boldsymbol{q})$ may be obtained experimentally when measurements are made, for example, with samples prepared with some of their atoms replaced by isotopes. When a sufficient number of such independent intensity functions is available, it is then possible to have all the partial pair distribution functions $g_{\alpha\beta}(\boldsymbol{r})$ individually determined, as will be elaborated on shortly. When only a single intensity function is available from x-ray or neutron scattering, however, what can be obtained from a Fourier inversion of the interference function is some type of weighted average of all $g_{\alpha\beta}(\boldsymbol{r})$ functions. The exact relationship between such an averaged function and $g_{\alpha\beta}(\boldsymbol{r})$s is as follows.

In the case of a multiatom sample the interference function $i(\boldsymbol{q})$ is evaluated from the observed intensity according to

$$i(\boldsymbol{q}) = \frac{I(\boldsymbol{q})/N - \sum_{\alpha=1}^{m} x_\alpha b_\alpha^2}{\left(\sum_{\alpha=1}^{m} x_\alpha b_\alpha \right)^2} \tag{4.13}$$

in place of Equation (4.6). The inverse Fourier transform of $i(\boldsymbol{q})$ then gives the *averaged* or *gross pair distribution function* $\hat{g}(\boldsymbol{r})$ defined by

$$i(\boldsymbol{q}) = \langle n \rangle \int_V \left[\hat{g}(\boldsymbol{r}) - 1 \right] e^{-i\boldsymbol{q}\boldsymbol{r}}\, d\boldsymbol{r} \tag{4.14}$$

Comparison of (4.13) and (4.14) with (4.12) shows that $\hat{g}(\boldsymbol{r})$ is related to the partial functions $g_{\alpha\beta}(\boldsymbol{r})$ by

$$\int_V \hat{g}(\boldsymbol{r}) e^{-i\boldsymbol{q}\boldsymbol{r}}\, d\boldsymbol{r} = \sum_{\alpha=1}^{m}\sum_{\beta=1}^{m} w_\alpha w_\beta \int_V g_{\alpha\beta}(\boldsymbol{r}) e^{-i\boldsymbol{q}\boldsymbol{r}}\, d\boldsymbol{r} \tag{4.15}$$

where w_α is the weighting factor for the type α atom:

$$w_\alpha = \frac{x_\alpha b_\alpha}{\sum_{\alpha=1}^{m} x_\alpha b_\alpha} \tag{4.16}$$

In the case of x-ray scattering, the relationship between $\hat{g}$ and $g_{\alpha\beta}$s given by (4.15) is complicated, because the atomic scattering factor f_α for x-rays is q dependent, and therefore the weighting factor w_α is also q dependent. (See Waser and Schomaker[4] and Pings and Waser[5] for further discussions on the relationship between $\hat{g}$ and $g_{\alpha\beta}$s.) On the other hand, in the case of neutron scattering, w_α is a constant independent of q, and therefore Equation (4.15) can be further simplified to

$$\hat{g}(\boldsymbol{r}) = \sum_{\alpha=1}^{m}\sum_{\beta=1}^{m} w_\alpha w_\beta\, g_{\alpha\beta}(\boldsymbol{r}) \tag{4.17}$$

showing that $\hat{g}(\boldsymbol{r})$ is a simple weighted average of $g_{\alpha\beta}(\boldsymbol{r})$s.

The x-ray atomic scattering factor $f(q)$ of a C atom is about six times that of an H atom, and therefore when a hydrocarbon polymer is studied by means of x-ray scattering, $g_{CC}(\boldsymbol{r})$ makes the predominant contribution to $\hat{g}(\boldsymbol{r})$. In such a case, $\hat{g}(\boldsymbol{r})$ may be taken as a reasonable approximation to $g_{CC}(\boldsymbol{r})$, which is usually the object of primary interest. However, when the weighting factors w_α for different atomic species are comparable, each of the partial pair distribution functions $g_{\alpha\beta}(\boldsymbol{r})$ makes a substantial contribution to $\hat{g}(\boldsymbol{r})$, and this makes meaningful interpretation of the latter difficult.

As was alluded to briefly earlier, it is possible to determine all the partial pair distribution functions $g_{\alpha\beta}(\boldsymbol{r})$ if a sufficient number of independent $I(\boldsymbol{q})$s can be obtained with the same or similar material. As an illustration, let us again consider a hydrocarbon polymer, and suppose that measurements are made for the intensities, $I_X(\boldsymbol{q})$ and $I_H(\boldsymbol{q})$, of x-ray and neutron scattering from an ordinary sample, and the intensity $I_D(\boldsymbol{q})$ of neutron scattering from a specially prepared sample in which all hydrogens are replaced by deuteriums. The interference functions $i_X(\boldsymbol{q})$, $i_H(\boldsymbol{q})$, and $i_D(\boldsymbol{q})$ corresponding to each of these measurements are then evaluated by means of Equation (4.13), in which the scattering lengths b_α are assigned values appropriate to each radiation used. Now we define the *partial interference function* $i_{\alpha\beta}(\boldsymbol{q})$ by

$$i_{\alpha\beta}(\boldsymbol{q}) = \langle n \rangle \int_V \left[g_{\alpha\beta}(\boldsymbol{r}) - 1\right] e^{-i\boldsymbol{q}\boldsymbol{r}}\, d\boldsymbol{r} \tag{4.18}$$

which allows us to write (4.15) as

$$i(q) = \sum_{\alpha=1}^{m} \sum_{\beta=1}^{m} w_\alpha w_\beta i_{\alpha\beta}(q) \tag{4.19}$$

For each of the three interference functions $i_X(q)$, $i_H(q)$, and $i_D(q)$ determined as mentioned above, Equation (4.19) is applicable, where the $i_{\alpha\beta}(q)$s [i.e., $i_{CC}(q)$, $i_{CH}(q)$, and $i_{HH}(q)$] are common among the three cases and are unknown and yet to be determined. The weighting factors w_α, on the other hand, depend, as seen from (4.16), on the scattering lengths b_α and assume different values in the three measurements. For a given q value, Equation (4.19) therefore constitutes a set of simultaneous linear equations with three unknowns $i_{\alpha\beta}(q)$, whose values can be determined by solving the simultaneous equations. The partial pair distribution functions $g_{\alpha\beta}(r)$ are then obtained from them by Fourier inversion as implied by (4.18).

4.1.3 Isotropic Polymers

When the polymer is unoriented, so that its properties are isotropic, the radial distribution function depends only on the magnitude and not on the direction of r. The intensity function is then also isotropic and depends only on the magnitude of q. Equation (4.14) can now be written (cf. Section B.5) as

$$i(q) = \langle n \rangle \int_0^\infty \left[\hat{g}(r) - 1\right] 4\pi r^2 \frac{\sin qr}{qr} dr \tag{4.20}$$

Equations (4.5), (4.7), (4.11), (4.12), (4.14), (4,15), and (4.18) can all be written similarly in terms of the Fourier sine transform. Writing (4.20) in a slightly modified form, we have

$$qi(q) = \langle n \rangle \int_0^\infty 4\pi r \left[\hat{g}(r) - 1\right] \sin qr \, dr \tag{4.21}$$

from which by taking the inverse sine transform we obtain

$$\langle n \rangle r \left[\hat{g}(r) - 1\right] = \frac{1}{2\pi^2} \int_0^\infty qi(q) \sin qr \, dq \tag{4.22}$$

In the literature there are reports of radial distribution function analyses performed with polystyrene,[6,7] polycarbonate of bisphenol-A,[7,8] and a number of other amorphous polymers.[9] As an illustration, we present results obtained with atactic polystyrene. Figure 4.2 shows the x-ray scattering intensity data obtained with Cu$K\alpha$ radiation. The strong peak at 2θ around 20° represents the so-called amorphous halo, whereas the smaller peak at around 10° is called the polymerization peak by some and has attracted interest with regard to its structural origin. The experimentally measured intensity is first corrected for background, polarization, absorption, etc.,

and then the Compton-modified scattering, calculated from theory, is subtracted; the resulting intensity function thus obtained is what constitutes the "observed" intensity $I(q)$ referred to in the above discussion. The interference function $i(q)$ is then calculated according to (4.13). In Figure 4.3, $i(q)$ multiplied by q is plotted against q. Some oscillations in $qi(q)$, reflecting the presence of fine details in the structure, persist even at the highest q shown in Figure 4.3.[10] Taking the inverse sine transform according to (4.22) gives the gross radial distribution function $\hat{g}(r)$ shown in Figure 4.4. Here, the ordinate is $4\pi r^2 \langle n \rangle [\hat{g}(r) - 1]$, which may be regarded, in an approximate sense, as the weighted-average number of atoms, in excess of the overall average, found at distance r from an arbitrarily selected atom. As stated earlier, in x-ray scattering, a carbon–carbon pair has a much higher weighting than pairs involving hydrogen atoms, and therefore $\hat{g}(r)$ may approximately track the carbon–carbon radial distribution function. In fact, the first peak at r around 1.4 Å can be considered to arise mainly from the nearest-neighbor covalently-bonded carbon pairs, and the peak at around 2.4 Å from the second-nearest-neighbor carbon pairs. The peaks at higher r are, however, more difficult to identify in this manner and undoubtedly result from overlap of many different types of atomic pairings.

At this point several brief remarks are made about the experimental and data-reduction processes that are needed before the radial distribution function such as shown in Figure 4.4 is finally obtained.

Necessity of a Wide q Range. Since in the sine transform (4.22) the integration is in principle to be performed from 0 to infinity in q, and since the interference

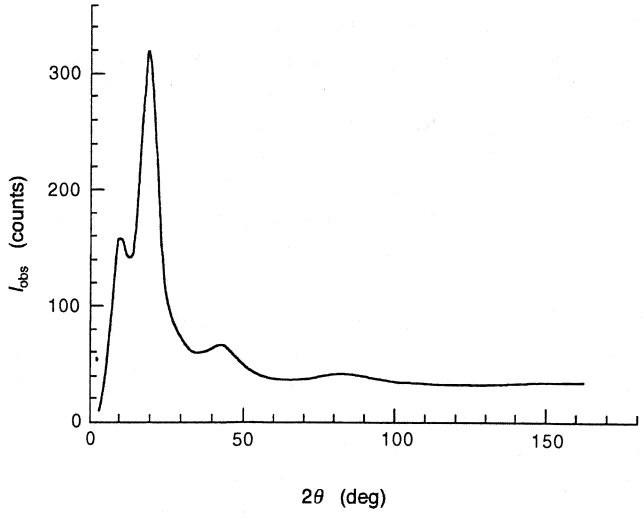

Figure 4.2 Intensity of x-ray scattering from atactic polystyrene, as observed using Cu$K\alpha$ radiation.

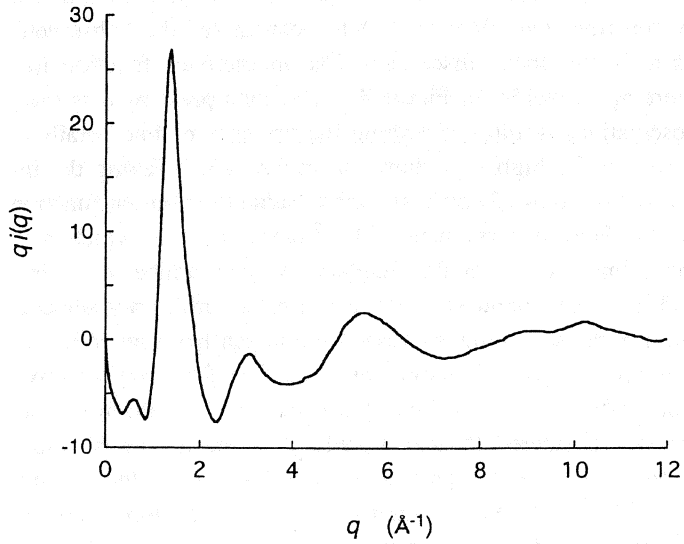

Figure 4.3 Plot of $qi(q)$ for atactic polystyrene, where $i(q)$ is the interference function defined by (4.13). (From Mitchell and Windle.[10])

function $i(q)$ exhibits deviations from zero even at relatively high q, it is necessary that the intensity $I(q)$ be determined experimentally to as high a value of q as possible. For this reason, a radiation with a shorter wavelength, such as the one from a Mo target in the case of x-rays, is often used. In measuring the intensity, more time must be spent at higher q, since the scattering is generally weaker, and moreover any measurement error is magnified more in the process of converting $I(q)$ into $qi(q)$ at higher q.

Compton Scattering. It is difficult to eliminate the Compton-modified x-ray scattering reliably by experimental means, because the wavelength shift of the modified from the coherent scattering is rather small, especially at small scattering angles. The preferred practice is to include all the Compton-modified scattering in the measured intensity and then subsequently to subtract the Compton-modified intensity calculated theoretically from it.

Normalization. The practice of subtracting the theoretical Compton-modified intensity works only if the measured intensity is available on an absolute scale. Similarly, before the intensity function $I(q)$ can be converted into the interference function $i(q)$ by means of Equation (4.13), $I(q)$ must be on an absolute scale. In principle, the intensity can of course be measured from the beginning in absolute units by means of an instrument calibrated for absolute intensity, as discussed in Section 2.7. The more usual practice, however, is to measure the intensity first in relative units and then to scale it by the normalization constant determined according to the following criterion. The normalization condition is satisfied when the following is obeyed in the limit of large q

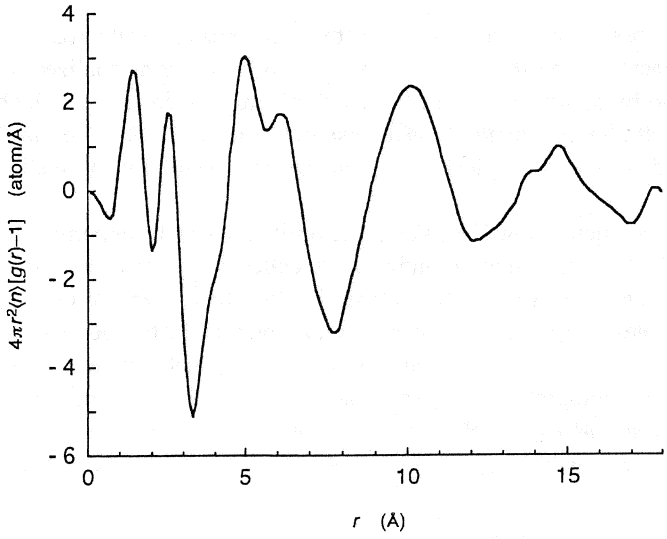

Figure 4.4 Gross radial distribution function $\hat{g}(r)$ of polystyrene given by the inverse Fourier sine transform of $qi(q)$ according to (4.22). (From Schubach *et al.*[7])

$$\lim_{q\to\infty} \frac{I(q)/N}{\sum_{\alpha=1}^{m} x_\alpha b_\alpha^2} = 1 \tag{4.23}$$

In other words, the coherent scattering intensity per atom, $I(q)/N$, should be equal to the average independent scattering per atom, $\sum x_\alpha b_\alpha^2$, at large q where the effect of interference among waves scattered from different atoms is expected to be largely smeared out. Alternatively, a more accurate result is obtained when the following is satisfied:[11,12]

$$\frac{(1/2\pi^2)\int_0^\infty q^2[I(q)/N]\,dq + \langle\rho\rangle^2 V/N}{(1/2\pi^2)\int_0^\infty q^2 \sum_{\alpha=1}^{m} x_\alpha b_\alpha^2 dq} = 1 \tag{4.24}$$

where $\langle\rho\rangle$ is the average scattering length density in the sample (at $q = 0$). Equation (4.24) is based on the concept of the invariant discussed in Section 1.5.4. The quantity in the numerator of (4.24) is the invariant Q evaluated on the basis of the observed intensity $I(q)$. The term $\langle\rho\rangle^2 V/N$ is the contribution to the invariant due to the unobservable null scattering. The quantity in the denominator of (4.24) is the invariant Q based on the scattering from independent atoms. The total scattering power of the sample, which the quantity Q represents, should remain invariant irrespective of how the atoms are arranged, as long as the numbers and types of atoms contained in it remain the same. Thus, the value of the invariant Q (the numerator) evaluated from

the observed intensity should agree with the value (the denominator) evaluated from the known atomic content, when the observed intensity is properly normalized. In contrast to the method based on Equation (4.23), where only the intensity at high q values is compared, the second method makes use of the intensity observed over the whole q range and is expected to lead to a more accurate value for the scaling constant.

Truncation Error. No matter how large the upper limit of q is in the experimental determination of $I(q)$, it is still short of infinity, as called for in the theoretical sine transform (4.22). The truncation of the integration at a finite upper limit q_{max} produces spurious ripples in the vicinity of any peaks present in the derived radial distribution function $\hat{g}(r)$ (see Waser and Schomaker[4]). Such ripples can be suppressed or eliminated altogether if the integrand $qi(q)$ in (4.22) is multiplied by a *modification function* $M(q)$, which is equal to unity at $q = 0$ but smoothly decreases to zero as q approaches q_{max}. An example of such a modification function is

$$M(q) = \begin{cases} \dfrac{\sin(\pi q/q_{max})}{\pi q/q_{max}} & \text{for } q \leq q_{max} \\ 0 & \text{for } q > q_{max} \end{cases} \tag{4.25}$$

which was used in the derivation of the radial distribution function plotted in Figure 4.4 (Schubach et al.[7]). It should be remarked, however, that although the use of a modification function alleviates the effect of ripples due to the integration truncation, its trade-off is to broaden and smear out sharp peaks present in the radial distribution function.

The radial distribution function $\hat{g}(r)$ obtained from the experimental data thus suffers from the smearing effect because of the presence of more than one type of atom and is also distorted as a result of the truncation of integration or the use of a modification function $M(q)$. We may naturally ask whether, in spite of all these undesirable effects, it is still possible to obtain useful and reliable information about the short-range order present. The question can be answered if we have a known, model structure of an amorphous polymer, from it calculate both $\hat{g}(r)$ and $g_{CC}(r)$, and compare them to see how well $\hat{g}(r)$ in fact represents $g_{CC}(r)$. For this purpose we make use of the result of a molecular dynamics simulation of bulk atactic polystyrene (Mondello *et al.*[13]). From the atomic coordinates obtained in the simulation $g_{CC}(r)$ can be immediately evaluated. To evaluate $\hat{g}(r)$ we first calculate the x-ray scattering intensity from the structure obtained by the simulation, and then we follow exactly the same data reduction procedure used to derive the results in Figure 4.4, including the use of the modification function given by (4.25). Here the issue is not how well the simulation approximates the real structure, but rather how well the two functions, $\hat{g}(r)$ and $g_{CC}(r)$, based on exactly the same model structure, compare with each other. The result is shown in Figure 4.5, where the solid curve represents $g_{CC}(r)$ and the broken curve $\hat{g}(r)$. As expected, the latter is appreciably more smeared in comparison to the former. However, the positions and relative weights of the peaks appear to be correctly represented in $\hat{g}(r)$.

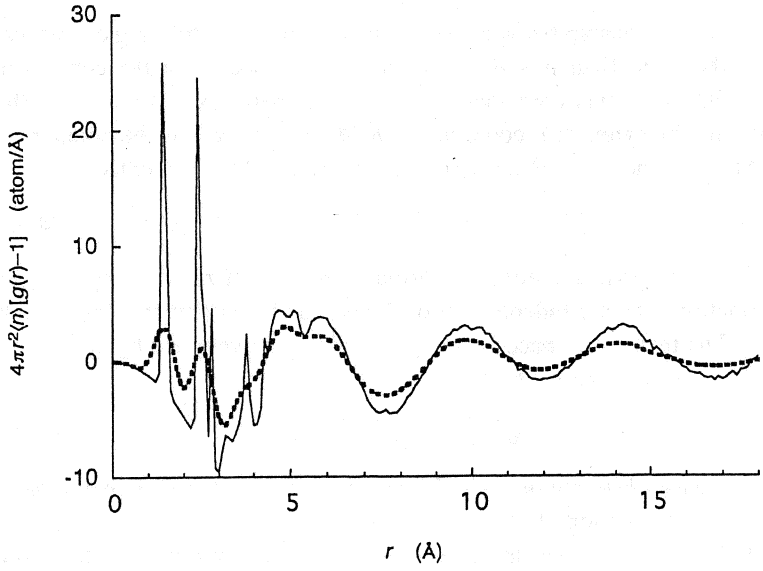

Figure 4.5 From the result of a molecular dynamics simulation, the x-ray scattering intensity was calculated, and from it $\hat{g}(r)$, given in the broken curve, was derived, by using exactly the same procedure as was used to treat experimental x-ray scattering intensities. The solid curve is the C–C atom pair distribution function calculated directly from the simulation result. (From Mondello *et al.*[13])

4.1.4 Uniaxially Oriented Polymers

With an amorphous polymer that has been stretched uniaxially, the structure is no longer isotropic and instead possesses cylindrical symmetry. This is reflected in the intensity of scattering that now depends, at a fixed scattering angle 2θ, on the orientation of the sample deformation axis with respect to the scattering vector. The scattered intensity therefore needs to be determined not only as a function of 2θ (or q) but also as a function of the sample orientation. It may then be noted that some of the broad peaks in the scattering curve are enhanced in the equatorial direction, whereas others are enhanced in the meridional direction. The "equatorial" (or "meridional") direction means that the scattering is observed when the sample axis is oriented perpendicular (or parallel) to the scattering vector. The enhancement of scattering in either the equatorial or meridional direction is often interpreted to indicate whether the particular peak concerned arises from an inter- or intramolecular correlation. This interpretation is based on the assumption that a pair of nearby atoms or groups in the same chain are likely to be aligned along the stretch direction on deformation. A more detailed and accurate interpretation of the changes in the structure may be obtained by having the intensity data converted to a cylindrical distribution function, as explained below.

To describe the relationship between the intensity function exhibiting cylindrical symmetry and the cylindrical pair distribution function, we adopt the coordinate system o-xyz with the z axis coincident with the symmetry axis. Vector $\boldsymbol{r}$ in the sample is specified by cylindrical coordinates (R, Φ, Z), where Z is the component of $\boldsymbol{r}$ in the z direction and R lies in the xy plane (see Figure 4.6). Evidently

$$r^2 = R^2 + Z^2 \tag{4.26}$$

In the presence of cylindrical symmetry, various functions of $\boldsymbol{r}$, including the pair distribution function $g(\boldsymbol{r})$, are independent of Φ and can be written as a function of R and Z alone. The reciprocal space vector $\boldsymbol{q}$ is similarly represented by cylindrical coordinates (ξ, α, ζ) (see Figure 4.6), where

$$q^2 = \xi^2 + \zeta^2 \tag{4.27}$$

The scattering intensity $I(\boldsymbol{q})$, having cylindrical symmetry and therefore being independent of α, is also a function of only ξ and ζ. This means that as long as the z axis coincides with the symmetry axis, the x axis can be chosen arbitrarily. We therefore choose the x axis such that α is equal to zero. The dot product $\boldsymbol{qr}$ is then equal to $\xi R \cos\Phi + \zeta Z$. Recognizing that the volume element $d\boldsymbol{r}$ is equal to $R\, dR\, d\Phi\, dZ$, we can write equation (4.14) as

$$i(\xi, \zeta) = \langle n \rangle \int_{-\infty}^{\infty} \int_0^{2\pi} \int_0^{\infty} \left[\hat{g}(R, Z) - 1\right] e^{-i(\xi R \cos\Phi + \zeta Z)} R\, dR\, d\Phi\, dZ \tag{4.28}$$

Since $\hat{g}(R, Z)$ is independent of Φ, the integration with respect to Φ can be performed immediately. Using the identity

$$J_0(x) = \frac{1}{\pi} \int_0^{\pi} \cos(x \cos\phi)\, d\phi \tag{4.29}$$

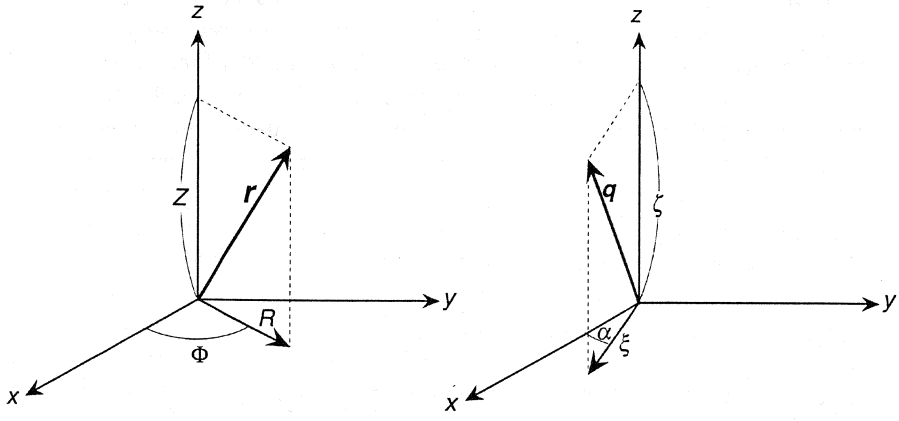

Figure 4.6 Definition of the cylindrical coordinates (R, Φ, Z) to represent $\boldsymbol{r}$ in real space, and the cylindrical coordinates (ξ, α, ζ) representing $\boldsymbol{q}$ in reciprocal space.

where J_0 is the Bessel function of the zeroth order (cf. Section B.5), (4.28) then becomes

$$i(\xi, \zeta) = \langle n \rangle \int_0^\infty \int_0^\infty 4\pi R \left[\hat{g}(R, Z) - 1\right] J_0(\xi R) \cos(\zeta Z)\, dR\, dZ \qquad (4.30)$$

Equation (4.30) is in the form of a Fourier–Bessel transform, and by taking its inverse transform (see Cormack[14]) we obtain

$$\langle n \rangle R \left[\hat{g}(R, Z) - 1\right] = \frac{1}{2\pi^2} \int_0^\infty \int_0^\infty \xi i(\xi, \zeta) J_0(\xi R) \cos(\zeta Z)\, d\xi\, d\zeta \qquad (4.31)$$

which shows how the cylindrical distribution function $\hat{g}(R, Z)$ can be obtained once the interference function $i(\xi, \zeta)$ is derived from the observed intensity $I(\xi, \zeta)$ according to (4.13).

As an illustration, we here quote the results obtained by Mitchell and Windle[10] with an atactic polystyrene stretched to an extension ratio 3 at 75°C. Figure 4.7 plots contour lines representing $qi(\xi, \zeta)$, where $i(\xi, \zeta)$ is the interference function derived according to Equation (4.13) from the observed intensity $I(\xi, \zeta)$. The dashed contour lines represent negative values. The equatorial section ($\zeta = 0$) of Figure 4.7 is plotted as the solid curve in Figure 4.8, and the meridional section ($\xi = 0$) is plotted as the broken curve. The so-called "polymerization peak" observable at q around 0.8 Å^{-1} shows up only in the equatorial direction, and this fact led many workers to consider the peak to reflect mainly interchain correlations. In comparison to this, the main amorphous peak at q around 1.4 Å^{-1} is enhanced in the meridional section, suggesting that it arises mainly from intrachain correlations. Figure 4.9 shows the gross cylindrical distribution function $\hat{g}(R, Z) - 1$ obtained by means of Equation (4.31) from the intensity data given in Figure 4.7.

4.2 THERMAL DENSITY FLUCTUATION

A hypothetical, perfectly homogeneous material, with a uniform scattering length density throughout, will give rise to no scattering at any q, except the unobservable null scattering at $q = 0$ discussed in Section 1.6. A large, perfect crystal can be considered to approach this ideal, when looked at on a size scale larger than the unit cell dimension, and indeed with crystals no scattering is observable at q smaller than the first Bragg peak. In the case of a gas or a liquid, however, a finite scattering occurs at all q, down to the smallest q approaching zero. This is because in a fluid inhomogeneities in density due to thermal motions of atoms and molecules always exist. In their random motion, some of the molecules may momentarily converge to create a region of a slightly higher density, whereas in another region molecules may happen to move simultaneously away from each other. Such an inhomogeneity in the atomic density (or more generally the scattering length density) from place to place in a fluid is called a *thermal density fluctuation* or simply a *density fluctuation*. Such density fluctuations exist at all size scales. Stated in another way, when the number of atoms found in a region of volume v is compared with the number found

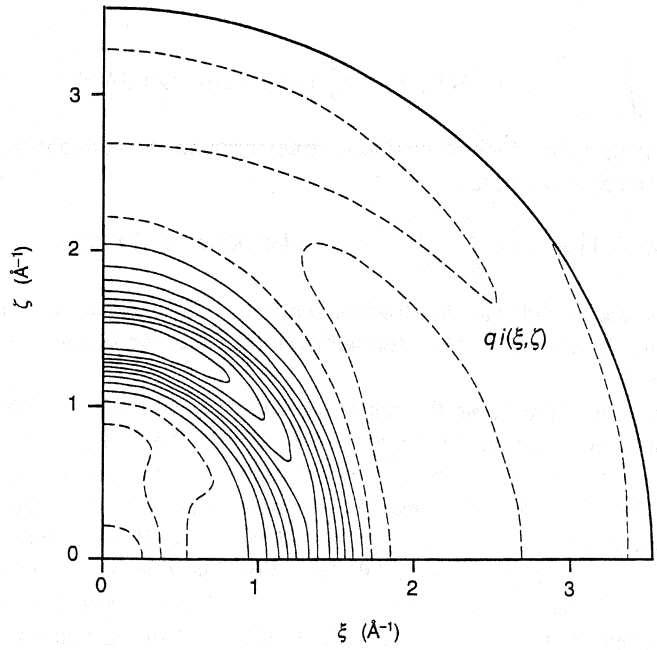

Figure 4.7 Interference function $i(\xi, \zeta)$ weighted by q (where $q^2 = \xi^2 + \zeta^2$), obtained with an atactic polystyrene stretched at 75°C to extension ratio 3. Dashed contour lines represent negative values. (From Mitchell and Windle.[10])

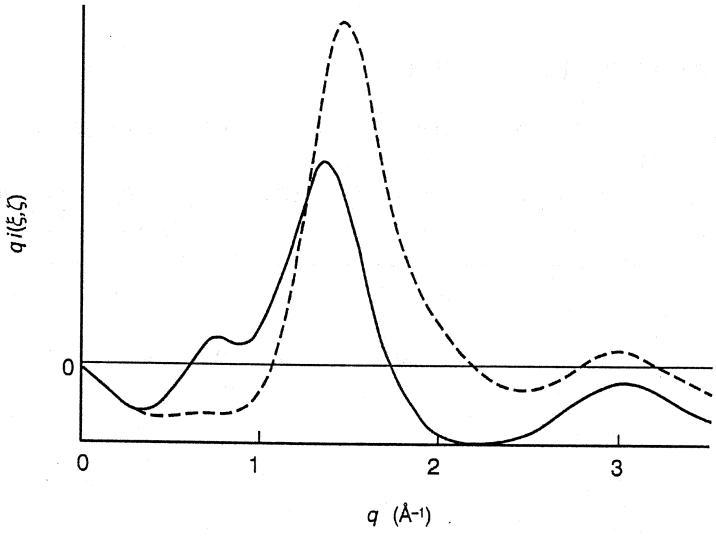

Figure 4.8 Plot of meridional (broken curve) and equatorial (solid curve) sections of Figure 4.7. (From Mitchell and Windle.[10])

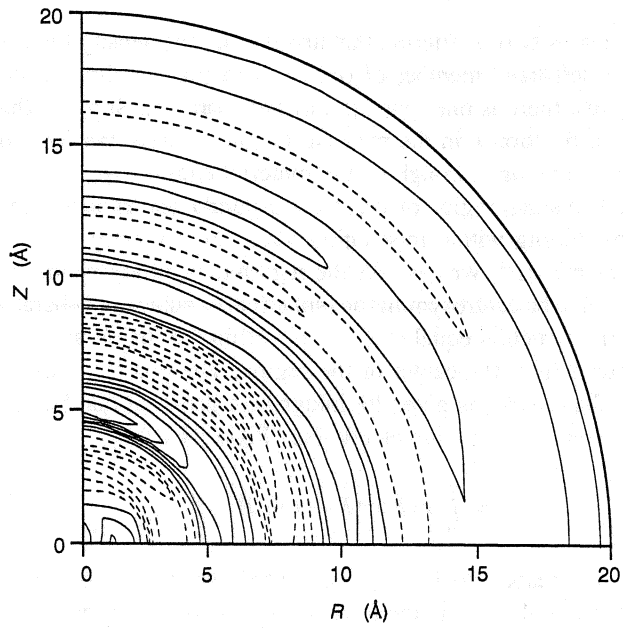

Figure 4.9 Cylindrical distribution function $\hat{g}(R, Z) - 1$ derived from the intensity data in Figure 4.7 by means of Equation (4.31). Dashed contour lines represent negative values. (From Mitchell and Windle.[10])

in another region of the same volume, a difference may be found no matter what the size v is. Such density fluctuations produce scattering intensities that are finite at all q values.

We are particularly interested at this point in the density fluctuations present on a macroscopic scale. As stated in any textbook on statistical mechanics, the fluctuation in the number N of atoms, contained in an open system under constant volume and temperature, can be calculated by means of the grand canonical ensemble formalism. The result shows that the mean square fluctuation $\langle(\Delta N)^2\rangle$ in N is on the order of N itself and is related, in a system of macroscopic size, to the isothermal compressibility β_T by

$$\frac{\langle(\Delta N)^2\rangle}{\langle N\rangle} = \langle n\rangle\, kT\beta_T \tag{4.32}$$

where $\langle n\rangle$ is the average number density, equal to N/V. Equation (4.32) states that the extent of the density fluctuation is proportional to the driving force, the thermal energy kT, and also the compressibility β_T, which may be thought of as the compliance toward the creation of a deviation in the density from its mean.

Now we derive the intensity of scattering that arises from the density fluctuation, defpprdomgined by the left-hand member of (4.32). In doing this, for the sake of simplicity, we assume that there is only one kind of atom present. Suppose that the density of atoms around position $\boldsymbol{r}$ in the material (found at an instant of time) is specified by $n(\boldsymbol{r})$, with its average throughout the material equal to $\langle n \rangle$. Let us now consider (after Ruland[15]) a small region of volume v around $\boldsymbol{r}$ and examine how the number $N_v(\boldsymbol{r})$ of atoms falling within this region varies as it is moved around to different locations in the material. We can take the region to be of any shape, but for convenience we assume it to be centrosymmetric (spherical or cubic) and characterize it by a shape factor $\sigma(\boldsymbol{r})$, which is equal to 1 if $\boldsymbol{r}$ is within the region and 0 if it is outside, $\boldsymbol{r}$ being measured from the center of the region. The Fourier transform of $\sigma(\boldsymbol{r})$ is designated by $\Sigma(\boldsymbol{q})$. $N_v(\boldsymbol{r})$ is given by integrating the local number density $n(\boldsymbol{r})$ over the region of volume v, or equivalently (see Figure 4.10) by

$$N_v(\boldsymbol{r}) = \int_V n(\boldsymbol{R})\sigma(\boldsymbol{R} - \boldsymbol{r})\, d\boldsymbol{R} \tag{4.33}$$

where the integration with respect to $\boldsymbol{R}$ is over the whole scattering volume V. We recognize that the integral in (4.33) is in the form of the convolution product defined in Section B.3 and write (4.33) as

$$N_v(\boldsymbol{r}) = n(\boldsymbol{r}) * \sigma(-\boldsymbol{r}) \tag{4.34}$$

The deviation of $N_v(\boldsymbol{r})$ from its mean is then

$$\begin{aligned} \Delta N_v(\boldsymbol{r}) &= N_v(\boldsymbol{r}) - \langle N_v \rangle \\ &= \Delta n(\boldsymbol{r}) * \sigma(-\boldsymbol{r}) \end{aligned} \tag{4.35}$$

where

$$\Delta n(\boldsymbol{r}) = n(\boldsymbol{r}) - \langle n \rangle \tag{4.36}$$

What we need to calculate is the variance in $N_v(\boldsymbol{r})$ as the region of volume v is placed at different locations throughout the material, that is

$$\begin{aligned} \langle (\Delta N_v)^2 \rangle &= \frac{1}{V} \int_V [\Delta N_v(\boldsymbol{r})]^2 \, d\boldsymbol{r} \\ &= \frac{1}{V} \int_V [\Delta n(\boldsymbol{r}) * \sigma(-\boldsymbol{r})]^2 \, d\boldsymbol{r} \end{aligned} \tag{4.37}$$

We now invoke in succession *Parseval's* (or *Raleigh's*) *theorem* (see Bracewell[16]) stating that

$$\int_{-\infty}^{\infty} |f(\boldsymbol{r})|^2 \, d\boldsymbol{r} = \frac{1}{(2\pi)^3} \int_{-\infty}^{\infty} |\mathcal{F}\{f(\boldsymbol{r})\}|^2 \, d\boldsymbol{q} \tag{4.38}$$

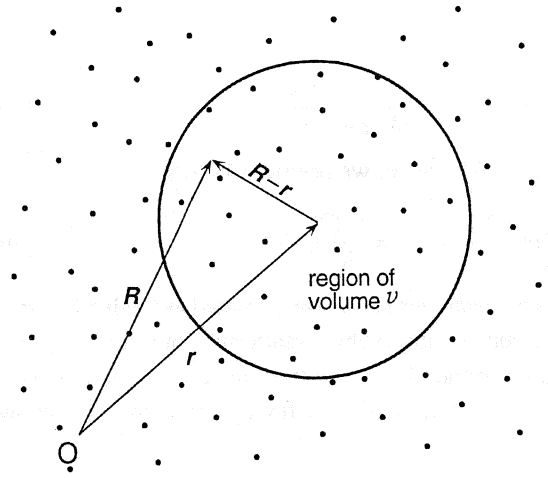

Figure 4.10 Diagram illustrating Equation (4.33). O is the arbitrarily chosen origin of the coordinate system. The center of the region of volume v is specified by vector $\boldsymbol{r}$.

and the convolution theorem (see Section B.3) stating that

$$\mathcal{F}\{f(\boldsymbol{r}) * g(\boldsymbol{r})\} = \mathcal{F}\{f(\boldsymbol{r})\} \cdot \mathcal{F}\{g(\boldsymbol{r})\} \tag{4.39}$$

and obtain

$$\langle (\Delta N_v)^2 \rangle = \frac{1}{V} \frac{1}{(2\pi)^3} \int_V |\mathcal{F}\{\Delta n(\boldsymbol{r})\}|^2 \, |\mathcal{F}\{\sigma(-\boldsymbol{r})\}|^2 \, d\boldsymbol{q} \tag{4.40}$$

The Fourier transform of $\sigma(-\boldsymbol{r})$ is equal to $\Sigma(\boldsymbol{q})$, when $\sigma(\boldsymbol{r})$ is centrosymmetric as we have assumed. The Fourier transform of $b\Delta n(\boldsymbol{r})$ gives the amplitude $A(\boldsymbol{q})$ of scattering, the absolute square of which is equal to the intensity $I(\boldsymbol{q})$. Therefore Equation (4.40) can be written as

$$\langle (\Delta N_v)^2 \rangle = \frac{1}{V} \frac{1}{(2\pi)^3} \int_V \frac{I(\boldsymbol{q})}{b^2} [\Sigma(\boldsymbol{q})]^2 \, d\boldsymbol{q} \tag{4.41}$$

This establishes the relationship between the density fluctuation expressed as $\langle (\Delta N_v)^2 \rangle$, on the one hand, and the scattering intensity $I(\boldsymbol{q})$ and the shape $\sigma(\boldsymbol{r})$ of the region of volume v being assumed, on the other hand. As the volume v is increased, its Fourier transform $\Sigma(\boldsymbol{q})$ becomes more sharply peaked around $\boldsymbol{q} = 0$, and therefore we see that only the part of the intensity curve $I(\boldsymbol{q})$ observable at very small $\boldsymbol{q}$ has a bearing on the density fluctuation for large v. We are mainly interested in the density fluctuation on a macroscopic scale, that is, in the limit of $v \to \infty$, in which case $\Sigma(\boldsymbol{q})$ approaches the delta function. Noting, by use of Parseval's theorem, that

$$\frac{1}{(2\pi)^3} \int |\Sigma(\boldsymbol{q})|^2 \, d\boldsymbol{q} = \int_V |\sigma(\boldsymbol{r})|^2 \, d\boldsymbol{r} = v \tag{4.42}$$

we find from (4.41) that

$$\lim_{v\to\infty} \langle(\Delta N_v)^2\rangle = \frac{v}{V} \lim_{q\to 0} \frac{I(q)}{b^2} \tag{4.43}$$

Recognizing that $N = \langle n\rangle V$ and $\langle N_v\rangle = \langle n\rangle v$, we rewrite (4.43) as

$$\lim_{v\to\infty} \frac{\langle(\Delta N_v)^2\rangle}{\langle N_v\rangle} = \frac{I(0)}{Nb^2} \tag{4.44}$$

where $I(0)/N$ is the intensity of scattering per atom, extrapolated to the limit of $q \to 0$. Note that $I(0)$ is not the true, but unobservable, scattering intensity at $q = 0$ that includes the null scattering, but rather the one extrapolated from the intensities observed at finite qs. Comparing (4.44) with (4.32), we finally obtain the well-known relationship

$$\frac{I(0)}{Nb^2} = \langle n\rangle kT\beta_T \tag{4.45}$$

The physical fact embodied in Equations (4.44) and (4.45) has been known from the time of Smoluchowski[17] and Einstein[18] in connection with the scattering of light.

The variation with q in the intensity $I(q)$ scattered from pure liquids or single-component amorphous polymers is very moderate in the small-angle region, and the extrapolation is easily accomplished. Figure 4.11[19] shows the x-ray scattering

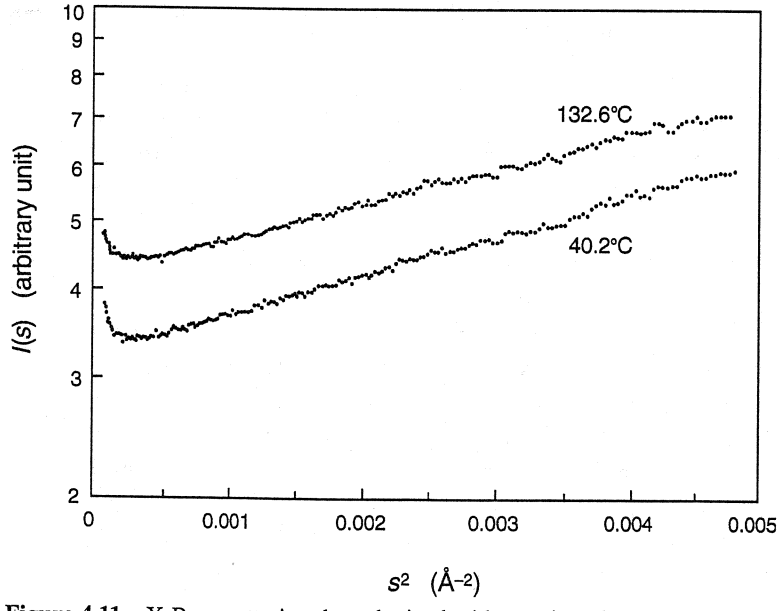

Figure 4.11 X-Ray scattering data obtained with atactic polystyrene at temperatures above and below the glass transition temperature, showing how the intensity $I(q)$, arising mostly from density fluctuations, depends on q as q approaches zero. (From Roe and Curro.[19])

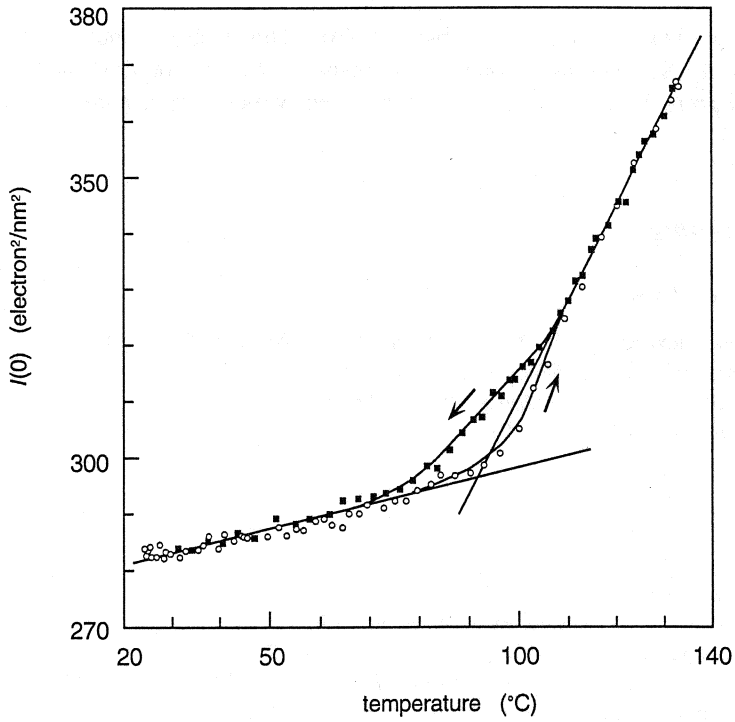

Figure 4.12 Points are the extrapolated x-ray scattering intensity $I(0)$, obtained with atactic polystyrene on heating and cooling through the glass transition temperature. (From Roe and Curro.[19])

intensities obtained with polystyrene at two temperatures, one above and the other below its glass transition temperature 100°C. In both cases the intensity increases moderately with increasing q, with the logarithm of $I(q)$ being approximately linear with q^2. This rise continues and eventually joins the more rapid rise toward the peaks found at q around 1.5 $Å^{-1}$ and beyond. The sharp upturn in intensity observed as q decreases toward zero is considered to arise from some unknown impurities in the polymer and is therefore ignored in carrying out the extrapolation to $q = 0$. The extrapolated intensity $I(0)$ determined with polystyrene is plotted in Figure 4.12[19] as a function of temperature. There is a change in the slope of the plot at around the glass transition temperature, in a manner resembling the one observed in the plot of volume against temperature. Some hysteresis is also exhibited between the heating and cooling cycles. The absolute value and the temperature coefficient of $I(0)$ agree well with those predicted from Equation (4.45) on the basis of the known isothermal compressibility of polystyrene and its temperature dependence. Similar agreements were seen with other polymers above their glass transition temperatures (Wendorff and Fischer[20] and Wiegand and Ruland[21]). The compressibility is known to decrease substantially when the temperature is brought below the glass transition temperature, but no indication of a corresponding drop,

either abrupt or gradual, is seen in the observed $I(0)$. This probably means that some of the density fluctuations produced as a result of thermal motions in the polymer above T_g remain frozen in the glassy polymer, which is in a nonequilibrium state.

FURTHER READING

Pair Distribution Function

1. Klug, H. P., and Alexander, L. E., *X-ray Diffraction Procedures for Polycrystalline and Amorphous Materials,* 2nd ed., Wiley-Interscience, New York, 1974, Chapter 12.
2. Furukawa, K., *Rept. Progr. Phys. (Japan)* **25**, 935 (1962).
3. Kruh, R. F., *Chem. Rev.* **62**, 319 (1962).

REFERENCES

4. Waser, J., and Schomaker, V., *Rev. Mod. Phys.* **25**, 671 (1953).
5. Pings, C. J., and Waser, J., *J. Chem. Phys.* **48,** 3016 (1968).
6. Wecker, S. M., Davidson, T., and Cohen, J. B., *J. Mater. Sci.* **7**, 1249 (1972).
7. Schubach, H. R., Nagy, E., and Heise, B., *Colloid Polymer Sci.* **259**, 789 (1981).
8. Wignall, G. D., and Longman, G. W., *J. Mater. Sci.* **8**, 1439 (1973).
9. Londono, J. D., Havenschuss, A., Curro, J. G., and Rajasekaran, J. J., *J. Polymer Sci. Part B: Polymer Phys.* **34**, 3055 (1996).
10. Mitchell, G. R., and Windle, A. H., *Polymer* **25**, 906 (1984).
11. Krogh-Moe, J., *Acta Crystallogr.* **9**, 951 (1956).
12. Norman, N., *Acta Crystallogr.* **10**, 370 (1957).
13. Mondello, M., Yang, H. J., Furuya, H., and Roe, R. J., *Macromolecules* **27**, 3566 (1994).
14. Cormack, A. M., *Acta Crystallogr.* **10**, 354 (1957).
15. Ruland, W., *Progr. Colloid Polymer Sci.* **57**, 192 (1975).
16. Bracewell, R. N., *The Fourier Transform and Its Applications*, 2nd ed., McGraw-Hill, New York, 1978, p. 112.
17. Smoluchowski, M. V., *Ann. Phys.* **25**, 205 (1908).
18. Einstein, A., *Ann. Phys.* **33**, 1275 (1910).
19. Roe, R. J., and Curro, J. J., *Macromolecules* **16**, 426 (1983).
20. Wendorff, J. H., and Fischer, E. W., *Kolloid-Z. Z. Polymere* **251**, 876, 884 (1973).
21. Wiegand, W., and Ruland, W., *Progr. Colloid Polymer Sci.* **66**, 355 (1979).

Small-Angle Scattering

5

5.1 MODEL STRUCTURES STUDIED BY SMALL-ANGLE SCATTERING

The technique of small-angle scattering is used to study structures of size on the order of 10 Å or larger. Information on such relatively large-scale structures is contained in the intensity of the scattered x-rays or neutrons at small angles, typically at 2θ less than 2°. The reciprocity between $\boldsymbol{r}$ and $\boldsymbol{q}$ means that information on relatively large $\boldsymbol{r}$ is contained in $I(\boldsymbol{q})$ at relatively small $\boldsymbol{q}$. To make the discussion more concrete, let us examine it in terms of the Bragg law:

$$\sin\theta = \frac{\lambda}{2d} \tag{5.1}$$

Thus, when distance d, representing the period of repetition in the structure or the spacing between crystallographic planes, is on the order of a few Ångstroms and when λ is equal to 1 Å, the scattering angle 2θ is typically about 20°. On the other hand, to take an example, a block copolymer sample having an ordered arrangement of spherical microdomains, with distance d between microdomains about 100 Å, will exhibit a scattering peak at 2θ around 0.6°. Whenever the sample contains a scattering length density inhomogeneity of dimension larger than $\sim$ 10 Å, scattering becomes observable in the small-angle region, and its study requires the techniques of small-angle scattering, with respect to both the experimental method of measuring intensity at such small scattering angles and the method of analysis of the observed data.

A basic concern in experimental measurements at small angles is the spatial proximity of the scattered rays to the incident beam transmitted unmodified through the sample. The flux of the transmitted primary beam is usually at least several orders of magnitude higher than the scattered beam flux, and consequently even a minor intrusion of the tail of the primary beam can seriously degrade the observed data. To eliminate such contamination the incident beam must be very carefully collimated. A very fine collimation, irrespective of how it is achieved, is always accompanied by a proportionate reduction in the incident beam flux. To alleviate this difficulty, a slit collimation has often been employed. Some problems associated with the use of slit collimation, both in the measurement itself and in the analysis of the data, are discussed in Section 5.6. This collimation-vs.-flux dichotomy has become less

of a problem in recent years as high brilliance x-ray sources, such as rotating anode generators and synchrotron radiation sources, have become more widely available.

The theoretical tools we employ to analyze the small-angle scattering data are all based on the same basic principles discussed in Chapter 1. All the methods developed for the analysis of wide-angle data are therefore applicable to the analysis of small-angle data as well. In addition, however, there are theoretical results that have been developed specifically for the analysis of small-angle data. These incorporate some additional assumptions about the nature of the sample or some additional approximations applicable only to small-angle scattering. For example, in small-angle scattering, $\sin\theta$ can always be approximated by θ. Similarly, in discussing the structure of a sample, any details of size scale less than about 10 Å are usually assumed not to exist. Such a practice corresponds to ignoring any scattering intensity observable at 2θ larger than a few degrees and performing the analysis on data observed in the small-angle region only.

As already stated in Section 1.5.3, although the intensity $I(\boldsymbol{q})$ of scattering can always be calculated from knowledge of the structure or the scattering length density distribution $\rho(\boldsymbol{r})$ in the sample, the reverse is not true. In other words, the inverse Fourier transform operation applied to the observed intensity $I(\boldsymbol{q})$ merely leads to the autocorrelation function $\Gamma_\rho(\boldsymbol{r})$, from which there is no unique way to recover $\rho(\boldsymbol{r})$. As an alternative we usually seek direct interpretation of either $I(\boldsymbol{q})$ or $\Gamma_\rho(\boldsymbol{r})$ in terms of a plausible model, chosen on the basis of some additional information, as may be available from other physical measurements or from independent knowledge about the sample. Most of the models that are adopted in practice for analysis of small-angle data belong to one of the following four: a dilute particulate system, a nonparticulate two-phase system, a periodic system, and a soluble blend system. Methods for evaluating parameters characterizing such systems have been developed by many workers over the years and are discussed in detail in the following sections. Here we give a brief description of the distinguishing features of each of the models.

1. In the *dilute particulate system*, particles (polymer molecules, colloidal particles, etc.) of one material are dispersed in a uniform matrix of a second material. When the concentration of the particles is sufficiently dilute, the positions of individual particles, far apart from each other, are uncorrelated. Under this circumstance the waves scattered from different particles are incoherent among them, and the observed intensity simply becomes a sum of the individual scattering. If the shape of the particles is known or assumed on the basis of independent information, the intensity of scattering from individual particles can be calculated and compared with the observation. If the particles are of irregular or unknown shape, the data may be analyzed according to the Guinier law to determine the radius of gyration characterizing the size of the particles. When the concentration is not sufficiently dilute, so that the effect of interference among rays scattered by different particles may no longer be ignored, then accounting for such interference effects becomes an important concern of the analysis.

2. In the *nonparticulate two-phase system*, two different materials are irregularly intermixed, and neither of them is considered the host matrix or the dispersed phase.

Such a material system may be realized, for example, when two immiscible polymers are blended or when a miscible polymer blend has phase separated. The two "phases" could be the different phases of a single material in a true thermodynamic sense, such as the crystalline and amorphous phases in a semicrystalline polymer. Neither of the two phases is required to be dilute, and as such a particulate system, in which the particle concentration is no longer dilute, can be regarded as belonging to this system. The analysis of the scattering data from such a system leads to determination of parameters characterizing the state of dispersion of the materials in the sample, and these include the correlation length characterizing the mean domain size, the specific interphase boundary area, and possibly the thickness of the phase boundaries.

3. The *soluble blend system* is a single phase material in which two components (such as two polymeric species or a polymer and a solvent) are dissolved molecularly as a homogeneous solution in the thermodynamic sense. A miscible polymer blend, a block copolymer in a disordered state, and a polymer solution are examples. Whether a homogeneous solution of this kind is regarded as a soluble blend system or as a dilute particulate system discussed above is often simply a matter of viewpoint. When there is a dilute solution of polymer molecules in a solvent and the focus of interest is the size and shape of the polymer molecules, the theoretical tools developed for the dilute particulate systems are more useful. If, on the other hand, the investigator is interested in the thermodynamic properties of the solution, the equations developed for the blend system are more appropriate.

4. To the *periodic system* belong, for example, semicrystalline polymers consisting of stacks of lamellar crystals and block copolymers having ordered, segregated microdomains. Many biological materials also possess periodic structures, and some animal tail tendons and myelin membranes in the nerve are well known for their particularly well-developed lamellar structures. Some micellar aggregates of organic and inorganic substances also exhibit good periodicity. The methods developed for the analysis of wide-angle diffraction from crystalline solids are directly applicable to such periodic systems. However, the degree of periodic order present in these systems is much poorer than in small molecule crystals in almost all cases, and dealing with the effects of such "lattice distortion" becomes an important consideration in the analysis.

In this chapter the dilute particulate system, the nonparticulate two-phase system, and the periodic system are discussed in Sections 5.2, 5.3, and 5.5, respectively. Section 5.4 deals with scattering from a fractal object, which may be regarded as a special kind of nonparticulate two-phase system. The soluble blend system is dealt with in Chapter 6. The method discussed in Section 4.2 for determining, for a single component amorphous polymer, the thermal density fluctuation from the intensity $I(q)$ extrapolated to $q \to 0$ can also be regarded as a small-angle technique.

5.2 DILUTE PARTICULATE SYSTEM

In the dilute particulate system the matrix is assumed to be devoid of any internal structure and simply presents a uniform, homogeneous background. In a real material,

whether liquid or solid, there is always a granularity due to the presence of atoms as its basic building blocks, but as long as such inhomogeneity is of a size scale much smaller than $1/q$, the effect does not manifest itself in the small-angle q range of interest here. The important assumption of the dilute particulate model is that the positions of the particles in it are uncorrelated, so that the waves scattered by different particles lack a phase coherence. The overall intensity is then simply the sum of the intensities of rays independently scattered from individual particles. Another assumption usually invoked in the discussion of the particulate system, although it is not always necessary, is that the system is isotropic. In the discussions below, we follow this practice and assume that the particles are not only at random positions but also take all different orientations with equal probabilities.

5.2.1 Radius of Gyration

The size of a particle, irrespective of whether it is geometrically well defined or irregular in shape, can be conveniently characterized by its *radius of gyration* R_g. On the other hand, a complete specification of the shape of a particle, as far as its scattering behavior is concerned, requires the knowledge of the scattering length density distribution $\rho(\boldsymbol{r})$ in the particle. The radius of gyration R_g is then given by

$$R_g^2 = \frac{\int \boldsymbol{r}^2 \rho(\boldsymbol{r})\, d\boldsymbol{r}}{\int \rho(\boldsymbol{r})\, d\boldsymbol{r}} \tag{5.2}$$

where in defining $\rho(\boldsymbol{r})$ the origin of $\boldsymbol{r}$ is taken to be at the center of mass (of scattering length density) of the particle, so that the following should hold:

$$\int x\rho(\boldsymbol{r})\, d\boldsymbol{r} = 0, \quad \int y\rho(\boldsymbol{r})\, d\boldsymbol{r} = 0, \quad \int z\rho(\boldsymbol{r})\, d\boldsymbol{r} = 0 \tag{5.3}$$

If the particle is of a constant scattering length density in its entirety, Equation (5.2) is simplified to

$$R_g^2 = \frac{1}{v} \int \boldsymbol{r}^2 \sigma(\boldsymbol{r})\, d\boldsymbol{r} \tag{5.4}$$

where v is the volume of the particle and $\sigma(\boldsymbol{r})$ is its shape function, equal to 1 within it and 0 otherwise. The definitions (5.2) and (5.4) show that the radius of gyration is the root-mean-square distance of all points in the particle from its center of mass (with each point weighted according to its scattering length density). If the particle is regarded as consisting of discrete scattering centers (e.g., atoms or segments), the radius of gyration can also be written as

$$R_g^2 = \frac{\sum_j b_j^2 \boldsymbol{r}_j^2}{\sum_j b_j^2} \tag{5.5}$$

where b_j is the scattering length of the jth scattering center located at position $\boldsymbol{r}_j$. If all the scattering centers are of the same kind, (5.5) is further simplified to

$$R_g^2 = \frac{1}{N}\sum_{j=1}^{N} r_j^2 \tag{5.6}$$

where N is the total number of such scattering centers.

As examples of the radius of gyration of particles of well-defined geometric shape, we obtain for a solid sphere of radius R

$$R_g = \sqrt{\frac{3}{5}}R \tag{5.7}$$

while for a solid ellipsoid of half axes a, b, and c

$$R_g = \frac{1}{\sqrt{5}}\left(a^2 + b^2 + c^2\right)^{1/2} \tag{5.8}$$

For a solid rod having length L and circular cross section of radius R it becomes

$$R_g^2 = \frac{L^2}{12} + \frac{R^2}{2} \tag{5.9}$$

which reduces to

$$R_g = \frac{1}{\sqrt{12}}L \tag{5.10}$$

for a thin rod of length L and

$$R_g = \frac{1}{\sqrt{2}}R \tag{5.11}$$

for a thin disk of radius R.

An idealized polymer chain can be modeled by a random flight chain, consisting of $(N + 1)$ "beads" (or "segments") connected by N bonds of fixed length l, each of which takes an orientation that is entirely uncorrelated with the orientation of its neighbors. When one end of the chain is at the origin, the probability $w(N,r)\,d\boldsymbol{r}$ that the other end is found at a volume element $d\boldsymbol{r}$ at distance r from the origin is given, when N is sufficiently large, by the Gaussian approximation

$$w(N, r)\,d\boldsymbol{r} = \left(\frac{3}{2\pi N l^2}\right)^{3/2} \exp\left(-\frac{3r^2}{2Nl^2}\right) d\boldsymbol{r} \tag{5.12}$$

The radius of gyration of such a *Gaussian chain*, calculated according to (5.6) (see Flory[9]), is

$$\left\langle R_g^2 \right\rangle = \frac{Nl^2}{6} \tag{5.13}$$

Note that the instantaneous value of the radius of gyration can change as the polymer conformation undergoes continual change with time and the above expression (5.13) holds only for the radius of gyration $\left\langle R_g^2 \right\rangle$ averaged over time (or, equivalently, over an ensemble of identical chains).

5.2.2 Independent Scattering from Particles of Simple Geometric Shape

For many of the particles having well-defined, simple geometric shape it is possible to calculate the intensity curve for the whole range of q without making any approximations. The amplitude $A(\boldsymbol{q})$ of scattering from a single particle is calculated according to

$$A(\boldsymbol{q}) = \int_v \rho(\boldsymbol{r}) e^{-i\boldsymbol{q}\boldsymbol{r}}\, d\boldsymbol{r} \tag{1.73}$$

where the integration is now performed over only the particle volume v. When the particle is suspended in a continuous matrix, $\rho(\boldsymbol{r})$ here should be replaced by the excess $\eta(\boldsymbol{r})$ of the scattering length density in the particle over the average $\langle\rho\rangle$ throughout the system, as discussed in Section 1.6. For a dilute particulate system the average scattering length density $\langle\rho\rangle$ is essentially the same as the scattering length density of the uniform background offered by the continuous matrix. If the latter is a "vacuum," $\eta(\boldsymbol{r})$ is then practically identical to $\rho(\boldsymbol{r})$. With this understanding, the symbol $\rho(\boldsymbol{r})$ will continue to be used to stand for the "excess" scattering length density in the calculation of $A(\boldsymbol{q})$. The intensity $I(q)$ of scattering per particle, in an isotropic sample, is then obtained by evaluating the absolute square of $A(\boldsymbol{q})$, followed by averaging over all possible orientations of the particle, in recognition of the fact that the system contains a large number of particles oriented in random directions.

5.2.2.1 Sphere

Deriving the scattering function for a sphere is particularly simple, because a sphere has spherical symmetry by itself and does not require orientational averaging. A solid sphere of radius R with a uniform density ρ_0 is defined by

$$\rho(r) = \begin{cases} \rho_0 & \text{for } r \le R \\ 0 & \text{for } r > R \end{cases} \tag{5.14}$$

Substituting (5.14) into (1.73) and evaluating the Fourier transform according to Equation (B.50) that applies to isotropic samples, we obtain

$$\begin{aligned} A(q) &= \int_0^\infty \rho(r) 4\pi r^2 \frac{\sin qr}{qr}\, dr \\ &= \frac{\rho_0}{q} \int_0^R 4\pi r \sin(qr)\, dr \end{aligned} \tag{5.15}$$

which, on integration by parts, yields

$$A(q) = \rho_0 v \frac{3(\sin qR - qR\cos qR)}{(qR)^3} \tag{5.16}$$

where v is the volume of the sphere, $(4/3)\pi R^3$. The intensity of scattering from a sphere is therefore

$$I(q) = \rho_0^2 v^2 \frac{9(\sin qR - qR\cos qR)^2}{(qR)^6} \tag{5.17}$$

The behavior of Equation (5.17) is shown in Figure 5.1, where the ordinate is given in a logarithmic scale to bring out clearly the nearly periodic variation of $I(q)$. The zeros occur for values of q satisfying

$$qR = \tan qR \tag{5.18}$$

or at $qR = 4.493, 7.725, 10.90, 14.07, \ldots, \cong (2k+1)\pi/2$, and the maxima occur at $qR = 5.763, 9.095, 12.32, 15.51, \ldots, \cong k\pi (k$: integers). Note that $\rho_0 v$ is the total scattering length of the particle (the sum of the scattering lengths of all the atoms in the particle), and that the intensity $I(q)$ is proportional to $(\rho_0 v)^2$.

5.2.2.2 Thin Rod

Take a thin rod of length L and cross-sectional area a of a material with uniform scattering length density ρ_0. When a is very small compared to L, the rod can be regarded as a virtual thin line with a scattering length density $\rho_0 a$ per unit length concentrated on the axis. Let us now take the origin of the coordinate system at the center of the rod. If the angle between its axis and vector $\boldsymbol{q}$ is Θ, then $\boldsymbol{qr} = qr\cos\Theta$, and Equation (1.73) becomes

$$\begin{aligned} A(\boldsymbol{q}) &= \rho_0 a \int_{-L/2}^{L/2} e^{-iqr\cos\Theta}\, dr \\ &= \rho_o a \frac{2}{q\cos\Theta} \sin\left(\frac{qL}{2}\cos\Theta\right) \end{aligned} \tag{5.19}$$

Its square is the intensity:

$$I(\boldsymbol{q}) = \rho_0^2 v^2 \left(\frac{2}{qL\cos\Theta}\right)^2 \sin^2\left(\frac{qL}{2}\cos\Theta\right) \tag{5.20}$$

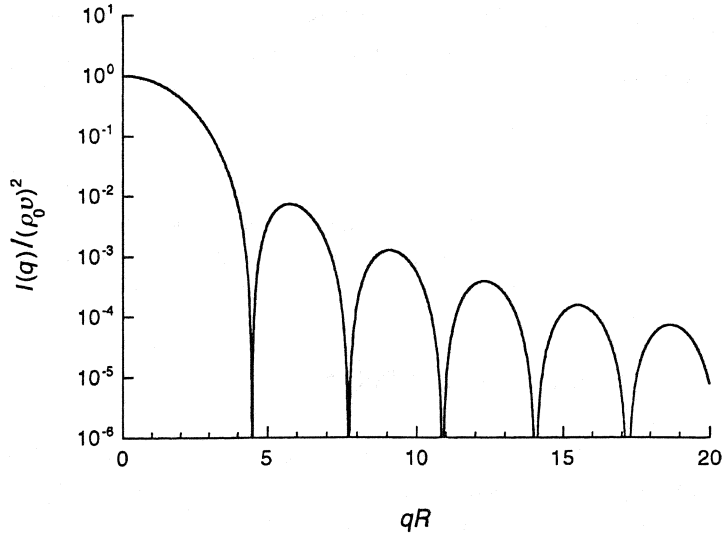

Figure 5.1 Single particle scattering intensity $I(q)$ for a solid sphere of radius R.

where $v = aL$. The average of (5.20) for all orientations can be evaluated (see Neugebauer[10]) by

$$I(q) = \rho_0^2 v^2 \frac{1}{2} \int_0^{\pi} \left(\frac{2}{qL \cos \Theta} \right)^2 \sin^2 \left(\frac{qL}{2} \cos \Theta \right) \sin \Theta d\Theta$$

$$= \rho_0^2 v^2 \frac{2}{qL} \left[\mathrm{Si}(qL) - \frac{1 - \cos qL}{qL} \right] \tag{5.21}$$

where $\mathrm{Si}(x)$ is the sine integral function defined as

$$\mathrm{Si}(x) = \int_0^x \frac{\sin u}{u} du \tag{5.22}$$

5.2.2.3 Thin Circular Disk

In a dilute suspension of thin circular disks of radius R, the contributions by individual particles scattering independently can be derived in a manner similar to that for thin rods, but here we will simply present the result (see Kratky and Porod[11] for the derivation):

$$I(q) = \rho_0^2 v^2 \frac{2}{q^2 R^2} \left[1 - \frac{J_1(2qR)}{qR} \right] \tag{5.23}$$

where $J_1(x)$ is the first-order Bessel function.

5.2.2.4 Comparison of the Three Intensity Curves

In Figure 5.2 the three intensity curves given by Equations (5.17), (5.21), and (5.23) are plotted together. Note that here the abscissa is qR_g, where the radius of gyration R_g is $\sqrt{3/5}R$ for a sphere, $L/\sqrt{12}$ for a thin rod, and $R/\sqrt{2}$ for a thin circular disk. It is seen that for very small q the three curves merge together, despite the large difference in the shape of the particles. This commonality of the curve shape at small q provides the basis for the Guinier law to be discussed in Section 5.2.4. As q is increased, the curve falls off rapidly for spheres and less so for disks and rods. Since in Equations (5.17), (5.21), and (5.23) the sine, cosine, sine integral, and Bessel functions all remain finite as $q \to \infty$, the asymptotic form of the intensity curves at large q can be represented by

$$I(q) \sim q^{-\alpha} \tag{5.24}$$

The exponent α is equal to 4 for spheres (three dimensional), 2 for thin disks (two dimensional), and 1 for thin rods (one dimensional), and is thus seen to reflect the dimensionality of the object.

5.2.3 Independent Scattering from a Polymer Chain

5.2.3.1 Gaussian Chain

We now consider the intensity of independent scattering from a random coil polymer molecule, consisting of $(N + 1)$ "beads" connected by N bonds and obeying the Gaussian approximation (5.12). We assume that the volume of a "bead" is v_u and the volume of the chain is $v = (N + 1)v_u$. Each bead thus contributes $\rho_0 v_u$ to the

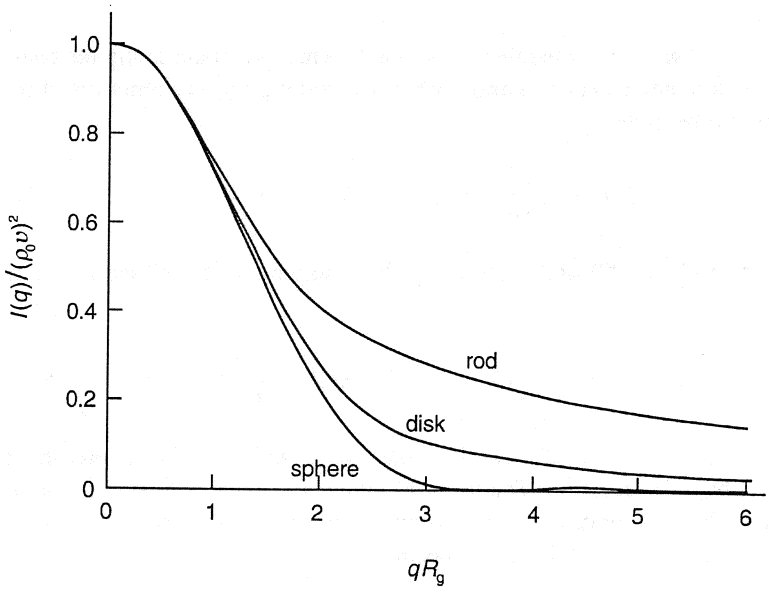

Figure 5.2 Plot of independent scattering intensities from spheres, thin disks, and thin rods.

scattering length, which we assume is concentrated at the center of the bead. The amplitude of scattering is then

$$A(\boldsymbol{q}) = \rho_0 v_u \sum_{j=0}^{N+1} e^{-i\boldsymbol{q}\boldsymbol{r}_j} \tag{5.25}$$

and the intensity is

$$I(\boldsymbol{q}) = \rho_0^2 v_u^2 \sum_{j=0}^{N+1} \sum_{k=0}^{N+1} e^{-i\boldsymbol{q}\boldsymbol{r}_{jk}} \tag{5.26}$$

where $\boldsymbol{r}_{jk} = \boldsymbol{r}_j - \boldsymbol{r}_k$. We replace the summation in (5.26) by an integration and obtain

$$I(\boldsymbol{q}) = \rho_0^2 v_u^2 \int P(\boldsymbol{r}) e^{-i\boldsymbol{q}\boldsymbol{r}}\, d\boldsymbol{r} \tag{5.27}$$

where $P(\boldsymbol{r})$ represents the number of those bead pairs that have their members separated from each other by $\boldsymbol{r}$ (with both the direction and distance taken into account) and the integration is over the whole scattering volume. We now take the average of (5.27) over an ensemble of chains (or over time). When such an average is taken, $P(r)$ becomes a function of the magnitude r only.

$P(r)$ must obviously be related to the end-to-end distance distribution $w(N,r)$ given by Equation (5.12). The exact relationship between the two is obtained as follows. For $P(r)$ we have to include not only the end bead pair separated by N bonds, but all other bead pairs separated by one bond, two bonds, three bonds, etc., and also those separated by zero bonds (i.e., the beads by themselves). In a chain of $(N + 1)$ beads

there are $(N + 1 - K)$ pairs separated by K bonds when we count along the chain going one direction, and an equal number when we count going the other direction. $P(r)$ can therefore be given by

$$P(r) = 2\sum_{K=0}^{N}(N + 1 - K)w(K, r) \tag{5.28}$$

Substituting (5.28) in (5.27) and performing the Fourier transform [see Equation (B.17)] give

$$I(q) = \rho_0^2 v_u^2 2 \sum_{K=0}^{N}(N + 1 - K) \exp\left(-\frac{q^2 l^2}{6} K\right) \tag{5.29}$$

Although the summation in (5.29) can be evaluated exactly, we will approximate the summation by an integration. This is valid when N is large, which is the same assumption already incorporated in the Gaussian approximation. On using the variable $u = K/N$ and letting $N + 1 \cong N$, (5.29) becomes

$$\begin{aligned} I(q) &= \rho_0^2 v_u^2 2N^2 \int_0^1 (1 - u) \exp\left(\frac{-q^2 N l^2}{6} u\right) du \\ &= \rho_0^2 v^2 D(x) \end{aligned} \tag{5.30}$$

where

$$D(x) = \frac{2(e^{-x} + x - 1)}{x^2}, \quad x = \frac{q^2 N l^2}{6} = q^2 \left\langle R_g^2 \right\rangle \tag{5.31}$$

Equation (5.31), first derived by Debye,[12] is known as the *Debye function*. Figure 5.3 shows the behavior of $D(x)$ in comparison to the independent scattering functions for a thin rod and a thin disk. The Debye function can be approximated, for $q \to 0$, by

$$D(x) = 1 - \frac{q^2 \left\langle R_g^2 \right\rangle}{3} + \cdots \tag{5.32}$$

in agreement with the Guinier law to be discussed in Section 5.2.4. Over the whole range of q it can also be approximated fairly well (within 15%) by

$$D(x) \cong \frac{1}{1 + x/2} \tag{5.33}$$

as seen in Figure 5.4. For $q \to \infty$ $D(x)$ thus varies as $q^{-\alpha}$ with the exponent α equal to 2. This is to be contrasted with the exponent 4 for solid spheres as shown in Section 5.2.2.4. The smaller exponent reflects the fact that although a Gaussian coil is a three-dimensional entity, it in effect behaves like a two-dimensional object because of its openness.

5.2.3.2 Worm-like Chain

The Gaussian chain is obviously an oversimplification of the real polymer chain. The description of the shape of a polymer chain can in fact vary greatly according to the size scale with which we examine it.

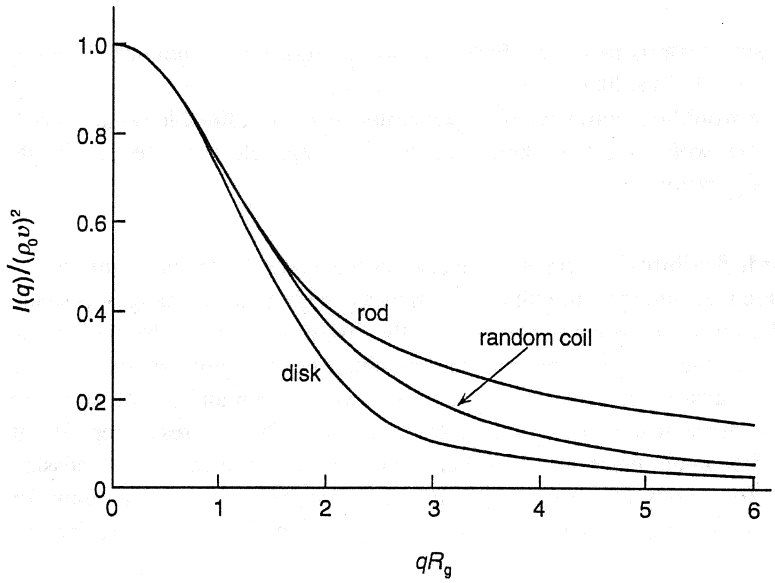

Figure 5.3 The Debye function, Equation (5.31), for a random coil chain is plotted and compared with the independent scattering intensity function for a thin rod and a thin circular disk.

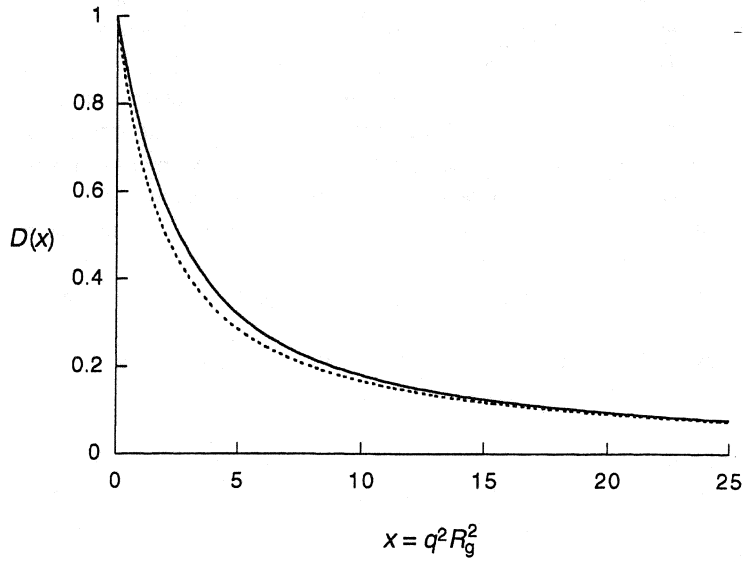

Figure 5.4 Plot (solid curve) of the Debye function $D(x)$, showing that it can be approximated fairly well over the whole range of x by Equation (5.33) (thin broken curve).

1. On the smallest scale, we would see only atoms.
2. On a slightly larger scale, we would recognize the presence of monomeric units.

3. As the size scale is increased further, a short sequence of monomers strung together would look like a more or less rigid rod.
4. Next, we would recognize the polymer molecule to be a flexible random coil.
5. Finally, we would see the whole molecule as a particle characterized by its radius of gyration.

(Here the words flexibility and rigidity are used as a measure of the curvature of the chain, unrelated to its dynamic flexibility, i.e., the ease with which it changes its shape with time.) The above sequence corresponds to the different types of information that we will derive as we analyze scattering curves obtained in regions of smaller and smaller q. The Gaussian chain represents a very flexible chain and is well suited to model the random coil feature recognized in step (4) above. The features in step (3) that arise from limited chain flexibility, however, cannot be represented by the Gaussian chain model. To remedy this, Kratky and Porod[13] proposed a *worm-like chain* (or *Kratky–Porod chain*) model. The main features of their model can be described as follows.

In the random flight model, from which the Gaussian approximation is derived, the directions of any two succeeding steps are completely uncorrelated. As a result, in a chain of N steps starting from the origin, the position of the chain ends, averaged over a large number of such chains, is independent of the direction of the first step, if N is sufficiently large. We, however, expect that if the chain retains a degree of rigidity, the influence of the direction of the first step will remain irrespective of how long the chain is. In the worm-like chain this expectation is incorporated in the construction of the model, such that the projection of the averaged end-to-end vector onto the first bond direction, in the limit of infinite N, does not vanish but rather approaches a finite limit, which is termed the *persistence length*. For details on how the model is in fact constructed, the reader is referred to the original papers by Kratky and Porod[11,13] and to the description of it by Flory.[14] Properties of the worm-like chain have been investigated by a number of workers, both analytically and by generation of chains by a Monte Carlo method (see Kirste and Oberthür[15]). Here we quote only the following results.

The main features of the intensity curve of the Kratky–Porod chain can be represented schematically by the diagrams in Figure 5.5. At very small q the intensity curve falls exponentially according to the Guinier law and is characterized by the radius of gyration R_g. As q is increased, the curve reflects the random coil nature of the molecule and follows the Debye function, decreasing as q^{-2}. The scattering at still larger q is governed by the behavior of still smaller sections of the molecule, which can be considered as more or less rigid, and the intensity curve now shows the q^{-1} behavior of thin rods. The difference in the shape of the scattering curve in different regions of q is even more clearly brought out when we plot $I(q)q^2$ against q. (Such a plot is called the *Kratky plot.*) The Debye behavior is now represented by a horizontal line, while the q^{-1} branch becomes a sloped straight line that extrapolates back to the origin. The value of q^* at which the transition between these two q regions occurs (see Figure 5.5b) is inversely related to the persistence length.

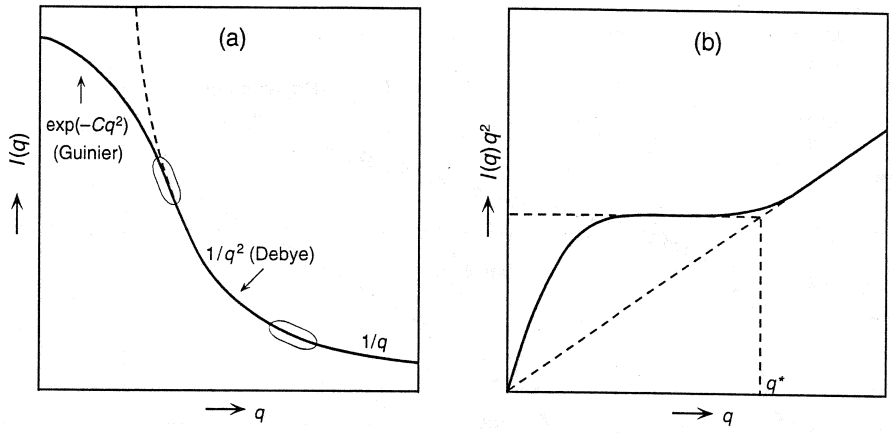

Figure 5.5 (a, b) Schematic presentation of the expected characteristics of the single chain scattering function in different q regions. (After Kratky and Porod.[11,13])

The scattering curve of a more realistic polymer molecule can be calculated from an atomistic model of the molecule obtained by Monte Carlo or molecular dynamic simulation techniques. In Figure 5.6 the points give the scattering function calculated for a polyethylene chain[16] of molecular weight 14,000 by combining the rotational isomeric states model with a Monte Carlo method. The solid curve gives the fit[15] obtained with a Kratky–Porod chain. Also shown are the expected behavior of a random coil and an asymptotic thin rod. It is seen that a polyethylene chain seems to behave approximately as expected of a Kratky–Porod chain.

5.2.4 Guinier Law

In Sections 5.2.2 and 5.2.3 scattering functions were derived for particles of known shape. It turns out, however, that even when the shape is unknown, or when the shape is irregular and not describable in simple terms, the scattering function still follows a certain universal form, in the limit of small q, that is given by

$$I(q) = \rho_0^2 v^2 \exp\left(-\frac{1}{3}q^2 R_g^2\right) \tag{5.34}$$

where $I(q)$ is the intensity of independent scattering by a particle. Equation (5.34), called the *Guinier law*, allows determination of the radius of gyration R_g of a particle of unknown shape and size from small-angle scattering measurement. The Guinier law is valid provided that (1) q is much smaller than $1/R_g$, (2) the system is dilute, so that the particles in the system scatter independently of each other, and (3) the system is isotropic as a result of the particles assuming random orientations. Actually there is an additional condition that must also be satisfied for (5.34) to be valid, and this is that the matrix (or the solvent) in which the particles are dispersed is of constant density and is devoid of any internal structure that can by itself give scattering in the interested range of q. Since thermal density fluctuations present in any amorphous

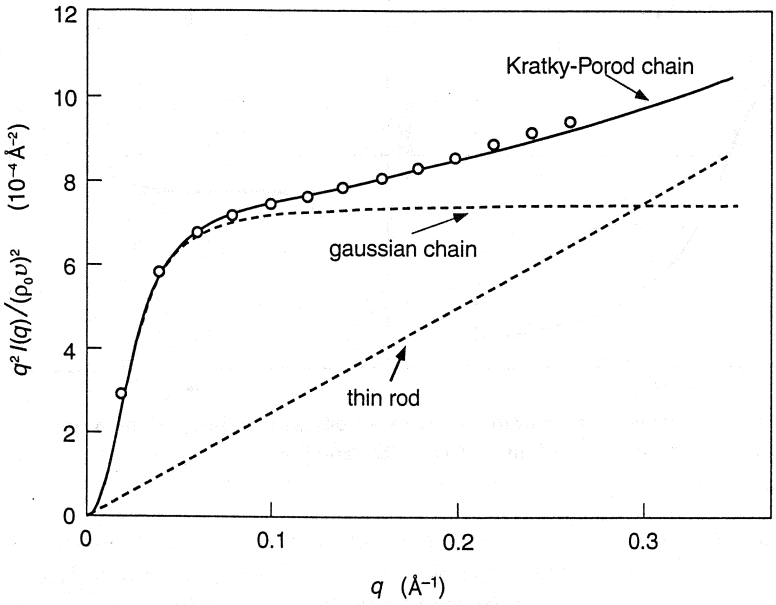

Figure 5.6 Kratky plot of the scattering function (circles) calculated[16] from an atomistic model of polyethylene. The curves shown are those calculated for a Kratky–Porod chain, a Gaussian chain, and an asymptotic thin rod. (After Kirste and Oberthür.[15])

material give rise to a scattering in the small q region, as discussed in Section 4.2; this condition can be met only if the intensity referred to here is understood to mean the one from which the solvent scattering has been subtracted.

5.2.4.1 Derivation of Guinier Law

We start from Equation (1.73) giving the amplitude $A(\boldsymbol{q})$ of scattering from a particle with its scattering length density distribution given by $\rho(\boldsymbol{r})$. Focusing our attention on the cases where $\boldsymbol{q}$ is very small, we expand the exponential as a power series:

$$A(\boldsymbol{q}) = \int \rho(\boldsymbol{r}) e^{-i\boldsymbol{q}\boldsymbol{r}}\, d\boldsymbol{r}$$

$$= \int \rho(\boldsymbol{r})\, d\boldsymbol{r} - i \int \boldsymbol{q}\boldsymbol{r}\rho(\boldsymbol{r})\, d\boldsymbol{r} - \frac{1}{2!}\int (\boldsymbol{q}\boldsymbol{r})^2 \rho(\boldsymbol{r})\, d\boldsymbol{r} + \cdots \qquad (5.35)$$

The first term is equal to $\rho_0 v$, where ρ_0 is the average scattering length density and v is the volume of the particle. Since the final expression for the intensity does not depend on the choice of the origin, we take the origin of $\boldsymbol{r}$ to be at the center of mass of the particle. Then, in view of (5.3), the second term in (5.35) is seen to vanish. In the third term we make the substitution

$$(\boldsymbol{q}\boldsymbol{r})^2 = (q_x x + q_y y + q_z z)^2 \qquad (5.36)$$

The integral can then be expressed in terms of the various second moments defined, for example, by

$$\overline{xy} = \frac{\int xy\,\rho(r)\,dr}{\int \rho(r)\,dr} = \frac{\int xy\,\rho(r)\,dr}{\rho_0 v} \tag{5.37}$$

leading to

$$\frac{1}{2!}\int (qr)^2 \rho(r)\,dr = \frac{\rho_0 v}{2}$$
$$\left(q_x^2\overline{x^2} + q_y^2\overline{y^2} + q_z^2\overline{z^2} + 2q_xq_y\overline{xy} + 2q_yq_z\overline{yz} + 2q_zq_x\overline{zx}\right) \tag{5.38}$$

The intensity is obtained by taking the absolute square of (5.35), and in doing so we remember the fact that for small q the quantity represented by (5.38) is much smaller than $\rho_0 v$. In the presence of a large number of identical particles oriented in random directions, the average intensity per particle becomes

$$I(q) = \rho_0^2 v^2$$
$$\left[1 - \left\langle q_x^2\overline{x^2} + q_y^2\overline{y^2} + q_z^2\overline{z^2} + 2q_xq_y\overline{xy} + 2q_yq_z\overline{yz} + 2q_zq_x\overline{zx}\right\rangle + \cdots\right] \tag{5.39}$$

For an isotropic system the following holds:

$$\left\langle\overline{x^2}\right\rangle = \left\langle\overline{y^2}\right\rangle = \left\langle\overline{z^2}\right\rangle = \frac{1}{3}R_g^2 \tag{5.40}$$

and also

$$\langle\overline{xy}\rangle = \langle\overline{yz}\rangle = \langle\overline{zx}\rangle = 0 \tag{5.41}$$

since variations in x, y, z are uncorrelated with each other, leading to $\langle xy\rangle = \langle x\rangle\,\langle y\rangle = 0$.

Equation (5.39) can therefore be written as

$$I(q) = \rho_0^2 v^2\left(1 - \frac{1}{3}q^2R_g^2 + \cdots\right)$$
$$= \rho_0^2 v^2 \exp\left(-\frac{1}{3}q^2R_g^2\right) \tag{5.42}$$

which is the Guinier law.

The Guinier law suggests that when the logarithm of $I(q)$ is plotted against q^2 the initial slope gives $R_g^2/3$. For the purpose of determining the radius of gyration it suffices to have the intensity determined in relative units. If, on the other hand, the intensity is measured in absolute units by means of an instrument suitably calibrated (see Section 2.7), it is possible to determine the value of $\rho_0^2 v^2$ as well. For this purpose it is also necessary to know the concentration of the particles in the scattering volume, since $I(q)$ in (5.42) is the average intensity *per particle*. Then, from the extrapolation of the observed intensity to $q \to 0$, $I(0) = \rho_0^2 v^2$ is determined. Since the value of ρ_0, the average scattering length density in the particle, is usually known from its chemical composition, this provides the means of evaluating the particle volume v. Knowledge of both the radius of gyration R_g and the particle volume v provides a

clue about the shape of the particle. Equation (5.42), in a slightly modified form, provides the basis for determining the molecular weight of polymer molecules in dilute solution by light scattering.

5.2.4.2 Samples Containing Nonidentical Particles

When the particles the sample contains are not all identical, the Guinier law is still applicable, with the radius of gyration R_g and the particle volume v interpreted to represent some types of averages. If, of the N total particles, $N_j (j = 1, 2, \ldots)$ have volume v_j and radius of gyration R_{gj}, then assuming that the particles are all of the same average density ρ_0 and that scattering from different particles is uncorrelated, we have

$$\begin{aligned} I(q) &= \frac{\rho_0^2}{N} \sum_j N_j v_j^2 \left[1 - \frac{1}{3} q^2 R_{gj}^2 + \cdots \right] \\ &= \frac{\rho_0^2}{N} \left(\sum_j N_j v_j^2 \right) \left[1 - \frac{q^2}{3} \frac{\sum_j N_j v_j^2 R_{gj}^2}{\sum_j N_j v_j^2} + \cdots \right] \\ &= \rho_0^2 \langle v^2 \rangle_n \exp \left[-\frac{q^2}{3} \left\langle R_g^2 \right\rangle_z \right] \end{aligned} \tag{5.43}$$

where $\langle v^2 \rangle_n$ is the number-average of v^2 given by

$$\langle v^2 \rangle_n = \frac{\sum N_j v_j^2}{N} \tag{5.44}$$

and $\left\langle R_g^2 \right\rangle_z$ is the z-average of R_g^2 defined as

$$\left\langle R_g^2 \right\rangle_z = \frac{\sum N_j v_j^2 R_{gj}^2}{\sum N_j v_j^2} = \frac{\sum N_j W_j^2 R_{gj}^2}{\sum N_j W_j^2} \tag{5.45}$$

W_j being the mass of the jth size particle (proportional to v_j).

5.2.5 Effect of Dense Packing

So far we have discussed only independent scattering from particles, that is, the particles are so far apart from each other that the effect of interference among the waves scattered by different particles can be ignored. We now consider what happens to the observed intensity as the concentration of particles in the system is increased and the interference effect becomes no longer negligible.

Let us first consider the simplest case in which the system contains N spherical particles of radius R and uniform scattering length density ρ_0. The amplitude of the scattered radiation is then given by

$$A(\boldsymbol{q}) = \sum_{j=1}^{N} A_1(q) e^{-i\boldsymbol{q}\boldsymbol{r}_j} \tag{5.46}$$

where $\boldsymbol{r}_j$ is the position of the center of the jth sphere relative to an arbitrary origin, and $A_1(q)$ is the amplitude of scattering from a single sphere with its center at the origin, as given by Equation (5.16). The intensity is obtained by taking the absolute square $A(\boldsymbol{q})A^*(\boldsymbol{q})$, which is then averaged over time (or over an ensemble of similar systems):

$$I(\boldsymbol{q}) = I_1(q)\left\langle \sum_{j=1}^{N}\sum_{k=1}^{N} e^{-i\boldsymbol{q}\boldsymbol{r}_{jk}} \right\rangle \tag{5.47}$$

where $\boldsymbol{r}_{jk} = \boldsymbol{r}_j - \boldsymbol{r}_k$, and $I_1(q)$, the absolute square of $A_1(q)$, is given by (5.17). Separating out the terms for which j equals k, Equation (5.47) is rewritten as

$$I(\boldsymbol{q}) = I_1(q)\left[N + \left\langle \sum_{j=1}^{N}\sum_{k\neq j} e^{-i\boldsymbol{q}\boldsymbol{r}_{jk}} \right\rangle \right] \tag{5.48}$$

Here the first term represents the independent scattering and the second term represents the contribution by the interference effect.

To be able to calculate the second term, we obviously need information on the statistics of interparticle distances. We introduce the pair distribution function $g(\boldsymbol{r})$ by saying that $\langle n\rangle g(\boldsymbol{r})\, d\boldsymbol{r}$ is the probability of finding another particle in the volume element $d\boldsymbol{r}$ a distance $\boldsymbol{r}$ from a given particle, and $\langle n\rangle$ is the average number density of the particles in the system (cf. Section 4.1.1). In terms of $g(\boldsymbol{r})$, Equation (5.48) can be rewritten as

$$I(\boldsymbol{q}) = NI_1(q)\left[1 + \langle n\rangle \int g(\boldsymbol{r}) e^{-i\boldsymbol{q}\boldsymbol{r}}\, d\boldsymbol{r} \right] \tag{5.49}$$

Eliminating the null scattering that shows up only at $q = 0$ (cf. Section 1.6), (5.49) is further rewritten as

$$I(\boldsymbol{q}) = NI_1(q)\left[1 + \langle n\rangle \int \{g(\boldsymbol{r}) - 1\} e^{-i\boldsymbol{q}\boldsymbol{r}}\, d\boldsymbol{r} \right] \tag{5.50}$$

If the system is isotropic, $g(r)$ depends only on the magnitude r, and the integration with respect to the orientation of $\boldsymbol{r}$ can be performed at once, leading to

$$I(q) = NI_1(q)\left[1 + \langle n\rangle \int_0^\infty 4\pi r^2 \{g(r) - 1\} \frac{\sin qr}{qr}\, dr \right] \tag{5.51}$$

The pair distribution function $g(r)$ depends on the interaction forces between the particles. In general, for a fairly dilute dispersion of particles as we are discussing here, a good approximation is afforded by

$$g(r) = \exp\left[-\frac{\varepsilon(r)}{kT} \right] \tag{5.52}$$

where $\varepsilon(r)$ is the energy of interaction as a function of the separation distance r. In the case of hard spheres that we are considering now

$$\varepsilon(r) = \begin{cases} \infty \\ 0 \end{cases}, \quad g(r) - 1 = \begin{cases} -1 & \text{for } r \leq 2R \\ 0 & \text{for } r > 2R \end{cases} \tag{5.53}$$

and on performing the integration (5.51) becomes

$$I(q) = NI_1(q)\left[1 - 8\langle n\rangle v\frac{3(\sin 2qR - 2qR\cos 2qR)}{(2qR)^3}\right] \tag{5.54}$$

where v is the volume of the sphere and $\langle n\rangle v$ is equal to the fraction of the total volume occupied by the spheres. Figure 5.7 shows the intensities of scattering per particle calculated by (5.54) when the volume fractions of the spheres are equal to 0.0, 0.02, 0.04, and 0.06. The most noticeable feature seen in Figure 5.7 is that as the concentration of the spheres is increased, the intensity per particle at very small q is progressively more depressed, and the curve eventually develops a maximum at a finite q.

When the particles are of irregular shape, the analysis can still be carried out in a similar manner, but the result naturally turns out more complicated. The amplitude of scattering from a system containing N identical, irregularly shaped particles is given by

$$A(\boldsymbol{q}) = \sum_{j=1}^{N} A_j(\boldsymbol{q})e^{-i\boldsymbol{q}\boldsymbol{r}_j} \tag{5.55}$$

in place of Equation (5.46). $A_j(\boldsymbol{q})$ are different for different particles, even when the particles are all identical, because of the different orientations they assume. The intensity is then

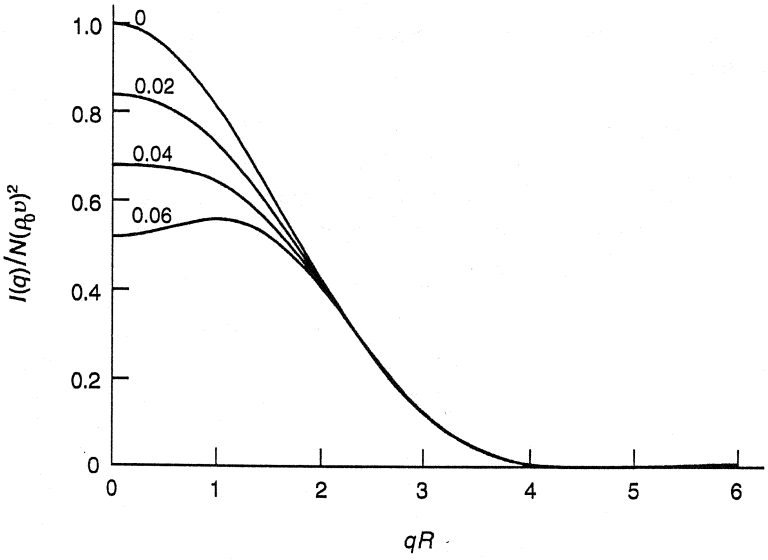

Figure 5.7 Intensity of scattering, per particle, from a dilute suspension of hard spheres of radius R, according to Equation (5.54). The four curves are for the cases in which the volume fraction of the spheres is equal to 0.0, 0.02, 0.04, and 0.06, respectively.

$$I(\boldsymbol{q}) = \left\langle \sum_{j=1}^{N} \sum_{k=1}^{N} A_j(\boldsymbol{q}) A_k^*(\boldsymbol{q}) e^{-i\boldsymbol{q}\boldsymbol{r}_{jk}} \right\rangle \tag{5.56}$$

When terms with $j = k$ are split, (5.56) becomes

$$I(\boldsymbol{q}) = \sum_{j=1}^{N} \langle A_j(\boldsymbol{q}) A_j^*(\boldsymbol{q}) \rangle + \left\langle \sum_{j=1}^{N} \sum_{k \neq j}^{N} A_j(\boldsymbol{q}) A_k^*(\boldsymbol{q}) e^{-i\boldsymbol{q}\boldsymbol{r}_{jk}} \right\rangle \tag{5.57}$$

The first term again represents the independent scattering by individual particles each assuming a random orientation. The second term, as before, represents the interference effect.

To be able to make some further sense out of (5.57), we make the assumption that there is no correlation between the orientations of different particles j and k or between the separation distance $\boldsymbol{r}_{jk}$ and the orientation of the particles. This is a reasonable assumption when the asymmetry of the particles is not severe and the concentration is at most moderate. The averaging in the second term can then be performed separately for the three factors $A_j(\boldsymbol{q})$, $A_k^*(\boldsymbol{q})$, and $\exp(-i\boldsymbol{q}\boldsymbol{r}_{jk})$, and (5.57) becomes

$$I(q) = N I_1(q) \left[1 + \langle n \rangle \frac{\langle A(\boldsymbol{q}) \rangle^2}{\langle A^2(\boldsymbol{q}) \rangle} \int_0^\infty 4\pi r^2 \{ g(r) - 1 \} \frac{\sin qr}{qr} \, dr \right] \tag{5.58}$$

where $I_1(q) = \langle A^2(\boldsymbol{q}) \rangle$. In general, irrespective of whether the particles tend to attract or repel each other, they exclude each other at very short distances where they overlap, so that $g(r) - 1 \to -1$ when $r \to 0$. At large distances $g(r)$ approaches unity in the absence of a long-range order, so that $g(r) - 1 \to 0$ when $r \to \infty$. The contribution of the interference term in (5.58) is therefore negative for small q, whereas it is negligibly small at large q. The overall effect of the interference term is therefore similar to the case of the hard spheres, that is, the tendency remains that the intensity curve at very small q values is depressed as the concentration of the particles is increased. The above discussion makes it clear that as long as the particles have a finite volume and exclude each other on close approach, the effect of moderate packing will manifest itself as a depression of the intensity curve at very small q.

In systems in which individual polymer coils are regarded as the particles, the effect of finite concentrations has to be analyzed in a somewhat different manner, since polymer coils are more open and can interpenetrate each other. The volume around the immediate vicinity of a segment is, however, still excluded from occupancy by other segments belonging either to the same molecule or to a different molecule. In calculating the interference term in the scattered intensity, the distribution of segments around the center of each polymer coil and the effect of the volume exclusion on segment–segment contacts must be taken into account fully. Such segment–segment contacts also affect the thermodynamic properties of the polymer solution. It is therefore not surprising that the scattering function from a dilute polymer solution is intimately related to the polymer solution theory.

According to Zimm[17] and Flory and Bueche[18] the intensity $I(q,c)$ of scattered light (as well as x-rays and neutrons) as a function of q and the concentration c (usually expressed in grams per cubic centimeter) can be given as

$$\frac{Kc}{I(q,c)} = \frac{1}{MP(q)} + 2A_2Q(q)c + \cdots \tag{5.59}$$

where K is a constant, M is the molecular weight of the polymer, and A_2 is the second virial coefficient that can also be determined from osmotic pressure measurement. $P(q)$, which is sometimes called the *form factor* or *shape factor*, is the independent scattering intensity $I_1(q)$ normalized so as to have $P(0) = 1$. $Q(q)$ is another shape factor that is related to the overall shape of the two approaching molecules and is not far from unity. Equation (5.59) forms the basis for the Zimm plot for determining the molecular weight of polymers by light scattering from dilute polymer solutions. By extrapolating to infinite dilution in the Zimm plot the molecular weight and the radius of gyration are determined according to

$$\lim_{c\to 0} \frac{Kc}{I(q,c)} = \frac{1}{MP(q)} = \frac{1}{M}\left(1 + \frac{1}{3}\left\langle R_g^2 \right\rangle q^2 + \cdots\right) \tag{5.60}$$

A special simplification arises when a deuterated polymer is blended with its hydrogenous counterpart of exactly the same molecular weight. In this case, the interference component of the scattered intensity turns out to be simply proportional to the independent scattering component, and as a result the form factor can be determined even when the concentration of the deuterated polymer is not dilute. This will be discussed more when the technique of deuterium labeling is described in Section 6.3.

5.3 NONPARTICULATE TWO-PHASE SYSTEM

5.3.1 Correlation Function and Invariant

By way of introduction we here summarize a few results of general validity, before focusing on the nonparticulate two-phase system that will be discussed in the rest of Section 5.3. For the present we stipulate only that the system of study is characterized by its scattering length density distribution $\rho(\boldsymbol{r})$, which is not restricted in any way. The intensity of scattering $I(\boldsymbol{q})$ is then given by

$$I(q) = \int \Gamma_\rho(\boldsymbol{r}) e^{-i\boldsymbol{q}\boldsymbol{r}}\, d\boldsymbol{r} \tag{1.78}$$

where $\Gamma_\rho(\boldsymbol{r})$ is the autocorrelation function of $\rho(\boldsymbol{r})$. As was done in Section 1.6, introducing the deviation $\eta(\boldsymbol{r})$ of the scattering length density $\rho(\boldsymbol{r})$ from its mean $\langle\rho\rangle$,

$$\eta(\boldsymbol{r}) - \rho(\boldsymbol{r}) - \langle\rho\rangle \tag{1.88}$$

allows us to rewrite Equation (1.78) as

$$I(\boldsymbol{q}) = \int \Gamma_\eta(\boldsymbol{r}) e^{-i\boldsymbol{q}\boldsymbol{r}}\, d\boldsymbol{r} \tag{5.61}$$

where $\Gamma_\eta(\boldsymbol{r})$ is the autocorrelation function of $\eta(\boldsymbol{r})$. In writing (5.61) [cf. equation (1.92)] we have ignored the unobservable "null scattering" that is due to the scattering from the sample as a whole. We take Equation (5.61) as the starting point for the present discussion.

The normalized version of $\Gamma_\eta(\boldsymbol{r})$ can be defined as

$$\gamma(\boldsymbol{r}) = \frac{\Gamma_\eta(\boldsymbol{r})}{\Gamma_\eta(0)} \tag{5.62}$$

so that $\gamma(0)$ is equal to 1. The function $\gamma(\boldsymbol{r})$ is sometimes referred to as the *Debye correlation function* (Debye and Bueche[19]). Porod[20] calls it the *characteristic function.* The normalization constant $\Gamma_\eta(0)$ is

$$\Gamma_\eta(0) = \int \eta(\boldsymbol{u})\eta(0+\boldsymbol{u})\, d\boldsymbol{u} = V\langle\eta^2\rangle \tag{5.63}$$

where $\langle\eta^2\rangle$ is the mean square fluctuation of the scattering length density about its mean throughout the system. An alternative way of writing Equation (5.61) is therefore

$$I(\boldsymbol{q}) = V\langle\eta^2\rangle \int \gamma(\boldsymbol{r}) e^{-i\boldsymbol{q}\boldsymbol{r}}\, d\boldsymbol{r} \tag{5.64}$$

The correlation function $\Gamma_\eta(\boldsymbol{r})$, according to (5.61), can be obtained by taking the inverse Fourier transform of the scattered intensity $I(\boldsymbol{q})$, which, however, must be measured in absolute units if $\Gamma_\eta(\boldsymbol{r})$ is to be obtained also in absolute units. When the intensity is known only in arbitrary (relative) units, $\gamma(\boldsymbol{r})$ can still be obtained in view of the normalization condition $\gamma(0) = 1$.

The invariant Q was defined, in Section 1.5.4, as the quantity that represents the total scattering power of the sample, and it can be evaluated by integrating the observed intensity $I(\boldsymbol{q})$ over the whole reciprocal space, as indicated by Equation (1.85), or in the case of an isotropic material by

$$Q = 4\pi \int_0^\infty s^2 I(s)\, ds = \frac{1}{2\pi^2} \int_0^\infty q^2 I(q)\, dq \tag{1.86}$$

The integration in (1.86) should, strictly speaking, extend to infinity as the upper limit, but in the context of small-angle scattering the integration is usually confined to small q regions with the intensity $I(q)$ at larger q ignored. Substitution of (5.61) into (1.85) and changing the order of integration give

$$\begin{aligned} Q &= \int \Gamma_\eta(\boldsymbol{r}) \left[\frac{1}{(2\pi)^3} \int e^{-i\boldsymbol{q}\boldsymbol{r}}\, d\boldsymbol{q} \right] d\boldsymbol{r} \\ &= \int \Gamma_\eta(\boldsymbol{r})\delta(\boldsymbol{r})\, d\boldsymbol{r} \\ &= \Gamma_\eta(0) \end{aligned} \tag{5.65}$$

which, from (5.63), is seen to be equal to $V\langle\eta^2\rangle$. Experimental evaluation of Q is useful since it gives a measure of the severity of scattering length density inhomogeneity in the sample. However, it should be noted that for evaluation of Q according to (1.85) or

(1.86) the intensity $I(q)$ must be determined in absolute units. The term invariant was coined by Porod,[20] who first recognized the usefulness of the concept in the context of small-angle scattering studies.

The intensity and the correlation function are the Fourier transforms of each other, and therefore they contain identical information. To extract information about the structure, either one of them may be analyzed, and, in principle, the choice is arbitrary. Because of the reciprocity between $\boldsymbol{r}$ and $\boldsymbol{q}$, information on large structural features, for example, can be obtained from $\Gamma_\eta(\boldsymbol{r})$ or $\gamma(\boldsymbol{r})$ at large $\boldsymbol{r}$, or equivalently from $I(\boldsymbol{q})$ at small $\boldsymbol{q}$. Some workers prefer analyzing the correlation function since this is a function in direct space $\boldsymbol{r}$ and affords a more intuitive interpretation. However, to be able to perform the inverse Fourier transform and obtain the correlation function reliably, the intensity $I(\boldsymbol{q})$ must be available over a sufficiently extended range of $\boldsymbol{q}$ with accuracy, a task that may not always be practical. Because of the lack of phase information in the observed intensity, neither the intensity nor the correlation function offers a direct means of determining the scattering length density $\rho(\boldsymbol{r})$, and it is necessary to make additional assumptions about the structure based on knowledge from independent sources. Section 5.3 discusses what can be determined from the analysis of $I(\boldsymbol{q})$ or the correlation function under the assumption that the system of study consists of a two-phase structure. A similar treatment can be extended to the analysis of a three-phase structure, but the results are naturally more complicated, and the reader is instead referred to literature reports.[21]

5.3.2 Ideal Two-Phase Model

As an idealized example of the nonparticulate two-phase system, we first consider the *ideal two-phase system* defined as follows. We assume (1) that the system contains only two different regions (or phases), each of constant scattering length density ρ_1 or ρ_2, and (2) that the boundary between these two regions is sharp with no measurable thickness (see Figure 5.8). We further assume that these two phases are irregularly intermixed, so that the system as a whole is isotropic and there is no long-range order. (The dilute particulate system considered in Section 5.2 can also be included as an ideal two-phase system in a broader sense if the particles are of uniform scattering length density.) Two parameters characterizing such a system are the volume fractions of the two phases and the specific interface area between the two phases. Both can be determined from the observed intensity data. From these two, a parameter characterizing the mean dimension of each of the two phases can also be calculated. The model is of course an idealization that no real material system fulfills literally. By assuming a constant scattering length density within each phase, we are ignoring the granularity in the material that arises from its atoms and molecules. In addition, in real liquids (and glasses) there are also long-range inhomogeneities that arise from thermal density fluctuations, as discussed in Section 4.2. Theoretical results derived from the ideal two-phase model can therefore be applied to the analysis of observed intensities only after the effect of such granularity has been subtracted. The assumption of sharp phase boundaries also does not agree with reality, and as a result observed intensity curves may exhibit a certain systematic deviation from

the predictions of the idealized model. Such discrepancies can in fact be analyzed to yield information about the width of the diffuse phase boundaries, as discussed in Section 5.3.3.

5.3.2.1 Invariant

In an ideal two-phase system, in which the volume fractions of the two phase are ϕ_1 and $\phi_2(= 1 - \phi_1)$, the average scattering length density is

$$\langle \rho \rangle = \phi_1 \rho_1 + \phi_2 \rho_2 \tag{5.66}$$

and η_1 and η_2 are given by

$$\eta_1 = \rho_1 - \langle \rho \rangle = \Delta\rho\phi_2 \tag{5.67}$$

and

$$\eta_2 = \rho_2 - \langle \rho \rangle = -\Delta\rho\phi_1 \tag{5.68}$$

where

$$\Delta\rho = \rho_1 - \rho_2 = \eta_1 - \eta_2 \tag{5.69}$$

The invariant is then

$$\begin{aligned} Q = V\langle \eta^2 \rangle &= V\left(\eta_1^2\phi_1 + \eta_2^2\phi_2\right) \\ &= V\,(\Delta\rho)^2\,\phi_1\phi_2 \end{aligned} \tag{5.70}$$

This simple relationship turns out to be useful in a surprising variety of situations, provided the intensity is determined in absolute units so that the invariant Q can also be evaluated in absolute units. If the scattering length densities of the two phases are known, for example, from knowledge of their chemical compositions, the experimental value of Q can be used to provide the relative amounts of the two phases. If, on the other hand, the relative amounts are known beforehand, for example, when the sample is prepared by mixing known quantities of two substances, the invariant can be used to determine the difference $\rho_1 - \rho_2$. An instance in which such information could be useful is with a polymer blend in which a partial miscibility is suspected. When known quantities of two polymers are mixed together, any decrease in $\rho_1 - \rho_2$

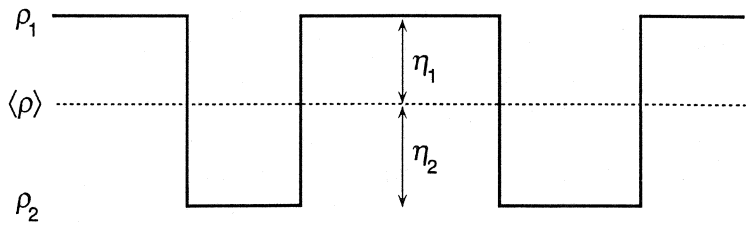

Figure 5.8 Scattering length density profile in an ideal two-phase model.

below the expected value can be a sign of partial miscibility. Another instance is the determination of the degree of crystallinity of a semicrystalline polymer. The mass densities, and hence the scattering length densities, of the crystalline and amorphous phases are known for most polymers, and therefore knowledge of the value of Q can provide the relative amount of the crystalline phase. An application of this method to polyethylene samples gave degrees of crystallinity that are in good agreement with those obtained by conventional methods.[22]

5.3.2.2 Porod Law

The most important theoretical result for the ideal two-phase model is the prediction that $I(q)$ should decrease as $\sim q^{-4}$ for large q, and moreover that the proportionality constant should be related to the total area S of the boundaries between the two phases in the scattering volume. In other words, as $q \to \infty$,

$$I(q) \to \frac{2\pi(\Delta\rho)^2 S}{q^4} \tag{5.71}$$

This is called the *Porod law*.[20,23] Before proceeding to the derivation of the law, it is instructive to examine a special case, the scattering from a suspension of spheres. A collection of solid spheres with a uniform density ρ_1 provides a good example of an ideal two-phase system.

The intensity of scattering from a system containing N solid spheres of radius R, dispersed in a medium of scattering length density ρ_2, can be written, after (5.17), as

$$\begin{aligned} I(q) &= N(\Delta\rho)^2 \left(\frac{4}{3}\pi R^3\right)^2 \frac{9(\sin qR - qR\cos qR)^2}{(qR)^6} \\ &= N(\Delta\rho)^2 8\pi^2 \left[\frac{R^2(1+\cos 2qR)}{q^4} - \frac{2R\sin 2qR}{q^5} + \frac{1-\cos 2qR}{q^6}\right] \end{aligned} \tag{5.72}$$

For large q the second and third terms within the square brackets in (5.72) become insignificant. In the first term, $\cos 2qR$ contributes either positively or negatively as q increases, but if the spheres are all of different radii the average of $\cos 2qR$ is equal to zero. With $S = \sum 4\pi R^2 = 4\pi N\langle R^2\rangle$, Equation (5.72) thus reduces to (5.71).

To derive the Porod law, we first evaluate the correlation function $\Gamma_\eta(r)$. Imagine that the whole sample volume is divided into four regions, by regarding those in the shell within distance r from the phase boundary to be distinct from the inner regions (see Figure 5.9). These regions are the bulk region 1B of phase 1, the surface region 1S of phase 1, the bulk region 2B of phase 2, and the surface region 2S of phase 2. When r is small compared to the radius of curvature of the boundary, the volumes of regions 1S and 2S are both equal approximately to Sr. The volumes of regions 1B and 2B are $V\phi_1 - Sr$ and $V\phi_2 - Sr$ respectively, where V is the total sample volume. For a sample with overall isotropic symmetry, the correlation function $\Gamma_\eta(r)$ is a function of the magnitude of $\boldsymbol{r}$ only, and can be written as

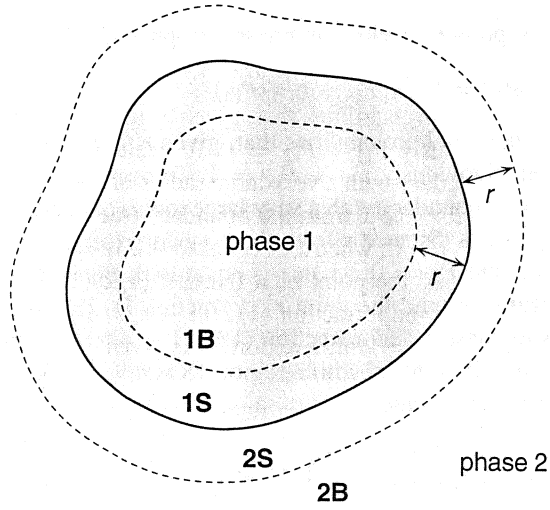

Figure 5.9 The diagram illustrates the four regions into which the sample volume is divided: bulk region 1B of phase 1, surface region 1S of phase 1, surface region 2S of phase 2, and bulk region 2B of phase 2.

$$\Gamma_\eta(r) = V\left\langle \eta\left(\boldsymbol{r}'\right)\eta\left(\boldsymbol{r}''\right)\right\rangle \tag{5.73}$$

where $\langle\cdots\rangle$ denotes taking the average throughout the sample volume while keeping $r = |\boldsymbol{r}' - \boldsymbol{r}''|$ constant. $\Gamma_\eta(r)$ can be considered to be the sum of four separate contributions $\Gamma_{1B}(r)$, $\Gamma_{1S}(r)$, $\Gamma_{2B}(r)$, and $\Gamma_{2S}(r)$. $\Gamma_{1B}(r)$, for example, is the contribution to $\Gamma_\eta(r)$ when $\boldsymbol{r}'$ is within region 1B, that is,

$$\Gamma_{1B}(r) = V_{1B}\left\langle \eta(\boldsymbol{r}')\eta(\boldsymbol{r}'')\right\rangle_{1B} \tag{5.74}$$

where V_{1B} is the volume of region 1B and $\langle\cdots\rangle_{1B}$ denotes that the average is taken only when $\boldsymbol{r}'$ is within region 1B (while $r = |\boldsymbol{r}' - \boldsymbol{r}''|$ is still kept constant, so that $\boldsymbol{r}''$ is allowed to go outside region 1B).

We now evaluate each of the four separate contributions to $\Gamma_\eta(r)$. When point $\boldsymbol{r}'$ is in region 1B, point $\boldsymbol{r}''$ must be in phase 1 (either in region 1B or 1S), so that $\Gamma_{1B}(r)$ is given by

$$\Gamma_{1B}(r) = (V\phi_1 - Sr)\eta_1^2 \tag{5.75}$$

Similarly, we have

$$\Gamma_{2B}(r) = (V\phi_2 - Sr)\eta_2^2 \tag{5.76}$$

When point $\boldsymbol{r}'$ is in region 1S, point $\boldsymbol{r}''$ is either in phase 1 or phase 2. Thus we write

$$\Gamma_{1S}(r) = Sr(\eta_1^2 P_{11} + \eta_1 \eta_2 P_{12}) \tag{5.77}$$

where P_{11} and P_{12} are the conditional probabilities that, given $\boldsymbol{r}'$ in region 1S, $\boldsymbol{r}''$ is in phase 1 and 2, respectively. Obviously $P_{11} + P_{12} = 1$. To evaluate P_{11} and P_{12} consider a planar boundary (or a boundary with a very large radius of curvature) and a point $\boldsymbol{r}'$ in region 1S located at a distance x from the boundary (see Figure 5.10). When x is equal to r, $P_{11} = 1$ and $P_{12} = 0$; when x is equal to 0, $P_{11} = P_{12} = 0.5$. If a sphere of radius r is drawn around the point $\boldsymbol{r}'$, a fraction $(1/2)(1 + x/r)$ of the surface of the sphere is in phase 1 and a fraction $(1/2)(1 - x/r)$ is in phase 2. The average probability P_{11} for all points $\boldsymbol{r}'$ within region 1S is given by integrating $(1/2)(1 + x/r)$ for x between 0 and r, and is

$$P_{11} = \frac{1}{r} \int_0^r \frac{1}{2} \left(1 + \frac{x}{r}\right) dx = \frac{3}{4} \tag{5.78}$$

Equation (5.77) thus becomes

$$\Gamma_{1S}(r) = Sr \left(\frac{3}{4}\eta_1^2 + \frac{1}{4}\eta_1 \eta_2\right) \tag{5.79}$$

In a similar manner, one can show that

$$\Gamma_{2S}(r) = Sr \left(\frac{3}{4}\eta_2^2 + \frac{1}{4}\eta_1 \eta_2\right) \tag{5.80}$$

Taking the sum of (5.75), (5.76), (5.79), and (5.80), we obtain

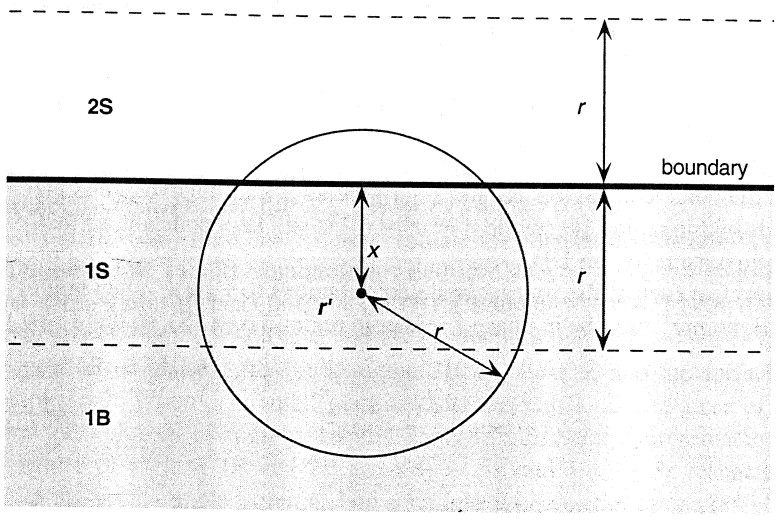

Figure 5.10 When a point $\boldsymbol{r}'$ is in region 1S, the conditional probability P_{12} that a point $\boldsymbol{r}''$ (with $r = |\boldsymbol{r}' - \boldsymbol{r}''|$) is in region 2S is equal to the fraction of the sphere surface area above the boundary plane.

$$\begin{aligned}\Gamma_\eta(r) &= V\left(\eta_1^2\phi_1 + \eta_2^2\phi_2\right) - \frac{Sr}{4}(\Delta\rho)^2 \\ &= V\langle\eta^2\rangle\left[1 - \frac{1}{4}\frac{S}{V}\frac{(\Delta\rho)^2}{\langle\eta^2\rangle}r\right] \\ &= V\langle\eta^2\rangle\left(1 - \frac{r}{l_\mathrm{P}}\right)\end{aligned} \tag{5.81}$$

where l_P is defined as

$$l_\mathrm{P} = 4\frac{V}{S}\frac{\langle\eta^2\rangle}{(\Delta\rho)^2} \tag{5.82}$$

For $r \ll l_\mathrm{P}$ (5.81) can be approximated by

$$\Gamma_\eta(r) = V\langle\eta^2\rangle\exp\left(-\frac{r}{l_\mathrm{P}}\right) \tag{5.83}$$

and substitution of (5.83) into (5.61) gives

$$\begin{aligned}I(q) &= \int_0^\infty V\langle\eta^2\rangle\exp\left(-\frac{r}{l_\mathrm{P}}\right)4\pi r^2\frac{\sin qr}{qr}\,dr \\ &= V\langle\eta^2\rangle\frac{8\pi l_\mathrm{p}^3}{\left(1 + l_\mathrm{p}^2q^2\right)^2}\end{aligned} \tag{5.84}$$

In the limit of $q \to \infty$, (5.84) becomes

$$I(q) \to \frac{8\pi V\langle\eta^2\rangle}{l_\mathrm{P}}\frac{1}{q^4} \tag{5.85}$$

which is the Porod law, Equation (5.71). The approximation introduced in the derivation, that r be small, is justified in the limit of large q.

5.3.2.3 Specific Interface Area and Length of Inhomogeneity

By comparing the experimentally obtained intensity function $I(q)$ against the Porod law (5.71), one can determine the total interfacial area S in the sample. To accomplish this the intensity must be available in absolute units. If the intensity is determined only in relative units, there is still a way out. When the invariant Q is evaluated according to (1.86) and divided into $I(q)$, the relative unit scale used to express the intensity is canceled out from the ratio, and we obtain, in place of the Porod law (5.71),

$$\frac{I(q)}{Q} \to \frac{2\pi}{\phi_1\phi_2}\frac{S}{V}\frac{1}{q^4} \tag{5.86}$$

which can be used to evaluate S/V provided ϕ_1 and ϕ_2 are known. The ratio S/V is the *specific surface* (or *interfacial*) *area*, and is of course more meaningful than S itself when the total scattering volume V is not well defined.

The ratio V/S has dimension of length and can be regarded as the length scale that characterizes the structure. To elaborate on this, let us consider a line, as in Figure 5.11, that crosses the system in an arbitrary direction and cuts out alternating chords l_1 and l_2 from the two phases. The average chord lengths $\langle l_1 \rangle$ and $\langle l_2 \rangle$ are related to V/S by

$$\langle l_1 \rangle = 4\frac{V}{S}\phi_1 \quad \text{and} \quad \langle l_2 \rangle = 4\frac{V}{S}\phi_2 \tag{5.87}$$

To see these relationships, imagine that the line crossing through the system in Figure 5.11 is replaced by a long, straight tube of cross-sectional area δA. A short section of such a tube, cut out by phase 1, will be of length l_1 and capped at two ends by small pieces of the interfacial boundary $\delta S'$ and $\delta S''$, as in Figure 5.12. With the normal to the end surface making angle θ' and θ'' with the tube axis respectively, the areas of the boundary cut out by the tube are $\delta S' = \delta A/\cos\theta'$ and $\delta S'' = \delta A/\cos\theta''$, and the volume of the tube section is $\delta V = l_1 \delta A$. Eliminating δA from these quantities, we have

$$\delta V = \frac{1}{2} l_1 \left(\delta S' \cos\theta' + \delta S'' \cos\theta''\right) \tag{5.88}$$

Now imagine that the whole system is filled with such tubes packed tightly parallel to each other. Summing (5.88) for all the tube sections in the system, we then have

$$\sum \delta V = \frac{1}{2} \langle l_1 \rangle \left(\langle \cos\theta' \rangle \sum \delta S' + \langle \cos\theta'' \rangle \sum \delta S''\right) \tag{5.89}$$

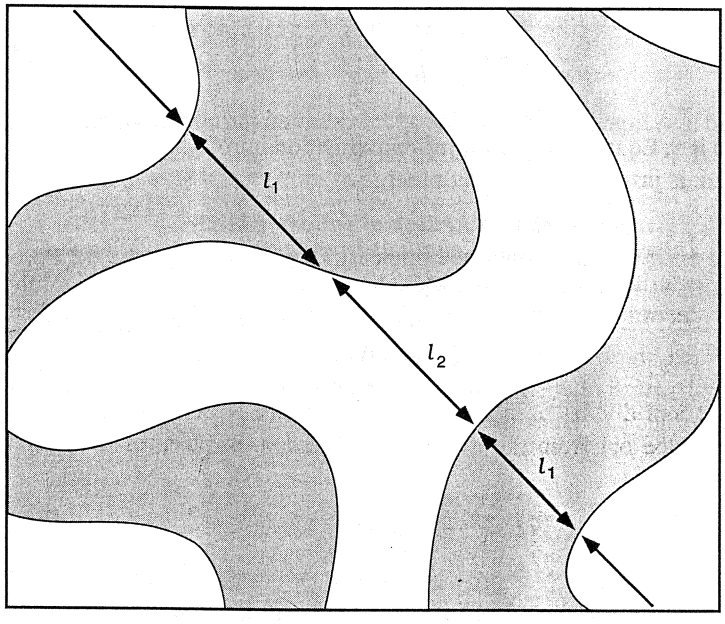

Figure 5.11 A line crossing the system in an arbitrary direction cuts out alternating chords of l_1 and l_2 in the two phases between boundaries.

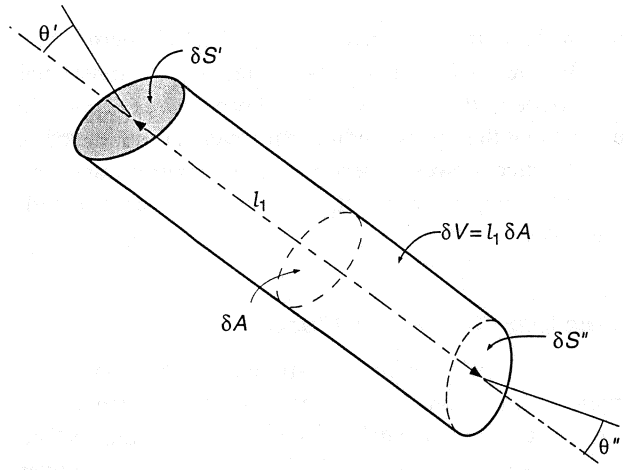

Figure 5.12 A section of length l_1, cut out by phase 1, from a straight tube of cross section δA crossing through the system in an arbitrary direction as in Figure 5.11.

where the averaging for l_1 and cos θ is performed separately since there is no correlation between them. We recognize that

$$\sum \delta V = V\phi_1 \tag{5.90}$$

and

$$\sum (\delta S' + \delta S'') = S \tag{5.91}$$

where $V\phi_1$ is the total volume of phase 1 and S is the total interfacial boundary area. Since the average of cos θ is 1/2, (5.89) leads to (5.87).

The length l_P, defined by (5.82), can be written, in view of (5.70), as

$$l_P = 4\frac{V}{S}\phi_1\phi_2 \tag{5.92}$$

which is then seen, in view of (5.87), to be related to the average chord lengths by

$$\frac{1}{l_P} = \frac{1}{\langle l_1 \rangle} + \frac{1}{\langle l_2 \rangle} \tag{5.93}$$

The length l_P, known by some as *Porod's length of inhomogeneity*, is thus a measure of the average size of the heterogeneities present in the system. Equation (5.83) shows that for any ideal two-phase system, the correlation function $\Gamma_\eta(r)$ decays exponentially, at least for small r, and l_P plays the role of the *correlation length*. Taking the slope of the correlation function (5.83) at $r = 0$, we obtain

$$\left[\frac{d\Gamma_\eta(r)}{dr}\right]_{r=0} = -\frac{V\langle \eta^2 \rangle}{l_P} = -\frac{1}{4}(\Delta\rho)^2 S \tag{5.94}$$

It is therefore entirely feasible to have the observed intensity $I(q)$ converted first into the correlation function by Fourier inversion, and then determine the interfacial boundary area S from the initial slope of the latter. Since the Porod law is applicable in the limit of $q \to \infty$, it is natural that the corresponding information is contained in $\Gamma_\eta(r)$ in the limit of $r \to 0$. In practice, however, performing the Fourier transform on observed intensity data and obtaining the correlation function for small r with sufficient accuracy are difficult tasks.

5.3.3 Deviations from the Ideal Two-Phase Model

A real material never completely fulfills the idealization stipulated in the ideal two-phase model. Therefore certain modifications have to be introduced either to the theoretical expressions derived or to the experimentally observed intensity data before the two can be compared. We discuss separately the effects arising from the presence of heterogeneities within each phase and from the diffuseness of the interface boundaries.

5.3.3.1 Density Fluctuation within the Phases

In a real two-phase specimen, there are inhomogeneities within the individual phases, due to the atomic nature of the material and to the density fluctuations at all size scales arising from thermal motions of atoms (or frozen-in thermal motions, in the case of glasses). Thus the scattering from such a specimen consists of four components:

$$I(q) = I_0(q) + I_1(q) + I_2(q) + I_{12}(q) \tag{5.95}$$

where $I_0(q)$ is the scattering that would have been realized if the two phases were of uniform density as in the idealized model, $I_1(q)$ and $I_2(q)$ are the scattering due to the density fluctuations present independently in the two phases, and $I_{12}(q)$ represents the effect associated with the interaction of the waves scattered in the different phases (Filipovich[24]). The contributions $I_1(q)$ and $I_2(q)$ are equal, respectively, to the intensities scattered from the pure substances, weighted in proportion to their relative amounts present. Any correlation between the density fluctuations in the two phases across the phase boundaries is likely to be of short range, and consequently for small q $I_{12}(q)$ is small and can be neglected. Thus, to make a correction for the thermal density fluctuations, it is only necessary to make additional measurements to determine the scattering from the two pure components. In practice, however, such a "background correction" is usually made empirically, estimating the magnitude of $I_1(q) + I_2(q)$ in the range of interest simply by extrapolating the behavior of the intensity curve beyond the small-angle region (see Figure 5.13). Empirical equations of the type

$$ae^{-bq^2} \quad \text{or} \quad a + bq^n \tag{5.96}$$

with arbitrary constants a, b, and n (an even integer) have been found to fit the curve well from the end of the small-angle region toward the beginning of the amorphous halo. The fitted curve is then extrapolated to smaller values of q, and the result subtracted from the observed intensity $I(q)$.

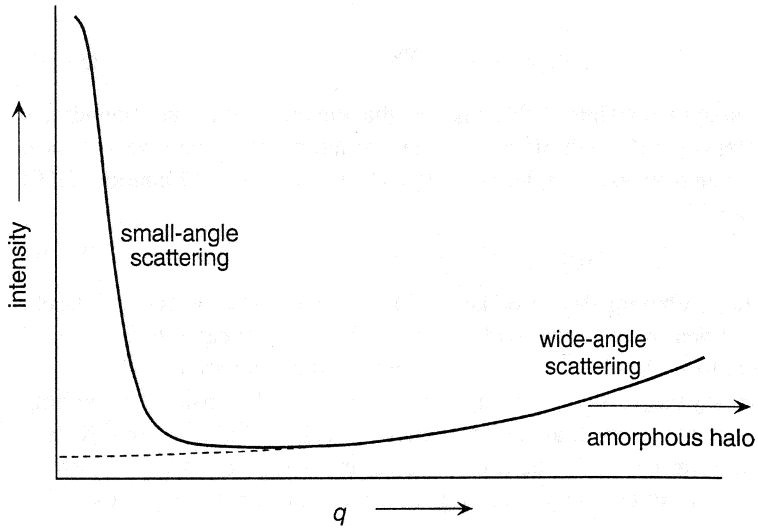

Figure 5.13 The scattering due to the presence of density inhomogeneities within the phases is eliminated by subtracting the "background," which is obtained by extrapolating the intensity observed beyond the small-angle region.

5.3.3.2 Diffuse Interface Boundary

The main theoretical results derived from the ideal two-phase model, i.e., Equation (5.70) relating the invariant Q to the phase volumes and the Porod law (5.71), are no longer valid and need be modified when in the two-phase system the phase boundaries are diffuse. To see the modifications necessary to these theoretical results, we represent by $\rho(\boldsymbol{r})$ the scattering length density distribution in a two-phase material with diffuse boundaries and by $\rho_{\text{id}}(\boldsymbol{r})$ the density distribution in the (hypothetical) system in which all the diffuse boundaries in the above have been replaced by sharp boundaries. The two are then related to each other[25] by a convolution product

$$\rho(\boldsymbol{r}) = \rho_{\text{id}}(\boldsymbol{r}) * g(\boldsymbol{r}) \tag{5.97}$$

where $g(\boldsymbol{r})$ is a "smoothing" function characterizing the diffuse boundary. For most cases $g(\boldsymbol{r})$ can be approximated well by a three-dimensional Gaussian function:

$$g(r) = \left(\frac{1}{\sqrt{2\pi}\sigma}\right)^3 e^{-r^2/2\sigma^2} \tag{5.98}$$

where σ is related to the width of the transition zone. The intensity of scattering is given by the absolute square of the Fourier transform of (5.97), that is, by

$$I(\boldsymbol{q}) = I_{\text{id}}(\boldsymbol{q})G^2(\boldsymbol{q}) \tag{5.99}$$

where $G(\boldsymbol{q})$ is the Fourier transform of $g(\boldsymbol{r})$. When $g(\boldsymbol{r})$ is approximated by (5.98), $G(\boldsymbol{q})$ is given by

$$G(\boldsymbol{q}) = e^{-(\sigma^2/2)q^2} \tag{5.100}$$

and on substitution of (5.100) into (5.99) it is seen that the effect of diffuse boundaries is to make the intensity curve fall off more rapidly at large q than the inverse fourth power dictated, for an isotropic sample, by the Porod law. For small σ Equation (5.99) can be approximated by

$$I(\boldsymbol{q}) = I_{\mathrm{id}}(\boldsymbol{q})\left(1 - \sigma^2 q^2\right) \tag{5.101}$$

Therefore, with $I_{\mathrm{id}}(q)$ obeying the Porod law (5.71), a plot of $q^4 I(q)$ against q^2 should give, at large q, a linear relationship with its intercept at $q = 0$ equal to $2\pi(\Delta\rho)^2 S$ and its slope equal to $-[2\pi(\Delta\rho)^2 S]\sigma^2$, thus permitting the evaluation of σ.

To see more clearly the physical meaning of σ and the three-dimensional smoothing function (5.98), consider a small area of the boundary region and take the direction normal to it as the x direction. If the diffuse boundary is now replaced by a sharp planar boundary, $\rho_{\mathrm{id}}(\boldsymbol{r})$ in the immediate neighborhood can be represented by

$$\rho_{\mathrm{id}}(\boldsymbol{r}) = \rho_1 + (\rho_2 - \rho_1)H(x) \tag{5.102}$$

where $H(x)$ is the Heaviside function equal to 0 for $x < 0$ and to 1 for $x > 0$. Obviously $\rho_{\mathrm{id}}(\boldsymbol{r})$ depends only on x and is independent of y and z. Substituting (5.98) and (5.102) into (5.97) and performing the convolution operations in the x, y, and z directions individually, we obtain

$$\rho(\boldsymbol{r}) = \rho_1 + (\rho_2 - \rho_1)H(x) * g_1(x) \tag{5.103}$$

where g_1(x) is the one-dimensional Gaussian function

$$g_1(x) = \frac{1}{\sqrt{2\pi}\sigma} e^{-x^2/2\sigma^2} \tag{5.104}$$

The convolution product $H(x) * g_1(x)$ becomes

$$\begin{aligned} H(x) * g_1(x) &= \frac{1}{\sqrt{2\pi}\sigma}\int_0^\infty \exp\left[-\frac{(x-u)^2}{2\sigma^2}\right] du \\ &= \frac{1}{2} + \frac{1}{2}\mathrm{erf}\left(\frac{x}{\sqrt{2}\sigma}\right) \end{aligned} \tag{5.105}$$

where erf(x) is the error function defined as

$$\mathrm{erf}(x) = \frac{2}{\sqrt{\pi}}\int_0^x e^{-t^2} dt \tag{5.106}$$

The relationship among $g_1(x)$, $H(x)$, and $H(x) * g_1(x)$ is illustrated in Figure 5.14. The "effective" width t of the diffuse interface may be defined by

$$t = (\rho_2 - \rho_1)/\rho'(0) \tag{5.107}$$

where $\rho'(0)$ is the slope of the interface density profile $\rho(x)$ at the mid-point. For the density profile defined by (5.103) and (5.105), the interface thickness becomes

$$t = \sqrt{2\pi}\sigma \tag{5.108}$$

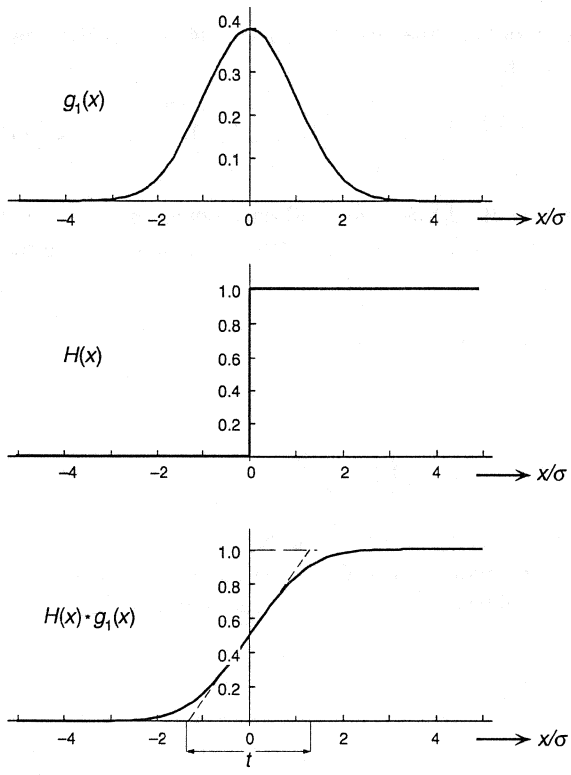

Figure 5.14 Plots illustrating the relationship among the one-dimensional Gaussian "smoothing" function $g_1(x)$, the Heaviside function $H(x)$ representing the sharp boundary, and the convolution product of $g_1(x)$ and $H(x)$. The broken line in the last shows how the effective thickness t of the diffuse interface is defined.

The diffuse phase boundaries affect not only the scattering curve in the Porod region, but also the value of the invariant $Q = V\langle\eta^2\rangle$. The value of Q would now be smaller than that given by (5.70), since the deviations η of the scattering length density from the mean will be smaller in the diffuse interface zone than when the interface is sharp. To calculate $\langle\eta^2\rangle$, we approximate by assuming that the density is different appreciably from either ρ_1 or ρ_2 only to the depth x_0 on either side of the interface (x_0 being slightly larger than $t/2$). The fraction ε of the total volume belonging to the interface region is then approximately equal (if x_0 is much smaller than the radius of curvature) to

$$\varepsilon = 2x_0 \frac{S}{V} \tag{5.109}$$

The volume fraction of phase 1 excluding the transition zone is now equal to $\phi_1 - \varepsilon/2$, and the volume fraction of phase 2 is equal to $\phi_2 - \varepsilon/2$. We therefore have

$$\langle\eta^2\rangle = \left(\phi_1 - \frac{\varepsilon}{2}\right)(\rho_1 - \langle\rho\rangle)^2 + \left(\phi_2 - \frac{\varepsilon}{2}\right)(\rho_2 - \langle\rho\rangle)^2 + \frac{S}{V}\int_{-x_0}^{x_0} [\rho(x) - \langle\rho\rangle]^2 \, dx \tag{5.110}$$

Substituting for $\rho(x)$ the density profile defined by (5.103), (5.104) and (5.105), and after some regrouping of terms, we find

$$\langle \eta^2 \rangle = (\Delta\rho)^2 \phi_1 \phi_2 - \frac{(\Delta\rho)^2}{2} \frac{S}{V} \int_0^{x_0} \left[1 - \mathrm{erf}\left(\frac{x}{\sqrt{2}\sigma} \right)^2 \right] dx \qquad (5.111)$$

The integrand in (5.111) is significantly different from 0 only when x is small, and therefore the upper integration limit can be extended to infinity with negligible error. Using the fact that

$$\int_0^{\infty} \left[1 - \mathrm{erf}(x)^2 \right] dx = \sqrt{2/\pi} \qquad (5.112)$$

we obtain[26]

$$\langle \eta^2 \rangle = (\Delta\rho)^2 \phi_1 \phi_2 \left(1 - \frac{t}{l_P} \right) \qquad (5.113)$$

where l_P is Porod's length of inhomogeneity. The result in (5.113) is what would have been expected, that is, the fractional reduction in Q due to the diffuse interface is equal to the ratio of the interface thickness t to the average "domain size" l_P.

5.4 FRACTAL OBJECTS

5.4.1 Definitions

In Section 5.2.2 it was shown that at large q the intensity $I(q)$ of scattering from a sphere decays as q^{-4}, from a thin disk as q^{-2}, and from a thin rod as q^{-1}. The power-law exponent at large q is therefore seen to be related to the dimensionality of the scattering object. There are, however, many cases in which the intensity varies as an unexpected or even *fractional* power of q. In the case of a Gaussian model of a polymer chain, the intensity was seen to decrease as q^{-2} even though a chain obviously is a three-dimensional object. The inverse power-law exponents that differ from 1, 2, or 4 can be explained in terms of the concept of a *fractal*.

Ever since Mandelbrot[27] promulgated the description of complex patterns in nature in terms of fractal geometry, the concept has been applied[28–30] to the study of increasing numbers of irregular objects in all branches of science including polymer science. A well-known example of a fractal is the length of a coast line, which increases in length as the yard stick with which it is measured is made smaller. Other examples are the irregular aggregates of tiny silica or soot particles, the pattern of dendritic growth of crystals, the trace left by an electric discharge starting from a point in a dielectric, and the shape of a polymer coil under both Θ and non-Θ conditions.

A fractal possesses a *dilation symmetry*, that is, it retains a *self-similarity* under scale transformations. In other words, if we magnify part of the structure, the enlarged portion looks just like the original. Figure 5.15 shows a fractal shape, the Koch curve. If we magnify by three the part of the Koch curve in the interval (0, 1/3), it becomes exactly identical to the whole shape. The same is true if the part in (0, 1/9) is enlarged

by nine, etc. In a mathematically defined fractal object such as the Koch curve, this self-similarity extends from an infinitesimally small to an infinitely large scale, but in an object occurring in nature, there are of course an upper bound imposed by the largest dimension of the object and a lower bound due to the size of the basic building blocks of the structure.

A fundamental characteristic of a fractal is its *fractal dimension*. Suppose we draw a sphere of radius r around a point in the object. If the fractal object is a line, the mass $M(r)$ within the sphere will be proportional to r. If it is a sheet, then $M(r) \propto r^2$. If it is a solid three-dimensional object, $M(r)$ would be proportional to r^3. In a fractal, the following general relation is obeyed,

$$M(r) \propto r^d \tag{5.114}$$

where the fractal dimension d is a number between 1 and 3 (that can be fractional). The smaller the value of d, the more open the structure is, and as d is reduced to 1, the object becomes a line if it remains singly connected. Since the volume of the sphere is proportional to r^3, the density $\tilde{\rho}(r)$ of actual material embedded in it is

$$\tilde{\rho}(r) \propto r^{d-3} \tag{5.115}$$

which shows that the density is no longer a constant of the object but rather decreases as the size of the volume being considered is increased.

Some objects possess a surface that is rough and exhibit fractal properties. Such an object is called a *surface fractal*; the fractal object discussed in the preceding paragraph is called a *mass fractal.* The moon pock-marked with craters of all sizes and a clump of cauliflower are examples of a surface fractal. An island with a fractal coastline mentioned earlier is an example of a surface fractal in two-dimensional space. We first examine this two-dimensional example, since it is easier to visualize than a three-dimensional one. Imagine we cover the island completely with square tiles of edge length l, and we mark those tiles that at least partially overlap the coastline. Suppose $N(l)$ is the number of tiles so marked. If the coastline is smooth and nearly straight, $N(l)$ will be proportional to l^{-1} as we use tiles of different size l. If the coastline is irregular and fractal, the number $N(l)$ of marked tiles depends

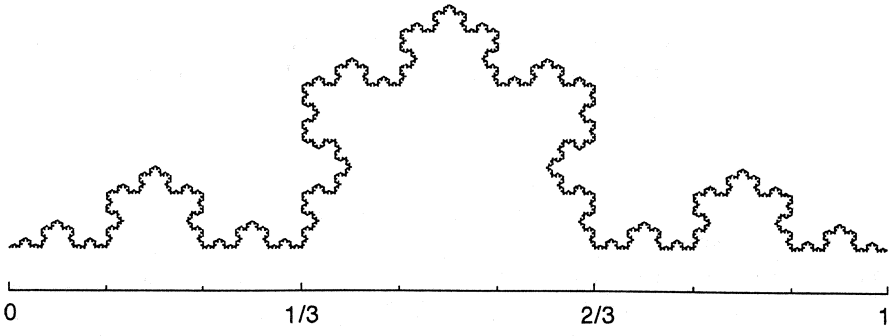

Figure 5.15 The Koch curve.

more strongly on l, and is proportional to l^{-d_S} where d_s is a number larger than 1. The length $L(l)$ of the coastline can be regarded as equal to $lN(l)$ or

$$L(l) \propto l^{1-d_S} \tag{5.116}$$

The number d_s is the fractal dimension of this two-dimensional surface fractal. The fractal dimension of a three-dimensional surface fractal can be defined in a similar manner. In particular, if $S(r)$ is the surface area measured with a measuring tool of characteristic area r^2, it depends on r as

$$S(r) \propto r^{2-d_S} \tag{5.117}$$

The value of d_s ranges from 2 to 3 for a surface fractal in three-dimensional space. It is equal to 2 when the surface is perfectly smooth and approaches 3 when the surface is so folded that it almost completely fills the space (imagine a tightly crumpled napkin).

5.4.2 Scattering from Fractal Objects

5.4.2.1 Scattering from a Mass Fractal

If we consider a mass fractal object as a distribution of mass points, the normalized correlation function $\gamma(r)$ is the probability of finding a mass point a distance r apart from an arbitrary mass point selected within the object. We construct a spherical shell of radius r and thickness dr around the selected point. The number of mass points enclosed in the shell is proportional to $4\pi r^{d-1}\,dr$ in view of Equation (5.114). Since the volume of the shell is equal to $4\pi r^2\,dr$, the correlation function is

$$\gamma(r) \propto r^{d-3} \tag{5.118}$$

The range of validity of (5.118) is $R \gg r \gg a$, where R is the overall dimension of the object ($\sim R_g$), and a is the size of the basic building block of the structure, which could be as small as an atom or a molecule. On substituting (5.118) into (5.61) the intensity of scattering for an isotropic material is given by

$$I(q) \propto \frac{1}{q}\int_0^\infty r^{d-2} \sin qr\,dr \tag{5.119}$$

Evaluation of the integral in (5.119) requires care because of the limited range of validity of (5.118). Without dwelling on the intricacy of the problem, we may simply quote the result:

$$I(q) \propto q^{-d} \tag{5.120}$$

which is valid for $1/R \ll q \ll 1/a$. Figure 5.16 illustrates an experimental result obtained with a colloidal aggregate of silica particles by combining small-angle light and x-ray scattering measurements (Schaefer *et al.*[31]). The slope of the log–log plot gives the fractal dimension $d = 2.1$ over a fairly wide range of q. For q larger than $1/a$ the slope is -4 suggesting a Porod law scattering from the individual silica particles.

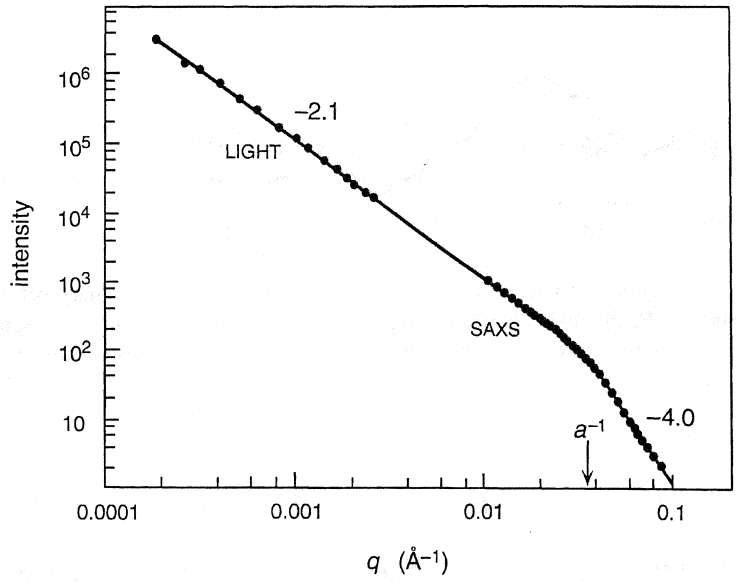

Figure 5.16 Combined small-angle light and x-ray scattering results for a colloidal aggregate of silica particles. (From Schaefer *et al.*[31])

5.4.2.2 Scattering from a Surface Fractal

The intensity of scattering from a surface fractal can be derived by following a procedure that is essentially the same as the derivation of the Porod law in Section 5.3.2.2. We regard the system as still obeying the ideal two-phase model, except that the interface boundary, instead of being smooth, is now fractal. Often the second phase is simply a vacuum, but that does not affect our discussion. To derive the correlation function $\Gamma_\eta(r)$, we divide our system into four regions, 1B, 1S, 2B, and 2S, as before, but in view of the roughness of the phase boundary, we have to be a little more careful in drawing the division between the regions 1S and 1B (and, similarly, between 2S and 2B). Region 1S consists of all points in phase 1 from which at least some part of the phase boundary can be reached within a distance r or less. If we draw a sphere of radius r from every point on the phase boundary (designated A in Figure 5.17), the envelope (designated B in Figure 5.17) of all such spheres is the dividing surface between regions 1S and 1B. Obviously the larger the radius r, the smoother the surface B. Its area $S(r)$ is given by

$$S(r) = S_0 r^{2-d_S} \tag{5.121}$$

where S_0 is a constant, which is the surface area itself when $d_S = 2$ (smooth surface). The volume of region 1S, bounded by the two surfaces A and B, is given[32] by

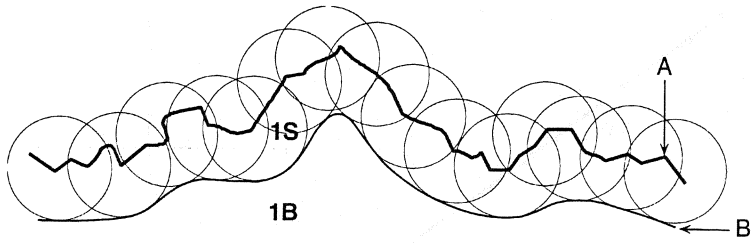

Figure 5.17 An illustration showing how region 1S is defined. A, the boundary between phase 1 and phase 2. B, the dividing surface between region 1S and reghion 1B. A sphere of radius r is drawn at every point on A, and the envelope of all such spheres constitutes the dividing surface B.

$$V_{1S} = \int_a^r S(r)\,dr = \frac{S_0}{3 - d_S}\left(r^{3-d_S} - a^{3-d_S}\right) \tag{5.122}$$

where the fractal behavior is assumed to extend down to the smallest length scale a. The volume of region 1B is given by

$$V_{1B} = V\phi_1 - V_{1S} \tag{5.123}$$

By substituting (5.122), (5.123), and similar expressions for V_{2S} and V_{2B} in the appropriate places in the derivation of $\Gamma_\eta(r)$ described in Section 5.3.2.2, we obtain

$$\Gamma_\eta(r) = V\langle\eta^2\rangle\left[1 - \frac{1}{4\phi_1\phi_2 V}\frac{S_0}{3 - d_S}\left(r^{3-d_S} - a^{3-d_S}\right)\right] \tag{5.124}$$

The scattered intensity $I(q)$ can be obtained by substituting (5.124) into (5.61) and performing the integration. Here, again, we simply quote the final result, which is

$$I(q) \propto q^{-(6-d_S)} \tag{5.125}$$

A log–log plot of $I(q)$ against q will therefore give a straight line, with the slope equal to $6 - d_S$. Since d_S (for a three-dimensional surface fractal) is between 2 and 3, the exponent of q is to be between -3 and -4 (the latter limit corresponds to the Porod law for a smooth interface boundary). As seen in Equation (5.120), the intensity of scattering from a mass fractal decays with q with an exponent between -1 and -3. Figure 5.18 shows an example of the small-angle x-ray scattering curve obtained with a sample of coal (Bale and Schmidt[33]). The plot is linear over a remarkably wide range of q and gives the surface fractal dimension d_s equal to 2.56.

The exponent $-(6-d_S)$ for surface fractals, given by Equation (5.125), can also be understood by the following simplified argument. The surface area of a surface fractal depends on the scale with which the object is viewed. In the scattering measurement, as we increase q, we are in effect looking at the object at an ever decreasing size scale. The effective surface area S perceived therefore varies, as a function of q, as

$$S \propto r^{2-d_S} \propto q^{-(2-d_S)} \tag{5.126}$$

Since, according to the Porod law,

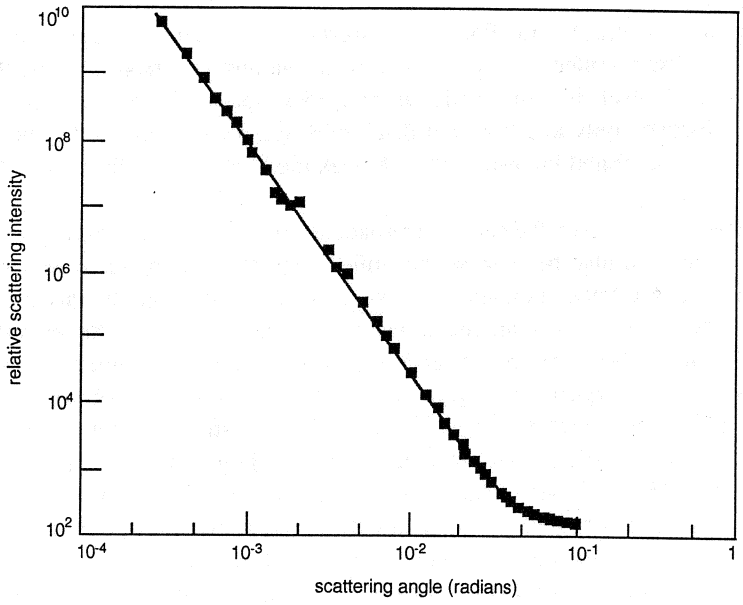

Figure 5.18 Small-angle x-ray scattering intensity for a lignite coal. (From Bale and Schmidt.[33])

$$I(q) \propto Sq^{-4} \tag{5.127}$$

substitution of (5.126) into (5.127) leads to (5.125).

5.5 PERIODIC SYSTEM

Among polymeric materials there are many examples of ordered structures having a period of repetition on the order of 1 to 100 nm, and such structures are amenable to study by small-angle scattering. The methods developed for the analysis of wide-angle diffraction from crystalline solids, discussed in Chapter 3, are directly applicable to the study of periodic systems, without any modifications in most cases. However, the degree of periodic order present in these systems is usually much poorer than in crystals, and dealing with the effects of such "imperfections" constitutes a significant part of the effort in the analysis.

As with a crystalline specimen, the structure of interest in the present context can be represented by a scattering length density distribution $\rho(\boldsymbol{r})$ written as

$$\rho(\boldsymbol{r}) = \rho_u(\boldsymbol{r}) * z(\boldsymbol{r}) \tag{1.95}$$

where $\rho_u(\boldsymbol{r})$ is the scattering length density distribution associated with a single repeating motif (equivalent to a unit cell) in the structure, and $z(\boldsymbol{r})$ is the function describing the lattice or the ordered arrangement of such motifs. The intensity of scattering is then given by

$$I(\boldsymbol{q}) = |F(\boldsymbol{q})|^2 \, |Z(\boldsymbol{q})|^2 \tag{5.128}$$

where $F(\boldsymbol{q})$ and $Z(\boldsymbol{q})$ are the Fourier transforms of $\rho_u(\boldsymbol{r})$ and $z(\boldsymbol{r})$, respectively. If the real lattice, represented by $z(\boldsymbol{r})$, is large in extent and free from defects, the lattice factor $|Z(\boldsymbol{q})|^2$ itself is also a lattice in reciprocal space. The intensity of scattering is then observed only as a series of discrete Bragg peaks, with the height (or, more exactly, the integrated intensity) of each peak modulated according to the "structure factor" $|F(\boldsymbol{q})|^2$.

In practice, however, the peaks are broadened because of the imperfections present in the lattice and also because of the limited size of the domains within which the coherence of the lattice is maintained. As a consequence, usually only the first few Bragg reflections, at most, are recognizable as separate peaks. At higher q the lattice factor $|Z(\boldsymbol{q})|^2$ often smears out and degenerates into a continuum of essentially constant height independent of q. If there is any variation in $I(q)$ observable in this q region, it may in fact reflect the q dependence of the "structure factor" $|F(q)|^2$. This can be seen especially clearly when the scattering length density distribution $\rho_u(\boldsymbol{r})$ is such that $|F(q)|^2$ itself exhibits peaks. Figure 5.19 shows small-angle neutron scattering data (Bates *et al.*[34]) obtained with a styrene-butadiene diblock copolymer, which by transmission electron microscopy was shown to have spherical butadiene microdomains ordered on a cubic lattice. The peaks at q below about 0.04 $Å^{-1}$ are considered to arise from the lattice structure, and their positions are consistent with a body-centered cubic lattice with $a = 491$ Å. The intensity curve at higher q can be fitted well by the solid curve that was calculated (see Section 5.2.2.1) for independent scattering by a collection of solid spheres of mean radius 124 Å.

The periodic systems that are subjected to small-angle scattering studies are mostly of lamellar morphology, as in folded-chain lamellar crystals, membrane structures, and block copolymers with lamellar ordering. We will therefore confine our discussion to lamellar systems only and discuss them in more detail in the rest of this section.

If, in a stack of such lamellae, the individual lamellae are perfectly parallel to each other and their lateral expanses are sufficiently wide, the scattering length density distribution in the system can be represented by a one-dimensional function $\rho(x)$, x being the direction perpendicular to the lamella plane. The intensity of scattering is then concentrated on $\boldsymbol{q}$ along a line normal to the lamellae. Such a one-dimensional intensity pattern is designated by the symbol $I_1(q)$. If the sample under consideration contains only a single such stack of lamellae, the observed three-dimensional intensity pattern $I(\boldsymbol{q})$ will be zero everywhere except for $\boldsymbol{q}$ along the lamella normal. If, on the other hand, the specimen contains many such stacks oriented in all random directions, as is usually the case, the observed intensity pattern $I(q)$ is isotropic, and $I_1(q)$ can be obtained from it by

$$I_1(q) \propto 4\pi q^2 I(q) \tag{5.129}$$

5.5.1 Scattering from Lamellar Structure

5.5.1.1 Ideal Two-Phase Lamellar Structure

Let us first consider an ideal two-phase lamellar structure (see Figure 5.20) in which lamellae of phase A, of thickness d_a and uniform scattering length density ρ_a, alternate

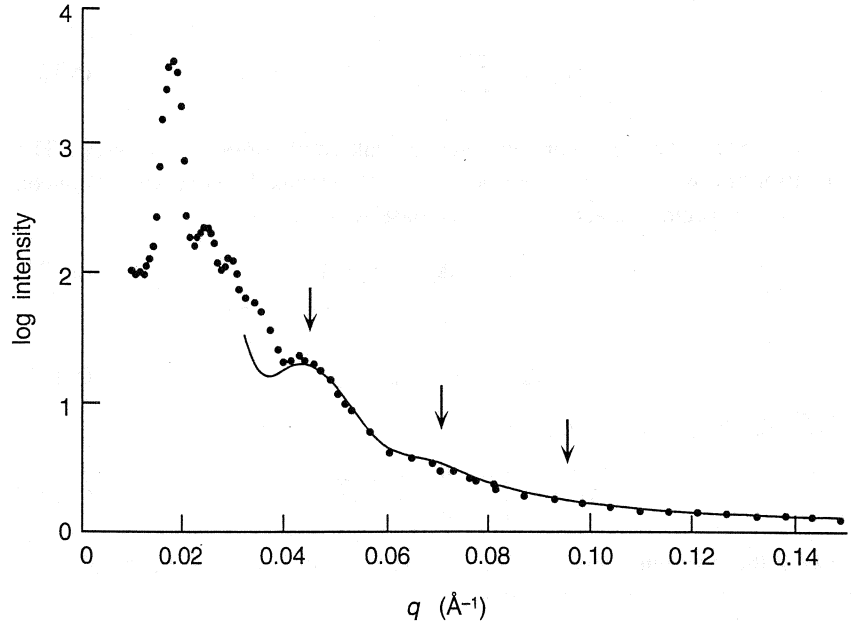

Figure 5.19 Small-angle neutron scattering intensity obtained with a styrene-butadiene diblock copolymer having spherical butadiene microdomains. The peaks at very small q are due to a body-centered cubic lattice structure of ordered microdomains. The solid curve is the calculated intensity of independent scattering from solid spheres of mean radius 124 Å. (From Bates *et al.*[34])

with lamellae of phase B, of thickness d_b and uniform scattering length density ρ_b. The scattering length density profile $\rho(x)$ in the stack of such parallel lamellae can be written as

$$\rho(x) = \rho_u(x) * z(x/d) \tag{5.130}$$

where $z(x)$ is defined as

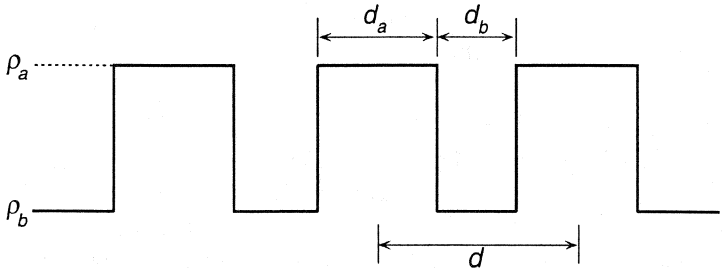

Figure 5.20 Scattering length density profile in the direction perpendicular to the lamella plane in the ideal two-phase lamellar system.

$$z(x) = \sum_{n=-\infty}^{\infty} \delta(x - n) \tag{5.131}$$

and therefore $z(x/d)$ represents a one-dimensional lattice of period $d(= d_a + d_b)$. The density distribution within a single period can be represented by $\rho_u(x)$ for x between 0 and d (with the origin of x at the center of phase A) given as

$$\rho_u(x) = \rho_b + \Delta\rho \; \Pi(x/d_a) \tag{5.132}$$

where

$$\Delta\rho = \rho_a - \rho_b \tag{5.133}$$

and $\Pi(x)$ is the step function defined as

$$\Pi(x) = \begin{cases} 1 & \text{for } |x| < \frac{1}{2} \\ 0 & \text{for } |x| > \frac{1}{2} \end{cases} \tag{5.134}$$

By taking the absolute square of the Fourier transform of $\rho(x)$ in (5.130), the intensity of scattering $I_1(x)$ is obtained as

$$I_1(q) \propto |F(q)|^2 \; z(dq/2\pi) \tag{5.135}$$

The lattice factor $z(dq/2\pi)$ expresses the fact that the square of the Fourier transform of $z(x/d)$ is itself a lattice of period $2\pi/d$ (in q) in reciprocal space. A proportionality instead of an equality sign is used in (5.135) to acknowledge that the proportionality constant arising from the squaring of the delta functions in $z(q)$ is here not explicitly accounted for. With $\rho_u(x)$ given by (5.132), we obtain

$$|F(q)|^2 = (\Delta\rho)^2 \frac{4}{q^2} \sin^2\left(\frac{d_a q}{2}\right) \tag{5.136}$$

Equations (5.135) and (5.136), together, state that Bragg peaks occur at a series of q values satisfying $dq/2\pi = n$ or $q = 2\pi n/d$, and that the height of (or, more exactly, the integrated area under) the nth order peak is proportional to $\sin^2(\pi n\phi_a)/n^2$, where $\phi_a(= d_a/d)$ is the volume fraction of phase A. This means that from the measurement of the relative heights of successive peaks, the relative volumes of the two phases can be determined. It also shows that when the volumes of the two phases are equal, all even order peaks are reduced to zero heights.

5.5.1.2 Structure with Variable Lamella Thickness

The sharp peaks predicted by Equation (5.135) are broadened and reduced in height if various types of imperfections degrade the structure from the ideal two-phase model envisioned above. Most of such imperfections find their counterparts in three-dimensional crystals, and the methods of analysis to account for such imperfections, developed in Section 3.4, can be applied to the small-angle scattering equally well and need not be elaborated here again. There is, however, one type of imperfection

that will be described here in some detail, since this is a type that is expected to occur more frequently in one-dimensional lamellar structures than in three-dimensional crystals. Here we consider a modification to the ideal two-phase lamellar system in such a way that the lamellae are still strictly parallel, but the thickness of the lamellae is no longer fixed to either d_a or d_b but varies more or less randomly from one to the next. More specifically, we assume that the thickness of phase A lamellae is distributed according to the probability $p_a(a)\,da$ of finding it between a and $a + da$ (with the average of a equal to d_a) and similarly the thickness of phase B lamellae is distributed according to the probability $p_b(b)\,db$ (with the average of b equal to d_b). We further assume that there is no correlation between the thicknesses of neighboring lamellae. Such an imperfection is called paracrystalline or an imperfection of the second kind, as described in Section 3.4.3. Since the scattering intensity depends on the deviation from the mean ($\eta = \rho - \langle\rho\rangle$) and not on the absolute value of the scattering length density ρ, we will from now on assume, without loss of generality, that ρ_b is equal to zero or that phase B is a vacuum.

The amplitude $A(q)$ of scattering from such a parallel stack of lamellae is given by

$$A(q) = \sum_{j=1}^{N} A_j(q) \tag{5.137}$$

where $A_j(q)$ is the contribution to $A(q)$ by the jth A lamella. The number N of A lamellae in the stack is considered sufficiently large, so that, in the interest of avoiding unnecessary details due to end effects, we will from now on regard N as being practically equal to infinity whenever it occurs as the upper limit of a summation. For $A_j(q)$ in (5.137) we can write

$$\begin{aligned} A_j(q) &= \int_{x_j}^{x_j+a_j} \Delta\rho\, e^{-iqx}\, dx \\ &= \frac{\Delta\rho}{iq} e^{-iqx_j}(1 - e^{-iqa_j}) \end{aligned} \tag{5.138}$$

where x_j is the x-coordinate of the point where the jth A lamella starts, and a_j is its thickness (see Figure 5.21). The intensity of scattering is then

$$\begin{aligned} I_1(q) &= \sum_{j=1}^{N} A_j \sum_{k=1}^{N} A_k^* \\ &= \sum_{j=1}^{N} A_j A_j^* + \sum_{j=1}^{N} \sum_{m=1}^{N} (A_j A_{j+m}^* + A_{j+m} A_j^*) \end{aligned} \tag{5.139}$$

Note that the upper limit of the summation with respect to m is written as N instead of $N - j$ in view of the aforementioned approximation of regarding N as practically equal to infinity.

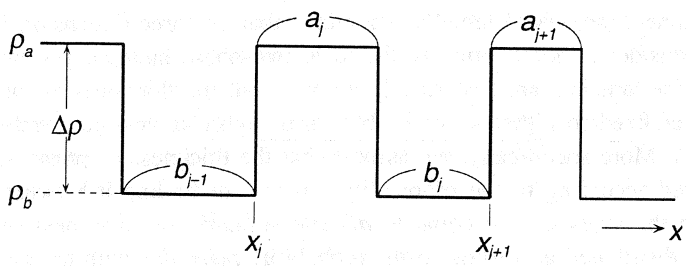

Figure 5.21 Stack of lamellae of varying thicknesses.

We now consider the first sum in (5.139), which, with (5.138) substituted for $A_j(q)$, becomes

$$\sum_{j=1}^{N} A_j A_j^* = \left(\frac{\Delta\rho}{q}\right)^2 \sum_{j=1}^{N} (2 - e^{-iqa_j} - e^{iqa_j})$$

$$= \left(\frac{\Delta\rho}{q}\right)^2 N \left(2 - \langle e^{-iqa}\rangle - \langle e^{iqa}\rangle\right) \tag{5.140}$$

where $\langle\ \ \rangle$ represents an average over the N lamellae. Recognizing that $p_a(a) = 0$ for $a < 0$, we have

$$\langle e^{-iqa}\rangle = \int_0^\infty e^{-iqa} p_a(a)\, da = \int_{-\infty}^\infty e^{-iqa} p_a(a)\, da = P_a(q) \tag{5.141}$$

where $P_a(q)$ is the Fourier transform of $p_a(a)$. Similarly, by recognizing that $p_a(a)$ is real, we find

$$\langle e^{iqa}\rangle = \int_0^\infty e^{iqa} p_a(a)\, da = \int_{-\infty}^\infty e^{iqa} p_a(a)\, da = P_a^*(q) \tag{5.142}$$

Equation (5.140) thus becomes

$$\sum_{j=1}^{N} A_j A_j^* = \left(\frac{\Delta\rho}{q}\right)^2 N 2\,\mathrm{Re}(1 - P_a) \tag{5.143}$$

where $\mathrm{Re}(z)$ denotes the real part of a complex quantity z, obtainable by taking $(z + z^*)/2$.

Next, we take up the terms in (5.139) for $m = 1$. First we consider

$$\sum_{j=1}^{N} A_j A_{j+1}^* = \left(\frac{\Delta\rho}{q}\right)^2 \sum_{j=1}^{N} e^{-iqx_j}(1 - e^{-iqa_j}) e^{iqx_{j+1}}(1 - e^{iqa_{j+1}}) \tag{5.144}$$

Since x_{j+1} is equal to $x_j + a_j + b_j$, it becomes

$$\sum_{j=1}^{N} A_j A_{j+1}^* = \left(\frac{\Delta\rho}{q}\right)^2 \sum_{j=1}^{N} e^{iqb_j}(e^{iqa_j} - 1 - e^{iqa_j} e^{iqa_{j+1}} + e^{iqa_{j+1}})$$

$$= \left(\frac{\Delta\rho}{q}\right)^2 N\left\langle e^{iqb_j}\right\rangle\left(\left\langle e^{iqa_j}\right\rangle - 1 - \left\langle e^{iqa_j}\right\rangle\left\langle e^{iqa_{j+1}}\right\rangle + \left\langle e^{iqa_{j+1}}\right\rangle\right) \quad (5.145)$$

In the above, in replacing the exponential factors with their expectation values, we recognize the fact that the thicknesses of the neighboring lamellae are uncorrelated. Making use of (5.142) we then find

$$\sum_{j=1}^{N} A_j A_{j+1}^* = \left(\frac{\Delta\rho}{q}\right)^2 N P_b^*(2P_a^* - 1 - P_a^{*2})$$

$$= -\left(\frac{\Delta\rho}{q}\right)^2 N P_b^*(1 - P_a^*)^2 \quad (5.146)$$

Since $A_{j+1}A_j^*$ is the complex conjugate of $A_j A_{j+1}^*$, we obtain

$$\sum_{j=1}^{N}(A_j A_{j+1}^* + A_{j+1}A_j^*) = -\left(\frac{\Delta\rho}{q}\right)^2 N2\mathrm{Re}\left[P_b(1 - P_a)^2\right] \quad (5.147)$$

Proceeding in the similar way, it can be shown that

$$\sum_{j=1}^{N}(A_j A_{j+m}^* + A_{j+m}A_j^*) = -\left(\frac{\Delta\rho}{q}\right)^2 N2\mathrm{Re}\left[P_b(1 - P_a)^2(P_a P_b)^{m-1}\right] \quad (5.148)$$

Substituting (5.143), (5.147), and (5.148) into (5.139) leads to

$$I_1(q) = 2N\left(\frac{\Delta\rho}{q}\right)^2 \mathrm{Re}\left[\frac{(1 - P_a)(1 - P_b)}{1 - P_a P_b}\right] \quad (5.149)$$

This is the expression giving the scattering intensity $I_1(q)$ in terms of the lamellae thickness distributions. The above derivation is based on the one given by Hosemann and Bagchi.[35]

To make the discussion more concrete, we now assume the lamella thickness distributions to be Gaussian, so that

$$p_a(a) = \frac{1}{\sqrt{2\pi}\sigma_a}\exp\left[-\frac{(a - d_a)^2}{2\sigma_a^2}\right] \quad (5.150)$$

where d_a is the average and σ_a the standard deviation of a. A similar expression is assumed for $p_b(b)$. The Fourier transform of (5.150) is given by

$$P_a(q) = e^{-\frac{1}{2}\sigma_a^2 q^2} e^{-iqd_a} \quad (5.151)$$

Substitution of (5.151) and the similar expression for $P_b(q)$ into (5.149) leads, after some tedious algebra, to

$$I_1(q) = 2N\left(\frac{\Delta\rho}{q}\right)^2 \frac{1}{(1 - g_a g_b)^2 + 4g_a g_b \sin^2(qd/2)}$$
$$\times\left[(1 - g_a)(1 - g_b)(1 - g_a g_b) + 2g_a(1 - g_b^2)\sin^2(qd_a/2) + \right. \quad (5.152)$$
$$\left. 2g_b(1 - g_a^2)\sin^2(qd_b/2)\right]$$

where

$$g_a \equiv e^{-\frac{1}{2}\sigma_a^2 q^2}, \qquad g_b \equiv e^{-\frac{1}{2}\sigma_b^2 q^2} \tag{5.153}$$

Figure 5.22 shows the intensity function $I_1(q)$ calculated from (5.152) for $\phi_a = d_a/d = 0.3, \sigma_a = 0.15d_a, \sigma_b = 0.15d_b$ (solid curve), and for $\phi_a = 0.3, \sigma_a = 0.3d_a, \sigma_b = 0.3d_b$ (broken curve). As expected, the peaks are broader and lower in height as σ_a and σ_b become larger. The relative height of the peak of the successive order n can be estimated from the following approximation to Equation (5.152):

$$I_1(q) = 16N\frac{(\Delta\rho)^2}{q^4}\frac{\sigma_b^2 \sin^2(qd_a/2) + \sigma_a^2 \sin^2(qd_b/2)}{(\sigma_a^2 + \sigma_b^2)^2 + (16/q^4)\sin^2(qd/2)} \tag{5.154}$$

which is valid for small values of σ_a and σ_b. The denominator of (5.154) tells us that the peaks are located near the q values that make $\sin^2(qd/2)$ equal to zero, that is, $q = 2\pi n/d$. The exact locations of the maxima are slightly shifted from these q values because of the distortion to the peak shape imparted by the numerator of (5.154). The heights of the successive peaks at the q values exactly equal to $2\pi n/d$ are given by

$$I_1\left(\frac{2\pi n}{d}\right) = N(\Delta\rho)^2\frac{d^4}{n^4\pi^4}\frac{\sin^2(n\pi\phi_a)}{(\sigma_a^2 + \sigma_b^2)} \tag{5.155}$$

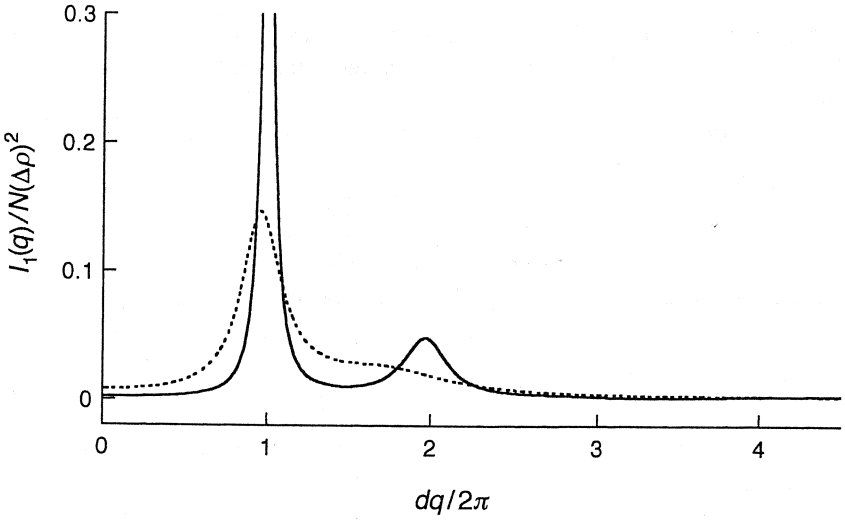

Figure 5.22 Scattering intensity $I_1(q)$ from a stack of parallel lamellae of alternating phases A and B, in which the thicknesses of the lamellae vary according to Gaussian probability functions. Solid line: $\phi_a = 0.3, \sigma_a = 0.15d_a, \sigma_b = 0.15d_b$. Broken line: $\phi_a = 0.3, \sigma_a = 0.3d_a, \sigma_b = 0.3d_b$.

This equation shows that the heights of the successive peaks decrease as n^{-4}. From Equation (5.136) we have already seen that in the ideal lamellar structure the area under the peak varies as n^{-2}. Combination of these two results suggests that the width of the peak increases as n^2 in the present variable thickness model.

5.5.2 Correlation Function of Lamellar Structure

Instead of comparing the observed intensity with the one calculated on the basis of an assumed model, we may derive the correlation function from the observed intensity and then analyze it directly or compare it with the one calculated from the model. The potential advantage of such a correlation function approach has been stressed by some workers.[36,37] From the observed one-dimensional intensity $I_1(q)$, the one-dimensional correlation function $\Gamma_1(x)$ can be obtained by

$$\Gamma_1(x) = \frac{1}{2\pi}\int_{-\infty}^{\infty} I_1(q)e^{iqx}\,dq = \frac{2}{2\pi}\int_0^{\infty} I_1(q)\cos qx\,dq \tag{5.156}$$

If $I_1(q)$ is known only in arbitrary units, as is usually the case in practice, the normalized correlation function $\gamma_1(x)$ may instead be evaluated by

$$\gamma_1(x) = \frac{\int_0^{\infty} I_1(q)\cos qx\,dq}{\int_0^{\infty} I_1(q)\,dq} \tag{5.157}$$

The correlation function, on the other hand, can be calculated from the assumed structure by

$$\Gamma_1(x) = \int_{-\infty}^{\infty} \eta(u)\eta(u+x)\,du \tag{5.158}$$

and

$$\gamma_1(x) = \frac{\int_{-\infty}^{\infty} \eta(u)\eta(u+x)\,du}{\int_{-\infty}^{\infty}[\eta(u)]^2\,du} \tag{5.159}$$

where $\eta(x)$ is the deviation in the scattering length density $\rho(x)$ from the mean.

For the ideal two-phase lamellar structure shown in Figure 5.20, $\langle\rho\rangle$ is equal to $\phi_a\rho_a+\phi_b\rho_b$ where ϕ_a and ϕ_b are the volume fractions of the two phases. The deviations $\eta(x)$ in the two phases are

$$\eta_a = \rho_a - \langle\rho\rangle = \phi_b\Delta\rho \tag{5.160}$$

and

$$\eta_b = \rho_b - \langle\rho\rangle = -\phi_a\Delta\rho \tag{5.161}$$

and the denominator of (5.159) is equal to $L\langle\eta^2\rangle = L(\Delta\rho)^2\phi_a\phi_b$, where L, equal to Nd, is the total length of the stack in the x direction. The correlation function calculated according to (5.159) for the ideal two-phase lamellar structure is shown in Figure 5.23, and is seen to consist of a series of triangles with their peaks separated from each other by the lamellar repeat period d. The central triangle at $x = 0$ arises

from self-correlation of every lamella, whereas those with peaks at $x = \pm d, \pm 2d$, etc. result from correlations between first neighbors, second neighbors, etc. When the number N of lamellae in the stack is sufficiently large so that the end effect is negligibly small, the triangular peaks near the central region are all essentially of the same height.

Certain features of the "self-correlation triangle" centered at the origin are of interest and can be interpreted directly in terms of the structural parameters. In view of the definition of the correlation function, Equation (5.159), we find the following:

$$\overline{\mathrm{OA}} = \gamma_1(0) = 1 \tag{5.162}$$

$$\overline{\mathrm{BD}} = d_\mathrm{a} = \phi_\mathrm{a} d \tag{5.163}$$

$$\overline{\mathrm{BO}} = \gamma_1(d_\mathrm{a}) = \phi_\mathrm{a}/\phi_\mathrm{b} \tag{5.164}$$

$$\overline{\mathrm{BA}} = 1/\phi_\mathrm{b} \tag{5.165}$$

$$\overline{\mathrm{OC}} = \phi_\mathrm{a}\phi_\mathrm{b} d \tag{5.166}$$

and

$$\text{slope of line } \overline{\mathrm{AD}} = -1/\phi_\mathrm{a}\phi_\mathrm{b} d \tag{5.167}$$

As imperfections are introduced into the structure, thereby distorting the density profile $\rho(x)$ from that of the strictly periodic system shown in Figure 5.20, the correlation function suffers a corresponding deterioration. The two curves shown in Figure 5.24 are the correlation functions calculated for the two model lamellar structures for which the intensity functions were plotted in Figure 5.22, that is, a model in which ϕ_a is equal to 0.3, and the lamellar thicknesses vary according to Gaussian probabilities with $\sigma_\mathrm{a} = 0.15 d_\mathrm{a}$ and $\sigma_\mathrm{b} = 0.15 d_\mathrm{b}$ (solid curve) and another with $\sigma_\mathrm{a} = 0.3 d_\mathrm{a}$ and $\sigma_\mathrm{b} = 0.3 d_\mathrm{b}$ (broken curve). With the second model, in particular, an appreciable degree of smearing of the second and third triangles

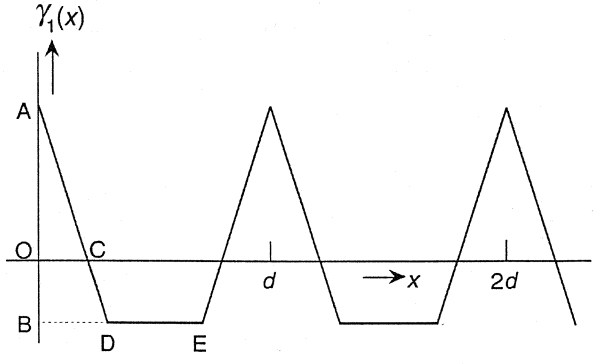

Figure 5.23 The correlation function $\gamma_1(x)$ calculated for the ideal two-phase lamellar structure given in Figure 5.20.

is clearly seen. The two curves shown here were calculated by taking the inverse Fourier transform of the intensity curves in Figure 5.22 in accordance with Equation (5.157), but a method of calculating the correlation function directly from the assumed structure of these variable thickness models has been described by Vonk and Kortleve.[36]

In Figure 5.24 we note that despite the substantial degrees of smearing, the "self-correlation triangle" retains its shape largely intact. This is because the self-correlation triangle results from the simple superposition of the self-correlations of every lamella, which differ from each other only by the width of the triangular base (BD in Figure 5.23), which is equal to d_a. This suggests the possibility (see Strobl and Schneider[37]) that some of the parameters characterizing the structure might be read off directly from the self-correlation triangle: (1) The initial slope of the triangle is equal to $-1/\bar{d}\phi_a\phi_b$ where $\bar{d}$ is the number-average of the repeat period d. (2) If the "baseline" (equivalent to DE in Figure 5.23) is clearly defined, as is the case with the solid curve in Figure 5.24, the distance from the baseline to the tip of the triangle gives $1/\phi_b$. (3) By combining these two measurements ϕ_a, $\phi_b(= 1 - \phi_a)$, and $\bar{d}$ can therefore be evaluated

Throughout the discussion of lamellar structures in Sections 5.5.1 and 5.5.2 it has been assumed that the transition between phase A and phase B is sharp and the scattering length density changes abruptly from ρ_a to ρ_b. When there exists a transition layer between the two phases, the most noticeable consequence is that around the very top of the self-correlation triangle the line is somewhat rounded, instead of being straight as in Figures 5.23 and 5.24. Even in the presence of such a

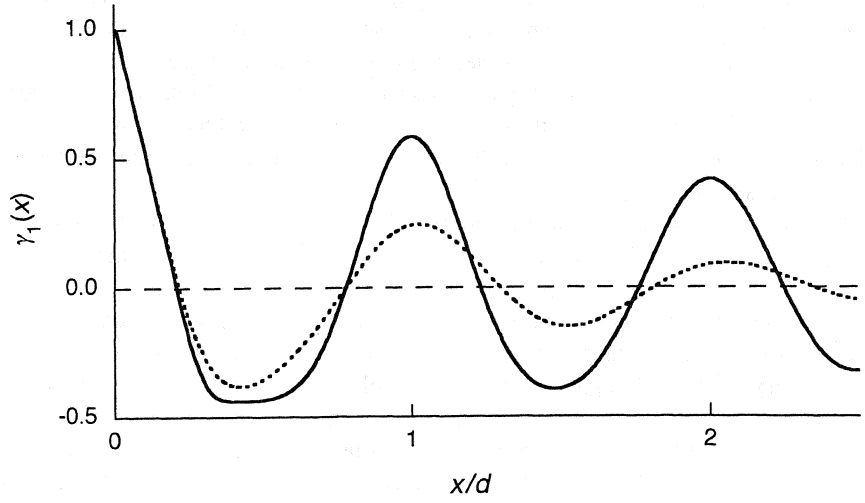

Figure 5.24 The correlation functions calculated for lamellar structures in which the thickness of the lamellae varies according to a Gaussian distribution function. The solid curve is based on the model that gave the solid intensity curve in Figure 5.22, and the broken curve here matches the broken curve in Figure 5.22.

transition layer, useful parameters characterizing the structure can still be obtained from examination of the self-correlation triangle, about which the readers are referred to the original literature.[37]

5.6 SLIT COLLIMATION AND DESMEARING

5.6.1 Slit Collimation

Although most of the considerations given in Chapter 2 on the experimental techniques are as valid for small-angle scattering measurements as for wide-angle studies, there is one additional aspect that is of particular importance to small-angle scattering, that is, the need to have an extremely well-collimated primary beam. To be able to measure the intensity of scattering at angles as small as, say, $\theta_{\min}$, the divergence of rays within the primary beam itself must be no greater than $\theta_{\min}$ (cf. Section 2.5.1). This means that if a pinhole collimation is used, the pinhole diameter must be extremely small (in comparison to the distance L_0 or L_1 in Figure 2.21). With small pinholes only a small fraction of the radiation emitted by the source is allowed to pass and illuminate the sample. The flux of the scattered beam is accordingly very weak, and a long measurement time is required for an acceptable level of precision in the obtained intensity data. To alleviate this difficulty, the use of a slit collimation has long been practiced in many small-angle studies, especially in those employing x-rays from a sealed tube. Among the slit collimating systems devised by many over the years, those due to Kratky[38–40] and to Bonse and Hart[41] are noted for their superior characteristics. A slit with a long opening, say, in the horizontal direction can be thought of as a series of pinholes tightly spaced along a straight, horizontal line. The total amount of the primary beam energy reaching the sample is obviously many times the energy from a single pinhole, and yet, if the measurement is made by moving the detector in the vertical direction, the smearing due to the divergence of the primary beam in the vertical direction is no worse than with a single pinhole. On the other hand, the spread of the beam in the horizontal direction introduces a distortion of another kind, which we may, however, be able to correct for, once the nature of such *slit smearing* is properly understood.

In the following discussion of the slit smearing effect[1,42] we assume the sample is isotropic. In Figure 5.25 the primary beam is collimated with a horizontal slit, so that, in the absence of a sample, the area illuminated in the detector plane is a thin, horizontal line, whose thickness in the vertical direction is here assumed to be negligibly small. The normalized intensity distribution along the horizontal direction in the primary beam is designated by $W(x)$. In place of the position coordinate x, it is actually more convenient to use the corresponding scattering vector defined by $t = (2\pi/\lambda)(x/D)$ as the independent variable, so that the beam intensity distribution is now written as $W(t)$. With a sample placed in the sample plane, the intensity of scattering is measured at the detector placed along the vertical axis OY and is recorded as $\tilde{I}(q)$, where $q = (2\pi/\lambda)(y/D)$. Designating the intensity that would have been obtained with a pinhole collimation by $I(q)$, we are seeking the relationship between $\tilde{I}(q)$ and $I(q)$.

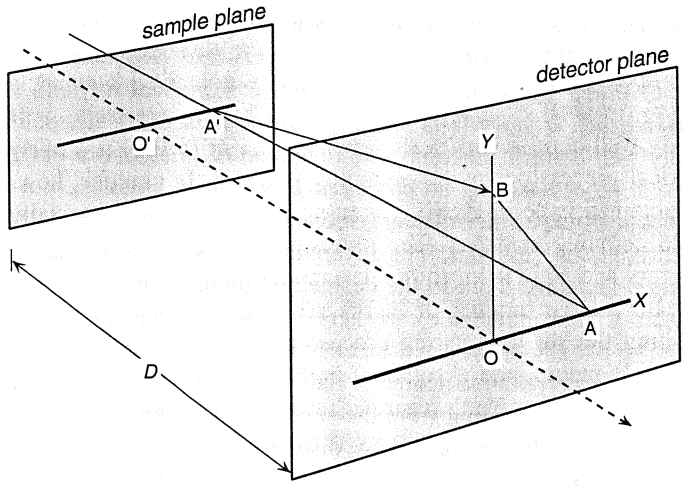

Figure 5.25 Geometry to illustrate the slit smearing effect.

Suppose that in Figure 5.25 the ray in the primary beam that strikes the sample at A′ reaches the detector plane at A. (The direction A′A is assumed, for the sake of simplicity, to be parallel to the beam center direction O′O.) We note that if OA = x and OB = y, AB is equal to $(x^2 + y^2)^{1/2}$. The contribution $\delta\tilde{I}(q)$ to the intensity measured at B by the ray scattered at A′ is then given by

$$\delta\tilde{I}(q) = W(t)I\left(\sqrt{q^2 + t^2}\right) dt \tag{5.168}$$

Integrating over the whole range of the primary beam intensity distribution $W(t)$, we find

$$\tilde{I}(q) = \int_{-\infty}^{\infty} W(t)I\left(\sqrt{q^2 + t^2}\right) dt \tag{5.169}$$

Stated in words, Equation (5.169) expresses that a ray in the primary beam, proceeding toward a position in the detector plane that corresponds to an angle t, is actually scattered at an angle $\sqrt{q^2 + t^2}$ before it is registered at the nominal scattering angle q, and that the smeared intensity $\tilde{I}(q)$ is the weighted sum of contributions from all such rays contained in the primary beam.

5.6.2 Slit Desmearing

In using a slit collimation the advantage gained from the increased flux is offset by the smearing of the observed intensity curve, as expressed by Equation (5.169), unless a way is found to remove the effect of smearing. The function $W(t)$, often called the *slit-length weighting function*, can be determined experimentally by measuring the intensity distribution along the slit length direction while the sample and the beam stop have been removed and the primary beam attenuated. It is also possible

to calculate $W(t)$ from knowledge of the detailed geometry of the slit collimating system and the camera.[43] When both $W(t)$ and $\tilde{I}(q)$ are thus available, $I(q)$ may be recovered by inverting Equation (5.169) through a numerical method, a process called *slit desmearing*. If both $W(t)$ and $\tilde{I}(q)$ are known precisely, or if both are mathematically well-defined functions, the inversion of (5.169) is a fairly straightforward numerical process posing no particular problem. In practice, however, $W(t)$ and $\tilde{I}(q)$ obtained experimentally are subject to errors and especially to uncertainties due to counting statistics. The inversion process greatly magnifies these statistical errors and adds them to the desmeared intensity function $I(q)$ obtained. Over the years a large number of workers[44–56] devised and published algorithms for performing the slit desmearing process numerically, and all these different methods implicitly incorporate a degree of data smoothing as part of their desmearing processes. As a result, starting from the same set of experimental data $W(t)$ and $\tilde{I}(q)$, desmearing may be performed by different methods and lead to desmeared intensity curves $I(q)$ that sometimes show significant differences from each other.

5.6.3 Infinite Slit Approximation

A way to avoid the possibility of an erroneous interpretation of data due to amplification of errors is to refrain altogether from desmearing the observed intensity $\tilde{I}(q)$ and, instead, to analyze it directly by means of theoretical expressions that have themselves been modified to take the collimation smearing effect into account. Such an alternative approach is especially worthwhile when the slit in the collimating system can be approximated by an "infinite slit," since then the various theoretical expressions acquire particularly simple forms[20] permitting convenient data analysis. The *infinite slit approximation* is valid when the intensity of scattering due to the portions of the primary beam in the end regions of the slit makes a negligibly small contribution to the overall $\tilde{I}(q)$ at any q of interest. More precisely, it is valid provided that the slit weighting function $W(t)$ remains finite and essentially constant over a relatively wide range of t between $-t_{\max}$ and $t_{\max}$, and at the same time that the intensity function $I(q)$ decays at large q sufficiently rapidly so that $I(t > t_{\max})$ makes a negligibly small contribution to $\tilde{I}(q)$ in the q range of interest. Under the infinite slit approximation Equation (5.169) is simplified to

$$\tilde{I}(q) = W_q \int_{-\infty}^{\infty} I\left(\sqrt{q^2 + t^2}\right) dt \tag{5.170}$$

where W_q is the constant value of $W(t)$ independent of t .

The Guinier law, as given by Equation (5.34), allows evaluation of the radius of gyration R_g from the slope of the logarithm of $I(q)$ plotted against q^2. Substituting (5.34) into (5.170) and performing the integration, we obtain

$$\begin{aligned} \tilde{I}(q) &= \rho_0^2 v^2 2 W_q \int_0^{\infty} \exp\left[-\tfrac{1}{3}(q^2 + t^2) R_g^2\right] dt \\ &= \rho_0^2 v^2 \frac{\sqrt{3\pi}}{R_g} W_q \exp\left(-\tfrac{1}{3} q^2 R_g^2\right) \end{aligned} \tag{5.171}$$

which shows that R_g can still be evaluated from the slope of $\tilde{I}(q)$ plotted against q^2, without the need to go through the process of desmearing $\tilde{I}(q)$.

The Porod law, given in Equation (5.71), shows the asymptotic behavior of $I(q)$ at large q. A similar expression can be derived in terms of $\tilde{I}(q)$. Thus, substituting (5.71) into (5.170) gives

$$\begin{aligned}\tilde{I}(q) &\rightarrow 2\pi(\Delta\rho)^2 S\, 2W_q \int_0^\infty \frac{dt}{(q^2+t^2)^2} \\ &= \frac{\pi(\Delta\rho)^2 S\, W_q}{q^3}\end{aligned} \tag{5.172}$$

showing that $\tilde{I}(q)$ decays as q^{-3} at large q , in contrast to $I(q)$ decaying as q^{-4}. To be able to evaluate the interfacial area S, both $\tilde{I}(q)$ and W_q must be determined in absolute units. In Equation (5.86) it was shown that if $I(q)$ is not known in absolute units, taking the ratio of $I(q)$ to the invariant Q permits evaluation of the specific interfacial area S/V. A similar recourse is also available in the case of the slit smeared intensity. To see this, let us first examine how the invariant Q, defined by (1.85) or (1.86) (see also Section 5.3.1), can be evaluated directly from the infinite-slit-smeared intensity . For this purpose, first the following integral must be evaluated.

$$\int_0^\infty q\tilde{I}(q)\, dq = 2W_q \int_0^\infty \int_0^\infty q I\left(\sqrt{q^2+t^2}\right)\, dt\, dq \tag{5.173}$$

Regarding q and t as Cartesian coordinates in two-dimensional space, and making a change of variables to polar coordinates R and Φ, where $q = R\, \cos\Phi$, $t = R\, \sin\Phi$, and $dtdq = R\, dR\, d\Phi$, we can transform (5.173) into

$$\begin{aligned}\int_0^\infty q\tilde{I}(q)\, dq &= 2W_q \int_0^\infty \int_0^{\pi/2} R\, \cos\Phi\, I(R) R\, d\Phi\, dR \\ &= 2W_q \int_0^\infty R^2 I(R)\, dR \\ &= 2W_q \int_0^\infty q^2 I(q)\, dq \\ &= 4\pi^2 W_q Q\end{aligned} \tag{5.174}$$

where in the last equality the definition of Q given by (1.86) is utilized. Dividing (5.172) by (5.174), and recognizing that Q for an ideal two-phase system is equal to $V(\Delta\rho)^2\phi_1\phi_2$, as given in (5.70), we find

$$\frac{\lim_{q\to\infty} q^3\tilde{I}(q)}{\int_0^\infty q\tilde{I}(q)\, dq} = \frac{1}{4\pi}\frac{S}{V}\phi_1\phi_2 \tag{5.175}$$

which allows determination of S/V, even when $\tilde{I}(q)$ is available only in arbitrary units, provided the volume fractions ϕ_1 and ϕ_2 of the two phases are known.

FURTHER READING

1. Guinier, A., and Fournet, G., *Small Angle Scattering of X-Rays*, Wiley, New York, 1955.
2. Brumberger, H., *Small-Angle X-Ray Scattering*, Gordon and Breach, New York, 1967.
3. Glatter, O., and Kratky, O., *Small Angle X-Ray Scattering*, Academic Press, New York, 1982.
4. Feigin, L. A., and Svergun, D. I., *Structure Analysis by Small-Angle X-Ray and Neutron Scattering*, Plenum Press, New York, 1987.
5. Baltá-Calleja, F. J., and Vonk, C. G., *X-Ray Scattering of Synthetic Polymers*, Elsevier, New York, 1989, Chapter 7.
6. Lindner, P., and Zemb, Th., *Neutron, X-Ray and Light Scattering*, North-Holland, New York, 1991.
7. Higgins, J. S., and Benoît, H. C., *Polymers and Neutron Scattering*, Clarendon Press, Oxford, 1994.
8. Brumberger, H., *Modern Aspects of Small-Angle Scattering*, Kluwer Academic Publishers, Dordrecht, 1995.

REFERENCES

9. Flory, P. J., *Principles of Polymer Chemistry*, Cornell University Press, Ithaca, New York, 1953, p. 428.
10. Neugebauer, T., *Ann. Phys.* **42**, 509 (1943).
11. Kratky, O., and Porod, G., *J. Colloid Interface Sci.* **4**, 35 (1949).
12. Debye, P., *J. Phys. Colloid Chem.* **51**, 18 (1947).
13. Kratky, O., and Porod, G., *Rec. Trav. Chim.* **68**, 1106 (1949).
14. Flory, P. J., *Statistical Mechanics of Chain Molecules*, Wiley, New York, 1969, reprinted by Hanser Publishers, New York, 1989, p. 401.
15. Kirste, R. G., and Oberthür, R. C., in *Small Angle X-ray Scattering*, O. Glatter and O. Kratky, Eds., Academic Press, New York, 1982, p. 387.
16. Yoon, D. Y., and Flory, P. J., *Macromolecules* **9**, 294 (1976).
17. Zimm, B. H., *J. Chem. Phys.* **16**, 1093 (1948).
18. Flory, P. J., and Bueche, A. M., *J. Polymer Sci.* **27**, 219 (1958).
19. Debye, P., and Bueche, A. M., *J. Appl. Phys.* **20**, 518 (1949).
20. Porod, G., *Kolloid-Z.* **124**, 83 (1951).
21. Wu, W.-L., *Polymer* **23**, 1907 (1982).
22. Roe, R. J., and Gieniewski, C., *Macromolecules* **6**, 212 (1973).
23. Debye, P., Anderson, H. R., Jr., and Brumberger, H., *J. Appl. Phys.* **28**, 679 (1957).
24. Filipovich, V. N., *Soviet Phys.—Tech. Phys.* **1**, 391 (1956).
25. Ruland, W., *J. Appl. Crystallogr.* **4**, 70 (1971).
26. Roe, R. J., Fishkis, M., and Chang, J. C., *Macromolecules* **14**, 1091 (1981).
27. Mandelbrot, B. B., *The Fractal Geometry of Nature*, Freeman, San Fransisco, 1983.
28. Liu, S. H., *Solid State Physics* **39**, 207 (1986).
29. Martin, J. E., and Hurd, A. J., *J. Appl. Crystallogr.* **20**, 61 (1987).
30. Schmidt, P. W., in *The Fractal Approach to Heterogeneous Chemistry*, D. Avnir, Ed., Wiley, New York, 1989, p. 67.
31. Schaefer, D. W., Martin, J. E., Wiltzius, P., and Cannell, D. S., *Phys. Rev. Lett.* **52**, 2371 (1984).

32. Wong, P.-Z., and Bray, A. J., *J. Appl. Crystallogr.* **21**, 786 (1988).
33. Bale, H. D., and Schmidt, P. W., *Phys. Rev. Lett.* **53**, 596 (1984).
34. Bates, F. S., Cohen, R. E., and Berney, C. V., *Macromolecules* **15**, 589 (1982).
35. Hosemann, R., and Bagchi, S. N., *Direct Analysis of Diffraction by Matter*, North-Holland, Amsterdam, 1962, p. 410.
36. Vonk, C. G., and Kortleve, G., *Kolloid-Z. Z. Polymer* **220**, 19 (1967).
37. Strobl, G. R., and Schneider, M., *J. Polymer Sci.: Polymer Phys. Ed.* **18**, 1343 (1980).
38. Kratky, O., *Z. Elektrochem.* **58**, 49 (1954).
39. Kratky, O., *Z. Elektrochem.* **62**, 66 (1958).
40. Kratky, O., in *Small Angle X-ray Scattering,* O. Glatter and O. Kratky, Eds., Academic Press, New York 1982, Chapter 3.
41. Bonse, U., and Hart, M., *Appl. Phys. Lett.* **7**, 238 (1968).
42. Guinier, A., and Fournet, G., *J. Phys. Radium* **8**, 345 (1947).
43. Hendricks, R. W., and Schmidt, P. W., *Acta Phys. Austr.* **26**, 97 (1967); **37**, 20 (1973).
44. Lake, J. A., *Acta Crystallogr.* **23**, 191 (1967).
45. Strobl, G. R., *Acta Crystallogr.* **A26**, 367 (1970).
46. Schelten, J., and Hossfeld, F., *J. Appl. Crystallogr.* **4**, 210 (1971).
47. Vonk, C. G., *J. Appl. Crystallogr.* **4**, 340 (1971).
48. Glatter, O., *J. Appl. Crystallogr.* **7**, 147 (1974).
49. Sŏler, J., and Baldrian, J., *J. Appl. Crystallogr.* **7**, 398 (1974).
50. Deutsch, M., and Luban, M., *J. Appl. Crystallogr.* **11**, 87, 98 (1978).
51. Schmidt, P. W., and Fedorov, B. A., *J. Appl. Crystallogr.* **11**, 411 (1978).
52. Moor, P. B., *J. Appl. Crystallogr.* **13**, 168 (1980).
53. Schmidt, P. W., *J. Appl. Crystallogr.* **21**, 602 (1988).
54. Svergun, D. I., *J. Appl. Crystallogr.* **24**, 485 (1991).
55. Gerber, T., Walter, G., and Schmidt, P. W., *J. Appl. Crystallogr.* **24**, 278 (1991).
56. Singh, M. A., Ghosh, S. S., and Shannon, R. F. , Jr., *J. Appl. Crystallogr.* **26**, 787 (1993).

Polymer Blends, Block Copolymers, and Deuterium Labeling

6

6.1 POLYMER BLENDS

6.1.1 Zero-Angle Scattering

In the discussion of scattering from amorphous polymers in Chapter 4, we confined our attention to a single-component material. We now consider scattering from an amorphous, homogeneous, two-component system, such as a (miscible) polymer blend, a polymer solution, or a solution of two liquids in general. In the case of a single-component material, it is the presence of density inhomogeneity that gives rise to scattering. As discussed in Chapter 4, the density inhomogeneity on the local scale can be described in terms of the radial distribution function $g(\boldsymbol{r})$, and on the larger length scale in terms of the so-called thermal density fluctuation, whose magnitude depends on the compressibility β_T. In the case of a two-component material, the inhomogeneity in it that gives rise to scattering is due not only to density fluctuations but also to concentration fluctuations that are present at the same time. The scattering due to the latter is, in fact, usually much stronger and dominating.

According to Equation (4.43), for a single-component liquid the zero-angle scattering intensity $I(0)$, that is, the intensity of scattering $I(q)$ extrapolated to $q \to 0$, is proportional to the mean square fluctuation $\langle(\Delta N_v)^2\rangle$ in the number N_v of atoms present in a macroscopic volume v. In an equilibrium liquid (or an amorphous polymer above T_g) the mean square fluctuation $\langle(\Delta N_v)^2\rangle$ is related to the isothermal compressibility β_T of the liquid according to (4.32), so that $I(0)$ is given by

$$I(0) = Nb^2 \langle n \rangle kT\beta_T \tag{4.45}$$

where $\langle n \rangle = N/V$ is the number density of the atoms. With a two-component system, $I(0)$ reflects both the density *and* concentration fluctuations that are present on a macroscopic scale. The two effects are additive. The component of $I(0)$ due to the concentration fluctuations can therefore be obtained from the observed $I(0)$ by subtracting the density fluctuation contribution, which can be estimated very approximately, for example, as the weighted average of $I(0)$s measured with the individual pure components. The density fluctuation component is usually the much weaker of the two and is often simply ignored. An expression equivalent to (4.45) but describing the effect of the concentration fluctuations then relates $I(0)$ to the

thermodynamic forces that give rise to the concentration fluctuations. Deriving such an expression from first principles, however, involves considerations beyond the scope of the present book. Instead we here take the heuristic approach of "translating" expression (4.45) into the language of concentration fluctuations. Readers who are interested in a more rigorous derivation of the expression, Equation (6.6) given below, are advised to consult other textbooks such as Higgins and Benoît[3] and Doi.[4]

We call component 1 the solvent and component 2 the solute throughout this chapter. By "concentration fluctuation" we mean the fluctuation in the number N_2 of the solute molecules in a system of total volume V. We therefore replace N in (4.45) by N_2, and similarly $\langle n \rangle = N/V$ by N_2/V. The scattering length b of the atom (or molecule) in (4.45) is now replaced by the excess of the scattering length of the solute molecule above the solvent background. The scattering length of a solute molecule is given by b_2, the sum of the scattering lengths of all the atoms in the molecule. The excess above the solvent background is then

$$\Delta b = b_2 - b_1 \tag{6.1}$$

where b_1 is the sum of the scattering lengths of the solvent molecules in a volume that is equal to the solute molecular volume v_2. The compressibility β_T in (4.45) is $-(1/V)(\partial V/\partial p)_T$, but the pressure p is now replaced by the osmotic pressure Π. Expressing the concentration in terms of the volume fraction ϕ_2 of the solute:

$$\phi_2 = \frac{N_2 v_2}{V} \tag{6.2}$$

we can write

$$\frac{\partial \Pi}{\partial V} = \frac{\partial \Pi}{\partial \phi_2}\frac{\partial \phi_2}{\partial V} = \frac{\partial \Pi}{\partial \phi_2}\left(-\frac{N_2 v_2}{V^2}\right) \tag{6.3}$$

Putting all these replacements together in (4.45) we obtain

$$I(0) = V\left(\frac{\Delta b}{v_2}\right)^2 kT\phi_2 \Big/ \frac{\partial \Pi}{\partial \phi_2} \tag{6.4}$$

We recall that Δb is the difference between the scattering length of a solute molecule and the equivalent volume of the solvent. Therefore the ratio $\Delta b/v_2$ is equal to the difference $\Delta\rho$ in the scattering length density ρ of the solute and solvent

$$\frac{\Delta b}{v_2} = \Delta\rho = \rho_2 - \rho_1 \tag{6.5}$$

Equation (6.4) can therefore be rewritten as

$$\frac{I(0)}{V(\Delta\rho)^2} = kT\phi_2 \Big/ \frac{\partial \Pi}{\partial \phi_2} \tag{6.6}$$

which is the equivalent of (4.45) and gives the contribution to the extrapolated zero-angle intensity $I(0)$ by the concentration fluctuations in a two-component system.

6.1.1.1 Dilute Polymer Solution

For a dilute polymer solution it is customary to express the concentration in terms of c (mass of solute per unit volume) defined as

$$c = \frac{N_2 M_2}{V} = \tilde{\rho}_2 \phi_2 \tag{6.7}$$

where M_2 is the molecular mass and $\tilde{\rho}_2$ is the mass density of the solute. Equation (6.6) then becomes

$$\frac{I(0)}{V(\Delta\rho/\tilde{\rho}_2)^2} = kTc \Big/ \frac{\partial \Pi}{\partial c} \tag{6.8}$$

From the theory of dilute polymer solution[5] it is known that the osmotic pressure can be expressed as a function of concentration in a virial expansion

$$\frac{\Pi}{kT} = \frac{1}{M_2} c + A_2 c^2 + A_3 c^3 + \cdots \tag{6.9}$$

where A_2, A_3, etc., are the virial coefficients. Substitution of (6.9) into (6.8) gives

$$\frac{V(\Delta\rho/\tilde{\rho}_2)^2 c}{I(0)} = \frac{1}{M_2} + 2A_2 c + 3A_3 c^2 + \cdots \tag{6.10}$$

which constitutes the fundamental theoretical basis for the method of determining the molecular weight M_2 of a polymer and its second virial coefficient A_2 in a solution from measurement of the intensity of scattering (of light, in particular) from a dilute solution.

6.1.1.2 Polymer Blend

To be able to measure the osmotic pressure Π, a semipermeable membrane that permits passage of the solvent molecules but not the solute molecules is needed. This can, in practice, be realized only when there is a large disparity between the sizes of the solute and solvent molecules, as in a solution of a polymer in a small-molecule solvent. However, the existence of osmotic pressure can be envisioned, at least mentally, with any kind of solution, such as a solution of two small-molecule liquids or a miscible blend of two polymers. Equation (6.6) is thus valid for any two-component (amorphous) system, as long as it is in equilibrium and classical thermodynamics is applicable to it. For applications to these general cases, it is more convenient if Equation (6.6) is reformulated in terms of the free energy of mixing and no explicit reference to osmotic pressure is made in it.

The osmotic pressure is related to the chemical potential μ_1 of the solvent in the solution by

$$-\Pi v_1 = \Delta\mu_1 = \mu_1 - \mu_1^\circ \tag{6.11}$$

where v_1 is the molecular volume of the solvent and μ_1° is the chemical potential of the pure solvent. The chemical potential change $\Delta\mu_1$ of the solvent due to the presence of the solute is related to the Gibb's free energy of mixing $G_m(N_1, N_2, p, T)$ by

$$\Delta\mu_1 = \left(\frac{\partial G_m}{\partial N_1}\right)_{N_2,p,T} \tag{6.12}$$

The free energy of mixing $G_m(N_1,N_2,p,T)$ is the Gibb's free energy $G(N_1,N_2,p,T)$ of the mixture (containing N_1 and N_2 molecules, respectively, of the two components) from which the pure component free energies $G_1(N_1,p,T)$ and $G_2(N_2,p,T)$ have been subtracted. It is often more convenient to use, instead of G_m, the *free energy density* of mixing defined as

$$g_m \equiv G_m/V \tag{6.13}$$

Whereas the free energy of mixing G_m is an extensive property and is a function of N_1 and N_2 (and of course p and T), the free energy density of mixing g_m is an intensive property depending only on the composition of the mixture besides p and T. Equation (6.12) can then be written as

$$\begin{aligned}\Delta\mu_1 &= V\left(\frac{\partial g_m}{\partial N_1}\right)_{N_2,p,T} + \left(\frac{\partial V}{\partial N_1}\right)_{N_2,p,T} g_m \\ &= V\left(\frac{\partial g_m}{\partial N_1}\right)_{N_2,p,T} + v_1 g_m\end{aligned} \tag{6.14}$$

where in the last equality any possible small difference between the molecular volume v_1 and the partial molecular volume has been ignored. Noting that

$$\begin{aligned}\left(\frac{\partial g_m}{\partial N_1}\right)_{N_2,p,T} &= \left(\frac{\partial g_m}{\partial \phi_1}\right)_{p,T}\left(\frac{\partial \phi_1}{\partial N_1}\right)_{N_2,p,T} \\ &= \left(\frac{\partial g_m}{\partial \phi_1}\right)_{p,T}\frac{\phi_1\phi_2}{N_1}\end{aligned} \tag{6.15}$$

we can rewrite Equation (6.14) as

$$\begin{aligned}\Delta\mu_1 &= v_1\left[g_m + \phi_2\left(\frac{\partial g_m}{\partial \phi_1}\right)_{p,T}\right] \\ &= v_1\left[g_m - \phi_2\left(\frac{\partial g_m}{\partial \phi_2}\right)_{p,T}\right]\end{aligned} \tag{6.16}$$

In view of (6.11), we then have

$$\left(\frac{\partial \Pi}{\partial \phi_2}\right)_{p,T} = \phi_2\left(\frac{\partial^2 g_m}{\partial \phi_2^2}\right)_{p,T} \tag{6.17}$$

This is the desired expression relating the osmotic pressure to the free energy of mixing. Equation (6.6) for the extrapolated zero-angle scattering intensity is then written as

$$\frac{I(0)}{V(\Delta\rho)^2} = kT\Big/\frac{\partial^2 g_m}{\partial \phi_2^2} \tag{6.18}$$

Since $d\phi_1 = -d\phi_2$, (6.18) can also be written as

$$\frac{I(0)}{V(\Delta\rho)^2} = kT \Big/ \frac{\partial^2 g_m}{\partial \phi_1^2} \tag{6.19}$$

showing the symmetrical role the two components play in the expression for $I(0)$. Equation (6.18) illustrates the close relationship between the scattering and the thermodynamic properties of the mixture. The zero-angle intensity $I(0)$ is inversely related to the curvature of the plot of free energy density g_m against composition ϕ_1 or ϕ_2, and if $I(0)$ is measured as a function of composition, it is possible, at least in principle, to integrate the result and determine the free energy of mixing.

Figure 6.1a shows an example of the free energy density of mixing, g_m, plotted as a function of ϕ_2, for a mixture that exhibits a miscibility gap. The relationship between the shape of such a g_m–ϕ_2 curve and the miscibility behavior is discussed in most textbooks on polymers and polymer blends. The following is a very brief description of the significance of the binodal and spinodal points in phase diagrams.

The whole composition range, $\phi_2 = 0 \sim 1$, is subdivided into five sections by the binodal compositions ϕ_2^A and ϕ_2^B and the spinodal compositions ϕ_2^C and ϕ_2^D. The binodal points A and B are defined as points of common tangent to the free energy density curve. For compositions between 0 and ϕ_2^A and between ϕ_2^B and 1, the free energy of the mixture increases whenever it separates into two phases of

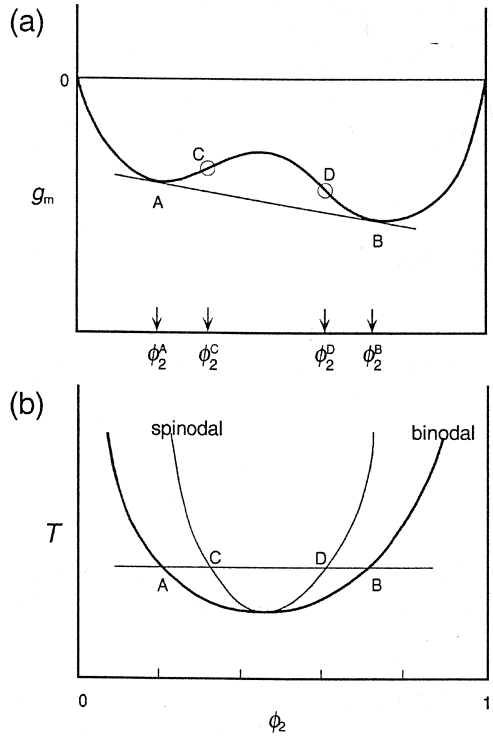

Figure 6.1 (a) Free energy density of mixing, g_m, plotted as a function of ϕ_2. A and B, points of common tangent to the curve, give the binodal compositions. C and D, points of inflection, give the spinodal compositions. (b) Phase diagram giving the varations in the binodal and spinodal compositions with temperature. The example shown illustrates a system exhibiting a lower critical solution temperature behavior.

any composition, and therefore the mixture is stable against phase separation. For compositions between ϕ_2^A and ϕ_2^B the free energy of the system is rendered lowest if the mixture separates into two phases of compositions ϕ^A and ϕ_2^B, respectively. The inflection points C and D, at which the derivative $\partial^2 g_m/\partial\phi_2^2$ vanishes, mark the spinodal points. Between points A and C and between D and B the free energy curve is concave upward (i.e., $\partial^2 g_m/\partial\phi_2^2 > 0$), and the mixture is stable against phase separation into two phases of small composition differences. The mixture in these composition ranges is therefore said to be metastable, and the phase separation can proceed only if it is seeded by nuclei having a composition sufficiently different from the original composition of the mixture. In the region between ϕ_2^C and ϕ_2^D the mixture is unstable against phase separation into two phases of any compositions, and composition fluctuations induced by thermal motions will spontaneously grow. The spinodal point is recognized in scattering measurements as the point at which the zero-angle scattering intensity diverges.

If the binodal and spinodal points are determined at various temperatures and are plotted together, a phase diagram such as the one shown in Figure 6.1b may result. The temperature at which the binodal and spinodal curves merge together is the critical temperature. The phase diagram shown illustrates a case in which the miscibility gap occurs at temperatures above the critical temperature, and the system is said to exhibit a lower critical solution temperature (LCST) behavior. A system, on the other hand, may display an upper critical solution temperature (UCST) behavior, in which the miscibility gap occurs below the critical temperature.

As an example of experimental studies in which Equation (6.18) is used, we quote the neutron scattering study by Schwahn *et al.*[6] of three samples of a blend of poly(vinyl methyl ether) and deuterated polystyrene. In Figure 6.2 the reciprocal of the extrapolated zero-angle intensity $I(0)$ obtained at different temperatures is plotted against $1/T$. The extrapolation to obtain $I(0)$ is accomplished by plotting, against q^2, the inverse of $I(q)$ observed in the small q region, as is illustrated in Figure 6.3. More will be said in Section 6.1.2.3 about such a linear dependence of $I(q)^{-1}$ on q^2. The blend is miscible at low temperatures but phase separates at higher temperatures, exhibiting a LCST behavior. For a mixture of fixed composition the observed $I(0)$ accordingly increases with increasing temperature. The spinodal temperature T_s is identified as the temperature at which $I(0)^{-1}$ eventually vanishes. To see the significance of the linear dependence of $I(0)^{-1}$ on T^{-1} exhibited in Figure 6.2, we need to examine how the free energy of mixing itself depends on temperature, as discussed in Section 6.1.2.3.

6.1.1.3 Flory–Huggins Free Energy of Mixing

The free energy of mixing N_1 molecules of a polymer with N_2 molecules of a solvent is usually written in the following form that is due to Flory and Huggins[5]:

$$\frac{G_m(N_1, N_2, p, T)}{kT} = N_1 \ln\phi_2 + N_2 \ln\phi_2 + \chi N_1\phi_2 \tag{6.20}$$

In the original derivation based on a lattice model, the quantity $kT\chi$ was meant to represent the enthalpy of interaction between a solvent molecule and a segment of the polymer. In this lattice model approximation the Flory interaction parameter χ is thus

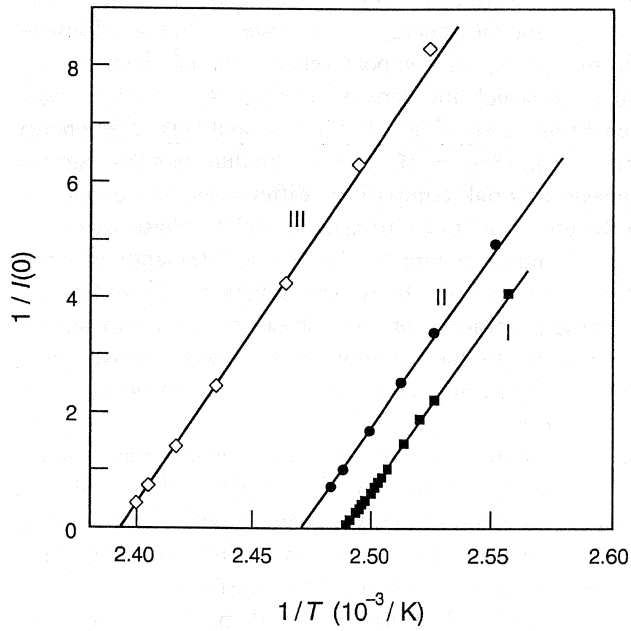

Figure 6.2 Plot of $I(0)^{-1}$ against $1/T$, where the extrapolated zero-angle intensity $I(0)$ was obtained by neutron scattering with blends of poly(vinyl methyl ether) and deuterated polystyrene. The molecular weight of poly(vinyl methyl ether) is 64.3×10^3, and the molecular weight and volume fraction of the deuterated polystyrene are, respectively, 783×10^3 and 0.13 for sample I, 379×10^3 and 0.13 for sample II, and 232×10^3 and 0.20 for sample III. (From Schwahn *et al.*[6])

expected to be proportional to $1/T$. The value of the χ parameter is determined, in practice, by comparing experimental measurements against expressions derived from (6.20). The consequence of this is that the term $kT\chi N_1\phi_2$ ends up including the effect of all the shortcomings of (6.20), that is, it includes not only the interaction enthalpy but also any entropic effect not adequately accounted for by the combinatory entropy, the first two terms on the right of (6.20). The values of χ determined experimentally thus seldom vary with temperature simply as $1/T$.

From (6.20) the free energy density of mixing is written as

$$\frac{g_m(\phi_2, p, T)}{kT} = \frac{1}{v_1}\phi_1 \ln\phi_1 + \frac{1}{v_2}\phi_2 \ln\phi_2 + \frac{\chi}{v_1}\phi_1\phi_2 \tag{6.21}$$

For a blend of two polymers (6.21) is generalized to

$$\frac{g_m(\phi_2, p, T)}{kT} = \frac{1}{v_1}\phi_1 \ln\phi_1 + \frac{1}{v_2}\phi_2 \ln\phi_2 + \frac{\chi}{v_u}\phi_1\phi_2 \tag{6.22}$$

where v_1 and v_2 are the molecular volumes of polymers 1 and 2, and v_u is the "lattice volume" or the volume of a "segment." In the original formulation by Flory for a polymer solution, v_u is equated to the volume v_1 of the solvent molecule. For a blend

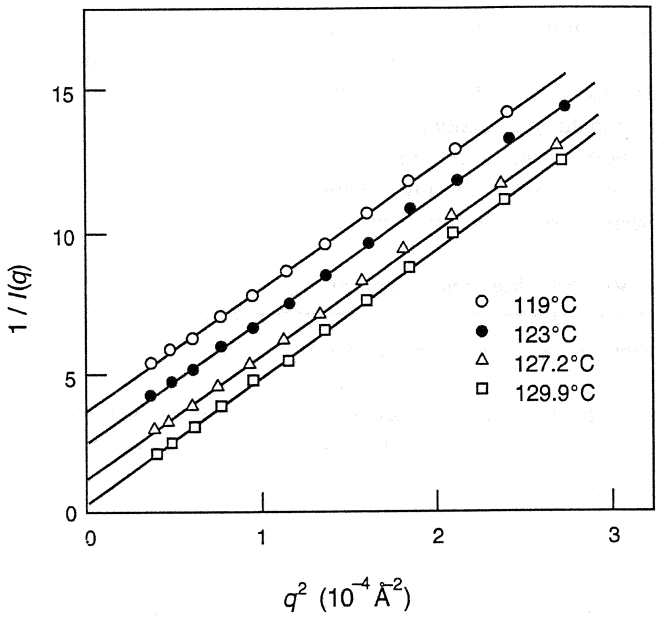

Figure 6.3 Results shown here illustrate how $I(0)$ values, plotted in Figure 6.2, were obtained by linear extrapolation of the inverse of the observed intensity, $I(q)^{-1}$, against q^2. The data are for sample II mentioned in Figure 6.2. (From Schwahn *et al.*[6])

of two polymers, v_u is commonly taken to be equal to the monomeric volume of one of the polymers, although v_u can actually be taken arbitrarily without invalidating Equation (6.22). However, it is important to note that the numerical value of χ must be proportional to the size of the segment assumed, and only the ratio χ/v_u is physically meaningful and assumes a unique value, under a given condition, for a given pair of polymers being considered.

By taking the second derivative of g_m with respect to ϕ_2 as indicated by (6.18), we find

$$\frac{V(\Delta\rho)^2}{I(0)} = \frac{1}{v_1}\frac{1}{\phi_1} + \frac{1}{v_2}\frac{1}{\phi_2} - 2\frac{\chi}{v_u} \tag{6.23}$$

Thus in the plot of $I(0)^{-1}$ against T or $1/T$, as in Figure 6.2, it is in fact the temperature dependence of the χ parameter that is being explored. In the example shown in Figure 6.2 it is seen that χ happens to vary as $A + B/T$, with A and B representing the entropic and enthalpic effects, respectively.

6.1.2 Finite-Angle Scattering

The intensity of zero-angle scattering, discussed in the previous section, reflects the concentration fluctuations present in the system on a macroscopic scale and is directly related to its thermodynamic properties, such as the free energy of mixing.

The intensity of scattering at finite q, on the other hand, reflects the concentration fluctuations that exist on a more local scale. In the case of a single-component system, as discussed in Section 4.1, the finite-angle intensity data can be converted, through an inverse Fourier transform, to a radial distribution function $g(\boldsymbol{r})$. With a two-component system a comparable general procedure is not available, and information on the structure is derived usually by comparing the observed intensity data, on the q plane, with expressions derived from theoretical models.

6.1.2.1 Some General Relationships and Assumptions

Before proceeding further, it is useful at this point to introduce some general relationships, notations, and assumptions to be used in the rest of the chapter.

Segment. As discussed in Chapter 1, the intensity of scattering depends on the positions of all the atoms or atomic nuclei in the system. The amplitude $A(\boldsymbol{q})$ of scattering is specified completely by

$$A(\boldsymbol{q}) = \sum_j b_j e^{-i\boldsymbol{q}\boldsymbol{r}_j} \tag{1.71}$$

where $\boldsymbol{r}_j$ is the position of the jth atom and b_j is its scattering length. In small-angle scattering studies, however, we generally seek less detailed information about the structure. Thus, in the study of polymer blends, we are concerned with the overall shape of the polymer molecules rather than the details of the positions of individual atoms. It is then sufficient to regard the polymer molecule simply as a connected sequence of identical segments, each acting as a single scattering center without any internal detail. The segment is often chosen to coincide with the chemical monomeric unit or with the so-called Kuhn segment of the polymer. A degree of arbitrariness is, however, allowed in the choice of the size of the segment, as will be seen shortly. A polymer molecule then consists of Z such segments, where $Z = v/v_u$, v being the volume of the polymer molecule and v_u the volume of the segment. The scattering power of the segment as a single scattering center is represented by the *segmental scattering length* $\hat{b}$, which is the sum of the scattering lengths of all the atoms belonging to it. The scattering amplitude in (1.71) is then approximated by

$$A(\boldsymbol{q}) = \sum_m \hat{b}_m e^{-i\boldsymbol{q}\boldsymbol{r}_m} \tag{6.24}$$

where $\boldsymbol{r}_m$ stands for the position of the center of the mth segment. The approximation amounts to saying that

$$\sum_{\substack{\text{atoms in the} \\ m\text{th segment}}} b_j e^{-i\boldsymbol{q}\boldsymbol{r}_j} = \left(\sum_{\substack{\text{atoms in the} \\ m\text{th segment}}} b_j \right) e^{-i\boldsymbol{q}\boldsymbol{r}_m} \equiv \hat{b}_m e^{-i\boldsymbol{q}\boldsymbol{r}_m} \tag{6.25}$$

Such an approximation is allowed as long as the intensity data of interest is confined to regions of small q. To see this in more detail we rewrite (6.25) as follows:

$$\sum_j b_j e^{-i\boldsymbol{q}\boldsymbol{r}_j} = e^{-i\boldsymbol{q}\boldsymbol{r}_m} \sum_j b_j e^{-i\boldsymbol{q}(\boldsymbol{r}_j - \boldsymbol{r}_m)}$$

$$= e^{-i\boldsymbol{q}\boldsymbol{r}_m} \sum_j b_j \left[1 - i\boldsymbol{q}(\boldsymbol{r}_j - \boldsymbol{r}_m) - \frac{1}{2}q^2(\boldsymbol{r}_j - \boldsymbol{r}_m)^2 + \cdots\right] \tag{6.26}$$

$$= e^{-i\boldsymbol{q}\boldsymbol{r}_m} \left(\sum_j b_j\right) \left[1 - i\boldsymbol{q}\frac{\sum_j b_j(\boldsymbol{r}_j - \boldsymbol{r}_m)}{\sum_j b_j} - \frac{1}{2}q^2 \frac{\sum_j b_j(\boldsymbol{r}_j - \boldsymbol{r}_m)^2}{\sum_j b_j} + \cdots\right]$$

where the summation with respect to j is over all the atoms in the mth segment. In the last member of (6.26) the second term within the bracket is identically equal to zero, if the segment center $\boldsymbol{r}_m$ is defined as

$$\boldsymbol{r}_m = \frac{\sum b_j \boldsymbol{r}_j}{\sum b_j} \tag{6.27}$$

that is, if it is identified as the center of mass of scattering lengths in the segment. The third and higher-order terms in the last member of (6.26) can also be neglected provided $q << 1/|\boldsymbol{r}_j - \boldsymbol{r}_m|$ for all the atoms in the segment.

Partial Structure Factor. We consider a binary mixture containing N_α molecules of polymer α ($\alpha = 1$ or 2), each of molecular volume v_α so that there are $Z_\alpha = v_\alpha / v_{u\alpha}$ segments per molecule ($v_{u\alpha}$ being the volume of a polymer α segment). Taking the square of (6.24), the intensity of scattering can be written as

$$I(\boldsymbol{q}) = \hat{b}_1^2 \sum_{m_1} \sum_{n_1} \exp(-i\boldsymbol{q}\boldsymbol{r}_{m_1 n_1}) + 2\hat{b}_1\hat{b}_2 \sum_{m_1} \sum_{n_2} \exp(-i\boldsymbol{q}\boldsymbol{r}_{m_1 n_2})$$
$$+ \hat{b}_2^2 \sum_{m_2} \sum_{n_2} \exp(-i\boldsymbol{q}\boldsymbol{r}_{m_2 n_2}) \tag{6.28}$$

where $\boldsymbol{r}_{mn} = \boldsymbol{r}_m - \boldsymbol{r}_n$, and the summation indices m_1 and n_1 for polymer 1 and m_2 and n_2 for polymer 2 run from 1 to $N_1 Z_1$ and 1 to $N_2 Z_2$, respectively . We now introduce the three *partial structure factors* $S_{11}(\boldsymbol{q})$, $S_{12}(\boldsymbol{q})$, and $S_{22}(\boldsymbol{q})$ defined as

$$S_{\alpha\beta}(\boldsymbol{q}) = \frac{v_{u\alpha} v_{u\beta}}{V} \sum_{m_\alpha} \sum_{n_\beta} \exp(-i\boldsymbol{q}\boldsymbol{r}_{m_\alpha n_\beta}) \tag{6.29}$$

where V is the system volume. Equation (6.28) can then be written in a compact form as

$$I(\boldsymbol{q}) = V\left[\rho_1^2 S_{11}(\boldsymbol{q}) + 2\rho_1\rho_2 S_{12}(\boldsymbol{q}) + \rho_2^2 S_{22}(\boldsymbol{q})\right] \tag{6.30}$$

where ρ_α is the scattering length density given by

$$\rho_\alpha = \hat{b}_\alpha / v_{u\alpha} \tag{6.31}$$

[Note that $S_{\alpha\beta}(\boldsymbol{q})$ as defined in (6.29) has dimension of volume. The partial structure

factor is often defined to be dimensionless by other workers, without the front factor $v_{u\alpha}v_{u\beta}/V$. The number of terms in the double summation with respect to m_α and n_β in (6.29) is inversely proportional to $v_{u\alpha}$ and $v_{u\beta}$, and therefore the magnitude of the partial structure factor as defined here is independent of the size of the segments assumed. See also the remarks made in connection with Equation (6.41).]

The partial structure factor defined by (6.29) can be written in an alternative way. In terms of the local number density $n_\alpha(\boldsymbol{r})$ of type α segments at position $\boldsymbol{r}$, it becomes

$$\begin{aligned} S_{\alpha\beta}(\boldsymbol{q}) &= \frac{v_{u\alpha}v_{u\beta}}{V}\int_V\int_V n_\alpha(\boldsymbol{r})n_\beta(\boldsymbol{r}')e^{-i\boldsymbol{q}(\boldsymbol{r}-\boldsymbol{r}')}\,d\boldsymbol{r}\,d\boldsymbol{r}' \\ &= \frac{v_{u\alpha}v_{u\beta}}{V}\int_V\int_V n_\alpha(\boldsymbol{u})n_\beta(\boldsymbol{u}+\boldsymbol{r})e^{-i\boldsymbol{q}\boldsymbol{r}}\,d\boldsymbol{u}\,d\boldsymbol{r} \end{aligned} \tag{6.32}$$

We recognize that the product $v_{u\alpha}n_\alpha(\boldsymbol{r})$ is equal to the volume fraction $\phi_\alpha(\boldsymbol{r})$ of type α segments at position $\boldsymbol{r}$, and write (6.32) as

$$S_{\alpha\beta}(\boldsymbol{q}) = \frac{1}{V}\int_V\int_V \phi_\alpha(\boldsymbol{u})\phi_\beta(\boldsymbol{u}+\boldsymbol{r})e^{-i\boldsymbol{q}\boldsymbol{r}}\,d\boldsymbol{u}\,d\boldsymbol{r} \tag{6.33}$$

In analogy to the density autocorrelation function $\Gamma_\rho(\boldsymbol{r})$ introduced in Section 1.5.2, we can define the concentration correlation function $\Gamma_{\alpha\beta}(\boldsymbol{r})$ as

$$\Gamma_{\alpha\beta}(\boldsymbol{r}) = \int_V \phi_\alpha(\boldsymbol{u})\phi_\beta(\boldsymbol{u}+\boldsymbol{r})d\boldsymbol{u} = V\left\langle\phi_\alpha(0)\phi_\beta(\boldsymbol{r})\right\rangle \tag{6.34}$$

Equation (6.33) thus shows that the partial structure factor $S_{\alpha\beta}(\boldsymbol{q})$ is the Fourier transform of $\Gamma_{\alpha\beta}(\boldsymbol{r})$:

$$S_{\alpha\beta}(\boldsymbol{q}) = \frac{1}{V}\int_V \Gamma_{\alpha\beta}(\boldsymbol{r})e^{-i\boldsymbol{q}\boldsymbol{r}}\,d\boldsymbol{r} = \int_V \left\langle\phi_\alpha(0)\phi_\beta(\boldsymbol{r})\right\rangle e^{-i\boldsymbol{q}\boldsymbol{r}}\,d\boldsymbol{r} \tag{6.35}$$

As discussed in Section 1.6, it is more convenient to separate out, from $I(\boldsymbol{q})$, the "null scattering" at $\boldsymbol{q} = 0$ that is unobservable and ignored in practice. When such a subtraction of the null scattering is carried out, it is easily seen that the result leaves the expression for $I(\boldsymbol{q})$ unchanged from Equation (6.30), providing the partial structure factors $S_{\alpha\beta}(\boldsymbol{q})$ are now understood to be the Fourier transform, not of $\Gamma_{\alpha\beta}(\boldsymbol{r})$ defined by (6.34), but of another correlation function defined as

$$\Gamma_{\alpha\beta}(\boldsymbol{r}) = \int_V \delta\phi_\alpha(\boldsymbol{u})\delta\phi_\beta(\boldsymbol{u}+\boldsymbol{r})d\boldsymbol{u} \tag{6.36}$$

where $\delta\phi_\alpha(\boldsymbol{r})$ is the fluctuation of the local concentration from the overall mean in the scattering volume:

$$\delta\phi_\alpha(\boldsymbol{r}) = \phi_\alpha(\boldsymbol{r}) - \langle\phi_\alpha\rangle \tag{6.37}$$

We note here that Equations (6.30) and (6.33)–(6.36) do not contain any quantities, such as $v_{u\alpha}$, $\hat{b}_\alpha$, and $n_\alpha(\boldsymbol{r})$, that depend on the size of the segment assumed, and this confirms the earlier statement that the choice of the segment size is arbitrary and does not affect the final results of the analysis.

Incompressibility Assumption. As stated in the discussion of zero-angle scattering in Section 6.1.1, both the density and concentration fluctuations contribute additively to the scattering from a two-component system. The effect of the density fluctuations is usually relatively small and may be eliminated approximately (at least in the small-angle region) by subtracting the weighted sum of the intensities of scattering from individual pure components. The observed intensity that has been modified in this way corresponds to the scattering intensity expected from a hypothetical system that is incompressible but otherwise identical to the system under consideration. Such an approach is useful, since many of the theoretical expressions required for the analysis become much simpler under the *incompressibility assumption.* An example of such a simplification is seen if we examine Equation (6.36). In an incompressible solution, any deviation $\delta\phi_1(\boldsymbol{r})$ in the local concentration of component 1 from its mean $\langle\phi_1\rangle$ is allowed only when there is a compensating deviation $\delta\phi_2(\boldsymbol{r})$ in the concentration of component 2 in the opposite direction, so that the relationship $\delta\phi_1(\boldsymbol{r}) = -\delta\phi_2(\boldsymbol{r})$ is obeyed for all $\boldsymbol{r}$. It is then evident from (6.36) that

$$\Gamma_{11}(\boldsymbol{r}) = \Gamma_{22}(\boldsymbol{r}) = -\Gamma_{12}(\boldsymbol{r}) = -\Gamma_{21}(\boldsymbol{r}) \tag{6.38}$$

Taking their Fourier transforms, we then also have

$$S_{11}(\boldsymbol{q}) = S_{22}(\boldsymbol{q}) = -S_{12}(\boldsymbol{q}) = -S_{21}(\boldsymbol{q}) \equiv S(\boldsymbol{q}) \tag{6.39}$$

Equation (6.30) can now be further simplified to

$$I(\boldsymbol{q}) = V(\Delta\rho)^2 S(\boldsymbol{q}) \tag{6.40}$$

where $\Delta\rho = \rho_2 - \rho_1$. For the incompressible system, the scattered intensity $I(\boldsymbol{q})$ is thus governed by the difference $\Delta\rho$, and not by ρ_1 and ρ_2 individually as in (6.30). In other words, the intensity is determined essentially by the structure built by component 1, and the role of component 2 is simply to fill the void left behind. In this regard the incompressible system is similar to the ideal two-phase model, discussed in Section 5.3.2, for which the intensity $I(\boldsymbol{q})$ and the invariant Q are both proportional to $(\Delta\rho)^2$.

We may regard Equation (6.40) as defining the *structure factor* $S(\boldsymbol{q})$, in other words, we may *define* $S(\boldsymbol{q})$ to represent the scattered intensity per unit volume per unit contrast factor $\Delta\rho$. It should be noted that the structure factor is frequently defined by other workers as

$$S(\boldsymbol{q}) = I(\boldsymbol{q})/N(\Delta\hat{b})^2 \tag{6.41}$$

where $\Delta\hat{b}$ is the contrast factor expressed in terms of the scattering length of a scattering unit (either a segment or a small molecule) and N is the number of such scattering units present in the system. In either case, the structure factor is a measure of the scattered intensity normalized with respect to the contrast factor ($\Delta\rho$ or $\Delta\hat{b}$) and the system size (V or N). In other contexts the term *structure factor* has very different meanings. For example, in crystal structure analysis it refers to the Fourier transform of the atomic (or electron density) distribution within a unit cell (see Section 3.3.1). In the small-angle scattering study of a periodic system, as discussed in Section 5.5, it

denotes the Fourier transform of the scattering length density distribution associated with a single macrolattice point. In contrast, in the present context it is basically a normalized intensity function.

6.1.2.2 Dilute Polymer Solution

The intensity $I(q)$ of scattering from a single random-coil polymer molecule in solution, obeying Gaussian statistics, can be written (see Section 5.2.3.1) as

$$I(q) = (\Delta\rho)^2 v_2^2 D(q^2 R_g^2) \tag{6.42}$$

where $D(x)$ is the Debye function defined in (5.31), v_2 is the volume of the polymer molecule, and $\Delta\rho$ is the excess of the scattering length density of the polymer over that of the solvent. When the solution is sufficiently dilute, the scattering from individual molecules does not interfere with each other, and the total intensity of scattering from the system of volume V containing N_2 polymer molecules is given by

$$\begin{aligned} I(q) &= N_2(\Delta\rho)^2 v_2^2 D(q^2 R_g^2) \\ &= V(\Delta\rho)^2 \phi_2 v_2 D(q^2 R_g^2) \end{aligned} \tag{6.43}$$

where $\phi_2 = N_2 v_2 / V$. In considering the intensity of scattering from a binary system under the incompressibility assumption we need to include only the scattering from the solute in view of Equation (6.40). Gaussian statistics describe the shape of the polymer molecule when it is in the *unperturbed* state, that is, when the dilute solution is in the Θ condition. When the solvent is a good solvent, the coil is expanded more as a result of the so-called excluded volume effect, and Equation (6.43) is written more generally as

$$I(q) = V(\Delta\rho)^2 \phi_2 v_2 P(q) \tag{6.44}$$

where $P(q)$ is the *shape factor* or *form factor*, that is, a single-chain structure factor that is normalized so as to have $P(0) = 1$. $P(q)$ reduces to $D(q^2 R_g^2)$ for a Gaussian chain.

As discussed in Section 5.2.5, for small but finite concentrations the effect of interchain interference can be expressed in a virial expansion. When terms up to the second order are retained, the scattered intensity may be approximated in the following form[7]

$$\frac{V(\Delta\rho/\tilde{\rho}_2)^2 c}{I(q)} = \frac{1}{M_2 P(q)} + 2A_2 c \tag{6.45}$$

or

$$\frac{V(\Delta\rho)^2}{I(q)} = \frac{1}{v_2 \phi_2 P(q)} + 2A_2 \tilde{\rho}_2^2 \tag{6.46}$$

Extrapolating (6.45) for $q \to 0$ gives (6.10) in Section 6.1.1.1 that was discussed in connection with zero-angle scattering. For a Θ solvent for which A_2 is equal to 0, Equation (6.46) reduces to (6.44).

6.1.2.3 *Polymer Blend*

For a miscible blend of two polymers, an expression giving $I(q)$ was derived by deGennes by using a theoretical technique called "random phase approximation." The discussion of this technique or the derivation of $I(q)$ unfortunately requires an excursion into a realm of polymer physics far beyond the scope of the present book, and we are here left with simply quoting the result. Interested readers are advised to consult other textbooks (deGennes[1] and Doi[4]) for the derivation. The expression for $I(q)$ derived by deGennes can be written, in our present notation, as

$$\frac{V(\Delta\rho)^2}{I(q)} = \frac{1}{v_1\phi_1 D(q^2R_{g1}^2)} + \frac{1}{v_2\phi_2 D(q^2R_{g2}^2)} - \frac{2\chi}{v_u} \tag{6.47}$$

where R_{g1} and R_{g2} are the radii of gyration of polymers 1 and 2. The incompressibility assumption was used in deriving (6.47), as can be seen from the fact that $I(q)$ is proportional to $(\Delta\rho)^2$. The Debye function $D(x)$ arises in (6.47) because in polymer blends the shape of polymer molecules is in general little disturbed from their unperturbed Gaussian shape. The interaction between the segments of two different types of polymers is expressed by the Flory interaction parameter χ, with the assumption that the segments of both polymers are of volume v_u.

When the extrapolation $q \to 0$ is carried out in (6.47), noting that $D(0) = 1$, we obtain an expression that is identical to (6.23) derived in Section 6.1.1.3 on the basis of the Flory–Huggins free energy of mixing. This shows that the assumptions embodied in (6.47) are essentially equivalent to those in the Flory–Huggins theory. Using the approximation for the Debye function given by (5.33), Equation (6.47) can be written as

$$\frac{V(\Delta\rho)^2}{I(q)} = \frac{1}{S(q)} = \frac{1}{S(0)}(1 + q^2\xi^2) \tag{6.48}$$

where

$$\frac{1}{S(0)} = \frac{1}{v_1\phi_1} + \frac{1}{v_2\phi_2} - \frac{2\chi}{v_u} \tag{6.49}$$

and

$$\xi^2 = \frac{S(0)}{2}\left(\frac{R_{g1}^2}{v_1\phi_1} + \frac{R_{g2}^2}{v_2\phi_2}\right) \tag{6.50}$$

The quantity ξ, having dimension of length, is called the *correlation length*. It is a measure of the distance over which the concentration fluctuations remain correlated. Equation (6.48) shows that a plot of $I(q)^{-1}$ against q^2 will give a straight-line relationship, a fact demonstrated by the results shown in Figure 6.3. Such a plot of $I(q)^{-1}$ against q^2 is often referred to as an *Ornstein–Zernike plot* after the two scientists who in 1914 showed[8] that such a linear q^2 dependence of the inverse intensity function is obeyed by a small-molecule liquid mixture near the critical point.

6.2 BLOCK COPOLYMERS

In a block copolymer a long sequence of segments of type A is followed by another long sequence of segments of type B. For the sake of simplicity, only diblock copolymers are discussed here, although of course there exist other types of block copolymers such as triblock or multiblock copolymers. The two kinds of blocks, linked together covalently, are in general not miscible with each other, unless the blocks are relatively short and the two monomer types A and B are mutually compatible. The blocks thus tend to segregate out from each other and aggregate with their own kind, forming microphases (or microdomains) of about the same order of magnitude in size as the radii of gyration of the blocks. The methods for synthesizing block copolymers are such that the block lengths usually turn out to be fairly uniform, and this uniformity in length causes the segregated microdomains to be uniform in size also and to arrange themselves into a regularly ordered structure, as mentioned in Section 5.5. Changing the temperature of the block copolymer alters the χ parameter denoting the interaction between the two types of segments, making the contact between them more or less costly energetically. When the χ parameter is reduced sufficiently by such a temperature change, the two blocks may eventually be induced to mix with each other, and the ordered structure may disappear. This type of transition, from the ordered to the disordered state of a block copolymer, or vice versa, is called the *order–disorder transition (ODT)*, and the temperature of the transition is called the *microphase separation temperature (MST)*. Scattering from such an ordered phase has been discussed in Section 5.5, and the present section is concerned with the scattering from disordered block copolymers.

Although two types of segments and blocks are present in the system, they are covalently linked into a single molecule, and therefore from a thermodynamic point of view the block copolymer is a single-component material. There is only one kind of molecule present in the system. In other words, on a macroscopic scale, there can be no concentration fluctuations, and the extrapolated zero-angle intensity $I(0)$ arises only from density fluctuations and is therefore very weak. On a more local scale, however, there are two types of segments, A and B, existing together, and their relative concentrations will vary from place to place, as they do in systems in which two homopolymers A and B are mixed together. In the region of intermediate and large q, the scattering curve will therefore be similar to what has been discussed in Section 6.1.2.3 for polymer blends, that is, $I(q)^{-1}$ increases linearly with q^2. This means that as q is *decreased* from a large to an intermediate range, $I(q)$ will *increase*. As q is further decreased toward zero, $I(q)$ must then go through a maximum before it eventually attains, at $q = 0$, the very small intensity commensurate with the density fluctuations alone. Such a maximum in fact occurs at the value of q for which $1/q$ is of the order of the average distance between the centers of the blocks.

A theoretical expression giving the scattering intensity $I(q)$ through the full range of q can be derived by using the same random phase approximation method used for a polymer blend. Again, we can only quote the final result here, which was obtained by Leibler,[9] under exactly the same assumptions as those used for the derivation of

Equation (6.47). The system considered consists of diblock copolymer molecules of volume v each, in which the volume fractions of the two types of blocks are f_1 and f_2 $(= 1 - f_1)$, respectively. It is assumed that the flexibilities of the two block chains are similar, such that

$$R_{g1}^2 = f_1 R_g^2, \qquad R_{g2}^2 = f_2 R_g^2, \qquad R_g^2 = R_{g1}^2 + R_{g2}^2 \tag{6.51}$$

where R_{g1} and R_{g2} are the radii of gyration of the two blocks, and R_g that of the whole copolymer molecule. The intensity of scattering, according to Leibler,[9] is then given by

$$\frac{V(\Delta\rho)^2}{I(q)} = \frac{1}{S(q)} = \frac{F(q)}{v} - \frac{2\chi}{v_u} \tag{6.52}$$

where

$$F(q) = \frac{D(x)}{f_1^2 D(x_1) f_2^2 D(x_2) - \frac{1}{4}\left[D(x) - f_1^2 D(x_1) - f_2^2 D(x_2)\right]^2} \tag{6.53}$$

and

$$x_1 = q^2 R_{g1}^2, \qquad x_2 = q^2 R_{g2}^2, \qquad x = q^2 R_g^2 = x_1 + x_2 \tag{6.54}$$

For $qR_g << 1$, $D(x) \approx 1 - x/3$ as shown in Equation (5.32), and Equation (6.52) becomes

$$S(q) = \frac{2}{3} v f_1^2 f_2^2 q^2 R_g^2 \tag{6.55}$$

The intensity therefore approaches zero as $q \to 0$, and this is a consequence of the incompressibility assumption. For $qR_g >> 1$, on the other hand, the structure factor $S(q)$ can be approximated by

$$S(q) = \frac{2 v f_1 f_2}{q^2 R_g^2} \tag{6.56}$$

For a homopolymer blend with equal numbers of molecules of type 1 and type 2, Equation (6.47) reduces, in the limit $q >> 1$, to

$$S(q) = \frac{2(v_1 + v_2)\phi_1\phi_2}{q^2(R_{g1}^2 + R_{g2}^2)} \tag{6.57}$$

which is in fact identical to (6.56), thus confirming that on a local scale the concentration fluctuations in a disordered block copolymer are exactly the same as in the corresponding homopolymer blend.

Figure 6.4 gives plots of $S(q)$ calculated from (6.52) for $f_1 = 0.25$ and for three values of the χ parameter. The curves all show a maximum. This example clearly shows that the presence of a peak in the scattered intensity curve does not necessarily mean that a lattice-like regularity or a well-defined repeat distance d exists in the structure. A crude estimate of the peak position can be obtained by equating (6.55) and (6.56) to each other and solving for q_{max}, and is given by

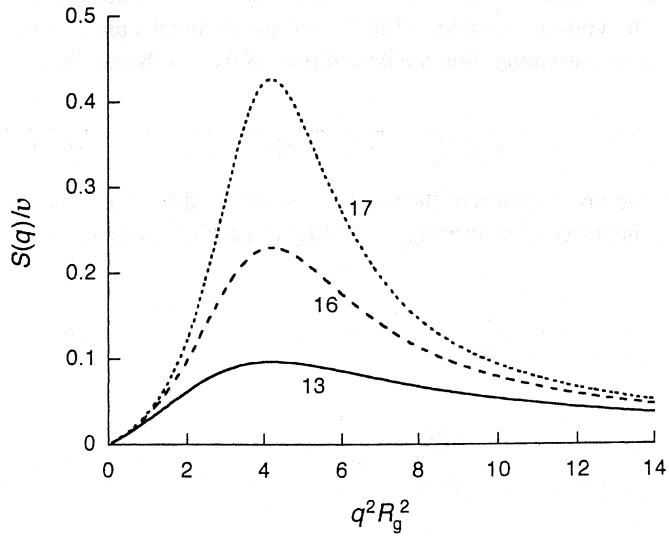

Figure 6.4 The structure factor of a copolymer, with $f_1 = 0.25$, calculated from Equation (6.52), with three values of $\chi(v/v_u)$ equal to 13, 16, and 17, respectively.

$$q_{\max}^2 = \sqrt{\frac{3}{f_1 f_2}} \frac{1}{R_g^2} \tag{6.58}$$

which agrees, within at least 9%, with the exact value evaluated by setting the derivative of $S(q)$ equal to zero. If the two blocks are made less compatible with each other, by changing the temperature to increase χ, the local concentration fluctuations increase and so does the peak intensity. The latter should diverge as the temperature reaches the spinodal temperature T_s, at which the disordered phase becomes unstable in comparison to the microphase-separated state. By plotting the inverse of the peak intensity against T or $1/T$ (depending on how the χ parameter varies with temperature) and extrapolating it to zero, one can determine the spinodal temperature. In practice, however, the actual transition to the ordered phase takes place before the spinodal temperature T_s is eventually reached, much in the same way as the phase separation of a binary liquid mixture is realized before the spinodal temperature is actually reached. Figure 6.5[10] shows the intensity data obtained by neutron scattering from a diblock copolymer of hydrogenous 1,2-polybutadiene and deuterated 1,4-polybutadiene. Here the peak intensity and hence the χ value increase with decreasing temperature, suggesting that the corresponding homopolymer blend should exhibit an UCST-type phase-separation behavior. In Figure 6.5 the peak position $q_{\max}$ is seen to vary somewhat with temperature, in disagreement with the prediction made using Equation (6.52). Figure 6.6[10] plots the inverse of the peak intensity, as a function of temperature, for the same sample used in Figure 6.5, and it shows how the

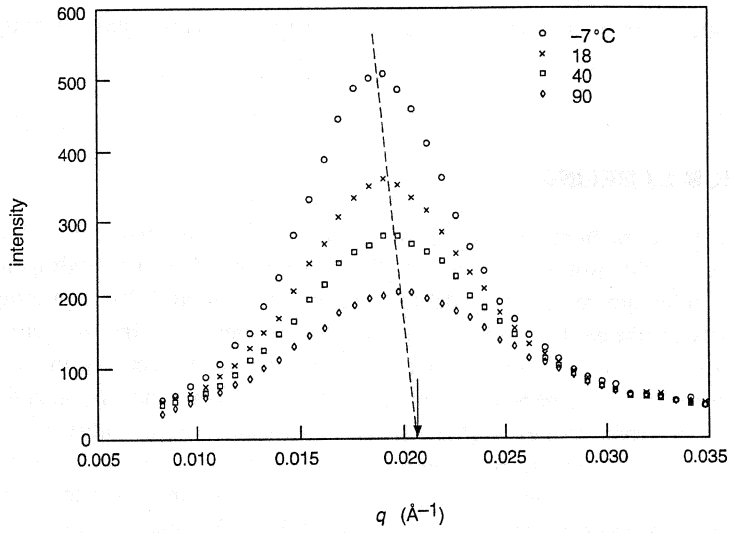

Figure 6.5 Neutron scattering intensity data obtained with a diblock copolymer of deuterated 1,4-polybutadiene and hydrogenous 1,2-polybutadiene. (From Bates and Hartney.[10])

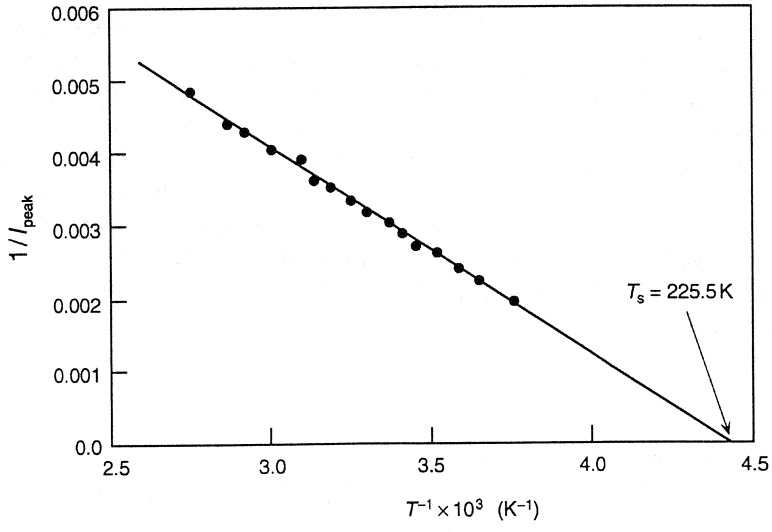

Figure 6.6 This plot illustrates how to determine the spinodal temperature by varying the temperature and extrapolating the reciprocal peak intensity to zero. These results were obtained with the same diblock copolymer used in Figure 6.5. (From Bates and Hartney.[10])

spinodal temperature can be determined by extrapolating the inverse peak intensity to zero.

6.3 DEUTERIUM LABELING

Neutron scattering is a much more powerful technique for studying polymers when used in conjunction with deuterium labeling. When some or all of the hydrogens in polymer molecules are replaced by deuterium, the cross section for scattering neutrons is greatly modified, but all the other physical properties of the molecules remain essentially unaltered. This results from the very fortunate fact that the two isotopes, hydrogen ^{1}H and deuterium ^{2}D, have coherent neutron scattering lengths b_{coh} that are very different from each other. As given in Table 1.2, the value of b_{coh} for ^{1}H is -0.374×10^{-12} cm and the value for ^{2}D is 0.667×10^{-12} cm. In many instances, it is of interest to know the shape of a single polymer molecule that is in the midst of many other molecules of exactly the same kind. We may, for example, want to know the radius of gyration of a molecule in an amorphous bulk polymer, or the manner by which a polymer molecule is folded in a crystalline polymer. These can be determined only if we can make that single molecule stand out among all the other similar molecules. The technique that is used is deuterium labeling.

It might at first appear that to be able to "see" the shape of an isolated molecule, the concentration of the labeled molecule must be very small, so that the effect of interference by rays scattered from other labeled molecules is negligibly small, in much the same way that the concentration of the particles must be small for the Guinier law to be valid (cf. Section 5.2.4). Alternatively, one might expect that the measurement would have to be made at several different concentrations of the labeled molecules and the results extrapolated to zero concentration to eliminate the effect of the interference. Initially, when neutron scattering facilities first became generally available to the polymer science community, measurements were indeed made in this manner. When only a small concentration of labeled polymers was present, the intensity was of course low, and making measurements was difficult. Soon, however, it was realized, as explained below, that a single-chain form factor can be obtained from measurements made with samples having a high concentration of the labeled polymer. Such a high concentration labeling has made it possible to obtain a much stronger scattered beam intensity and consequently greater precision in the data obtained.

6.3.1 High Concentration Labeling

Here we consider how to obtain the single-particle form factor even when labeled molecules are present at a high concentration. For this purpose let us first consider a single-component, bulk polymer, consisting of N molecules in volume V, each molecule with $Z = v/v_u$ segments. The amplitude of scattering from such a polymer is

$$A(\boldsymbol{q}) = \hat{b} \sum_{\alpha=1}^{N} \sum_{m=1}^{Z} \exp(-i\boldsymbol{q}\boldsymbol{r}_{\alpha m}) \tag{6.59}$$

where index α designates molecules and index m segments in each molecule. We assume, for the sake of simplicity, that the segments are all of the same type, so that the scattering length $\hat{b}$ is pulled out in front of the summation. The intensity of scattering is then

$$I(\boldsymbol{q}) = \hat{b}^2 \sum_{\alpha=1}^{N} \sum_{\beta=1}^{N} \sum_{m=1}^{Z} \sum_{n=1}^{Z} \exp\left[-i\boldsymbol{q}(\boldsymbol{r}_{\alpha m} - \boldsymbol{r}_{\beta n})\right] \tag{6.60}$$

We define the single-particle (or intramolecular) *form factor* $P(\boldsymbol{q})$ by

$$P(\boldsymbol{q}) = \frac{1}{Z^2} \left\langle \sum_{m=1}^{Z} \sum_{n=1}^{Z} \exp\left[-i\boldsymbol{q}(\boldsymbol{r}_{\alpha m} - \boldsymbol{r}_{\alpha n})\right] \right\rangle \tag{6.61}$$

where both indices m and n refer to segments belonging to the same molecule. The form factor represents the intensity of independent scattering by a single molecule, averaged over an ensemble of such molecules. The factor $1/Z^2$ renders $P(0)$ equal to unity. The corresponding contributions to the intensity arising from interference between segments belonging to different molecules can be represented by

$$Q(\boldsymbol{q}) = \frac{1}{Z^2} \left\langle \sum_{m=1}^{Z} \sum_{n=1}^{Z} \exp\left[-i\boldsymbol{q}(\boldsymbol{r}_{\alpha m} - \boldsymbol{r}_{\beta n})\right] \right\rangle \qquad (\alpha \neq \beta) \tag{6.62}$$

Separating intramolecular from intermolecular contributions, we can then write Equation (6.60) as

$$I(\boldsymbol{q}) = \hat{b}^2 N Z^2 P(\boldsymbol{q}) + \hat{b}^2 N^2 Z^2 Q(\boldsymbol{q}) \tag{6.63}$$

where in the second term on the right the approximation $N(N-1) \approx N^2$ has been used.

In most instances it is the form factor $P(\boldsymbol{q})$ that we wish to determine. The form factor gives information about the average shape of the molecule. Suppose we have a blend of hydrogenous and deuterated polymers, both having the same chemical structure and the same number of segments, Z, per molecule, and their volume fractions are ϕ_H and ϕ_D, respectively ($\phi_H + \phi_D = 1$). In the blend there are thus $N_H = N\phi_H$ hydrogenous molecules and $N_D = N\phi_D$ deuterated molecules, and instead of (6.63) the scattering intensity is now written as

$$\begin{aligned} I(\boldsymbol{q}) = {} & \hat{b}_H^2 N\phi_H Z^2 P_H(\boldsymbol{q}) + \hat{b}_H^2 (N\phi_H)^2 Z^2 Q_{HH}(\boldsymbol{q}) \\ & + \hat{b}_D^2 N\phi_D Z^2 P_D(\boldsymbol{q}) + \hat{b}_D^2 (N\phi_D)^2 Z^2 Q_{DD}(\boldsymbol{q}) \\ & + 2\hat{b}_H \hat{b}_D (N\phi_H)(N\phi_D) Z^2 Q_{HD}(\boldsymbol{q}) \end{aligned} \tag{6.64}$$

where the first and second terms arise from the hydrogenous molecules only, the third and fourth terms from the deuterated molecules only, and the last term from the interference effect between dissimilar molecules. The hydrogenous and deuterated molecules are expected to be identical in all their properties except for the neutron scattering lengths, and therefore we can write

$$P_{\mathrm{H}}(q) = P_{\mathrm{D}}(q) \equiv P(q) \tag{6.65}$$

and

$$Q_{\mathrm{HH}}(q) = Q_{\mathrm{DD}}(q) = Q_{\mathrm{HD}}(q) \equiv Q(q) \tag{6.66}$$

Equation (6.64) is then simplified to

$$\begin{aligned} I(q) &= (\hat{b}_{\mathrm{H}}^2\phi_{\mathrm{H}} + \hat{b}_{\mathrm{D}}^2\phi_{\mathrm{D}})NZ^2P(q) + (\hat{b}_{\mathrm{H}}\phi_{\mathrm{H}} + \hat{b}_{\mathrm{D}}\phi_{\mathrm{D}})^2\, N^2Z^2Q(q) \\ &= \left\langle \hat{b}^2 \right\rangle NZ^2P(q) + \left\langle \hat{b} \right\rangle^2 N^2Z^2Q(q) \end{aligned} \tag{6.67}$$

In (6.67) the average scattering lengths, $\langle \hat{b}^2 \rangle$ for the $P(q)$ term and $\langle \hat{b} \rangle^2$ for the $Q(q)$ term, depend differently on ϕ_{D}. Therefore, when measurements are made at two different concentrations of labeled polymers, a set of two simultaneous linear equations (6.67) with two unknowns $P(q)$ and $Q(q)$ is obtained, which can then be solved readily (Williams *et al.*[11] and Akcasu *et al.*[12]).

An even simpler relationship is obtained when the incompressibility assumption is justified. The scattering intensity from a sample containing only a hydrogenous or deuterated polymer, due solely to density fluctuations, is weak for q in the small-angle region and can be completely neglected under the incompressibility assumption. This means that in (6.63) we can set $I(q) = 0$ and obtain

$$NQ(q) = -P(q) \tag{6.68}$$

The form factors $P(q)$ and $Q(q)$ and their relationship represented by (6.68) remain of course unchanged even when some of the hydrogens are replaced by deuteriums. Thus for a blend of hydrogenous and deuterated polymers, substituting (6.68) into (6.67) gives

$$I(q) = (\hat{b}_{\mathrm{H}} - \hat{b}_{\mathrm{D}})^2\phi_{\mathrm{H}}\phi_{\mathrm{D}}NZ^2P(q) \tag{6.69}$$

Equation (6.69) shows that the form factor $P(q)$ can therefore be determined by a single measurement of the scattered intensity at any relative concentration ϕ_{H} (Wignall *et al.*[13]). Since the intensity is proportional to $\phi_{\mathrm{H}}\phi_{\mathrm{D}}$ in (6.69), the best signal-to-noise ratio can be obtained when a mixture containing about equal amounts of hydrogenous and deuterated polymers is used.

6.3.2 Method of Contrast Variation

When the system of study is binary to begin with, for example, a polymer dissolved in a solvent or a blend of two polymers, the practice of deuterating one of the components

leads to greatly enhanced contrast and a much higher intensity of scattering. As has been seen throughout the discussions in Chapters 5 and 6, the scattered intensity $I(q)$ from a binary system is proportional (under the incompressibility assumption) to the square of the difference $\Delta\rho$ in the scattering length density between the two components. Table 6.1[14] lists the values of scattering length density calculated for hydrogenous and deuterated varieties of several of the common polymers and solvents. Clearly, the contrast is enhanced greatly when one of the two components is deuterated. The choice of which component to deuterate is usually based on the criterion that the overall hydrogen content in the sample should be made as small as possible to minimize the undesirable incoherent scattering.

The fact that the scattered intensity is proportional to $(\Delta\rho)^2$ can be clearly demonstrated by performing the following simple experiment. Suppose the scattered intensity $I(q)$ is measured with a polymer solution in which the solvent is a mixture of hydrogenated and deuterated varieties. By mixing the two in different proportions the scattering length density ρ_s of the solvent can be systematically varied. Plotting the square root of $I(q)$ (at a fixed q) against ρ_s will give a linear plot, such as shown in Figure 6.7a, and extrapolating it to $I(q) = 0$ will allow determination of the solvent composition for the *contrast match*, at which ρ_s is equal to the scattering length density of the polymer and such that the polymer essentially becomes "invisible." Incidentally, if the polymer happens to contain more than one species differing in scattering length density from each other, the intensity $I(q)$ will fail to reach zero even when ρ_s matches the *average* scattering length density of the polymer, as illustrated schematically in Figure 6.7b.

When the sample is a ternary system, analysis of the scattering data is in general much more difficult than has been discussed in this and previous chapters, but the need to investigate a ternary system is encountered often. Examples of such ternary systems are a diblock copolymer in a common solvent, a suspension of latex particles having a core-shell structure, and an incompatible binary polymer blend in which one of the polymers is semicrystalline. By employing the technique of *contrast matching*

TABLE 6.1
Neutron Scattering Length Densities of Several Common Polymers and Solvents

	Neutron Scattering Length Density ρ (10^{10} cm^{-2})	
Polymer or Solvent[a]	For Hydrogenous Variety	For Deuterated Variety
Water	−0.56	6.4
Cyclohexane	−0.28	6.69
Xylene	0.79	6.04
Toluene	0.94	5.66
Benzene	1.18	5.4
Polyethylene	−0.28	6.71
Polyisoprene	0.27	5.12
Polystyrene	1.41	6.47
Poly(methyl methacrylate)	1.06	7.09

[a] Most of the data are taken from Wignall.[14]

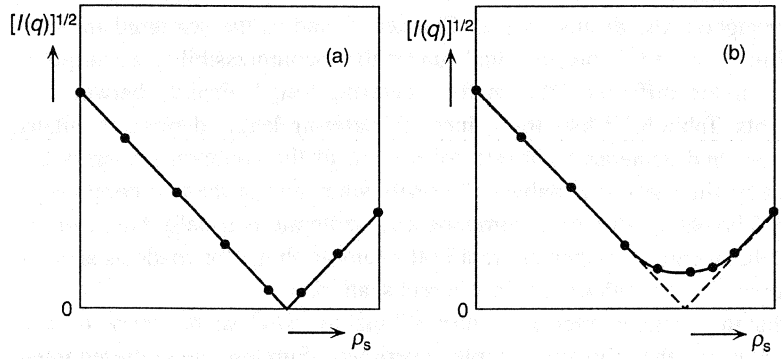

Figure 6.7 Schematic plot showing the square root of the scattered intensity $I(q)$ at a fixed q against the scattering length density ρ_s of the solvent, the latter being varied by mixing the hydrogenated and deuterated varieties to different proportions. $I(q)$ goes to zero at the contrast match point, as is illustrated in (a), provided the solute particles are all of the same scattering length density; otherwise $I(q)$ is not zero even when the *average* scattering length density of the solute is matched by the solvent, as in (b).

it is, however, possible to render one of the components "invisible," thereby letting the sample appear as if it were a binary system. By choosing the third component (usually the solvent) to be a mixture of isotopes and by adjusting the isotopic composition to render its scattering length density equal to that of the second component, one can essentially make the second component indistinguishable from the solvent background. Thus, for example, one can determine the radii of gyration of the A and B blocks in a diblock copolymer individually by first using a solvent whose scattering length density matches that of the B block and then using a solvent whose isotopic composition is adjusted to match the A block. Such a contrast matching is permissible as long as the thermodynamic properties of the solvent can be considered to be unaffected by the changes in its isotopic composition.

Instead of seeking to match the solvent scattering length density with that of the second component exactly, one may alternatively make a series of measurements in which the solvent composition is systematically varied. The desired structural information is then extracted by an interpolation (or extrapolation) from these observed results. To illustrate such an approach, consider the example in which the radii of gyration of individual blocks of a diblock copolymer are determined. The diblock copolymer consists of a deuterated styrene block jointed to a hydrogenous isoprene block, and the copolymer is dissolved in a mixture of deuterated and hydrogenated toluene. When the radius of gyration is determined through use of the Guinier law or the Zimm plot, the apparent radius of gyration $\langle R^2_{app} \rangle$ obtained depends on the scattering length density ρ_s of the mixed solvent. If ρ_s is equal to the scattering length density ρ_B of the B block, the observed $\langle R^2_{app} \rangle$ will be equal to the radius of gyration $\langle R^2_A \rangle$ of the A block, and if ρ_s is equal to ρ_A, $\langle R^2_{app} \rangle$ will be equal to $\langle R^2_B \rangle$. When ρ_s is not exactly equal to either ρ_A or to ρ_B, $\langle R^2_{app} \rangle$ is given, as can be shown readily (Ionescu *et al.*[15]), by

$$\left\langle R_{\text{app}}^2 \right\rangle = Y \left\langle R_{\text{A}}^2 \right\rangle + (1 - Y) \left\langle R_{\text{B}}^2 \right\rangle + Y(1 - Y) \left\langle L^2 \right\rangle \tag{6.70}$$

where $\langle L^2 \rangle$ is the mean-square distance between the centers of mass of the A and B blocks, and the contrast factor Y is given by

$$Y = \frac{(\rho_{\text{A}} - \rho_{\text{s}})v_{\text{A}}}{(\rho_{\text{A}} - \rho_{\text{s}})v_{\text{A}} + (\rho_{\text{B}} - \rho_{\text{s}})v_{\text{B}}} \tag{6.71}$$

v_{A} and v_{B} being the volumes of the A and B blocks, respectively. Equation (6.70) suggests that measurements of $\langle R_{\text{app}}^2 \rangle$ with mixed solvents of three different ρ_{s} values will enable the determination of $\langle R_{\text{A}}^2 \rangle$, $\langle R_{\text{B}}^2 \rangle$, and $\langle L^2 \rangle$. Or, alternatively, one may measure $\langle R_{\text{app}}^2 \rangle$ with more than three mixed solvents and determine the best values of the three parameters by fitting Equation (6.70) to the observed $\langle R_{\text{app}}^2 \rangle$. Such a procedure is illustrated in Figure 6.8.[16]

6.3.3 Deuterium Isotope Effect

The practice of deuterium labeling and isotopic substitution rests on the premise that replacing hydrogens with deuteriums in an organic molecule alters the neutron scattering length without affecting the physical properties of the molecule in any other way. This is nearly, but not totally, true. A hydrogen and a deuterium atom differ in their mass, and as a result the isotopic substitution often brings about some subtle differences in some of the properties. For example, hydrogenous and deuterated polyethylenes are known to exhibit a difference in melting temperature of about 6°C (Stehling *et al.*[17]), which makes the two isotopic varieties of polyethylene segregate out from each other on crystallization from a melt of their mixture. Similarly, the theta

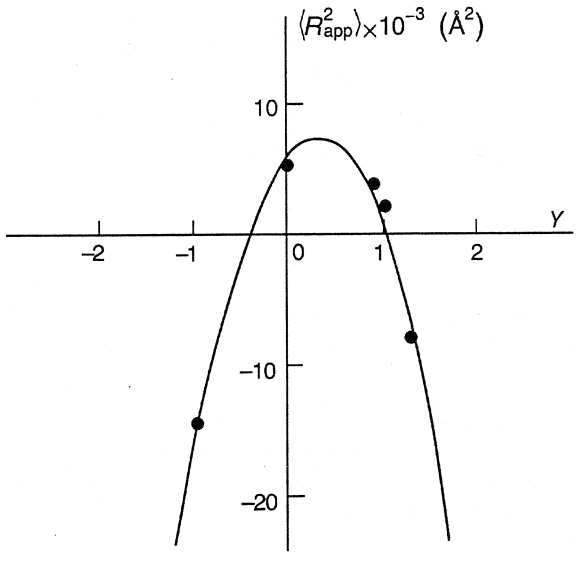

Figure 6.8 Points are the values of $\left\langle R_{\text{app}}^2 \right\rangle$ determined with a diblock copolymer of deuterated polystyrene and hydrogenous polyisoprene, dissolved in a solvent that is a mixture of hydrogenous and deuterated cyclohexane. The contrast factor Y, defined by (6.71), depends on the proportions of the two isotopic species in the solvent. The curve is the theoretical parabola calculated according to Equation (6.70) with best-fitting values of $\langle R_{\text{A}}^2 \rangle$, $\langle R_{\text{B}}^2 \rangle$, and $\langle L^2 \rangle$. (From Ionescu *et al.*[16])

temperature of deuterated polystyrene in cyclohexane is different by about 5°C from that of ordinary polystyrene in cyclohexane (Strazielle and Benoît[18]). More recently it has also become known that a mixture of an ordinary amorphous polymer with its deuterated variety can phase separate if the chain lengths are sufficiently long. As an example we quote a result of neutron scattering measurements obtained with a mixture (50% by volume) of an ordinary polystyrene (molecular weight 870,000) and a deuterated polystyrene (molecular weight 1,150,000) that was annealed at 160°C (Bates and Wignall[19]). The data are presented in an Ornstein–Zernike plot in Figure 6.9. The observed data were fitted by the solid curve calculated according to the deGennes equation (6.47) based on the random-phase approximation, with the value of χ adjusted to 1.9×10^{-4} to attain the best fit. If the deuterated polystyrene behaved exactly the same as the hydrogenous polystyrene, the χ value would have been equal to zero, and the data would have followed the upper broken curve in the figure. The lower broken curve represents the one that is expected if the mixture is on the limit of stability (spinodal), that is, if the χ value is equal to χ_s given by

$$2\frac{\chi_s}{v_u} = \frac{1}{v_1}\frac{1}{\phi_1} + \frac{1}{v_2}\frac{1}{\phi_2} \tag{6.72}$$

[for which $I(0)$ is equal to ∞, as seen from Equation (6.23)]. With a blend of even higher molecular weight polystyrenes, the observed data, when plotted in the same manner as in Figure 6.9, were actually below the spinodal curve, indicating that phase

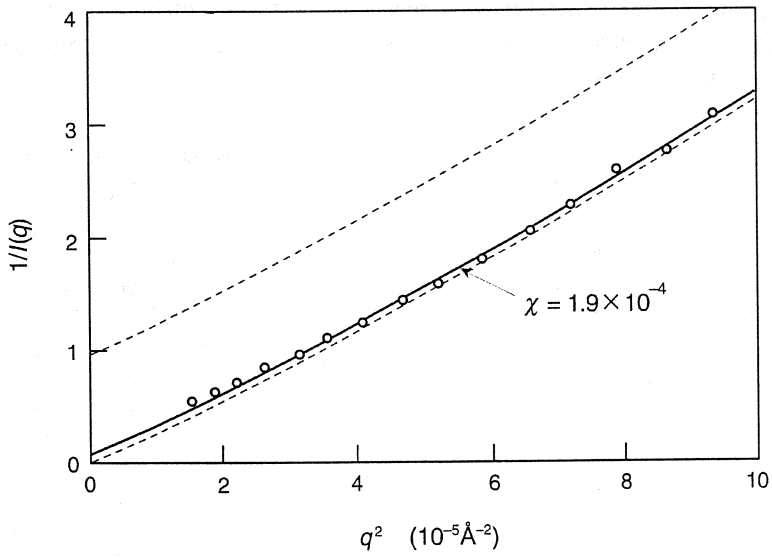

Figure 6.9 Neutron scattering data from a binary mixture, annealed at 160°C, of a hydrogenous polystyrene (molecular weight 870,000) and a deuterated polystyrene (molecular weight 1,150,000). The solid curve is a fitted theoretical curve with χ equal to 1.9×10^{-4}, and the upper broken curve is for $\chi = 0$ expected in the absence of the deuterium isotope effect. (From Bates and Wignall.[19])

separation had indeed taken place. There are other examples reported in the literature in which the χ parameter for a blend of hydrogenous and deuterated species of the same polymer was found not to be equal to zero. All these findings point to the need to guard against possible artifacts when data involving deuterated polymers are interpreted.

FURTHER READING

1. deGennes, P.-G., *Scaling Concepts in Polymer Physics*, Cornell University Press, Ithaca, New York, 1979.
2. Lindner, P., and Zemb, Th., *Neutron, X-Ray and Light Scattering,* North-Holland, New York, 1991.
3. Higgins, J. S., and Benoît, H. C., *Polymers and Neutron Scattering*, Oxford University Press, Oxford, 1994.
4. Doi, M., *Introduction to Polymer Physics*, Oxford University Press, Oxford, 1996.

REFERENCES

5. Flory, P. J., *Principles of Polymer Chemistry*, Cornell University Press, Ithaca, 1953.
6. Schwahn, D., Janssen, S., and Springer, T., *J. Chem. Phys.* **97**, 8775 (1992).
7. Zimm, B. H., *J. Chem. Phys.* **16**, 1093 (1948).
8. Ornstein, L. S., and Zernike, F., *Proc. Acad. Sci. Amsterdam* **17**, 793 (1914).
9. Leibler, L., *Macromolecules* **13**, 1602 (1980).
10. Bates, F. S., and Hartney M. A., *Macromolecules* **18**, 2478 (1985).
11. Williams, C. E., Nierlich, M., Cotton, J. P., Jannink, G., Boué, F., Daoud, M., Farnoux, B., Picot, C., deGennes, P. G., Rinaudo, M., Moan, M., and Wolff, C., *J. Polymer Sci., Polymer Lett. Ed.* **17**, 379 (1979).
12. Akcasu, A. Z., Summerfield, G. C., Jahshan, S. N., Han, C. C., Kim, C. Y., and Yu, H., *J. Polymer Sci., Polymer Phys. Ed.* **18**, 863 (1980).
13. Wignall, G. D., Hendricks, R. W., Koehler, W. C., Lin, J. S., Wai, M. P., Thomas, E. L., and Stein, R. S., *Polymer* **22**, 886 (1981).
14. Wignall, G. D., in *Physical Properties of Polymers Handbook*, Mark, J. E., Ed., American Institute of Physics, New York, 1996, p. 299.
15. Ionescu, L., Picot, C., Duval, M., Duplessix, R., Benoît, H., and Cotton, J. P., *J. Polymer Sci.: Polymer Phys. Ed.* **19**, 1019 (1981).
16. Ionescu, L., Picot, C., Duplessix, R., Duval, M., Benoît, H., Lingelser, J. P., and Gallot, Y., *J. Polymer Sci.: Polymer Phys. Ed.* **19**, 1033 (1981).
17. Stehling, F. C., Ergos, E., and Mandelkern, L., *Macromolecules* **4**, 672 (1971).
18. Strazielle, C., and Benoît, H., *Macromolecules* **8**, 203 (1975).
19. Bates, F. S., and Wignall, G. D., *Macromolecules* **19**, 932 (1986).

Study of Surfaces and Interfaces

7

7.1 INTRODUCTION

The study of polymer surfaces and interfaces has attracted increasing interest in recent years. The scattering (or reflection) of x-rays and neutrons from surfaces offers a valuable means of examining the nature of surfaces and interfaces, and the method complements other techniques of surface study such as scanning electron microscopy (SEM), atomic force microscopy (AFM), secondary ion mass spectroscopy (SIMS), x-ray photoelectron spectroscopy (XPS), etc. The technique of x-ray and neutron reflectivity measurement has undergone rapid evolution in recent years, with the scope of its application expanding every year, and can now claim a place among the major techniques for utilizing x-ray and neutron scattering.

As discussed in Section 5.3, the intensity of scattering in the small-angle regime obeys the Porod law asymptotically as the scattering vector q is increased, and the absolute value of the intensity is proportional to the total area of interfaces within the sample. It was further shown that examination of any deviation of the observed intensity curve from the Porod law can give a measure of the diffuseness of the interfaces. The method of reflectivity measurement can be thought of as an extension of the Porod law method to surfaces that are essentially flat and interfaces that are close to exposed surfaces and parallel to them. As with small-angle scattering we are concerned with measuring phenomena at small q, in which the radiation strikes the surface at a small, glazing angle and is reflected (or scattered) from the surface at a similarly small angle.

Figure 7.1 depicts the geometry of scattering at a surface, where the incident, reflected and refracted rays are represented by wave vectors $\boldsymbol{k}_0$, $\boldsymbol{k}$, and $\boldsymbol{k}_1$. A wave vector is defined as $(2\pi/\lambda)\boldsymbol{S}$, where $\boldsymbol{S}$ is a unit vector in the beam direction and λ is the wavelength of the radiation in the medium concerned. With the normal to the surface designated as the z axis, the plane of incidence is defined as the plane containing z and $\boldsymbol{k}_0$. Note that in general $\boldsymbol{k}$ and $\boldsymbol{k}_1$ are not necessarily in the plane of incidence. Thus the angle ϕ in Figure 7.1, between the y axis and the projection of $\boldsymbol{k}$ on the xy plane, is not necessarily equal to zero. The detector is placed to measure the reflected (or scattered) beam in the direction of $\boldsymbol{k}$, where the scattering vector $\boldsymbol{q}$ is equal to $\boldsymbol{k} - \boldsymbol{k}_0$.

If in Figure 7.1 ϕ is zero and θ is equal to θ_0, the reflection is termed *specular*. The wave vectors $\boldsymbol{k}_0$ and $\boldsymbol{k}$ are then related to each other in the same way as they

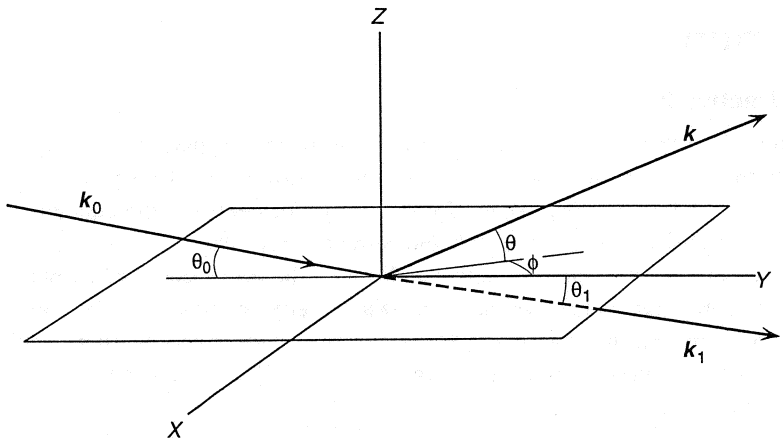

Figure 7.1 Geometry of scattering (and reflection) from surface. $\boldsymbol{k}_0$, $\boldsymbol{k}$, and $\boldsymbol{k}_1$ are the wave vectors for the incident, reflected, and refracted rays.

are when a beam of light incident on a mirror is reflected by it. The scattering vector $\boldsymbol{q}(= \boldsymbol{k} - \boldsymbol{k}_0)$ for such a specular reflection is normal to the surface, and its x and y components are both equal to zero. Such specular reflection occurs when the surface is perfectly flat and, at the same time, there is no variation in the scattering length density in the x and y directions in the layer of material immediately below the surface. The *reflectivity* R, the ratio of the reflected beam energy to the incident beam energy, is then measured as a function of the magnitude of $\boldsymbol{q}$ while its direction is kept normal to the surface. The changes in $\boldsymbol{q}$ can be accomplished either by changing the angles θ_0 and $\theta(= \theta_0)$ of incidence and reflection at the same time or by changing the wavelength λ while keeping the geometry of the scattering fixed. The result of measurement of R as a function of q is then analyzed to obtain information about the variation in the scattering length density, $\rho(z)$, in the material as a function of depth z from the surface. Most studies of x-ray and neutron reflectivity are concerned with the measurement of such specular reflectivity.

When the surface is not perfectly flat or when the material near the surface contains some inhomogeneities in scattering length density in the direction parallel to the surface, scattering in nonspecular directions may no longer be vanishingly small. This is referred to as *off-specular* or *diffuse* scattering, and the scattered intensity may be measured off the specular direction within a few degrees of it. The scattering vector $\boldsymbol{q}$ in such a diffuse scattering measurement contains a finite q_x or q_y component. The result is then analyzed to derive information about the surface topology or scattering length density inhomogeneities in the x or y direction. Theoretical tools for analyzing off-specular scattering are being actively developed by many workers at present, but they will not be discussed in this book. For a summary of recent work on this topic, readers are referred to the review article by Foster.[2]

7.2 REFLECTIVITY

7.2.1 Refractive Index

When radiation is incident on an interface between two materials, part of the energy is reflected at the interface and the rest is transmitted through it. Irrespective of whether the radiation involved is a beam of light, x-rays, or neutrons, the geometry and the relative intensities of the reflected and refracted rays can be described by the principles of optics,[4] once the refractive indices of the two media are known. The concept of refractive indices of neutrons was briefly introduced in Section 2.1.2.2 in connection with neutron guide tubes. For both x-rays and neutrons, the refractive index n of a material is in general slightly less than 1 and is given to a good approximation by

$$n = 1 - \delta + i\beta \tag{7.1}$$

where

$$\delta = \frac{\lambda^2 \rho}{2\pi} \tag{7.2}$$

ρ being the scattering length density of the material, and

$$\beta = \frac{\lambda \rho_{\text{abs}}}{4\pi} \tag{7.3}$$

ρ_{abs} being the absorption cross-section density (or the linear absorption coefficient μ mentioned in Section 2.3.1). For most materials δ is of the order of 10^{-6} for both x-rays and neutrons. A special case to be noted is that the neutron scattering length of protons is negative (see Table 1.2), and therefore a substance with a high concentration of hydrogen can exhibit a neutron refractive index slightly larger than 1, as is the case with saturated hydrocarbon polymers. The imaginary component of n arises only when the material is absorbing. For neutrons the absorption cross-section density is sufficiently small such that β in (7.1) can be neglected in most cases, except when the material contains isotopes of Li, B, Cd, or Gd (see Table 2.2). With Cu$K\alpha$ x-rays β for most organic materials is about 10^{-2} to 10^{-3} times δ and therefore can also be ignored without introducing significant errors.

It is instructive to examine the derivation of refractive index n, due to Fermi,[5] and see why it depends on the scattering length density ρ as shown in Equations (7.1) and (7.2). Consider a plane wave traveling in a vacuum in the z direction. The amplitude of the wave at point z along its path is represented by e^{-ikz} where $k = 2\pi/\lambda$, λ being the wavelength in a vacuum. We now insert an infinite slab of material of refractive index n and thickness a, as in Figure 7.2. Within the slab the wavelength is λ/n, and the amplitude of the wave reaching z after passing through the slab is therefore given by

$$\begin{aligned} A(z) &= \exp\left\{-i\left[\frac{2\pi}{\lambda/n}a + \frac{2\pi}{\lambda}(z-a)\right]\right\} \\ &= \exp\{-ik[na + (z-a)]\} \end{aligned} \tag{7.4}$$

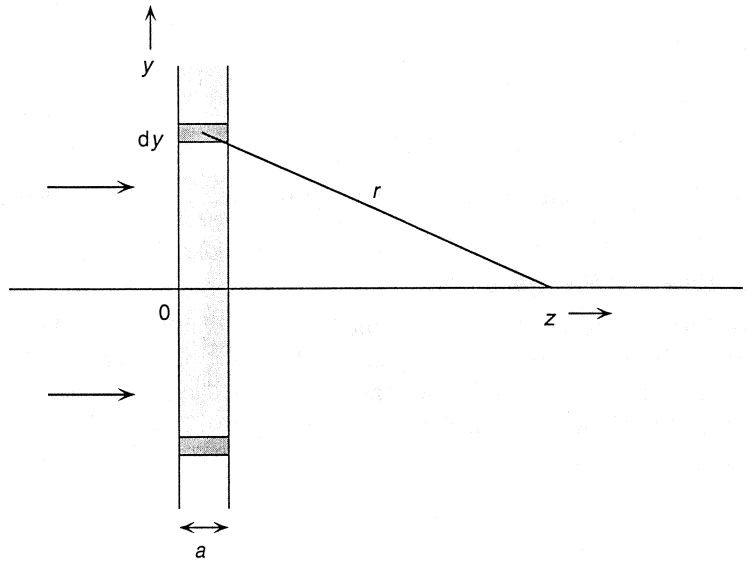

Figure 7.2 Calculation of refractive index. A plane wave traveling to the right is transmitted through an infinite slab of thickness a.

Here it is assumed that the slab is sufficiently thin so that the absorption effect is negligible.

Next we take the viewpoint that the wave reaching a point on the right of the slab can be considered to result from the sum of the waves scattered at every point on the slab plus the unmodified incident wave, and thus its amplitude is given by

$$A(z) = e^{-ikz} + \int_0^\infty (-1)\frac{\rho}{r} e^{-ikr} a 2\pi y \, dy \tag{7.5}$$

where $a2\pi y \, dy$ is the volume of the slab of thickness a within the ring of radius y and width dy, and ρ is the scattering length density of the slab material. r is the distance from the point of scattering to point z on the axis at which the amplitude is considered. The negative sign in the integral comes from the conventions used for the definition of scattering length. On substituting $y^2 = r^2 - z^2$, (7.5) becomes

$$\begin{aligned} A(z) &= e^{-ikz} - 2\pi a\rho \int_0^\infty e^{-ikr} \, dr \\ &= e^{-ikz}\left(1 + i\frac{2\pi a\rho}{k}\right) \end{aligned} \tag{7.6}$$

(Some mathematical subtlety is involved in evaluating the integral in (7.6) at the upper limit, for which the interested reader is referred to the original reference.[5]) The amplitudes calculated by these two approaches should lead to the same result, and therefore by equating (7.6) with (7.4) we obtain

$$n = 1 - \frac{2\pi\rho}{k^2}$$
$$= 1 - \frac{\lambda^2\rho}{2\pi} \tag{7.7}$$

which is Equation (7.1) for the cases in which the absorption effect can be neglected.

7.2.2 Snell's Law and Fresnel's Law

At a sharp, planar boundary between two homogeneous media of refractive indices n_0 and n_1 both the reflected and refracted rays are in the plane of incidence (the plane containing the incident ray and the normal to the boundary). The angle θ of reflection is related to the angle θ_0 of incidence (see Figure 7.3) by the *law of reflection*

$$\cos\theta_0 = \cos\theta \tag{7.8}$$

and the angle θ_1 of refraction is given by *Snell's law*

$$n_0 \cos\theta_0 = n_1 \cos\theta_1 \tag{7.9}$$

In a medium of refractive index n, the wavelength is equal to λ/n and the magnitude of the wave vector $\boldsymbol{k}$ is equal to $2\pi n/\lambda$, where λ is the wavelength in a vacuum. The two laws, (7.8) and (7.9), therefore state that the y component of the wave vector is invariant at the boundary on reflection and refraction.

In most cases we consider the first medium is a vacuum (or air), and therefore n_0 is equal to 1. Since n_1 is less than 1 in general, the refraction angle θ_1 is smaller than the incident angle θ_0. Consequently at incident angles below a certain *critical angle* θ_c the radiation is totally reflected back into the medium 0 (air). The critical angle is thus given by

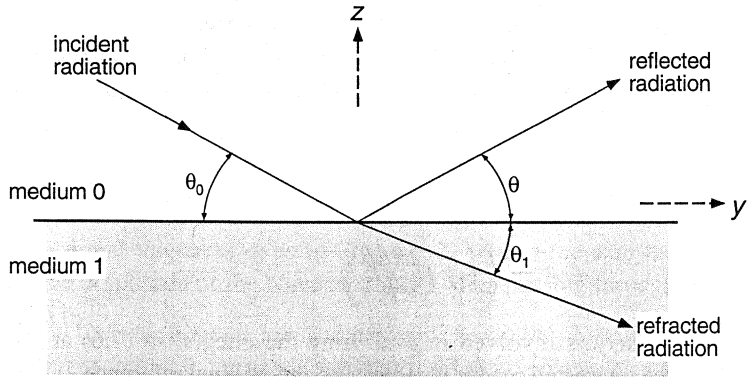

Figure 7.3 Geometry of reflection and refraction.

$$\cos\theta_c = n_1 \tag{7.10}$$

Since $\cos\theta = 1 - \theta^2/2 + \cdots$ for small θ, from (7.1) we find that, to a good approximation,

$$\theta_c = \sqrt{2\delta} = \lambda\sqrt{\rho/\pi} \tag{7.11}$$

For both Cu$K\alpha$ x-rays and neutrons, δ with polymers is mostly $\sim 10^{-6}$ as stated before, and therefore θ_c is on the order of milliradians (see Table 7.1).

The *reflectivity* R is defined as the fraction of the incident energy that is reflected. For an incident angle θ_0 larger than θ_c, R is less than 1 and generally decreases as the angle θ_0 is made larger. From (7.9) we can write

$$n_1^2(1 - \sin^2\theta_1) = n_0^2(1 - \sin^2\theta_0) \tag{7.12}$$

Similarly, from (7.10) (or its equivalent, written in the form $n_0\cos\theta_c = n_1$) we can write

$$n_0^2(1 - \sin^2\theta_c) = n_1^2 \tag{7.13}$$

Taking the difference between (7.12) and (7.13) leads to

$$n_1^2\,\sin^2\theta_1 = n_0^2\,\sin^2\theta_0 - n_0^2\,\sin^2\theta_c \tag{7.14}$$

which can be written as

$$k_{z1} = \left(k_{z0}^2 - k_{zc}^2\right)^{1/2} \tag{7.15}$$

where k_{z0} and k_{z1} are the z components of the wave vectors of the incident and refracted rays and k_{zc} is the value of k_{z0} when θ_0 is equal to the critical angle θ_c.

Taking the origin of z at the boundary and considering only the z dependency of the wave amplitude, we now represent the incident wave at height z as $A(z) = \exp(ik_{z0}z)$. If r and $t(= 1 - r)$ are the fractions of amplitudes of the wave reflected and transmitted at the boundary respectively, the wave amplitude in medium 0 is given by

TABLE 7.1
Refractive Indices and Critical Angles for Selected Materials[a]

Material	δ_x ($\times 10^6$)	$\theta_{c,x}$ (milliradian)	β_x ($\times 10^6$)	δ_N ($\times 10^6$)	$\theta_{c,N}$ (milliradian)
Si	7.44	3.85	0.19	0.791	1.260
Polystyrene	3.33	2.58	0.005	0.509	1.010
Deuterated polystyrene	3.33	2.58	0.005	2.336	2.160
Polyethylene	3.48	2.63	0.009	−0.128	—
Deuterated polyethylene	3.48	2.63	0.009	3.067	2.477
Poly(vinyl chloride)	4.56	3.02	0.119	0.591	1.087

[a] Data are for x-rays and neutrons of wavelength 1.54 Å.

$$A_0(z) = \exp(ik_{z0}z) + r\exp(-ik_{z0}z) \tag{7.16}$$

and the same in medium 1 by

$$A_1(z) = t\exp(ik_{z1}z) \tag{7.17}$$

The wave must be continuous and smoothly varying across the interface. By imposing the requirement that the values of $A(z)$ and $dA(z)/dz$ on either side of the interface must be the same, Equations (7.16) and (7.17) can be solved to give

$$r = \frac{k_{z0} - k_{z1}}{k_{z0} + k_{z1}} \tag{7.18}$$

The reflectivity R is the absolute square of r and is given by

$$R = \left|\frac{k_{z0} - k_{z1}}{k_{z0} + k_{z1}}\right|^2 \tag{7.19}$$

Equation (7.19) is called *Fresnel's law.* It applies for both neutrons and x-rays. However, for electromagnetic waves it is valid, strictly speaking (see Lekner[6]), for only the *s* wave, that is, the wave with its electric vector polarized perpendicular to the plane of incidence (the label *s* stands for *senkrecht* meaning perpendicular in German). In the limit of the small incident angles that we are here considering, Equation (7.19) is valid approximately also for the *p* wave, and therefore the expression can be used irrespective of the state of polarization of x-rays.

Substitution of (7.15) for k_{z1} in (7.19) leads to

$$R = \left|\frac{k_{z0} - \sqrt{k_{z0}^2 - k_{zc}^2}}{k_{z0} + \sqrt{k_{z0}^2 - k_{zc}^2}}\right|^2 \tag{7.20}$$

The reflectivity of Cu$K\alpha$ x-rays from a perfectly smooth silicon surface, calculated according to (7.20) with the values of δ and θ_c given in Table 7.1 (and with the absorption effect ignored), is plotted against the scattering vector $q = 2k_{z0}$ in Figure 7.4. For $k_{z0} >> k_{zc}$ Equation (7.20) can be approximated by

$$R = \left|\frac{1 - \left[1 - (k_{zc}/k_{z0})^2\right]}{1 + \left[1 - (k_{zc}/k_{z0})^2\right]}\right|^2 \cong \frac{1}{16}\left(\frac{k_{zc}}{k_{z0}}\right)^4 \tag{7.21}$$

showing that the tail of the reflectivity curve decays as q^{-4} for large q, as in the Porod law. When the absorption effect is fully taken into account,[7,8] the calculated reflectivity curve is modified as given in Figure 7.5. It shows that the effect is important only for incident angles θ in the vicinity of the critical angle θ_c. Note that to accentuate the effect, the plot is given with the ordinate on a linear scale, and only values of q in a limited range around q_c are shown. Had it been plotted in the same way as in Figure 7.4, the absorption effect would have been recognizable only as a slight rounding off of the curve around q_c.

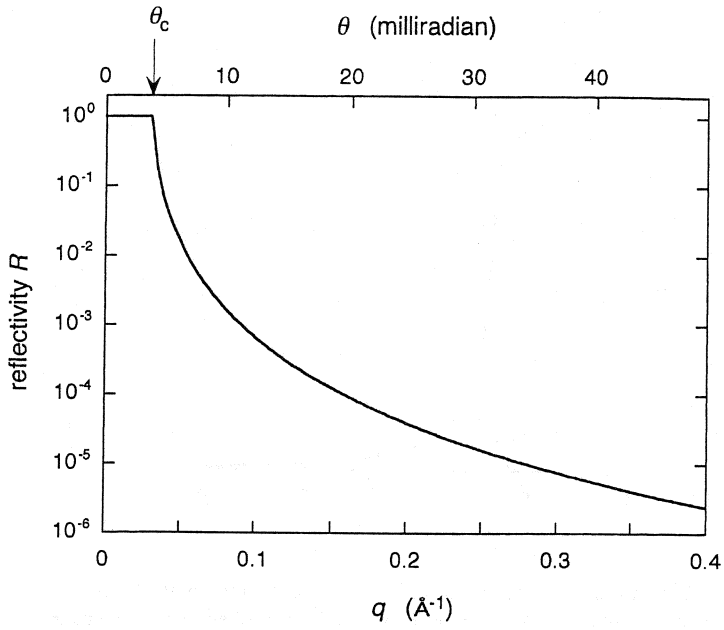

Figure 7.4 X-Ray reflectivity of silicon against air calculated according to Equation (7.20), with the absorption effect ignored.

7.2.3 Reflectivity from a System with Two Parallel Interfaces

In the preceding section we examined the reflectivity from an interface between two media. Next we consider the case (see Heavens[9]) in which a thin film (medium 1) of thickness t is now interposed between a vacuum (medium 0) and a substrate (medium 2) as in Figure 7.6. A thin film deposited on a thick, flat substrate will correspond to such a system. In this case the reflected radiation that is observed will consist not only of rays reflected at the 0–1 interface but will also of rays transmitted from medium 1 to medium 0 after having been reflected at the 1–2 interface once, twice, etc.

To keep track of all these contributions systematically, let us first consider the general case pertaining to the event that takes place at a single interface between medium j and medium $k(= j + 1)$. The amplitude of the wave incident in medium j and striking the j–k interface will be partly reflected back into medium j and partly transmitted to medium k. We designate the fraction of the amplitude that is reflected back to medium j by r_{jk} and call it the *reflection coefficient* (or the *Fresnel coefficient for reflection*). We similarly designate the fraction that is transmitted to medium k by t_{jk} and call it the *transmission coefficient* (or the *Fresnel coefficient for transmission*). Obviously $r_{jk} + t_{jk}$ is equal to one. The argument leading to Equation (7.18), given in the preceding section, is applicable also to this general case, and we find

$$r_{jk} = \frac{k_{zj} - k_{zk}}{k_{zj} + k_{zk}} \tag{7.22}$$

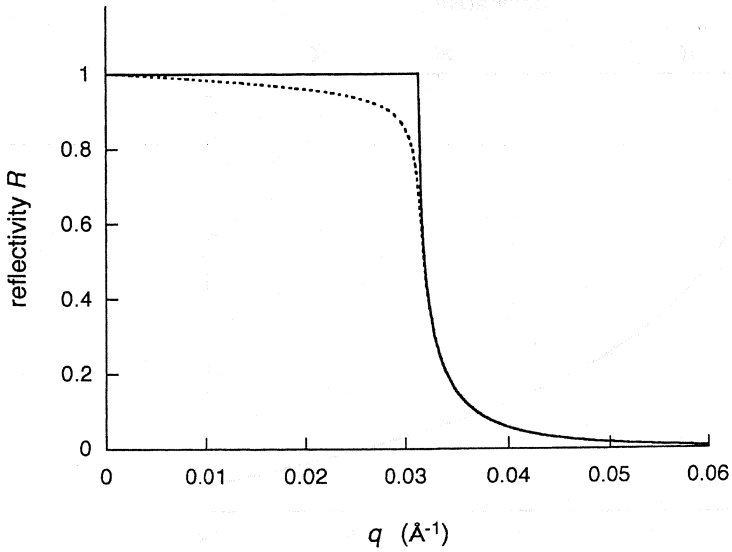

Figure 7.5 Effect of absorption in the reflectivity R of x-ray, calculated for the silicon surface ($\mu = 151\text{cm}^{-1}$) against air. Solid line, without absorption effect; broken line, with absorption effect.

and

$$t_{jk} = \frac{2k_{zk}}{k_{zj} + k_{zk}} \tag{7.23}$$

We now look at one particular beam that emerges from the 0–1 interface after having been reflected twice at the 1–2 interface, as shown in Figure 7.7. If the amplitude of the beam incident on the 0–1 interface has a magnitude 1, each time the beam encounters an interface its magnitude is reduced by a factor equal to the Fresnel coefficient of either transmission or reflection as indicated in Figure 7.7. When the beam finally emerges from the 0–1 interface, its magnitude is reduced to $t_{01}r_{12}r_{10}r_{12}t_{10}$. The beam, in addition, has suffered a phase shift equal to $4\phi_1$ in comparison to the beam reflected directly at the 0–1 interface, where ϕ_1, given by

$$\phi_1 = \frac{2\pi}{\lambda} n_1 \sin\theta_1 t = k_{z1}t \tag{7.24}$$

is the phase shift incurred on traversing the film of thickness t once. The overall coefficient r of reflection is then the sum of amplitudes of all the beams (see Figure 7.6) emerging from the 0–1 interface, and is therefore given by

$$r = r_{01} + t_{01}r_{12}t_{10}e^{-i2\phi_1} + \cdots + t_{01}r_{12}(r_{10}r_{12})^{m-1}t_{10}e^{-i2m\phi_1} + \cdots \tag{7.25}$$

where $m(= 1 \cdots \infty)$ is the number of times the beam has been reflected at the 1–2 interface before emerging into medium 0. Equation (7.25) can be summed to give

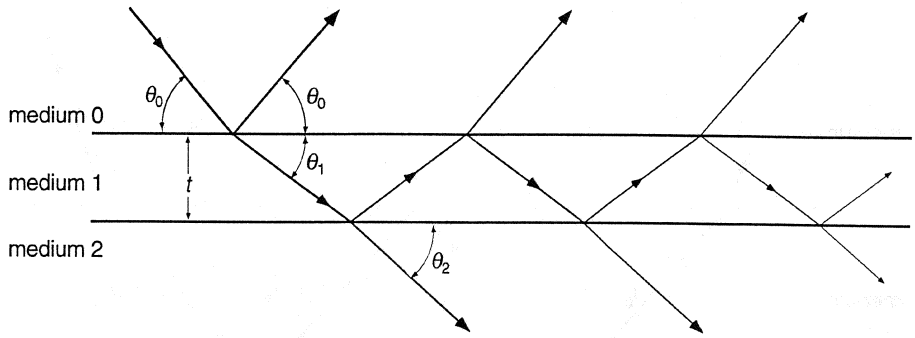

Figure 7.6 The reflected radiation observed will consist of the rays reflected directly at the 0–1 interface but also of those rays transmitted from medium 1 to medium 0 after having been reflected at the 1–2 interface once, twice, etc.

$$r = r_{01} + \frac{t_{01}t_{10}r_{12}e^{-i2\phi_1}}{1 - r_{10}r_{12}e^{-i2\phi_1}} \tag{7.26}$$

We note from (7.22) and (7.23) that r_{10} is equal to $-r_{01}$ and that

$$t_{01}t_{10} = 1 - r_{01}^2 \tag{7.27}$$

Equation (7.26) is therefore rewritten as

$$r = \frac{r_{01} + r_{12}e^{-i2\phi_1}}{1 + r_{01}r_{12}e^{-i2\phi_1}} \tag{7.28}$$

The reflectivity R, which is the fraction of the incident *energy* that is reflected, is obtained as $|r|^2$, or

$$R = \left| \frac{r_{01} + r_{12}e^{-i2\phi_1}}{1 + r_{01}r_{12}e^{-i2\phi_1}} \right|^2 \tag{7.29}$$

Figure 7.8 shows the x-ray reflectivity R calculated (again ignoring the absorption effect) for a polystyrene film of thickness 200 Å deposited on a silicon substrate. The overall trend of the curve is similar to the one in Figure 7.4 calculated for the substrate only, but here a pronounced oscillation is superimposed. The maxima in R occur when the rays, emerging from the 0–1 interface after having been reflected at the 1–2 interface one or more times, differ in phases by a multiple of 2π from each other and interfere constructively. This fact enables us to determine the thickness t of the film from the interval in q between successive maxima or minima, as

$$t = \frac{2\pi}{2\Delta k_{z1}} \cong \frac{2\pi}{2\Delta k_{z0}} = \frac{2\pi}{\Delta q} \tag{7.30}$$

7.2.4 Reflectivity from a Multilayer Film

Next we consider the reflection from a system consisting of a large number of thin parallel layers of different refractive indices. A sample with a continuously varying

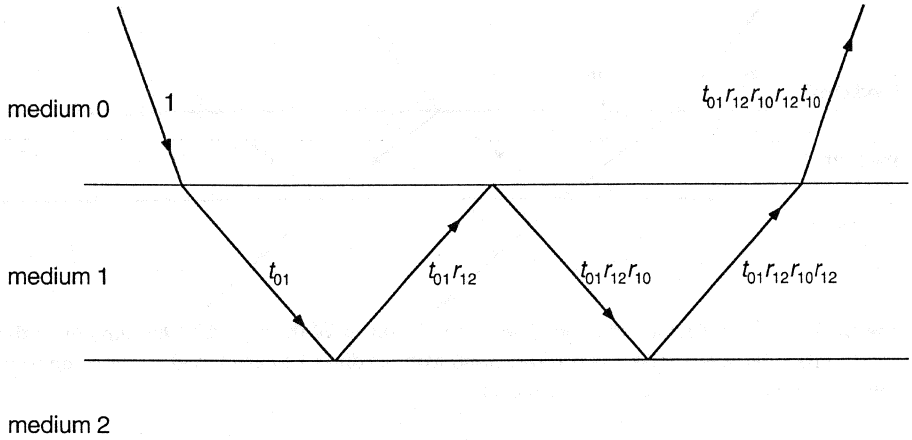

Figure 7.7 Shown is the successive change in the magnitude of the amplitude of a ray, as it is either refracted or reflected on encountering an interface.

scattering length density $\rho(z)$ across the surface can be approximated by such a multilayer system. The reflectivity R for such a system can be calculated, in principle, by extending the method in the preceding section that was discussed to treat a system having two parallel interfaces. Suppose, for instance, we consider a system consisting of four media, 0, 1, 2, and 3, and three interfaces 0–1, 1–2, and 2–3. At first we focus our attention on the system consisting of only three media 1, 2, and 3 and apply the same kind of analysis used for the three media system in the preceding section. We thereby obtain the effective reflection coefficient $\hat{r}_{12}$ at the 1–2 interface as

$$\hat{r}_{12} = \frac{r_{12} + r_{23}\exp(-i2\phi_2)}{1 + r_{12}r_{23}\exp(-i2\phi_2)} \tag{7.31}$$

where

$$\phi_j = \frac{2\pi}{\lambda} n_j \sin\theta_j \, t_j = k_{zj} t_j \tag{7.32}$$

The system now effectively reduces to one consisting of two interfaces: the 0–1 interface and the virtual interface at the 1–2 boundary with the effective reflection coefficient $\hat{r}_{12}$. The overall reflection coefficient r is then obtained as

$$r = \frac{r_{01} + \hat{r}_{12}\exp(-i2\phi_1)}{1 + r_{01}\hat{r}_{12}\exp(-i2\phi_1)} \tag{7.33}$$

and the reflectivity R as $|r|^2$.

Although the above method of calculating the reflectivity can be extended to multilayer systems with any number of discrete layers, it becomes unwieldy as soon as the number of layers involved exceeds four or five. A computationally more efficient method is offered by the use of an optical transfer matrix. Here we simply summarize the method as described by Lekner.[6] For any single layer j within the multilayer

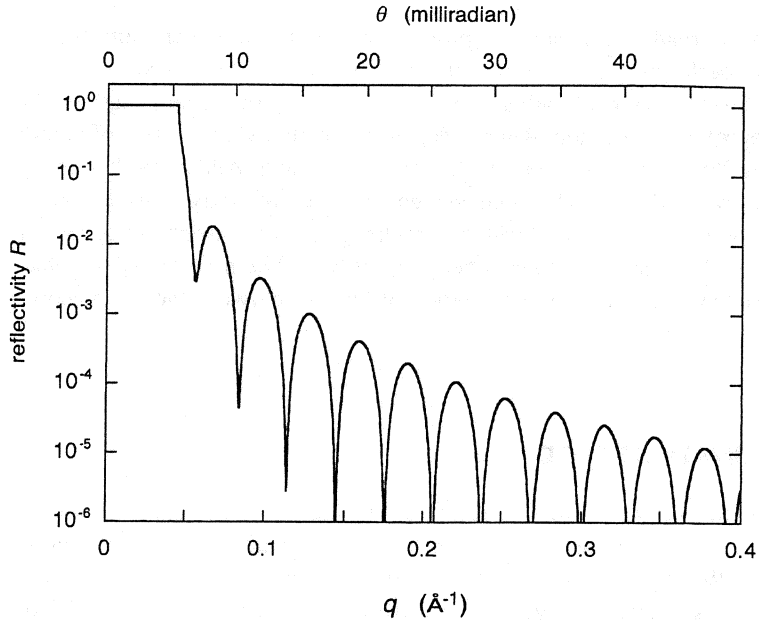

Figure 7.8 X-Ray reflectivity calculated with Equation (7.29) for a polystyrene film of thickness 200 Å deposited on a silicon substrate.

system its optical characteristics can be concisely summarized in the transfer matrix $\boldsymbol{M}_j$ defined as

$$\boldsymbol{M}_j = \begin{bmatrix} \cos\phi_j & -(1/k_{zj})\sin\phi_j \\ k_{zj}\sin\phi_j & \cos\phi_j \end{bmatrix} \tag{7.34}$$

with ϕ_j given by (7.32). The matrix $\boldsymbol{M}_j$ describes how the amplitude and its derivative of a wave propagating through layer j and reaching boundary $(j, j+1)$ are related to the amplitude and derivative at the preceding boundary $(j-1, j)$. As noted in the derivation of Fresnel's law in Section 7.2.2, the amplitude and its derivative of a wave at a boundary are continuous, and this fact allows the construction of the transfer matrix $\boldsymbol{M}$ for the whole stack of $N-1$ layers sitting on top of a substrate (medium N) by

$$\boldsymbol{M} = \begin{bmatrix} m_{11} & m_{12} \\ m_{21} & m_{22} \end{bmatrix} = \boldsymbol{M}_{N-1}\boldsymbol{M}_{N-2}\cdots\boldsymbol{M}_2\boldsymbol{M}_1 \tag{7.35}$$

The reflection coefficient r from the surface of the 0–1 interface is then obtained, in terms of the matrix elements of $\boldsymbol{M}$, by

$$r = \frac{(k_{z0}k_{zN}m_{12} + m_{21}) - i(k_{zN}m_{11} - k_{z0}m_{22})}{(k_{z0}k_{zN}m_{12} - m_{21}) + i(k_{zN}m_{11} + k_{z0}m_{22})} \tag{7.36}$$

The reader may want to verify that for a system consisting of a single layer of film on a substrate (i.e., $N = 2$), as in the preceding section, (7.36) indeed leads to (7.28).

This method is readily amenable to programming into computers, and the calculation can be performed for models with any number of layers, each of different thickness if necessary. A model with a continuously varying scattering length density $\rho(z)$ can be approximated, to any desired degree of accuracy, by a stack of parallel layers with a uniform scattering length density within each. Additional knowledge of the system, obtained from other independent methods of study, is usually indispensable to come up with an initial trial model that gives a fair degree of agreement between the calculated and observed reflectivity curves. The model may then have to be refined successively, by trial and error, until the fit between the two becomes satisfactory.

7.3 APPROXIMATE METHOD

The method of numerical calculation discussed in the previous section allows reflectivity curves to be obtained that are exact except for any numerical round-off errors and any other errors associated with replacing the continuous profile with a set of discrete density steps. However, the method, being entirely numerical, does not easily lend itself to providing insight into the relationship between the scattering length density profile assumed and the reflectivity curve calculated. All the theoretical results in Section 7.2 started from Snell's and Fresnel's laws, without any direct reference to scattering. Reflection, however, occurs as a result of scattering of the radiation by individual particles (electrons or atomic nuclei) in the material, followed by interference among these scattered rays. In this regard reflection is no different from any of the other phenomena associated with scattering and diffraction of x-rays and neutrons discussed in the previous chapters in this book. The only important difference is that the so-called *kinematic* (or *first Born*) *approximation*, which we have been tacitly assuming all along, becomes no longer valid as we approach the regime of total reflection.

The kinematic approximation is valid when the scattered wave amplitude is sufficiently small that the interaction between the incident and the scattered waves can be neglected. All the theories of scattering presented in Chapter 1, including the statement that the scattered intensity is the absolute square of the Fourier transform of the scattering length density distribution in the system, are based on this assumption. Here we reexamine the phenomenon of reflection within the kinematic approximation. This will provide the link between the interpretation of reflectivity curves and the analysis of intensity data obtained by other types of scattering measurements, such as small-angle scattering. Another advantage of this approach will be that the contributions to the reflectivity curve by various features in the structure can more easily be understood and identified individually. It should, however, be kept in mind that the results based on the kinematic approximation are valid only for weak interactions, that is, when the incident angle θ is much larger than the critical angle θ_c.

7.3.1 Reflectivity under the Kinematic Approximation

In the kinematic approximation the intensity of scattering, as discussed in Section 1.5.2, is given by

$$I(\boldsymbol{q}) = |\mathcal{F}\{\rho(\boldsymbol{r})\}|^2 \tag{7.37}$$

where $\rho(\boldsymbol{r})$ is the scattering length distribution in the material and $\mathcal{F}\{\ \}$ denotes the (three-dimensional) Fourier transform. We will now recast (7.37) into a form appropriate for reflectivity measurements.[10] We consider a sample in which the scattering length density in the z direction normal to the surface is given by $\rho(z)$ and the scattering length density in the direction parallel to the surface is invariant. The scattering length density distribution $\rho(\boldsymbol{r})$, formally written as a function of three-dimensional position variable $\boldsymbol{r}$, can therefore be written as

$$\rho(\boldsymbol{r}) = \sigma_x(x)\sigma_y(y)\rho(z) \tag{7.38}$$

where $\sigma_x(x)\sigma_y(y)$ represents the shape of the illuminated surface, assumed to be rectangular, and is equal to 1 if the point (x,y) is in the illuminated area and is equal to 0 otherwise. Equation (7.37) can now be written as

$$\begin{aligned} I(\boldsymbol{q}) &= \left| \int\int\int \sigma_x(x)\sigma_y(y)\rho(z) \exp\left[-i(q_x x + q_y y + q_z z)\right] dx\, dy\, dz \right|^2 \\ &= |\mathcal{F}\{\sigma_x(x)\}|^2 \left|\mathcal{F}\{\sigma_y(y)\}\right|^2 |\mathcal{F}\{\rho(z)\}|^2 \end{aligned} \tag{7.39}$$

where $\mathcal{F}\{\ \}$ now represents the one-dimensional Fourier transform. When area A of the illuminated surface is large compared to q^{-2}, $\mathcal{F}\{\sigma_x(x)\}$ and $\mathcal{F}\{\sigma_y(y)\}$ are concentrated around $q_x = 0$ and $q_y = 0$, respectively, and $I(\boldsymbol{q})$ can be written in the form

$$I(\boldsymbol{q}) = C_x\delta(q_x)C_y\delta(q_y)\,|\mathcal{F}\{\rho(z)\}|^2 \tag{7.40}$$

The constants C_x and C_y are equal to $2\pi L_x$ and $2\pi L_y$, respectively, L_x and L_y being the dimensions of the illuminated surface ($L_x L_y = A$).

For the sake of interested readers the demonstration that C_xC_y is equal to $(2\pi)^2 A$ is given as follows. That C_xC_y should be proportional to L_xL_y can easily be rationalized from the fact that the intensity must be proportional to the illuminated area. The factors 2π in C_x and C_y essentially arise from the use of $\boldsymbol{q}$ instead of $\boldsymbol{s}$ as the scattering vector. To see this, we make use of Parseval's theorem[11] that states that

$$\int_{-\infty}^{\infty} |f(x)|^2\, dx = \frac{1}{2\pi}\int_{-\infty}^{\infty} |\mathcal{F}\{f(x)\}|^2\, dq_x \tag{7.41}$$

[Note that (7.41) is the one-dimensional version of Equation (4.38) cited previously.] By substituting $\sigma_x(x)$ for $f(x)$ in (7.41) and recognizing that $|\sigma_x(x)|^2$ is nonvanishing and equal to unity only in the x interval of length L_x, the left-hand member of (7.41) is found to equal L_x. On the other hand, by substituting $C_x\delta(q_x)$

for $|\mathcal{F}\{f(x)\}|^2$, the right-hand member of (7.41) is found to equal $C_x/2\pi$. C_x is therefore equal to $2\pi L_x$.

The term *intensity* or $I(\boldsymbol{q})$ is used throughout this book to denote the differential scattering cross section $d\sigma/d\Omega$ (see Section 1.2.1), that is, the ratio of the flux of the scattered beam *per unit solid angle* to the incident beam flux. The reflectivity R, on the other hand, is the ratio of the reflected beam energy to the incident beam energy. Suppose the surface is illuminated by an incident beam of unit flux. The amount of energy, ε_0, contained in the incident beam of cross-sectional area L_x by $L_y \sin\theta$ is then equal to $L_x L_y \sin\theta$. To calculate the amount of energy, ε, contained in the reflected beam, we must integrate $I(\boldsymbol{q})$ given by (7.40) over a range of solid angles Ω around the specular reflection direction. To do this we need first to establish the relationship between $d\Omega$ and $dq_x dq_y$. This relationship can be obtained as follows. For θ and ϕ defined as in Figure 7.1, $d\Omega$ is equal to $d\theta\, d\phi$. In terms of θ and ϕ the components k_x and k_y of the scattering wave vector $\boldsymbol{k}$ are given as

$$k_x = k\ \cos\theta\ \sin\phi, \qquad k_y = k\ \cos\theta\ \cos\phi \tag{7.42}$$

from which we obtain

$$\begin{aligned} dk_x\, dk_y &= \begin{vmatrix} \dfrac{\partial k_x}{\partial\theta} & \dfrac{\partial k_x}{\partial\phi} \\ \dfrac{\partial k_y}{\partial\theta} & \dfrac{\partial k_y}{\partial\phi} \end{vmatrix} d\theta\, d\phi \\ &= k^2\ \sin\theta\ \cos\theta\, d\theta\, d\phi \\ &\cong k^2\ \sin\theta\, d\theta\, d\phi \end{aligned} \tag{7.43}$$

Since $\boldsymbol{q} = \boldsymbol{k} - \boldsymbol{k}_0$, we have $dk_x = dq_x$ and $dk_y = dq_y$, and therefore

$$d\Omega = \frac{1}{k^2 \sin\theta} dq_x\, dq_y \tag{7.44}$$

Integrating (7.40) with respect to $d\Omega$ to obtain the reflected beam energy ε, we find

$$\begin{aligned} \varepsilon &= \int\int (2\pi)^2 L_x L_y \delta(q_x)\delta(q_y)\, |\mathcal{F}\{\rho(z)\}|^2 \frac{1}{k^2\ \sin\theta} dq_x\, dq_y \\ &= 4(2\pi)^2 L_x L_y \sin\theta \frac{1}{q^2} |\mathcal{F}\{\rho(z)\}|^2 \end{aligned} \tag{7.45}$$

where in the last member q is substituted for $2k \sin\theta$. The reflectivity R is given by the ratio $\varepsilon/\varepsilon_0$, or

$$R = \frac{16\pi^2}{q^2} |\mathcal{F}\{\rho(z)\}|^2 \tag{7.46}$$

Using (B.18), which states that the Fourier transform of the derivative of a function is iq times the Fourier transform of the function, (7.46) can be written also as

$$R = \frac{16\pi^2}{q^4}\left|\mathcal{F}\left\{\frac{d\rho(z)}{dz}\right\}\right|^2 \tag{7.47}$$

We see that the reflectivity R is governed by the Fourier transform of the scattering length density, according to (7.46), or equivalently by the Fourier transform of the scattering length density *gradient* normal to the surface, according to (7.47).

7.3.2 Comparison with Exact Results

To see how well the results of the kinematic approximation represented by (7.46) or (7.47) reproduce the exact results, let us consider the reflection from a planar surface of a material with uniform scattering length density ρ_1. The scattering length density profile $\rho(z)$ for such a system can be represented mathematically as $\rho_1 H(-z)$, where $H(z)$ is the Heaviside unit step function, equal to 0 for $z < 0$ and equal to 1 for $z > 0$, as illustrated in Figure 7.9. The derivative of the Heaviside function is a delta function, and therefore $d\rho(z)/dz$ is equal to $\rho_1\delta(-z) = r_1\delta(z)$. Since the Fourier transform of a delta function is equal to unity, we obtain, from (7.47),

$$R = \frac{16\pi^2}{q^4}\rho_1^2 \tag{7.48}$$

The exact result applicable to the same system is the Fresnel reflectivity given by (7.19). For $k_{z0} >> k_{zc}$ it was already shown in (7.21) that (7.19) can be approximated by $(1/16)(k_{zc}/k_{z0})^4$. We recognize that $k_{z0} = (1/2)q_z = (1/2)q$ and also that, in view of (7.11), $k_{zc} = (2\pi/\lambda)\sin\theta_c = 2(\pi\rho_1)^{1/2}$. Substituting these results for k_{zc} and k_{z0} then gives an approximate expression for the Fresnel reflectivity that is exactly the same as (7.48). This agreement is consistent with the expectation that the kinematic approximation, which is valid when the scattering is relatively weak, gives a result that agrees with Fresnel law when θ is much larger than θ_c. The reflectivity R calculated from (7.48) is plotted in Figure 7.10 as the dotted curve, and the agreement with the

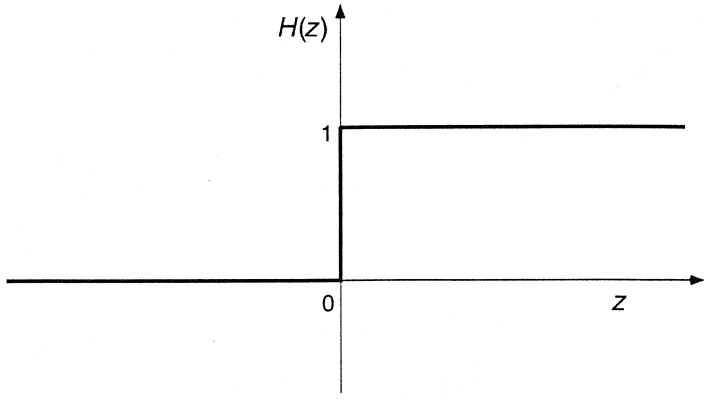

Figure 7.9 Definition of the Heaviside function $H(z)$.

exact result (solid curve) calculated according to Fresnel's law (7.19) is excellent except in the vicinity of the critical angle. It is seen that the phenomenon of total reflection for $\theta < \theta_c$ is completely missed by the kinematic approximation.

As another example we make a similar comparison for the case in which a film of thickness t and scattering length density ρ_1 is deposited on a planar substrate of scattering length density ρ_2. The scattering length density profile $\rho(z)$ can now be represented as

$$\rho(z) = \rho_1 H(-z) + (\rho_2 - \rho_1) H(-z - t) \tag{7.49}$$

leading to

$$\frac{d\rho(z)}{dz} = \rho_1 \, \delta(-z) + (\rho_2 - \rho_1)\delta(-z - t) \tag{7.50}$$

The Fourier transform of (7.50) is obtained with the help of the shift theorem (see Appendix B), which shows that the Fourier transform of $\delta(-z-t)$ is equal to $\exp(iqt)$ times the Fourier transform of $\delta(-z)$. We thus obtain

$$\mathcal{F}\left\{\frac{d\rho(z)}{dz}\right\} = \rho_1 + (\rho_2 - \rho_1)e^{iqt} \tag{7.51}$$

Substitution of (7.51) into (7.47) gives

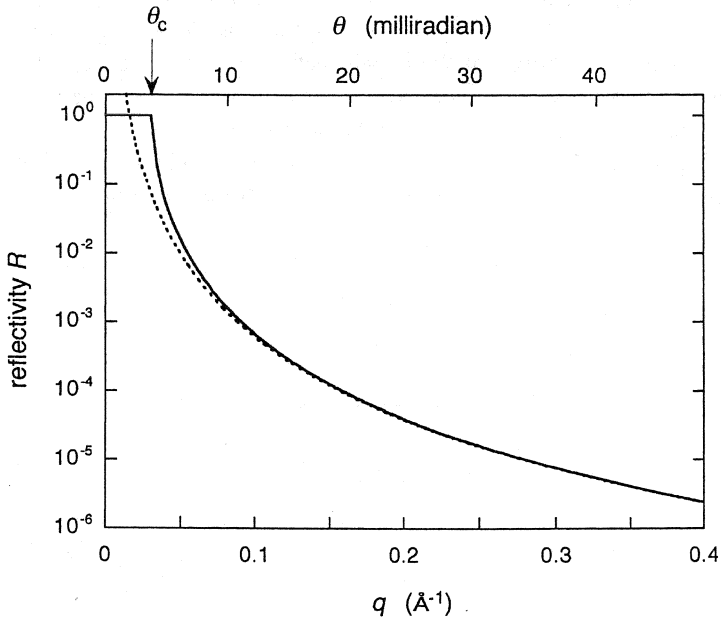

Figure 7.10 X-Ray reflectivity of silicon against air. The exact result (solid line) calculated according to Fresnel's law (7.19) is compared with the result (broken line) calculated according to (7.48) based on the kinematic approximation.

$$R = \frac{16\pi^2}{q^4}\left[\rho_1^2 + (\rho_2 - \rho_1)^2 + 2\rho_1(\rho_2 - \rho_1)\cos(qt)\right] \tag{7.52}$$

In Figure 7.11 the curve calculated from (7.52) for the neutron reflectivity from a 500-Å film of deuterated polystyrene deposited on a silicon substrate is compared with the exact result calculated from (7.29). The overall features are again well represented as long as θ is much larger than the critical angle θ_c, but the positions of the maxima and minima in the interference fringes deviate progressively more severely from the correct ones as θ decreases toward θ_c.

7.3.3 Diffuse and Rough Interfaces

7.3.3.1 Diffuse Interface

The result of the kinematic approximation, expressed in the form of Equation (7.46) or (7.47), allows the effect of diffuse interfaces to be incorporated in a straightforward and transparent manner. Suppose that in a system of a single planar interface the scattering length density in the normal direction varies not abruptly at the interface but undergoes a gradual transition from zero in vacuum to the bulk density ρ_1 in medium 1. The scattering length density distribution $\rho(z)$ for such a diffuse interface can be represented by

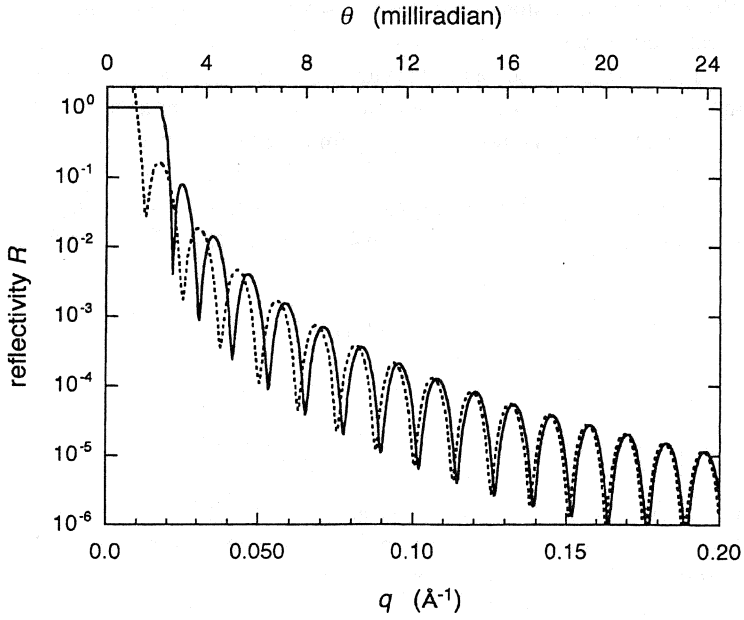

Figure 7.11 Neutron reflectivity calculated from a thin polystyrene film deposited on a silicon substrate. The solid curve is the exact result calculated according to (7.29) and the broken curve is the approximate result based on the kinematic approximation.

$$\rho(z) = \rho_1 H(-z) * g(z) \tag{7.53}$$

where $g(z)$ is the "smearing" function that characterizes the nature of the diffuseness of the interface. Usually $g(z)$ can be approximated by a Gaussian function

$$g(z) = \frac{1}{\sqrt{2\pi\sigma^2}} \exp\left(-\frac{z^2}{2\sigma^2}\right) \tag{7.54}$$

with σ characterizing the "width" of the diffuse interface. Making use of the result (B.24) showing that the derivative of $f(x) * g(x)$ is equal to $f'(x) * g(x)$, we obtain

$$\frac{d\rho(z)}{dz} = \rho_1 \delta(z) * g(z) = \rho_1 g(z) \tag{7.55}$$

Substitution of (7.55) into (7.47) gives the reflectivity

$$R = \frac{16\pi^2}{q^4} \rho_1^2 \exp(-\sigma^2 q^2) = R_F \exp(-\sigma^2 q^2) \tag{7.56}$$

where R_F is the reflectivity expected from a sharp interface as given by (7.48). Equation (7.56) shows that with a diffuse interface the reflectivity falls off more rapidly than it would with a sharp interface. The q^{-4} dependence of R in (7.48) has the same physical origin as the familiar q^{-4} dependence of scattered intensity in the Porod law. In the case of small-angle scattering it is known that the Porod law is not strictly obeyed if the interface between the two phases within the sample is diffuse rather than sharp. For such a sample, as discussed in Section 5.3.3.2, the scattered intensity is expected rather to follow Equation (5.99), that is, one in which the ideal Porod law behavior $I_{id}(q)$ is modified by a factor $\exp(-\sigma^2 q^2)$. Equation (5.99) is the exact equivalent of Equation (7.56) according to which the ideal Fresnel reflectivity is modified by a similar factor when the interface is diffuse.

Suppose that in a system with a film of thickness t deposited on a substrate, the two interfaces are diffuse. The scattering length density profile $\rho(z)$ is then modified from (7.49) to

$$\rho(z) = \rho_1 H(-z) * g_1(z) + (\rho_2 - \rho_1) H(-z - t) * g_2(z) \tag{7.57}$$

which leads to

$$\mathcal{F}\left\{\frac{d\rho(z)}{dz}\right\} = \rho_1 G_1(q) + (\rho_2 - \rho_1) e^{iqt} G_2(q) \tag{7.58}$$

where $G_j(q)$ is the Fourier transform of the smearing function $g_j(z)$. When the latter is approximated by a Gaussian function as in (7.54), $G_j(q)$ is equal to $\exp(-\sigma_j^2 q^2)$. Insertion of (7.58) into (7.47) then gives the reflectivity

$$\begin{aligned} R = \frac{16\pi^2}{q^4} & \left[\rho_1^2 G_1^2(q) + (\rho_2 - \rho_1)^2 G_2^2(q)\right. \\ & \left. + 2\rho_1(\rho_2 - \rho_1) G_1(q) G_2(q) \cos(qt)\right] \end{aligned} \tag{7.59}$$

which is to be compared with (7.52). Figure 7.12 gives numerical results that illustrate the effect of diffuse interfaces, as predicted by Equation (7.59). Here neutron reflectivity curves have been calculated for a system of a 500-Å deuterated polystyrene film laid over a Si substrate. The solid curve shows the result obtained when the interfaces between air and the polymer and between the polymer and the substrate are both sharp ($\sigma_1 = \sigma_2 = 0$), the thin broken curve is when the air–polymer interface is diffuse ($\sigma_1 = 20$Å, $\sigma_2 = 0$), and the thick broken curve is when the polymer–Si interface is diffuse ($\sigma_1 = 0, \sigma_2 = 20$Å).

7.3.3.2 Coherence Length and Rough Interface

The scattering length density profile $\rho(z)$, which determines the reflectivity R according to Equations (7.46) and (7.47), has hitherto been assumed to vary only in the z direction and to be constant in the directions parallel to the interface. If, however, there is in fact a moderate variation in the scattering length density in the x and y directions, $\rho(z)$ is to be understood to be the average over an x–y area at a given z. A question naturally arises over how large an area the average is to be taken. The answer is given in reference to the concept of the *coherence area* and *coherence length.* The coherence length is the distance between two points on the sample from which scattered rays will interfere coherently at the detector. It is known that on the wave front of a plane wave the coherence length is of the order of $\lambda/2\alpha$, where α is the angular divergence of the incident beam.[4,12] With $\lambda = 1$Å and $\alpha = 0.005° = 0.1$

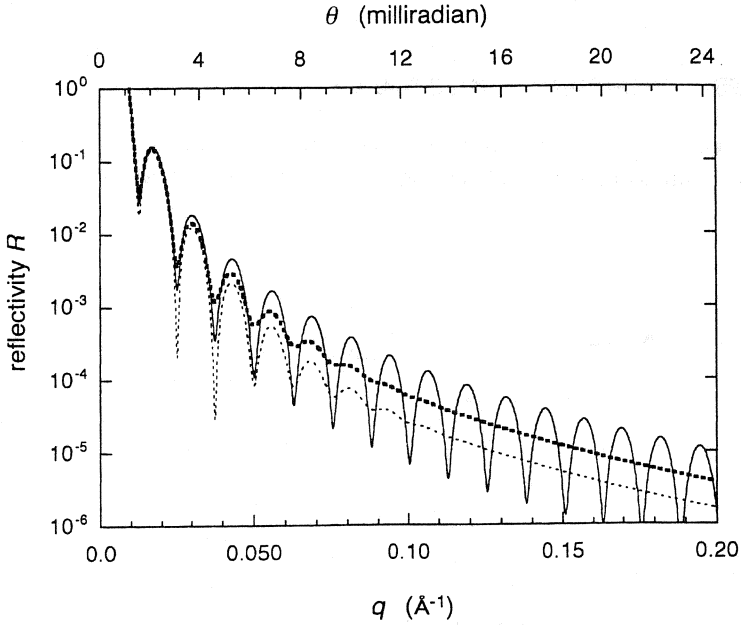

Figure 7.12 Reflectivity calculated for a deuterated polystyrene film of thickness 500 Å deposited on a Si substrate, to illustrate the effect of diffuse interfaces. Thin solid curve, $\sigma_1 = \sigma_2 = 0$; thin broken curve, $\sigma_1 = 20$Å, $\sigma_2 = 0$; thick broken curve, $\sigma_1 = 0, \sigma_2 = 20$Å.

milliradian, $\lambda/2\alpha$ is of the order of 5×10^3 Å. When the beam is incident on a planar surface at an angle θ of 1°(~ 0.02 radian), the rays scattered from two points on the surface separated by $(\lambda/2\alpha)/\sin\theta = 2.5 \times 10^5$ Å can still interfere with each other. If the scattering length density averaged over the coherence area still varies somewhat as the area is moved parallel to the interface, then an additional nonspecular diffuse scattering will become superimposed on the specular reflectivity that we have been discussing in this chapter.

So far we have also regarded the interface to be perfectly planar and smooth. We now consider what happens to the reflectivity if the interface contains some degree of roughness (or waviness). The answer depends on the size scale of the roughness. In Figure 7.13a the curvature of the interface is so small in comparison to the coherence length l_c that locally the interface can be regarded as planar and smooth, but the angle of incidence, θ_1, θ_2, etc., varies from place to place. The overall effect is then similar to the one produced when a beam containing a degree of divergence is incident on a planar, smooth interface. Figure 7.13b, on the other hand, shows the case in which the roughness is of a much smaller size scale than l_c. In this case the scattering length density averaged over a coherence area no longer changes abruptly as the interfacial boundary is crossed. As long as the height of the local peaks varies randomly from peak to peak, the averaged scattering length density $\rho(z)$ will undergo a gradual transition, as a function of z, from one medium to the next. The effect on the reflectivity would then be exactly the same as that produced by the diffuse interface discussed in the preceding section.

7.4 EXAMPLES OF EXPERIMENTAL STUDIES

A couple of examples from the literature are cited here to show how well the reflectivity curves obtained experimentally can be fitted by theoretical calculations and

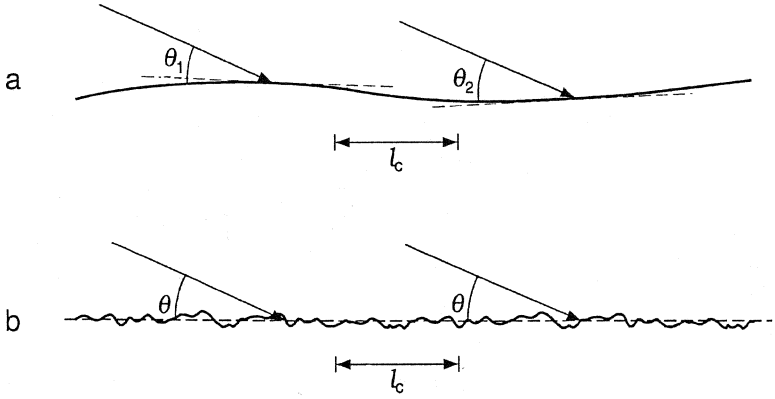

Figure 7.13 Rough interfaces in which the radii of curvature are (a) larger than the coherence length l_c and (b) smaller than l_c.

how sensitive the fit is to the details of the assumed models. For more experimental examples, the reader is referred to other review articles.[1-3,8,13]

Figure 7.14 shows the x-ray reflectivity curve (repeated three times) obtained by Tidswell *et al.*[14] with a sample that has a monolayer of alkylsiloxane $CH_3(CH_2)_{17}SiO_3$ deposited on a silicon substrate. In the plot the reflectivity $R(q)$, observed as a function of q, has been normalized by the Fresnel reflectivity $R_F(q)$ that is expected of a bare silicon surface. The solid curves are the reflectivities calculated on the basis of the models of scattering length density profile given in Figure 7.15, where $z = 0$ denotes the surface against air. The models assume (a) a single layer film, (b) a double layer film, and (c) a triple layer film sitting on top of the substrate, all the interfaces being diffuse in the sense discussed in Section 7.3.3.1. The best agreement is obtained with model (c) where the alkylsiloxane monolayer consists of a SiO_2 layer of 23.5 Å, followed by an intervening layer of 0.7 Å, and finally a hydrocarbon layer of thickness 17 Å. An equation in the form of (7.57) and (7.59) but generalized for a larger number of diffuse interfaces was used to calculate the reflectivity. Models (a) and (b) are clearly unable to fit the reflectivity curve at higher q values.

Figure 7.16 shows the neutron reflectivity determined by Anastasiadis *et al.*[15] with a sample in which a thin film of a diblock copolymer was deposited on a silicon substrate. The diblock copolymer, of molecular weight 100,000, consists of a block of deuterated polystyrene joined to a block of hydrogenous poly(methyl methacrylate) of about equal length and is therefore expected to organize itself into a lamellar

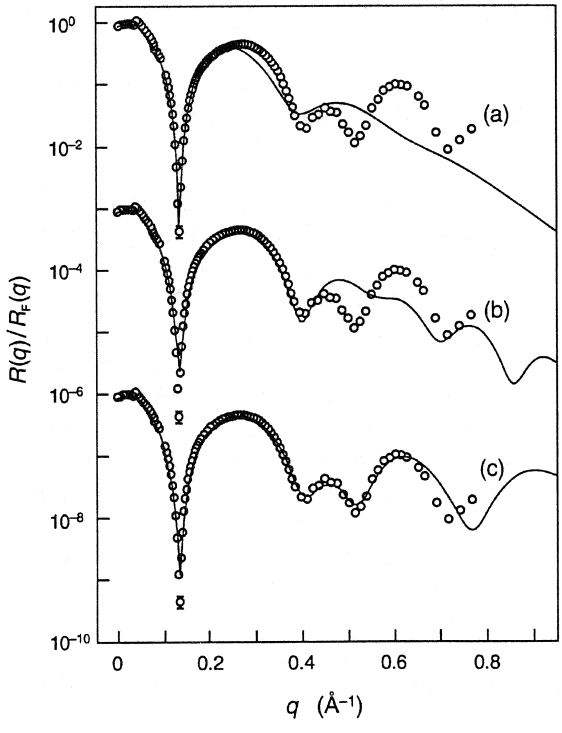

Figure 7.14 Normalized x-ray reflectivity from an alkylsiloxane monolayer on a silicon substrate. The solid curves are those calculated from the (a) one-, (b) two-, and (c) three-layer models shown in Figure 7.15. (From Tidswell *et al.*[13])

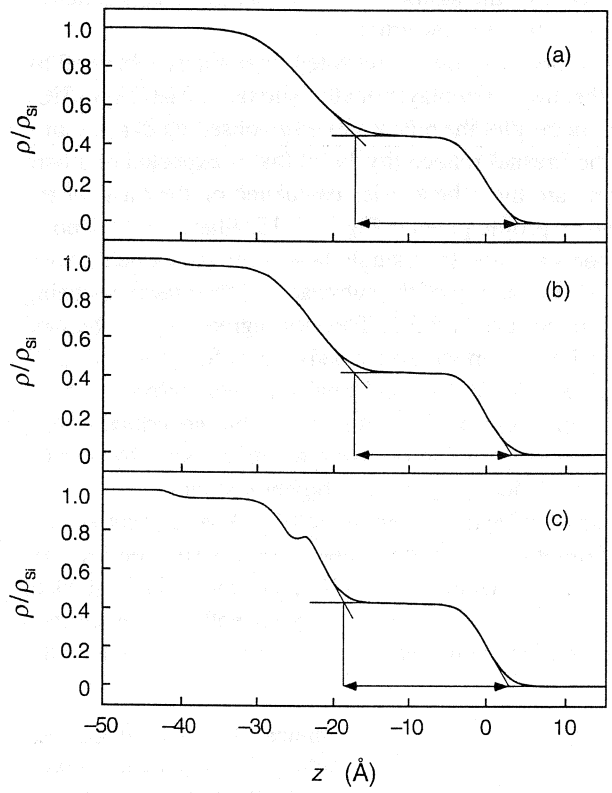

Figure 7.15 Electron density profiles for the (a) one-, (b) two-, and (c) three-layer models used to fit the reflectivity data shown in Figure 7.14. (From Tidswell *et al.*[13])

structure aligned parallel to the substrate surface. The inset in the figure gives the model scattering length density profile assumed for calculation of the reflectivity curve. Here the air–polymer interface is at $z = 0$ and the polymer–Si interface is at $z = 1400$ Å. Within the block copolymer the deuterated polystyrene layer has a higher scattering length density than the poly(methyl methacrylate) layer, and the former layer, with its lower surface free energy, is expected to place itself preferentially at the air–polymer interface. The diffuse interface between different block layers is assumed to have an effective thickness of 50 Å, and the solid curve in the inset is drawn according to an expression involving a hyperbolic tangent function predicted on theoretical grounds. The reflectivity calculated from this model is shown in the main plot of Figure 7.16 as the solid curve and is seen to agree well with the observed data. In the inset the thin dotted line gives the scattering length density model when the interfacial profile between block copolymer layers is replaced by a linear function. This model gives the reflectivity curve indicated by the broken line, which is clearly seen to be unable to reproduce the observed data completely. This example thus illustrates the degree to which small details in the model can be discriminated by comparing the calculation with observation.

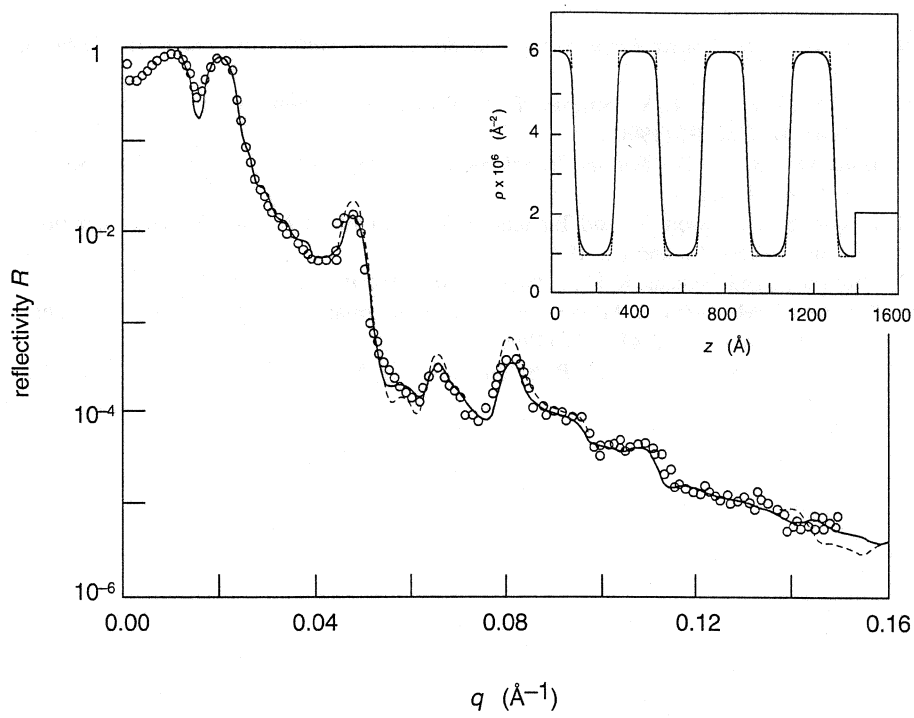

Figure 7.16 Neutron reflectivity determined with a layer of a diblock copolymer deposited on a silicon substrate, the copolymer being poly(deuterostyrene-co-methylmethacrylate) of molecular weight 100,000. (From Anastasiadis *et al.*[14]) The inset shows the scattering length density profile assumed to fit the observed data.

FURTHER READING

1. Russell, T. P., *Mat. Sci. Rep.* **5**, 171 (1990).
2. Foster, M., *Crit. Rev. Anal. Chem.* **24**, 179 (1993).
3. Higgins, J. S., and Benoît, H. C., *Polymers and Neutron Scattering,* Oxford University Press, Oxford, 1994, Chapter 10.

REFERENCES

4. Born, M., and Wolf, E., *Principle of Optics*, 6th ed., Pergamon Press, New York, 1980.
5. Fermi, E., *Nuclear Physics*, University of Chicago Press, Chicago, 1950.
6. Lekner, J., *Theory of Reflection*, Martinus Nijhoff Publishers, Dordrecht, 1987.
7. Parratt, L. G., *Phys. Rev.* **95**, 359 (1954).
8. Als-Nielsen, J., and Kjaer, K., in *Phase Transitions in Soft Condensed Matter*, T. Riest and D. Sherrington, Eds., Plenum Press, New York, 1989, p. 113.

9. Heavens, O. S., *Optical Properties of Thin Solid Films,* Butterworths Scientific, London, 1955.
10. Crowley, T. L., Lee, E. M., Simister, E. A., Thomas, R. K., Penfold, J., and Rennie, A. R., *Colloids Surf.* **52**, 85 (1990).
11. Bracewell, R. N., *The Fourier Transform and Its Applications*, 2nd ed., McGraw-Hill, New York, 1978, p. 112.
12. Lipson, S. G., Lipson, H., and Tannhauser, D. S. , *Optical Physics*, 3rd ed., Cambridge University Press, Cambridge, 1995.
13. Penfold, J., and Thomas, R. K., *J. Phys. Condens. Matter* **2**, 1396 (1990).
14. Tidswell, I. M., Ocko, B. M., Pershan, P. S., Wasserman, S. R., Whitesides, G. M., and Axe, J. D., *Phys. Rev. B* **41**, 1111 (1990).
15. Anastasiadis, S. H., Russell, T. P., Satija, S. K., and Majkrzak, C. F., *J. Chem. Phys.* **92**, 5677 (1990).

Inelastic Neutron Scattering

8

One of the important advantages of neutrons over x-rays, as mentioned in Section 1.1, is that measurements of inelastic neutron scattering yield information on atomic and molecular motions in polymers and other materials. This arises because neutrons whose wavelengths are of the order of atomic or molecular dimensions possess energy that is comparable to the thermal energies of atomic motions. Both the (kinetic) energy E and the wavelength λ of a neutron are related to its velocity v by

$$E = \frac{1}{2}mv^2 \tag{1.4}$$

and

$$\lambda = \frac{h}{mv} \tag{1.8}$$

which give the dependence of E on λ as

$$E = \frac{h^2}{2m\lambda^2} \tag{8.1}$$

Using the numerical values of the physical constants m and h given in Appendix D, we find from (1.4) and (8.1) the following relationship:

$$E = 5.228 \times 10^{-6}\, v^2 = 81.79\, \lambda^{-2} \tag{8.2}$$

where E, v, and λ are given in meV, m/s, and Å, respectively. For neutrons of wavelength 0.5–10 Å the energy is thus in the range of 300–0.8 meV, which is comparable to the thermal energy kT equal to about 20 meV at room temperature. The energy that may be exchanged during the inelastic scattering process can therefore be a sizable fraction of the energy of incident neutrons and is thus amenable to experimental determination.

8.1 THEORY OF INELASTIC SCATTERING

The wave vector $\boldsymbol{k}$ of the neutron is defined to have magnitude

$$k = \frac{2\pi}{\lambda} \tag{8.3}$$

and direction coinciding with that of $\boldsymbol{v}$. Its momentum $\boldsymbol{p} = m\boldsymbol{v}$ is then given, in view of (1.8), by

$$\boldsymbol{p} = \hbar \boldsymbol{k} \tag{8.4}$$

In terms of the frequency ν or the *angular frequency* $\omega (= 2\pi\nu)$ the energy of a neutron is $E = h\nu = \hbar\omega$. The energy is related to the magnitude of the momentum $p = \hbar k$ by

$$E = \frac{p^2}{2m} \qquad \text{and} \qquad \hbar\omega = \frac{\hbar^2 k^2}{2m} \tag{8.5}$$

Consider an incident neutron of wave vector $\boldsymbol{k}_0$ that is scattered by the sample into a solid angle $d\Omega$. If the wave vector of the scattered neutron is $\boldsymbol{k}_1$, the momentum transferred *to the neutron from the sample* is equal to $\hbar\boldsymbol{q}$ given by

$$\hbar\boldsymbol{q} = \hbar\boldsymbol{k}_1 - \hbar\boldsymbol{k}_0 \tag{8.6}$$

In inelastic scattering the energy $E_1 = \hbar\ \omega_1$ of the scattered neutron is not equal to the energy $E_0 = \hbar\ \omega_0$ of the incident neutron, and the amount of energy transferred *to the neutron from the sample* on scattering is

$$\Delta E = \hbar\omega_1 - \hbar\omega_0 = \frac{\hbar^2 k_1^2}{2m} - \frac{\hbar^2 k_0^2}{2m} \tag{8.7}$$

From now on the symbol ω without a subscript is used to denote the change in the angular frequency on scattering, i.e., $\omega = \omega_1 - \omega_0$ and $\Delta E = \hbar\omega$. If $\Delta E = 0$, the scattering is termed elastic; for $\Delta E \neq 0$ the scattering is inelastic, and for the particular cases in which ΔE is very close to zero, the term quasielastic is often used. In inelastic (and quasielastic) scattering where $k_1 \neq k_0$, the magnitude of the momentum change $\hbar q$ suffered by the neutron on scattering is no longer determined solely by the scattering angle 2θ but depends also on the energy change $\hbar\omega$ (see Figure 8.1):

$$q^2 = k_0^2 + k_1^2 - 2k_0 k_1 \cos 2\theta \tag{8.8}$$

In inelastic scattering the scattered intensity needs to be determined as a function of both the scattering angle Ω and the magnitude of energy exchange $\hbar\omega$. This function, called the *double* (or *partial*) *differential scattering cross section* $d^2\sigma/d\Omega\, d\omega$, is a

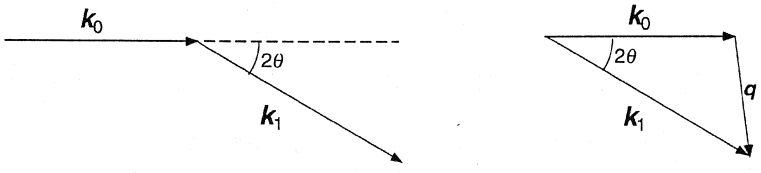

Figure 8.1 Relationship between wave vector, momentum transfer, and energy transfer on inelastic scattering.

measure of the probability of scattering per unit solid angle per unit energy transfer, and is the generalization of the differential scattering cross section $d\sigma/d\Omega$ defined in Section 1.2.1.

8.1.1 Inelastic Scattering Cross Section

We start the discussion of the theory of inelastic scattering by first quoting the basic equation that relates the double differential scattering cross section to the structure and motion of nuclei in the scattering system. Unfortunately the derivation of this fundamental equation requires the use of quantum mechanics much beyond the scope of this book. The scattering system is characterized by the positions $\boldsymbol{r}_j(t)$ of all the nuclei ($j = 1, \ldots, N$) in it as a function of t. The equation we take as the starting point of our discussion is then

$$\frac{d^2\sigma}{d\Omega\, d\omega} = \frac{k_1}{k_0}\frac{1}{2\pi}\sum_j\sum_k b_j b_k \int_{-\infty}^{\infty} \left\langle \exp\left[-i\boldsymbol{q}\boldsymbol{r}_j(t)\right] \exp\left[i\boldsymbol{q}\boldsymbol{r}_k(0)\right]\right\rangle \exp(i\omega t)\, dt \tag{8.9}$$

We will merely content ourselves by examining the "significance" of the various elements in (8.9) in comparison with those in the analogous equation valid in the static approximation. The differential scattering cross section $d\sigma/d\Omega$, in the static approximation in which the time dependence of the system is ignored, is obtained by taking the absolute square of the amplitude as given by (1.71):

$$\begin{aligned}\frac{d\sigma}{d\Omega} &= \left\langle \left| \sum_j b_j \exp(-i\boldsymbol{q}\boldsymbol{r}_j) \right|^2 \right\rangle \\ &= \sum_j\sum_k b_j b_k \left\langle \exp(-i\boldsymbol{q}\boldsymbol{r}_j) \exp(i\boldsymbol{q}\boldsymbol{r}_k)\right\rangle \end{aligned} \tag{8.10}$$

The factor k_1/k_0 present in (8.9) arises from the fact that the flux of neutrons measured at the detector depends on the velocity of the neutrons. Equation (8.10) can be "derived" from equation (8.9) by letting $k_1 = k_0$, by eliminating the time dependence of $\boldsymbol{r}_j(t)$, and by recognizing that

$$\frac{1}{2\pi}\int_{-\infty}^{\infty} e^{i\omega t}\, dt = \delta(\omega) \tag{8.11}$$

which embodies the assumption of no energy exchange on scattering.

Equation (8.9) can be written in various alternative forms using several functions defined below. In doing so, we assume, for the sake of simplicity, that the scattering system consists of nuclei of a single element, and moreover the element contains a single isotope whose nuclear spin is zero, so that the scattering lengths b_j in (8.9) all have the same numerical value b.

The *intermediate scattering function* $F(\boldsymbol{q},t)$ is defined as

$$F(\boldsymbol{q}, t) = \frac{1}{N} \sum_{j=1}^{N} \sum_{k=1}^{N} \left\langle \exp\left[-i\boldsymbol{q}\boldsymbol{r}_j(t)\right] \exp\left[i\boldsymbol{q}\boldsymbol{r}_k(0)\right] \right\rangle \tag{8.12}$$

which allows (8.9) to be written as

$$\frac{d^2\sigma}{d\Omega\, d\omega} = \frac{k_1}{k_0} b^2 N \frac{1}{2\pi} \int_{-\infty}^{\infty} F(\boldsymbol{q}, t) e^{i\omega t}\, dt \tag{8.13}$$

Next we define the *time-dependent pair correlation function* or *van Hove correlation function*[5] $G(\boldsymbol{r},t)$ as the inverse Fourier transform of $F(\boldsymbol{q},t)$ in space, that is,

$$G(\boldsymbol{r}, t) = \frac{1}{(2\pi)^3} \int F(\boldsymbol{q}, t) e^{i\boldsymbol{q}\boldsymbol{r}}\, d\boldsymbol{q} \tag{8.14}$$

which allows (8.9) to be written as

$$\frac{d^2\sigma}{d\Omega\, d\omega} = \frac{k_1}{k_0} b^2 N \frac{1}{2\pi} \int_{-\infty}^{\infty} \int_{V} G(\boldsymbol{r}, t) e^{-i(\boldsymbol{q}\boldsymbol{r} - \omega t)}\, d\boldsymbol{r}\, dt \tag{8.15}$$

The *dynamic structure factor* $S(\boldsymbol{q},\omega)$ (also called the *scattering function* or *scattering law* by some) is defined as

$$\begin{aligned} S(\boldsymbol{q}, \omega) &= \frac{1}{2\pi} \int_{-\infty}^{\infty} F(\boldsymbol{q}, t) e^{i\omega t}\, dt \\ &= \frac{1}{2\pi} \int_{-\infty}^{\infty} \int_{V} G(\boldsymbol{r}, t) e^{-i(\boldsymbol{q}\boldsymbol{r} - \omega t)}\, d\boldsymbol{r}\, dt \end{aligned} \tag{8.16}$$

which allows (8.9) to be written in the compact form

$$\frac{d^2\sigma}{d\Omega\, d\omega} = \frac{k_1}{k_0} b^2 N S(\boldsymbol{q}, \omega) \tag{8.17}$$

The three functions $G(\boldsymbol{r},t)$, $F(\boldsymbol{q},t)$, and $S(\boldsymbol{q},\omega)$ are related to each other by Fourier transforms in space and/or in time, as illustrated in Figure 8.2. Note that $F(\boldsymbol{q},t)$ is dimensionless, $G(\boldsymbol{r},t)$ has dimension [volume^{-1}], and $S(\boldsymbol{q},\omega)$ has dimension [time].

8.1.2 van Hove Correlation Function

We now examine the physical meaning of the van Hove correlation function $G(\boldsymbol{r},t)$ defined by (8.14). From (8.12) and (8.14) it follows that

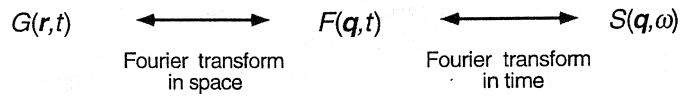

Figure 8.2 Fourier transform relationships among the van Hove correlation function $G(\boldsymbol{r}, t)$, the intermediate scattering function $F(\boldsymbol{q}, t)$, and the dynamic structure factor $S(\boldsymbol{q}, \omega)$.

$$G(\boldsymbol{r}, t) = \frac{1}{N} \sum_{j=1}^{N} \sum_{k=1}^{N} \frac{1}{(2\pi)^3} \int \left\langle \exp\left[-i\boldsymbol{q}\boldsymbol{r}_j(t)\right] \exp\left[i\boldsymbol{q}\boldsymbol{r}_k(0)\right] \right\rangle e^{i\boldsymbol{q}\boldsymbol{r}}\, d\boldsymbol{q} \tag{8.18}$$

Using the following relationship

$$\delta(\boldsymbol{r} - \boldsymbol{a}) = \frac{1}{(2\pi)^3} \int e^{-i\boldsymbol{q}\boldsymbol{a}}\, e^{i\boldsymbol{q}\boldsymbol{r}}\, d\boldsymbol{q} \tag{8.19}$$

that can be derived from (B.13) and (B.36), we rewrite (8.18) as

$$G(\boldsymbol{r}, t) = \frac{1}{N} \sum_{j-1}^{N} \sum_{k=1}^{N} \left\langle \delta\left[\boldsymbol{r} - \left\{\boldsymbol{r}_j(t) - \boldsymbol{r}_k(0)\right\}\right] \right\rangle \tag{8.20}$$

If the nuclei are equivalent, then for fixed k the sum over j in (8.20) gives the same value whatever the value of k is. So the sum over k is N times the term with $k = 1$. Thus

$$G(\boldsymbol{r}, t) = \sum_{j=1}^{N} \left\langle \delta\left[\boldsymbol{r} - \left\{\boldsymbol{r}_j(t) - \boldsymbol{r}_1(0)\right\}\right] \right\rangle \tag{8.21}$$

Taking $\boldsymbol{r}_1(0)$ as the origin, we interpret this equation to mean that $G(\boldsymbol{r},t)\, d\boldsymbol{r}$ is the probability that given a particle at the origin at time $t = 0$, any particle (including the original particle) is in the volume $d\boldsymbol{r}$ at position $\boldsymbol{r}$ at time t.

The double differential scattering cross section, according to (8.15), is proportional to the space–time Fourier transform of $G(\boldsymbol{r},t)$. This is analogous to the fact, discussed in Section 1.5.2, that in the static approximation the intensity $I(\boldsymbol{q})$ (or the differential scattering cross section $ds/d\Omega$) is given by the spatial Fourier transform of the density–density autocorrelation function defined in (1.79). In the special case of $t = 0$, $G(\boldsymbol{r},0)$ denotes the probability of finding a particle at $\boldsymbol{r}$ when there is already a particle at position 0. $G(\boldsymbol{r},0)$ is therefore related to the pair distribution function $g(\boldsymbol{r})$ discussed in Section 4.1.1, as in

$$G(\boldsymbol{r}, 0) = \delta(\boldsymbol{r}) + \langle n \rangle\, g(\boldsymbol{r}) \tag{8.22}$$

where $\langle n \rangle$ is the average number density of the particles (or nuclei, in the present discussion). The first term $\delta(\boldsymbol{r})$ in (8.22) represents the self-correlation of the particles, and the second term denotes correlation between different particles. Following the example set by (8.22) we may split $G(\boldsymbol{r},t)$ into its "self (s)" and "distinct (d)" parts, as in

$$G(\boldsymbol{r}, t) = G_{\mathrm{s}}(\boldsymbol{r}, t) + G_{\mathrm{d}}(\boldsymbol{r}, t) \tag{8.23}$$

where $G_{\mathrm{s}}(\boldsymbol{r},t)$ is the probability that the particle, which was at position 0 at time 0, will be found at position $\boldsymbol{r}$ at time t, and $G_{\mathrm{d}}(\boldsymbol{r},t)$ is the probability that after seeing a particle at the origin at time 0, we see a *different* particle at $\boldsymbol{r}$ at time t. By comparing (8.23) with (8.22) we note that $G_{\mathrm{s}}(\boldsymbol{r},0)$ is equal to $\delta(\boldsymbol{r})$ and $G_{\mathrm{d}}(\boldsymbol{r},0)$ is equal to $\langle n \rangle\, g(\boldsymbol{r})$.

$G_s(\boldsymbol{r},t)$ is in general simpler to visualize and calculate theoretically than $G_d(\boldsymbol{r},t)$ since the former describes the motion of a single particle.

In the limit of large t both G_s and G_d become independent of $\boldsymbol{r}$, while the behavior at large $\boldsymbol{r}$ is the same as that at large t. It follows that

$$\lim_{r\to\infty} G_s(\boldsymbol{r},t) = \lim_{t\to\infty} G_s(\boldsymbol{r},t) = \frac{1}{V} \approx 0 \tag{8.24}$$

and

$$\lim_{r\to\infty} G_d(\boldsymbol{r},t) = \lim_{t\to\infty} G_d(\boldsymbol{r},t) \approx \langle n\rangle \tag{8.25}$$

The variation of G_s and G_d (in an isotropic amorphous material) as a function of r for $t \ll \tau, t \sim \tau$, and $t \gg \tau$ is illustrated schematically in Figure 8.3, where τ is the characteristic relaxation time of the material system. At very short time, G_s is not very different from a delta function, indicating that there is only a small probability that the atom has moved very far away. Likewise, G_d indicates the position of *other* atoms, and evidently there is no likelihood that some other atom has already replaced the one at the origin. On the other hand, at t long compared to τ, the curve for G_s indicates that the atom that was originally at the origin is likely to have diffused away from it, although it is still slightly more likely to be found at the origin than in any other particular position. The curve for G_d on the other hand shows that so far as other atoms are concerned, diffusion has produced practically a uniform density.

8.1.3 Coherent and Incoherent Scattering

In Section 1.4 it was shown that when there is random variation in the scattering length b from nucleus to nucleus, the scattering of neutrons from an assemblage of atomic nuclei consists of coherent and incoherent components. Such random variation in the scattering length arises when the element is a mixture of isotopes or when the nuclear spin is nonzero so that the scattering length realized is either b^+ or b^- depending on the orientation of the nuclear spin. The inelastically scattered neutrons also consist of coherent and incoherent components as demonstrated as follows.

For the sake of simplifying the argument, we again assume that the system contains a single type of element. To reflect the random variability in the scattering length b of individual nuclei, Equation (8.9) is now written as

$$\frac{d^2\sigma}{d\Omega\, d\omega} = \frac{k_1}{k_0}\frac{1}{2\pi}\sum_j\sum_k \langle b_j b_k\rangle \int_{-\infty}^{\infty} \left\langle \exp\left[-i\boldsymbol{q}\boldsymbol{r}_j(t)\right]\exp[i\boldsymbol{q}\boldsymbol{r}_k(0)]\right\rangle \exp(i\omega t)\, dt \tag{8.26}$$

where $\langle b_j b_k\rangle$ is the expectation value of $b_j b_k$. As was done in Section 1.4, the summation in (8.26) is now separated into two sums, one in which j equals k and the other in which j does not equal k, leading to

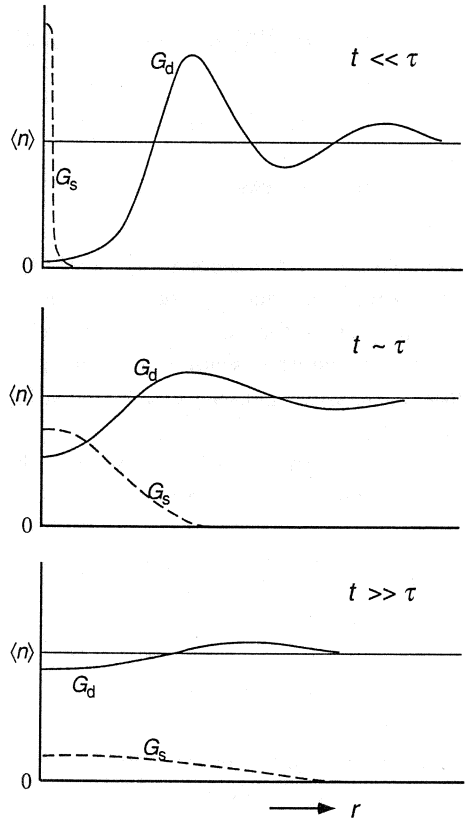

Figure 8.3 Qualitative behavior of the van Hove correlation functions. The full curve is $G_d(r, t)$ and the broken curve is $G_s(r, t)$. (After van Hove.[5])

$$\frac{d^2\sigma}{d\Omega\, d\omega} = \frac{k_1}{k_0}\frac{\langle b^2\rangle}{2\pi}\sum_j \int_{-\infty}^{\infty} \left\langle \exp\left[-i\boldsymbol{q}\boldsymbol{r}_j(t)\right]\exp[i\boldsymbol{q}\boldsymbol{r}_j(0)]\right\rangle \exp(i\omega t)\, dt$$

$$+ \frac{k_1}{k_0}\frac{\langle b\rangle^2}{2\pi}\sum_j\sum_{j\neq k} \int_{-\infty}^{\infty} \left\langle \exp\left[-i\boldsymbol{q}\boldsymbol{r}_j(t)\right]\exp[i\boldsymbol{q}\boldsymbol{r}_k(0)]\right\rangle \exp(i\omega t)\, dt \quad (8.27)$$

In terms of the coherent and incoherent scattering lengths, b_{coh} and b_{inc}, defined as

$$b_{\text{coh}} = \langle b\rangle \quad (1.65)$$

and

$$b_{\text{inc}} = \left(\langle b^2\rangle - \langle b\rangle^2\right)^{1/2} \quad (1.66)$$

(8.27) can be rewritten as

$$\frac{d^2\sigma}{d\Omega\, d\omega} = \frac{k_1}{k_0}\frac{b_{\text{inc}}^2}{2\pi}\sum_j \int_{-\infty}^{\infty} \left\langle \exp[-i\boldsymbol{q}\boldsymbol{r}_j(t)]\exp[i\boldsymbol{q}\boldsymbol{r}_j(0)]\right\rangle \exp(i\omega t)\, dt$$

$$+\frac{k_1}{k_0}\frac{b_{\text{coh}}^2}{2\pi}\sum_j\sum_k\int_{-\infty}^{\infty}\langle\exp[-i\boldsymbol{q}\boldsymbol{r}_j(t)]\exp[i\boldsymbol{q}\boldsymbol{r}_k(0)]\rangle\exp(i\omega t)\,dt \quad (8.28)$$

[Note that to obtain (8.28),

$$\frac{k_1}{k_0}\frac{\langle b\rangle^2}{2\pi}\sum_j\int_{-\infty}^{\infty}\langle\exp[-i\boldsymbol{q}\boldsymbol{r}_j(t)]\exp[i\boldsymbol{q}\boldsymbol{r}_j(0)]\rangle\exp(i\omega t)\,dt$$

was subtracted from the first term of (8.27) and added to the second.] The first term in (8.28) is called the incoherent scattering component and contains information about the motions of individual nuclei but nothing about their correlation with other nuclei. On the other hand, the second term, the coherent scattering component, contains information about the relative motion between nuclei j and k (including the contributions from the cases in which $j = k$).

In view of (8.28) and from the definition of $G_s(\boldsymbol{r},t)$ in Section 8.1.2, we find the incoherent component of the double differential scattering cross section to be

$$\left(\frac{d^2\sigma}{d\Omega\,d\omega}\right)_{\text{inc}} = \frac{k_1}{k_0}\frac{Nb_{\text{inc}}^2}{2\pi}\int_{-\infty}^{\infty}\int G_s(\boldsymbol{r},t)e^{-(\boldsymbol{q}\boldsymbol{r}-\omega t)}\,d\boldsymbol{r}\,dt \quad (8.29)$$

and its coherent counterpart to be

$$\left(\frac{d^2\sigma}{d\Omega\,d\omega}\right)_{\text{coh}} = \frac{k_1}{k_0}\frac{Nb_{\text{coh}}^2}{2\pi}\int_{-\infty}^{\infty}\int G(\boldsymbol{r},t)e^{-(\boldsymbol{q}\boldsymbol{r}-\omega t)}\,d\boldsymbol{r}\,dt \quad (8.30)$$

The intermediate scattering function $F(\boldsymbol{q},t)$ and the dynamic structure factor $S(q,\omega)$ can also be split into their respective "self" and "distinct" parts, as in

$$F(\boldsymbol{q},t) = F_s(\boldsymbol{q},t) + F_d(\boldsymbol{q},t) \quad (8.31)$$

and

$$S(\boldsymbol{q},\omega) = S_s(\boldsymbol{q},\omega) + S_d(\boldsymbol{q},\omega) \quad (8.32)$$

where the "self" part $F_s(\boldsymbol{q},t)$ or $S_s(\boldsymbol{q},\omega)$ is associated with the incoherent scattering cross section, as, for example, in

$$\left(\frac{d^2\sigma}{d\Omega\,d\omega}\right)_{\text{inc}} = \frac{k_1}{k_0}b_{\text{inc}}^2 N S_s(\boldsymbol{q},\omega) \quad (8.33)$$

In view of the definition (8.12) of the intermediate scattering function, its self part $F_s(\boldsymbol{q},t)$ can be written as

$$F_s(\boldsymbol{q},t) = \frac{1}{N}\sum_{j=1}^{N}\langle\exp[-i\boldsymbol{q}\{\boldsymbol{r}_j(t) - \boldsymbol{r}_j(0)\}]\rangle \quad (8.34)$$

If all the nuclei are dynamically equivalent, $F_s(\boldsymbol{q},t)$ can be represented by the behavior of any single nucleus, and can thus be written as

$$F_s(\boldsymbol{q},t) = \langle\exp[-i\boldsymbol{q}\{\boldsymbol{r}(t) - \boldsymbol{r}(0)\}]\rangle \quad (8.35)$$

where $\boldsymbol{r}(t)$ stands for $\boldsymbol{r}_j(t)$ with the index j taken arbitrarily.

Experimentally, it is difficult to separate incoherent from coherent scattering. However, with most polymers in their unmodified, hydrogenous form, scattering is predominantly incoherent, owing to the large incoherent scattering cross section of protons. The coherent scattering is usually concentrated in a few Bragg peaks or broader maxima so that provided these regions in q are avoided, the scattered intensity observed is almost entirely incoherent. In such cases neutron scattering results can be interpreted solely in terms of the self motions of protons, which simplifies interpretation considerably. In the remainder of this chapter, unless otherwise mentioned, we will confine our attention to incoherent scattering from protons and its interpretation in terms of the self parts, $G_s(\boldsymbol{r},t)$, $F_s(\boldsymbol{q},t)$, and $S_s(\boldsymbol{q},\omega)$, of the functions defined in this section.

8.2 SIMPLE MODELS OF MOTIONS

Motions that are observed in polymer systems are very complex and result from the superposition of many different types of motions taking place on widely different time scales. To understand such complex dynamics, it is, however, helpful initially to consider scattering functions that can be derived theoretically on the basis of several very simple models. With some oversimplification, one may recognize in polymers three representative types of motions: the vibration of atoms around their average positions, the rotation of side groups attached to the main chain, and the slow relaxation in the positions of individual segments in the main chain. In corresponding small molecule liquids, one may similarly recognize three types of motions: vibration of atoms, reorientation of the molecule about its center of mass, and translational diffusion of the molecule as a whole. The time scales of these motions are sufficiently distinct from each other such that in inelastic neutron scattering spectra, features characteristic of these different motions tend to appear in separate regions of ω. In Sections 8.2.1–8.2.3 that follow, the dynamic scattering functions are derived for these simple models, and this is followed in Section 8.2.4 by a brief discussion of how these functions could be combined to represent the overall behavior.

8.2.1 Translational Diffusion

The self part $G_s(\boldsymbol{r},t)$ of the van Hove correlation function represents the probability that a proton, which was at the origin at time 0, will be at position $\boldsymbol{r}$ at time t. For a particle undergoing a translational diffusion with diffusion coefficient D, $G_s(\boldsymbol{r},t)$ therefore obeys the Fickian diffusion equation

$$\frac{\partial G_s^T(\boldsymbol{r},t)}{\partial t} = D\nabla^2 G_s^T(\boldsymbol{r},t) \tag{8.36}$$

Solution of (8.36) with the initial condition $G_s^T(\boldsymbol{r},0) = \delta(\boldsymbol{r})$ leads to

$$G_s^T(r,t) = \frac{1}{(4\pi D\,|t|)^{3/2}} \exp\left(-\frac{r^2}{4D\,|t|}\right) \tag{8.37}$$

The spatial Fourier transform of (8.37) is

$$F_s^T(q, t) = \exp(-q^2 D\,|t|) \tag{8.38}$$

which, after a further Fourier transformation in time, yields

$$S_s^T(q, \omega) = \frac{1}{\pi} \frac{Dq^2}{(Dq^2)^2 + \omega^2} \tag{8.39}$$

The intermediate scattering function $F_s^T(q, t)$, plotted in Figure 8.4, is a simple exponential $\exp(-t/\tau)$ whose relaxation time $\tau (= 1/Dq^2)$ decreases with increasing q. The dynamic structure factor $S_s^T(q, \omega)$ is a simple Lorentzian, whose half-width at half-maximum Dq^2 increases with q, as illustrated in Figure 8.5.

8.2.2 Rotation

To discuss the scattering function due to a rotational motion, we start with Equation (8.35) for the intermediate scattering function $F_s(\boldsymbol{q},t)$ but with $\boldsymbol{r}$ now replaced by the radius vector $\boldsymbol{R}$, which represents the position of the proton relative to the center of the rotating body. Let us first consider the function in the limit of $t \to \infty$. Since at long t any correlation between $\boldsymbol{R}(0)$ and $\boldsymbol{R}(t)$ is totally lost, we can write

$$\begin{aligned} F_s^R(\boldsymbol{q}, \infty) &= \langle \exp[-i\boldsymbol{q}\{\boldsymbol{R}(\infty) - \boldsymbol{R}(0)\}] \rangle \\ &= \langle \exp[-i\boldsymbol{q}\boldsymbol{R}(\infty)] \rangle \langle \exp[i\boldsymbol{q}\boldsymbol{R}(0)] \rangle \end{aligned} \tag{8.40}$$

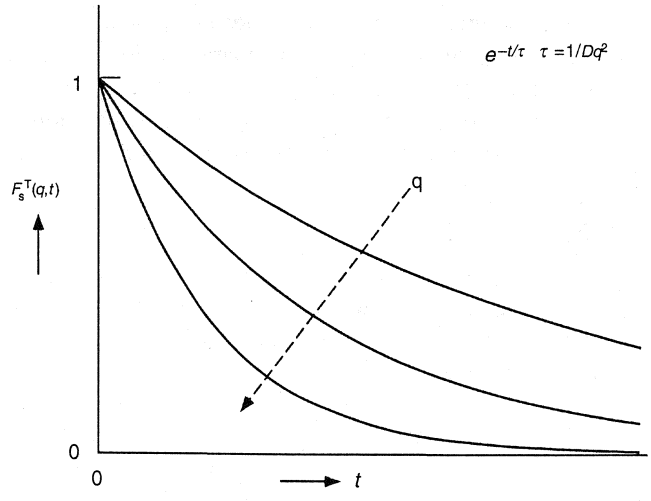

Figure 8.4 Plot of the incoherent intermediate scattering function $F_s^T(q, t)$ calculated for translational diffusion, for different q values.

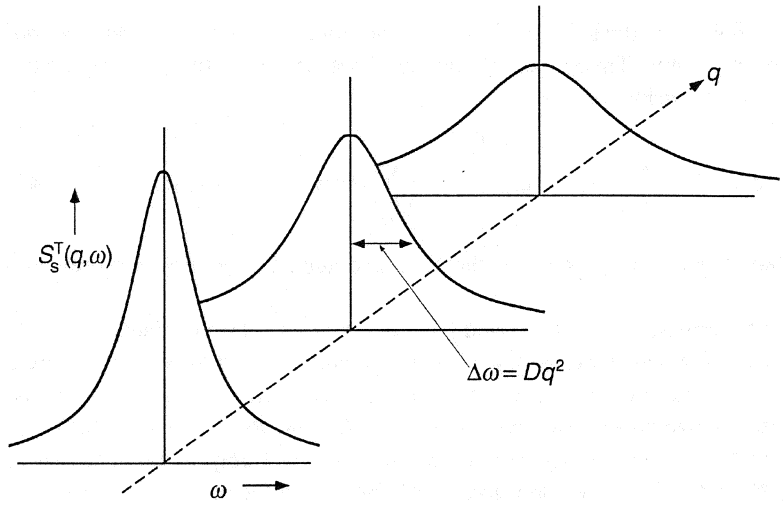

Figure 8.5 Schematic representation of the incoherent dynamic structure factor $S_s^T(q, \omega)$ for translational diffusion, at different q values.

In taking the thermal averages $\langle\ \ \rangle$ we recognize that the distribution of $\boldsymbol{R}(0)$ among different protons should be the same as the distribution of $\boldsymbol{R}(\infty)$, and therefore $F_s^R(\boldsymbol{q}, \infty)$ is given by

$$\begin{aligned} F_s^R(\boldsymbol{q}, \infty) &= \langle \exp[-i\boldsymbol{q}\boldsymbol{R}(0)] \rangle \langle \exp[i\boldsymbol{q}\boldsymbol{R}(0)] \rangle \\ &= |\langle \exp[-i\boldsymbol{q}\boldsymbol{R}(0)] \rangle|^2 \end{aligned} \tag{8.41}$$

In rotation, unlike in totally free translational diffusion, $\boldsymbol{R}$ is confined to a restricted volume of space, so that $F_s^R(\boldsymbol{q}, \infty)$ is not equal to zero. We therefore split $F_s^R(\boldsymbol{q}, t)$ into this time-independent term and a time-dependent one:

$$F_s^R(\boldsymbol{q}, t) = F_s^R(\boldsymbol{q}, \infty) + [F_s^R(\boldsymbol{q}, t) - F_s^R(\boldsymbol{q}, \infty)] \tag{8.42}$$

Remembering that the Fourier transform of unity is a delta function, we can write the time Fourier transform of (8.42) in the form

$$S_s^R(\boldsymbol{q}, \omega) = A_0(\boldsymbol{q})\delta(\omega) + \{1 - A_0(\boldsymbol{q})\} f_{qe}(\boldsymbol{q}, \omega) \tag{8.43}$$

where the factor $A_0(\boldsymbol{q})$, which is equal to $F_s^R(\boldsymbol{q}, \infty)$, is called the *elastic incoherent structure factor* (EISF). Equation (8.43) shows that $S_s^R(\boldsymbol{q}, \omega)$ always contains a purely elastic component, $A_0(\boldsymbol{q})\delta(\omega)$, superimposed on the quasielastic component represented by the second term. The latter is written in the form shown in (8.43) in recognition of the normalization conditions:

$$\int_{-\infty}^{\infty} f_{qe}(\boldsymbol{q}, \omega)\, d\omega = 1 \qquad \text{and} \qquad \int_{-\infty}^{\infty} S_s^R(\boldsymbol{q}, \omega)\, d\omega = 1 \tag{8.44}$$

It is seen from (8.41) that the EISF gives a direct measure of the time-averaged *spatial distribution* of the proton. This should be compared with the static (coherent) structure factor, which can be written as

$$S(\boldsymbol{q}) \propto \left\langle \left| \sum_j \exp(-i\boldsymbol{q}\boldsymbol{r}_j) \right|^2 \right\rangle = \left\langle \sum_{j,k} \exp[-i\boldsymbol{q}(\boldsymbol{r}_j - \boldsymbol{r}_k)] \right\rangle \tag{8.45}$$

indicating that it gives a measure of the time-averaged *correlation* between two nuclei.

The explicit expressions for $A_0(\boldsymbol{q})$ and $f_{\mathrm{qe}}(\boldsymbol{q},\omega)$ in (8.43) of course depend on the specifics of the rotational motion that is being considered. To provide a concrete example as an illustration, we consider the simplest[6] of such motions, in which the vector $\boldsymbol{R}$ jumps between only two rotational sites $\boldsymbol{R}_1$ and $\boldsymbol{R}_2$ (see Figure 8.6). We assume that the two sites are equivalent and are equally likely to be occupied at $t = 0$. Let $p(\boldsymbol{R}_k, t|\boldsymbol{R}_j, 0)$ be the conditional probability that the proton is at $\boldsymbol{R}_k$ at time t provided it was at $\boldsymbol{R}_j$ at time 0 ($j, k = 1, 2$). Obviously $p(\boldsymbol{R}_1, t|\boldsymbol{R}_j, 0)+p(\boldsymbol{R}_2, t|\boldsymbol{R}_j, 0)$ is equal to 1. In the cases in which the proton happens to be at $\boldsymbol{R}_1$ at $t = 0$, the following kinetic equation holds for the rate of change in $p(\boldsymbol{R}_1, t|\boldsymbol{R}_1, 0)$:

$$\frac{d}{dt}p(\boldsymbol{R}_1, t|\boldsymbol{R}_1, 0) = -\frac{1}{\tau}p(\boldsymbol{R}_1, t|\boldsymbol{R}_1, 0) + \frac{1}{\tau}p(\boldsymbol{R}_2, t|\boldsymbol{R}_1, 0) \tag{8.46}$$

where τ, the average time interval between successive transitions, is assumed to be the same for the transitions from $\boldsymbol{R}_1$ to $\boldsymbol{R}_2$ and from $\boldsymbol{R}_2$ to $\boldsymbol{R}_1$. Solving (8.46) with the initial condition $p(\boldsymbol{R}_1, 0|\boldsymbol{R}_1, 0) = 1$, we find

$$p(\boldsymbol{R}_1, t|\boldsymbol{R}_1, 0) = \frac{1}{2}(1 + e^{-2t/\tau}) \equiv p(t) \tag{8.47}$$

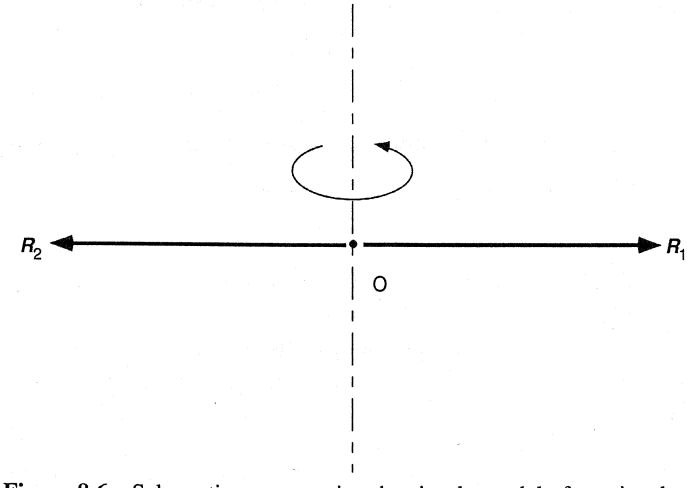

Figure 8.6 Schematics representing the simple model of rotational transitions between two sites R_1 and R_2.

and

$$p(\boldsymbol{R}_2, t|\boldsymbol{R}_1, 0) = 1 - p(t) \tag{8.48}$$

By a similar argument we find

$$p(\boldsymbol{R}_2, t|\boldsymbol{R}_2, 0) = p(t) \tag{8.49}$$

and

$$p(\boldsymbol{R}_1, t|\boldsymbol{R}_2, 0) = 1 - p(t) \tag{8.50}$$

In view of the physical meaning of the self part of the intermediate scattering function given by (8.35), we have

$$\begin{aligned} F_s^R(\boldsymbol{q}, t) &= \langle \exp[-i\boldsymbol{q}\{\boldsymbol{R}(t) - \boldsymbol{R}(0)\}]\rangle \\ &= \frac{1}{2}\left[p(\boldsymbol{R}_1, t|\boldsymbol{R}_1, 0) + p(\boldsymbol{R}_2, t|\boldsymbol{R}_1, 0)\exp\{-i\boldsymbol{q}(\boldsymbol{R}_2 - \boldsymbol{R}_1)\}\right] \\ &\quad + \frac{1}{2}\left[p(\boldsymbol{R}_2, t|\boldsymbol{R}_2, 0) + p(\boldsymbol{R}_1, t|\boldsymbol{R}_2, 0)\exp\{-i\boldsymbol{q}(\boldsymbol{R}_1 - \boldsymbol{R}_2)\}\right] \end{aligned} \tag{8.51}$$

where the factors 1/2 arise from the fact that the proton is equally likely to be at $\boldsymbol{R}_1$ and $\boldsymbol{R}_2$ at time zero. Substituting (8.47)–(8.50) into (8.51) gives

$$F_s^R(\boldsymbol{q}, t) = \frac{1}{2}(1 + e^{-2t/\tau}) + \frac{1}{2}(1 - e^{-2t/\tau})\cos \boldsymbol{qd} \tag{8.52}$$

where $\boldsymbol{d}$ is equal to $\boldsymbol{R}_2 - \boldsymbol{R}_1$. Finally its time Fourier transform leads to

$$S_s^R(\boldsymbol{q}, \omega) = \frac{1}{2}(1 + \cos \boldsymbol{qd})\delta(\omega) + \frac{1}{2}(1 - \cos \boldsymbol{qd})\frac{1}{\pi}\frac{2/\tau}{(2/\tau)^2 + \omega^2} \tag{8.53}$$

The dynamic structure factor $S_s^R(\boldsymbol{q}, \omega)$, as given by (8.53), depends on the orientation of $\boldsymbol{d}$ relative to $\boldsymbol{q}$. For an isotropic sample in which there is a random orientation of the molecules to which the vectors $\boldsymbol{R}_1$ and $\boldsymbol{R}_2$ are attached, we have to take the orientational average of (8.53), and $S_s^R(q, \omega)$, now a function of the magnitude of $\boldsymbol{q}$ only, becomes

$$S_s^R(q, \omega) = \frac{1}{2}\left(1 + \frac{\sin qd}{qd}\right)\delta(\omega) + \frac{1}{2}\left(1 - \frac{\sin qd}{qd}\right)\frac{1}{\pi}\frac{2/\tau}{(2/\tau)^2 + \omega^2} \tag{8.54}$$

By comparing (8.54) with (8.43) it is seen that the EISF $A_0(q)$ is given by

$$A_0(q) = \frac{1}{2}\left(1 + \frac{\sin qd}{qd}\right) \tag{8.55}$$

and the quasielastic component $f_{qe}(q, \omega)$ is a Lorentzian function given by

$$f_{qe}(q, \omega) = \frac{1}{\pi}\frac{2/\tau}{(2/\tau)^2 + \omega^2} \tag{8.56}$$

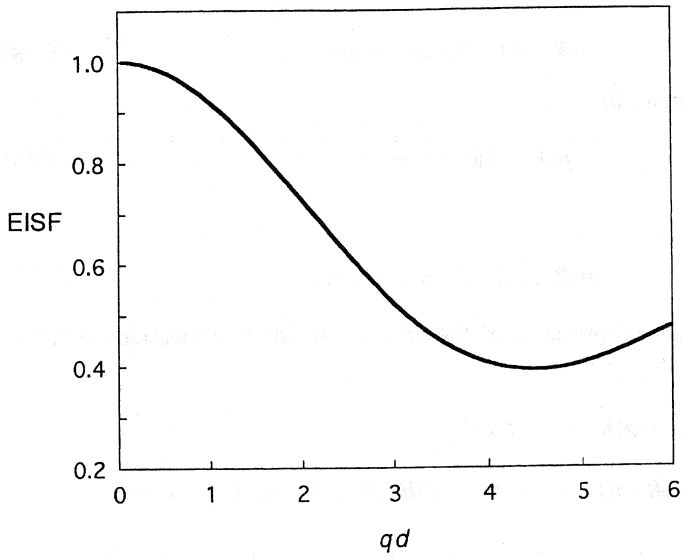

Figure 8.7 Elastic incoherent structure factor $A_0(q)$ calculated according to Equation (8.53) for the jump rotational motion between two sites.

Figure 8.7 shows the plot of $A_0(q)$ given by (8.55), and Figure 8.8 illustrates $S_s^R(q, \omega)$ given by (8.54) and how it changes as q increases. The central, elastic peak is drawn with a finite width since experimentally the observed central peak is broadened due to finite resolution of the instrument (and from the superposition of translational diffusion).

8.2.3 Vibration

We now consider the incoherent scattering due to vibrational motions of individual protons. We begin the discussion with the intermediate scattering function $F_s(\boldsymbol{q},t)$ as given by (8.35). Expressing the position of a proton at time t measured from its equilibrium position as $\boldsymbol{u}(t)$, and expanding the exponential and neglecting terms higher than the second order, we obtain

$$\begin{aligned} F_s^V(\boldsymbol{q}, t) &= \langle \exp[-i\boldsymbol{q}\{\boldsymbol{u}(t) - \boldsymbol{u}(0)\}]\rangle \\ &= 1 - i\,\langle \boldsymbol{q}[\boldsymbol{u}(t) - \boldsymbol{u}(0)]\rangle - \frac{1}{2}\left\langle \{\boldsymbol{q}[\boldsymbol{u}(t) - \boldsymbol{u}(0)]\}^2 \right\rangle \end{aligned} \tag{8.57}$$

in which the term linear in $\boldsymbol{q}$ vanishes because $\langle \boldsymbol{u}(0)\rangle = \langle \boldsymbol{u}(t)\rangle = 0$. Equation (8.57) thus becomes

$$\begin{aligned} F_s^V(\boldsymbol{q}, t) &= 1 - \frac{1}{2}\left\langle [\boldsymbol{q}\boldsymbol{u}(t) - \boldsymbol{q}\boldsymbol{u}(0)]^2 \right\rangle \\ &\cong \exp\left\{ -\frac{1}{2}\left\langle [\boldsymbol{q}\boldsymbol{u}(t) - \boldsymbol{q}\boldsymbol{u}(0)]^2 \right\rangle \right\} \end{aligned}$$

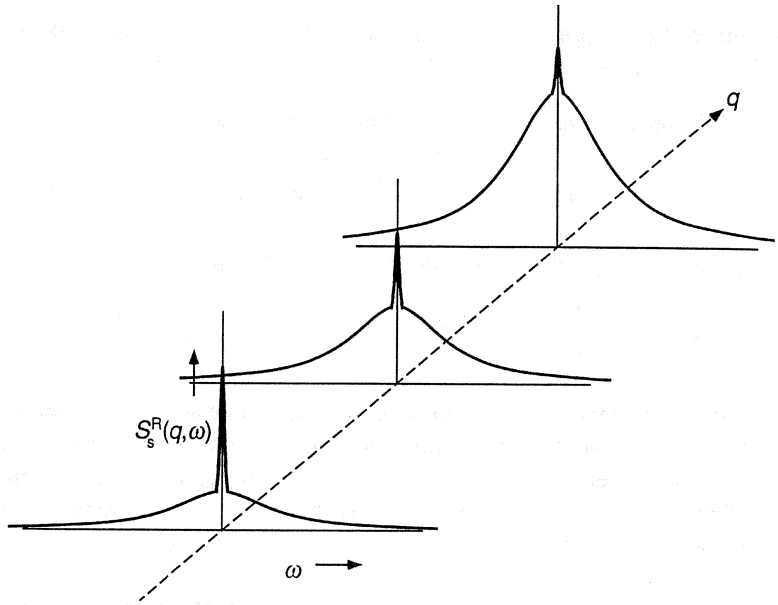

Figure 8.8 Schematic representation of the incoherent dynamic structure factor $S_s^R(q, \omega)$ for the rotational motion, at different q values.

$$= \exp\left\{-\frac{1}{2}\left\langle[\boldsymbol{qu}(t)]^2\right\rangle - \frac{1}{2}\left\langle[\boldsymbol{qu}(0)]^2\right\rangle + \left\langle[\boldsymbol{qu}(t)][\boldsymbol{qu}(0)]\right\rangle\right\} \tag{8.58}$$

Recognizing that $\left\langle[\boldsymbol{qu}(t)]^2\right\rangle$ is the same as $\left\langle[\boldsymbol{qu}(0)]^2\right\rangle$, we rewrite (8.58) as

$$F_s^V(\boldsymbol{q}, t) = \exp\left[-\left\langle(\boldsymbol{qu})^2\right\rangle\right] \exp\left\{\left\langle[\boldsymbol{qu}(t)][\boldsymbol{qu}(0)]\right\rangle\right\} \tag{8.59}$$

The first exponential factor in (8.59) does not depend on t, and it therefore represents a purely elastic scattering. It is identical to the *Debye–Waller factor* introduced earlier in Sections 1.7.1 and 3.4.4. It is usually expressed as $\exp(-2W)$ or $\exp(-2M)$, the former preferentially in the neutron scattering community and the latter by those engaged in x-ray scattering. Thus

$$\exp(-2W) = \exp\left(-\left\langle(\boldsymbol{qu})^2\right\rangle\right) = \exp\left(-q^2\left\langle u_q^2\right\rangle\right) = \exp\left(-q^2\frac{\left\langle u^2\right\rangle}{3}\right) \tag{8.60}$$

where u_q is the component of $\boldsymbol{u}$ in the $\boldsymbol{q}$ direction, and the factor 1/3 arises from the fact that in isotropic vibration $\left\langle u_x^2\right\rangle = \left\langle u_y^2\right\rangle = \left\langle u_z^2\right\rangle = \left\langle u^2\right\rangle/3$.

For a classic harmonic oscillator of angular frequency ω_0, $\boldsymbol{u}(t)$ can be written as

$$\boldsymbol{u}(t) = \boldsymbol{u}_0 \cos(\omega_0 t + \phi) \tag{8.61}$$

where ϕ is the initial phase angle at time 0 and $\boldsymbol{u}_0$ is the modulus of the oscillation. It can be easily seen from (8.61) that when averaged over many oscillators with

randomly varying ϕ, $\langle[\boldsymbol{qu}(t)][\boldsymbol{qu}(0)]\rangle$ is equal to $\langle[\boldsymbol{qu}(0)]^2\rangle \cos\omega_0 t$. Equation (8.59) can therefore be written as

$$\begin{aligned} F_s^V(\boldsymbol{q}, t) &= \exp(-2W)\left(1 + \langle[\boldsymbol{qu}(0)]^2\rangle \cos\omega_0 t\right) \\ &= \exp(-2W)\left(1 + \frac{q^2\langle u^2\rangle}{3}\cos\omega_0 t\right) \end{aligned} \tag{8.62}$$

The time Fourier transform of (8.62) gives the dynamic structure factor

$$S_s^V(q, \omega) = \exp(-2W)\left\{\delta(\omega) + \frac{q^2\langle u^2\rangle}{6}[\delta(\omega - \omega_0) + \delta(\omega + \omega_0)]\right\} \tag{8.63}$$

It shows that the spectrum consists of three delta functions; the one at $\omega = 0$ represents elastic scattering without change in the energy, and the two at $\omega = \pm\omega_0$ represent scattering events in which energy is either given to or subtracted from the incident neutrons. Note that as q increases, the intensity of scattering at $\pm\omega_0$ is strengthened as q^2, while the Debye–Waller factor attenuates it according to $\exp(-2W)$ where $W \propto q^2$.

Although the derivation of (8.63) given in the previous paragraph provides a useful insight into the factors leading to the dynamic structure factor $S_s^V(q, \omega)$, a treatment of vibrational motions should more properly be based on quantum mechanics. A full quantum mechanical derivation[7] of $S_s^V(q, \omega)$ is, however, beyond the scope of the present book, and we here simply quote the final result. Thus for a single harmonic oscillator, the dynamic structure factor is given by

$$\begin{aligned} &S_s^V(q, \omega) = \\ &e^{-2W}\left\{\delta(\omega) + \frac{\hbar q^2}{6m\omega_0}[n(\omega_0)\delta(\omega - \omega_0) + (n(\omega_0) + 1)\delta(\omega + \omega_0)]\right\} \end{aligned} \tag{8.64}$$

where m is the mass of the oscillating nuclei (proton in the present case), and $n(\omega)$, known as the *Bose occupation number*, is defined as

$$n(\omega) = \frac{1}{\exp(\hbar\omega/kT) - 1} \tag{8.65}$$

In the high temperature limit $T \to \infty$ we have

$$n(\omega) \approx n(\omega) + 1 \to kT/\hbar\omega \tag{8.66}$$

and at the same time the energy E_{quantum} of a quantum harmonic oscillator approaches kT. On the other hand, the energy $E_{\text{classical}}$ of a classical oscillator represented by (8.61) is given by

$$\begin{aligned} E_{\text{classical}} &= \frac{1}{2}m\omega_0^2 u_0^2 \\ &= m\omega_0^2\langle u^2\rangle \end{aligned} \tag{8.67}$$

Equating E_{quantum} to $E_{\text{classical}}$ and using results (8.66) and (8.67), we find that (8.64) reduces to the classical result (8.63) in the high temperature limit.

If the system contains a large number of independent vibrational modes (i.e., normal modes), with frequency distribution $g(\omega_0)$ ($\omega_0 > 0$), then $S_s^V(q, \omega)$ is now given by

$$S_s^V(q,\omega) = e^{-2W}\left\{\delta(\omega) + \int_0^\infty g(\omega_0)\frac{\hbar q^2}{6m\omega_0}[n(\omega_0)\delta(\omega-\omega_0) + (n(\omega_0)+1)\delta(\omega+\omega_0)]\,d\omega_0\right\} \tag{8.68}$$

which, on use of identity (B.32), becomes

$$S_s^V(q,\omega) = e^{-2W}\left\{\delta(\omega) + \frac{\hbar q^2}{6m}\frac{g(\omega)}{\omega}[n(\omega)+\tfrac{1}{2}\pm\tfrac{1}{2}]\right\} \tag{8.69}$$

where $g(-\omega) = g(\omega)$ and the + sign is associated with $\omega < 0$ and the − sign with $\omega > 0$. Equation (8.69) shows that the spectrum no longer consists of sharp lines but is given rather by a continuous curve extending to both sides of $\omega = 0$. Measurement of $S_s^V(q, \omega)$ thus allows determination of the frequency distribution $g(\omega)$, which is called *the density of vibrational states, the phonon density of states,* or simply *the density of states.* Figure 8.9 schematically illustrates how $S_s^V(q, \omega)$ changes with q.

8.2.4 Combination of Different Kinds of Motions

The motions encountered in polymeric materials are obviously much more complex than those discussed in the above idealized models, and they usually contain elements of all the three types of motions, vibrational, rotational, and translational, at the same time. The spectrum that is expected from the combined effect of these different types

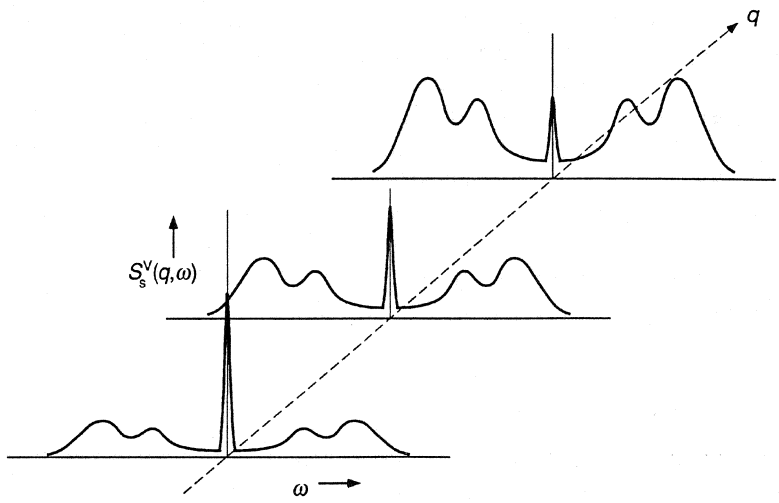

Figure 8.9 Schematic representation of the incoherent dynamic structure factor $S_s^V(q, \omega)$ for vibration, at different q values.

of motions can, however, be deduced fairly readily if we make the assumption that the motions are *dynamically independent* of each other. Suppose that the time-dependent position vector $\boldsymbol{r}(t)$ of a proton is represented as

$$\boldsymbol{r}(t) = \boldsymbol{a}(t) + \boldsymbol{R}(t) + \boldsymbol{u}(t) \tag{8.70}$$

where $\boldsymbol{a}(t)$ denotes the center of mass of a segment, $\boldsymbol{R}(t)$ is the radius vector of the proton relative to the center of mass, and $\boldsymbol{u}(t)$ is the displacement of the proton from its average position due to vibration. The dynamic independence means that the time dependence of $\boldsymbol{u}(t)$, for example, is not influenced by the particular values that $\boldsymbol{a}(t)$ and $\boldsymbol{R}(t)$ happen to possess at any given moment. Fortunately the vibrational, rotational, and translational motions occur in general on widely different time scales, and this makes the assumption of the dynamic independence justified in most cases.

Substitution of (8.70) into (8.35) leads to

$$\begin{aligned} F_s(\boldsymbol{q}, t) = \langle &\exp[-i\boldsymbol{q}\{\boldsymbol{a}(t) - \boldsymbol{a}(0)\}] \exp[-i\boldsymbol{q}\{\boldsymbol{R}(t) - \boldsymbol{R}(0)\}] \\ &\exp[-i\boldsymbol{q}\{\boldsymbol{u}(t) - \boldsymbol{u}(0)\}]\rangle \end{aligned} \tag{8.71}$$

Under the dynamic independence assumption, the thermal average in (8.71) can be performed separately for the individual factors, and we obtain

$$F_s(\boldsymbol{q}, t) = F_s^{\mathrm{T}}(\boldsymbol{q}, t) F_s^{\mathrm{R}}(\boldsymbol{q}, t) F_s^{\mathrm{V}}(\boldsymbol{q}, t) \tag{8.72}$$

where the three factors represent the individual intermediate scattering functions due to the translational, rotational, and vibrational motions, respectively. By taking the time Fourier transform of (8.72) and making use of the multiplication theorem (B.24), we obtain

$$S_s(\boldsymbol{q}, \omega) = S_s^{\mathrm{T}}(\boldsymbol{q}, \omega) * S_s^{\mathrm{R}}(\boldsymbol{q}, \omega) * S_s^{\mathrm{V}}(\boldsymbol{q}, \omega) \tag{8.73}$$

where * represents a convolution operation with respect to ω at constant q.

Figure 8.10 gives a schematic representation of the combined incoherent dynamic structure factor $S_s(\boldsymbol{q}, \omega)$ that is expected on the basis of (8.73). It consists of three different ω regions commonly termed "elastic," "quasielastic," and "inelastic," although strictly speaking all arise from inelastic neutron scattering. The width of the "elastic" component, which is the central peak around $\omega = 0$, reflects the instrumental resolution as well as the slow diffusional motion of the polymer segment or the polymer molecule as a whole. The "quasielastic" component in the intermediate ω region has contributions from both rotational and translational motions. At still larger q, the "inelastic" peaks are due mostly to vibrational motions but are broadened somewhat as a result of the other two types of motions.

8.3 SPECTROMETERS

Most of the experimental techniques discussed in Chapter 2 are relevant to both elastic and inelastic scattering studies, but for the latter it is in addition necessary to be able to determine the amount of energy exchange the neutrons has sustained on scattering.

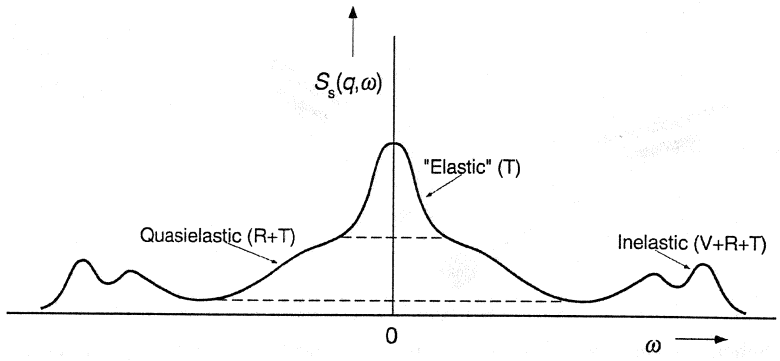

Figure 8.10 Schematic representation of the incoherent dynamic structure factor $S_s(q,\omega)$, at constant q, where translational (T), rotational (R), and vibrational (V) motions all make contributions.

In place of the diffractometer discussed in Section 2.5.3, a *spectrometer* is used, which allows measurement of the energy spectrum of scattered neutrons at different scattering angles. There are four main types of spectrometers in use today, the triple-axis spectrometer, the time-of-flight spectrometer, the back-scattering spectrometer, and the spin-echo spectrometer, each of which is briefly described in the following section.

8.3.1 Triple-Axis Spectrometer

The triple-axis spectrometer most closely resembles the conventional diffractometer discussed in Section 2.5.3. In it (see Figure 8.11) the incident neutron beam, which is either continuous or pulsed, is monochromatized by Bragg reflection from a monochromator crystal. The wavelength of the incident beam can be altered by rotating the monochromator crystal and the whole spectrometer, including the sample holder and the analyzer–detector arm, about the monochromator axis to a new setting. To change the scattering angle 2θ the analyzer–detector arm is rotated about the axis at the sample holder. For the analysis of the spectrum of the scattered beam the detector and the analyzer crystal are rotated about the analyzer crystal axis. There are thus three axes of rotations, all parallel to each other. With three axes of rotation that allow independent variations in the incident beam energy E_0, the scattered beam energy E_1, and the scattering angle 2θ, the instrument offers versatility in choosing the range of q and ω over which the scattering intensity is measured. Counterbalancing this versatility is the fact that the intensity must be determined point by point as a function of both q and ω, and as a result the whole measurement can be very time consuming.

8.3.2 Time-of-Flight Spectrometer

In the time-of-flight spectrometer, shown schematically in Figure 8.12, the incident neutron beam is converted into pulses and, at the same time, monochromatized by

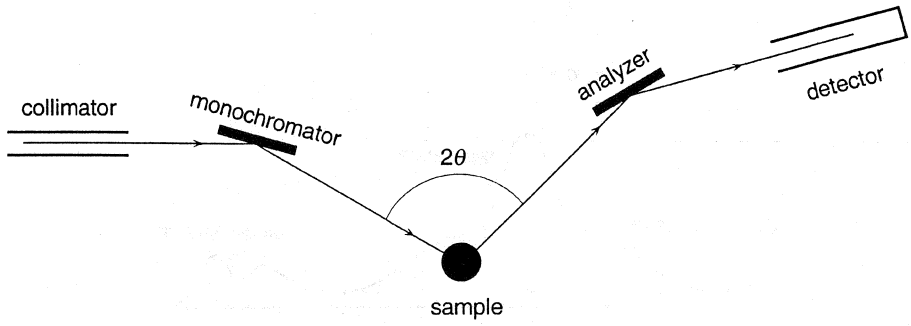

Figure 8.11 Schematic diagram of the triple-axis spectrometer. The three axes are at the monochromator crystal, the sample holder, and the analyzer crystal.

means of a set of (usually four) disk choppers rotating around a common, horizontal axis. The phase angle difference between the first and the last disks and their common rotating speed define the desired wavelength. The second disk removes higher order contaminations from the beam. The repetition rate of the neutron pulse is controlled by the third disk, which may be allowed to rotate at a slower rate than the other disks. This third disk is to lengthen the time interval between successive pulses, so as to permit complete time analysis of each pulse without a "frame-overlap." Monitors placed in the direct beam at set distances apart allow determination of the incident beam wavelength. The neutrons scattered from the sample are collected by a bank of detectors placed several meters away around the sample, covering a wide range of scattering angles. The neutrons arriving at each detector are sorted according to their time of arrival and accumulated in multichannel analyzers. The counting efficiency is thus very much higher than in the triple-axis instrument.

8.3.3 Back-Scattering Spectrometer

The time-of-flight spectrometer does not provide sufficient energy resolution to detect the slow relaxational motions in polymers. The best resolution of the time-of-flight instrument is typically of the order of 1% in $\Delta E/E$, or about 20 μeV in E, or about 5×10^9 Hz in frequency (see the conversion factors in Table 8.1). The back-scattering spectrometer has been designed to attain a higher resolution, by using the fact that the best resolution from a monochromator or analyzer crystal is obtained when the Bragg reflection occurs at a scattering angle 2θ equal to 180°. This is because differentiating the Bragg law gives

$$\frac{\Delta\lambda}{\lambda} = \cot\theta \; \Delta\theta \tag{8.74}$$

showing that for a given spread $\Delta\theta$ (due to mosaic spread of the crystal and beam divergence) $\Delta\lambda$ is minimized when θ is close to 90°.

A schematic view of a back-scattering spectrometer is shown in Figure 8.13. The incident neutrons brought in a straight guide tube are back-scattered from a monochromator crystal mounted on a velocity drive. An example of the monochromator crystal

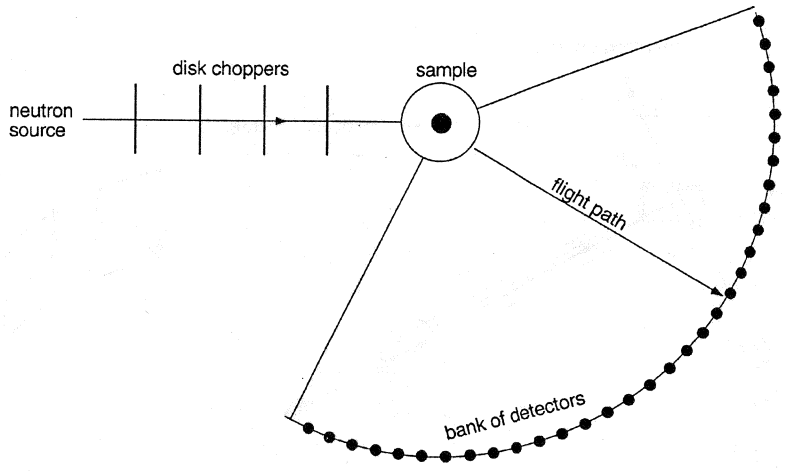

Figure 8.12 Schematic diagram of a time-of-flight spectrometer.

is a polished silicon with its (111) plane oriented to back-reflect 6.27-Å neutrons. The energy spread produced by the Doppler effect is then superimposed on the sharp monochromatic energy of the beam. The beam is now deflected by a graphite crystal and thereby sent toward the sample, past a disk chopper. The neutrons scattered by the sample are reflected back and focused by the analyzer crystals toward the detector placed behind the sample. The purpose of the chopper is to interrupt the steady beam so that the detector is able to sort out electronically those neutrons scattered directly into it from those coming after reflection from the analyzer crystal. Among the incident neutrons that have gained or lost energy δE by the Doppler drive, only those that have lost or gained almost exactly the same amount δE of energy by inelastic scattering at the sample will then be registered in the detector. The spectrometer therefore works by "inverse spectroscopy"; the final energy of the detected neutrons is in a narrow band about a precise value [6.27 Å in the case of a (111)-oriented silicon crystal], whereas the initial energy of these neutrons is varied around this value. In this way the energy resolution that can be achieved with a back-scattering machine is very high ($\sim$ 1 μeV) but the range of energy that can be scanned by the Doppler motion is rather limited ($\sim$ 30 μeV). To improve the counting rates, a bank of analyzer crystals is mounted on a spherically curved surface aligned such that neutrons back-reflected from the crystals are focused into a single detector. Because of the relatively large area covered by the bank of crystals, the scattering angle is less well defined and $\Delta q/q$ attained is of the order of 10%.

8.3.4 Spin-Echo Spectrometer[8,9]

The spin-echo spectrometer offers an exceptionally high-energy resolution ($\Delta E/E \sim 10^{-5}$) and is based on a design first conceived by Mezei.[10] Here the Larmor precession

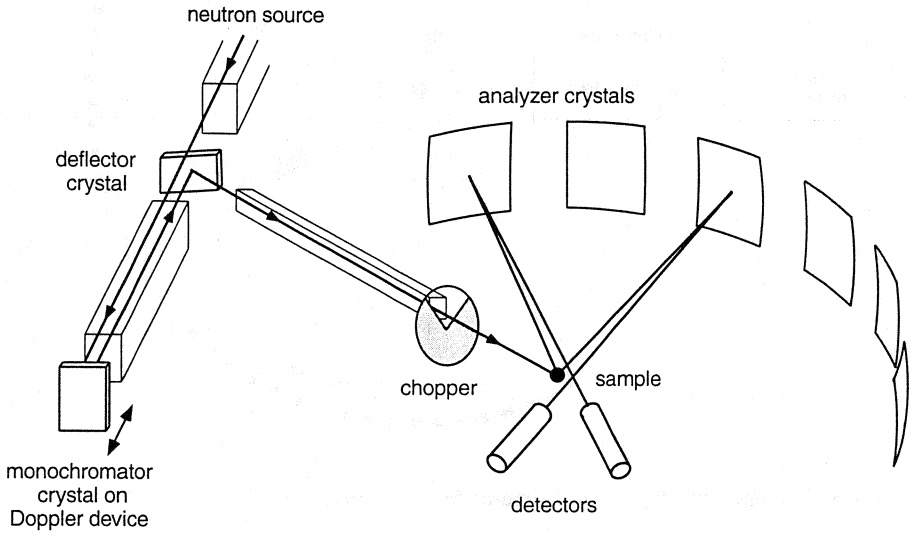

Figure 8.13 Schematic view of a back-scattering spectrometer. The neutrons incident from the neutron guide are back-scattered by the monochromator mounted on a Doppler drive, deflected by a graphite crystal to the sample, scattered to the analyzers and then back-scattered again to the detectors located close to the sample. The chopper interrupts the beam and makes it possible to discriminate the neutrons scattered directly into the detectors.

of the neutron spin in a magnetic field is utilized as an individual counter to measure a very small change in velocity of each neutron. As only the wavelength change resulting from scattering is measured, a relatively wide spectrum of incident wavelengths can be used to increase the flux. It also differs from other types of spectrometers in that the intermediate scattering function $F(\boldsymbol{q},t)$ is measured instead of the dynamic structure factor $S(\boldsymbol{q},\omega)$, which is determined by other instruments. Although $F(\boldsymbol{q},t)$ can in principle be obtained from $S(\boldsymbol{q},\omega)$ by Fourier transformation, in reality such a transformation is difficult because of the limited range of ω for which data are available. The intermediate scattering function $F(\boldsymbol{q},t)$, being in the time domain, is in some cases easier to interpret than $S(\boldsymbol{q},\omega)$ in terms of a physical picture.

The basic experimental setup of a neutron spin-echo spectrometer is presented in Figure 8.14. It has two identical arms on either side of the sample, each consisting of a length of solenoid providing a magnetic guide field directed along the flight path. A helical velocity selector defines the wavelength in the incident beam to have some moderate degree of spread, typically about 10% in $\Delta\lambda/\lambda$. Such a monochromatization is unnecessary for the energy resolution but affects the q resolution. The beam is reflected from the "supermirror" polarizer crystal such that the neutrons are polarized in the direction of the beam propagation, which we will call the z direction. The first $\pi/2$ spin-turn coil then flips the spins in the x direction perpendicular to z. In guide field 1, under the influence of the magnetic field of strength B oriented in the z direction, the neutron spin precesses in the xy plane at the Larmor frequency given by

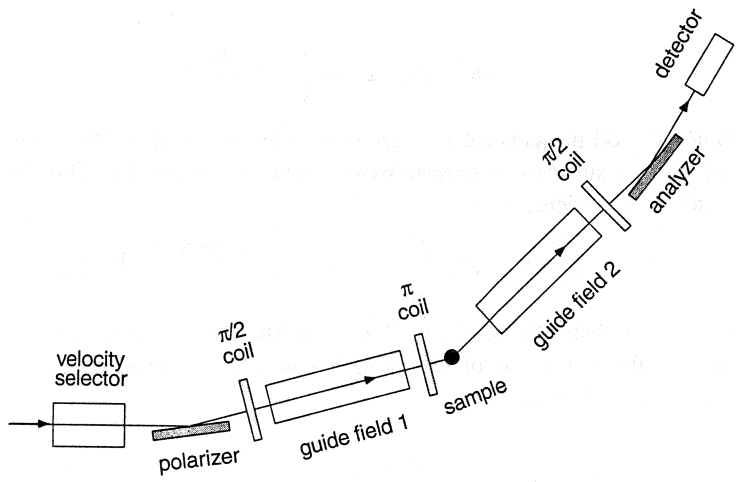

Figure 8.14 Schematic drawing of a neutron spin-echo spectrometer.

$$\omega_L = \gamma B \tag{8.75}$$

where γ is a constant known as the gyromagnetic ratio. The length of time dt spent by the neutron in traveling distance dz in the guide field is $dt = dz/v = (m\lambda/h)\,dz$, and the phase angle of precession undergone during this time period is $\omega_L\,dt$. A neutron of wavelength λ traveling in guide field 1 therefore undergoes a phase-angle change ϕ_1 given by

$$\phi_1 = \frac{m\lambda}{h}\gamma \int B\,dz \tag{8.76}$$

which consists of N_0 complete 2π precessions and an additional fractional precession $\Delta\phi_1$:

$$\phi_1 = 2\pi N_0 + \Delta\phi_1 \tag{8.77}$$

The π coil flips the spin 180° to transform the angle $\Delta\phi_1$ to $-\Delta\phi_1$. The π coil is positioned such that the field integrals $\int B\,dz$ are exactly equal over guide fields 1 and 2. If the scattering is elastic the wavelength λ is unchanged, and in traveling through guide field 2 the neutron undergoes a phase-angle change ϕ_2, which is exactly equal to ϕ_1 as given by (8.76). Therefore between the first and the second $\pi/2$ coils the neutron spin undergoes $2N_0$ complete 2π precessions, and by the time the neutron reaches the second $\pi/2$ coil the spin points again in the x direction irrespective of the wavelength λ.

If, however, the neutron energy is changed due to inelastic scattering by the sample, which is positioned near the π coil, the wavelength is modified from λ to $\lambda' = \lambda + \delta\lambda$. In this case, by the time the neutron reaches the second $\pi/2$ coil, it has undergone a phase change

$$\phi_2' = \frac{m\lambda'}{h}\gamma \int B\,dz \tag{8.78}$$

which is different from $\phi_2 (= \phi_1)$. The x component of the neutron spin at the second $\pi/2$ coil has thus been reduced from 1 to

$$\cos(\phi_2' - \phi_2) \cong \cos\left(2\pi N_0 \frac{\delta\lambda}{\lambda}\right) \tag{8.79}$$

The second $\pi/2$ coil projects the x component of the spin in the z direction, which is then analyzed by a subsequent supermirror analyzer and a detector. The net polarization $\langle P_z \rangle$ detected is therefore

$$\langle P_z \rangle = \int_0^\infty f(\lambda)\, d\lambda \int_{-\infty}^\infty P(\lambda, \delta\lambda) \cos\left(\frac{2\pi N_0 \delta\lambda}{\lambda}\right) d(\delta\lambda) \tag{8.80}$$

where $f(\lambda)$ is the distribution of wavelengths in the incident beam and $P(\lambda, \delta\lambda)$ is the probability that a neutron of wavelength λ will be scattered with a wavelength change $\delta\lambda$. From (8.1) we find

$$\hbar\omega = \delta E = \frac{h^2}{m} \frac{\delta\lambda}{\lambda^3} \tag{8.81}$$

Changing the variable from λ to ω, and recognizing that

$$P(\lambda, \delta\lambda)\, d(\delta\lambda) = S(\boldsymbol{q}, \omega)\, d\omega \tag{8.82}$$

we obtain

$$\langle P_z \rangle = \int_0^\infty f(\lambda)\, d\lambda \int_{-\infty}^\infty S(\boldsymbol{q}, \omega)\, \cos\left(\frac{m N_0 \lambda^2}{h} \omega\right) d\omega \tag{8.83}$$

The factor $m N_0 \lambda^2 / h$ has dimension of time and is a function of the guide field strength B [see Equations (8.76) and (8.77)]. Therefore, designating it by t, we rewrite (8.83) as

$$\begin{aligned} \langle P_z \rangle &= \int_0^\infty f(\lambda)\, d\lambda \int_{-\infty}^\infty S(\boldsymbol{q}, \omega)\, \cos(\omega t)\, d\omega \\ &= \int_0^\infty f(\lambda)\, d\lambda\, F(\boldsymbol{q}, t) \end{aligned} \tag{8.84}$$

Thus, in the neutron spin-echo measurement, $F(\boldsymbol{q},t)$ is measured as a function of t (by adjusting the magnetic guide field strength B) at fixed $\boldsymbol{q}$, covering a time scale of about two decades from 1 to 100 ns. The energy resolution attained is as small as 0.1 μeV. This high resolution is usually won at the expense of q resolution. The fairly large spread $\Delta\lambda/\lambda$ in wavelength, necessary for the sake of increasing the flux, leads to a corresponding spread in q, even though in the spectrometer the beam is highly collimated and the direction of scattering is well defined.

8.4 EXAMPLES OF EXPERIMENTAL STUDIES

In presenting the experimentally observed spectrum, i.e., either the double differential scattering cross section $d^2\sigma/d\Omega d\omega$ or the dynamic structure factor $S(\boldsymbol{q},\omega)$ as a function of the energy exchange ω, different workers often use different energy units for ω. To facilitate conversion between these energy units, Table 8.1 gives the relationships between them.

TABLE 8.1
Relationships between Energy Units Commonly Used in Neutron Scattering

Energy Units	Symbol	Conversion from E (meV)
Frequency (Hz)	ν	$\nu = E/h = E \cdot 2.418 \times 10^{11}$ Hz
Angular frequency (rad s^{-1})	ω	$\omega = E/\hbar = E \cdot 1.519 \times 10^{12}$rad s^{-1}
Wave number (cm^{-1})	$\bar{\nu}$	$\bar{\nu} = E/hc = E \cdot 8.066$ cm^{-1}
Time of flight (s m^{-1})	τ	$\tau = (m/2E)^{1/2} = E^{-1/2} \cdot 2.286 \times 10^{-3}$ s m^{-1}

Figure 8.15 shows the time-of-flight spectrum obtained by Danner *et al.*[11] with linear polyethylene (Marlex 6050, degree of crystallinity 85%) at 100 K. At such a low temperature any motion observed in the polymer is expected to be almost exclusively vibrational. Because of the high hydrogen content of polyethylene, the scattering is predominantly incoherent, and the spectrum obtained therefore corresponds mostly to the self part of the dynamic structure factor, $S_s(q,\omega)$. For monochromatization the incident beam was passed through a Be polycrystalline filter, which sharply cuts off neutrons with energies greater than 5.2 meV ($\sim$ 4.0 Å). The neutrons scattered at a scattering angle $2\theta = 90°$ were analyzed, by a multichannel analyzer, for their flight times over a 5-m flight path. The steep rise in the number of counts observed for channel numbers larger than 152 (flight times longer than 152×32 μs over the 5-m path, or energy smaller than 5.2 meV) thus reflects elastic scattering. Counts at lower channel numbers represent neutrons that have gained energy on scattering, i.e., $\Delta E = \hbar\omega > 0$. The incident beam energy is relatively modest to begin with and is therefore not sufficient to allow determination of the spectrum for neutrons that have lost energy on scattering ($\omega < 0$). From the data in Figure 8.15 and by use of Equation (8.66), the density of vibrational states $g(\omega)$ was calculated and is shown in Figure 8.16.

The second example is taken from the study of the torsional rotation of ester methyl groups in poly(methyl methacrylate) by Gabrys *et al.*[12] They synthesized samples of poly(methyl methacrylate) in which all the hydrogens, except the three on the ester methyl groups, were replaced by deuteriums. Scattering from the samples is still dominated by the incoherent scattering due to the hydrogens in the ester methyl groups. The spectra, obtained with time-of-flight spectrometers, were converted to the dynamic structure factors $S_s(q, \omega)$, and one of them, obtained with a syndiotactic polymer at 298 K for $q = 2.06$ Å^{-1}, is shown in Figure 8.17. At this temperature, which is far below the glass transition temperature ($\sim$ 380 K) of the polymer, little relaxational motion of the main chain segments is expected, and the plot in Figure 8.17 is very much in the form expected from Equation (8.43) or (8.54) derived for a model of rotational motion. The central elastic peak, broadened mostly by the instrumental resolution, is superposed on top of the quasielastic wing decaying in a Lorentzian manner. The EISF $A_0(q)$, defined in Equation (8.43), can be evaluated by

$$A_0(q) = \frac{I_{el}}{I_{el} + I_{qe}} \tag{8.85}$$

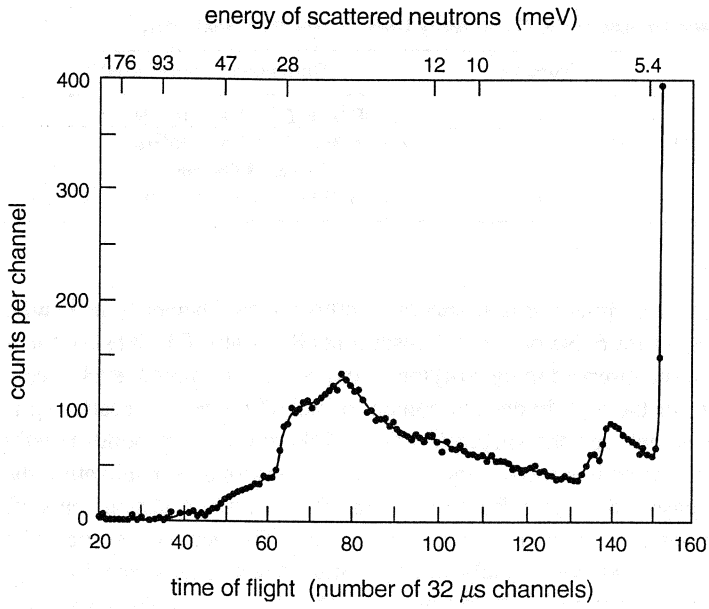

Figure 8.15 Time-of-flight spectrum obtained with linear polyethylene at 100 K. (From Danner *et al.*[11])

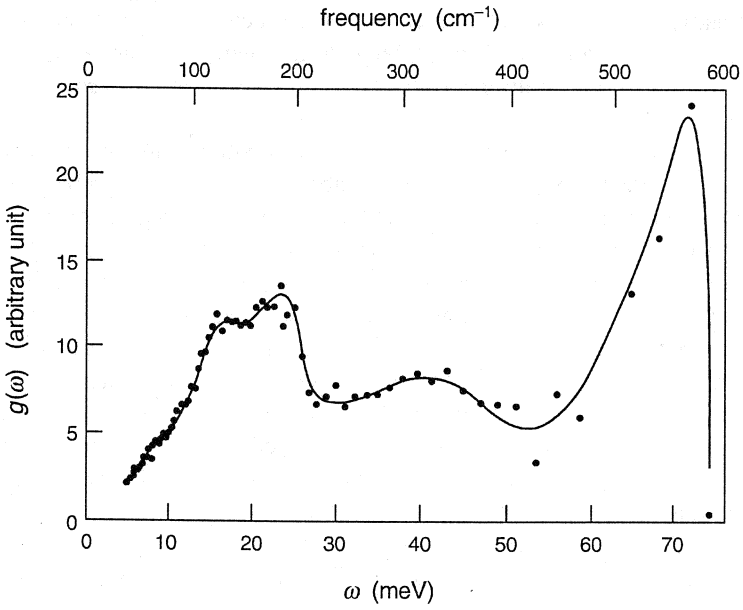

Figure 8.16 Density of vibrational states $g(\omega)$ of linear polyethylene derived, by use of Equation (8.66), from the time-of-flight spectrum shown in Figure 8.15. (From Danner *et al.*[11])

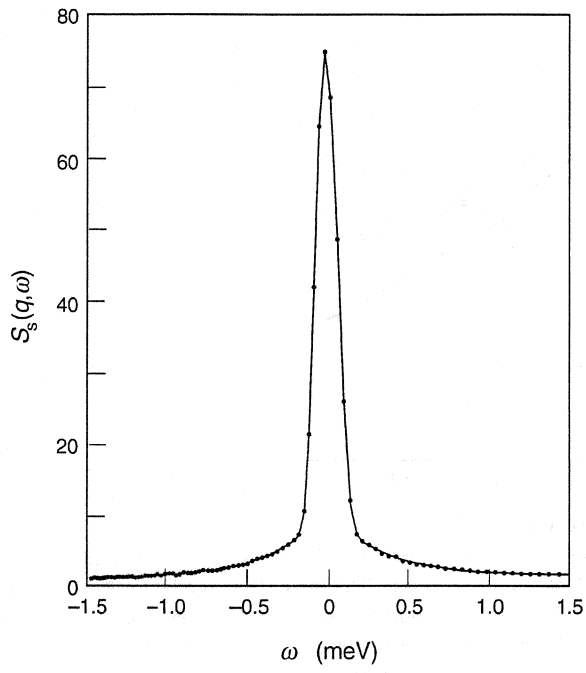

Figure 8.17 Dynamic structure factor $S_s(q, \omega)$ (predominantly incoherent) obtained, at 25°C, with a sample of poly(methyl methacrylate) in which all the hydrogens, except the ones in the ester methyl group, were replaced by deuteriums. (From Gabrys *et al.*[12])

where I_{el} and I_{qe} are the relative intensities of the elastic and quasielastic components, respectively, integrated over ω at constant q. The values of $A_0(q)$, evaluated as a function of q at 150 K and 290 K, are plotted in Figure 8.18. Also given in Figure 8.18 is the solid curve calculated from the model of instantaneous jumps among three rotational positions, similar to the model of jumps between two sites considered in detail in Section 8.2.2. The discrepancy between the experimental points and the calculated curve is due, according to the authors,[12] to the observed intensity being contaminated by the coherent scattering component, which in this case is not negligible. The values calculated from the theoretical model were therefore corrected for the coherent contamination, and the resulting values, plotted as the broken curve in Figure 8.18, agree well with the observed data points.

As an example of the application of neutron inelastic scattering to the study of motion in glass-forming polymers, we examine the dynamic structure factor of poly(vinyl chloride), shown in Figure 8.19, that was determined by Colmenero *et al.*[13] at temperatures both above and below its glass-transition temperature $\sim$ 358 K. The broken curve in the figure gives the measured instrumental resolution. Since the fraction of the incoherent component in the scattering cross section of poly(vinyl chloride) is 0.92, the data obtained reflect mostly the self motion of protons. At the two temperatures 110 and 290 K, both below the T_g, the spectra show only almost flat contributions merging with the central elastic peak. According to the

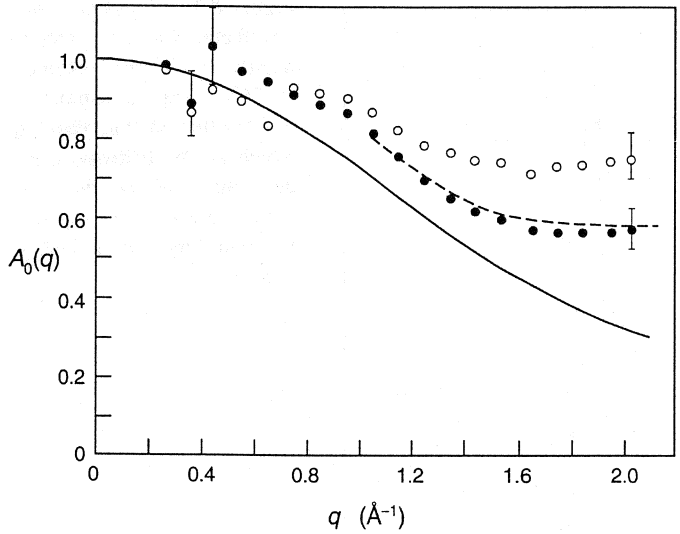

Figure 8.18 Elastic incoherent structure factor $A_0(q)$ obtained with poly(methyl methacrylate) at 150 K (open circles) and 290 K (solid circles). The theoretical prediction based on a model of rotation among three symmetric sites is given by the solid curve, whereas the broken curve was obtained by modifying the theoretical curve for the amount of contamination by coherent scattering in the experimental results. (From Gabrys *et al.*[12])

authors,[13] these arise almost exclusively from harmonic vibrations, since the difference between the spectra at these two temperatures (and at any other temperatures below T_g) can be explained on the basis of the temperature dependence of the Debye–Waller factor and the Bose occupation number $n(\omega)$ [defined by Equation (8.65)].

As the temperature is raised above the T_g, a quasielastic component, undoubtedly arising from the onset of slow segmental motion, is seen to broaden the central elastic peak progressively. To see the nature of the motion above T_g more clearly, the data were now converted into the intermediate scattering function $F_s(q,t)$ by Fourier transformation of $S_s(q,\omega)$. This Fourier transformation was, however, carried out with the values of $S_s(q,\omega)$ from which the contribution by the harmonic vibrations had been subtracted, and therefore the intermediate scattering function $F_s(q,t)$ obtained by the transformation and plotted in Figure 8.20 reflects only the contribution from the relaxational motion. There are evidently two types of motions present: one that takes place below about 2×10^{-12} s can be represented by

$$F_D(q, t) = A_D \exp(-t/\tau_D) \tag{8.86}$$

(as fitted by the solid curve for the data at 450 K in Figure 8.20), and another that follows the first can be represented by

$$F_W(q, t) = A_W \exp\left[-(t/\tau_W)^{\beta}\right] \tag{8.87}$$

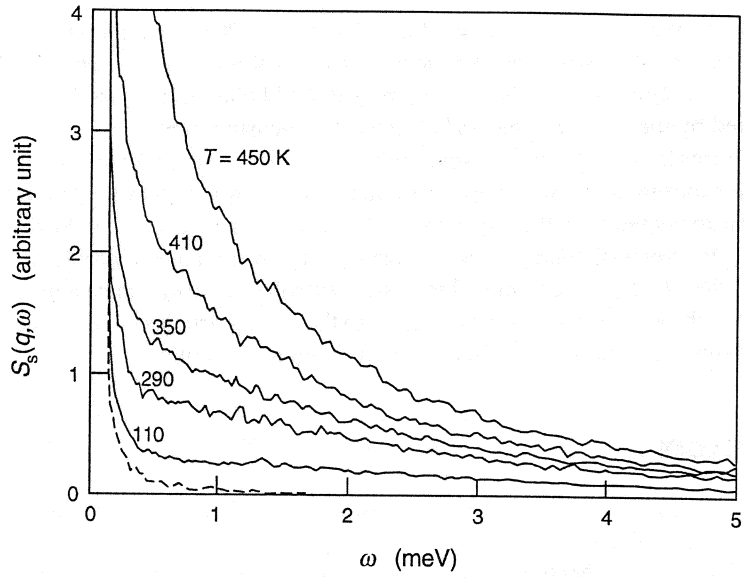

Figure 8.19 Incoherent dynamic structure factor measured with poly(vinyl chloride) for $q = 1.5\text{Å}^{-1}$ at temperatures above and below the glass transition temperature 358 K. The broken curve is the instrumental resolution function measured. (From Colmenero *et al.*[13])

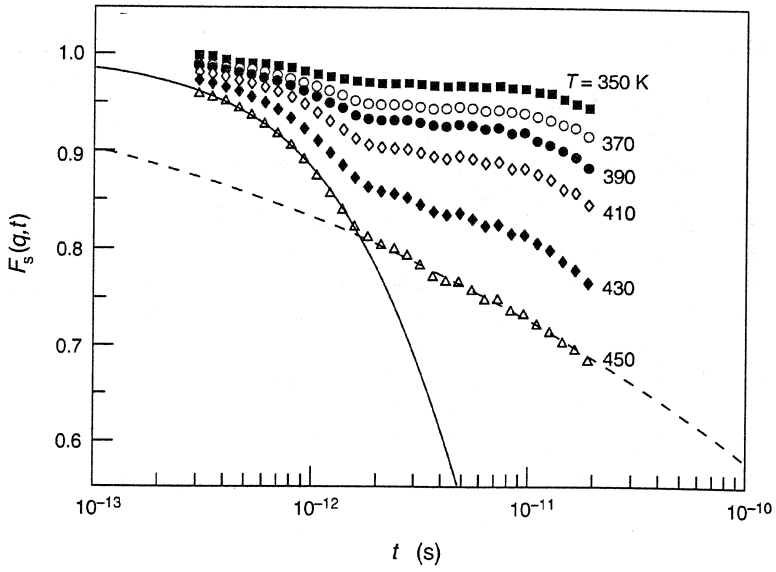

Figure 8.20 Intermediate scattering function obtained by Fourier transformation of $S_s(q, \omega)$ in Figure 8.19 from which the harmonic vibration contribution has been removed. (From Colmenero *et al.*[13])

(as fitted by the broken curve, with $\beta = 0.23$, in Figure 8.20). Equation (8.87) is in the form of the so-called stretched exponential or the Kohlrausch–Williams–Watt function, which is widely used to describe the relaxational behavior in glass-forming polymers studied by means of mechanical or dielectric measurements.

The above examples are cited here to give some feeling for the types of spectra that can be obtained experimentally with polymers and also to show how they resemble or differ from those expected from the idealized models of motions discussed in Section 8.2. These three examples of course do not do justice to the wide range of problems in polymer science to which the technique of inelastic neutron scattering can be applied, and to learn more about them the reader is referred to the review articles on the subject by Higgins,[14] Wignall,[15] Higgins and Benoît,[4] and Ewen and Richter.[9]

FURTHER READING

1. Squires, G. L., *Introduction to the Theory of Thermal Neutron Scattering*, Cambridge University Press, Cambridge, 1978.
2. Lovesey, S. W., *Theory of Neutron Scattering from Condensed Matter*, Clarendon Press, Oxford, 1984.
3. Bée, M., *Quasielastic Neutron Scattering*, Adam Hilger, Bristol, 1988.
4. Higgins, J. S., and Benoît, H. C., *Polymers and Neutron Scattering*, Clarendon Press, Oxford, 1994.

REFERENCES

5. van Hove, L., *Phys. Rev.* **95**, 249 (1954).
6. See, for example, Bée[3], p. 189.
7. Zemach, A. C., and Glauber, R. J., *Phys. Rev.* **101**, 118 (1956).
8. Nicholson, L. K., *Contemp. Phys.* **22**, 451 (1981).
9. Ewen, B., and Richter, D., *Adv. Polymer Sci.* **134**, 1 (1997).
10. Mezei, F., *Z. Phys.* **255**, 146 (1972).
11. Danner, H. R., Safford, G. J., Boutin, H., and Berger, M., *J. Chem. Phys.* **40**, 1417 (1964).
12. Gabrys, B., Higgins, J. S., Ma, K. T., and Roots, J. E., *Macromolecules* **17**, 560 (1984).
13. Colmenero, J., Arbe, A., and Alegria, A., *Phys. Rev. Lett.* **71**, 2603 (1993).
14. Higgins, J. S., in *Developments in Polymer Characterization–4*, J. V. Dawkins, Ed., Applied Science Publishers, London, 1983, p. 131.
15. Wignall, G. D., in *Encyclopedia of Polymer Science and Engineering*, Vol. 10, Wiley, New York, 1987, p. 112.

Refresher on Complex Numbers

Appendix **A**

The following is a short summary of the basic properties of complex numbers, presented here to refresh the reader's memory.

A complex number is essentially an ordered pair of two ordinary numbers, (x, y) or $x + iy$, in which i is $(-1)^{1/2}$. It is frequently convenient to employ a graphical representation of a complex number $z = x + iy$. By plotting x, the *real* part of z, as the abscissa and y, the *imaginary* part of z, as the ordinate, we have the *complex plane* shown in Figure A.1. Since $x = r\cos\phi$ and $y = r\ \sin\phi$, we can also write the complex number z as

$$z = r(\cos\phi + i\ \sin\phi) \tag{A.1}$$

By expanding $e^{i\phi}$ into a power series we find

$$\begin{aligned} e^{i\phi} &= \sum_{n=0}^{\infty} \frac{(i\phi)^n}{n!} \\ &= \sum_{k=0}^{\infty} \frac{(i\phi)^{2k}}{(2k)!} + \sum_{k=0}^{\infty} \frac{(i\phi)^{2k+1}}{(2k+1)!} \\ &= \sum_{k=0}^{\infty} (-1)^k \frac{\phi^{2k}}{(2k)!} + i \sum_{k=0}^{\infty} (-i)^k \frac{\phi^{2k+1}}{(2k+1)!} \\ &= \cos\ \phi + i\ \sin\ \phi \end{aligned} \tag{A.2}$$

We can therefore write (A.1) as

$$z = re^{i\phi} \tag{A.3}$$

In this *polar representation*, r is called the *modulus* or *magnitude* of z ($r = |z|$), and the angle ϕ is called the *argument* or *phase* of z. Note that as ϕ varies from 0 to 2π, $e^{i\phi}$ scribes a circle of unit radius in the complex plane (see Figure A.2), while its real part oscillates as $\cos\phi$.

The *complex conjugate* of $z = x + iy$ is $z^* = x - iy$. The product zz^* is therefore equal to $x^2 + y^2 = |z|^2$. Sometimes one writes z^2 for short to mean $|z|^2$. Thus we have

$$z^2 = |z|^2 = zz^* = x^2 + y^2 \tag{A.4}$$

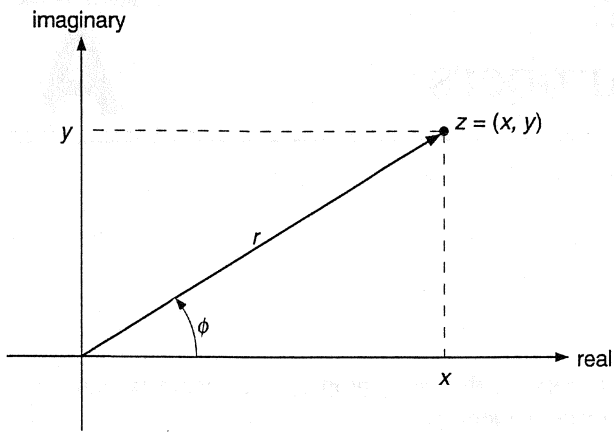

Figure A.1 Complex plane.

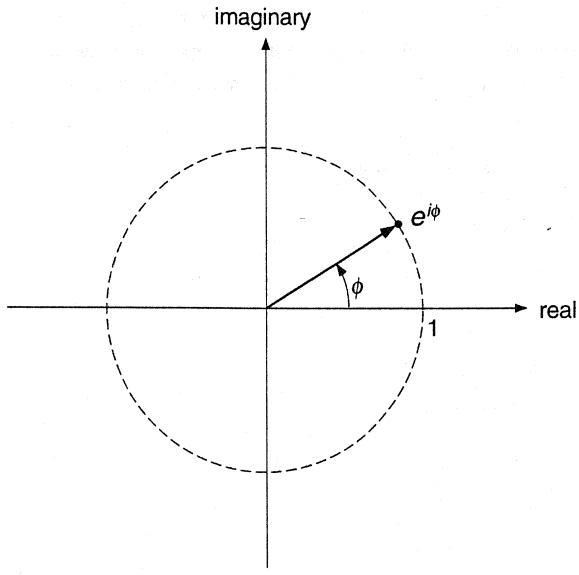

Figure A.2 Representation of $e^{i\phi}$ in the complex plane.

Adding or subtracting the expression for $e^{-i\phi}$ to or from (A.2) we obtain the following expressions, which are worth remembering.

$$\sin \phi = \frac{e^{i\phi} - e^{-i\phi}}{2i} \tag{A.5}$$

and

$$\cos \phi = \frac{e^{i\phi} + e^{-i\phi}}{2} \tag{A.6}$$

Fourier Transform

Appendix **B**

B.1 DEFINITIONS

B.1.1 Fourier Transform

We first discuss the Fourier transform in one dimension. The Fourier transform of a function $f(x)$ is defined as

$$F(s) = \int_{-\infty}^{\infty} f(x)e^{-i2\pi sx}\,dx \tag{B.1}$$

by which the function $f(x)$ of a variable x is transformed to another function $F(s)$ of a variable s. The original function $f(x)$ can be recovered from $F(s)$ by taking the inverse Fourier transform given by

$$f(x) = \int_{-\infty}^{\infty} F(s)e^{i2\pi sx}\,ds \tag{B.2}$$

A short-hand notation for Equation (B.1) is $F(s) = \mathcal{F}\{f(x)\}$, and for Equation (B.2) we write $f(x) = \mathcal{F}^{-1}\{F(s)\}$. Since the product sx, in the exponent of an exponential function, must be dimensionless, the dimension of s is the reciprocal of the dimension of x. Thus, if x has dimension [length], s has dimension [length^{-1}]. By the Fourier transform operation all the information contained in the function $f(x)$ in direct space is converted into the information contained in $F(s)$ in reciprocal space. The two functions $f(x)$ and $F(s)$ are often called a Fourier transform pair. Note that some workers define the Fourier transform with a plus sign in the exponent, but in this book the minus-i transform as in (B.1) is taken as the definition of the Fourier transform. If the use of the variable $q = 2\pi s$ instead of s is preferred, the Fourier transform pair can be written as

$$F(q) = \int_{-\infty}^{\infty} f(x)e^{-iqx}\,dx \tag{B.3}$$

and

$$f(x) = \frac{1}{2\pi}\int_{-\infty}^{\infty} F(q)e^{iqx}\,dq \tag{B.4}$$

B.1.2 Cosine and Sine Transforms

The *cosine transform* $F_c(s)$ and the *sine transform* $F_s(s)$ of a function $f(x)$ are defined as

$$F_c(s) = 2\int_0^\infty f(x)\ \cos(2\pi sx)\ dx \tag{B.5}$$

and

$$F_s(s) = 2\int_0^\infty f(x)\ \sin(2\pi sx)\ dx \tag{B.6}$$

It should be noted that both the cosine and sine transforms take no account of $f(x)$ to the left of the origin. To see the relationship of the cosine and sine transforms to the Fourier transform, let us now write (B.1) as

$$F(s) = \int_{-\infty}^\infty f(x)\ \cos(2\pi sx)\ dx - i\int_{-\infty}^\infty f(x)\ \sin(2\pi sx)\ dx \tag{B.7}$$

If $f(x)$ is an *even function*, i.e., $f(-x) = f(x)$, then the second integral in (B.7) is zero, and we see that the Fourier transform $F(s)$ is the same as the cosine transform $F_c(s)$. Since $F_c(s)$ is also an even function, $f(x)$ can be recovered by taking the cosine transform of $F_c(s)$:

$$f(x) = 2\int_0^\infty F_c(s)\ \cos(2\pi sx)\ ds \tag{B.8}$$

If $f(x)$ is an *odd function*, i.e., $f(-x) = -f(x)$, then the first integral in (B.7) is zero, and we have

$$F(s) = -i2\int_0^\infty f(x)\ \sin(2\pi sx)\ dx \tag{B.9}$$

$F(s)$ is then an odd function, and therefore its inverse transformation becomes

$$f(x) = i2\int_0^\infty F(s)\ \sin(2\pi sx)\ ds \tag{B.10}$$

On comparing (B.6) with (B.9) we note that $F(s)$ is equal to $-iF_s(s)$. From (B.10) we therefore find

$$f(x) = 2\int_0^\infty F_s(s)\ \sin(2\pi sx)\ ds \tag{B.11}$$

which is the inverse of the sine transformation (B.6).

B.2 PROPERTIES OF FOURIER TRANSFORM

B.2.1 Addition

From the definition (B.1) it is obvious that

$$\mathcal{F}\{f(x) + g(x)\} = \mathcal{F}\{f(x)\} + \mathcal{F}\{g(x)\} \tag{B.12}$$

which is the consequence of the linearity of the Fourier transform.

B.2.2 Shift

$$\begin{aligned}\mathcal{F}\{f(x-a)\} &= \int_{-\infty}^{\infty} f(x-a)e^{-i2\pi sx}\,dx \\ &= \int_{-\infty}^{\infty} f(x')e^{-i2\pi s(x'+a)}\,dx' \qquad (x' = x-a) \\ &= F(s)e^{-i2\pi sa}\end{aligned} \tag{B.13}$$

This shows that when a function $f(x)$ is shifted in the positive direction by an amount a (see Figure B.1a), its Fourier transform is affected only by a phase change, equal in magnitude to $2\pi sa$.

For example, consider that $f(x)$ represents the scattering length density distribution (of a one-dimensional object) and $F(s)$ the amplitude of scattering from it. A second object of exactly the same structure but displaced by a from the first has the scattering length density distribution given by $f(x-a)$. The amplitude of scattering from the latter then differs from that from the former by a factor $e^{-i2\pi sa}$. The absolute square of $e^{-i2\pi sa}$ is equal to unity, and therefore on squaring the amplitude function to obtain intensity, the intensities of scattering from the two objects are exactly equal to each other, as expected on physical grounds.

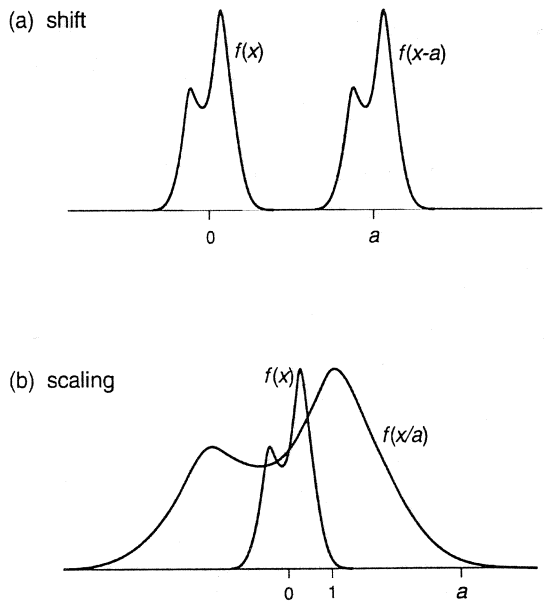

Figure B.1 Relationships (a) between $f(x)$ and $f(x-a)$ and (b) between $f(x)$ and $f(x/a)$.

B.2.3 Scaling

For a positive

$$\int_{-\infty}^{\infty} f(ax)e^{-i2\pi sx}\,dx = \frac{1}{a}\int_{-\infty}^{\infty} f(x')e^{-i2\pi s(x'/a)}\,dx' \qquad (x' = ax)$$

$$= \frac{1}{a}F\left(\frac{s}{a}\right) \tag{B.14}$$

Performing a similar calculation for the case where a is negative, and combining the results we obtain

$$\mathcal{F}\{f(ax)\} = \frac{1}{|a|}F\left(\frac{s}{a}\right) \tag{B.15}$$

This theorem shows that if a function $f(x)$ is scaled by *shrinking* its width by a factor a, its Fourier transform is *expanded* in width by the same factor (while the height is altered by a factor $1/|a|$). It clearly illustrates the reciprocity relationship between $f(x)$ and $F(s)$.

As an example illustrating the use of the scaling theorem (B.15), consider the normalized Gaussian function written as

$$g(x) = \frac{1}{\sqrt{2\pi}\sigma}\exp\left(-\frac{x^2}{2\sigma^2}\right) \tag{B.16}$$

where σ is the standard deviation. To obtain the Fourier transform of (B.16), we start from the Fourier transform pair $\exp(-\pi x^2)$ and $\exp(-\pi s^2)$. Regarding $1/\sqrt{2\pi}\sigma$ as a and using (B.15), we then find that

$$\mathcal{F}\{g(x)\} = \exp(-2\pi^2\sigma^2 s^2) \tag{B.17}$$

B.2.4 Differentiation

The Fourier transform of the derivative of $f(x)$ is equal to $i2\pi sF(s)$. Derivation:

$$\int_{-\infty}^{\infty}\frac{df(x)}{dx}e^{-i2\pi sx}\,dx = \int_{-\infty}^{\infty}\lim_{\Delta x\to 0}\frac{f(x+\Delta x)-f(x)}{\Delta x}e^{-i2\pi sx}\,dx$$

$$= \lim_{\Delta x\to 0}\frac{1}{\Delta x}\left[\int_{-\infty}^{\infty} f(x+\Delta x)e^{-i2\pi sx}\,dx - \int_{-\infty}^{\infty} f(x)e^{-i2\pi sx}\,dx\right]$$

$$= \lim_{\Delta x\to 0}\frac{e^{i2\pi s\Delta x}F(s)-F(s)}{\Delta x}$$

$$= \left[\lim_{\Delta x\to 0}\frac{e^{i2\pi s\Delta x}-1}{\Delta x}\right]F(s)$$

$$= i2\pi sF(s) \tag{B.18}$$

which shows that the definition of convolution is symmetrical with respect to the two functions, so that

$$f(x) * g(x) = g(x) * f(x) \tag{B.22}$$

B.3.2 Convolution Theorem

Consider the Fourier transform of the convolution $f(x) * g(x)$:

$$\begin{aligned}\mathcal{F}\{f(x) * g(x)\} &= \int_{-\infty}^{\infty} \left[\int_{-\infty}^{\infty} f(u)g(x-u)\,du \right] e^{-i2\pi sx}\,dx \\ &= \int_{-\infty}^{\infty} f(u) \left[\int_{-\infty}^{\infty} g(x-u)e^{-i2\pi sx}\,dx \right] du \\ &= \int_{-\infty}^{\infty} f(u)e^{-i2\pi su}\,G(s)\,du \\ &= F(s)G(s)\end{aligned} \tag{B.23}$$

where $G(s)$ is the Fourier transform of $g(x)$. Thus, the Fourier transform of the convolution of two functions is the product of the Fourier transforms of the two individual functions. This is called the *convolution theorem,* which has many applications to scattering and diffraction phenomena as well as to other areas of science. Similarly, it can be shown that the Fourier transform of the product of two functions is equal to the convolution of the Fourier transforms of the individual functions, i.e.,

$$\mathcal{F}\{f(x) \cdot g(x)\} = F(s) * G(s) \tag{B.24}$$

This is sometimes called the *multiplication theorem.*

These two theorems provide a useful means of evaluating or visualizing a convolution operation, since multiplication is usually much simpler than the integration implied in the convolution process. For example, the result given in (B.20) can be obtained more easily by applying the convolution theorem and the multiplication theorem in succession and by recognizing that the Fourier transform of a Gaussian function (B.16) is given by (B.17).

B.3.3 Derivative

The derivative of a convolution is the convolution of either of the functions with the derivative of the other, that is,

$$\frac{d}{dx}[f(x) * g(x)] = f'(x) * g(x) = f(x) * g'(x) \tag{B.25}$$

This can be shown as follows. According to (B.18) and the convolution theorem,

$$\mathcal{F}\left\{ \frac{d}{dx}[f(x) * g(x)] \right\} = i2\pi s[F(s)G(s)]$$

Associating the factor $i2\pi s$ with $F(s)$ we then have

$$\frac{d}{dx}[f(x) * g(x)] = \mathcal{F}^{-1}\{[i2\pi s F(s)]G(s)\} = f'(x) * g(x) \tag{B.26}$$

while associating $i2\pi s$ with $G(s)$ will give the second equality in (B.25).

B.4 DELTA FUNCTION

B.4.1 Definition

Delta function $\delta(x)$ is defined by

$$\delta(x) = \begin{cases} 0 & \text{for } x \neq 0 \\ \infty & \text{for } x = 0 \end{cases} \tag{B.27}$$

and

$$\int_{-\infty}^{\infty} \delta(x)\, dx = 1 \tag{B.28}$$

Thus the delta function is an infinitely narrow and infinitely tall function having the area under the curve equal to unity. It can be considered as the limit of a set of real continuous functions, such as those given by the Gaussian function $g(x)$ in (B.16) in which a successively smaller value is assigned to the standard deviation σ. As σ tends to zero, the properties of $g(x)$ approach those of $\delta(x)$ as defined by Equations (B.27) and (B.28).

B.4.2 Multiplication by $\delta(x)$

If any function $f(x)$ is multiplied by $\delta(x)$, we have

$$f(x)\delta(x) = f(0)\delta(x) \tag{B.29}$$

since the product is zero everywhere except at $x = 0$, and the values of $f(x)$ for $x \neq 0$ are irrelevant in any case. Integration of (B.29) then gives

$$\int_{-\infty}^{\infty} f(x)\delta(x)\, dx = f(0) \tag{B.30}$$

showing that $f(x)\delta(x)$ is a sharply peaked function similar to $\delta(x)$ but its area is equal to $f(0)$ instead of unity. An infinitely narrow spike placed at $x = a$, instead of $x = 0$, can be represented by $\delta(x - a)$. In analogy to (B.29) we can write

$$f(x)\delta(x - a) = f(a)\delta(x - a) \tag{B.31}$$

which, on integration, leads to

$$\int_{-\infty}^{\infty} f(x)\delta(x - a)\, dx = f(a) \tag{B.32}$$

B.4.3 Convolution with $\delta(x)$

By making the change of variables $x \to u$ and $a \to x$ and recognizing that $\delta(x)$ is an even function, Equation (B.32) can be rewritten in the form

$$\int_{-\infty}^{\infty} f(u)\delta(u-x)\,du = \int_{-\infty}^{\infty} f(u)\delta(x-u)\,du = f(x) \tag{B.33}$$

The second equality in (B.33) can be interpreted to mean

$$f(x) * \delta(x) = f(x) \tag{B.34}$$

Convoluting $f(x)$ with a delta function thus leaves the function $f(x)$ unchanged. Such an operation leaving the operand unmodified is called the *identity operation*, as is the case when zero is added to a number or a matrix is multiplied with a unit matrix.

B.4.4 Fourier Transform of $\delta(x)$

By taking the Fourier transforms of both sides of (B.34) and by making use of the convolution theorem, we obtain

$$\mathcal{F}\{f(x)\} \cdot \mathcal{F}\{\delta(x)\} = \mathcal{F}\{f(x)\} \tag{B.35}$$

which shows that the Fourier transform of $\delta(x)$ is equal to unity, that is,

$$\int_{-\infty}^{\infty} \delta(x)e^{-i2\pi sx}\,dx = 1 \tag{B.36}$$

By taking the inverse Fourier transform of (B.36), we then find that

$$\delta(x) = \int_{-\infty}^{\infty} e^{i2\pi sx}\,ds \tag{B.37}$$

which in some textbooks is considered the definition of the delta function. By exchanging the variables x and s, and recognizing the symmetry of the delta function, we can write (B.37) as

$$\delta(s) = \int_{-\infty}^{\infty} e^{-i2\pi sx}\,dx \tag{B.38}$$

which shows that the Fourier transform of unity is the delta function.

B.4.5 Lattice Function $z(x)$

A one-dimensional lattice with a regular spacing a between neighboring lattice points can be written as

$$z(x) = \sum_{n=-\infty}^{\infty} \delta(x-na) \tag{B.39}$$

If $z(x)$ is multiplied by an arbtrary function $f(x)$, the product is given, in view of (B.31), by

$$f(x)z(x) = \sum_{n=-\infty}^{\infty} f(x)\delta(x - na)$$
$$= \sum_{n=-\infty}^{\infty} f(na)\delta(x - na) \tag{B.40}$$

which is still a collection of delta functions located at the lattice sites, but their height (or, more accurately, the area under the peak) is modulated according to $f(x)$.

To obtain the convolution product of $z(x)$ with $f(x)$, we first need to establish the following relationship

$$f(x) * \delta(x - a) = f(x - a) \tag{B.41}$$

which includes (B.34) as a special case. Taking the Fourier transform of the left-hand member of (B.41) and using the convolution theorem, we obtain

$$\mathcal{F}\{f(x) * \delta(x - a)\} = \mathcal{F}\{f(x)\}\mathcal{F}\{\delta(x - a)\}$$
$$= \mathcal{F}\{f(x)\}e^{-i2\pi sa} \tag{B.42}$$

where in the last equality the shift theorem, (B.13) was applied in taking the Fourier transform of $\delta(x)$. On the other hand, taking the Fourier transform of the righ-hand member of (B.41) and applying the shift theorem lead directly to the last member of (B.42), thus proving the relation (B.41). The convolution of $f(x)$ with $z(x)$ is then

$$f(x) * z(x) = \sum_{n=-\infty}^{\infty} f(x) * \delta(x - na)$$
$$= \sum_{n=-\infty}^{\infty} f(x - na) \tag{B.43}$$

If $f(x)$ is narrower than the lattice spacing a, (B.43) represents a repetition of function $f(x)$ at every lattice site.

B.5 THREE-DIMENSIONAL FOURIER TRANSFORM

The three-dimensional Fourier transform can be defined in a manner entirely analogous to (B.1)–(B.4). Thus, if $f(x,y,z)$ is a function of Cartesian coordinates x, y, z in real space, its Fourier transform is defined as

$$F(s_x, s_y, s_z) = \int_{-\infty}^{\infty}\int_{-\infty}^{\infty}\int_{-\infty}^{\infty} f(x, y, z)e^{-i2\pi(s_x x + s_y y + s_z z)}\, dx\, dy\, dz \tag{B.44}$$

where s_x, s_y, s_z are the Cartesian components of vector $\boldsymbol{s}$ in reciprocal space. Expressing the vector with components x, y, z as $\boldsymbol{r}$, we can rewrite (B.44) in the compact form

$$F(\boldsymbol{s}) = \int_V f(\boldsymbol{r})e^{-i2\pi \boldsymbol{s}\cdot\boldsymbol{r}}\, d\boldsymbol{r} \tag{B.45}$$

TABLE B.1
Summary of theorems and properties

Theorem	$f(x)$	$F(s)$
Addition	$f(x) + g(x)$	$F(s) + G(s)$
Scaling	$f(ax)$	$\frac{1}{\lvert a\rvert} F\left(\frac{s}{a}\right)$
Shift	$f(x - a)$	$e^{-i2\pi as} F(s)$
Derivative	$f'(x)$	$i2\pi s F(s)$
Convolution	$f(x) * g(x)$	$F(s)G(s)$
Delta function	$\delta(x)$	1
Convolution with delta function	$f(x) * \delta(x) = f(x)$ $f(x) * \delta(x - a) = f(x - a)$	
Derivative of convolution	$\frac{d}{dx}[f(x) * g(x)] = f'(x) * g(x)$ $= f(x) * g'(x)$	

where $d\boldsymbol{r}$ is the volume element in three-dimensional space ($d\boldsymbol{r} = dx\, dy\, dz$). $\int_V$ denotes that the integration is over the whole available volume in real space, and it is thus a short hand notation for $\int_{-\infty}^{\infty} \int_{-\infty}^{\infty} \int_{-\infty}^{\infty}$.

In the sections above, various properties of Fourier transforms were discussed first with reference to the one-dimensional Fourier transform, which is simpler and easier to understand. With the three-dimensional transform, expressions analogous to those discussed above hold and can be obtained from the one-dimensional versions by exchanging $x \to \boldsymbol{r}$, $s \to \boldsymbol{s}$, and $\int_{-\infty}^{\infty} \to \int_V$, as has been done in obtaining (B.45) from (B.1). An exception to this is that Equation (B.15), expressing the scaling theorem, needs to be modified to read

$$\mathcal{F}\{f(a\boldsymbol{r})\} = \frac{1}{|a|^3} F\left(\frac{\boldsymbol{s}}{a}\right) \tag{B.46}$$

which reflects the fact that a factor $1/|a|$ is associated with each integration with respect to x, y, and z. Similarly, when $\boldsymbol{q}$ instead of $\boldsymbol{s}$ is used as the reciprocal space variable, the three-dimensional version of the inverse Fourier transform (B.4) requires a front factor $1/(2\pi)^3$ in place of $1/(2\pi)$, so that

$$f(\boldsymbol{r}) = \frac{1}{(2\pi)^3} \int F(\boldsymbol{q}) e^{i\boldsymbol{q}\boldsymbol{r}}\, d\boldsymbol{q} \tag{B.47}$$

If $\boldsymbol{r}$ is expressed in spherical polar coordinates in terms of three variables r, Θ, Φ (see Figure B.4a), $d\boldsymbol{r}$ is equal to $r^2 \sin\Theta\, dr\, d\Theta\, d\Phi$, and (B.45) can be written as

$$F(\boldsymbol{s}) = \int_{\Phi=0}^{2\pi} \int_{\Theta=0}^{\pi} \int_{r=0}^{\infty} f(r, \Theta, \Phi) e^{-i2\pi \boldsymbol{s}\cdot\boldsymbol{r}}\, r^2 \sin\Theta\, dr\, d\Theta\, d\Phi \tag{B.48}$$

If $f(\boldsymbol{r})$ is real and depends only on the length of the vector $\boldsymbol{r}$, the function $F(\boldsymbol{s})$ is also a real function of the length of $\boldsymbol{s}$. In such a case the integration with respect to Θ and Φ can be performed without knowledge of $f(r)$. To do this, we choose the polar axis to coincide with the direction of the vector $\boldsymbol{s}$, thereby letting

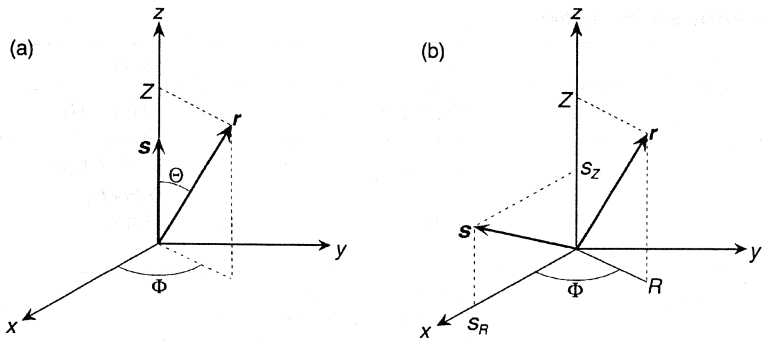

Figure B.4 Diagram (a) defining r, Θ, and Φ in the spherical polar coordinate system and (b) defining R, Θ, and Z in the circular cylindrical coordinate system.

$$\boldsymbol{s} \cdot \boldsymbol{r} = sr \cos\Theta \tag{B.49}$$

With the change of variable $\cos\Theta \rightarrow u$ (B.48) becomes

$$\begin{aligned} F(s) &= \int_{\Theta=0}^{2\pi} \int_{u=-1}^{1} \int_{r=0}^{\infty} f(r) e^{-i2\pi sru} r^2 \, dr \, du \, d\Phi \\ &= 2\pi \int_{r=0}^{\infty} f(r) r^2 \frac{e^{i2\pi sr} - e^{-i2\pi sr}}{i2\pi sr} dr \\ &= 4\pi \int_{0}^{\infty} f(r) r^2 \frac{\sin(2\pi sr)}{2\pi sr} dr \end{aligned} \tag{B.50}$$

The inverse operation of recovering $f(r)$ from $F(s)$ can be written, in view of (B.6) and (B.11), as

$$rf(r) = 2 \int_{0}^{\infty} sF(s) \sin(2\pi sr) \, ds \tag{B.51}$$

If $f(\boldsymbol{r})$ is cylindrically symmetric, it is convenient to adopt the circular cylindrical coordinates (R, Φ, Z) with the Z axis coincident with the symmetry axis and R lying in the plane perpendicular to it (see Figure B.4b). $f(\boldsymbol{r})$ is then a function of R and Z only. The transform $F(\boldsymbol{s})$ is then also a function of two variables, s_R and s_Z, where s_Z is the component of $\boldsymbol{s}$ in the symmetry axis direction and s_R is the component in the direction perpendicular to it. When the x axis direction is chosen so that the vector $\boldsymbol{s}$ is in the XOZ plane, we have

$$\boldsymbol{s} \cdot \boldsymbol{r} = Rs_R \cos\Phi + Zs_Z \tag{B.52}$$

Since $d\boldsymbol{r}$ is equal to $R \, dR \, d\Phi \, dZ$, Equation (B.45) is rewritten as

$$F(s_R, s_Z) = \int_{-\infty}^{\infty} \int_{0}^{2\pi} \int_{0}^{\infty} f(R, Z) e^{-i2\pi(s_R R \cos\Phi + s_Z Z)} \, R \, dR \, d\Phi \, dZ$$

$$= \int_{-\infty}^{\infty} \left[\int_0^{\infty} 2\pi R f(R, Z) J_0(2\pi s_R R) dR \right] e^{-i2\pi s_Z Z} \, dZ \qquad \text{(B.53)}$$

where $J_0(x)$ is the zeroth order Bessel function that is defined, for example, as

$$J_0(x) = \frac{1}{2\pi} \int_0^{2\pi} e^{-ix\cos\Phi} \, d\Phi \qquad \text{(B.54)}$$

FURTHER READING

1. Bracewell, R. N., *The Fourier Transform and Its Applications*, 2nd ed., McGraw-Hill, New York, 1978.
2. Cowley, J. M., *Diffraction Physics*, 3rd ed., Elsevier, Amsterdam, 1995, Chapter 2.

EXERCISES

1. Verify the following relationships where $F(s)$ is the Fourier transform of $f(x)$.

(a) $f(x) = 1 + \delta(x)$; $\quad F(s) = 1 + \delta(s)$

(b) $f(x) = \dfrac{2}{1 + (2\pi x)^2}$; $\quad F(s) = e^{-|s|}$

(c) rectangle

$$f(x) \begin{cases} = 1 & \text{for } |x| < 1/2 \\ = 0 & \text{for } |x| > 1/2 \end{cases}; \qquad F(s) = \frac{\sin \pi s}{\pi s}$$

(d) triangle

$$f(x) \begin{cases} = 1 - |x| & \text{for } |x| < 1 \\ = 0 & \text{for } |x| > 1 \end{cases}; \qquad F(s) = \left(\frac{\sin \pi s}{\pi s} \right)^2$$

(e) $f(x) = \operatorname{sech} \pi x$; $\quad F(s) = \operatorname{sech} \pi s$

(f) $f(x) = \operatorname{sech}^2 \pi x$; $\quad F(s) = 2s \operatorname{cosech} \pi s$

2. Make a plot of the Fourier transform pairs in the preceding problem.

3. Verify the following Fourier transform pairs in three dimensions, where $f(\boldsymbol{r})$ in every case is a function of the length r only.

(a) $f(\boldsymbol{r}) = \left(\dfrac{1}{2\pi\sigma^2} \right)^{3/2} \exp\left(-\dfrac{r^2}{2\sigma^2} \right)$; $\quad F(s) = \exp(-2\pi^2\sigma^2 s^2)$

(b) $f(\boldsymbol{r}) = \dfrac{1}{r} e^{-ar}$; $\quad F(s) = \dfrac{4\pi}{a^2 + (2\pi s)^2}$

(c) solid sphere of radius R

$$f(\boldsymbol{r}) \begin{cases} = 1 & \text{for } r \le R \\ = 0 & \text{for } r > R \end{cases}; \quad F(s) = \frac{4\pi R^3}{3} \frac{3[\sin 2\pi s R - (2\pi s R) \cos 2\pi s R]}{(2\pi s R)^3}$$

(d) spherical shell of inner radius R and outer radius $(R + a)$ $(a \ll R)$

$$f(\boldsymbol{r}) \begin{cases} = 1 & \text{for } R \le r \le (R + a) \\ = 0 & \text{otherwise} \end{cases}; \qquad F(s) = 4\pi R^2 a \frac{\sin 2\pi s R}{2\pi s R}$$

4. Give the sketch of the following two functions, $\Pi(x) \cdot f(x)$ and $\Pi(x) * f(x)$, where $\Pi(x)$ is a "rectangle" function equal to 1 for $|x| < 1/2$ and equal to 0 otherwise and $f(x)$ is equal to $\exp(-x^2)$.

5. Show that among any three functions, $a(x)$, $b(x)$, and $c(x)$, the following relationship holds.

   $[a(x) * b(x)] * c(x) = a(x) * [b(x) * c(x)]$

6. Show that if a is a constant

   $a[f(x) * g(x)] = [af(x)] * g(x) = f(x) * [ag(x)]$

7. Show that

   $$\mathcal{F}\{f(ax - b)\} = \frac{1}{|a|} \exp\left(-i2\pi \frac{b}{a} s\right) F\left(\frac{s}{a}\right)$$

8. Prove that $|F(s)|^2$ is an even function if $f(x)$ is real.

9. Compare the results of the following operations.

   (a) $f(x)\delta(x - a)$

   (b) $f(x - a)\delta(x)$

   (c) $\displaystyle\int_{-\infty}^{\infty} f(x)\delta(x - a)\, dx$

   (d) $\displaystyle\int_{-\infty}^{\infty} f(x - a)\delta(x)\, dx$

   (e) $f(x) * \delta(x - a)$

   (f) $f(x - a) * \delta(x)$

Reciprocal Lattice

Appendix C

C.1 DEFINITION

The concept of the *reciprocal lattice* is very useful in discussing the diffraction of x-rays and neutrons from crystalline materials, especially in conjunction with the Ewald sphere construction discussed in Section 1.5.3. The regular arrangement of atoms and atomic groupings in a crystal can be described in terms of the crystal lattice, which is uniquely specified by giving the three unit cell vectors $\boldsymbol{a}$, $\boldsymbol{b}$, and $\boldsymbol{c}$. It turns out that the diffraction from a crystal is similarly associated with a lattice in reciprocal space. The *reciprocal lattice* is specified by means of the three unit cell vectors $\boldsymbol{a}^*$, $\boldsymbol{b}^*$, and $\boldsymbol{c}^*$ in the same way as the crystal lattice is based on $\boldsymbol{a}$, $\boldsymbol{b}$, and $\boldsymbol{c}$. In fact, the crystal lattice and the reciprocal lattice are related to each other by the Fourier transform relationship.

The basis vectors $\boldsymbol{a}^*$, $\boldsymbol{b}^*$, and $\boldsymbol{c}^*$ of the reciprocal lattice are defined as

$$\boldsymbol{a}^* = \frac{1}{V_u}(\boldsymbol{b} \times \boldsymbol{c}), \qquad \boldsymbol{b}^* = \frac{1}{V_u}(\boldsymbol{c} \times \boldsymbol{a}), \qquad \boldsymbol{c}^* = \frac{1}{V_u}(\boldsymbol{a} \times \boldsymbol{b}) \tag{C.1}$$

where $\times$ denotes the vector product, and V_u is the unit cell volume given by

$$V_u = \boldsymbol{a} \cdot (\boldsymbol{b} \times \boldsymbol{c}) = \boldsymbol{b} \cdot (\boldsymbol{c} \times \boldsymbol{a}) = \boldsymbol{c} \cdot (\boldsymbol{a} \times \boldsymbol{b}) \tag{C.2}$$

By multiplying (C.1) with $\boldsymbol{a}$, $\boldsymbol{b}$, and $\boldsymbol{c}$ in turn, we find

$$\begin{aligned} \boldsymbol{a} \cdot \boldsymbol{a}^* &= 1, & \boldsymbol{a} \cdot \boldsymbol{b}^* &= 0, & \boldsymbol{a} \cdot \boldsymbol{c}^* &= 0 \\ \boldsymbol{b} \cdot \boldsymbol{a}^* &= 0, & \boldsymbol{b} \cdot \boldsymbol{b}^* &= 1, & \boldsymbol{b} \cdot \boldsymbol{c}^* &= 0 \\ \boldsymbol{c} \cdot \boldsymbol{a}^* &= 0, & \boldsymbol{c} \cdot \boldsymbol{b}^* &= 0, & \boldsymbol{c} \cdot \boldsymbol{c}^* &= 1 \end{aligned} \tag{C.3}$$

Figure C.1 illustrates how the reciprocal vector $\boldsymbol{c}^*$ is related to the unit cell vectors $\boldsymbol{a}$, $\boldsymbol{b}$, and $\boldsymbol{c}$. The relationships $\boldsymbol{a} \cdot \boldsymbol{c}^* = 0$ and $\boldsymbol{b} \cdot \boldsymbol{c}^* = 0$ show that the vector $\boldsymbol{c}^*$ is perpendicular to both $\boldsymbol{a}$ and $\boldsymbol{b}$ and hence to the base OACB of the unit cell. The relationship $\boldsymbol{c} \cdot \boldsymbol{c}^* = 1$ means that its length $|\boldsymbol{c}^*|$ is equal to the reciprocal of OP, the projection of $\boldsymbol{c}$ to $\boldsymbol{c}^*$. In the special case in which the directions of $\boldsymbol{c}$ and $\boldsymbol{c}^*$ coincide, i.e., when $\boldsymbol{c}$ is perpendicular to both $\boldsymbol{a}$ and $\boldsymbol{b}$, $|\boldsymbol{c}^*|$ is equal to $1/|\boldsymbol{c}|$. Figure C.2 illustrates the relationship between the crystal and reciprocal lattices, drawn for a monoclinic crystal where $\boldsymbol{b}$ and $\boldsymbol{b}^*$ are normal to the plane of the drawing. Note that

in making such a drawing, the reciprocal Ångstrom can be drawn to any convenient length scale.

C.2 FOURIER TRANSFORM RELATIONSHIP

Given the unit cell vectors $\boldsymbol{a}$, $\boldsymbol{b}$, and $\boldsymbol{c}$, a lattice point in real space can be written as

$$\boldsymbol{r}_{uvw} = u\boldsymbol{a} + v\boldsymbol{b} + w\boldsymbol{c} \tag{C.4}$$

where u, v, and w are integers (positive, negative, or zero). The crystal lattice of a perfect, infinitely large crystal, as a whole, can then be expressed as

$$z(\boldsymbol{r}) = \sum_{u=-\infty}^{\infty} \sum_{v=-\infty}^{\infty} \sum_{w=-\infty}^{\infty} \delta(\boldsymbol{r} - \boldsymbol{r}_{uvw}) \tag{C.5}$$

We now want to evaluate the Fourier transform of $z(\boldsymbol{r})$. Writing the Fourier transform as $Z(\boldsymbol{s})$, we have

$$\begin{aligned} Z(\boldsymbol{s}) &= \int \sum_u \sum_v \sum_w \delta(\boldsymbol{r} - \boldsymbol{r}_{uvw}) e^{-i2\pi \boldsymbol{s}\boldsymbol{r}}\, d\boldsymbol{r} \\ &= \sum_u \sum_v \sum_w \exp(-i2\pi \boldsymbol{s}\boldsymbol{r}_{uvw}) \end{aligned} \tag{C.6}$$

where, in the last equality, the relationship (B.32) has been used. With substitution of (C.4) Equation (C.6) becomes

$$Z(s) = \left(\sum_{u=-\infty}^{\infty} e^{-i2\pi usa} \right) \left(\sum_{v=-\infty}^{\infty} e^{-i2\pi vsb} \right) \left(\sum_{w=-\infty}^{\infty} e^{-i2\pi wsc} \right) \tag{C.7}$$

To see how each of the three infinite sums in Equation (C.7) behaves, we first consider the finite sum extending for u, v, or w from $-N/2$ to $N/2$ (for N even). Thus

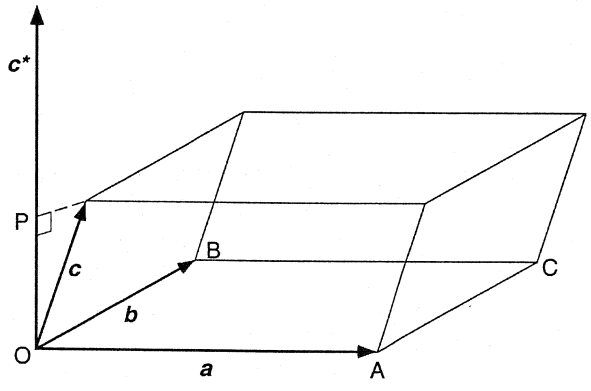

Figure C.1 Reciprocal lattice vector $\boldsymbol{c}^*$ in relation to the unit cell vectors $\boldsymbol{a}$, $\boldsymbol{b}$, and $\boldsymbol{c}$ in real space.

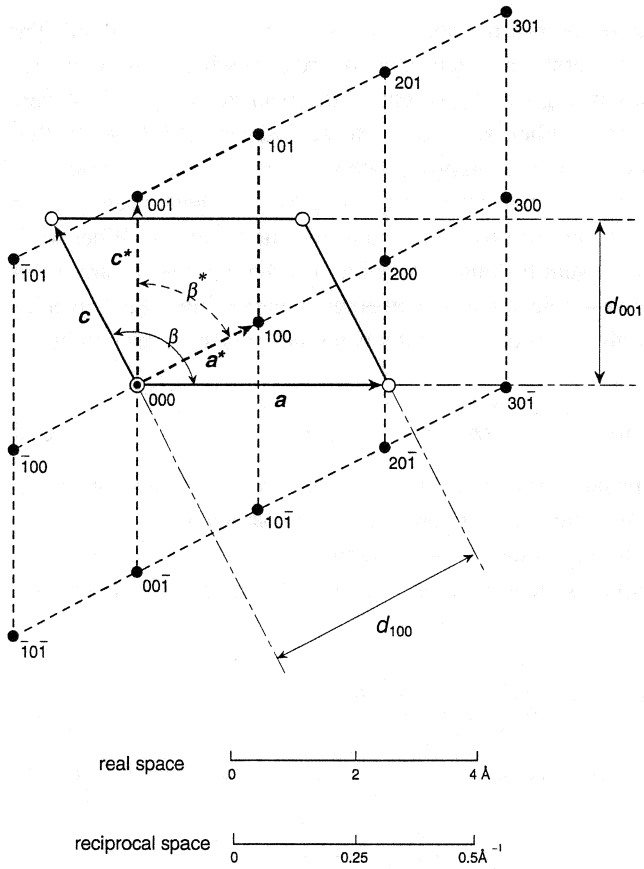

Figure C.2 Diagram showing the relationship between the crystal lattice (open circles connected with solid lines) and the reciprocal lattice (solid circles connected with broken lines). The crystal is assumed monoclinic, so that $\boldsymbol{b}$ and $\boldsymbol{b}^*$ vectors are both normal to the plane of the drawing.

$$\begin{aligned}\sum_{u=-\frac{N}{2}}^{\frac{N}{2}} e^{-i2\pi usa} &= e^{i\pi Nsa}\sum_{u=0}^{N} e^{-i2\pi usa} \\ &= \frac{e^{i\pi(N+1)sa}}{e^{i\pi sa}}\,\frac{1-e^{-i2\pi(N+1)sa}}{1-e^{-i2\pi sa}} \\ &= \frac{e^{i\pi(N+1)sa}-e^{-i\pi(N+1)sa}}{e^{i\pi sa}-e^{-i\pi sa}} \\ &= \frac{\sin[\pi(N+1)sa]}{\sin(\pi sa)} \qquad \text{(C.8)}\end{aligned}$$

Figure C.3 shows the plot of the last member of (C.8) calculated for $N = 40$. The sine functions in both the numerator and denominator are zero when $\boldsymbol{sa}$ is an integer, and the use of l'Hospital's rule gives the height of the peak to be $N + 1$. A zero of the numerator occurs again when $\boldsymbol{sa}$ is equal to an integer $\pm 1/(N + 1)$, thus suggesting that the width of the peak is approximately $1/(N + 1)$. The infinite sums in (C.7) are obtained if we let N tend to infinity in (C.8). The peak present at an integral value of $\boldsymbol{sa}$ then becomes infinitely tall and infinitely narrow. When $\boldsymbol{sa}$ is different from an integer, the sum becomes so rapidly oscillating that for any value of $\boldsymbol{s}$, the only physically observable value is its average, which is zero. $Z(\boldsymbol{s})$ given by (C.7) is therefore zero for all values of $\boldsymbol{s}$, except when $\boldsymbol{s}$ satisfies the three conditions simultaneously

$$\boldsymbol{sa} = h, \qquad \boldsymbol{sb} = k, \qquad \boldsymbol{sc} = l \tag{C.9}$$

where h, k, and l are any positive or negative integers (or zero). This means that $Z(\boldsymbol{s})$ given by (C.7) is an infinite lattice in the reciprocal space spanned by $\boldsymbol{s}$.

This infinite lattice in fact coincides with the reciprocal lattice based on $\boldsymbol{a}^*$, $\boldsymbol{b}^*$, and $\boldsymbol{c}^*$ as defined in the previous section. Mathematically, this statement is equivalent to saying that

$$Z(\boldsymbol{s}) = K \sum_{h=-\infty}^{\infty} \sum_{k=-\infty}^{\infty} \sum_{l=-\infty}^{\infty} \delta(\boldsymbol{s} - \boldsymbol{r}^*_{hkl}) \tag{C.10}$$

where K is a proportionality constant, and $\boldsymbol{r}^*_{hkl}$ representing the reciprocal lattice point is given by

$$\boldsymbol{r}^*_{hkl} = h\boldsymbol{a}^* + k\boldsymbol{b}^* + l\boldsymbol{c}^* \tag{C.11}$$

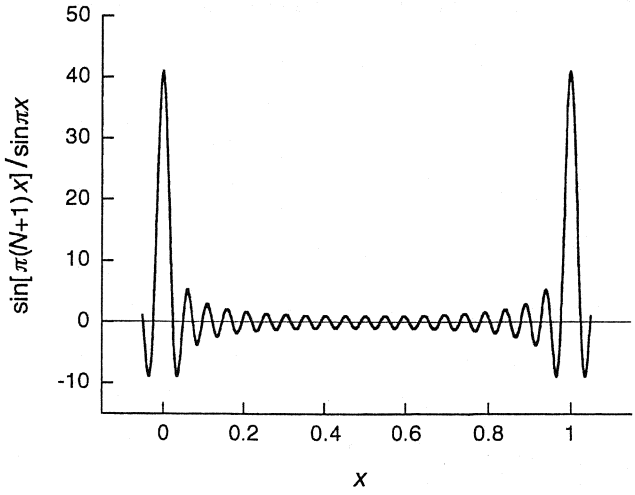

Figure C.3 Plot of $\sin[\pi(N + 1)x]/\sin \pi x$ against x computed for $N = 40$.

h, k, and l being integers. The validity of (C.10) can be proven readily, since, when $\boldsymbol{s}$ is equal to $\boldsymbol{r}^*_{hkl}$ given in (C.11), we have

$$\begin{aligned}(h\boldsymbol{a}^* + k\boldsymbol{b}^* + l\boldsymbol{c}^*)\boldsymbol{a} &= h \\ (h\boldsymbol{a}^* + k\boldsymbol{b}^* + l\boldsymbol{c}^*)\boldsymbol{b} &= k \\ (h\boldsymbol{a}^* + k\boldsymbol{b}^* + l\boldsymbol{c}^*)\boldsymbol{c} &= l\end{aligned} \tag{C.12}$$

showing that the conditions (C.9) are indeed satisfied. The proportionality constant K in Equation (C.10) is equal to $1/V_u$, but we do not reproduce its derivation[1] here since comparing the size of two delta functions, one in real space and the other in reciprocal space, is a rather delicate affair.

C.3 PROPERTIES OF THE RECIPROCAL LATTICE

The important characteristics of the reciprocal lattice that should be noted are (1) that the vector $\boldsymbol{r}^*_{hkl}$ is normal to the crystallographic plane whose Miller indices are (hkl), and (2) that the length $|\boldsymbol{r}^*_{hkl}|$ of the vector is equal to the reciprocal of the interplanar spacing d_{hkl}.

To demonstrate these facts, we select, from the set of parallel (hkl) crystal planes, the particular plane that is next to the one passing through the origin (see Figure C.4). Then, according to the definition of the Miller indices,

$$OH = \frac{\boldsymbol{a}}{h}, \qquad OK = \frac{\boldsymbol{b}}{k}, \qquad OL = \frac{\boldsymbol{c}}{l} \tag{C.13}$$

We prove that $\boldsymbol{r}^*_{hkl}$ is perpendicular to the selected (hkl) plane by showing that two nonparallel vectors lying in it are perpendicular to $\boldsymbol{r}^*_{hkl}$. For this purpose we choose the vectors $\boldsymbol{HK}$ $(= \boldsymbol{OK} - \boldsymbol{OH})$ and $\boldsymbol{HL}$ $(= \boldsymbol{OL} - \boldsymbol{OH})$. Thus we have

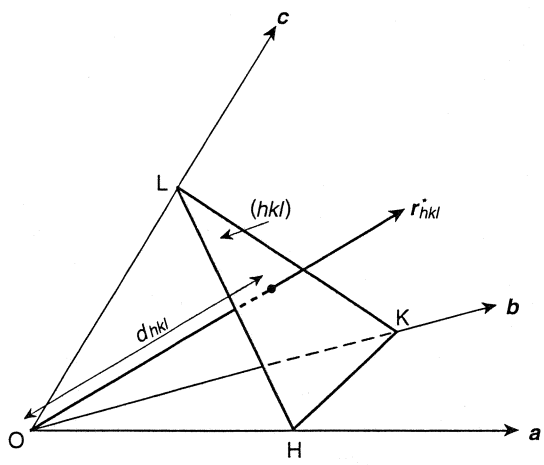

Figure C.4 Relation between the reciprocal lattice vector $\boldsymbol{r}^*_{hkl}$ and the (hkl) plane of the crystal lattice.

$$\begin{aligned} \boldsymbol{r}^*_{hkl} \cdot \boldsymbol{HK} &= (h\boldsymbol{a}^* + k\boldsymbol{b}^* + l\boldsymbol{c}^*) \cdot \left(\frac{\boldsymbol{b}}{k} - \frac{\boldsymbol{a}}{h}\right) \\ \boldsymbol{r}^*_{hkl} \cdot \boldsymbol{HL} &= (h\boldsymbol{a}^* + k\boldsymbol{b}^* + l\boldsymbol{c}^*) \cdot \left(\frac{\boldsymbol{c}}{l} - \frac{\boldsymbol{a}}{h}\right) \end{aligned} \tag{C.14}$$

Using (C.3), we find the above two products to be both zero, thus indicating that $\boldsymbol{r}^*_{hkl}$ is perpendicular to $\boldsymbol{HK}$ and $\boldsymbol{HL}$ and therefore to the plane HKL, which is the (hkl) plane.

Next, to prove that $|\boldsymbol{r}^*_{hkl}|$ is equal to $1/d_{hkl}$, we note that d_{hkl} is given by the dot product of $\boldsymbol{a}/h$ with the unit vector normal to (hkl) and hence parallel to $\boldsymbol{r}^*_{hkl}$. We therefore have

$$\begin{aligned} d_{hkl} &= \frac{\boldsymbol{a}}{h} \cdot \frac{\boldsymbol{r}^*_{hkl}}{|\boldsymbol{r}^*_{hkl}|} \\ &= \frac{1}{|\boldsymbol{r}^*_{hkl}|} \frac{\boldsymbol{a}}{h} (h\boldsymbol{a}^* + k\boldsymbol{b}^* + l\boldsymbol{c}^*) \\ &= \frac{1}{|\boldsymbol{r}^*_{hkl}|} \end{aligned} \tag{C.15}$$

It is left to the reader, as an exercise, to figure out that the unit cell volume of the reciprocal lattice is equal to $1/V_u$.

The fact that the Fourier transform of the crystal lattice is equal (within a proportionality constant) to the reciprocal lattice means that the intensity of diffraction will be observable only when the scattering vector $\boldsymbol{s}$ coincides with one of the reciprocal lattice vectors, that is, only when

$$\boldsymbol{s} = \boldsymbol{r}^*_{hkl} \tag{C.16}$$

By taking the absolute value of (C.16) and recalling that $|\boldsymbol{s}|$ is equal to $2 \sin\theta/\lambda$, we find

$$\frac{2 \sin\theta}{\lambda} = \frac{1}{d_{hkl}} \tag{C.17}$$

which is the familiar *Bragg law.*

C.4 ROTATING-CRYSTAL METHOD AND FIBER DIAGRAM

As an example illustrating the usefulness of the reciprocal lattice concept, we will examine the diffraction pattern that is obtainable by the rotating-crystal method. Suppose that a single crystal is mounted with one of its principal directions, say, the c axis, aligned perpendicular to the incident beam direction. The crystal is then rotated around the c axis, while the diffraction pattern is recorded on a cylindrically shaped film placed around the crystal, with the cylinder axis coinciding with the rotation axis (see Figure C.5). An essentially equivalent arrangement is attained when a semicrystalline polymer that is highly elongated uniaxially is mounted at

the center of a cylindrical film. In a highly stretched polymer the molecular chain axes (which usually coincide with the crystalline c axis) tend to align more or less perfectly in the stretch direction. The random orientation distribution of crystallites maintained around the stretch direction is then equivalent to having the single crystal rotated around its c axis. The diffraction pattern obtained is a fiber diagram, an example of which is shown in Figure 3.3. The Bragg reflection from each hkl crystallographic plane is recorded as a small spot, which is arranged in *layer lines*, the equatorial layer line arising from $hk0$ planes, the first layer line arising from $hk1$ planes, etc.

To see why the diffraction spots are arranged in layer lines, we assume the crystal to be orthorhombic for the sake of simplifying the discussion. As the crystal is rotated, the reciprocal lattice associated with it also rotates about the c axis (which coincides with the c^* axis for the orthorhombic crystal being considered). At the instant when, during the rotation, one of the reciprocal lattice point $\boldsymbol{r}^*_{hkl}$ cuts across the surface of the Ewald sphere at P, the crystal is in the right orientation that satisfies the Bragg condition, and a reflection takes place in the direction given by MP (see Figure C.6). As the crystal continues to rotate, moments later another reciprocal lattice point crosses the Ewald sphere surface, giving rise to another Bragg reflection, and so forth. Those reciprocal lattice points for l equal to, say, 2 cut the Ewald sphere surface on the same horizontal plane through P, and if the axis of the cylindrical film is imagined to be vertical and go through M, it is easy to see that the corresponding diffraction spots must be arranged on the same layer line.

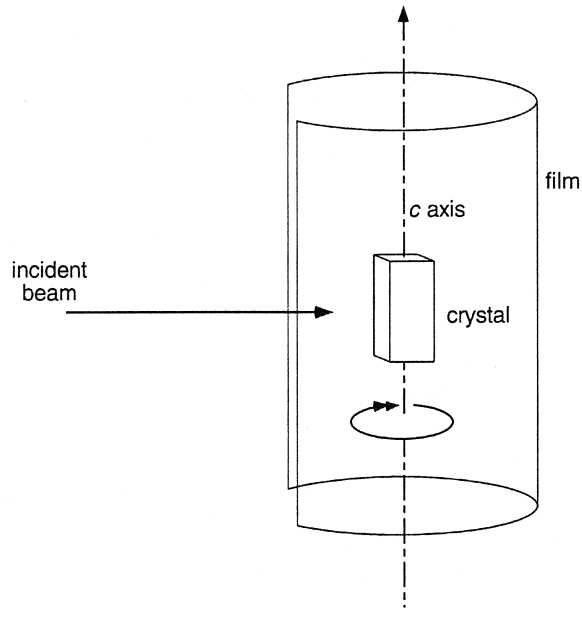

Figure C.5 Schematics of the rotating-crystal method.

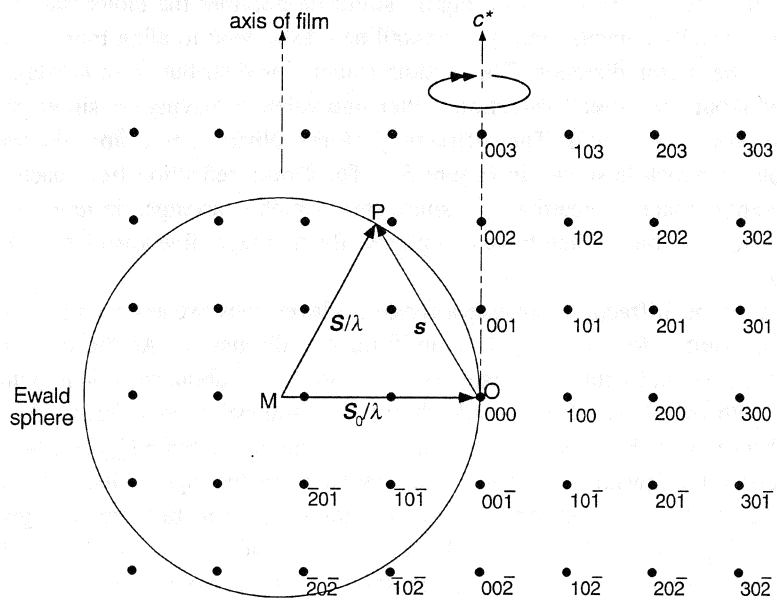

Figure C.6 As the crystal is rotated, the reciprocal lattice also rotates, and when one of the reciprocal lattice points cuts across the Ewald sphere surface, a Bragg reflection takes place.

REFERENCES

1. Guinier, A., *X-ray Diffraction in Crystals, Imperfect Crystals, and Amorphous Bodies*, Freeman, San Fransisco, 1963, p. 86.

EXERCISES

1. Demonstrate graphically in the diagram in Figure C.2 that the reciprocal lattice vectors $\boldsymbol{r}^*_{101}$ and $\boldsymbol{r}^*_{201}$ are indeed perpendicular to the (101) and (201) planes, respectively.

2. Sketch the $h0l$ layer of the reciprocal lattice of a monoclinic crystal having $a = 3.2$ Å, $b = 2.8$ Å, $c = 4.0$ Å, and the angle between a and c axes equal to 60°. Choose a suitable scale constant to show all the reciprocal lattice points up to $h = 4$ and $l = 6$.

3. What is the length of $\boldsymbol{a}^*$ in a cubic crystal with $a = 5$ Å, in a tetragonal crystal with $a = 5$ Å and $c = 10$ Å, and in a hexagonal crystal with $a = 5$ Å and $c = 10$ Å?

4. Given the angles α, β, and γ between the axes of the crystal lattice, derive the expression for the angles α^*, β^*, and γ^* between the axes of the reciprocal lattice.

5. Polyethylene normally forms an orthorhombic crystal with $a = 7.42$ Å, $b = 4.95$ Å, and $c = 2.54$ Å. What are the unit cell parameters a^*, b^*, and c^* of the reciprocal lattice? Calculate the lengths of the reciprocal lattice vectors $\boldsymbol{r}^*_{hkl} = h\boldsymbol{a}^* + k\boldsymbol{b}^* + l\boldsymbol{c}^*$ for all combinations of integral values of h, k, l from 0 to 4. Using the fact that $|\boldsymbol{r}^*_{hkl}|$ is equal to $1/d_{hkl}$ and d_{hkl} is related to the diffraction angle 2θ by the Bragg law (C.17), calculate the diffraction angles corresponding to the above combinations of h, k, l, when λ is 1.54 Å.

6. Show that the unit cell volume of the reciprocal lattice is equal to $1/V_u$, where V_u is the unit cell volume of the real lattice.

7. In the plot of Figure C.3, calculate the full width at half-height of the peak at $x = 0$ by solving the equation $\sin[\pi(N+1)x] / \sin \pi x = (N+1)/2$ for $x_{1/2}$ numerically.

8. Show that the inverse Fourier transform of the function $Z(\boldsymbol{s})$ defined by (C.10) and (C.11) indeed leads to the lattice function $z(\boldsymbol{r})$ given by (C.5), ignoring the exact value of the proportionality constant.

Constants and Conversion Factors

Appendix **D**

CONSTANTS

Avogadro's number, N_A	$6.023 \times 10^{23}\ \text{mol}^{-1}$
electron mass, m	$9.110 \times 10^{-28}\ \text{g}$
neutron mass, m	$1.675 \times 10^{-24}\ \text{g}$
electron charge, e	$1.602 \times 10^{-19}\ \text{C}$
Boltzmann's constant, k	$1.381 \times 10^{-23}\ \text{J/K} = 8.620 \times 10^{-5}\ \text{eV/K}$
Planck's constant, h	$6.626 \times 10^{-34}\ \text{J} \cdot \text{s} = 4.136 \times 10^{-12}\ \text{meV} \cdot \text{s}$
Planck's constant, $\hbar = h/2\pi$	$1.055 \times 10^{-34}\ \text{J} \cdot \text{s} = 6.583 \times 10^{-13}\ \text{meV} \cdot \text{s}$
speed of light in vacuum, c	$2.998 \times 10^{8}\ \text{m/s}$
classical electron radius, r_e	$2.818 \times 10^{-15}\ \text{m}$

CONVERSION FACTORS

$$
\begin{aligned}
1\ \text{J} &= 1\text{N} \cdot \text{m} \\
&= 1\ \text{kg} \cdot \text{m}^2/\text{s}^2 \\
&= 6.242 \times 10^{18}\ \text{eV} \\
&= 0.2389\ \text{cal} \\
1\ \text{meV} &= 1.602 \times 10^{-22}\ \text{J} \\
&= 2.418 \times 10^{11}\ \text{Hz} \\
1\ \text{Å} &= 10^{-10}\ \text{m} \\
1\ \text{barn} &= 10^{-28}\ \text{m}^2
\end{aligned}
$$

Glossary of Symbols

The symbol is followed by the section number in which it is introduced or defined. The number in square brackets refers to the defining equation. The same symbol may be listed more than once if it is used in different meanings in different contexts. Symbols of only a local significance are not listed.

$\boldsymbol{a}, \boldsymbol{b}, \boldsymbol{c}$	crystalline lattice unit cell vectors. C.1
$\boldsymbol{a}^*, \boldsymbol{b}^*, \boldsymbol{c}^*$	reciprocal lattice unit cell vectors. C.1 [C.1]
A	cross-sectional area. 2.5.3, 5.3.2.3
A, $A(\boldsymbol{q})$	amplitude. 1.2.1, 1.5.1
A_2	second virial coefficient. 5.2.5
b	scattering length. 1.2.2, 1.5.1
b_{coh}, b_{inc}	coherent and incoherent scattering length of a nucleus. 1.4
b_{e}	scattering length of an electron. 1.3.1 [1.37], 1.5.1
$\hat{b}$	scattering length of a polymer segment. 6.1.2.1
c	velocity of light.
c	concentration (mass per unit volume). 6.1.1.1
d	interplanar spacing.
d_{hkl}	interplanar spacing for (hkl) crystallographic planes.
d, d_{a}, d_{b}	repeat distance in a periodic system. 5.5.1.1
d	fractal dimension. 5.4.1
d_{s}	surface fractal dimension. 5.4.1
$d\sigma/d\Omega$	differential scattering cross section. 1.2.1 [1.10]
$d^2\sigma/d\Omega\, d\omega$	double differential scattering cross section. 8.1
D	Debye–Waller factor, e^{-2M} or e^{-2W}. 1.7.1 [1.100]
D	diffusion coefficient. 8.2.1
$D(x)$	Debye function. 5.2.3.1 [5.31]
e	electronic charge.

E	energy.
f, $f(s)$	atomic scattering factor. 1.3.3 [1.43]
f	Hermans orientation parameter. 3.6.2.1 [3.75]
f_1, f_2	volume fraction of block 1 and 2 in a diblock copolymer. 6.2
$F(\boldsymbol{q}, t)$	intermediate scattering function. 8.1.1 [8.12]
$F_s(\boldsymbol{q}, t)$, $F_d(\boldsymbol{q}, t)$	self and distinct part of the intermediate scattering function. 8.1.3
$F(\boldsymbol{s})$	structure factor. 1.7
F_{hkl}	structure factor $F(\boldsymbol{s})$ at $\boldsymbol{s} = \boldsymbol{r}^*_{hkl}$. 1.7 [1.98]
$\mathcal{F}\{f(x)\}$	Fourier transform of a function $f(x)$. B.1.1
$\mathcal{F}^{-1}\{F(s)\}$	inverse Fourier transform of a function $F(s)$. B.1.1
$g(r)$	pair correlation function, radial distribution function. 4.1.1 [4.1]
$\hat{g}(r)$	gross pair distribution function. 4.1.1 [4.14]
$g(\boldsymbol{r})$	smoothing function. 5.3.3.2
g_m	free energy density of mixing. 6.1.1.2 [6.13]
G_m	Gibb's free energy of mixing. 6.1.1.2
$G(\boldsymbol{r}, t)$	van Hove correlation function. 8.1.1 [8.14]
$G_s(\boldsymbol{r}, t)$, $G_d(\boldsymbol{r}, t)$	self and distinct part of the van Hove correlation function. 8.1.3
$G(\boldsymbol{s})$	smearing function. 3.4.1
h	Plank's constant
$\hbar$	Plank's constant, $= h/2\pi$. 1.2.2
$H(x)$	Heaviside function. 5.3.3.2, 7.3.2
$i(\boldsymbol{q})$	intensity of scattering per unit volume of the sample. 2.5.3
$i(\boldsymbol{q})$	interference function, reduced intensity function. 4.1.1 [4.6]
$i_{\alpha\beta}(\boldsymbol{q})$	partial interference function. 4.1.2 [4.18]
I, $I(\boldsymbol{q})$	intensity. 1.2.1 [1.75]
$I_{eu}(\boldsymbol{q})$	intensity in electron units. 1.3.2 [1.41]
$I_1(q)$	one-dimensional intensity pattern. 5.5 [5.129]
$\tilde{I}(q)$	slit-smeared intensity. 5.6.1
J, $J(\boldsymbol{q})$	scattered beam flux. 1.2.1
J_0	incident beam flux. 1.2.1
k	Boltzmann's constant.
$\boldsymbol{k}$	wave vector. 1.2.2, 8.1

k	magnitude of wave vector. 8.1
$\boldsymbol{k}_0$	incident beam wave vector. 1.2.2
l_P	Porod's length of inhomogeneity. 5.3.2.2 [5.82]
m	mass (of electron, neutron, or atom).
M	molar mass of a polymer molecule. 5.2.5
n	refractive index. 2.1.2.2, 7.2.1
n	number density of particles. 1.2.2
$\langle n \rangle$	average number density. 4.1.1
$n(\boldsymbol{r})$	local number density at position $\boldsymbol{r}$. 1.2.2
$n_2(\boldsymbol{r})$	number density of atoms at position $\boldsymbol{r}$ when there is an atom at $\boldsymbol{r} = 0$. 4.1.1
N	number of particles, atoms, molecules, etc.
N_v	number of particles in a region of volume v. 4.2
N_A	Avogadro's number.
$p, \boldsymbol{p}$	momentum. 1.1, 8.1
$P(\boldsymbol{q})$	shape factor, form factor. 5.2.5 [6.61]
$P_m^l(x)$	normalized associated Legendre function. 3.6.3
$\boldsymbol{q}$	scattering vector, $= 2\pi \boldsymbol{s}$. 1.2.2 [1.27]
q	magnitude of the scattering vector $\boldsymbol{q}$.
Q	invariant. 1.5.4 [1.85]
r	reflection coefficient. 7.2.2
r_e	classical radius of the electron. 1.3.1
$\boldsymbol{r}$	position vector. 1.2.2
$\boldsymbol{r}^*_{hkl}$	reciprocal lattice vector. C.2 [C.11]
R	reflectivity. 7.2.2
R	radius of a sphere or a circular disk. 5.2.2
R_g	radius of gyration. 5.2.1
$\mathrm{Re}(z)$	real part of a complex quantity z.
$\boldsymbol{s}$	scattering vector. 1.2.2 [1.18]
s	magnitude of the scattering vector.
$\boldsymbol{S}$	unit vector in the direction of a ray. 1.2.2
$\boldsymbol{S}_0$	unit vector in the direction of the incident ray. 1.2.2
S	total interfacial area. 5.3.2.2
$S(\boldsymbol{q})$	structure factor. 6.1.2.1 [6.40]
$S_{\alpha\beta}(\boldsymbol{q})$	partial structure factor. 6.1.2.1 [6.29]
$S(\boldsymbol{q}, \omega)$	dynamic structure factor. 8.11 [8.16]

$S_s(\boldsymbol{q}, \omega)$, $S_d(\boldsymbol{q}, \omega)$	self and distinct part of the dynamic structure factor. 8.1.3
t	time.
t	thickness. 2.5.3
t	transmission coefficient. 7.2.2
$t(\Theta)$, $t(\Theta, \Phi)$	plane-normal orientation distribution. 3.6.1.1
T	absolute temperature.
v	velocity. 1.1
v	volume of a region. 4.2
v	volume of a particle, a molecule, etc. 5.2.1, 6.1.1
v_u	volume of a polymer segment. 6.1.1.3
V	scattering volume. 1.2.2
V_u	unit cell volume. 3.3.1
$w(\alpha, \beta, \gamma)$	crystallite orientation distribution function. 3.6.3
$w(N, r)$	end-to-end distribution of a Gaussian chain. 5.2.1 [5.12]
$W(t)$	slit-length weighting function. 5.6.1
W_q	constant value of $W(t)$ with infinite slit approximation. 5.6.3
$z(\boldsymbol{r})$	mathematical representation of crystalline lattice. 1.7 [1.94]
$Z(\boldsymbol{s})$	lattice factor, Fourier transform of $z(\boldsymbol{r})$. 1.7
$Z_{lmn}(x)$	generalized Legendre function. 3.6.3
Z	atomic number. 1.3.3
Z	number of segment per polymer molecule. 6.1.2.1
β	imaginary component of the refractive index. 7.2.1 [7.3]
β_T	isothermal compressibility
$\gamma(\boldsymbol{r})$	normalized autocorrelation function. 5.3.1 [5.62]
$\Gamma(\boldsymbol{r})$	autocorrelation function. 1.5.2 [1.79]
δ	deviation of the refractive index from unity. 7.2.1 [7.2]
$\delta(x)$	delta function. B.4.1
$\eta(\boldsymbol{r})$	deviation of scattering length density $\rho(\boldsymbol{r})$ from its mean. 1.6 [1.88]
θ	one-half of the scattering angle. 1.2.2
θ_c	critical angle for total reflection. 2.1.2.2, 7.2.2
Θ	polar angle in the spherical polar coordinate system.
λ	wavelength.
μ	linear absorption coefficient. 2.3.1
μ_j	chemical potential of component j. 6.1.1.2

ν	frequency.
ξ	correlation length. 6.1.2.3 [6.50]
Π	osmotic pressure. 6.1.1
$\rho, \rho(\boldsymbol{r})$	scattering length density. 1.5.1 [1.74]
ρ_0	the constant scattering length density within a particle. 5.2.2
$\rho_u(\boldsymbol{r})$	scattering length density distribution in a unit cell. 1.7
$\tilde{\rho}$	mass density. 2.3.1
σ	standard deviation
σ_{tot}	total scattering cross section. 1.2.1 [1.13]
$\sigma_{coh}, \sigma_{inc}$	coherent and incoherent scattering cross section. 1.4
σ_{abs}	absorption cross section. 2.3.1
$\sigma(\boldsymbol{r})$	shape function. 3.4.2
$\Sigma(s)$	Fourier transform of $\sigma(\boldsymbol{r})$. 3.4.2
Σ_{abs}	absorption cross section per unit volume. 2.3.1 [2.7]
Φ	azimuthal angle in the spherical polar coordinate system.
ϕ	phase angle of a wave. 1.2.2
ϕ_1	volume fraction of phase 1. 5.3.2.1
χ	Flory interaction parameter. 6.1.1.3
ω	angular frequency, $= 2\pi\nu$. 8.1
Ω	solid angle. 1.2.1

Index

S

T

U

V

W